Physics of the Solid State, Vol. 45, No. 1, 2003, pp. 1–5. Translated from Fizika Tverdogo Tela, Vol. 45, No. 1, 2003, pp. 3–7.

METALS AND SUPERCONDUCTORS

Annihilation of Positrons in Hydrogen-Saturated Titanium

K. P. Aref'ev*, O. V. Boev*, O. N. Imas*, A. M. Lider*, A. S. Surkov, and I. P. Chernov***

** Tomsk Polytechnical University, Tomsk, 634034 Russia*

*** Fraunhofer Institute of Nondestructive Control Methods, Saarbrücken, D-66123 Germany*

e-mail: kpa@hm.tpu.ru

Received May 4, 2002

Abstract—The effect of atomic hydrogen on the electronic structure of α-titanium samples is studied using the electron–positron annihilation methods. It is shown that different states of hydrogen atoms are manifested in different ways in the positron lifetime distribution spectrum. The results of theoretical calculations of the first component of the positron lifetime are in accord with the obtained experimental data. © *2003 MAIK "Nauka/Interperiodica".*

1. INTRODUCTION

Metals are the most important structural materials. However, hydrogen corrosion of metals can become a hazard. In this respect, commercial operation of equipment used in the oil-and-gas, chemical, and nuclear-power industries, where hydrogen and hydrogenous media constitute a considerable part of the working atmosphere, can be highly dangerous. The change in the physical and mechanical properties of metals and alloys under the action of hydrogen is a serious problem. The materials used usually have to combine resistance to high stresses with an admissible high-temperature strain. However, the effect of hydrogen on their strength parameters is determined to a considerable extent by the chemical composition of the material. For example, the limiting admissible concentration of hydrogen is 0.5 at. % for commercially pure titanium (BT1-0) and 1.0 at. % for the alloy $TiV_{13}Cr_{11}Al_{13}$ [1].

This study is devoted to the effect of atomic hydrogen on the mechanical properties of titanium. Upon the absorption of hydrogen under normal pressure, the crystal lattice of α titanium expands and the ratio *c*/*a* of the hcp-lattice parameters decreases. Hydrogen dissolution in a metal is characterized by a nonuniform distribution of this gas from the surface to the bulk. It is this nonuniform distribution that explains the occurrence of different extents of material degradation at the surface and in the bulk. For example, after electrolytic saturation of titanium samples with hydrogen for 360 min, "traces of damage" can be fixed on the surface in the form of an elevated concentration of dislocations [2]. However, we did not observe destruction of the entire titanium sample in the atomic-hydrogen concentration range up to 11×10^{-5} at. %. We endeavored to establish the mechanisms of variation of the properties of titanium under the action of hydrogen by comparing the calculated electronic structures of ideal and hydrogenated titanium and the experimental data. A unique instrument for solving this problem is the electron–positron annihilation (EPA) method, which directly provides information on the electronic structure of defects in the material under investigation. In this work, the EPA method was used in the diagnostics of the state of titanium articles and structures in contact with hydrogenous media at the stage preceding brittle fracture. We measured the positron lifetime and Doppler broadening of the annihilation γ line (DBAL). The DBAL parameters, the mean positron lifetime, and its different components associated with annihilation of positrons in the region of positron-sensitive defects provide quantitative and qualitative information on the type and concentration of such defects.

Positron annihilation in metal hydrides was studied earlier in [3–5] by analyzing the angular distribution of annihilation photons (ADAP) and the positron lifetime. The lifetime of quasi-free positrons was calculated theoretically only for "complete" hydrides (TiH_2) [6]. The effect of hydrogen on the dynamics of formation of defects (craters and cracks) in titanium BT1-0 was investigated visually in [2] with the help of scanning microscopy and by measuring the mean positron lifetime. In this work, we investigated samples of commercially pure titanium hydrogenated to the composition $TiH_{0.01}$ and calculated the electronic structure, the positron spectrum, and positron characteristics of α-Ti and α-$TiH_{0.125}$, which were then compared with the experimental data obtained by the EPA method.

2. MATERIALS AND EXPERIMENTAL TECHNIQUE

The electronic band structures of pure α-Ti and α-$TiH_{0.125}$ were calculated using the self-consistent method of linearized muffin-tin orbitals in the atomic-sphere approximation (LMTO-ASA) with the Ceper-

1063-7834/03/4501-0001$24.00 © 2003 MAIK "Nauka/Interperiodica"

Table 1. Parameters of the electronic structure of ideal α-Ti: Fermi energy E_F relative to zero crystal energy, width $E_F - \Gamma_1$ of the occupied part of the conduction band, total energy E_{tot}, density of states $N(E_F)$ at the Fermi level, and hcp lattice parameters a and c

Parameter	Simple unit cell (2 atoms/cell)	Large unit cell (8 atoms/cell)	Simple unit cell, APW method [8]*
a, nm	0.2951	0.5902	0.2951
c, nm	0.4684	0.4684	0.4684
E_F, Ry	0.630	0.631	0.5953
$E_F - \Gamma_1$, Ry	0.475	0.474	0.466
E_{tot}, Ry	–15.107	–15.101	
$N(E_F)$, states/Ry	30.37	24.25	16.12

* The augmented plane wave method.

Table 2. Theoretically calculated positron lifetime τ and the positron probability distribution w over atomic spheres s, as well as the corresponding electron charge Q in atomic spheres and the probability ω of positron annihilation with conduction electrons

	α-Ti τ = 158.1 ps	α-$TiH_{0.125}$ τ = 154.5 ps		
	s_{Ti}	s_{Ti}	s_H	s_E
w, %	100	32.25	4.90	62.85
ω, %	100	42.19	5.35	52.46
Q, el./atom	22	20.47	2.48	1.48

ley–Alder exchange-correlation potential [7]. The crystal lattice was simulated by repetitive hexagonal large unit cells with eight titanium atoms (the lattice parameters for titanium are a = 0.2951 nm and c = 0.4684 nm [8]). A hydrogen atom was placed in an octahedral pore with coordinates (1/4; $\sqrt{3}/12$; $c/4$) in the units of the lattice parameter a. The remaining seven octahedral pores were filled with additional empty spheres (E) with zero charge density to include the crystal-potential anisotropy in the model. The self-consistence procedure was carried out over 90 k points in the irreducible part of the Brillouin zone for an hcp unit cell and terminated when the change in the energy eigenvalues did not exceed 0.003 Ry and when the change in pressure calculated from the Pettifor formula [9] on each iteration did not exceed 1 kbar. The quasi-free states of a positron in the crystal were described under the assumption that the effect of the positron on the electron system is negligibly small; positron states were calculated on the basis of the electron density, which was self-consistent in the absence of a positron. The positron potential and the positron wave function obtained in this way were used for calculating the probabilities of positron location in various atomic spheres (including the sphere occupied by a defect such as hydrogen), as well as the annihilation rates and the positron lifetime. The method of calculating positron states is described in detail in [10, 11].

Annihilation parameters of positrons were measured on paired BT1-0 titanium samples (with contents of Fe less than 0.18 at. %, Si less than 0.10 at. %, C less than 0.07 at. %, O less than 0.12 at. %, and N less than 0.04 at. %). A sample of BT1-0 was subjected to preliminary annealing at 750°C in vacuum, followed by slow cooling to 20°C. Paired samples were saturated electrochemically with hydrogen in monomolar electrolyte LiOH (the electrolyte was thermostatically controlled at 20°C) for 20, 60, 120, and 360 min. Immediately after the saturation of a sample with hydrogen, the lifetime and Doppler spectra were measured simultaneously at T = 25°C. An Na^{22} isotope having an activity of the order of 10^6 Bq was placed between two identical parts of the sample under investigation and used as a source of positrons. The radioactive source was $Na^{22}Cl$ salt vapor-deposited on a 20-μm-thick aluminum foil. The instant of position creation was detected by nuclear γ radiation with an energy of 1.28 MeV emitted almost simultaneously with the positron, while the instant of annihilation was determined from the annihilation γ radiation with energy 0.511 MeV; the time resolution of the setup used was 240 ps. The positron lifetime distribution was processed using the standard Resolution program [12]. The DBAL was measured synchronously with the positron lifetime by using a Ge detector with a resolution of 1.2 keV operating on the 0.5-MeV line. The DBAL spectrum was processed with the help of the LIFESPECFIT program [13, 14].

3. DISCUSSION

In the low-hydrogen-concentration simulation of the unit cell of the titanium crystal, an hcp unit cell with a doubled parameter a was used for calculating the electronic structure. In order to unify the approach, the electronic structure of perfect α-Ti was calculated using the same algorithm. The correctness of this approach is confirmed by the closeness of the results obtained with different schemes [calculations with a simple and a large unit cell (two and eight atoms per unit cell, respectively)] in our work and in the literature [8] (Table 1). The electron energy spectrum and the lower positron band for $TiH_{0.125}$ are shown in Fig. 1. The positron band has a parabolic form corresponding to the quasi-free positron state [10]. Table 2 lists the charge distribution, the positron probability distribution over atomic spheres, and the positron annihilation probability in the atomic spheres, as well as the positron lifetime, which will be henceforth associated with the first, short-lived time-distribution component (τ_1 in Table 3) for α-Ti and α-$TiH_{0.125}$. For the given choice of the radii of atomic spheres (the radii of the Ti

and H atomic spheres and empty spheres *E* are identical), the calculations showed that valence electrons of titanium are transferred in large numbers to empty interstitial spheres *E* and to the hydrogen sphere. A positron in a unit cell is distributed over the interstitial region both in pure α-Ti and in hydrogenated Ti. It can be seen from Table 2 that, in the case of interstitial hydrogen, the positron location probability near hydrogen is half the corresponding value in the absence of hydrogen, which can be explained by the expulsion of the positron by the Coulomb field of the hydrogen nucleus to the region of lowest electron density. Calculations of the positron lifetime showed an insignificant decrease in the value of τ upon the introduction of hydrogen into the titanium structure. This fact can be interpreted as follows: (i) in our calculations, we disregarded the lattice expansion due to hydrogenation of the titanium matrix, which occurs in the given case and must cause a certain decrease in the electron density and a corresponding increase in the positron lifetime, and (ii) the electron concentration in the impurity defect (hydrogen) and its electron density (one electron) are small against the background of the electrons in the titanium matrix, which is confirmed by the insignificant variation of the first short-lived component (150–154 ps, Table 3). We also calculated the contributions from the core electrons and valence electrons (90.32% in α-Ti and 90.11% in α-$TiH_{0.125}$) to the EPA. In spite of an insignificant discrepancy in the theoretical, as well as experimental, data, our results confirm that hydrogen is a positron-sensitive defect.

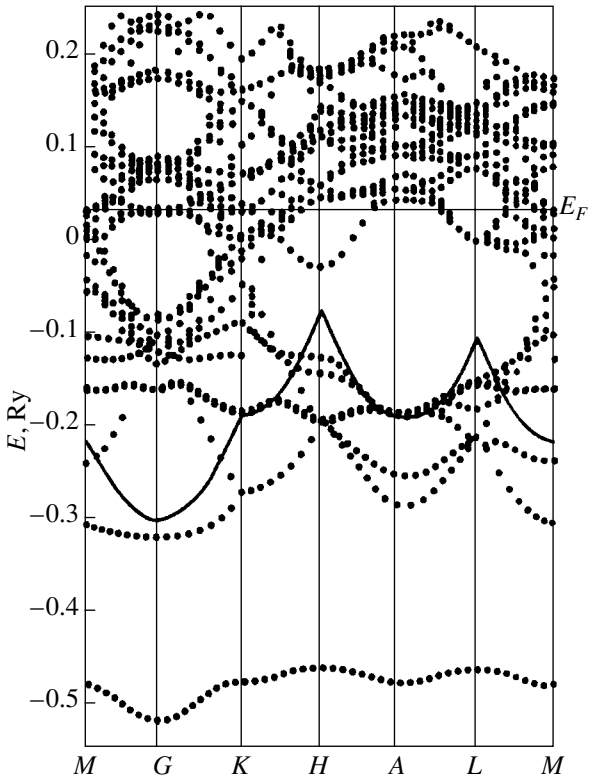

Fig. 1. Electronic energy spectrum (dotted curves) and the lower positron band (solid curve) of α-$TiH_{0.125}$.

Table 3 gives the parameters of experimentally measured positron lifetime components. The first two rows in the table correspond to samples cut from different regions of the same BT1-0 plate. Let us discuss the obtained results. The first component τ_1, associated with the quasi-free positron annihilation, displays stable values in different samples and is in satisfactory agreement with the calculated value of τ (Table 2). The changes in the long-lived component τ_3, associated with positron annihilation in air, may be due to changes in the experimental geometry (different positions of the positron source and the samples). Since the third-component intensity is very low, a change in the value of τ_3 even by 30% can be regarded as insignificant; we will not return to the discussion of τ_3 in our subsequent analysis. More significant changes are observed in the values of τ_2 (due to positron annihilation in the source and in the region of structural vacancies in the sample under investigation) and, accordingly, in the mean positron lifetime τ. These changes are obviously due to differences in the concentration and structure of the initial

Table 3. Experimental values of the three-component decomposition of the positron lifetime distribution and the parameters *S* and *W* of Doppler broadening of the annihilation γ line in α-titanium samples

Treatment	Positron lifetime components, ps			Component intensity, %			Mean lifetime, ps	DBAL parameters, arb. units	
	$\tau_1 \pm 1$	$\tau_2 \pm 10$	τ_3	$I_1 \pm 0.6$	$I_2 \pm 0.6$	$I_3 \pm 0.03$	τ	$W \pm 0.0003$	$S \pm 0.0003$
Without treatment	150	390	1326	96.1	3.7	0.2	163	0.0757	0.4322
	150	369	1419	94.3	5.3	0.3	167	0.0759	0.4332
Hydrogenation for 20 min	152	356	1376	94.4	5.4	0.2	167	0.0748	0.4327
60 min	153	362	1344	94.0	5.7	0.3	170	0.0752	0.4328
120 min	154	321	1015	91.5	8.1	0.3	174	0.0766	0.4337
360 min	154	331	1298	91.7	8.0	0.3	174	0.0746	0.4347

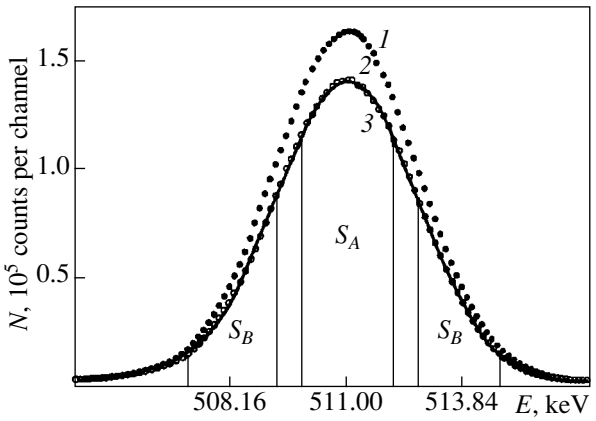

Fig. 2. Doppler broadening of the annihilation γ line for (*1*) pure α-Ti and (*2*, *3*) titanium hydrogenated for 120 and 360 min, respectively.

vacancies and indicate a nonuniform distribution of such defects in the BT1-0 plate.

The saturation times 120 and 360 min of titanium with hydrogen (during which the maximum hydrogen concentration is attained) correspond to the chemical composition $TiH_{0.01}$ in the surface layer and in a layer ~100 μm wide, which are in the sensitivity region of the EPA method. In this case, we also singled out three positron lifetime components which differed from the initial components and were associated with the presence of hydrogen both in the matrix and in the region of titanium vacancies. The small increase in the first component τ_1, along with the decrease in the corresponding values of I_1, shows that no considerable changes in the free-electron density are observed during hydrogenation (nor in calculations). In hydrogenated samples, a decrease in the second component τ_2 and, hence, an increase in its intensity occur, as compared to the initial titanium samples. This result can be explained only by an increase in the contribution from positrons annihilating in the region of structural vacancies filled with hydrogen atoms. In this case, the electron density of a vacancy increases, which must reduce the lifetime of positrons localized in such defects. The increase in the τ_2 component intensity shows that the positron capture by these defects becomes more efficient when there are hydrogen atoms present in them (obviously, due to an increase in their size), which is also manifested in a considerable increase in the mean positron lifetime. This point of view is logically confirmed by the results obtained on the titanium samples with a lower hydrogen concentration: the samples saturated for 60 and 20 min exhibit a smooth decrease in the mean lifetime and in the second-component intensity down to the initial values for nonhydrogenated samples.

Figure 2 shows the DBAL spectrum for the initial and hydrogenated titanium samples. The DBAL spectrum for metals and alloys is usually approximated by a superposition of the parabolic component corresponding to annihilation of positrons with conduction electrons and a Gaussian corresponding to the contribution of core electrons (in analogy with the ADAP curves). This approach was used by us to determine the parameters $S = S_A/S_0$ and $W = S_B/S_0$, where S_0 is the total area under the curve, S_A is the area under the parabolic component, and S_B is the area under the wings of the Gaussian. It can be seen from Fig. 2 that hydrogenation of titanium does not lead to a considerable change in the shape of the DBAL line, which is in accord with the general form of variation of the positron lifetime distribution. However, the parameters of the DBAL spectrum (*S* and *W*) increase upon the introduction of hydrogen into titanium samples (hydrogenation for 120 and 360 min); the integrated value of S_0 in this case corresponds to 5.6052×10^6, 4.8682×10^6, and 4.8358×10^6 pulses for samples without and with hydrogenation for 120 and 360 min, respectively. This increase can be due to the following reasons (as in the case of the observed variations in the positron lifetime distribution). The increase in the parameter *S* is associated with the contribution to positron annihilation from electrons of hydrogen (both dissolved in the titanium matrix and localized in the region of vacancies). The increase in the parameter *W* is associated with a distortion of the positron wave function localized in the region of a vacancy containing hydrogen atoms. Insignificant changes in these parameters indicate the absence of defect clusters and the stability of the α phase of titanium in the bulk of the hydrogenated sample for a concentration of 11×10^{-5} at. % H.

4. CONCLUSIONS

Thus, the theoretical and experimental investigations have revealed the sensitivity of the EPA method to the presence and state of hydrogen atoms in titanium. The presence of hydrogen dissolved in the titanium matrix is manifested in the first, short-lived, positron lifetime component and in the parameter *S* of the DBAL spectrum. Hydrogen localized in titanium vacancies makes a contribution to the second, long-lived component of the positron lifetime distribution and is manifested indirectly in the parameter *W* of the DBAL spectrum.

REFERENCES

1. N. D. Tomashov and R. M. Al'tovskiĭ, *Corrosion and Protection of Titanium* (Moscow, 1963).
2. I. P. Chernov, A. M. Lider, Yu. P. Cherdantsev, *et al.*, Fiz. Mezomekh. **3** (6), 97 (2000).
3. V. I. Savin, R. A. Andrievskiĭ, V. V. Gorbachev, and A. D. Tsiganov, Fiz. Tverd. Tela (Leningrad) **14** (11), 3320 (1972) [Sov. Phys. Solid State **14**, 2815 (1973)].
4. A. D. Tsiganov, R. A. Andrievskiĭ, V. V. Gorbachev, and V. I. Savin, Izv. Akad. Nauk SSSR, Neorg. Mater. **10** (6), 1030 (1974).

5. A. Gainotti, C. Ghezzi, M. Manfredi, and L. Zecchina, Nuovo Cimento B **56** (1), 47 (1968).
6. S. E. Kul'kova, O. N. Muryzhnikova, and K. A. Beketov, Int. J. Hydrogen Energy **21** (11/12), 1041 (1996).
7. D. M. Ceperley and B. J. Alder, Phys. Rev. Lett. **45** (7), 566 (1980).
8. D. A. Papaconstantopoulos, *Handbook of the Band Structure of Elemental Solids* (Plenum, New York, 1986).
9. D. J. Pettifor, Commun. Phys. **1** (5), 151 (1976).
10. E. B. Boronski and R. M. Nieminen, Phys. Rev. B **34**, 3820 (1986).
11. O. V. Boev, M. J. Puska, and R. M. Nieminen, Phys. Rev. B **36** (15), 7786 (1987).
12. P. Kirkegaard, M. Eldrup, O. E. Mogensen, and N. J. Pedersen, Comput. Phys. Commun. **23**, 307 (1981).
13. P. Kirkegaard, N. J. Pedersen, and M. Eldrup, Comput. Phys. Commun. **7**, 401 (1974).
14. R. Unger, *POSIT: Programm zur Erfassung und Auswertung von Positronen-annihilationspektren. Benutzerhandbuch* (Halle, Saale, 1994).

Translated by N. Wadhwa

Physics of the Solid State, Vol. 45, No. 1, 2003, pp. 104–108. Translated from Fizika Tverdogo Tela, Vol. 45, No. 1, 2003, pp. 101–104.

MAGNETISM AND FERROELECTRICITY

Nitrogen-Containing Compounds $R\mathrm{Fe}_{11}\mathrm{TiN}_x$ (R = Gd or Lu)

I. S. Tereshina[1, 2], G. A. Beskorovaĭnaya[2], N. Yu. Pankratov[2, 3], V. V. Zubenko[2], I. V. Telegina[2], V. N. Verbetsky[2], and A. A. Salamova[2]

[1] *Baĭkov Institute of Metallurgy and Materials Technology, Russian Academy of Sciences, Leninskiĭ pr. 49, Moscow, 117119 Russia*

[2] *Moscow State University, Vorob'evy gory, Moscow, 119899 Russia*

[3] *International Laboratory of Strong Magnetic Fields and Low Temperatures, Wroclaw, 53-421 Poland*

Received January 9, 2002

Abstract—The structure and magnetic properties of $R\mathrm{Fe}_{11}\mathrm{TiN}$ compounds (R = Gd or Lu) containing nitrogen are investigated. Magnetic measurements are performed on a magnetometer in magnetic fields up to 100 kOe in the temperature range from 4.2 to 750 K with the use of $R\mathrm{Fe}_{11}\mathrm{TiN}$ single crystals, $R\mathrm{Fe}_{11}\mathrm{TiN}$ powders placed in a ceramic cell, and samples oriented in an external magnetic field. It is found that the nitridation leads to an increase in the Curie temperature and the saturation magnetization. The samples studied are uniaxial over the entire temperature range of magnetic ordering. The magnetic anisotropy decreases upon nitridation. It is demonstrated that, within the local anisotropy model, the decrease in the magnetic anisotropy constant K_1 can be explained by the redistribution of the electron density in the vicinity of the crystallographic positions occupied by iron atoms. © *2003 MAIK "Nauka/Interperiodica".*

1. INTRODUCTION

Nitrogen-containing iron compounds with rare-earth metals (R) of the general formula $R\mathrm{Fe}_{11}\mathrm{TiN}_x$ have a ThMn_{12}-type structure. Owing to their properties, these compounds are promising for use as permanent magnets [1]. The crystal structure of these materials involves two sublattices, namely, a rare-earth metal sublattice and a 3*d* transition metal sublattice. The magnetic properties of the iron sublattice, as a rule, are studied using compounds with nonmagnetic rare-earth metals, such as yttrium and lutecium. Earlier, Yang *et al.* [2] performed a detailed investigation into the magnetic properties of $\mathrm{YFe}_{11}\mathrm{TiN}_x$ (x = 0.1) compounds. The purpose of the present work was to elucidate how nitrogen affects the structure and magnetic properties of $\mathrm{LuFe}_{11}\mathrm{Ti}$ and $\mathrm{GdFe}_{11}\mathrm{Ti}$ compounds. The study of gadolinium-based compounds is of special interest, because a Gd^{3+} ion has no orbital angular momentum; hence, the effect of a crystal field on the rare-earth sublattice can be ignored in investigating the magnetocrystalline anisotropy of this material. Moreover, among the $R\mathrm{Fe}_{11}\mathrm{Ti}$ compounds, the $\mathrm{GdFe}_{11}\mathrm{Ti}$ compound has the highest temperature of transition to a magnetically ordered state (the Curie temperature T_C), whereas the $\mathrm{LuFe}_{11}\mathrm{Ti}$ compound is characterized by the lowest Curie temperature.

Compounds with a ThMn_{12}-type structure have a body-centered tetragonal lattice (space group $I4/mmm$) with a unit cell containing two formula units. As is known, no structures of the ThMn_{12} type are observed in binary iron compounds of the general formula $R\mathrm{Fe}_{12}$. However, the addition of a third component in small amounts leads to the formation of a compound with a stable structure of the formula $R\mathrm{Fe}_{11}T$, where T is a stabilizing element (in our case, Ti). In this structure, iron and titanium atoms occupy the 8*f*, 8*i*, and 8*j* positions, whereas rare-earth metal atoms are located in the 2*a* positions. Nitrogen atoms can be incorporated into the 2*b* positions [3]. As a result, the nitrogen environment involves two rare-earth metal atoms in the adjacent positions and four iron atoms in the 8*j* positions. Such an arrangement of nitrogen atoms should bring about an increase in the unit cell volume, ordering of valence bonds between atoms of the elements entering into the alloy composition, and a substantial change in the magnetic properties. In the present work, this effect of nitrogen on the magnetic properties was investigated over wide ranges of temperatures (from 4.2 K to T_C) and magnetic fields.

2. SAMPLE PREPARATION AND EXPERIMENTAL TECHNIQUE

The experiments were performed with $R\mathrm{Fe}_{11}\mathrm{Ti}$ alloys prepared by rf induction melting in a "Donets-1" apparatus in a special-purity argon atmosphere at the pressure P = 1.1 atm. High-purity iron (99.9%), gadolinium (99.5%), lutecium (99.5%), and titanium (99.9%) served as the initial components. The weights of the metals in the batch did not exceed the calculated values, because the saturation vapor pressure was relatively small at a synthesis temperature of ~1600°C.

Nitrides of the $R\mathrm{Fe}_{11}\mathrm{Ti}$ polycrystalline compounds were synthesized at temperatures ranging from 500 to 600°C and pressures up to 50 atm. The samples were

Structure parameters and magnetic properties of $R\mathrm{Fe}_{11}\mathrm{TiN}_x$ compounds (R = Gd, Lu; x = 0.1) at T = 4.2 K

Compound	a, Å	c, Å	V, Å^3	$\Delta V/V$, %	T_C, K	σ_S, emu/g	$K_1 \times 10^{-7}$, erg/cm^3	$K_2 \times 10^{-7}$, erg/cm^3
$\mathrm{LuFe}_{11}\mathrm{Ti}$	8.53	4.74	345	–	490	138	1.92	–
$\mathrm{LuFe}_{11}\mathrm{TiN}$	8.62	4.77	354	2.8	738	160	1.77	–
$\mathrm{GdFe}_{11}\mathrm{Ti}$	8.54	4.81	351	–	602	99	1.25	0.56
$\mathrm{GdFe}_{11}\mathrm{TiN}$	8.67	4.80	361	2.8	>750	110	0.41	0.40

preliminarily ground, and the size of particles in powdered samples did not exceed 5 μm. This made it possible to prepare samples with a sufficiently homogeneous nitrogen content. The amount of absorbed nitrogen was calculated from the van der Waals equation $p(V - nb) = nRT$, where b = 38.6 cm^3/mol is the van der Waals coefficient, p is the pressure (atm) of nitrogen in the system, $R = 82 \times 10^6$ cm^3 atm./(mol K) is the universal gas constant, V is the nitrogen volume (cm^3), T is the temperature (K), and n is the amount (mol) of nitrogen. The nitrogen content in the nitrides prepared from the initial intermetallic compounds was equal to one nitrogen atom per formula unit.

The structure investigation and quality control of the initial and nitrided samples were performed using x-ray powder diffraction analysis on a DRON-2 diffractometer (CuK_α radiation) with powder samples. It was demonstrated that $R\mathrm{Fe}_{11}\mathrm{TiN}$ nitrides (R = Gd or Lu) retain a ThMn_{12}-type tetragonal structure. The unit cell volume in the nitrided samples was approximately 2.8% larger than that in the initial samples. The samples had a single-phase composition, and the x-ray powder diffraction patterns contain no reflections of the α-Fe phase. The lattice parameters determined for the $\mathrm{GdFe}_{11}\mathrm{TiN}$ compound are in good agreement with the data available in the literature. The presented data for the $\mathrm{LuFe}_{11}\mathrm{TiN}$ compound were obtained for the first time in this work (see table).

The magnetic properties were investigated using single crystals of the initial alloys, nitride powders placed in ceramic cells, and $R\mathrm{Fe}_{11}\mathrm{TiN}$ powder particles oriented in a static magnetic field (~7 kOe). The orientation of powder particles was fixed with the use of epoxy resin. Samples were prepared in the form of spheres, which provided correct inclusion of the demagnetizing factor for these samples. The Curie temperatures T_C of the compounds under investigation were determined using thermomagnetic analysis. The temperature dependences of the magnetization were measured on a pendulum magnetometer in magnetic fields up to 12 kOe in the temperature range 78–750 K. The field dependences of the magnetization were measured using a capacitance magnetometer at the International Laboratory of Strong Magnetic Fields and Low Temperatures (Wroclaw, Poland) in the temperature range from 4.2 to 300 K in magnetic fields up to 100 kOe.

3. RESULTS AND DISCUSSION

It is found that the nitridation leads to a substantial increase in the Curie temperature. For example, the Curie temperature increases from T_C = 490 K for the $\mathrm{LuFe}_{11}\mathrm{Ti}$ initial compound to T_C = 738 K for the $\mathrm{LuFe}_{11}\mathrm{TiN}$ nitride. We failed to measure the Curie temperature T_C for gadolinium nitrides precisely because of the pronounced irreversible decrease in the magnetization in the vicinity of 750 K. Upon cooling, the magnetization did not regain its original value completely. This suggests that, at the above temperature, either interstitial atoms leave the crystal lattice of the $\mathrm{GdFe}_{11}\mathrm{Ti}$ compound or the samples undergo decomposition. The Curie temperature of the $\mathrm{GdFe}_{11}\mathrm{Ti}$ initial compound was determined to be T_C = 602 K. As was noted above, this Curie temperature is highest for all the $R\mathrm{Fe}_{11}\mathrm{Ti}$ compounds but is appreciably lower than the Curie point T_C for pure iron (T_C ~ 1050 K). Such a considerable decrease in the temperature T_C as compared to pure iron can be associated with the antiferromagnetic exchange interaction between individual atoms in the iron sublattice in these compounds. It is known [4] that, in the case when the distance between Fe atoms is less than a critical distance of 2.42 Å, the exchange interaction in Fe–Fe pairs has negative sign. In $R\mathrm{Fe}_{11}\mathrm{Ti}$ compounds, the distance between Fe atoms at the 8j positions is less than the critical distance. The incorporation of nitrogen brings about an expansion of the lattice to such an extent that the distance between Fe atoms becomes larger than the critical value, the exchange interaction in Fe–Fe pairs is enhanced, and, consequently, the temperature T_C increases.

We analyzed the temperature and field dependences of the magnetization for $R\mathrm{Fe}_{11}\mathrm{Ti}$ compounds and their nitrides. Figure 1 displays the temperature dependences of the magnetization for the $\mathrm{GdFe}_{11}\mathrm{Ti}$ and $\mathrm{GdFe}_{11}\mathrm{TiN}$ compounds. For comparison, this figure shows the magnetization curve for the $\mathrm{GdFe}_{11}\mathrm{TiH}$ sample. It can be seen that the nitridation leads to a drastic increase in the magnetization (see table). It can be seen from Fig. 1 that, upon hydrogenation, the magnetization also increases but to a smaller extent. As is known, the unit cell volume increases, on average, by approximately 1% upon hydrogenation and by 3% upon nitridation. Thus, the magnetization changes in the following manner: the larger the unit cell volume, the higher the mag-

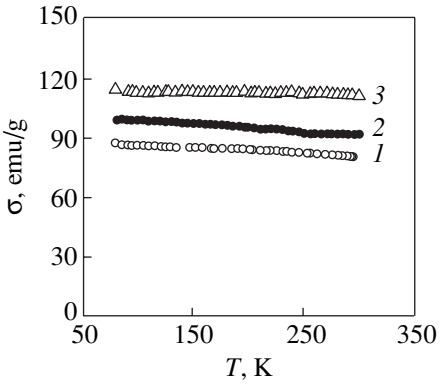

Fig. 1. Temperature dependences of the saturation magnetization for (*1*) $GdFe_{11}Ti$, (*2*) $GdFe_{11}TiH$, and (*3*) $GdFe_{11}TiN$ compounds.

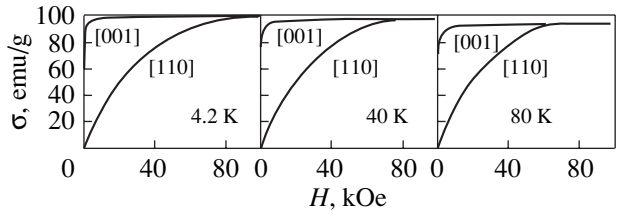

Fig. 2. Magnetization curves for the $GdFe_{11}Ti$ single crystal along the [100] and [110] crystallographic directions at temperatures of 4.2, 40, and 80 K.

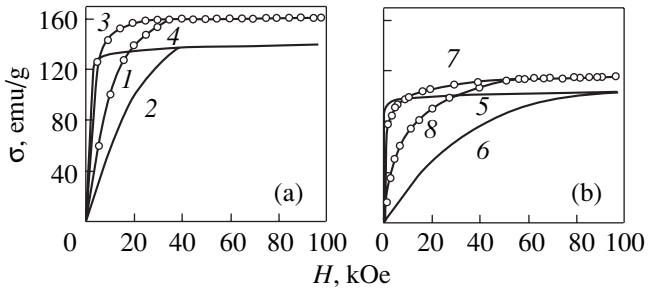

Fig. 3. Field dependences of the magnetization for (a) (*1*, *2*) the $LuFe_{11}Ti$ compound and (*3*, *4*) the $LuFe_{11}TiN$ nitride and (b) (*5*, *6*) the $GdFe_{11}Ti$ compound and (*7*, *8*) the $GdFe_{11}TiN$ nitride along (*1*, *3*, *5*, *7*) the easy magnetization axis and (*2*, *4*, *6*, *8*) the hard magnetization axis at 4.2 K.

netization of the studied compounds. The same is also true for lutecium compounds [5].

Iron atoms in the $ThMn_{12}$ structure are characterized by relatively small magnetic moments. For example, the mean magnetic moment in the $LuFe_{11}Ti$ compound is equal to $1.77\mu_B$ (for pure iron, $\mu_{Fe} = 2.2\mu_B$). The magnetic moments localized on iron atoms occupying the 8*i*, 8*j*, and 8*f* positions are equal to 1.99, 1.76, and $1.51\mu_B$, respectively.

According to Qi *et al.* [6], the nitridation is attended by an increase in the magnetic moments of the atoms located at the 8*i*, 8*j*, and 8*f* positions owing to a narrowing of the 3*d* band upon volume expansion, which, in turn, leads to a total increase in the magnetization observed in the experiments. Therefore, the lattice expansion due to the incorporation of nitrogen atoms into octahedral interstices is the main factor responsible for the increase in the magnetization.

Figure 2 depicts the magnetization curves measured for the $GdFe_{11}Ti$ initial compound along different crystallographic directions in magnetic fields up to 100 kOe at temperatures of 4.2, 40, and 80 K. It can be seen from Fig. 2 that the [001] crystallographic direction coincides with the easy magnetization axis, whereas the [110] direction is the hard magnetization axis. The effective magnetic anisotropy field is determined to be H_0 = 90 kOe at T = 4.2 K, rapidly decreases with an increase in the temperature, and reaches 60 kOe even at T = 80 K. Similar curves for an $LuFe_{11}Ti$ single crystal were obtained in our earlier work [7]. Unlike the R_2Fe_{17} compounds [8], the above compounds do not exhibit an anisotropy of saturation magnetization.

The field dependences of the magnetization measured for the $LuFe_{11}Ti$ and $GdFe_{11}Ti$ compounds and their nitrides along the easy and hard magnetization axes at T = 4.2 K are plotted in Fig. 3. As can be seen from this figure, the nitridation brings about an increase in the saturation magnetization and a decrease in the effective anisotropy field; however, all the crystals under investigation remain uniaxial. It is worth noting that, for yttrium compounds containing molybdenum as a stabilizing element, the nitridation leads to a change in the sign of the magnetic anisotropy constant K_1; in this case, the $YFe_{11}MoN$ compound is characterized by an in-plane anisotropy [9]. At the same time, yttrium compounds with a titanium stabilizing element retain axial anisotropy (the magnetic anisotropy constant K_1 for $YFe_{11}TiN$ decreases [2]). These findings indicate that the stabilizing dopant has a profound effect on the magnetic anisotropy constant K_1. In order to determine the magnetocrystalline anisotropy constants in our case, we used the Sucsmith–Thompson method [10], which involves a special mathematical processing of the magnetization curves measured along the easy and hard magnetization axes. The anisotropy constants for the initial compounds and their nitrides at T = 4.2 K are listed in the table. It follows from the table that, upon nitridation, the magnetic anisotropy constants K_1 decrease for both $LuFe_{11}TiN$ and $GdFe_{11}TiN$ compounds.

One of the known approaches to the interpretation of the magnetocrystalline anisotropy is based on first-principles band calculations. However, it should be

noted that rare-earth compounds are rather complex objects for investigation using standard methods of the band theory. Despite recent advances made in the band theory [11], the anisotropy energy can be determined only to within an order of magnitude and exact calculations present considerable difficulties. For this reason, simple qualitative treatment of the magnetocrystalline anisotropy in terms of the physically clear point-charge model can be used to advantage as before. According to this model, ions in a crystal are affected by a crystal electrostatic field whose potential $V(r)$ is induced by charges of the nearest neighbor ions. Strong uniaxial magnetocrystalline anisotropy of the $R\mathrm{Fe}_{11}\mathrm{Ti}$ initial compounds with nonmagnetic rare-earth elements and gadolinium (the orbital angular momentum of the 4*f* electron shell of gadolinium ions is equal to zero) can be explained by a partial defreezing of the orbital angular momentum L of iron ions in the anisotropic local crystal field, which significantly differs for crystallographically nonequivalent positions occupied by iron atoms (8*i*, 8*j*, and 8*f*). In this case, a small defrozen orbital angular momentum (the component of the orbital angular momentum L) is aligned with the easy magnetization axis and, in turn, orients the total spin angular momentum due to the spin–orbit interaction [12].

The nitridation brings about a decrease in the magnetocrystalline anisotropy of the $\mathrm{LuFe}_{11}\mathrm{TiN}$ and $\mathrm{GdFe}_{11}\mathrm{TiN}$ compounds. This can be associated either with the decrease in the orbital angular momentum L of iron ions or with the change in the local crystal field upon incorporation of nitrogen atoms into their nearest environment. The magnetic anisotropy constant K_1 for the $R\mathrm{Fe}_{11}\mathrm{Ti}$ initial compound can be represented as the sum of three partial constants corresponding to the contributions of the iron ions located at three crystallographically nonequivalent positions (8*i*, 8*j*, and 8*f*) [9]; that is,

$$K_1(T) = K_{1i} + K_{1j} + K_{1f}.$$

Upon introduction of nitrogen atoms into the ThMn_{12} crystal structure, light interstitial atoms are located in the closest proximity to the 8*j* positions and, hence, strongly affect the iron ions occupying these positions. This results in the hybridization of the Fe *d* and N *p* states and the redistribution of the electron density. As was noted earlier in [13], hydrogen and nitrogen atoms in the ThMn_{12} structure occupy the 2*b* positions along the *c* crystallographic axis. These atoms differently modify the electric field gradient at the rare-earth ion site and orient the quadrupole moment (and the related magnetic moment) of the rare-earth ions in the direction parallel or perpendicular to the *c* axis, depending on the Stevens factor α_J of the rare-earth ion.

In our previous work [13], we analyzed in detail how the hydrogenation and nitridation affect the magnetocrystalline anisotropy in $R\mathrm{Fe}_{11}\mathrm{Ti}$ compounds in the case when R is a magnetic rare-earth ion. It seems likely

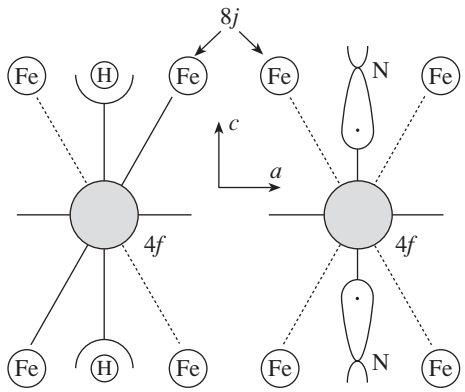

Fig. 4. A schematic diagram illustrating the interaction of the 4*f* electron shell of a rare-earth ion and Fe ions located at the 8*j* positions with interstitial atoms (hydrogen and nitrogen).

that the electric field gradient is also differently modified at the iron ion sites 8*j* (Fig. 4). In Fig. 4, the rare-earth (Gd or Lu) ion with a spherical distribution of the electron density of the 4*f* shell is located at the center. The nearest environment of the rare-earth ion involves iron atoms located at the 8*j* positions. These iron atoms, most probably, have a small, defrozen orbital angular momentum and are located in the immediate vicinity of the H and N interstitial atoms. It is known [14] that, in metals, nitrogen atoms retain 2*p* orbitals that are weakly distorted by the crystal lattice, because the *p* electron is tightly bound to the nitrogen anion. On the other hand, upon hydrogenation, hydrogen atoms reside in electronic states with a low energy to which electrons can readily transfer from the 3*d* band. The hydrogenation and nitridation bring about an increase in the magnetic moment at the 8*j* positions; however, hydrogen and nitrogen have opposite effects on the magnetocrystalline anisotropy. The introduction of hydrogen atoms into the crystal lattice most likely leads to an increase in the partial constant K_{1j} and, consequently, in the total constant K_1 [5]. By contrast, the incorporation of nitrogen atoms into octahedral holes results in a decrease in the constant K_{1j} and, hence, in the total constant K_1 for the $\mathrm{LuFe}_{11}\mathrm{TiN}$ and $\mathrm{GdFe}_{11}\mathrm{TiN}$ compounds.

4. CONCLUSION

Thus, the hydrogenation and nitridation of $R\mathrm{Fe}_{11}\mathrm{Ti}$ compounds (R = Y, Gd, or Lu) have opposite effects on the magnetocrystalline anisotropy. This can be explained by the fact that the electric field gradients at the 8*j* positions occupied by iron ions significantly differ upon incorporation of hydrogen and nitrogen atoms due to the difference in the distributions of the electron density around these atoms.

ACKNOWLEDGMENTS

We would like to thank K.P. Skokov for preparing the samples used in our investigation, Yu.V. Skourski for his assistance in performing the experiments, and S.A. Nikitin for his participation in discussions of the results and helpful remarks.

This work was supported by the State Program of Support for Leading Scientific Schools of the Russian Federation (project no. 00-15-96695) and the Russian Foundation for Basic Research (project nos. 99-02-17821 and 01-02-06490).

REFERENCES

1. S. P. Efimenko, Yu. K. Kovneristyĭ, and I. M. Milyaev, Fiz. Khim. Obrab. Mater., No. 3, 82 (1998).
2. J. Yang, Sh. Dong, W. Mao, *et al.*, Physica B (Amsterdam) **205**, 341 (1995).
3. Y. Yang, X. Zhang, L. Kong, and Q. Pan, Solid State Commun. **78** (4), 313 (1991).
4. I. B. Goodenough, *Magnetism and the Chemical Bond* (Interscience, New York, 1963).
5. I. S. Tereshina, S. A. Nikitin, N. Yu. Pankratov, *et al.*, J. Magn. Magn. Mater. **231**, 213 (2001).
6. Q. Nian Qi, Y. P. Li, and J. M. D. Coey, J. Phys.: Condens. Matter **4** (42), 8209 (1992).
7. S. A. Nikitin, I. S. Tereshina, Yu. V. Skourski, *et al.*, Fiz. Tverd. Tela (St. Petersburg) **43** (2), 279 (2001) [Phys. Solid State **43**, 290 (2001)].
8. S. A. Nikitin, I. S. Tereshina, N. Yu. Pankratov, *et al.*, Fiz. Tverd. Tela (St. Petersburg) **43** (9), 1651 (2001) [Phys. Solid State **43**, 1720 (2001)].
9. E. Tomey, D. Fruchart, and J. L. Soubeyroux, IEEE Trans. Magn. **30** (2), 684 (1994).
10. W. Sucsmith and J. E. Thompson, Proc. R. Soc. London, Ser. A **225**, 362 (1954).
11. S. Buck and M. Fahnle, J. Magn. Magn. Mater. **166** (2), 297 (1997).
12. S. A. Nikitin, I. S. Tereshina, V. N. Verbetsky, and A. A. Salamova, Fiz. Tverd. Tela (St. Petersburg) **40** (2), 285 (1998) [Phys. Solid State **40**, 258 (1998)].
13. S. A. Nikitin, I. S. Tereshina, V. N. Verbetsky, and A. A. Salamova, Metally, No. 1, 86 (2001).
14. V. K. Grigorovich, *Metallic Bonding and Structure of Metals* (Nauka, Moscow, 1988).

Translated by O. Borovik-Romanova

Physics of the Solid State, Vol. 45, No. 1, 2003, pp. 109–117. Translated from Fizika Tverdogo Tela, Vol. 45, No. 1, 2003, pp. 105–112.

MAGNETISM AND FERROELECTRICITY

Domain Structure in an Ultrathin Ferromagnetic Film: Three-Parameter Model

A. L. Sukstanskiĭ and K. I. Primak

Donetsk Physicotechnical Institute, National Academy of Sciences of Ukraine, Donetsk, 83114 Ukraine

e-mail: primak@purr.fti.ac.donetsk.ua

Received January 22, 2002

Abstract—A stripe domain structure (DS) was studied in an ultrathin ferromagnetic film under an in-plane magnetic field. The basic structure parameters (the amplitude and period of the DS, the thickness of domain walls) were determined within a unified variational approach, and transitions from the DS state to a homogeneous canted and a homogeneous planar phase were studied. © *2003 MAIK "Nauka/Interperiodica".*

1. Recently, considerable attention has been given to the properties of ultrathin magnetic films (UTMFs) a few monolayers thick ($\leq 10^{-7}$ cm) [1, 2]. This interest is stimulated by the development of novel UTMF technologies and experimental devices and, on the other hand, by the great potential applications of UTMFs.

Most of the studies of UTMFs are dedicated to their domain structure (DS) [3–6]. The existence of DSs in UTMFs was first predicted in [7, 8] by solving a complete set of micromagnetic (Landau–Lifshitz) equations for the magnetization vector **M** and of the magnetostatics equations for the demagnetization field $\mathbf{H}_m$ (with allowance for the boundary conditions at the film surface). In those works, the so-called critical DS (which arises in the vicinity of a second-order phase transition to a homogeneous magnetic state with the magnetization vector lying in the film plane) was studied and the corresponding phase diagrams were constructed (the critical DS in thick films was considered in [9]). The amplitude of the critical DS (i.e., the maximum value of the magnetization vector component normal to the film surface) was assumed to be a small parameter, which made it possible to find an analytical solution to the micromagnetics equations.

In general, analytical solution of these equations is impossible. Therefore, beginning with the pioneering work of Kittel [10], the DS in magnets has been theoretically studied using the variational approach, within which the character of the magnetization distribution is presupposed. A trial function describing the magnetization distribution in a DS contains unknown parameters (typically, the domain size), whose equilibrium values are found by minimizing the energy of the magnet with respect to these parameters.

A typical example of this approach as applied to an analysis of the DS in an UTMF is the study made in [11], where the simplest trial function corresponding to a uniform magnetization distribution in domains was used, the domain wall thickness Δ was assumed to be infinitesimal, and the domain size D was taken to be a single variational parameter. However, such a trial function ignores the fact that the domain wall thickness in ultrathin films is comparable to the thickness d of the film itself and depends on the film parameters. Moreover, as shown in [7–9], the DS that forms near a transition from a multidomain phase to a phase with a uniform distribution of magnetization (the critical DS) is sinusoidal in character. This structure cannot be approximated by wide domains separated by narrow domain walls; i.e., the concept of domain walls loses its meaning in this case. Therefore, the results of [11] are inapplicable to the critical DS; neglect of the finite thickness of a domain wall results in an incorrect dependence of the domain size D on the film thickness even in a region far from the phase transition [12].

To describe the DS in an UTMF, a more intricate trial function (with two variational parameters m and Δ) was suggested in [12]:

$$M_z(x) = m^{1/2} M_0 \mathrm{sn}\left(\frac{x}{\Delta}\middle| m\right), \qquad (1)$$

where $M_0 = |\mathbf{M}|$ is the saturation magnetization, M_z is the magnetization vector component along the normal to the film plane (axis z), and m is a parameter of the elliptic function (this parameter is equal to the squared modulus of the elliptic integral [13]). The DS period described by this function is $2D = 4\Delta K(m)$, where $K(m)$ is a complete elliptic integral of the first kind. The elliptic sine was chosen as a trial function, because the DS problem in the absence of a magnetic field has an analytical elliptic-sine-like solution if the demagnetizing field is ignored [14]. With such a trial function, the thickness Δ can be varied, which allows one to adequately describe both the critical and a finite-amplitude DS in an UTMF.

However, trial function (1) is inapplicable for the description of a DS in a film subject to an external in-

1063-7834/03/4501-0109$24.00

plane field, since the DS amplitude ($m^{1/2}M_0$) and period $2D$ are unambiguously related, which is not the case in the presence of an in-plane field. This study is dedicated to a generalization of the approach advanced in [12] to the case of the presence of an external in-plane field. We use a trial function for which the DS amplitude and period are not related but are, rather, independent variational parameters. To describe the DS, a trial function with three variational parameters is chosen:

$$M_z(x) = aM_0\mathrm{sn}\left(\frac{x}{\Delta}\middle| m\right). \quad (2)$$

These independent parameters are the DS amplitude aM_0, the domain wall thickness Δ, and the elliptic-function parameter m, which defines the DS period $L = 2D = 4\Delta K(m)$. It is noteworthy that the DS in a uniaxial ferromagnet can be assumed to be one-dimensional only in the case of sufficiently thin films, where the magnetization distribution over the film thickness (along axis Z) can be considered uniform. Furthermore, this description ignores the influence of morphological defects in an actual film (uncoated substrate areas, islands, etc.) and, hence, is inapplicable to the DS in a film that is not additionally processed to upgrade its quality. For example, in annealed films, structural defects are significant only if the film is as thin as a monolayer [6]; therefore, the DS in actual films can be adequately described [12]. An analysis of higher dimensional DSs and DSs closely related to morphological features of films is beyond the scope of this study.

The objective of this work is to determine the equilibrium parameters a, Δ, and m as functions of the parameters characterizing the film (thickness, exchange and anisotropy constants) and of the external magnetic field. Special attention is paid to the problem of the transition from the DS to a uniformly magnetized state. This transition can proceed in two ways: either through the DS amplitude (i.e., a) tending to zero or through the DS period increasing without limit; i.e., $\Delta \longrightarrow \infty$. In the first case, the critical DS with a smooth (sinusoidal) magnetization distribution emerges where, as indicated above, the domain wall concept loses its meaning [7, 8]. The second transition occurs in "thick" films under an external magnetic field perpendicular to the film plane [15]. However, as far as we know, these two types of transitions from the DS to a uniformly magnetized state have not yet been considered within a unified approach. We shall show that these transitions take place depending on the strength of the external in-plane field and on the film parameters.

2. Thus, we consider a ferromagnetic film with uniaxial magnetic anisotropy of the easy-axis type placed in an external in-plane field. We write the film energy as

$$W = \int dV\left\{\frac{\alpha}{2}(\nabla\mathbf{M})^2 - \frac{\beta}{2}M_z^2 - \frac{1}{2}\mathbf{M}\mathbf{H}_m - M_yH_y\right\}, \quad (3)$$

where $\mathbf{M}$ is the magnetization vector; α and β are the exchange and anisotropy constants, respectively; $\mathbf{H}_m$ is the demagnetizing field, which can be determined from the magnetostatics equations; H_y is the field in the film plane (without loss of generality, we assume that $H_y \geq 0$); and the anisotropy axis is normal to the film surface (along the Z axis).

Substituting Eq. (2) into Eq. (3), one arrives at the energy of the magnet (per unit length of the domain wall) as a function of parameters b, m, and u:

$$\begin{aligned} W &= M_0^2 d\sigma(b, m, u), \\ \sigma(b, m, u) &= \frac{\alpha}{d^2}\frac{2bK(m)I_1(b, m)}{u^2} \\ &\quad - \frac{\beta b}{2m}\left(1 - \frac{E(m)}{K(m)}\right) - h_y\frac{I_2(b, m)}{K(m)} \\ &\quad + \frac{4\pi^2 bu}{mK^2(m)}\sum_{n=1}^{\infty}\frac{q^{2n-1}\left[1 - \exp\left(-\frac{2n-\pi}{u}\right)\right]}{(2n-1)(1-q^{2n-1})^2}, \end{aligned} \quad (4)$$

where $b = a^2$, $u = D/d = 2K(m)\Delta/d$, $h_y = H_y/M_0$,

$$I_1 = \int_0^{K(m)}\frac{\mathrm{cn}^2(y|m)\mathrm{dn}^2(y|m)}{1 - b\mathrm{cn}^2(y|m)}dy,$$

$$I_2 = \int_0^{K(m)}\sqrt{1 - b\mathrm{sn}^2(y|m)}dy,$$

$$q = \exp[-\pi K(1-m)/K(m)],$$

and $E(m)$ is a complete elliptic integral of the second kind.

The equilibrium values of the parameters b, m, and u are found from the variational equations

$$\frac{\partial\sigma}{\partial b} = \frac{\partial\sigma}{\partial m} = \frac{\partial\sigma}{\partial u} = 0. \quad (5)$$

As a rule, the domain size D in ultrathin films significantly exceeds the film thickness d. In this case, i.e., as the inequality

$$u \gg 1 \quad (6)$$

is met, the exponential in the expression for the demagnetization energy σ_m [the last term in Eq. (4)] can be expanded into a power series in the small parameter

$u^{-1} \ll 1$. Restricting ourselves to the first two expansion terms, we reduce σ_m to the form

$$\sigma_m = \frac{4\pi^3 b}{mK^2(m)}\left[\Sigma_1(m) + \frac{\pi}{2u}\Sigma_2(m)\right], \quad (7)$$

where

$$\Sigma_1 = \sum_{n=1}^{\infty}\frac{q^{2n-1}}{(1-q^{2n-1})^2}, \quad \Sigma_2 = \sum_{n=1}^{\infty}\frac{(2n-1)q^{2n-1}}{(1-q^{2n-1})^2}.$$

The first sum in Eq. (7) can be calculated exactly, and the energy takes on the form

$$\sigma(b, m, u) = \frac{\alpha}{d^2}\frac{2bK(m)I_1(b, m)}{u^2} - \frac{\beta_* b}{2m}\left(1 - \frac{E(m)}{K(m)}\right) - h_y\frac{I_2(b, m)}{K(m)} - \frac{2\pi^4 b}{muK^2(m)}\Sigma_2(m), \quad (8)$$

where $\beta_* = \beta - 4\pi$.

From the equation $\partial\sigma/\partial u = 0$, one finds an expression for u,

$$u = \frac{\alpha}{d^2}\frac{2mK(m)^3 I_1(b, m)}{\pi^4\Sigma_2}. \quad (9)$$

Upon substituting Eq. (9) into Eq. (8), the energy σ becomes a function of only two parameters, b and m:

$$\sigma(b, m) = \frac{d^2}{\alpha}f_1(b, m) + \beta_* f_2(b, m) + h_y f_3(b, m), \quad (10)$$

where

$$f_1(b, m) = -\frac{\pi^2 b\Sigma_2^2}{2m^2K(m)^5 I_1(b, m)},$$

$$f_2(b, m) = -\frac{b}{2m}\left(1 - \frac{E(m)}{K(m)}\right), \quad (11)$$

$$f_3(b, m) = -\frac{I_2(b, m)}{K(m)}.$$

Both parameters b and m can take on any value within the interval [0, 1]. Their equilibrium values m_* and b_* are found from the variational equations

$$\frac{\partial\sigma}{\partial m} = 0, \quad \frac{\partial\sigma}{\partial b} = 0. \quad (12)$$

Equations (12) can be transformed as

$$\tilde{x}f_1^{(m)} + f_2^{(m)} + \tilde{h}f_3^{(m)} = 0,$$
$$\tilde{x}f_1^{(b)} + f_2^{(b)} + \tilde{h}f_3^{(b)} = 0, \quad (13)$$

where

$$\tilde{x} = \frac{d^2}{\alpha\beta_*}, \quad \tilde{h} = \frac{h_y}{\beta_*}, \quad f_i^{(x)} = \frac{\partial f_i}{\partial x}. \quad (14)$$

Thus, the DS of the film is determined by two dimensionless physical parameters, $\tilde{x}$ and $\tilde{h}$. We note that these parameters can take on both positive (at $\beta_* > 0$) and negative (at $\beta_* < 0$) values depending on the sign of β_*; $\tilde{x}$ and $\tilde{h} \longrightarrow \infty$ as $\beta_* \longrightarrow 0$.

3. First of all, we consider the DS with a small amplitude $b \ll 1$ (studied in [7, 8] within the micromagnetic approach). This DS is referred to as the critical DS (CDS). When studying the CDS, energy (4) can be expanded into a power series in the small parameter b (here, we do not restrict ourselves to the case of $u \gg 1$):

$$\sigma = g(m, u)b + g_1(m, u)b^2. \quad (15)$$

As shown in [7, 8], the CDS is described by a smooth sinusoidal function which corresponds to the limit $m \longrightarrow 0$ [$\mathrm{sn}(x|m) \longrightarrow \sin(x)$] when the DS is described by trial function (2). For this reason, we consider the parameters b and m to be of the same order of smallness and expand the functions $g(m, u)$ and $g_1(m, u)$ in Eq. (15) in a power series in parameter m:

$$g(m, u) = c_0(u)(1 + m/8) + c_1(u)m^2, \quad (16)$$

$$g_1(m, u) = \frac{\alpha\pi^2}{16d^2u^2} + \frac{(6 + m)h_y}{128}, \quad (17)$$

where

$$c_0(u) = \frac{\alpha\pi^2}{4d^2u^2} - \frac{\beta - h_y}{4} + u\left(1 - \exp\left(-\frac{\pi}{u}\right)\right),$$

$$c_1(u) = \frac{3\pi^2\alpha}{128d^2u^2} - \frac{\beta - h_y}{64} + \frac{u}{256}\left\{1 - \exp\left(-\frac{\pi}{u}\right) + \frac{1 - \exp\left(-\frac{3\pi}{u}\right)}{3}\right\}.$$

From variational equations (5) and Eqs. (15)–(17), one finds equations for determining the equilibrium values b and m:

$$b = -\frac{g(m, u)}{2g_1(m, u)}, \quad (18)$$

$$\frac{\partial g}{\partial m} + b\frac{\partial g_1}{\partial m} = 0. \quad (19)$$

Using the fact that b is small near the line of transition to the uniformly magnetized phase, the equilibrium

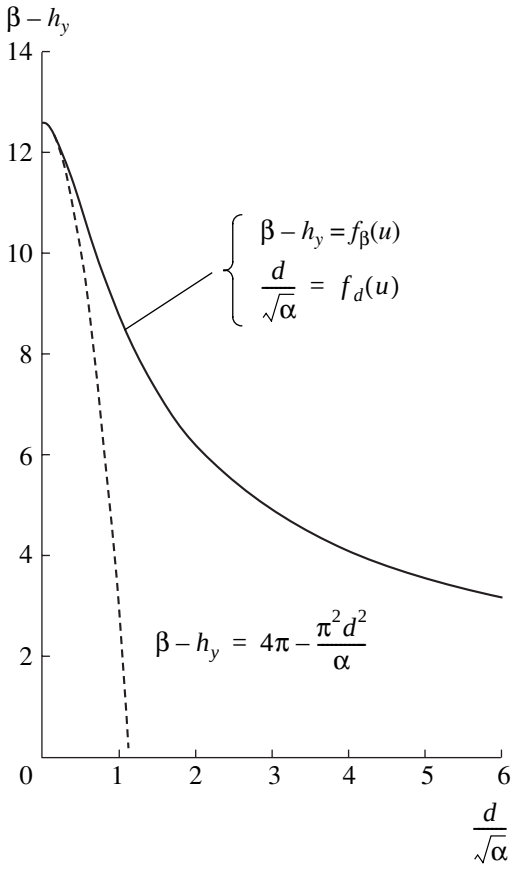

Fig. 1. Dependence of the critical anisotropy (field) on the film thickness. The solid line is the interface between the phase with DS and the homogeneous phase magnetized in the film plane, and the dashed line is the same interface in the $D/d \gg 1$ approximation.

parameters m_* and b_* are found from Eqs. (16) and (19) as functions of parameter u:

$$m_* = m_*(u) = -\frac{c_0(u)}{16c_1(u)}, \tag{20}$$

$$b_* = b_*(u) = -\frac{c_0(u)\left(1-\frac{c_0(u)}{256c_1(u)}\right)}{2g_1(u, m(u))}. \tag{21}$$

Along the transition line itself, we have $b_* = m_* = 0$, from which we find an equation for the value u in this line,

$$c_0(u) = 0. \tag{22}$$

The variational equation $\partial\sigma/\partial u = 0$ in the transition line, i.e., at $b_* = m_* = 0$, takes on the form

$$\frac{\partial c_0(u)}{\partial u} = 0. \tag{23}$$

Equations (22) and (23) define the relation between the field and the parameters of the magnet for which the DS amplitude in the film vanishes. This relation can be written in the parametric form:

$$\begin{aligned} \beta - h_y &= 2\left(3u - (\pi + 3u)\exp\left(-\frac{\pi}{u}\right)\right) \equiv f_\beta(u), \\ \frac{d}{\sqrt{\alpha}} &= \frac{\pi}{u}\left[2\left(u - (\pi + u)\exp\left(-\frac{\pi}{u}\right)\right)\right]^{-1/2} \equiv f_d(u). \end{aligned} \tag{24}$$

In fact, Eqs. (24) parametrically define the curve of the phase transition from the state with DS to a uniformly magnetized phase (solid curve in Fig. 1).

It is readily shown that condition (6) is equivalent to condition $d \ll \alpha^{1/2}$ in the case of the CDS. As this inequality is met, the dependence of the critical value of $\beta - h_y$ on the film thickness d in the phase transition line can be written in an explicit form:

$$\beta - h_y = 4\pi - \frac{\pi^2 d^2}{\alpha}, \tag{25}$$

which is identical to the result obtained in [7] on the basis of the micromagnetic approach (with $\beta - h_y$ in place of β) and the result obtained in [12] within the variational method (the film thickness dependence given by Eq. (25) is shown in Fig. 1).

It is significant that the domain size remains finite in the transition line, i.e., at $b_* = 0$. Let us introduce the dimensionless film thickness $\tilde{d}$ and the dimensionless domain width $\tilde{D}$ defined as

$$\tilde{d} = \frac{d}{(\alpha\beta_*)^{1/2}}, \quad \tilde{D} = D\frac{\beta_*^{1/2}}{\alpha^{1/2}}. \tag{26}$$

Then, if condition (6) is met, the relation between the CDS dimensionless period $\tilde{D}_{cr}$ and the critical dimensionless thickness $\tilde{d}_{cr}$ (i.e., the film thickness at which the transition to a homogeneous phase takes place) has a simple form:

$$\tilde{D}_{cr} = \frac{1}{\tilde{d}_{cr}}. \tag{27}$$

4. Now, we consider the second possible type of the DS transition to the uniformly magnetized phase, i.e., the transition through infinite growth of the structure period. This case corresponds to $m \longrightarrow 1$ [we recall that $K(m) \longrightarrow \infty$ and $D \sim K(m)$ as $m \longrightarrow 1$]. In the limiting case $m \longrightarrow 1$, it is convenient to use the elliptic integral $K(m)$ of the first kind rather than the quantity m as the variational parameter, i.e., to consider the structure energy σ in Eq. (10) as a function of parameters b and K.

Taking into account that $E(m) \sim 1$ and $q(K) \approx \exp(-\pi^2/2K)$, $(1 - m)K \approx 0$ for $m \longrightarrow 1$, as well as the

fact that the sum Σ_2 in the case under consideration can be approximated by the expression (see [12])

$$\Sigma_2(K) \approx \frac{2K^2}{\pi^4}(\ln K + c),$$

where $c \approx 0.7$, we find the functions $f_{1,2,3}(b, K)$ in Eq. (10) to be

$$f_1(b, K) = -\frac{b(\ln K + c)^2}{KI_1(b, 1)}, \quad f_2(b, K) = \frac{1}{2}\left(\frac{1-K}{K}\right),$$

$$f_3(b, K) = -\frac{(1-b)^{1/2}(K + \ln(1-b)^{1/2}) + b^{1/2}\arcsin b^{1/2}}{K},$$

$$I_1(b, 1) = \lim_{m \to 1} I_1(b, m) = \frac{1}{b}\left[1 - \frac{1-b}{b^{1/2}}\ln\left(\frac{1+b^{1/2}}{(1-b)^{1/2}}\right)\right].$$

The equations for the equilibrium values of the parameters b and K,

$$\frac{\partial\sigma(b, K)}{\partial b} = 0, \quad \frac{\partial\sigma(b, K)}{\partial K} = 0,$$

take on the form

$$\frac{\tilde{x}(\ln K + c)^2}{I_1(b, 1)}\left(1 - \frac{\partial(\ln I_1(b, 1))}{\partial(\ln b)}\right) + \frac{1-K}{2} + \frac{\tilde{h}}{2}\left[\frac{K + \ln(1-b)^{1/2}}{(1-b)^{1/2}} - \frac{\arcsin b^{1/2}}{2b^{1/2}}\right] = 0, \tag{28}$$

$$\frac{\tilde{x}b}{I_1(b, 1)}[(\ln K + c)^2 - 2(\ln K + c)] - \frac{b}{2} + \tilde{h}[1/2(1-b)^{1/2}\ln(1-b) + b^{1/2}\arcsin b^{1/2}] = 0. \tag{29}$$

The solution to Eq. (29) meeting the condition $\ln K \gg 1$ is

$$\ln K + c = r(b, \tilde{x}, \tilde{h}) \equiv 1 + \left\{1 + \frac{I_1(b, 1)}{2\tilde{x}} \times \left[1 - \tilde{h}\left(\frac{(1-b)^{1/2}\ln(1-b)}{b} + 2\frac{\arcsin b^{1/2}}{b^{1/2}}\right)\right]\right\}. \tag{30}$$

In the absence of an external field ($\tilde{h} = 0$), Eq. (30) reduces to the corresponding expression for the parameter K derived in [12]:

$$\ln K = 1 - c + \left(1 + \frac{1}{4\tilde{x}}\right)^{1/2}.$$

Analysis shows that the radicand in Eq. (30) is bounded for any value of b and, therefore, the condition $K \longrightarrow \infty$ can be met only for $\tilde{x} \longrightarrow 0$. Hence, the transition to a homogeneous phase through unlimited growth of the domain size can occur only for $\tilde{x} \longrightarrow 0$.

From Eq. (28), we find an expression for the equilibrium value $K = K_*$ as a function of variables b, $\tilde{x}$, and $\tilde{h}$:

$$K_* = \frac{(1-b)^{1/2}}{(1-b)^{1/2} - \tilde{h}}\left[1 - \frac{2\tilde{x}r^2}{I_1(b, 1)}\left(1 - \frac{\partial\ln I_1}{\partial\ln b}\right) - \tilde{h}\left(\frac{\ln(1-b)}{4(1-b)^{1/2}} - \frac{\arcsin b^{1/2}}{2b^{1/2}}\right)\right], \tag{31}$$

where r is defined by Eq. (30). It is evident that in the limit of $\tilde{x} \longrightarrow 0$ and $K \longrightarrow \infty$, the equilibrium amplitude b remains finite and is given by

$$b_* = 1 - \tilde{h}^2. \tag{32}$$

Thus, as in the case of zero field [12], the DS period becomes infinitely large in the limit of infinitesimal film thickness. In this case, in fact, the DS degenerates into a single domain wall, whose equilibrium amplitude b_* is defined by Eq. (32).

5. In Sections 3 and 4, we considered the DS near the boundaries of the domain of its existence. Now, we will study Eqs. (13) for the DS parameters for arbitrary values of parameters m and b [condition (6) is considered to be met; therefore, the parameter u is given by Eq. (9)].

In view of the rather complex structure of the functions $f_{1,2,3}$, it is difficult to solve Eqs. (13) analytically with respect to m and b. For this reason, in order to analyze Eqs. (13), we solve these equations with respect to the parameters $\tilde{x}$ and $\tilde{h}$:

$$\tilde{x}(b, m) = \frac{\Delta_x(b, m)}{\Delta_\infty(b, m)}, \tag{33a}$$

$$\tilde{h}(b, m) = \frac{\Delta_h(b, m)}{\Delta_\infty(b, m)}, \tag{33b}$$

where

$$\Delta_x(b, m) = f_2^{(b)}f_3^{(m)} - f_2^{(m)}f_3^{(b)},$$

$$\Delta_h(b, m) = f_1^{(b)}f_2^{(m)} - f_1^{(m)}f_2^{(b)},$$

$$\Delta_\infty(b, m) = f_3^{(b)}f_1^{(m)} - f_3^{(m)}f_1^{(b)},$$

the functions $f_{1,2,3}$ are defined by formulas (11), and the superscripts (b) and (m) indicate differentiation of these functions with respect to corresponding parameters. The problem to be solved is to determine the equilibrium parameters $m_* = m_*(\tilde{x}, \tilde{h})$ and $b_* = b_*(\tilde{x}, \tilde{h})$, i.e., to determine the functions inverse to $\tilde{x}(b, m)$ and $\tilde{h}(b, m)$ given by Eqs. (33).

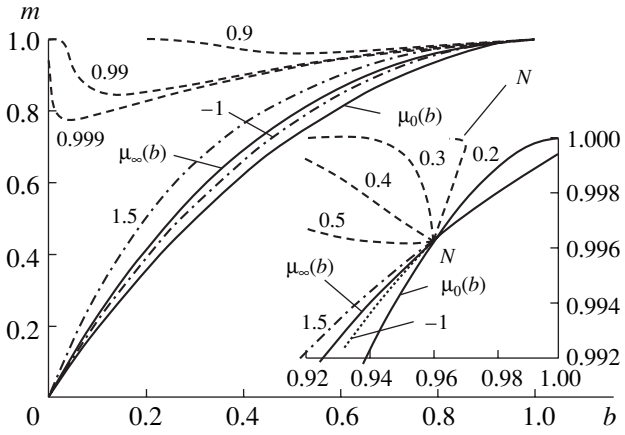

Fig. 2. Equilibrium DS parameters $m_* = \mu_h(b_*)$ at fixed values of the field. Dashed lines correspond to the cases with rather high anisotropy (in comparison with the external and demagnetization fields), and dash-dotted lines represent the typical dependences for films with low anisotropy.

An analysis showed that $\Delta_x(m, b) > 0$ for arbitrary values of m and b belonging to the domain of definition ($0 \le b \le 1$, $0 \le m \le 1$), while the signs of $\Delta_\infty(m, b)$ and $\Delta_h(m, b)$ can be arbitrary. Hence, the sign of function $\tilde{x}(b, m)$ is dictated only by the sign of function $\Delta_\infty(m, b)$, while the sign of $\tilde{h}(b, m)$ is determined by both the signs of $\Delta_\infty(m, b)$ and $\Delta_h(m, b)$. However, as follows from definition (14), the signs of the parameters $\tilde{x}$ and $\tilde{h}$ are controlled by the sign of β_*; these values are positive for $\beta_* > 0$ and negative for $\beta_* < 0$. Hence, only those values of m and b for which the signs of the functions $\tilde{x}(b, m)$ and $\tilde{h}(b, m)$ coincide will have physical meaning in solutions (33):

$$\operatorname{sgn}(\tilde{x}(b, m)) = \operatorname{sgn}(\tilde{h}(b, m)). \quad (34)$$

If the value of $\tilde{x}$ is fixed, then Eq. (33a) will parametrically describe the family of curves $m_* = \mu_x(b_*)$ in the (b, m) plane for equilibrium values m_* and b_*, while Eq. (33b) will give the dependence of the parameter $\tilde{h}$ on the equilibrium parameters m_* and b_*. If, conversely, the value of $\tilde{h}$ is fixed, then Eq. (33b) will parametrically describe the family of curves $m_* = \mu_h(b_*)$ in the (b, m) plane for equilibrium values m_* and b_*, while Eq. (33a) will give the dependence of the parameter $\tilde{x}$ on the equilibrium parameters m_* and b_*.

First, we consider two characteristic curves, $m = \mu_0(b)$ and $m = \mu_\infty(b)$, defined by

$$\Delta_h(m, b) = 0 \quad (35)$$

and

$$\Delta_\infty(m, b) = 0, \quad (36)$$

respectively.

The subscript 0 indicates that the parameter $\tilde{h}$ is zero in the $\mu_0(b)$ curve [according to (33)], and the superscript ∞ indicates that the parameter $\tilde{x}$ diverges in the $\mu_\infty(b)$ curve (as does $\tilde{h}$, except in the intersection points with the $\mu_0(b)$ curve). These two curves cross each other at the origin of coordinates (0, 0), at point (1, 1), and at a point $N(b_N, m_N)$ within the domain of definition of the parameters b and m (we recall that $0 \le b \le 1$, $0 \le m \le 1$), thus partitioning this domain of definition into four regions (see below).

According to Eq. (34), the region in which $\tilde{x}(b, m)$ and $\tilde{h}(b, m)$ have physical meaning is defined by the condition $m \ge \mu_0(b)$. The $\mu_\infty(b)$ curve, in turn, divides this region into two parts, $(m > \mu_\infty(b))$ and $(m < \mu_\infty(b))$, corresponding to domain structures existing at $\beta_* > 0$ and $\beta_* < 0$, respectively.

The equilibrium parameters m_* and b_* are further analyzed for a fixed value of one of the physical parameters $\tilde{h}$ and $\tilde{x}$.

(i) First, we consider the case of fixed $\tilde{h}$. Equation (33b) describes the curve $m_* = \mu_h(b_*)$, where the subscript h indicates that the parameter $\tilde{h}$ is constant along this curve. Figure 2 shows $m_* = \mu_h(b)$ curves constructed using a numerical solution to Eq. (33b) for various fixed values of $\tilde{h}$. Each point in this curve corresponds to equilibrium values m_* and b_* at a value of $\tilde{x}$ which can be calculated by substituting m_* and b_* into Eq. (33a).

The $\mu_h(b_*)$ curves all originate at the point $N(b_N, m_N)$ where the $\mu_0(b)$ and $\mu_\infty(b)$ curves cross each other; as the $\mu_\infty(b)$ curve is approached, the parameter $\tilde{x} \longrightarrow \infty$, since $\Delta_\infty \longrightarrow 0$. Thus, as the point N is approached along a curve corresponding to a fixed value of $\tilde{h}$, the thickness $\tilde{x}$ increases. Therefore, condition (6), defining the applicability of the approximation used, is violated in a certain vicinity of the point N.

The $\mu_h(b_*)$ curves describe the dependence of the DS equilibrium parameters m_* and b_* [as well as u_*, according to Eq. (9)] on $\tilde{x}$ at a fixed value of $\tilde{h}$. The shape of the $\mu_h(b_*)$ curves depends on the value and sign of the parameter $\tilde{h}$. There exist two typical $\mu_h(b_*)$ dependences (see below).

In the case of rather high anisotropy

$$\beta > h_y + 4\pi, \quad (37)$$

which corresponds to $0 < \tilde{h} < 1$, the $\mu_h(b_*)$ curves end at the point $m = 1$, $b = 1 - \tilde{h}^2$. As follows from the analysis of this extreme case performed above, these equi-

librium values of the DS parameters are (formally) achieved at a zero film thickness. This result is in line with the conclusion [7] that in thin films with high anisotropy, the DS exists no matter how small the film thickness. As indicated in Section 4, in the limit of zero film thickness, the DS represents a single domain wall and the extreme value of amplitude (32) is equal to the amplitude of a homogeneous canted phase (see, e.g., [7]). Obviously, the transition into a homogeneous phase in an actual film of finite size takes place at a finite film thickness, when the domain width becomes equal to the film dimensions.

In a film with low anisotropy, $\beta < h_y + 4\pi$ (which corresponds to two ranges of the parameter $\tilde{h}$: $\tilde{h} > 1$ and $\tilde{h} < 0$), the $\mu_h(b_*)$ curves end at the point $m = 0$, $b = 0$. This means that the CDS arises in such films (this extreme case is considered in Section 3 in detail). In this case, the DS transforms into a homogeneous phase with its magnetization vector lying in the film plane ($b = 0$) as the film thickness decreases to a certain critical value d_{cr}; the DS period remains finite ($D \sim K(m) \longrightarrow \pi/2$), and the DS itself becomes sinusoidal.

Using the $\mu_h(b_*)$ dependences, Eq. (9) for u, and Eq. (33) for $\tilde{x}(b_*, m_*)$, we find the parametric dependence of the equilibrium dimensionless period $\tilde{D}$ on the dimensionless film thickness $\tilde{d}$, which is defined, according to formula (27), at a fixed value of field $\tilde{h}$:

$$\tilde{D} = \frac{2\mu_h(b)K^3 I_1(b, \mu_h(b))}{\pi^4 \Sigma_2(\mu_h(b))\sqrt{\tilde{x}(b, \mu_h(b))}}, \qquad (38)$$
$$\tilde{d} = \sqrt{\tilde{x}(b, \mu_h(b))}.$$

The corresponding curves are shown in Fig. 3 for various values of the parameter $\tilde{h}$. One can see that, in the case of high anisotropy, the period $\tilde{D}$ increases infinitely as the thickness $\tilde{d}$ decreases to zero. In the case of low anisotropy, there exists a certain critical thickness d_{cr} at which the DS transforms into a homogeneous phase: the magnetization distribution becomes uniform at thicknesses smaller than d_{cr}. The critical values correspond to the $\tilde{D}_{cr}(\tilde{d}_{cr})$ curve, which is described by simple analytical expression (27) in the case of $u \gg 1$. We note that in the case of $\beta > 4\pi$ ($\beta_* > 0$), the dependence of the DS period on the film thickness can be switched (by varying the field $\tilde{h}$) between the modes corresponding to the cases of high and low anisotropy. This switching should experimentally manifest itself as follows. In a film with high anisotropy, i.e., when inequality (37) is met, the normal magnetization component should exist in films with arbitrarily small (down to monolayers) thicknesses (one should remember that the film morphology can have a significant effect on DS formation in monolayer films). As the field strengthens to the value at which inequality (37) is violated, the magnetization normal component disappears at a certain critical thickness depending on the field according to formula (25).

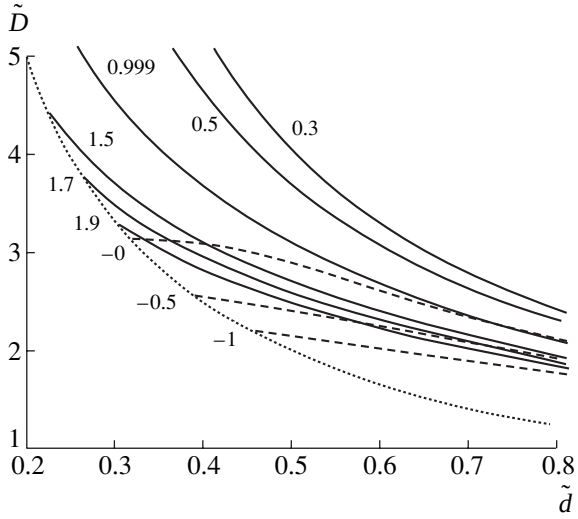

Fig. 3. Dependence of the domain size on the film thickness at fixed values of the field. The line labels indicate the values of the parameter $\tilde{h}$. The dashed line represents the relation between the critical domain size and the critical film thickness.

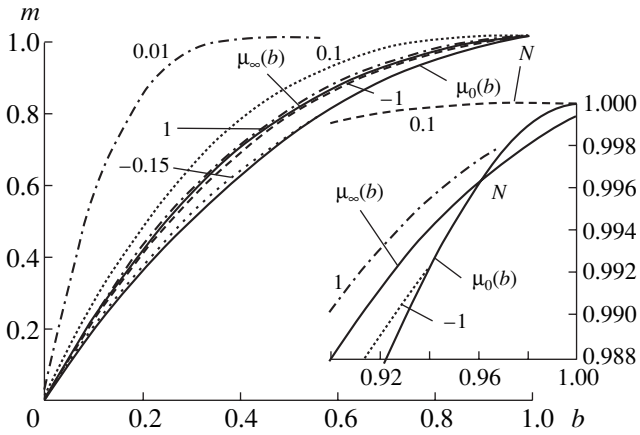

Fig. 4. Equilibrium values of the DS parameters $m_* = \mu_\chi(b_*)$ at fixed values of the film thickness (the values of the parameter $\tilde{x}$ are indicated near the lines).

(ii) Now, we consider solutions to Eqs. (33) at various fixed values of the parameter $\tilde{x}$. Figure 4 displays the $m_* = \mu_\chi(b_*)$ curves constructed by using a numerical solution to Eq. (33a), which parametrically describes these curves at a fixed value of $\tilde{x}$ (the sub-

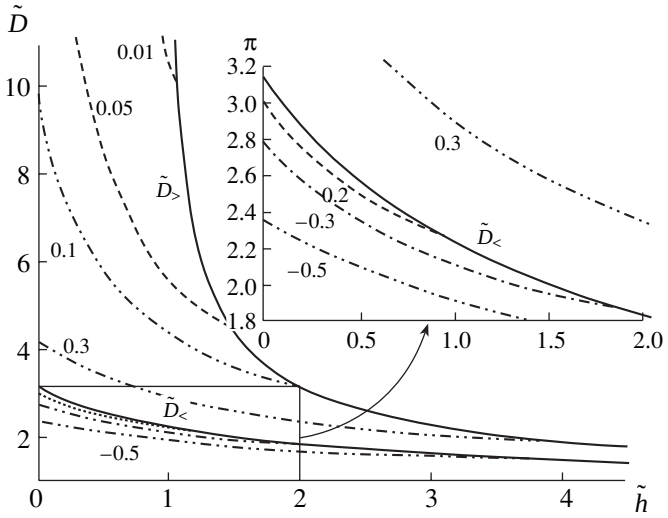

Fig. 5. Dependences of the domain size on the field at fixed values of the film thickness. $\tilde{D}_>$ and $\tilde{D}_<$ are the lines of the transition between the homogeneous phase and the DS under the field in the cases $\beta_* > 0$ and $\beta_* < 0$, respectively.

script x indicates that the parameter $\tilde{x}$ is fixed along the curve). Substituting $\mu_x(b_*)$ into Eq. (33b), we obtain the dependence of the DS parameters on the field $\tilde{h}$ at a fixed value of the thickness $\tilde{x}$. The motion along the $\mu_x(b_*)$ curve corresponds to the variation in the equilibrium values of the DS parameters caused by an $\tilde{h}$ variation at a fixed value of the parameter $\tilde{x}$. The initial points of all the $\mu_x(b_*)$ curves lie in the $\mu_0(b_*)$ curve, which, as was already indicated, corresponds to the equilibrium values of the DS parameters in a zero field and at various values of the film thickness. The increase in the field from zero to the value at which the CDS arises (and the transition to a homogeneous phase takes place) corresponds to motion along the $\mu_x(b_*)$ curve from the point $\mu_0(b_*)$ to point (0, 0).

It is noteworthy that the difference between the $\mu_x(b_*)$ curves and the $\mu_\infty(b_*)$ curve decreases as the parameter $|\tilde{x}|$ increases. However, one should remember that inequality (6), on which the theory presented above is based, is violated in the vicinity of the $\mu_\infty(b_*)$ curve.

In the case of low anisotropy ($\beta_* < 0$), the DS can exist in films for which the relation $|\tilde{x}| > 1/\pi^2$ is valid. Films with smaller values of $|\tilde{x}|$ are in the state with uniform magnetization in the film plane even in a zero field (the formation of a DS in such films can be conditioned by the morphological properties of the film).

Using the $\mu_x(b_*)$ dependences, Eq. (9) for u, and Eq. (33b) for $\tilde{h}(b_*, m_*)$, we find the parametric dependence of the DS dimensionless period $\tilde{D}$ on the normalized field $\tilde{h}$:

$$\tilde{D} = \frac{2\mu_x(b)K^3 I_1(b, \mu_x(b))}{\pi^4 \Sigma_2(\mu_x(b))\tilde{x}^{1/2}}, \qquad (39)$$
$$\tilde{h} = \tilde{h}(b, \mu_x(b)).$$

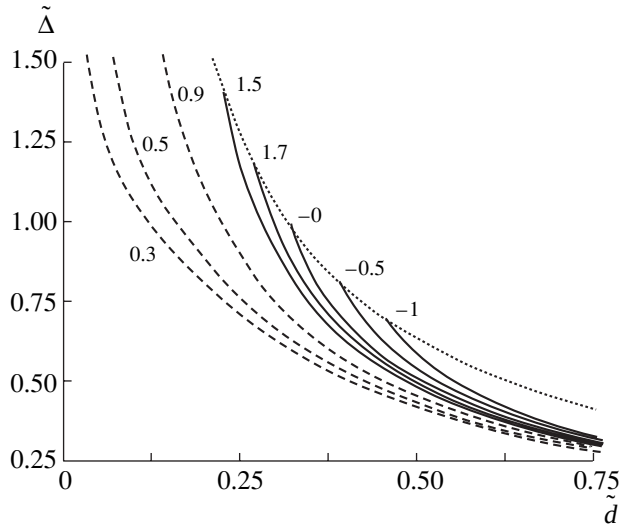

Fig. 6. Dependence of the domain wall thickness on the film thickness at fixed values of the field. The dashed line is the dependence of the domain wall thickness on the film thickness for the critical DS.

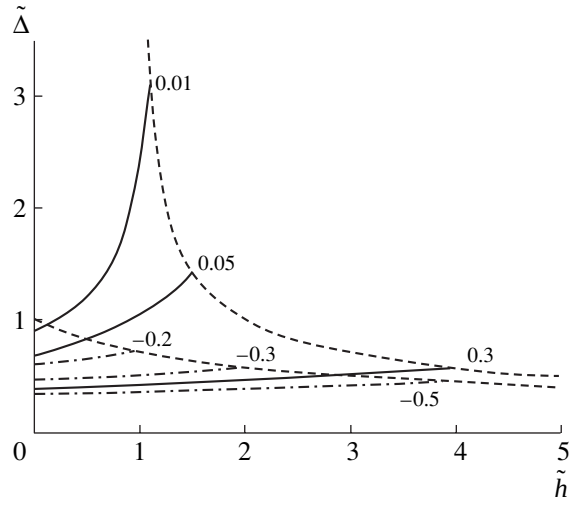

Fig. 7. Dependence of the domain wall thickness on the field at fixed values of the film thickness. Dashed lines are the dependences of the domain wall thickness on the critical field for the critical DS in the cases $\beta_* > 0$ (upper line) and $\beta_* < 0$ (lower line).

Figure 5 shows the $\tilde{D}_x(\tilde{h})$ curves (the subscript x indicates that the parameter $\tilde{x}$ is fixed). As indicated above, these curves originate at $\tilde{h} = 0$ and end at $\tilde{h}_{cr}(x)$, at which point the magnetization vector becomes parallel to the film plane (and the CDS arises). The critical-field dependence of the critical period $\tilde{D}_x(\tilde{h}_{cr})$ can be derived from Eq. (24) (taking into account the condition $u \gg 1$) to be

$$\tilde{D}_{cr} = \pi\left(\tilde{h}_{cr} - \frac{\beta_*}{|\beta_*|}\right)^{-1/2}. \quad (40)$$

These curves are labeled in Fig. 5 by $\tilde{D}_>$ for $\beta_* > 0$ and by $\tilde{D}_<$ for $\beta_* < 0$.

It is noteworthy that, when studying the DS in a uniaxial film, the domain wall thickness is often assumed to be sufficiently small in comparison with the DS period and is neglected. However, the analysis we carried out shows this assumption to be valid only in the case of high anisotropy (37) and small film thickness, i.e., when the condition

$$\frac{D}{\Delta} = 2K(m) \gg 1 \quad (41)$$

is met.

As Fig. 6 shows, the domain wall thickness essentially depends on the film thickness and, even in the case of high anisotropy, increases by a few times with small changes in the film thickness, with condition (41) remaining valid. This means that the domain wall energy does not remain unchanged as the film thickness changes, which should be taken into account in considering the DS.

The field dependence of the domain wall thickness is shown in Fig. 7. One can see that the domain wall thickness is maximum for the CDS. For films with a small thickness, the domain wall thickness increases by a few times as the field changes from 0 to $\tilde{h}_{cr}$.

Thus, by using a trial function with three variational parameters, we have described two probable scenarios of the DS transition to a homogeneous magnetized phase within a unified approach and taken into account the influence of the field on the equilibrium DS parameters.

REFERENCES

1. T. Duden, R. Zdyb, M. Altman, and E. Bauer, Surf. Sci. **480** (3), 145 (2001).
2. W. Kuch, J. Gilles, F. Offi, *et al.*, Surf. Sci. **480** (3), 153 (2001).
3. E. Allenspach, M. Stampanoni, and A. Bishof, Phys. Rev. Lett. **65** (26), 3344 (1990).
4. M. Stampanoni and E. Allenspach, J. Magn. Magn. Mater. **104–107** (3), 1805 (1992).
5. V. Grolier, J. Ferre, A. Maziewski, *et al.*, J. Appl. Phys. **73**, 10 (1993).
6. M. Speckmann, H. P. Oepen, and H. Ibach, Phys. Rev. Lett. **75** (10), 2035 (1995).
7. V. G. Bar'yakhtar and B. A. Ivanov, Zh. Éksp. Teor. Fiz. **72** (4), 1504 (1977) [Sov. Phys. JETP **45**, 789 (1977)].
8. B. A. Ivanov, V. P. Krasnov, and A. D. Sukstanskiĭ, Fiz. Nizk. Temp. **4** (2), 204 (1978) [Sov. J. Low Temp. Phys. **4**, 101 (1978)].
9. V. V. Tarasenko, I. E. Dikshteĭn, and E. V. Chenskiĭ, Zh. Éksp. Teor. Fiz. **70** (6), 2178 (1976) [Sov. Phys. JETP **43**, 1136 (1976)].
10. C. Kittel, Phys. Rev. **70** (11–12), 965 (1946).
11. B. Kaplan and G. A. Gehring, J. Magn. Magn. Mater. **128** (1), 111 (1993).
12. A. L. Sukstanskii and K. I. Primak, J. Magn. Magn. Mater. **169** (1), 31 (1997).
13. *Handbook of Mathematical Functions*, Ed. by M. Abramowitz and I. A. Stegun (National Bureau of Standards, Washington, 1964; Nauka, Moscow, 1979).
14. J. Kaczer, M. Zeleny, and P. Suda, Czech. J. Phys. **13** (4), 579 (1963).
15. K. Kooy and U. Enz, Philips Res. Rep. **15** (1), 7 (1960).

Translated by A. Kazantsev

Physics of the Solid State, Vol. 45, No. 1, 2003, pp. 11–15. Translated from Fizika Tverdogo Tela, Vol. 45, No. 1, 2003, pp. 12–16.

METALS AND SUPERCONDUCTORS

Electron Density Variation at Copper Sites at the Superconducting Transition in Cuprates

N. P. Seregin

Institute of Analytical Instrumentation, Russian Academy of Sciences, Rizhskiĭ pr. 26, St. Petersburg, 198103 Russia

Received March 15, 2002

Abstract—The temperature dependence of the center of gravity S of the Mössbauer spectrum produced by $^{67}Zn^{2+}$ impurity ions occupying copper and yttrium sites in $YBa_2Cu_3O_{6.6}$, $YBa_2Cu_3O_{6.9}$, $YBa_2Cu_4O_8$, $Bi_2Sr_2CaCu_2O_8$, $HgBa_2CuO_4$, and $HgBa_2CaCu_2O_6$ at temperatures above the superconducting transition point T_c was shown to be dominated by the second-order Doppler shift. For $T < T_c$, the quantity S is affected by the band mechanism associated with the formation of Cooper pairs and their Bose condensation. The variation of electron density at a metal site of the crystal was found to be related to the superconducting transition temperature. The variation of electron density created by the Cooper pair Bose condensate in compounds with two structurally inequivalent copper positions was shown to be different for these copper sites. The experimental dependence of the fraction of superconducting electrons on temperature agrees with the analogous dependence following from BCS theory for all the sites studied. © *2003 MAIK "Nauka/Interperiodica".*

1. INTRODUCTION

The electron density distribution over lattice sites is different for the superconducting and normal (metallic) phases, and this difference can be measured using Mössbauer spectroscopy. It was shown in [1] that the conditions for detecting Cooper pairs in cuprates using Mössbauer spectroscopy are most favorable for the ^{67}Zn isotope if one uses the emission variant of spectroscopy with the parent nuclei ^{67}Cu (with the daughter probe $^{67}Zn^{2+}$ sitting at copper sites) or ^{67}Ga (with the daughter probe $^{67}Zn^{2+}$ occupying yttrium or rare-earth metal sites).

We report here on a study of electron density distribution at copper lattice sites of the high-temperature superconductors $YBa_2Cu_3O_{6.9}$ (T_c = 90 K), $YBa_2Cu_3O_{6.6}$ (T_c = 50 K), and $YBa_2Cu_4O_8$ (T_c = 80 K) carried out using Mössbauer emission spectroscopy on the $^{67}Cu(^{67}Zn)$ and $^{67}Ga(^{67}Zn)$ isotopes. In these compounds, the copper atoms occupy two structurally inequivalent positions, Cu(1) and Cu(2), with the corresponding population ratio 1 : 2 (for $YBa_2Cu_3O_{6.9}$ and $YBa_2Cu_3O_{6.6}$) [2] or 1 : 1 (for $YBa_2Cu_4O_8$) [3]. It was assumed that the variation of the electron density at these sites at the transition of the compound to the superconducting state would be different. Also studied for comparison were the compounds $HgBa_2CuO_4$ (T_c = 79 K), $HgBa_2CaCu_2O_6$ (T_c = 93 K), and $Bi_2Sr_2CaCu_2O_8$ (T_c = 80 K), in which copper occupies the only position [4–6].

2. EXPERIMENTAL TECHNIQUE

The Mössbauer sources were prepared by diffusing radioactive ^{67}Cu and ^{67}Ga into polycrystalline samples in evacuated quartz ampules at 450°C for 2 h. The starting samples were synthesized using the techniques described in [4–8]. As reference samples that do not undergo the superconducting transition, we used materials obtained by annealing the starting (superconducting) samples in air at 600°C for 2 h.

The ^{67}Zn Mössbauer spectra were measured using an MS-2201 commercial spectrometer with a modified energy-modulating system. The modulator chosen was a piezoelectric transducer based on PZT ceramics. The maximum scan velocity was ±150 μm/s. The spectrometer was calibrated against the ^{67}Zn spectrum with a ^{67}Cu source. The gamma quanta were detected with a Ge(Li) semiconductor detector sensitized in the 100-keV region. The Mössbauer spectra were taken with a ^{67}ZnS absorber. The sample and the absorber were cooled in a cold helium flow, and the source heating was achieved with an electric furnace. The temperature was monitored with a semiconductor pickup. The temperature of the absorber was 10 ± 1 K, and the temperature of the source could be varied from 10 ± 2 to 90 ± 2 K.

3. EXPERIMENTAL RESULTS AND DISCUSSION

The $^{67}Cu(^{67}Zn)$ Mössbauer spectra of all the compounds studied were either quadrupole triplets (for compounds with only one copper position) or a super-

1063-7834/03/4501-0011$24.00

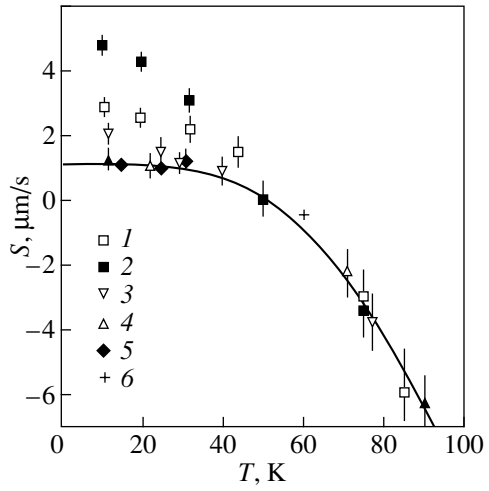

Fig. 1. Temperature dependences of the center of gravity S of the Mössbauer spectra of $^{67}Zn^{2+}$ at the Cu(1) [1, 4], Cu(2) [2, 5], and Y [3, 6] sites as measured relative to its value at 50 K for (*1–3*) $YBa_2Cu_3O_{6.6}$ and (*4–6*) $YBa_2Cu_3O_{6.5}$. Solid line is the theoretical temperature dependence of S for the case of a second-order Doppler shift for $\Theta = 420$ K.

position of two quadrupole triplets (for compounds having two structurally inequivalent copper positions). The fine structure of the spectra and assignment of the triplets to the corresponding copper site were described in [9–12]. The isomer shift (IS) of all spectra can be identified with the $^{67}Zn^{2+}$ ions (IS $\simeq$ 67–77 μm/s relative to the spectrum of the ^{67}Ga source in copper). It was assumed that, in the course of diffusion doping, the parent ^{67}Cu atoms enter the copper sites (this assumption is borne out by the data from [6, 7]) and, hence, that the $^{67}Zn^{2+}$ probe formed in the ^{67}Cu disintegration occupies a copper site.

The $^{67}Ga(^{67}Zn)$ Mössbauer spectra of $YBa_2Cu_3O_{6.9}$, $YBa_2Cu_3O_{6.6}$, and $YBa_2Cu_4O_8$ were quadrupole triplets with the isomer shift corresponding to the $^{67}Zn^{2+}$ ions (IS $\simeq$ 100–107 μm/s). The fine structure and assignment of the triplets to $^{67}Zn^{2+}$ centers at yttrium sites were described in [10, 13].

The quadrupole interaction constants C for the $^{67}Zn^{2+}$ centers at both the copper and yttrium sites are practically temperature-independent. This can be attributed to the fact that the electric field gradient at the ^{67}Zn nuclei detected by the $^{67}Zn^{2+}$ probe is generated primarily by the lattice ions and the lattice constants of the compounds studied vary very little in the temperature interval 4.2–100 K [2, 3].

The temperature dependence of the center of gravity S of the ^{67}Zn Mössbauer spectrum at constant pressure P can be determined using [14]

$$(\delta S/\delta T)_P = [\delta(\mathrm{IS})/\delta \ln V]_T(\delta \ln V/\delta T)_P + (\delta D/\delta T)_P + [\delta(\mathrm{IS})/\delta T]_V. \quad (1)$$

The first term in Eq. (1) describes the dependence of the isomer shift on volume V and becomes manifest in structural phase transitions. The second term is due to the temperature dependence of the second-order Doppler shift D and, in the Debye approximation, can be cast as [15]

$$(\delta D/\delta T)_P = -(3k_0E_0/2Mc^2)F(T/\Theta), \quad (2)$$

where k_0 is the Boltzmann constant, E_0 is the isomer transition energy, M is the probe nucleus mass, c is the speed of light in free space, Θ is the Debye temperature, and $F(T/\Theta)$ is the Debye function. The Debye model satisfactorily describes the vibrational properties of primitive lattices only; nevertheless, Eq. (2) fits quite well to the experimental $S(T)$ relations found for crystallochemically complex compounds [1]. This is accounted for by the fact that the $D(T)$ relation is dominated by the short-wavelength region of the phonon spectrum, which is described sufficiently well by the Debye approximation. Finally, the third term in Eq. (1) takes into account the temperature dependence of the isomer shift and is induced by the electron density variation at the Mössbauer nucleus sites, which is expected to occur in the host matrix undergoing the superconducting transition.

Figure 1 presents typical $S(T)$ relations for the Cu(1), Cu(2), and Y sites in the lattices of $YBa_2Cu_3O_{6.5}$ and $YBa_2Cu_3O_{6.6}$. It was found that the temperature dependence of the spectrum center of gravity S measured relative to its value at T_c is fitted well by Eq. (2) in the temperature interval 10–90 K for all reference samples if one uses the Debye temperatures 420 ± 10 K (for $YBa_2Cu_3O_{6.5}$), 400 ± 10 K (for $YBa_2Cu_4O_x$), 260 ± 10 K (for $Bi_2Sr_2CaCu_2O_x$), and 360 ± 10 K (for $HgBa_2CuO_x$ and $HgBa_2CaCu_2O_x$). (These Debye temperatures are in accord with the literature values derived from heat capacity measurements [16–19].) In other words, isomer shift variations, both due to a change in the volume and originating from temperature variations, virtually do not affect the $S(T)$ dependence for the nonsuperconducting samples. Because the compounds studied do not undergo structural phase transitions in the interval 10–90 K [2, 3], this behavior of $S(T)$ was to be expected.

For all superconducting samples, the $S(T)$ dependence for $T > T_c$ is likewise described by the second-order Doppler shift (2) and the Debye temperatures do not differ from those for the reference samples. In the $T < T_c$ region, S depends on temperature more strongly than would follow from Eq. (2); as a result, one must now take into account, in Eq. (1), the third term, which describes the temperature dependence of the isomer shift.

To describe the observed phenomenon qualitatively, we introduce the following parameters: the isomer shift $[\mathrm{IS}]_T$ at the given temperature T, found as the difference $[\mathrm{IS}]_T = S_T - D_T$ (where S_T and D_T are the center of grav-

ity and Doppler shift of the spectrum at temperature T, respectively), and the limiting isomer shift IS for $T \longrightarrow 0$, defined as the difference $[IS]_0 = S_0 - D_0$ (here, S_0 and D_0 are the center of gravity and Doppler shift of the spectrum for $T \longrightarrow 0$, respectively). As seen from Fig. 2, $[IS]_0$ is larger, the higher the superconducting transition temperature. The value of $[IS]_0$ also depends on the actual site occupied by the Mössbauer probe. $[IS]_0$ is the largest for the Cu(2) sites, substantially smaller for the Cu(1) sites, and the smallest for the Y sites, if one compares sites in the same lattice ($YBa_2Cu_3O_{6.6}$, $YBa_2Cu_3O_{6.9}$, or $YBa_2Cu_4O_8$; see table).

According to BCS theory, as the temperature is lowered and passes through T_c, Cooper pairs appear in the superconductor (the coupling electrons have opposite momenta and opposite spins, so that the total momentum, orbital angular momentum, and spin of a Cooper pair are zero) to form the Bose condensate [20]. This should change the electron density at lattice sites: the conduction electrons of the metallic phase are described by Bloch wave functions for temperatures $T > T_c$ and by a common coherent wave function for $T < T_c$. The isomer shift found as

$$IS = \alpha\Delta|\Psi(0)|^2 \qquad (3)$$

(here, $\Delta|\Psi(0)|^2$ is the difference between the relativistic electron densities at the nuclei of interest in two samples and α is a constant dependent on the nuclear parameters of the isotope used) is directly connected with the change in the electron density at the ^{67}Zn nucleus sites, with the value of $[IS]_0$ characterizing the electron density generated by the Bose condensate under the conditions where all conduction electrons are bound in Cooper pairs. In converting $[IS]_0$ to $\Delta|\Psi(0)|^2$, we made use of the value of α taken from [21]. Figure 2 plots the dependence of $\Delta|\Psi(0)|^2$ on T_c^{-1}; we see that the quantity $\Delta|\Psi(0)|^2 = |\Psi_c(0)|^2 - |\Psi_0(0)|^2$ increases with increasing T_c, which reflects the growth of electron density at the ^{67}Zn nuclei in going over from the nonsuperconducting [electron density $|\Psi_0(0)|^2$ at the ^{67}Zn nuclei] to superconducting phase [with electron density $|\Psi_c(0)|^2$ at the ^{67}Zn nuclei].

The dependence of $\Delta|\Psi(0)|^2$ on T_c becomes clear if we take into account that the standard correlation length ξ_0 (the "size" of a Cooper pair for $T \longrightarrow 0$) for anisotropic superconductors scales as $\xi_0 \sim T^{-1}$ and, thus, that Fig. 2 reflects the dependence of $[IS]_0$ and $\Delta|\Psi(0)|^2$ on T_c^{-1} and on the standard correlation length ξ_0. This dependence has an exponential character:

$$[IS]_0 = 7.9\exp[-31.4/T_c]$$

or

$$\Delta|\Psi(0)|^2 = 0.2\exp[-31.4/T_c],$$

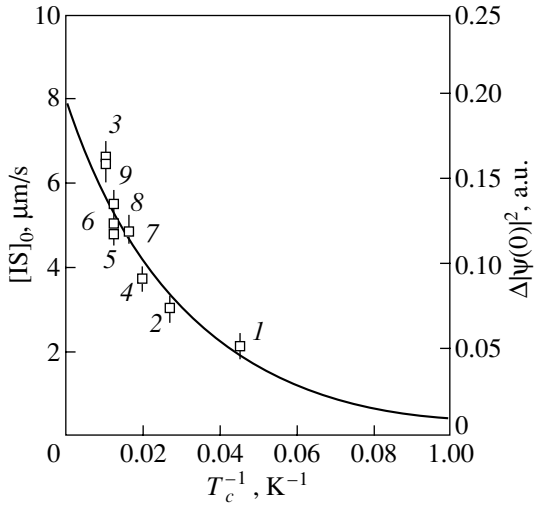

Fig. 2. Dependence of $[IS]_0$ and $\Delta|\Psi(0)|^2$ on T_c^{-1}. Symbols are data for (*1*) Cu in $Nd_{1.85}Ce_{0.15}CuO_4$, (*2*) Cu in $La_{1.85}Sr_{0.15}CuO_4$, (*3*) Cu(2) in $YBa_2Cu_3O_{6.9}$, (*4*) Cu(2) in $YBa_2Cu_3O_{6.6}$, (*5*) Cu(2) in $YBa_2Cu_4O_8$, (*6*) Cu in $Bi_2Sr_2CaCu_2O_8$, (*7*) Cu in $Tl_2Ba_2CaCu_2O_8$, (*8*) Cu in $HgBa_2CuO_4$, and (*9*) Cu in $HgBa_2CaCu_2O_6$. The data for $Nd_{1.85}Ce_{0.15}CuO_4$, $La_{1.85}Sr_{0.15}CuO_4$, and $Tl_2Ba_2CaCu_2O_8$ were taken from [1].

where IS is measured in μm/s, $|\Psi(0)|^2$ in atomic units, and T_c in kelvins.

We readily see that the experimental value of the change in the electron density at a ^{67}Zn nucleus site occurring at the superconducting transition does not exceed 0.2 a.u. and corresponds to the minimum possible size of a Cooper pair. The existence of such a minimum size is apparently associated with the physical impossibility of existence of Cooper pairs with a distance between the components of less than a certain critical length.

BCS theory permits one to find the temperature dependence of the effective density of superfluid elec-

The values of $[IS]_0$ for various lattice sites of $YBa_2Cu_3O_{6.6}$, $YBa_2Cu_3O_{6.9}$, and $YBa_2Cu_4O_8$

Compound	Site	$[IS]_0$, μm/s
$YBa_2Cu_3O_{6.6}$, T_c = 50 K	Cu(1)	1.8(3)
	Cu(2)	3.7(3)
	Y	1.0(3)
$YBa_2Cu_3O_{6.9}$, T_c = 90 K	Cu(1)	2.9(3)
	Cu(2)	6.6(3)
	Y	1.9(3)
$YBa_2Cu_4O_8$, T_c = 80 K	Cu(1)	2.2(3)
	Cu(2)	4.8(3)
	Y	1.0(3)

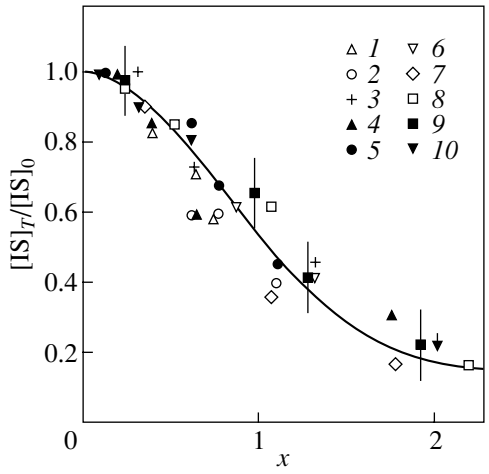

Fig. 3. Dependence of $[IS]_T/[IS]_0$ on the parameter $x = 1.76(k_0T/\Delta)$. Solid line shows a theoretical dependence of the effective density of superfluid electrons on the parameter x. Symbols refer to data obtained for the following sites: (*1*) Cu(1) in $YBa_2Cu_3O_{6.6}$, (*2*) Cu(1) in $YBa_2Cu_3O_{6.9}$, (*3*) Cu(1) in $YBa_2Cu_4O_8$, (*4*) Cu(2) in $YBa_2Cu_3O_{6.6}$, (*5*) Cu(2) in $YBa_2Cu_3O_{6.9}$, (*6*) Cu(2) in $YBa_2Cu_4O_8$, (*7*) Cu in $Bi_2Sr_2CaCu_2O_8$, (*8*) Cu in $HgBa_2CuO_4$, (*9*) Cu in $Hg_2Ba_2CaCu_2O_6$, and (*10*) Y in $YBa_2Cu_3O_{6.9}$.

trons $\rho(T)$ [20]; on the other hand, one may expect that $\rho(T) \sim [IS]_T/[IS]_0$. Figure 3 presents a theoretical dependence of ρ on the parameter $x = 1.76(k_0T/\Delta)$ (Δ is the energy gap in the elementary excitation spectrum of a superconductor taken from [20]) together with our data on the dependence of $[IS]_T/[IS]_0$ on the parameter x for various cuprates. The calculated and experimental temperature dependences of the effective density of superfluid electrons are seen to be in satisfactory agreement. This comes as a surprise; indeed, the problem of the inapplicability of BCS theory to the description of the properties of high-temperature superconductors has been discussed in the literature in considerable detail [22]; therefore, one should consider with caution our observation of agreement between the theoretical and experimental dependences of the effective density of superfluid electrons on the parameter x for the group of superconductors under study and the possibility of applying BCS theory in its unmodified form to the description of high-temperature superconductivity. This agreement should apparently be treated as an indication that the formation of Cooper pairs and their Bose condensation takes place in any theory of high-temperature superconductivity.

A specific feature of the compounds illustrated in Fig. 3 is the difference in the value of $[IS]_0$ observed to exist between the Cu(1) and Cu(2) sites. This is obviously a consequence of a spatial inhomogeneity in the electron density produced by the Bose condensate of Cooper pairs. Nevertheless, the calculated and experimental temperature dependences of the effective density of superfluid electrons exhibit satisfactory agreement for both the Cu(1) and Cu(2) (as well as for the Y) positions.

4. CONCLUSION

Thus, it has been established that the temperature dependence of the center of gravity S of the Mössbauer spectrum of the $^{67}Zn^{2+}$ crystal probe is dominated for the $YBa_2Cu_3O_{6.6}$, $YBa_2Cu_3O_{6.9}$, $YBa_2Cu_4O_8$, $Bi_2Sr_2CaCu_2O_8$, $HgBa_2CuO_4$, and $HgBa_2CaCu_2O_6$ compounds above the superconducting transition point T_c by the second-order Doppler shift. In the $T < T_c$ region, the quantity S is affected by the band mechanism associated with the formation of Cooper pairs and their Bose condensation. The change in the electron density at a metal site of a crystal is related to the superconducting transition temperature. As shown for the $YBa_2Cu_3O_{6.6}$, $YBa_2Cu_3O_{6.9}$, and $YBa_2Cu_4O_8$ compounds having two structurally inequivalent positions for the copper atoms, the variation of electron density produced by the Bose condensate of Cooper pairs is different for these cooper sites, as well as for the yttrium sites. The change in the electron density is the largest for the Cu(2) sites, considerably smaller for the Cu(1) sites, and the smallest for the Y sites. The experimentally established temperature dependence of the fraction of superconducting electrons for all the sites studied [Cu(1), Cu(2), Y] is in satisfactory agreement with the analogous dependence following from BCS theory.

ACKNOWLEDGMENTS

This study was supported by the Ministry of Education of the Russian Federation, project no. E 00-3.4-42.

REFERENCES

1. N. P. Seregin, F. S. Nasredinov, and P. P. Seregin, Fiz. Tverd. Tela (St. Petersburg) **43**, 587 (2001) [Phys. Solid State **43**, 609 (2001)].
2. J. Capponi, C. Chaillout, A. Hewat, *et al.*, Europhys. Lett. **3**, 1301 (1987).
3. E. Kaldis, P. Fischer, A. W. Hewat, *et al.*, Physica C (Amsterdam) **159**, 668 (1989).
4. O. Chmaissem, Q. Huang, S. N. Putilin, *et al.*, Physica C (Amsterdam) **212**, 259 (1993).
5. E. V. Antipov, J. J. Capponi, C. Chaillout, *et al.*, Physica C (Amsterdam) **218**, 348 (1993).
6. J. M. Tarascon, W. R. McKinnon, P. Barboux, *et al.*, Phys. Rev. B **38**, 8885 (1988).
7. J. D. Jorgensen, B. W. Veal, A. P. Paulikas, *et al.*, Phys. Rev. B **41**, 1863 (1990).
8. P. Gaptasarma, V. R. Palhar, and M. S. Multane, Solid State Commun. **77**, 769 (1991).
9. P. P. Seregin, V. F. Masterov, F. S. Nasredinov, *et al.*, Fiz. Tverd. Tela (St. Petersburg) **36**, 769 (1994) [Phys. Solid State **36**, 422 (1994)].

10. F. S. Nasredinov, V. F. Masterov, N. P. Seregin, and P. P. Seregin, J. Phys.: Condens. Matter **11**, 8291 (2000).
11. F. S. Nasredinov, V. F. Masterov, N. P. Seregin, and P. P. Seregin, J. Phys.: Condens. Matter **12**, 7771 (2000).
12. V. F. Masterov, F. S. Nasredinov, N. P. Seregin, and P. P. Seregin, Zh. Éksp. Teor. Fiz. **114**, 1079 (1998) [JETP **87**, 588 (1998)].
13. V. F. Masterov, F. S. Nasredinov, N. P. Seregin, and P. P. Seregin, Fiz. Tverd. Tela (St. Petersburg) **38**, 1986 (1996) [Phys. Solid State **38**, 1094 (1996)].
14. J. S. Shier and R. D. Taylor, Phys. Rev. **174**, 346 (1968).
15. D. L. Nagy, in *Mössbauer Spectroscopy of Frozen Solutions*, Ed. by A. Vértes and D. L. Nagy (Akadémiai Kiadó, Budapest, 1990; Mir, Moscow, 1998).
16. T. Sasaki, N. Kobayashi, O. Nakatsu, *et al.*, Physica C (Amsterdam) **153–155**, 1012 (1988).
17. H. M. Ledbetter, S. A. Kim, and R. B. Goldfarb, Phys. Rev. B **39**, 9689 (1989).
18. A. Junod, T. Craf, D. Sanchez, *et al.*, Physica C (Amsterdam) **165/166**, 1335 (1990).
19. S. J. Collocott, R. Driver, C. Audrikidis, and F. Pavese, Physica C (Amsterdam) **156**, 292 (1989).
20. J. R. Schrieffer, *Theory of Superconductivity* (Benjamin, New York, 1964; Nauka, Moscow, 1970).
21. A. Svane and E. Antoncik, Phys. Rev. B **34**, 1944 (1986).
22. *Physical Properties of High Temperature Superconductors*, Ed. by D. M. Ginsberg (World Scientific, Singapore, 1989; Mir, Moscow, 1990).

Translated by G. Skrebtsov

Physics of the Solid State, Vol. 45, No. 1, 2003, pp. 118–123. Translated from Fizika Tverdogo Tela, Vol. 45, No. 1, 2003, pp. 113–118.

MAGNETISM AND FERROELECTRICITY

Ferromagnetic Superstructure of an $La_{0.85}Sr_{0.15}MnO_3$ Manganite Single Crystal

S. F. Dubinin*, V. E. Arkhipov*, S. G. Teploukhov*, and Ya. M. Mukovskiĭ**

** Institute of Metal Physics, Ural Division, Russian Academy of Sciences, ul. S. Kovalevskoĭ 18, Yekaterinburg, 620219 Russia*

*** Moscow Institute of Steel and Alloys, Leninskiĭ pr. 4, Moscow, 117935 Russia*

Received February 14, 2002

Abstract—The elastic thermal-neutron scattering patterns of a $La_{0.85}Sr_{0.15}MnO_3$ manganite orthorhombic single crystal are investigated in the temperature range 4.2–300 K. It is found that, in addition to the known ferromagnetic ordering (T_C = 240 K), this compound exhibits a ferromagnetic superstructure with the $(010)2\pi/b$ wave vector (in the *Pnma* setting of the space group D_{2h}^{16}). The ferromagnetic superstructure is observed in the studied crystal at temperatures ranging from 4.2 to 200 K. It is shown that the formation of the ferromagnetic superstructure in this compound is directly associated with a 1/8-type charge ordering of Mn^{3+} and Mn^{4+} ions.

1. INTRODUCTION

The considerable interest expressed in neutron diffraction investigation of doped manganites of the formula

$$La_{0.85}^{3+}Sr_{0.15}^{2+}MnO_3, \quad (1)$$

in which a number of Mn^{3+} ions acquire a valence of 4+ in order to satisfy the electroneutrality condition, is associated with the giant magnetoresistance effect observed in ferromagnetic compounds of this class. In recent years, the giant magnetoresistance effect has assumed great practical importance.

Neutron diffraction investigations of doped manganites are also of particular scientific interest, because the question as to the nature of charge ordering in the $La_{0.85}^{3+}Sr_{0.15}^{2+}MnO_3$ compound remains open. In this respect, special mentioned should be made of two recent works [1, 2] devoted to neutron diffraction analysis of the magnetic and structural states of $La_{0.85}Sr_{0.15}MnO_3$ manganite single crystals.

Yamada *et al.* [1] investigated the structure and magnetic properties of $La_{0.85}Sr_{0.15}MnO_3$ crystals in the temperature range 10–300 K in the a^*c^* plane of the reciprocal orthorhombic lattice (unlike the notation used in [1], the designations of the reciprocal lattice axes are given here and below in the *Pnma* setting of the space group D_{2h}^{16} for convenience of comparison with our results). According to the results obtained in [1], the studied crystal, in its magnetic properties, is a collinear ferromagnet with the Curie temperature T_C = 240 K. These authors revealed two series of superstructure reflections with the fractional indices

$$(h \pm 1/2, 0, k \pm 1/2) \quad (2)$$

and

$$(h \pm 1/4, 0, k \pm 1/4). \quad (3)$$

In [1], series (3) of nuclear superstructure reflections was treated as an indication of the existence of charge (polaron) ordering in the crystal, i.e., as an indication of the formation of chains composed of identical ions alternating in the order

$$Mn^{3+}–Mn^{4+}–Mn^{3+} \quad (4)$$

in the initial lattice. Periods of type (4) appear in the neutron diffraction pattern of the crystal, because Mn^{4+} ions do not affect the surrounding oxygen octahedra (since these ions have no orbital angular momentum), whereas the Jahn–Teller Mn^{3+} ions strongly distort their environments due to interaction of the ionic orbital $d(z^2)$ with the crystal lattice.

More recently, Vasiliu-Doloc *et al.* [2] also thoroughly studied the magnetic and nuclear structures of an $La_{0.85}^{3+}Sr_{0.15}^{2+}MnO_3$ single crystal in the temperature range 10–380 K. It is interesting to note that, as in [1], these researchers observed superstructure reflections of type (2) in the diffraction pattern of the crystal. However, no superstructure reflections of type (3) were revealed in the diffraction pattern measured in [2]. This can be explained, for example, by the poor quality of the crystal or the deviation of the chemical composition of the manganite studied in [1] from the composition specified by formula (1). Most likely, the absence of

superstructure reflections of type (3) in the diffraction pattern was the reason why charge ordering in the studied compound was not considered in [2]. Vasiliu-Doloc *et al.* [2] analyzed in detail the origin of the weak magnetic superstructure reflection (030), which appears in the neutron diffraction pattern of the crystal at temperatures below T_{CA} = 205 K. According to the authors' opinion [2], this reflection can be associated with the formation of a weak antiferromagnetic component or a canted magnetic structure in the studied ferromagnet (T_C = 235 K) at temperatures below T_{CA}.

From the foregoing, it is seen that the neutron diffraction investigations performed in [1, 2] led to contradictory results regarding the occurrence of charge ordering of Mn^{3+} and Mn^{4+} ions in $La^{3+}_{0.85}Sr^{2+}_{0.15}MnO_3$ single crystals. In this respect, we undertook a detailed study of the structural and magnetic states in this manganite over a wide range of temperatures. In our previous experimental work [3], we measured the scattering patterns of thermal neutrons of crystals at relatively high temperatures (in the range 190–380 K). It should be noted that the diffraction patterns obtained in [3] are similar to those measured by Vasiliu-Doloc *et al.* [2]. The results obtained in [3] indicate that charge ordering in the $La^{3+}_{0.85}Sr^{2+}_{0.15}MnO_3$ manganite is characterized by a long-range order. Moreover, in [3], we determined the correlation lengths of the long-range order at temperatures above the Curie point for the compound under investigation.

However, in order to solve the problem of charge ordering in the La–Sr manganite conclusively, it is necessary to perform systematic neutron diffraction experiments at liquid-helium temperature and to compare the experimental results with the data obtained in [1, 2].

2. SAMPLES AND EXPERIMENTAL TECHNIQUE

In this work, we examined a manganite single crystal with the chemical composition specified by formula (1). The manganite single crystal was grown by zone melting. The misorientation of mosaic blocks in the crystal did not exceed 25′. A sample was prepared in the form of a cylinder with linear sizes d = 3 mm and l = 10 mm. The [110] crystallographic direction in a perovskite cubic reference sample deviated from the cylinder axis of the sample by approximately 15°.

Experiments on elastic scattering of thermal neutrons were performed using a special multichannel diffractometer designed for single-crystal investigations.

The wavelength λ of neutrons incident on the sample was equal to 1.567 Å. This was provided by a double crystal monochromator prepared from pyrolytic carbon and germanium. The efficient monochromatization of the primary beam and the appropriate choice of the wavelength of monochromatic neutrons made it possible to suppress multiple diffraction harmonics in the neutron diffraction pattern of the single crystal. For example, the relative intensity of Bragg reflections corresponding to the wavelength λ/2 in the diffraction pattern of the reference crystal reached only 0.02% of the intensity of the main Bragg reflections. (In other words, spurious peaks in the neutron diffraction pattern of a single crystal will arise only in the case when the intensity of the main Bragg reflections is greater than 10^5 pulses.) This appreciably increased the sensitivity of our neutron diffraction technique.

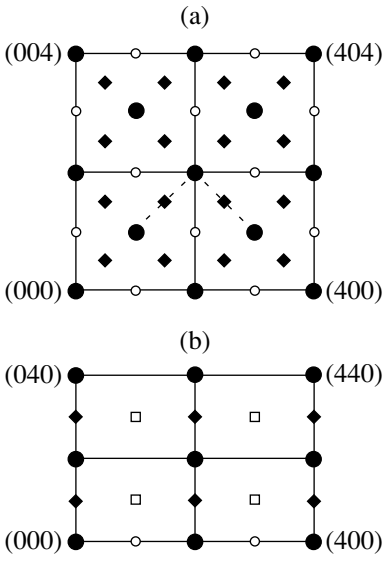

Fig. 1. A schematic representation of the neutron scattering patterns of the $La_{0.85}Sr_{0.15}MnO_3$ manganite orthorhombic single crystal at 4.2 K in (a) the a^*c^* plane and (b) the a^*b^* plane.

3. RESULTS AND DISCUSSION

The elastic neutron scattering patterns of the $La^{3+}_{0.85}Sr^{2+}_{0.15}MnO_3$ manganite orthorhombic single crystal were measured at a temperature of 4.2 K in the two principal planes a^*c^* and a^*b^* of the reciprocal lattice. The results obtained are schematically represented in Fig. 1. In this figure, the main Bragg reflections of the orthorhombic crystal are depicted by large closed circles. The superstructure reflections are indicated by other symbols. For example, the superstructure reflections associated with the rotational and Q_2 Jahn–Teller modes, which are well known in compounds of this class [4], are shown by squares and open circles, respectively.

It is worth noting that superstructure reflections of type (3), which should be observed midway between the main Bragg reflections in the reciprocal lattice and the superstructure reflections indicated by closed rhombs, are absent in Fig. 1. As an example, Fig. 2 shows two neutron diffraction patterns measured at 4.2 K along the paths depicted by dashed lines in

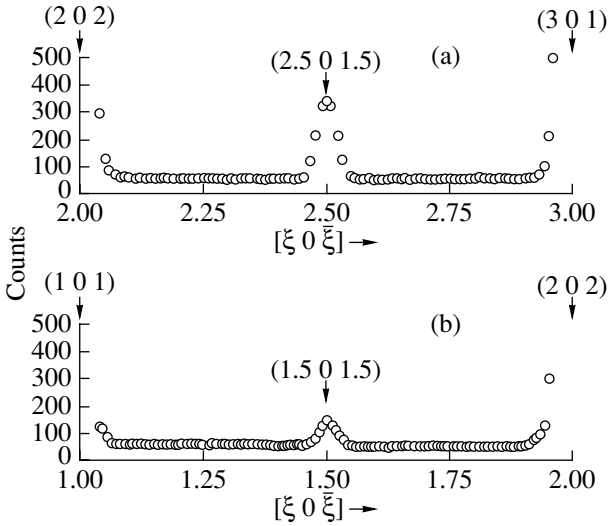

Fig. 2. Neutron diffraction patterns of the $La_{0.85}Sr_{0.15}MnO_3$ single crystal at 4.2 K in the a^*c^* plane of the reciprocal lattice: (a) scanning between the reflections (202) and (301) and (b) scanning between the reflections (101) and (202).

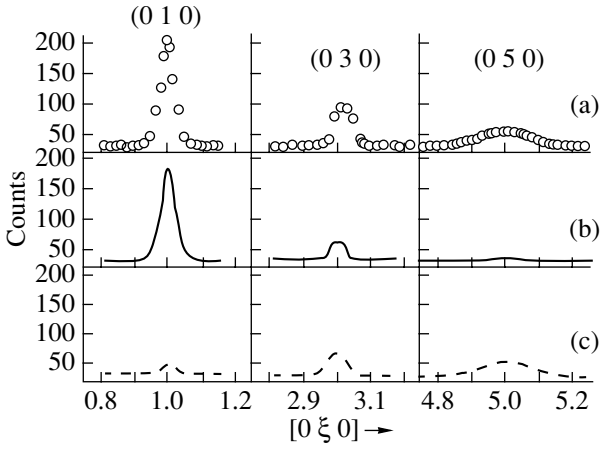

Fig. 3. (a) Experimental intensities of the (010), (030), and (050) superstructure reflections in the neutron diffraction pattern of the $La_{0.85}Sr_{0.15}MnO_3$ single crystal at 4.2 K; (b) calculated intensities of the (010), (030), and (050) reflections within the model of their magnetic nature; and (c) calculated intensities of the (010), (030), and (050) reflections within the model of structural distortions.

Fig. 1a. These scanning paths cover the reciprocal lattice points at which Yamada *et al.* [1] measured the temperature dependences of nuclear superstructure reflections of type (3). As can be seen from Fig. 2, reflections of series (3) are absent in our neutron diffraction pattern, which is in agreement with the results obtained in [2].

Consequently, there are good grounds to believe that, if charge ordering actually occurs in the manganite crystal under investigation, the superstructure reflections depicted by closed rhombs in Fig. 1 should provide information on this ordering. The original reflections of this series are as follows:

$$q_1 = (0 \;\; b^* \;\; 0) \tag{5}$$

$$q_2 = (a^*/2 \;\; 0 \;\; c^*/2). \tag{6}$$

According to the experimental results obtained in our earlier work [3], the intensities of superstructure reflections of type (6) involve both nuclear and magnetic components. Note that the nuclear component of these reflections is rather complicated, because it is determined by the distortion of oxygen octahedra and their spatial arrangement in the crystal. In the present work, as in [2], primary attention was concentrated on the origin of superstructure reflections of type (5), which are located along the b^* direction in the reciprocal lattice. The choice of this direction was motivated by the fact that the nuclear superstructure reflections $(0\ k\ 0)$ (associated with oxygen ion displacements of the Q_2 type [4]) with odd indices k are forbidden by *Pnma* symmetry in the scattering pattern of the studied crystal. It should be noted that, in this work, we measured the intensities of neutron scattering at the (010) and (050) reciprocal lattice points in addition to the reflections observed in [2].

The experimental neutron diffraction data obtained at a temperature of 4.2 K are shown by open circles in Fig. 3a. Figure 4 depicts the temperature dependence of the peak intensity of the (010) superstructure reflection. As can be seen from Fig. 4 and the results reported in our earlier work [3], the (010) weak reflection disappears at a temperature of 200 K. This critical temperature agrees well with the temperature T_{crit} = 205 K determined in [2] from the experimental temperature dependence of the intensity of the (030) reflection. Therefore, we can make the inference that the series of

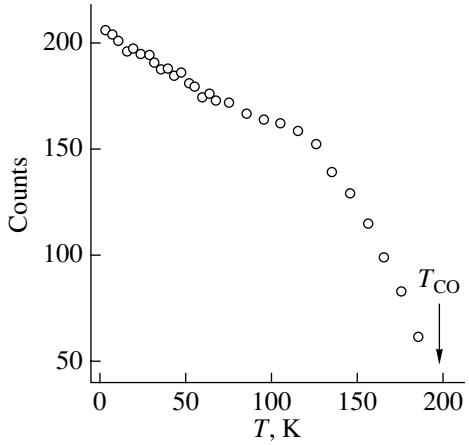

Fig. 4. Temperature dependence of the peak intensity of the (010) superstructure reflection in the neutron diffraction pattern of the $La_{0.85}Sr_{0.15}MnO_3$ single crystal.

weak reflections shown in Fig. 3a is associated with the same superstructure observed in the $La^{3+}_{0.85}Sr^{2+}_{0.15}MnO_3$ manganite orthorhombic single crystal.

In order to elucidate the nature of the superstructure observed, we compared the experimental data presented in Fig. 3a and the results of simple model calculations.

If we assume, for example, that the diffraction pattern shown in Fig. 3a is completely magnetic in nature, the intensity of superstructure (SS) reflections at different transferred momenta ($\kappa = 4\pi\sin\theta/\lambda$) can be represented by the standard relationship [5]

$$I \sim f^2(\kappa_{SS})P(\kappa_{SS}), \tag{7}$$

where $f(\kappa_{SS})$ is the magnetic form factor of the manganese ion and $P(\kappa_{SS})$ is the integral factor. In Fig. 3b, the solid lines correspond to the integrated intensities of reflections of the series under consideration. These intensities were calculated within the model of their magnetic nature. As can be seen from Figs. 3a and 3b, the results of calculations are in poor agreement with the experimental data. For example, the calculated intensity of the (030) reflection is almost half as high as the experimental intensity and the (050) reflection is virtually absent in Fig. 3b.

With the aim of fitting the experimental data to the calculated values, we assume that a magnetic density wave superposes on a nuclear density wave with the same period. Under this assumption, the nuclear superstructure reflections can be associated only with longitudinal ion displacements [with respect to the wave vector (5)] in the crystal. In this case, the dependence of the intensity of the superstructure reflections on the transferred momentum can be represented by the expression [5]

$$I \sim (\kappa_{SS}\mathbf{u})^2 P(\kappa_{SS}) \sim \kappa_{SS}^2 P(\kappa_{SS}), \tag{8}$$

where $\mathbf{u}$ is the vector of ion displacements along the κ_{SS} direction. In Fig. 3c, the dashed lines show the intensities of the (010), (030), and (050) reflections, which were calculated within the model of longitudinal structural distortions of the crystal (according to our experimental data, the calculations were performed under the assumption that the intensity of the (050) superstructure reflection is governed only by the nuclear component).

By combining the curves depicted in Figs. 3b and 3c, it can be easily shown that the results of simple calculations carried out in our work are in good agreement with the experimental data presented in Fig. 3a. This fact counts in favor of the magnetic and nuclear origin of the superstructure under consideration and is the first new result of the present work.

Now, we discuss one of the most interesting results of analyzing the diffraction patterns displayed in Fig. 3. Let us consider the experimental (010) peak and its magnetic and structural components. As is clearly seen from this figure, the magnetic contribution to the total intensity of the (010) superstructure reflection is greater than 90%. This circumstance is of fundamental importance, because it provides a means for constructing a model of the magnetic structure of the La–Sr manganite.

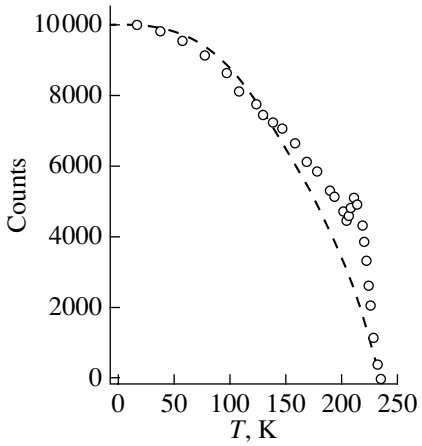

Fig. 5. Temperature dependence of the intensity of the ferromagnetic component of the (200) reflection in the neutron diffraction pattern of the $La_{0.85}Sr_{0.15}MnO_3$ manganite orthorhombic single crystal. Points are the experimental data taken from [2], and the dashed line corresponds to the results of calculations.

For this purpose, it is reasonable to compare the intensities of the structure (ST) ferromagnetic reflection (020) and the superstructure reflection (010); that is,

$$\frac{I^F_{(020)}}{I_{(010)}} = \frac{F^2_{(020)}\mathbf{M}^2_{(020)} f^2(\kappa_{ST})P(\kappa_{ST})}{F^2_{(010)}\mathbf{M}^2_{(010)} f^2(\kappa_{SS})P(\kappa_{SS})}, \tag{9}$$

where $F_{(010)}$ and $F_{(020)}$ are the superstructure and structure scattering amplitudes, respectively, and $\mathbf{M}_{(010)}$ and $\mathbf{M}_{(020)}$ are the vectors dependent on the mutual orientation of the scattering vector and the direction of the magnetic moments in the crystal [5].

The magnitudes of the vectors $\mathbf{M}_{(hkl)}$ for particular crystallographic planes substantially depend on the domain structure of a magnetic material. For example, in crystals with a random orientation of magnetic domains with respect to the crystallographic axes, the effective value M^2 is constant and equal to 2/3 for all ($h\,k\,l$) indices. For the manganite orthorhombic crystal studied in this work, the factor $M^2_{(hkl)}$ can significantly differ from 2/3. As an example, we analyze the temperature dependence of the intensity of the ferromagnetic component of the (200) reflection (in this case, the scattering vector $\boldsymbol{\kappa}$ coincides with the $\mathbf{a}^*$ direction). The experimental data taken from [2] are presented in Fig. 5. The dashed line in Fig. 5 shows the dependence of the quantity proportional to the square of the magnetization of the manganite orthorhombic single crystal.

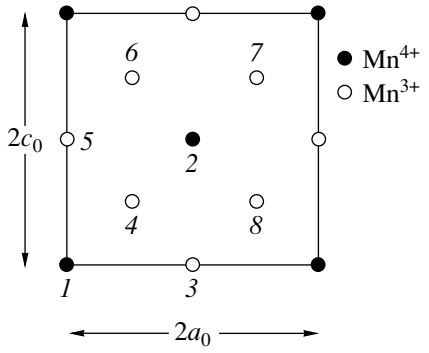

Fig. 6. A view of the unit cell of the ferromagnetic superstructure of the $La_{0.85}Sr_{0.15}MnO_3$ manganite in the a_0c_0 plane.

This curve is calculated within the mean-field approximation for spin $S = 2$. As can be seen from Fig. 5, the calculated and experimental data obtained in the low-temperature range (10–120 K) are in close agreement. However, at temperatures above 200 K, the experimental intensities substantially exceed the calculated values. This can be explained only by a considerable change in the domain structure of the ferromagnetic crystal. In other words, the factor $M^2_{(hkl)}$ for the (200) reflection plane depends on the temperature and, consequently, differs from 2/3. It is evident that the simplest ratios of the factors $\mathbf{M}^2_{(hkl)}$ in relationship (9) should be obtained for reflections corresponding to parallel crystallographic planes, for example, $\mathbf{M}^2_{(020)}/\mathbf{M}^2_{(010)}$.

It is well known that the structure factor $F^2_{(010)}$ depends on the magnetic structure of the material. For the manganite under investigation, there exist only two variants of magnetic ordering. One variant is the canted spin system proposed in [2]. For a canted magnetic structure of the crystal, the structure factor contains the antiferromagnetic component as a fitting parameter. The antiferromagnetic component obtained by fitting to the experimental data takes on a small fractional value. In our opinion, the formation of a canted magnetic structure in the $La^{3+}_{0.85}Sr^{2+}_{0.15}MnO_3$ compound at relatively high temperatures (T_{CA} = 200 K) is physically improbable. Indeed, it is common knowledge that the Néel temperature of antiferromagnetic ordering of solid solutions in the $La^{3+}_{1-x}Sr^{2+}_xMnO_3$ system (T_N = 140 K at $x = 0$) decreases with an increase in the dopant concentration [1]. This decrease in the temperature T_N can be explained by the increase in the concentration of Mn^{4+} ions, which encourage the formation of ferromagnetic ordering.

In the case of ferromagnetic ordering, the $La^{3+}_{0.85}Sr^{2+}_{0.15}MnO_3$ manganite can exhibit only a ferromagnetic superstructure. The superstructure with ferromagnetic order is directly associated with a 1/8-type charge ordering of Mn^{3+} and Mn^{4+} ions in the studied compound. The magnetic moments of trivalent and tetravalent manganese ions are equal to $4\mu_B$ and $3\mu_B$, respectively. The superstructure unit cell in the a_0c_0 plane is shown in Fig. 6. The closed and open circles in this figure indicate the positions of the Mn^{4+} and Mn^{3+} ions, respectively. According to formula (6) for the wave vector, the superstructure parameters are equal to twice the initial orthorhombic unit cell parameters. The size of the superstructure unit-cell along the axis $b_0 = 2b_C$ (where b_C is the parameter of the perovskite cubic unit cell) coincides with that of the initial unit cell. In this case, only the Mn^{3+} ions are located at a height $1/2b_0$ and the arrangement of manganese ions in the unit cell at a height b_0 is identical to that represented in Fig. 6. Thus, the unit cell of the ferromagnetic superstructure consists of 16 manganese ions (their numbering in the a_0c_0 plane is shown in Fig. 6), of which 2 ions are tetravalent and 14 ions have a valence of 3+. Within this model of the magnetic cell, the structure factors can be represented in the form

$$\begin{aligned} F^2_{(010)} &= [2(4\mu_B - 3\mu_B)]^2, \\ F^2_{(020)} &= [27 \times 4(\mu_B + 3\mu_B)]^2. \end{aligned} \tag{10}$$

By substituting expressions (10) into relationship (9) and taking into account the obvious equality $\mathbf{M}^2_{(010)} = \mathbf{M}^2_{(020)}$, we obtain the following intensity ratio:

$$(I^F_{(020)}/I^F_{(010)})_{exp} = 373. \tag{11}$$

Now, we compare the calculated intensity ratio (11) with the experimental data. The intensities of the (020) Bragg reflection in the neutron diffraction pattern of the $La^{3+}_{0.85}Sr^{2+}_{0.15}MnO_3$ single crystal are presented in Fig. 7. The closed and open circles indicate the results of measurements at temperatures of 4.2 and 300 K, respectively. (Recall that the Curie temperature of the studied manganite is 240 K.) The integrated intensity of the (020) structure ferromagnetic reflection is equal to the difference between the integrated intensities of the reflections shown in Fig. 7. Since the times of measuring the reflections displayed in Figs. 3 and 7 are identical, we can easily obtain the experimental intensity ratio

$$(I^F_{(020)}/I^F_{(010)})_{exp} = 358. \tag{12}$$

The experimental error in the determination of the intensity ratio (12) is equal to only 4.2%. The main advantage of our model of magnetic ordering resides in the fact that the close agreement between the experimental and calculated data is achieved (without resorting to fitting parameters) only with allowance made for the 1/8-type stoichiometric ratio of Mn^{4+} and Mn^{3+} ions

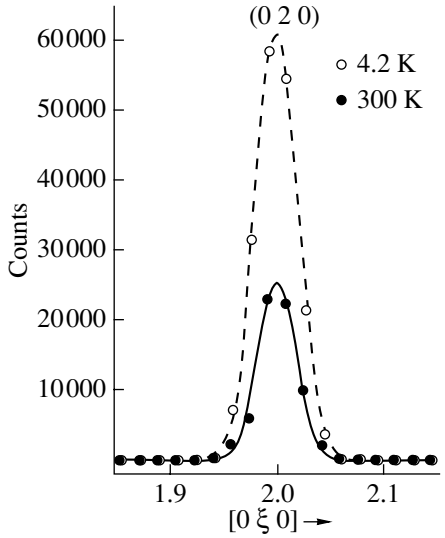

Fig. 7. Intensities of the (020) Bragg reflection in the neutron diffraction pattern of the $La_{0.85}Sr_{0.15}MnO_3$ single crystal at 4.2 and 300 K.

in relationships (10) and their ordered arrangement in the manganite crystal. It is this circumstance that should be considered main evidence of the occurrence of charge ordering in the $La^{3+}_{0.85}Sr^{2+}_{0.15}MnO_3$ manganite at temperatures below the transition point T_{CO} = 200 K. This is the principal result of the present work.

In our opinion, charge ordering is responsible for the aforementioned fact that longitudinal waves of static displacements of octahedral complexes (Fig. 3c) appear in the manganite compound at temperatures below T_{CO}. In turn, these waves directly affect the lattice parameters of the orthorhombic crystal. Actually, the energy of the crystal with ordered charges reaches a minimum when the charges are equally spaced in the lattice. This situation can occur only in compounds with cubic symmetry. To put it differently, the formation of charge ordering in the orthorhombic phase Q' can cause its transformation into the phase Q^*, which was experimentally observed by Vasiliu-Doloc *et al.* [2].

4. CONCLUSION

Thus, it was revealed that, in addition to the known ferromagnetic ordering at the Curie temperature T_C = 240 K, the $La^{3+}_{0.85}Sr^{2+}_{0.15}MnO_3$ manganite orthorhombic single crystal exhibits a ferromagnetic superstructure with the $(010)2\pi/b$ wave vector. The ferromagnetic superstructure is observed in the studied crystal at temperatures ranging from 4.2 to 200 K. It was demonstrated that the formation of the ferromagnetic superstructure in this compound is directly associated with a 1/8-type charge ordering of Mn^{3+} and Mn^{4+} ions.

ACKNOWLEDGMENTS

This work was supported by the State Scientific and Technical Program “Topical Directions in the Physics of Condensed Matter: Neutron Investigations of Condensed Matter” (project no. 107-19(00)-P-D01), the State Program of Support for Leading Scientific Schools of the Russian Federation (project no. 00-15-96581), and the Russian Foundation for Basic Research (project no. 99-02-16280).

REFERENCES

1. Y. Yamada, O. Hino, S. Nohdo, *et al.*, Phys. Rev. Lett. **77** (5), 904 (1996).
2. L. Vasiliu-Doloc, J. W. Lynn, A. H. Moudden, *et al.*, Phys. Rev. B **58** (22), 14913 (1998).
3. S. F. Dubinin, V. E. Arkhipov, Ya. M. Mukovskiĭ, *et al.*, Fiz. Met. Metallogr. **93** (3), 60 (2002).
4. J. L. Garcia-Munos, M. Suaaidi, J. Fontcuberta, and J. Rodriguez-Carvajal, Phys. Rev. B **55**, 34 (1997).
5. Yu. A. Izyumov, V. E. Naĭsh, and R. P. Ozerov, *Neutron Diffractometry of Magnetic Materials* (Atomizdat, Moscow, 1981).

Translated by O. Borovik-Romanova

Physics of the Solid State, Vol. 45, No. 1, 2003, pp. 124–129. Translated from Fizika Tverdogo Tela, Vol. 45, No. 1, 2003, pp. 119–123.

MAGNETISM AND FERROELECTRICITY

The Dynamics of Domain Walls in an Easy-Plane Magnet in the Field of an Acoustic Wave

V. S. Gerasimchuk and A. A. Shitov

Donbass State Academy of Civil Engineering, Makeevka, Donetsk oblast, 86123 Ukraine

e-mail: vme@dgasa.dn.ua

Received February 20, 2002

Abstract—The drift of a 180° domain wall is studied in an easy-plane weak two-sublattice ferromagnet subject to an elastic-stress field generated by an acoustic wave. The dependences of the drift velocity on the amplitude and polarization of the acoustic wave are found. The conditions of the drift of a stripe domain structure are determined. © *2003 MAIK "Nauka/Interperiodica".*

1. INTRODUCTION

In this paper, we study the interaction between a domain wall (DW) and an elastic wave in a weak easy-plane ferromagnet. One of the most interesting magnets of this type is iron borate $FeBO_3$ [1]. This compound is of particular interest, because $FeBO_3$ is transparent in the visible spectral region and has a Néel temperature T_N = 348 K, which makes it possible to study its properties at room temperature. In particular, the magnetoelastic properties of $FeBO_3$ were studied in [2].

Elastic strains produced by an acoustic wave change the energy of a DW and cause the DW to move [3]. Steady-state motion of the DW is possible at velocities smaller than the critical velocity $\tilde{V}$, determining the magnetoelastic gap in the DW velocity spectrum [4]. The dependence of the velocity $\tilde{V}$ on the compression stress in the plane of a sample was measured experimentally in [5]. As the DW velocity reaches the critical value $\tilde{V}$, the 180° DW may decay into two 90° DWs yielding a new 90° domain.

The direct influence of an elastic wave on an isolated 180° DW was experimentally studied in [6]. It was established that the directional motion of the DW is possible under the action of a longitudinal acoustic wave. Such a directional motion of the DW was theoretically investigated in [7–9]. In particular, the drift of the DW in a uniaxial ferromagnet was analyzed on the basis of the averaged Slonczevski equations [7]. By using the Lagrangian formalism and directly solving the equations of motion of the magnetization vector, the drift of the DW in a weak ferromagnet, such as rare-earth orthoferrite, was studied [8, 9].

2. MODEL AND EQUATION OF MOTION

Let us consider an arbitrary polarized acoustic wave. We suppose that the wave is defined as an external field and take into account the influence of the elastic subsystem on the magnetic subsystem, neglecting the backward action of the magnetic system on the elastic system. We consider the wavelength of the acoustic wave to be much larger than the DW width, which makes it possible not to consider the internal structure of the DW. It has been shown that there is a lattice potential relief for the DW motion in a magnet [10]. If the DW velocity is sufficient to overcome the lattice barrier, the DW can move in fields which are much smaller than the coercive force associated with the given potential barrier. In what follows, an external field is necessary only to compensate for dynamic losses. In this paper, we consider the steady motion of a DW. As indicated below, the DW drift velocity V_{dr} is much smaller than the critical velocity $\tilde{V}$.

The nonlinear macroscopic dynamics of a two-sublattice, weak easy-plane ferromagnet in an acoustic wave can be described on the basis of the Lagrangian density $L\{\mathbf{l}\}$ expressed in terms of the antiferromagnetism unit vector $\mathbf{l}$ [11]. If the vector $\mathbf{l}$ is defined by two angular variables θ and φ as

$$l_x + il_y = \sin\theta\exp(i\varphi), \quad l_z = \cos\theta, \tag{1}$$

the Lagrangian density can be written in the form

$$\begin{aligned} L\{\theta,\varphi\} = M_0^2\Bigg\{&\frac{\alpha}{2c^2}(\dot\theta^2 + \dot\varphi^2\sin^2\theta) \\ &- \frac{\alpha}{2}[(\nabla\theta)^2 + (\nabla\varphi)^2\sin^2\theta] - \left(\frac{\beta}{2} - \lambda + \frac{d^2}{2\delta}\right)\cos^2\theta \\ &- \gamma[\sin 2\theta(u_{zx}\cos\varphi + u_{yz}\sin\varphi) + u_{zz}\cos^2\theta \\ &+ \sin^2\theta(u_{xx}\cos^2\varphi + u_{xy}\sin 2\varphi + u_{yy}\sin^2\varphi)] \\ &+ 2\lambda\sin^2\theta\cos^2\varphi\Bigg\}, \end{aligned} \tag{2}$$

1063-7834/03/4501-0124$24.00 © 2003 MAIK "Nauka/Interperiodica"

where dots indicate differentiation with respect to time, M_0 is the magnitude of the sublattice-magnetization vector, $c = gM_0(\alpha\delta)^{1/2}/2$ is the minimum spin-wave phase velocity (with δ and α being the homogeneous- and inhomogeneous-exchange coupling constants, respectively), g is the gyromagnetic ratio, d is the Dzyaloshinskiĭ interaction constant, β is the uniaxial-anisotropy constant, λ is the effective orthorhombic-anisotropy constant, u_{ik} is the elastic-strain tensor, and γ is the magnetoelastic constant.

Let us introduce a dissipative function

$$F = \frac{\tilde{\lambda}M_0}{2g}\dot{\mathbf{l}}^2 = \frac{\tilde{\lambda}M_0}{2g}(\dot{\theta}^2 + \dot{\varphi}^2\sin^2\theta), \quad (3)$$

where $\tilde{\lambda}$ is the Gilbert damping constant.

With due regard for the dynamic losses, the equations of motion are expressed in terms of the angular variables as

$$\alpha\left(\Delta\theta - \frac{1}{c^2}\ddot{\theta}\right) + \sin\theta\cos\theta\left[\alpha\left(\frac{1}{c^2}\dot{\varphi}^2 - (\nabla\varphi)^2\right) + 4\lambda\cos^2\varphi + \beta - 2\lambda + \frac{d^2}{\delta}\right]$$
$$- \gamma[\sin 2\theta(u_{xx}\cos^2\varphi + u_{xy}\sin 2\varphi + u_{yy}\sin^2\varphi - u_{zz}) + 2\cos 2\theta(u_{xz}\cos\varphi + u_{yz}\sin\varphi)] = \frac{\tilde{\lambda}}{gM_0}\dot{\theta}, \quad (4)$$

$$\alpha\nabla[\nabla\varphi\sin^2\theta] - \frac{\alpha}{c^2}\frac{d}{dt}(\dot{\varphi}\sin^2\theta) - 4\lambda\sin^2\theta\sin\varphi\cos\varphi$$
$$- \gamma[[\sin^2\theta]\{(u_{yy} - u_{xx})\sin 2\varphi + 2u_{xy}\cos 2\varphi\} + \sin 2\theta(u_{zy}\cos\varphi - u_{zx}\sin\varphi)] = \frac{\tilde{\lambda}}{gM_0}\dot{\varphi}\sin^2\theta. \quad (5)$$

The equations of motion have two types of solutions describing planar 180° DWs in the ground state. Since the condition $(\beta - 2\lambda + d^2/\delta) > 4\lambda > 0$ is fulfilled, the vector **l** is collinear to the x axis in the absence of external fields and a domain wall in which **l** rotates in the xy plane is stable far away from the spin-reorientation region [12]. For this DW, we have $\theta = \theta_0 = \pi/2$ and the equation for the angular variable $\varphi_0(z)$ takes the form

$$\alpha\varphi_0'' - 4\lambda\sin\varphi_0\cos\varphi_0 = 0, \quad (6)$$

where the prime indicates differentiation with respect to z. Using the boundary conditions $\varphi_0(-\infty) = 0$, $\varphi_0(+\infty) = \pi$, we find the magnetization distribution in the static Bloch-type 180° DW:

$$\varphi_0' = \frac{1}{z_0}R\sin\varphi_0(z) = \frac{1}{z_0}R\rho\cosh^{-1}\frac{z}{z_0},$$
$$\cos\varphi_0(z) = -R\tanh\frac{z}{z_0}, \quad (7)$$

where $z_0 = \sqrt{\alpha/4\lambda}$ is the DW thickness, $R = \pm 1$ is the topological charge of the DW, and $\rho = \pm 1$ is a parameter defining the direction of rotation of the vector **l** in the DW.

The 180° DWs separating domains with opposite magnetization directions in a stripe domain structure have opposite topological charges R. The vector **l** can rotate in the domain wall from $-R$ to $+R$ (or in the opposite direction) either through the positive or the negative direction of the y axis; the direction of the rotation is defined by the parameter ρ. For this reason, to neighboring DWs in the stripe domain structure with the vector **l** rotating in the xy plane correspond the values $l_x(z = \pm\infty) = \mp R$ and one of the two values $l_y(z = 0) = \pm\rho$. For the isolated DW studied in [6], we have $R = +1$ and $\rho = +1$.

3. AN ACOUSTIC WAVE PROPAGATING IN THE PLANE OF A DOMAIN WALL

In order to solve equations of motion (4) and (5), we consider a monochromatic acoustic wave propagating in the DW plane: $\mathbf{u}(\mathbf{r}_\perp, t) = \mathbf{u}_0\exp(i\mathbf{k}_\perp\mathbf{r}_\perp - i\omega t)$, where $\mathbf{k}_\perp\mathbf{r}_\perp = k_x x + k_y y$. Let us introduce a collective variable $Z(\mathbf{r}_\perp, t)$ as the coordinate of the DW center. The DW drift velocity is determined as the instantaneous velocity $V(\mathbf{r}_\perp, t) = \dot{Z}(\mathbf{r}_\perp, t)$ averaged over a period of oscillations, $V_{dr} = \overline{V(\mathbf{r}_\perp, t)}$ (the bar means averaging over a period of oscillations). Supposing the amplitude of the acoustic wave to be sufficiently small, we seek a solution to the system of Eqs. (4) and (5) in terms of power-series expansions:

$$\theta(\mathbf{r}, t) = \pi/2 + \theta_1(\xi, \mathbf{r}_\perp, t) + \theta_2(\xi, \mathbf{r}_\perp, t) + \dots,$$
$$\varphi(\mathbf{r}, t) = \varphi_0(\xi) + \varphi_1(\xi, \mathbf{r}_\perp, t) + \varphi_2(\xi, \mathbf{r}_\perp, t) + \dots,$$
$$V = V_1 + V_2 + \dots, \quad (8)$$

where $\xi = z - Z(\mathbf{r}_\perp, t)$ and indices $n = 1, 2, \dots$ indicate the order of smallness with respect to the acoustic-wave amplitude. The function $\varphi_0(\xi)$ describes the motion of the nondisturbed DW and has a structure similar to that of the static solution to Eq. (7). The higher order functions θ_n and φ_n ($n = 1, 2 \dots$) describe motion of the disturbed DW and the excitation of spin waves.

3.1. Linear Approximation

The equations of the first-order perturbation theory have the form

$$\left(\hat{L} + \frac{1}{\omega_0^2}\frac{\partial^2}{\partial t^2} + \frac{\omega_r}{\omega_0^2}\frac{\partial}{\partial t}\right)\varphi_1(\xi, \mathbf{r}_\perp, t)$$

$$= \frac{R\sin\varphi_0(\xi)}{z_0\omega_0^2}\left(\frac{\partial^2 Z_1}{\partial t^2} + \omega_r\frac{\partial Z_1}{\partial t} - \omega_0^2 z_0^2\Delta_\perp Z_1\right) \quad (9)$$

$$-\frac{\gamma}{2\lambda}[(u_{yy}-u_{xx})\sin 2\varphi_0(\xi) + 2u_{xy}\cos 2\varphi_0(\xi)],$$

$$\left(\tilde{L} + \sigma + \frac{1}{\omega_0^2}\frac{\partial^2}{\partial t^2} + \frac{\omega_r}{\omega_0^2}\frac{\partial}{\partial t}\right)\theta_1(\xi, \mathbf{r}_\perp, t)$$

$$= \frac{\gamma}{2\lambda}(u_{xx}\cos\varphi_0 + u_{yz}\sin\varphi_0), \quad (10)$$

where $\Delta_\perp = \partial^2/\partial x^2 + \partial^2/\partial y^2$, $\sigma = (\beta - 2\lambda + d^2/\delta)(4\lambda)^{-1}$, $\omega_0 = c/z_0$ is the activation frequency of the lowest branch of the bulk-spin-wave spectrum, $\omega_r = \tilde{\lambda}\delta g M_0/4$ is the characteristic relaxation frequency, $\mathbf{k}_\perp$ is the wave vector of the sound wave, and $k_\perp = |\mathbf{k}_\perp| = \omega/s$, with s being the acoustic-wave velocity.

The operator $\hat{L} = -z_0^2 d^2/d\xi^2 + 1 - 2/\cosh^2(\xi/z_0)$ has the well-known eigenfunctions

$$f_0(\xi) = \frac{1}{\sqrt{2z_0}}\cosh^{-1}\frac{\xi}{z_0},$$

$$f_p(\xi) = \frac{1}{b_p\sqrt{L}}\left(\tanh\frac{\xi}{z_0} - ipz_0\right)\exp(ip\xi)$$

(L is the crystal length) and eigenvalues $\lambda_0 = 0$ and $\lambda_p = b_p^2 = 1 + p^2 z_0^2$. We seek a solution to the first-order-approximation equations (9) and (10) in the form of power-series expansion in terms of the complete set of eigenfunctions of the operator $\hat{L}$. The result is

$$\varphi_1(\xi, t) = R\rho\mathrm{Re}\left\{\frac{i\gamma}{8\lambda}[(k_y u_{0y} - k_x u_{0x})D_1(\xi) - (k_x u_{0y} + k_y u_{0x})D_2(\xi)]\exp(i\mathbf{k}_\perp\mathbf{r}_\perp - i\omega t)\right\},$$

$$\theta_1(\xi, t) = \frac{\gamma R}{4\lambda}\mathrm{Re}\left\{\left[\frac{ik_y u_{0z}}{\sigma - q}\sin\varphi_0(\xi) + \frac{ik_x u_{0z}}{1 + \sigma - q}\cos\varphi_0(\xi)\right]\exp(i\mathbf{k}_\perp\mathbf{r}_\perp - i\omega t)\right\}, \quad (11)$$

where

$$D_1(\xi) = \int_{-\infty}^{\infty}\frac{\tanh(\xi/z_0)\cos(p\xi) + pz_0\sin(p\xi)}{(\lambda_p - q)\cosh\dfrac{\pi p z_0}{2}}d(pz_0),$$

$$D_2(\xi) = \int_{-\infty}^{\infty}\frac{\tanh(\xi/z_0)\sin(p\xi) - pz_0\cos(p\xi)}{(\lambda_p - q)\sinh\dfrac{\pi p z_0}{2}}d(pz_0),$$

$$q = q_1 + iq_2, \quad q_1 = \left(\frac{\omega}{\omega_0}\right)^2, \quad q_2 = \left(\frac{\omega\omega_r}{\omega_0^2}\right).$$

Supposing the amplitude of the Goldstone mode to be zero [8, 9], the following equation for the determination of the DW velocity can be derived from Eq. (9):

$$\frac{\partial^2 Z_1}{\partial t^2} + \omega_r\frac{\partial Z_1}{\partial t} - \omega_1^2 z_0^2\Delta_\perp Z_1 = 0. \quad (12)$$

This equation indicates that, in the linear approximation with respect to the acoustic-wave amplitude, the sound does not cause the DW to move but results in the excitation of spin waves described by Eqs. (11). These excitations are caused by both longitudinal and transverse acoustic waves.

3.2. Second-Order Approximation

The second-order-approximation equation for the function $\varphi_2(\xi, \mathbf{r}_\perp, t)$ has the form

$$\left(\hat{L} + \frac{1}{\omega_0^2}\frac{\partial^2}{\partial t^2} + \frac{\omega_r}{\omega_0^2}\frac{\partial}{\partial t}\right)\varphi_2(\xi, \mathbf{r}_\perp, t)$$

$$= \left(\frac{\partial^2 Z_2}{\partial t^2} + \omega_r\frac{\partial Z_2}{\partial t} - \omega_0^2 z_0^2\Delta_\perp Z_2\right)\frac{R\sin\varphi_0}{\omega_0^2 z_0} + \frac{2}{\omega_0^2}\left(\frac{\partial Z_1}{\partial t}\right)$$

$$\times\ \dot{\varphi}_1'(\xi, \mathbf{r}_\perp, t) - 2z_0\theta_1(\xi, \mathbf{r}_\perp, t)\theta_1'(\xi, \mathbf{r}_\perp, t)R\sin\varphi_0$$

$$+\left[\Delta_\perp Z_1 - \left(\frac{1}{c}\frac{\partial Z_1}{\partial t}\right)^2\right]\frac{\sin 2\varphi_0}{2} + \varphi_1^2(\xi, \mathbf{r}_\perp, t)\sin 2\varphi_0$$

$$+\frac{\varphi_1'(\xi, \mathbf{r}_\perp, t)}{\omega_0^2}\left(\frac{\partial^2 Z_1}{\partial t^2} + \omega_r\frac{\partial Z_1}{\partial t} - \omega_0^2 z_0^2\Delta_\perp Z_1\right)$$

$$+\frac{\gamma}{2\lambda}[(u_{zy}\cos\varphi_0 - u_{xz}\sin\varphi_0)\theta_1(\xi, \mathbf{r}_\perp, t)$$

$$+((u_{xx} - u_{yy})\cos 2\varphi_0 + 2u_{xy}\sin 2\varphi_0)\varphi_1(\xi, \mathbf{r}_\perp, t)]. \quad (13)$$

We do not present the second-order-approximation equation for the function $\theta_2(\xi, \mathbf{r}_\perp, t)$, because it does not define the DW motion. Since we are interested in the induced DW motion only, it will suffice, when determining $V_2(t)$, to find the coefficient corresponding to the Goldstone mode in the expansion of $\varphi_2(\xi, \mathbf{r}_\perp, t)$ in

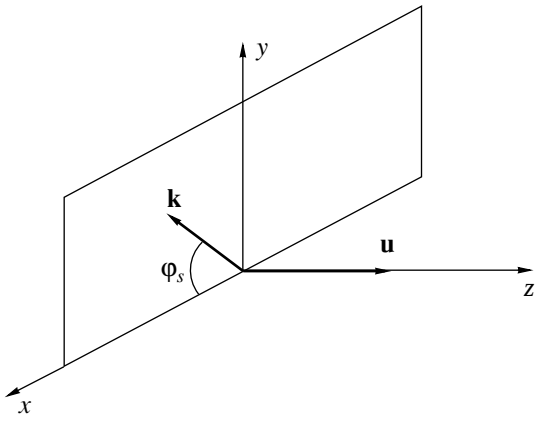

Fig. 1. Transverse wave. The displacement vector is perpendicular to the DW plane.

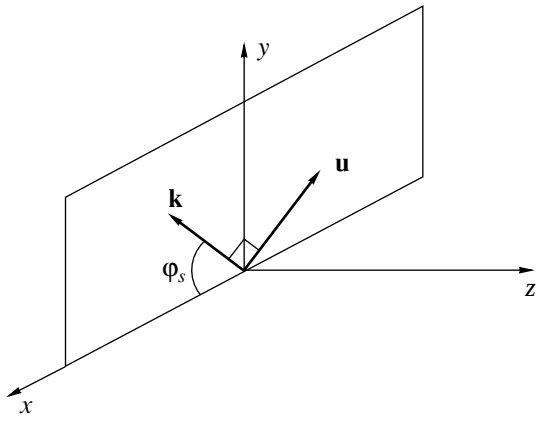

Fig. 2. Transverse wave. The displacement vector lies in the DW plane.

terms of the eigenfunctions of the operator $\hat{L}$ and to set this coefficient equal to zero [8, 9]. As a result, we have

$$R\rho\left(\frac{\partial^2 Z_2}{\partial t^2} + \omega_r\frac{\partial Z_2}{\partial t} - \omega_0^2 z_0^2\Delta_\perp Z_2\right) = N + N_1\exp(2i\omega t) + N_2\exp(-2i\omega t). \quad (14)$$

Here,

$$N = \omega_0^2 z_0\sqrt{2z_0}\,\mathrm{Re}\int_{-\infty}^{\infty} d\xi\, f_0(\xi)\left\{\frac{\theta_1^*\theta_1'}{2}\sin\varphi_0 - \varphi_1^*\varphi_1\frac{\sin 2\varphi_0}{4z_0} - \frac{(\varphi_1^*)'}{4\omega_0^2 z_0}\left(\frac{\partial^2 Z_1}{\partial t^2} + \omega_r\frac{\partial Z_1}{\partial t} - \omega_0^2 z_0^2\Delta_\perp Z_1\right) - \frac{\gamma}{2\lambda}[(u_{zy}\cos\varphi_0 - u_{xz}\sin\varphi_0)\theta_1^*(\xi, \mathbf{r}_\perp, t) + ((u_{xx} - u_{yy})\cos 2\varphi_0 + 2u_{xy}\sin 2\varphi_0)\varphi_1^*(\xi, \mathbf{r}_\perp, t)]\right\}, \quad (15)$$

where asterisks imply complex conjugation. We do not present explicit expressions for the coefficients N_1 and N_2, because they vanish after subsequent averaging of the solution to Eq. (14). Integrating Eq. (14) and averaging the obtained solution over a period of the acoustic wave yields the following expression for the DW drift velocity $V_{dr} = \overline{V}_2 = \overline{\partial Z_2}/\partial t$:

$$V_{dr} = R\rho\mu_1(\omega)k_x k_y(u_{0z})^2 + R\rho\mu_2(\omega) \times [k_x k_y(u_{0y}^2 - u_{0x}^2) + u_{0y}u_{0x}(k_y^2 - k_x^2)], \quad (16)$$

where $\mu_i(\omega)$ are the nonlinear DW mobilities,

$$\mu_1(\omega) = -\mu_0\frac{q_2^2}{[(1+\sigma-q_1)^2 + q_2^2][(\sigma-q_1)^2 + q_2^2]}, \qquad \mu_2(\omega) \approx \frac{\tau}{(1-q_1)^2 + q_2^2}. \quad (17)$$

Here, $\mu_0 = \pi z_0 g\gamma^2 M_0/(16\lambda\tilde{\lambda})$, $\tau = \eta\mu_0 \approx 1.2\times 10^5$ cm/s, and η is a numerical parameter. In estimating the drift velocity, we used the following parameters of iron borate [11, 13]: $z_0 \sim 10^{-4}$ cm, $\sigma \approx 2\times 10^4$, $g = 2.94\times 10^6$ (s Oe)$^{-1}$, $\gamma M_0^2 \sim 10^7$ erg/cm^3, $\mu_0 \approx 2.35\times 10^{19}$ cm/s, $\omega_0 \approx 1.4\times 10^{10}$ s^{-1}, and $\omega_r \approx 9.2\times 10^6$ s^{-1}.

Since the wavelength of the acoustic wave is much larger than the DW width (the relationship $\omega \ll 10^{10}$ s^{-1} corresponds to this condition), we have $q_1, q_2 \ll 1$. Hence, $\mu_2(\omega)$ depends on the frequency only weakly.

At the sound velocity $s = 4.71\times 10^5$ cm/s [11] and the limiting value of the strain tensor $ku_0 \sim 10^{-5}$, the DW drift velocity due to $\mu_2(\omega)$ can be as high as 10^{-5} cm/s.

The presence of the factor $R\rho$ in Eq. (16) for the DW drift velocity indicates that the stripe domain structure can drift as a whole. For this to happen, the vector **l** should rotate from one domain to another in the same direction.

Now, let us elucidate the dependence of the DW drift velocity on the acoustic-wave polarization. Since the wave propagates in the plane of the boundary (xy plane), the wave vector can be represented as $\mathbf{k} = (k_x, k_y, 0) = k(\cos\varphi_s, \sin\varphi_s, 0)$. The following polarizations of the wave are possible (Figs. 1–3).

(1) A transverse wave with the displacement vector perpendicular to the DW plane: $\mathbf{u} = u_0(0, 0, 1)$. In this

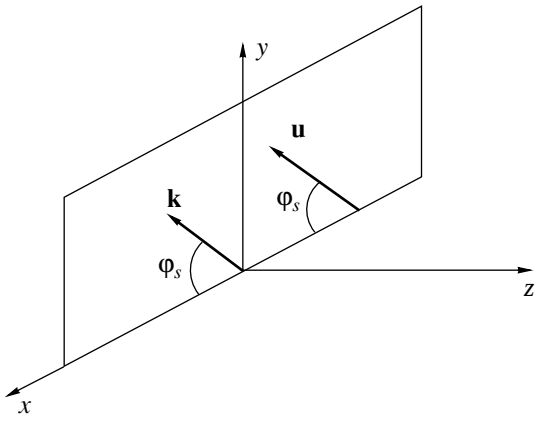

Fig. 3. Longitudinal wave.

case, the drift velocity given by Eq. (16) can be represented as

$$V_{\rm dr} = \frac{R\rho}{2}\mu_1(\omega)(k_t u_0)^2 \sin 2\varphi_s, \qquad (18)$$

where $k_t = \omega/s_t$, with s_t being the velocity of transverse sound.

(2) A transverse wave with the displacement vector in the DW plane: $\mathbf{u} = u_0(-\sin\varphi_s, \cos\varphi_s, 0)$. It follows from Eq. (16) that the drift velocity in this case is

$$V_{\rm dr} = \frac{R\rho}{2}\mu_2(\omega)(k_t u_0)^2 \sin 4\varphi_s. \qquad (19)$$

(3) A longitudinal wave with the displacement vector $\mathbf{u} = u_0(\cos\varphi_s, \sin\varphi_s, 0)$. The drift velocity of this wave is

$$V_{\rm dr} = -\frac{R\rho}{2}\mu_2(\omega)(k_l u_0)^2 \sin 4\varphi_s. \qquad (20)$$

Here, $k_l = \omega/s_l$, where s_l is the speed of the longitudinal sound.

It follows from Eqs. (18)–(20) that in the case of a sound wave propagating along a direction parallel to the DW plane, the DW can drift in both a longitudinal and a transverse acoustic wave. Equations (19) and (20) indicate that the drift of the domain structure defined by $\mu_2(\omega)$ occurs in opposite directions depending on the acoustic-wave type (transverse or longitudinal).

4. AN ACOUSTIC WAVE PROPAGATING PERPENDICULAR TO THE PLANE OF A DOMAIN WALL

Let us find solutions to the equations of motion (4) and (5) for the case when the sound wave propagates perpendicularly to the DW plane, $\mathbf{u} = \mathbf{u}_0\exp[i(k_z z - \omega t)]$. We introduce the collective coordinate of the DW center $Z(t)$, which, in contrast to the case considered above, does not depend on $\mathbf{r}_\perp$. The theory developed above can be generalized to this case. In the first-order perturbation theory, the sound also does not generate the DW drift but excites spin waves described by the relations

$$\varphi_1(\xi, t) = 0,$$
$$\theta_1(\xi, t) = \frac{\pi\gamma k^2 z_0}{8\lambda}\mathrm{Re}\{B(\xi)\exp[i(kZ - \omega t)]\}, \qquad (21)$$

where

$$B(\xi) = -\frac{z_0}{\pi}[\rho u_{0y} D_3(\xi) + iRu_{0x} D_4(\xi)] + b_1 f_k(\xi) + b_2 f_0(\xi),$$

$$D_3(\xi) = \sqrt{L}\int_{-\infty}^{\infty} \frac{f_p(\xi)\Omega(p, q)}{\cosh\dfrac{\pi z_0(p-k)}{2}}dp,$$

$$D_4(\xi) = \sqrt{L}\int_{-\infty}^{\infty} \frac{f_p(\xi)\Omega(p, q)}{\sinh\dfrac{\pi z_0(p-k)}{2}}dp,$$

$$b_1 = -\frac{2iR\sqrt{L}u_{0x}\Omega(k, q)}{\pi k z_0},$$

$$b_2 = \frac{\sqrt{2z_0}}{\sigma - q}\left(\frac{Ru_{0x}}{\cosh\dfrac{\pi k z_0}{2}} + \frac{i\rho u_{0y}}{\sinh\dfrac{\pi k z_0}{2}}\right),$$

$\Omega(n, q) = \{\sqrt{\lambda_n}(\lambda_n - q + \sigma)\}^{-1}$, $k = k_z$, and $\lambda_n = 1 + n^2 z_0^2$ $(n = p, k)$.

It is seen from these expressions that, in contrast to the case of the sound propagating in the DW plane, spin waves are excited only by transverse components of the field.

In the second-order perturbation theory, the DW drifts with velocity

$$V_{\rm dr} = \mu_{xx}(\omega)(ku_{0x})^2 + R\rho\mu_{xy}(\omega)(ku_{0x})(ku_{0y}) + \mu_{yy}(\omega)(ku_{0y})^2, \qquad (22)$$

where, at $\omega \ll 10^{10}$ s^{-1}, we have

$$\mu_{xy} = \eta_1\mu_0\frac{(kz_0)^2}{\sigma^2}, \quad \mu_{xx} = -\eta_2\mu_0\frac{kz_0 q_2}{\sigma^2}, \quad \mu_{yy} = -\eta_3\mu_0\frac{kz_0 q_2}{\sigma^2}. \qquad (23)$$

The numerical coefficients $\eta_1 \sim 1$, $\eta_2 \sim 0.05$, and $\eta_3 \sim 0.4$ are obtained as a result of estimating the expressions for $\mu_{ij}(\omega)$ in the long-wave limiting case. The nonlinear mobility μ_{xy} gives the main contribution the drift

velocity. The drift velocity due to this mobility is $V_{dr} \sim 0.1$ cm/s.

5. CONCLUSION

On the basis of the analysis carried out, it has been established that in a weak easy-plane ferromagnet, an isolated DW and a stripe domain structure can drift in an acoustic wave propagating along a direction either perpendicular or parallel to the DW plane. In the former case, the directional motion of DWs is caused by the transverse components of the acoustic wave. The drift velocity is maximum in an acoustic wave with two nonzero transverse components of the amplitude, u_{0x} and u_{0y}. When the acoustic wave propagates in the DW plane, the DW drift is due to both transverse and longitudinal components of the field. In this case, however, the DW drift velocity is much smaller than in the case of the acoustic wave propagating perpendicular to the DW plane.

REFERENCES

1. I. Bernal, C. W. Struck, and J. G. White, Acta Crystallogr. **16**, 849 (1963).
2. A. M. Kadomtseva, R. Z. Levitin, Yu. F. Popov, *et al.*, Fiz. Tverd. Tela (Leningrad) **14** (1), 214 (1972) [Sov. Phys. Solid State **14**, 172 (1972)].
3. V. G. Bar'yakhtar and B. A. Ivanov, Fiz. Met. Metalloved. **39** (4), 478 (1975).
4. A. K. Zvezdin, V. V. Kostyuchenko, and A. A. Mukhin, Preprint No. 209, FIAN SSSR (Lebedev Institute of Physics, Academy of Sciences of USSR, Moscow, 1983).
5. M. V. Chetkin, V. V. Lykov, and V. D. Tereshchenko, Fiz. Tverd. Tela (Leningrad) **32** (3), 939 (1990) [Sov. Phys. Solid State **32**, 555 (1990)].
6. M. V. Chetkin, V. V. Lykov, A. A. Makovozova, and A. G. Belonogov, Fiz. Tverd. Tela (Leningrad) **33** (1), 307 (1991) [Sov. Phys. Solid State **33**, 177 (1991)].
7. S. I. Denisov, Fiz. Tverd. Tela (Leningrad) **31** (11), 270 (1989) [Sov. Phys. Solid State **31**, 1992 (1989)].
8. V. S. Gerasimchuk and A. L. Sukstanskiĭ, Zh. Éksp. Teor. Fiz. **106** (4), 1146 (1994) [JETP **79**, 622 (1994)].
9. V. S. Gerasimchuk and A. L. Sukstanskiĭ, Zh. Éksp. Teor. Fiz. **118** (6), 1384 (2000) [JETP **91**, 1198 (2000)].
10. T. Egami, Phys. Status Solidi B **57**, 211 (1973).
11. B. A. Ivanov, A. L. Sukstanskiĭ, and A. V. Vershinin, Fiz. Tverd. Tela (Leningrad) **33** (7), 1978 (1991) [Sov. Phys. Solid State **33**, 1114 (1991)].
12. A. L. Sukstanskiĭ, Fiz. Tverd. Tela (Leningrad) **27** (11), 3509 (1985) [Sov. Phys. Solid State **27**, 2119 (1985)].
13. M. P. Petrov, G. A. Smolenskiĭ, A. P. Paugurt, *et al.*, Fiz. Tverd. Tela (Leningrad) **14** (1), 109 (1972) [Sov. Phys. Solid State **14**, 87 (1972)].

Translated by A. Poushnov

Physics of the Solid State, Vol. 45, No. 1, 2003, pp. 130–137. Translated from Fizika Tverdogo Tela, Vol. 45, No. 1, 2003, pp. 124–130.

MAGNETISM AND FERROELECTRICITY

Effect of a Magnetic Field on the Thermal and Kinetic Properties of the $Sm_{0.55}Sr_{0.45}MnO_{3.02}$ Manganite

A. M. Aliev*, Sh. B. Abdulvagidov*, A. B. Batdalov*, I. K. Kamilov*, O. Yu. Gorbenko, V. A. Amelichev**, A. R. Kaul'**, A. I. Kurbakov***, and V. A. Trunov*****

** Institute of Physics, Dagestan Scientific Center, Russian Academy of Sciences, ul. 26 Bakinskikh Komissarov 94, Makhachkala, 367003 Dagestan, Russia*

*** Moscow State University, Vorob'evy gory, Moscow, 119899 Russia*

**** St. Petersburg Institute of Nuclear Physics, Russian Academy of Sciences, Gatchina, Leningrad oblast, 188300 Russia*

e-mail: lowtemp@datacom.ru

Received November 27, 2001; in final form, April 1, 2002

Abstract—The temperature and magnetic-field dependences of the heat capacity, thermal conductivity, thermopower, and electrical resistivity of the $Sm_{0.55}Sr_{0.45}MnO_{3.02}$ ceramic material are studied in the temperature range 77–300 K and in magnetic fields up to 26 kOe. It is revealed that the quantities under investigation exhibit anomalous behavior due to a magnetic phase transition at the Curie temperature T_C. An increase in the magnetic field strength H leads to an increase in the Curie temperature T_C and a jump in the heat capacity ΔC_p at T_C. The temperature dependences of the measured quantities are characterized by hystereses that are considerably suppressed in a magnetic field of 26 kOe and depend neither on the thermocycling range nor on the rate of change in the temperature. The thermal conductivity K at temperatures above T_C shows unusual behavior for crystalline solids ($dK/dT > 0$) and, upon the transition to a ferromagnetic state, drastically increases as a result of a decrease in the phonon scattering by Jahn–Teller distortions. It is demonstrated that the hystereses of the studied properties of the $Sm_{0.55}Sr_{0.45}MnO_{3.02}$ manganite are caused by a jumpwise change in the critical temperature due to variations in the lattice parameters upon the magnetic phase transition. © *2003 MAIK "Nauka/Interperiodica".*

1. INTRODUCTION

Rare-earth substituted manganites with a perovskite structure are characterized by a unique combination of properties inherent in metals and dielectrics (and also properties exhibited by ionic and covalent crystals), the coexistence of ferromagnetic and antiferromagnetic ordering, phase separation, and giant magnetoresistance effects. This explains the considerable interest expressed by researchers in these physical objects. However, up to now, the nature of the anomalous properties observed in manganites has remained unclear. In particular, the giant magnetoresistance effect in conventional magnetic semiconductors is usually attributed to the strong indirect exchange interaction and the exchange-induced two-phase magnetic state. For manganites, this pattern is complicated by manifestations of the Jahn–Teller effect and a relative softness of the crystal lattice. As a consequence, the crystal structure of these compounds can undergo transformations under the action of temperature, magnetic fields, and pressure. A large number of models have been proposed for interpreting the unusual physical properties of manganites (see, for example, reviews [1–3]). In particular, the model of phase separation offers a satisfactory explanation of many experimental findings. However, this model also runs into certain problems [4–7]. In this respect, many researchers are inclined to believe that the great variety of properties of manganite materials cannot be interpreted in the framework of one particular model. Our interest in the $Sm_{1-x}Sr_xMnO_{3.02}$ ($x = 0.45$) manganite studied in the present work is associated with the following two factors: (i) owing to the large difference between the ionic radii of samarium and strontium ($r_{Sm} = 1.132$ Å and $r_{Sr} = 1.310$ Å), the intimate interrelation between the electronic, magnetic, and phonon subsystems (with the leading role played by the magnetic interactions) most clearly manifests itself in this compound, and (ii) the ferromagnetic metallic and antiferromagnetic dielectric phases can coexist in this system [8, 9]. The aim of the present work was to reveal these specific features. For this purpose, we experimentally investigated the temperature and magnetic-field dependences of the heat capacity, thermal conductivity, thermopower, and electrical resistivity of the $Sm_{0.55}Sr_{0.45}MnO_{3.02}$ ceramic material.

2. SAMPLE PREPARATION AND EXPERIMENTAL TECHNIQUE

The sample to be studied was prepared according to the procedure described earlier in [10]. Here, it should only be mentioned that the oxygen stoichiometric index

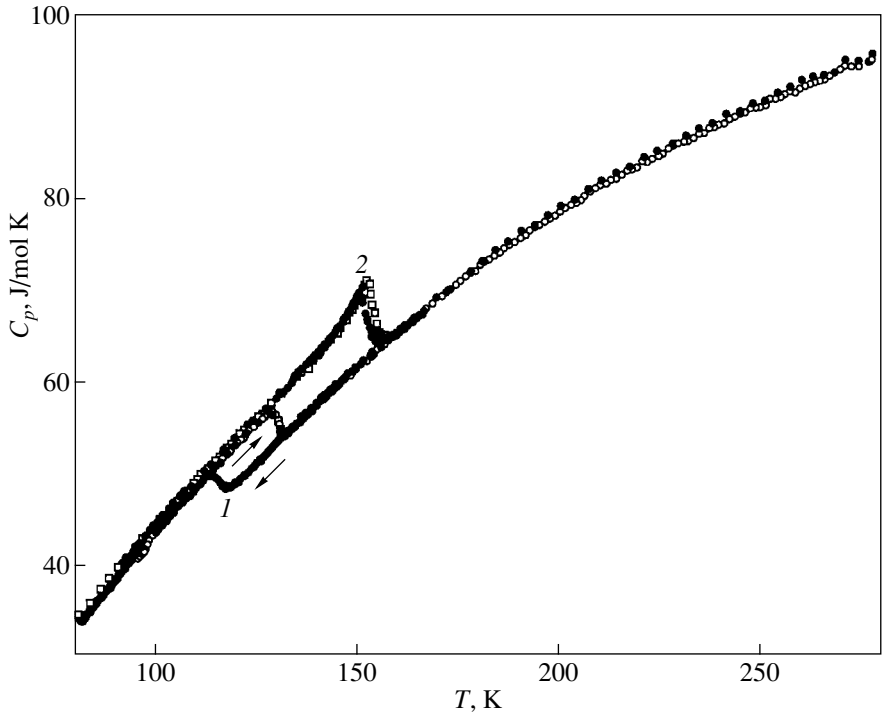

Fig. 1. Temperature dependences of the heat capacity of the $Sm_{0.55}Sr_{0.45}MnO_{3.02}$ manganite in magnetic fields H = (*1*) 0 and (*2*) 26 kOe.

was determined by iodometric titration [11] and proved to be 3.02(1). The content of Mn^{4+} ions was determined from data on the oxygen stoichiometry (with due regard for both the accuracy in the determination of the oxygen stoichiometry and the electroneutrality condition) and amounted to 47–49% of the total content of manganese ions. The heat capacity was measured using ac calorimetry [12]. The thermal conductivity was determined either by the method of stationary heat flux or as the product of the heat capacity C_p and the thermal diffusion coefficient η according to the technique described in [12]. This technique provides a means of performing measurements with a small temperature gradient across the sample ($\Delta T < 0.05$ K), which is especially important in studies in the vicinity of phase transitions. The electrical resistivity was measured using the standard four-point probe method. The magnetic field in the course of measurements was always directed perpendicularly to the heat flux.

3. RESULTS AND DISCUSSION

Figure 1 displays the temperature dependences of the heat capacity of the $Sm_{0.55}Sr_{0.45}MnO_{3.02}$ manganite in magnetic fields $H = 0$ and 26 kOe in the temperature range 80–280 K upon cooling and heating. The measurements of the heat capacity in a magnetic field were carried out after cooling of the sample to 77 K without a magnetic field. As can be seen from Fig. 1, the temperature dependences of the heat capacity of the $Sm_{0.55}Sr_{0.45}MnO_{3.02}$ sample both in the presence and in the absence of a magnetic field exhibit anomalies with a hysteresis in the vicinity of the Curie temperature T_C. The main specific features in the behavior of the heat capacity are as follows: the critical temperature depends on the magnetic field strength and the direction of the change in the temperature; in this case, an increase in the magnetic field strength is accompanied by an increase in the critical temperature and a decrease in the hysteresis width. Since the hysteresis in magnetic materials could be caused by long-term relaxation, the measurements were performed at different rates of change in the temperature and within different thermocycling ranges; however, the temperatures T_C and, hence, the values of ΔT_C remained unchanged. Note also that experimental points in the heat capacity curve for the $Sm_{0.55}Sr_{0.45}MnO_{3.02}$ manganite at temperatures below and above the transition cannot be approximated by a curve described by the Debye interpolation formula, as is the case with manganites of other compositions [13, 14]. This suggests that the phonon spectrum of the $Sm_{0.55}Sr_{0.45}MnO_{3.02}$ manganite substantially changes at the Curie temperature T_C and that the observed hystereses are associated with these changes.

The temperature dependences of the electrical resistivity of the $Sm_{0.55}Sr_{0.45}MnO_{3.02}$ manganite in magnetic fields $H = 0$ and 26 kOe upon cooling and heating are plotted in Fig. 2. As can be seen from this figure, the dependence of the electrical resistivity also exhibits a

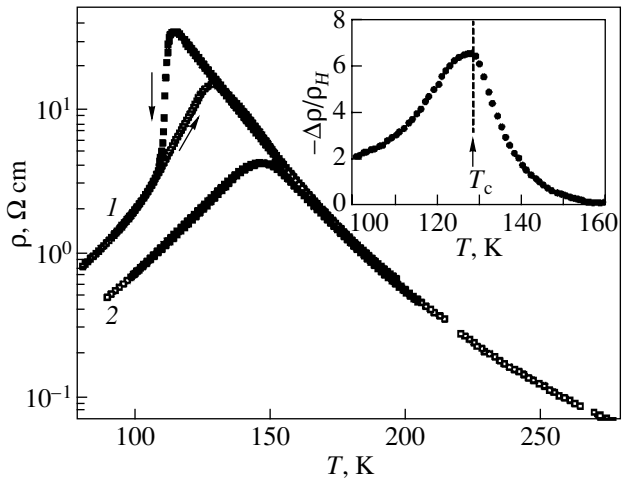

Fig. 2. Temperature dependences of the electrical resistivity of the $Sm_{0.55}Sr_{0.45}MnO_{3.02}$ manganite in magnetic fields H = (*1*) 0 and (*2*) 26 kOe. The inset shows the temperature dependence of the relative magnetoresistance $(\rho_0 - \rho_H)/\rho_H$ upon heating in a field of 26 kOe.

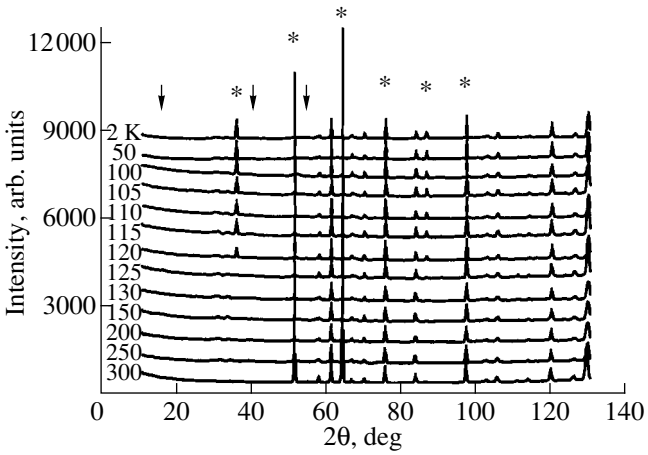

Fig. 3. Experimental neutron diffraction patterns of the $^{152}Sm_{0.55}Sr_{0.45}MnO_{3.02(1)}$ manganite at different temperatures. Asterisks mark the first (most intense) reflections attributed to the ferromagnetic phase. Arrows indicate positions at which the first reflections associated with the *A*-type antiferromagnetic phase (determined from the neutron diffraction pattern of the manganite with $x = 0.60$) should be observed.

hysteresis. This hysteresis is suppressed by the magnetic field and shifted to the high-temperature range, as is the case with the other quantities measured in our work. It can also be seen from Fig. 2 that the external magnetic field strongly suppresses the electrical resistivity, thus giving rise to a giant magnetoresistance effect, which is maximum in the vicinity of the Curie temperature T_C (see the inset in Fig. 2). Moreover, the crossover from semiconductor conductivity to metallic conductivity in the absence of a magnetic field occurs very sharply, whereas the reverse crossover (upon heating) proceeds in a gradual manner (Fig. 2).

In our earlier work [10], the experimental results were interpreted in the framework of the electron model of phase separation. Within this model, the $Sm_{0.55}Sr_{0.45}MnO_{3.02}$ manganite at $T < T_C$ can be represented as a dielectric matrix with embedded ferromagnetic metallic clusters. However, detailed analysis of more recent experimental data demonstrated that the results of measurements have defied unambiguous interpretation only in terms of the phase separation model. According to neutron diffraction investigations performed recently (the results of these investigations will be published in a separate work), no phase separation occurs in the $Sm_{0.55}Sr_{0.45}MnO_3$ manganite. At temperatures below T_C, the $Sm_{0.55}Sr_{0.45}MnO_3$ compound undergoes a phase transition to a homogeneous ferromagnetic state. This state is characterized by the magnetic moment $M = 3.36(5)\mu_B$/mol (where μ_B is the Bohr magneton) upon saturation at $T = 4$ K and corresponds to a nearly complete magnetic ordering without indications of the antiferromagnetic phase below T_C. Figure 3 displays the neutron diffraction patterns measured for the $^{152}Sm_{0.55}Sr_{0.45}MnO_{3.02(1)}$ manganite with a ^{152}Sm isotope at different temperatures and a neutron wavelength of 2.343 Å. The measurements were carried out on a G4.2 high-resolution neutron powder diffractometer situated in the neutron guide room of an ORPHEUS reactor (LLB, Saclay, France). The crystal structure for all temperatures is described by the space group *Pnma*. No additional peaks attributed to antiferromagnetic phases are observed at temperatures below $T \approx 130$ K. The result obtained turned out to be somewhat unexpected, because the investigations into the magnetic structure and transport properties of a sample with a close composition, namely, $^{154}Sm_{0.55}Sr_{0.45}MnO_3$, showed that, in this manganite, the low-temperature phase is magnetically inhomogeneous and the magnetization is substantially less than the theoretical value [15–17]. In order to confirm the reliability of the results obtained, we performed neutron diffraction analysis of a sample with a slightly different composition, namely, $Sm_{0.525}Sr_{0.475}MnO_3$. For this compound, the results were identical to those obtained earlier, which suggested the formation of a collinear ferromagnetic structure. Therefore, in Sm–Sr manganites, the homogeneous ferromagnetic state is observed in a narrow concentration range (in the vicinity of $x = 0.45$). Furthermore, in [8, 18], high magnetization ($\sim 3.3\mu_B$) was observed for a sample with a very close composition ($x = 0.44$). It seems likely that the high sensitivity of the physical properties to doping level is a specific feature of compounds in the $Sm_{1-x}Sr_xMnO_3$ system.

Moreover, the experimental neutron diffraction data obtained at temperatures close to T_C indicate a drastic decrease in the molar volume (lattice contraction) of the $Sm_{0.55}Sr_{0.45}MnO_{3.02}$ manganite upon transition to

the ferromagnetic phase. In our opinion, this is associated with the giant spontaneous magnetostriction. The space group (*Pnma*) remains the same over the entire temperature range; i.e., no structural phase transition occurs in accordance with the Ehrenfest and Landau classifications of phase transitions. The lattice parameters change in a specific manner: the rhombic base of the unit cell contracts sharply (the temperature dependences of the parameters *a* and *c* exhibit jumps), whereas the parameter *b* changes only slightly. The transition to the ferromagnetic phase is attended by ordering of MnO_6 octahedra. As a consequence, Jahn–Teller distortions of the lattice jumpwise decrease.

A change in the interatomic distances and angles in the plane of the unit cell base leads to an increase in the energy of the indirect exchange interaction between manganese ions and, hence, in the Curie temperature T_C corresponding to the ferromagnetic phase. The reverse transition from the ferromagnetic phase to the paramagnetic phase occurs in the crystal lattice with a different (higher, as follows from our data) temperature T_C'. This results in a hysteresis in the behavior of the studied properties of the $Sm_{0.55}Sr_{0.45}MnO_{3.02}$ manganite. The decrease in the difference $\Delta T_C = T_C' - T_C$ in a magnetic field can be explained by the following circumstance. Apart from the increase in the temperatures T_C and T_C' in a magnetic field, the lattice parameters of the $Sm_{0.55}Sr_{0.45}MnO_{3.02}$ manganite at temperatures below and above the phase transition point become closer to each other in magnitude owing to the giant magnetostriction, as is the case with a typical ferromagnet. Consequently, as follows from the above reasoning, the temperatures T_C and T_C' also become closer to each other and the difference ΔT_C decreases. In this respect, it should be noted that the notion of the Curie temperature T_C used in analyzing the magnetic phase transitions becomes conventional for systems with large hystereses. One further feature in the behavior of the heat capacity of the $Sm_{0.55}Sr_{0.45}MnO_{3.02}$ manganite is an increase in the jump $\Delta C_p(T)$ in a magnetic field. In our opinion, this can be caused by a drastic increase in the contribution of magnetic fluctuations to the heat capacity as the critical temperatures of the ferromagnetic and paramagnetic phases approach each other.

The field dependences of the heat capacity and the electrical resistivity (Fig. 4) are also worthy of notice. In a zero field, the $Sm_{0.55}Sr_{0.45}MnO_{3.02}$ sample at T = 147 K occurs in the paramagnetic state. An increase in the magnetic field to a certain critical field $H_c(T)$ (dependent on the temperature) leads to a magnetic phase transition, as judged from the increase in the heat capacity at H_c. The electrical resistivity begins to decrease drastically almost simultaneously with an increase in the heat capacity. This suggests that the delocalization of charge carriers occurs in the ferromagnetic phase and that the charge carriers in this phase possess a high mobility.

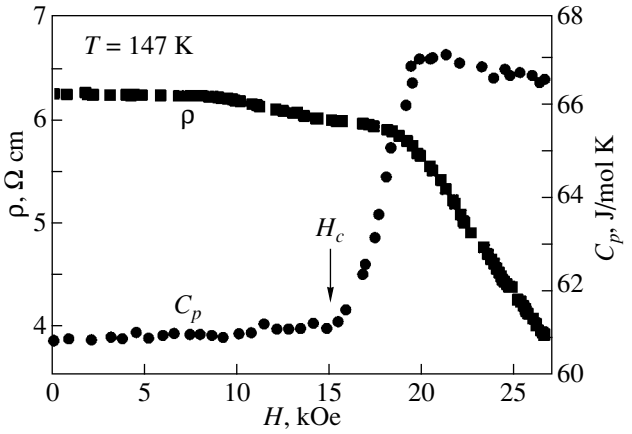

Fig. 4. Field dependences of the heat capacity and the electrical resistivity of the $Sm_{0.55}Sr_{0.45}MnO_{3.02}$ manganite.

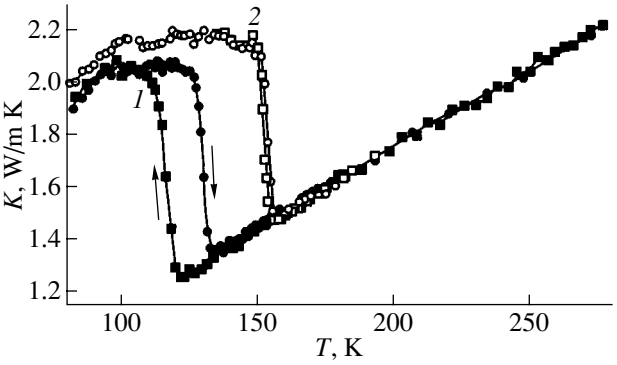

Fig. 5. Temperature dependences of the thermal conductivity of the $Sm_{0.55}Sr_{0.45}MnO_{3.02}$ manganite in magnetic fields H = (*1*) 0 and (*2*) 26 kOe.

Although it is universally accepted that the giant magnetoresistance effect and other unusual properties of manganites should be interpreted in terms of the double exchange mechanism with due regard for the electron–phonon interaction and that investigation of the thermal conduction is a proven way of revealing the specific features of this interaction, the thermal conduction in manganites remains poorly understood [19–22]. The temperature dependences of the thermal conductivity of the $Sm_{0.55}Sr_{0.45}MnO_{3.02}$ manganite upon heating and cooling in a zero magnetic field and a field of 26 kOe are shown in Fig. 5. The following specific features in the temperature dependence of the thermal conductivity are noteworthy: a sharp change in the phase transition range, anomalously small magnitudes (≤2 W/m K), unusual behavior of the dependence $K(T)$ ($dK/dT > 0$) for crystalline solids at temperatures above

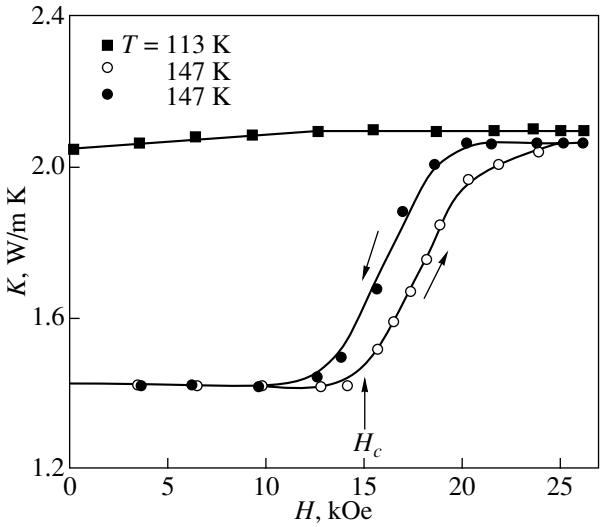

Fig. 6. Field dependences of the thermal conductivity of the $Sm_{0.55}Sr_{0.45}MnO_{3.02}$ manganite at different temperatures.

T_C, and the temperature hysteresis correlating with the hystereses of $C_p(T)$ and $\rho(T)$.

For magnetic materials, the total thermal conductivity can be represented as the sum of the electron (K_e), phonon (K_{ph}), and magnon (K_m) components: $K = K_e + K_{ph} + K_m$. These components each can contribute to the anomalies observed in the dependence $K(T)$. The estimation of the electron component K_e of the thermal conductivity with the use of the Wiedemann–Franz relationship $K_e = LT/\rho$ (where L is the Lorentz number) gives $K_e/K < 0.1\%$. Consequently, the electron component K_e does not make a noticeable contribution to the dependence $K(T)$. The magnon component can be estimated from the expression of the kinetic theory for thermal conductivity of magnons, which relates the heat capacity jump ΔC at T_C to the magnetic contribution: $K_m = \frac{1}{3}\Delta C v_m \tau_m$, where v_m and τ_m are the velocity of longitudinal magnons and their relaxation time, respectively. By using the experimental heat capacity jump $\Delta C = 2.5$ J/m^3 K and the characteristic values of $v_m = 600$ m/s and $\tau_m = 2 \times 10^{-12}$ s taken from [20], we obtain $K_m \approx 0.014$ W/m K. This value is negligible as compared to the anomalously large change in the thermal conductivity ($\Delta K \approx 0.8$ W/m K) at temperatures close to T_C. Furthermore, the measurements of the dependence $K(T)$ for an $La_{0.9}Ca_{0.1}MnO_3$ polycrystal revealed no noticeable anomalies at the Curie temperature T_C [19]. Therefore, we can draw the inference that the temperature dependence of the thermal conductivity of the $Sm_{0.55}Sr_{0.45}MnO_{3.02}$ manganite is determined by the specific features of phonon scattering.

The low values of the thermal conductivity and its behavior at $T > T_C$ ($kD/dT > 0$) recall the behavior of thermal conductivity of amorphous solids (for example, fused silica [23]). In these materials, the mean free path of phonons is limited by the size of structural units and a decrease in the heat transfer with a decrease in the temperature is due to a decrease in the thermal conductivity. A similar behavior is typical of ceramic samples in the case when grain-boundary scattering is the dominant mechanism of phonon scattering. However, taking into account the ratio of the phonon mean free path (~5.6 Å, see below) to the mean grain size (~2×10^4 Å) and the same behavior of the thermal conductivity observed for manganite single crystals [19, 20], the aforementioned circumstance cannot be used to explain the dependence $K(T)$ observed for manganites.

The mean free path of phonons l_{ph} can be estimated from the Debye relationship for phonon thermal conductivity $K_{ph} = \frac{1}{3} C_v v_s l_{ph}$ (where C_v is the heat capacity per unit volume and v_s is the velocity of sound), our experimental data on K_{ph} and C_v, and the available data on v_s [13, 24, 25]. In particular, from the data obtained at $T = 200$ K ($C_v = 1.86 \times 10^6$ J/m^3 K, $K_{ph} = 1.75$ W/m K, and $v_s = 5 \times 10^3$ m/s), we found $l_{ph} \approx 5.6$ Å. Hence, we can assume that the magnitudes of the structural distortions limiting the mean free path of phonons in manganites are of the order of the lattice parameter. The role of structural distortions can be played by Jahn–Teller local distortions of MnO_6 oxygen octahedra, which can significantly change upon phase transitions and in response to a magnetic field [24]. These distortions can drastically affect phonon heat transfer in these materials and bring about a sharp decrease in the phonon component K_{ph} upon transition to a paramagnetic (dielectric) phase. According to the neutron diffraction data, the transition to a ferromagnetic state is accompanied by symmetrization in the arrangement of oxygen octahedra due to a decrease in the Jahn–Teller distortions, which, in turn, results in a substantial increase in the thermal conductivity at temperatures below T_C. Visser *et al.* [19] and Cohn [20] analyzed the temperature and magnetic-field dependences of the thermal conductivity for different manganites (La–Sr–Mn–O, La–Ca–Mn–O, and other systems) and also reached the conclusion that the main mechanism limiting the phonon heat transfer in the materials studied is phonon scattering by Jahn–Teller static distortions. Upon transition to the ferromagnetic phase, these distortions disappear and, hence, the thermal conductivity increases.

As was noted above, the hysteresis in the behavior of $K(T)$ is associated with the difference in the critical temperatures corresponding to the ferromagnetic and paramagnetic phase.

The most important results were obtained in the study of the effect of a magnetic field on the thermal conductivity (Fig. 6). It can be seen from Fig. 6 that, in the ferromagnetic state ($T = 113$ K), the magnetic field only slightly affects the thermal conductivity K. This is

indirect evidence that the concentration of the ferromagnetic phase in the sample is close to saturation. At temperatures above T_C, the field dependence of the thermal conductivity K is similar to the field dependence of the heat capacity $C_p(H)$. An increase in the magnetic field to a certain critical value does not affect the thermal conductivity K. When the magnetic field strength H becomes high enough to restore the structural and magnetic orderings destroyed by the temperature, i.e., reaches the critical value H_c, the thermal conductivity increases drastically. The last circumstance is of particular importance: the observed effect of the magnetic field on the lattice thermal conductivity directly indicates that the lattice dynamics should be taken into account when constructing the theory explaining the mechanism of a giant magnetoresistance effect in perovskite manganites.

The sensitivity of the $Sm_{1-x}Sr_xMnO_3$ system to doping level can also be judged from the comparison of our results with the data obtained by Kasper *et al.* [26]. These authors measured the dependences $C_p(T)$, $K(T)$, and $S(T)$ for a sample of similar composition, namely, $Sm_{0.56}Sr_{0.44}MnO_{2.98}$ (in terms of the manganese valence, this sample efficiently corresponds to $Sm_{0.6}Sr_{0.4}MnO_3$), and did not observe specific features in the behavior of the studied quantities at temperatures close to T_C. It seems likely that, in [26], the authors did not perform measurements under different temperature conditions (upon cooling and heating). This can account for the absence of hystereses but cannot explain the absence of pronounced anomalies in the behavior of C_p and K. Possibly, the ratio of trivalent to tetravalent manganese ions in the sample plays a certain role. It is known that, in the case when these ions are contained in equal amounts, there occurs charge ordering accompanied by orbital ordering and the formation of a magnetic zigzag structure, which is referred to as the *CE* structure. The number of Mn^{4+} ions in our sample amounts to 47–49% of the total number of manganese ions; hence, charge ordering and related phenomena can play an important role (for comparison, this number in the sample studied in [26] amounts to 40% of the total number). However, we believe that such a large difference in the physical properties of $Sm_{0.55}Sr_{0.45}MnO_3$ and $Sm_{0.6}Sr_{0.4}MnO_3$ samples is associated with the qualitative difference in the magnetic structures of these manganites. According to the neutron diffraction data obtained in [15, 17], the manganite sample with $x = 0.40$ is characterized by three magnetically ordered phases, namely, ferromagnetic (below 130 K), *A*-type antiferromagnetic (below 120 K), and *CE*-type antiferromagnetic (below 160 K) phases, whereas the sample with $x = 0.45$ exists in a homogeneous ferromagnetic state at temperatures below the Curie point T_C.

It is generally believed that doping of lanthanum manganites with bivalent elements replacing La^{3+} should bring about the formation of holes and that, therefore, holes are charge carriers in manganites. The sign of the charge carriers is usually determined from the experimental data on the Hall effect or from the sign of the thermopower. In magnetic materials, the measurements of the Hall effect involve certain problems associated with the contribution of the so-called anomalous Hall effect, which is difficult to separate from the conventional Hall effect. For this reason, the sign of the charge carriers is often judged from the results of thermopower measurements. However, the experimental data on the thermopower of manganites are inconsistent with the concept of hole conduction. As a rule, the hole conduction manifests itself in lightly doped manganites ($x < 0.2$) and a complex dependence of the thermopower on the temperature and magnetic field is characteristic of manganites with an intermediate doping level ($0.2 < x < 0.5$) [26–28]. In this case, the thermopower S can reverse sign depending on the magnetic field H and the temperature T. Hundley and Neumeier [28] interpreted their results on the thermopower of $La_{1-x}Ca_xMnO_3$ manganites in the framework of a model according to which an increase in the temperature is accompanied by a redistribution of charge states of manganese ions in such a way that, in addition to Mn^{4+} and Mn^{3+} ions, there appear Mn^{2+} ions corresponding to hole carriers. Bivalent manganese ions possess a high mobility and provide the observed sign of the carriers. Bebenin *et al.* [29, 30] measured the Hall effect and the thermopower in manganites (both these quantities change sign with an increase in the temperature) and made the inference that there is a crossover from hole conduction to electron conduction. According to the authors' opinion, the change in the conduction type is caused by a shift of the mobility edge upon transition to the paramagnetic phase. Most likely, in the general case, the dependence $S(T)$ for manganites should be interpreted in terms of the two-band model, according to which carriers of different types predominate in different temperature ranges. Since charge carriers of both signs are involved in the conduction and the thermopower is determined as the difference between the corresponding contributions, the positive or negative sign of the thermopower implies the domination of the electron or hole contribution to the dependence $S(T)$. Our experimental dependences of the thermopower of the $Sm_{0.55}Sr_{0.45}MnO_{3.02}$ sample on the temperature T and the magnetic field H are plotted in Fig. 7. It can be seen that the thermopower is negative ($S < 0$) over the entire temperature range studied, is not very high (characteristic of metals) at temperatures below T_C, and drastically increases in magnitude upon transition to the paramagnetic phase. Moreover, the dependence of the thermopower exhibits a hysteresis similar to that observed in the dependences $\rho(T)$, $C_p(T)$, and $K(T)$.

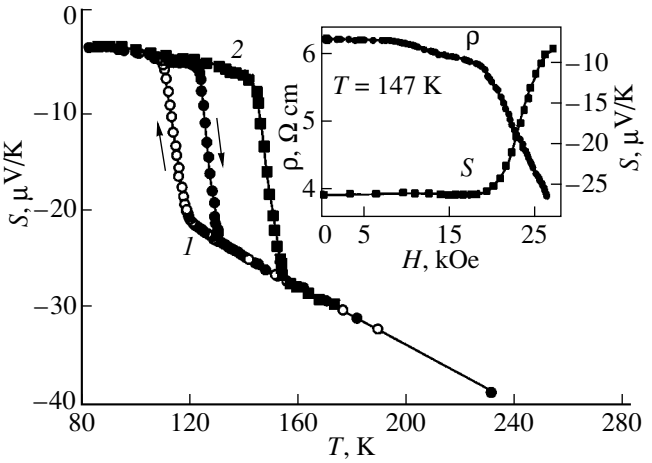

Fig. 7. Temperature dependences of the thermopower of the $Sm_{0.55}Sr_{0.45}MnO_{3.02}$ manganite in magnetic fields H = (*1*) 0 and (*2*) 26 kOe. The inset shows the field dependences of the thermopower and the electrical resistivity.

The dependences $S(T, H)$ can be explained using the Mott formula relating the quantity S and ρ; that is,

$$S = -\frac{\pi^2 k_B T}{3} \frac{\sigma'(\varepsilon_F)}{\sigma(\varepsilon_F)},$$

where k_B is the Boltzmann constant, e is the elementary charge, $\sigma(\varepsilon_F)$ is the conductivity at the Fermi level, and $\sigma'(\varepsilon_F) = \frac{\partial}{\partial \varepsilon}\sigma(\varepsilon)$.

Following Asamitsu and Moritomo [27], we can assume that $\sigma'(\varepsilon_F)$ = const and the conductivity $\sigma(\varepsilon_F) = \sigma$ (as in the isotropic case) is inversely proportional to the electrical resistivity; i.e., $\sigma^{-1} = \rho$. Therefore, the dependence of the thermopower S on H is completely determined by the dependence of the resistivity $\rho(H)$. Indeed, as can be seen from the inset in Fig. 7, the dependence $S(H)$ in a certain temperature range is similar to the dependence $\rho(H)$. Furthermore, the inequality $\left|\frac{\Delta S}{S_0}\right| > \left|\frac{\Delta \rho}{\rho}\right|$ is satisfied. Therefore, the giant magnetothermopower effect can be considered in addition to the giant magnetoresistance effect.

4. CONCLUSIONS

Thus, the above analysis of the experimental data on the heat capacity, thermal conductivity, thermopower, and electrical resistivity of the $Sm_{0.55}Sr_{0.45}MnO_{3.02}$ manganite sample allowed us to draw the following conclusions. (i) The temperature dependences of the studied quantities exhibit hystereses that correlate with each other and are suppressed by the magnetic field. (ii) The observed hystereses are caused by the change in the temperature T_C with variations in the lattice parameters (spontaneous magnetostriction) upon the magnetic phase transition. (iii) The anomalously small magnitudes of the thermal conductivity K and the features revealed in its temperature dependence are associated with local distortions of the crystal lattice, specifically with distortions of MnO_6 octahedra due to manifestations of the Jahn–Teller effect on Mn^{3+} ions. (iv) The dependence of the thermopower $S(H, T)$ should be interpreted in the framework of the two-band model.

ACKNOWLEDGMENTS

This work was supported by the Russian Foundation for Basic Research, project nos. 00-07-90241, 00-15-96662, 02-02-17895, and 02-07-06048.

REFERENCES

1. E. L. Nagaev, Phys. Rep. **346**, 387 (2001).
2. Yu. A. Izyumov and Yu. N. Skryabin, Usp. Fiz. Nauk **171**, 121 (2001) [Phys. Usp. **44**, 109 (2001)].
3. V. M. Loktev and Yu. G. Pogorelov, Fiz. Nizk. Temp. **26**, 231 (2000) [Low Temp. Phys. **26**, 171 (2000)].
4. N. N. Loshkareva, Yu. P. Sukhorukov, S. V. Naumov, *et al.*, Pis'ma Zh. Éksp. Teor. Fiz. **68**, 89 (1998) [JETP Lett. **68**, 97 (1998)].
5. A. I. Abramovich, R. V. Demin, L. I. Koroleva, *et al.*, Pis'ma Zh. Éksp. Teor. Fiz. **69**, 375 (1999) [JETP Lett. **69**, 404 (1999)].
6. I. F. Voloshin, A. V. Kalinov, S. E. Savel'ev, *et al.*, Pis'ma Zh. Éksp. Teor. Fiz. **71** (3), 157 (2000) [JETP Lett. **71**, 106 (2000)].
7. A. Machida, Y. Moritomo, E. Nishibori, *et al.*, Phys. Rev. B **62**, 3883 (2000).
8. C. Martin, A. Maignan, M. Hervieu, and B. Raveau, Phys. Rev. B **60**, 12191 (1999).
9. A. I. Abramovich, L. I. Koroleva, A. V. Michurin, *et al.*, Fiz. Tverd. Tela (St. Petersburg) **42**, 1451 (2000) [Phys. Solid State **42**, 1494 (2000)].
10. A. M. Aliev, Sh. B. Abdulvagidov, A. B. Batdalov, *et al.*, Pis'ma Zh. Éksp. Teor. Fiz. **72**, 668 (2000) [JETP Lett. **72**, 464 (2000)].
11. A. A. Bosak, O. Yu. Gorbenko, A. R. Kaul, *et al.*, J. Magn. Magn. Mater. **211**, 61 (2000).
12. Sh. B. Abdulvagidov, G. M. Shakhshaev, and I. K. Kamilov, Prib. Tekh. Éksp., No. 5, 134 (1996).
13. A. P. Ramirez, P. Schiffer, S.-W. Cheong, *et al.*, Phys. Rev. Lett. **76**, 3188 (1996).
14. M. N. Khlopkin, G. Kh. Panova, A. A. Shikov, *et al.*, Fiz. Tverd. Tela (St. Petersburg) **42**, 111 (2000) [Phys. Solid State **42**, 114 (2000)].
15. V. V. Runov, V. Yu. Chernyshev, A. I. Kurbakov, *et al.*, Zh. Éksp. Teor. Fiz. **118**, 1174 (2000) [JETP **91**, 1017 (2000)].
16. S. M. Dunaevskiĭ, A. I. Kurbakov, V. A. Trunov, *et al.*, Fiz. Tverd. Tela (St. Petersburg) **40**, 1271 (1998) [Phys. Solid State **40**, 1158 (1998)].
17. I. D. Luzyanin, V. A. Ryzhov, D. Yu. Chernyshov, *et al.*, Phys. Rev. B **64**, 094432 (2001).

18. F. Damay, N. Nguen, A. Maignan, *et al.*, Solid State Commun. **98**, 997 (1996).
19. D. W. Visser, A. P. Ramirez, and M. A. Subraminian, Phys. Rev. Lett. **78**, 3947 (1997).
20. J. L. Cohn, J. Supercond. **13**, 291 (2000).
21. K. H. Kim, M. Uehara, and S.-W. Cheong, Phys. Rev. B **62**, R11945 (2000).
22. S. Ulenbruck, B. Buchner, R. Gross, *et al.*, Phys. Rev. B **57**, R5571 (1998).
23. R. Berman, *Thermal Conduction in Solids* (Clarendon, Oxford, 1976; Mir, Moscow, 1979).
24. Yu. P. Gaĭdukov, N. P. Danilova, A. A. Mukhin, and A. M. Balbashov, Pis'ma Zh. Éksp. Teor. Fiz. **68**, 141 (1998) [JETP Lett. **68**, 153 (1998)].
25. R. G. Radaelli, M. Marezio, H. Y. Hwang, *et al.*, Phys. Rev. B **54**, 8992 (1996).
26. N. V. Kasper, A. Kattwinkel, N. Hamad, *et al.*, Physica B (Amsterdam) **292**, 54 (2000).
27. A. Asamitsu and Y. Moritomo, Phys. Rev. B **53**, R2952 (1996).
28. M. F. Hundley and J. J. Neumeier, Phys. Rev. B **55**, 11511 (1997).
29. N. G. Bebenin, R. I. Zaĭnullina, V. V. Mashkautsan, *et al.*, Fiz. Tverd. Tela (St. Petersburg) **43**, 482 (2001) [Phys. Solid State **43**, 501 (2001)].
30. N. G. Bebenin, R. I. Zaĭnullina, V. V. Mashkautsan, *et al.*, Zh. Éksp. Teor. Fiz. **113**, 981 (1998) [JETP **86**, 534 (1998)].

Translated by O. Borovik-Romanova

Physics of the Solid State, Vol. 45, No. 1, 2003, pp. 138–140. Translated from Fizika Tverdogo Tela, Vol. 45, No. 1, 2003, pp. 131–133.

MAGNETISM AND FERROELECTRICITY

Self-Propagating High-Temperature Synthesis and Magnetic Features of Fe–Al_2O_3 Granulated Films

V. G. Myagkov*, K. P. Polyakova*, G. N. Bondarenko, and V. V. Polyakov***

** Kirensky Institute of Physics, Siberian Division, Russian Academy of Sciences, Akademgorodok, Krasnoyarsk, 660036 Russia*

*** Institute of Chemistry and Chemical Technology, Siberian Division, Russian Academy of Sciences, Krasnoyarsk, 660036 Russia*

e-mail: miagkov@iph.krasn.ru

Received April 18, 2002

Abstract—The classical solid-phase reaction between Fe_2O_3 and Al layers in thin films is initiated. It is shown that, in the reaction products, Fe granulated films are formed in the Al_2O_3 nonconducting matrix. Analysis of the reaction equation demonstrates that the volume fraction of iron in the granulated films is less than the percolation threshold. This determines the magnetic properties of iron clusters in a superparamagnetic state. It is assumed that the nanocrystalline microstructure exists in thin films after solid-phase reactions proceeding under conditions of self-propagating high-temperature synthesis. *© 2003 MAIK "Nauka/Interperiodica".*

1. INTRODUCTION

Granulated films consisting of ferromagnetic nanoclusters contained in a nonconducting matrix have been intensively studied in recent years, because they exhibit very interesting properties, such as giant magnetoresistance [1], giant anomalous Hall effects [2], specific optical properties [3], and quantum-confinement effects [4]. From the practical point of view, these films can be used as media for magnetic and magneto-optical recording [5, 6]. Granulated magnetic films that contain nanoclusters of Fe, Ni, Co, and their alloys in SiO_2 and Al_2O_3 matrices have been the main subject of recent investigation in this field. A conventional method of producing metallic nanoclusters inside a nonconducting matrix in thin films is codeposition of a metal and an insulator onto a substrate. In this case, the nanoclusters are randomly distributed over the matrix and their size depends on the conditions of thermal annealing and deposition. However, the successive deposition of a metal and an insulator can result in self-organization in the formation of metallic nanoclusters [7]. The development of new techniques for preparing granulated samples is very important, because this makes it possible to extend the range of structural characteristics determining the physical properties of nanocomposites.

The purpose of this work was to investigate Fe nanogranulated films formed inside the Al_2O_3 matrix.

2. SAMPLE PREPARATION AND EXPERIMENTAL TECHNIQUE

The preparation procedure is based on initiating the classical solid-phase reaction in thin films:

$$Fe_2O_3 + 2Al = Al_2O_3 + 2Fe. \quad (1)$$

Earlier [8, 9], it was demonstrated that solid-phase reactions in bilayer thin films at high heating rates proceed under conditions of self-propagating high-temperature synthesis. The self-propagating high-temperature synthesis in thin films proceeds in the form of a surface combustion wave. This process is characterized by the initiation temperature T_0. In our case, the reagents for reaction (1) were bilayer and multilayer Al/Fe_2O_3 film samples, which were prepared by dc ion-plasma sputtering through successive deposition of Fe_2O_3 and aluminum layers without vacuum deterioration. The targets used in producing Al and Fe_2O_3 films were prepared in the form of wafers cut respectively from monolithic aluminum and a conducting ceramic coating of iron oxide, which was obtained by plasma deposition [10].

The films were evaporated on glass substrates at a temperature of ~320 K in an argon atmosphere at a pressure of 5×10^{-2} Pa. The evaporation rate was 0.3 nm/s for aluminum and 0.2 nm/s for iron oxide. The total thicknesses of the aluminum and iron oxide films lay within the ranges 15–50 and 40–120 nm, respectively. The samples obtained were heated at a rate no less than 20 K/s in order to initiate the wave of self-propagating high-temperature synthesis. For bilayer film samples, the solid-phase reaction proceeded at temperatures above the initiation temperature $T_0 \sim$ 800 K under conditions of self-propagating high-temperature synthesis. The front of the propagation of high-temperature synthesis, which was observed visually, is typical of self-propagating high-temperature synthesis in thin films [8, 9]. For multilayer film samples, the observation of the front of self-propagating high-temperature synthesis was hampered. For this rea-

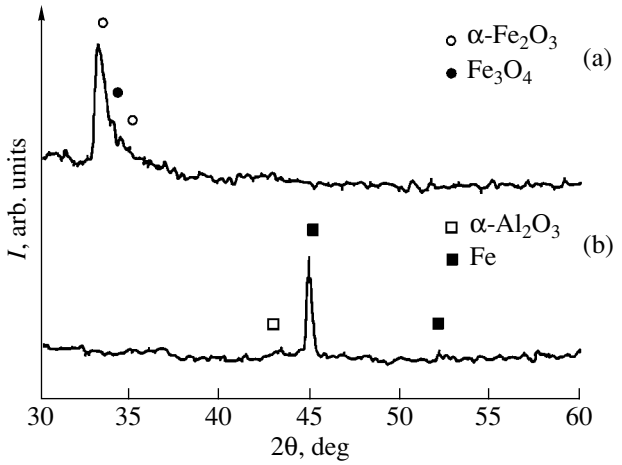

Fig. 1. X-ray diffraction patterns of the [Al(20 nm)/Fe_2O_3(40 nm)] × 4 multilayer film: (a) initial sample and (b) sample after thermal annealing at a temperature of 800 K for 10 min.

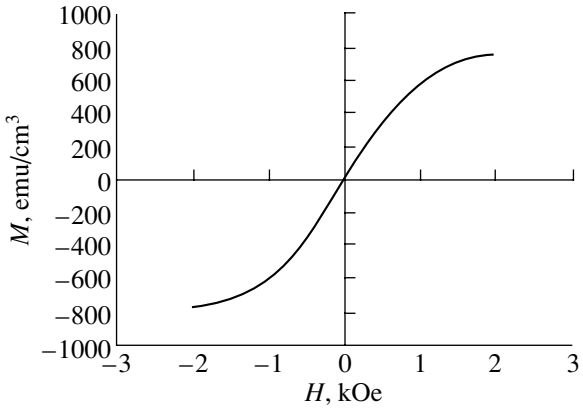

Fig. 2. Magnetization curve for the [Al(20 nm)/Fe_2O_3 (40 nm)] × 4 multilayer film after thermal annealing at a temperature of 800 K for 10 min. The magnetization is given per unit volume of iron.

son, these samples were subjected to thermal annealing through heating to a temperature 10–20 K higher than the initiation temperature T_0 and heat treatment at this temperature for 50 min (the time required for completing the reaction and subsequent annealing).

3. RESULTS AND DISCUSSION

Figure 1a shows a typical x-ray diffraction pattern for the [Al(20 nm)/Fe_2O_3(40 nm)] × 4 multilayer film sample prior to the solid-phase reaction. This pattern contains reflections attributed to α-Fe_2O_3. The formation of Fe_3O_4 in small amounts is also possible in the initial samples. The absence of reflections attributed to aluminum implies that aluminum is in an amorphous or finely crystalline state. After the solid-phase reaction (Fig. 1b), reflections from α-Fe_2O_3 and Fe_3O_4 disappear and the reflections assigned to iron and amorphous α-Al_2O_3 appear in the x-ray diffraction pattern. The presence of the reflections associated with Fe(110) in the x-ray diffraction patterns, along with other weak reflections or their complete absence, indicates that iron nanocrystallites are characterized by a preferred orientation of the (110) plane aligned parallel to the substrate surface. The size distribution of nanoclusters and the relative volume of the metallic fraction x are important factors responsible for the magnetic properties of granulated materials. It follows from the reaction equation that $x_r = 0.365$. This value is less than the percolation threshold x_p. For many granulated systems that contain metallic nanoclusters in a dielectric matrix, the percolation threshold is estimated as $x_p = 0.5$–0.6 [11]. This suggests that the metallic nanoclusters are separated from each other. The separation of iron nanoclusters is confirmed by a high resistivity of the samples, namely, $\rho = 10^{-6}$–10^{-4} Ω m, which is typical of metallic clusters in a nonconducting matrix below the percolation threshold.

The size of iron grains in the direction perpendicular to the sample surface was determined from the broadening of the diffraction peak of Fe(110) according to the Scherrer formula. The mean grain size was found to be 28 nm. As was shown by Chen *et al.* [12], particles with a smaller size exist in a one-dimensional state. Under the assumption that the iron cluster in other directions has the same size, the cluster should exhibit a magnetic single-domain structure. In this case, the sample can be treated as an ensemble of single-domain particles and its behavior can be described in terms of the Stoner–Wohlfahrt theory. The magnetization curve for an ensemble of single-domain particles has the form of a hysteresis loop with the following parameters: $M_r = 0.5M_S$ and $H_c = 0.958$ K/M_S (see, for example, [13]). Figure 2 depicts a typical magnetization curve for Fe–Al_2O_3 films obtained as a result of reaction (1). The absence of a hysteresis loop permits us to assume that the iron clusters predominantly occur in the superparamagnetic state. A similar hysteresis curve, which can be considered as a superposition of magnetization curves for iron nanoclusters in superparamagnetic and magnetic states, was observed earlier for Co–Ag granulated films [14]. The coexistence of the superparamagnetic and magnetic states can also be observed in ferromagnetic nanoclusters inside a nonconducting matrix [15]. The critical size below which the iron nanoclusters in the Al_2O_3 matrix are in the superparamagnetic state is approximately equal to 10 nm [12]. This suggests that the size distribution of iron nanoclusters in the samples under investigation is rather broad and covers sizes from several to tens of nanometers. It should be noted that no hysteresis loop is observed even at a temperature of 77 K. It follows that the blocking temperature T_B

for iron nanoparticles in the superparamagnetic state is below this temperature.

The reaction products are formed solely at the front of self-propagating high-temperature synthesis. The characteristic reaction time is determined from the formula $t = \tau/V_f^2$ where τ is the thermal diffusivity of the bilayer film sample and V_f is the front velocity at the initiation temperature of self-propagating high-temperature synthesis. Let us assume that τ is determined by the thermal diffusivity of the metal oxide; i.e., $\tau \sim (1–5) \times 10^{-7}$ m^2/s and $V_f \sim 1 \times 10^{-2}$ m/s [8, 9]. As a result, the characteristic reaction time is estimated as $t = (1–5) \times 10^{-3}$ s. Under the assumption that the reaction proceeds in the solid phase at a temperature close to the melting point of the metal and that the diffusion coefficient is determined to be $D \sim 10^{-12}$–10^{-14} m^2/s, the size of metallic clusters is estimated as $r \sim \sqrt{Dt} = (3–70)$ nm. This estimate is in good agreement with the aforementioned sizes of iron nanoclusters formed as a result of reaction (1). The dependence of the front velocity of self-propagating high-temperature synthesis V_f on the substrate temperature T_S ($T_S > T_0$) follows a law close to the Arrhenius law. Consequently, this velocity should determine the size distribution function and the mean size of iron nanoparticles. Therefore, the microstructure can be controlled both by varying the substrate temperature T_S upon initiating the self-propagating high-temperature synthesis in Al/Fe_2O_3 bilayer films and by choosing the conditions of subsequent heat treatment. In turn, the microstructure determines the magnetic properties of Fe–Al_2O_3 granulated films.

Note that the nanocrystalline microstructure should be predominant after passing the wave of self-propagating high-temperature synthesis in all the samples containing more than two phases in the reaction products. In particular, similar microstructure and magnetic properties are observed in Fe–TiO_2 films after the solid-phase reaction between Ti and Fe_2O_3 layers.

4. CONCLUSIONS

It was demonstrated that the solid-phase reactions proceeding under conditions of self-propagating high-temperature synthesis can be used for preparing granulated media. Specifically, the Fe–Al_2O_3 granulated films were obtained after the solid-phase reaction between Al and Fe_2O_3 layers. Analysis of the reaction equation proved that the volume fraction of iron is less than the percolation threshold. In the studied samples, the (110)-textured iron nanoclusters are in superparamagnetic and magnetic states.

ACKNOWLEDGMENTS

This work was supported by the Krasnoyarsk Regional Foundation for Research, project no. 11F001C.

REFERENCES

1. S. Mitani, S. Takahashi, K. Takahashi, *et al.*, Phys. Rev. Lett. **81** (13), 2799 (1998).
2. A. B. Pakhomov, X. Yan, and Y. Xu, J. Appl. Phys. **79** (8), 6140 (1996).
3. A. N. Drachenko, A. N. Yurasov, I. V. Bykov, *et al.*, Fiz. Tverd. Tela (St. Petersburg) **43** (5), 897 (2001) [Phys. Solid State **43**, 932 (2001)].
4. B. Raquet, M. Goiran, N. Negre, *et al.*, Phys. Rev. B **62** (24), 17144 (2000).
5. S. H. Liou and C. L. Chien, Appl. Phys. Lett. **52** (6), 512 (1988).
6. Z. S. Jiang, G. J. Jin, J. T. Ji, *et al.*, J. Appl. Phys. **78** (1), 439 (1995).
7. D. Babonneau, F. Petrov, J.-L. Maurice, *et al.*, Appl. Phys. Lett. **76** (20), 2892 (2000).
8. V. G. Myagkov and L. E. Bykova, Dokl. Akad. Nauk **354** (6), 777 (1997).
9. V. G. Myagkov, V. S. Zhigalov, L. E. Bykova, and V K. Mal'tsev, Zh. Tekh. Fiz. **68** (10), 58 (1998) [Tech. Phys. **43**, 1189 (1998)].
10. A. A. Lepeshev, V. N. Saunin, S. V. Telegin, *et al.*, Zh. Tekh. Fiz. **70** (5), 130 (2000) [Tech. Phys. **45**, 653 (2000)].
11. C. L. Chien, J. Appl. Phys. **69** (8), 5267 (1991).
12. C. Chen, O. Kitakami, and Y. Shimada, J. Appl. Phys. **84** (4), 2184 (1998).
13. M. Prutton, *Thin Ferromagnetic Films* (Butterworths, Washington, 1964; Sudostroenie, Leningrad, 1967).
14. S. Honda, M. Nawate, M. Tanaka, and T. Okada, J. Appl. Phys. **82** (2), 764 (1997).
15. Y. Xu, B. Zhao, and X. Yan, J. Appl. Phys. **79** (8), 6137 (1996).

Translated by N. Korovin

Physics of the Solid State, Vol. 45, No. 1, 2003, pp. 141–145. Translated from Fizika Tverdogo Tela, Vol. 45, No. 1, 2003, pp. 134–138.

MAGNETISM AND FERROELECTRICITY

Composition-Induced Transition of Spin-Modulated Structure into a Uniform Antiferromagnetic State in a $Bi_{1-x}La_xFeO_3$ System Studied Using ^{57}Fe NMR

A. V. Zalesskiĭ*, A. A. Frolov*, T. A. Khimich*, and A. A. Bush**

** Shubnikov Institute of Crystallography, Russian Academy of Sciences, Leninskiĭ pr. 59, Moscow, 119333 Russia*

e-mail: nmr@ns.crys.ras.ru

*** Moscow State Institute of Radio Engineering, Electronics, and Automation (Technical University), pr. Vernadskogo 78, Moscow, 117454 Russia*

Received March 20, 2002; in final form, April 26, 2002

Abstract—By analyzing the NMR line shape, the transformation of a spatially spin-modulated magnetic structure in $BiFeO_3$ into an ordinary spatially uniform structure of the $LaFeO_3$ orthoferrite in $Bi_{1-x}La_xFeO_3$ solid solutions is studied. The measurements are made using a spin-echo technique at temperatures of 77 and 4.2 K on ceramics with compositions $x = 0$, 0.1, 0.2, 0.61, 0.9, and 1.0 enriched by the ^{57}Fe isotope. It is shown that the spin-modulated structure disappears near the concentration $x = 0.2$, which corresponds, according to the published data, to the phase transition with a change in the unit-cell symmetry $R3c \longrightarrow C222$. A formula is obtained describing the NMR absorption line shape for the spin-modulated structure with account of local linewidth. Theoretical spectra adequately describe the evolution of the experimental spectrum in the concentration range $0 \le x \le 0.2$. Highly nonuniform local magnetic fields in the intermediate compositions make it impossible to detect NMR signals in a sample with $x = 0.61$. A uniform magnetic structure characterized by a single narrow line arises in the range of existence of a phase with the symmetry *Pnma* typical of the pure orthoferrite $LaFeO_3$.

The structure and properties of $BiFeO_3$ and its solid solutions were widely studied in the 1960s in connection with a great interest expressed at that time in magnetoelectrics, i.e., compounds possessing both magnetic (spin) and electric-dipole long-range ordering (see, e.g., monograph [1]). Bismuth ferrite $BiFeO_3$ is the most typical and extensively investigated representative of this class of compounds. In an early stage of studies, it was not known that $BiFeO_3$ also had a unique magnetic structure characterized by a spatial spin modulation of the cycloidal type, which was established using neutron diffraction in 1982 [2]. Antiferromagnetically ordered spins in such a structure rotate onto the plane containing the threefold axis (the *c* axis) of the rhombohedral unit cell of $BiFeO_3$, with the wave vector directed perpendicularly to this axis and the period $\lambda \approx 620$ Å being incommensurate with the lattice spacing.

A cycloid can be described by the equation [3, 4]

$$\cos\theta(x) = \mathrm{sn}\left(\pm\frac{4K(m)}{\lambda}x, m\right), \qquad (1)$$

where θ is the angle of spin rotation relative to the *c* axis, *x* is the coordinate along the cycloid propagation direction, $\mathrm{sn}(x, m)$ is the Jacobian elliptic function, *m* is its parameter, and $K(m)$ is a complete elliptic integral of the first kind.

Indirect evidence of the existence of a spatially spin-modulated structure (SSMS) in $BiFeO_3$ follows from studies of the mangnetoelectric effect, which is still given much attention [5–7].

The existence of an SSMS in $BiFeO_3$ has recently been confirmed in ^{57}Fe NMR studies [8, 9]. The rotation of spins in the plane of a cycloid results in the appearance of an NMR frequency band due to the anisotropic contribution to the local magnetic field H_n at ^{57}Fe nucleus sites. The anisotropic NMR frequencies in $BiFeO_3$ are described by the expression [8]

$$\nu(\theta) \approx \nu_\parallel - (\nu_\parallel - \nu_\perp)\sin^2\theta = \nu_\parallel - \delta\nu\sin^2\theta, \qquad (2)$$

where $\nu_\parallel$ and $\nu_\perp$ are the frequencies corresponding to the parts of the cycloid where the spins are oriented parallel and perpendicular to the *c* axis, respectively. Due to the specific density distribution of H_n (or of the NMR frequencies) in the coordinate *x* or in the angle θ for the cycloid, two edge absorption peaks arise in an NMR frequency band at the frequencies $\nu_\parallel$ and $\nu_\perp$ with a characteristic dip between them. The experimental NMR spectrum for $BiFeO_3$ at 77 K is shown in Fig. 1a (curve *1*). The profile of such an NMR line $P(\nu)$ for the SSMS in

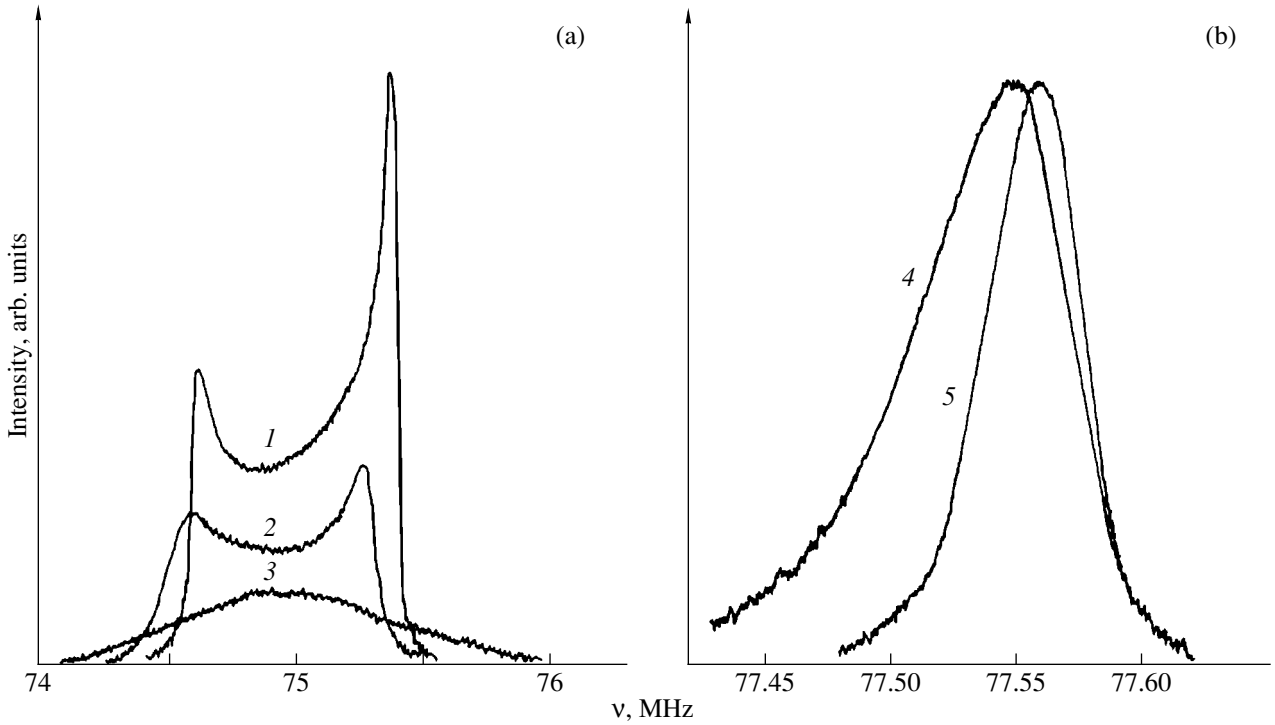

Fig. 1. Experimental ^{57}Fe NMR spectra for $Bi_{1-x}La_xFeO_3$ solid solutions with x = (*1*) 0, (*2*) 0.1, (*3*) 0.2, (*4*) 0.9, and (*5*) 1.0 at 77 K.

the case where the local line shape is represented by a δ function was calculated in [8] to be

$$P(\nu) \sim \{(\nu_\parallel - \nu)^{1/2}(\nu - \nu_\perp)^{1/2}[1/m - (\nu - \nu_\perp)/\delta\nu]^{1/2}\}^{-1}, \quad (3)$$

where ν is the running frequency.

The important feature of such a spectrum is the possibility of estimating the degree of anharmonicity of the cycloid by analyzing the shape of the spectrum. From Eqs. (1) and (3) it follows that if $m \longrightarrow 0$, the cycloid is sinusoidal and the spectrum has a symmetrical shape with edge peaks of equal heights and a minimum between them. If $m \longrightarrow 1$, the cycloid becomes more anharmonic, the ratio of the height of the higher frequency peak at the frequency $\nu_\parallel$ to that of the lower frequency peak at $\nu_\perp$ increases, and the dip minimum shifts towards $\nu_\perp$. Spectrum *1* in Fig. 1a gives evidence of an essential anharmonism of the cycloid in $BiFeO_3$.

From above, it follows that NMR allows one, comparatively easily, (in contrast with neutronography) not only to identify SSMS but also to obtain additional information about its properties.

In this connection, it would be advisable to use NMR for studying the transitions associated with the appearance or disappearance of an SSMS, for example, the transition to an ordinary spatially uniform magnetic structure. According to magnetoelectric-effect data [5–7], such a transition in $BiFeO_3$ takes place in strong magnetic fields (≈200 kOe). Unfortunately, a high-field NMR technique is not presently available. That is why we chose a simpler scenario, wherein the transition to a uniform magnetic structure is caused by a change in the composition of a binary solid solution in which one of the components is $BiFeO_3$ and the other component is an antiferromagnet with a uniform magnetic structure. As the latter component, the $LaFeO_3$ orthoferrite was chosen. The structure and properties of the $Bi_{1-x}La_xFeO_3$ system were studied in [10–14]. Ceramic samples of this system were studied in [10–12]. Four almost equal compositional phase ranges were found: $0 < x < 0.19$ (I), $0.2 < x < 0.5$ (II), $0.55 < x < 0.73$ (III), and $0.75 < x < 1.0$ (IV). In range I, there exists a phase with a rhombohedral unit cell (space group *R*3*c*) inherent in the pure $BiFeO_3$ compound, the compounds in range IV have the orthorhombic structure (space group *Pnma*) inherent in orthoferrites, and the intermediate phases, II and III, are characterized, as in [12], as orthorhombic.

Within the whole concentration range $0 \le x \le 1.0$, there exists a magnetic ordered state; the Néel temperature varies almost linearly with increasing x: from 643 K for $BiFeO_3$ to 738 K for $LaFeO_3$. Ferroelectric properties disappear at $x = 0.5$ according to [10, 11] or at $x = 0.75$ (in the vicinity of a boundary between phases III and IV) according to [12].

Publications [13, 14] were devoted to studies of the $Bi_{1-x}La_xFeO_3$ system performed on single crystals grown using spontaneous crystallization from the melt. Instead of the four phases I–IV, the authors of [13, 14]

found six phases, among them a low-symmetry triclinic phase (space group $P1$) in the range $0.06 < x < 0.24$ into which the $BiFeO_3$ structure transforms at $x > 0.06$. Ground crystals of one of the compositions ($Bi_{0.93}La_{0.07}FeO_3$) were studied using neutron diffraction [15]. However, the question of the existence of an SSMS in this composition remained open.

We studied the NMR spectra for samples with compositions $x = 0$, 0.1, 0.2, 0.61, 0.9, and 1.0. The sample with $x = 0$ was the same polycrystalline $BiFeO_3$ that was used in our previous NMR studies [8, 9]. The samples were prepared using the standard ceramic technology from the starting reagents Bi_2O_3, La_2O_3, and Fe_2O_3. In all cases, Fe_2O_3 enriched by the ^{57}Fe isotope up to 95.43 wt % was used. Solid-state synthesis and the mixture sintering were performed by increasing the temperature of calcination stepwise followed by cooling of the sample in a turned-off furnace. The sintering temperature increased with increasing La content from 800°C ($x = 0$) to 1250°C ($x = 1$).

The phase composition and the crystallographic characteristics of samples were determined with the help of an x-ray diffractometer DRON-4 (CuK_α radiation) by using the powder method with Ge powder as an internal reference. The lattice parameter of cubic Ge crystals was taken to be $a = 5.653$ Å.

Within an accuracy of 1–3%, the samples were found to be perovskite-like single-phase $Bi_{1-x}La_xFeO_3$ solid solutions. Their structural characteristics are given in Table 1.

NMR was observed using a spin-echo method in a zero magnetic field with the help of a semicommercial frequency-scanning pulsed radiospectrometer ISSh-1-13M (manufactured at the Institute of Radio Engineering and Electronics, Russian Academy of Sciences). The measurements were carried out at 77 and 4.2 K.

The spectra obtained at 77 K for compositions $x = 0.1$ and 0.2 are shown in Fig. 1a (curves *2*, *3*, respectively). For the $Bi_{0.9}La_{0.1}FeO_3$ sample, the double-peaked NMR spectrum typical of the SSMS is observed. For the $Bi_{0.8}La_{0.2}FeO_3$ sample, whose composition corresponds to the transitional range between phases I and II, the spectrum consists of a single broad maximum at a frequency of $\nu_{max} \approx 75$ MHz and has no edge peaks. The attempt to detect an NMR signal from the sample with $x = 0.61$ was unsuccessful despite the close-to-100% abundance of the ^{57}Fe isotope, which was most likely associated with the highly nonuniform local fields H_n in the intermediate orthorhombic phases. As the composition approached that of lanthanum orthoferrite in the range of phase IV, a single narrow line characteristic of a uniform magnetic structure appeared. For pure $LaFeO_3$, a narrow symmetric line with a halfwidth of only 500–600 kHz was observed (curve *5*, Fig. 1b; we note that the frequency scales in Figs. 1a, 1b differ by a factor of 10). The echo excitation conditions (pulses were 15 and 30 μs long at a high rf power) for the samples with $x = 0.9$ and 1.0 (possessing weak ferromagnetism) corresponded to the NMR lines for the nuclei in domains. Substitution of Bi for La (sample with $x = 0.9$, curve *4* in Fig. 1b) results only in an asymmetric broadening of the NMR line and a slight shift of the center of gravity of the line towards lower frequencies due to the appearance of a nonequivalent surrounding of oxygen anions involved in spin density transfer via the Fe–O–Fe superexchange coupling.

Table 1. Symmetry; lattice parameters a, b, c, α; and unit-cell volume V/z of $Bi_{1-x}La_xFeO_3$ solid solutions (z is the number of formula units in the unit cell)

x	Symmetry, phase	a, b, c, Å; α, deg	V/z, Å^3
0	Rhombohedral, *R*3*c*, I	$a = 3.963(2)$; $\alpha = 89.43(3)$	$V/z = 62.2(2)$, $z = 1$
0.1	Rhombohedral, *R*3*c*, I	$a = 3.959(2)$; $\alpha = 89.50(3)$	$V/z = 62.1(2)$, $z = 1$
0.2	Orthorhombic, *C*222, II	$a = 5.598(5)$, $b = 5.617(5)$, $c = 3.904(2)$	$V/z = 61.4(2)$, $z = 2$
0.61	Orthorhombic, $C222_1$, III	$a = 5.544(5)$, $b = 5.576(5)$, $c = 7.863(3)$	$V/z = 60.8(2)$, $z = 4$
0.9	Orthorhombic, *Pnma*, IV	$a = 5.543(5)$, $b = 5.564(5)$, $c = 7.856(3)$	$V/z = 60.2(2)$, $z = 4$
1.0	Orthorhombic, *Pnma*, IV	$a = 5.549(5)$, $b = 5.564(5)$, $c = 7.859(3)$	$V/z = 60.7(2)$, $z = 4$

The NMR spectra at 4.2 K have the same shape as those at 77 K, but all resonance frequencies are shifted towards higher values. The frequencies $\nu_\parallel$, $\nu_\perp$, and ν_{max} for the samples at 4.2 and 77 K are given in Table 2.

In order to theoretically describe the changes occurring in spectra upon the substitution of La for Bi, one should pass from simple equation (3), in which the δ function is taken as a local line shape function $f[\nu - \nu(\theta)]$, to a model which takes into account a finite local linewidth. For this purpose, we apply the method of calculation of the NMR absorption line shape used by Butler [16] in studying NMR in domain walls whose magnetic structure possesses a similar 180° periodicity. In contrast to domain walls, there is no need to consider the enhancement factor, since, as was shown in [8], the enhancement mechanism is ineffective in $BiFeO_3$. According to [16], the profile $P(\nu)$ of an NMR absorption line for a 180°-periodic structure is given by

$$P(\nu) = \int_0^\pi I(\theta)[\nu - \nu(\theta)]d\theta, \qquad (4)$$

Table 2. Frequencies $\nu_{\|}$, $\nu_{\perp}$, and ν_{max} for samples of various compositions of the $Bi_{1-x}La_xFeO_3$ system at 77 and 4.2 K

x	$\nu_{\|}$, MHz		$\nu_{\perp}$, MHz		ν_{max}, MHz	
	77 K	4.2 K	77 K	4.2 K	77 K	4.2 K
0	75.35	75.58	74.60	75.00		
0.1	75.25	75.50	74.60	74.90		
0.2					74.9–75.0	75.3–75.4
0.9					77.55	77.80
1.0					77.56	77.81

where $I(\theta)$ is the intensity of the signal in the part of the cycloid where spins make an angle θ with the c axis. The function $I(\theta)$ for the cycloidal magnetic structure in $BiFeO_3$ was calculated in [8] to be

$$I(\theta) \propto (m^{-1} - 1 + \sin^2\theta)^{-1/2}. \quad (5)$$

In order to take into account the finite width of a local line, we will describe the line using a Lorentzian with width Δ independent of the angle θ:

$$f[\nu - \nu(\theta)] = \frac{\Delta}{\pi}\frac{1}{\Delta^2 + (\nu - \nu(\theta))^2}. \quad (6)$$

Substituting Eqs. (2) and (5) into Eq. (4), we obtain

$$P(\nu) \propto \int_0^{\pi} (m^{-1} - 1 + \sin^2\theta)^{-1/2} \times [\Delta^2 + (\nu - \nu_{\|} + \delta\nu\sin^2\theta)^2]^{-1} d\theta. \quad (7)$$

The integration is conveniently performed by introducing dimensionless parameters:

$$\xi = (\nu - \nu_{\|})/\delta\nu; \quad \delta\nu/\Delta. \quad (8)$$

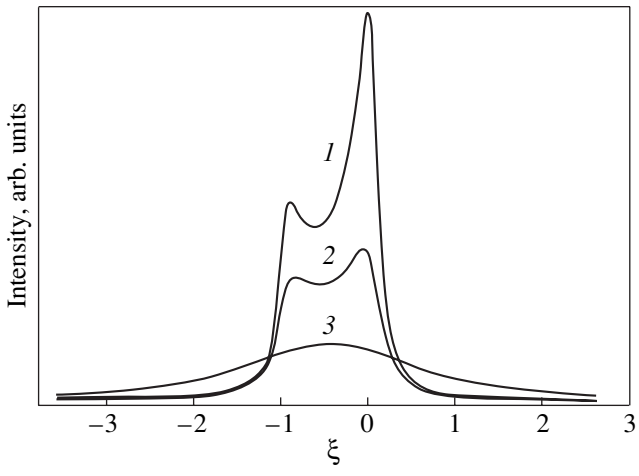

Fig. 2. Theoretical profile of the NMR lines obtained by calculating the integral in Eq. (9) with parameters $\delta\nu/\Delta$ and m equal to (*1*) 10, 0.83; (*2*) 6, 0.5; and (*3*) 1, 0.5, respectively.

From Eq. (8), it follows that $\xi = -1$ corresponds to the frequency $\nu_{\perp}$ ($\theta = \pi/2$) and $\xi = 0$, to the frequency $\nu_{\|}$ ($\theta = 0$). The integral in Eq. (7) reduces to

$$P(\nu) \propto \int_0^{\pi} (m^{-1} - 1 + \sin^2\theta)^{-1/2} \times [1 + (\delta/\nu/\Delta)^2(\sin^2\theta - \xi)^2]^{-1} d\theta. \quad (9)$$

Calculated curves *1–3* in Fig. 2 correspond to experimental spectra *1–3* in Fig 1a, respectively (the values of parameters m and $\delta\nu/\Delta$ used in calculating the integral in Eq. (9) are given in the caption to Fig. 2). Theoretical spectra well reproduce the line shape evolution caused by the substitution of La for Bi atoms within the concentration range $0 < x < 0.2$. The main cause of changes in the NMR spectra is the increased nonuniformity of local fields H_n, which results in an increase in the linewidth Δ. Indeed, for $BiFeO_3$, the value of Δ in frequency units is 75 kHz, whereas for the composition $x = 0.1$, $\Delta = 125$ kHz. Furthermore, the fact that the peaks tend to be equal in height and that m decreases from 0.83 to 0.5 indicates that the cycloid becomes more harmonic. When the local line shape Δ becomes comparable in magnitude with the frequency anisotropy $\delta\nu = 0.75$ MHz, the spectrum smears into a single broad line (curves *3* in Figs. 1a, 2) and looses the basic feature (two edge peaks) inherent in an SSMS. However, the fact that the NMR frequencies remain distributed over the range between $\nu_{\|}$ and $\nu_{\perp}$ suggests that the sample with composition $x = 0.2$ contains regions with spins distributed in the angle θ, although according to x-ray analysis, the crystal structure of the sample is orthorhombic (Table 1). Obviously, a further increase in the nonuniformity of H_n with increasing La concentration should result in such a large spread of NMR frequencies that the conditions for the formation of a pronounced NMR line will no longer be able to be fulfilled. This is the reason why NMR was not observed in the sample with $x = 0.61$. The conditions for NMR observation are restored only for compositions close to that of pure lanthanum orthoferrite.

From the results of the present NMR studies it follows that the SSMS is destroyed in a concentration range close to $x = 0.2$, which, according to the data pre-

sented in [10–12], corresponds to the transformation of rhombohedral phase I into orthorhombic phase II. Our results do no confirm the existence at $0 < x < 0.2$ of the triclinic phase identified in single crystals in [13, 14]. For the theoretical analysis of the NMR spectra, the local linewidth and its dependence on x had to be taken into account. With an increase in La concentration above $x = 0.2$ (in regions II and III), a large nonuniformity of H_n arises, which hinders the NMR observation. A uniform antiferromagnetic structure forms only in region IV, where a narrow single-peaked NMR line is observed.

ACKNOWLEDGMENTS

This study was supported by the Russian Foundation for Basic Research, project no. 02-02-16369.

REFERENCES

1. Yu. N. Venevtsev, V. V. Gagulin, and V. R. Lyubimov, *Magnetoelectrics* (Nauka, Moscow, 1982).
2. I. Sosnowska, T. Peterlin-Neumaier, and E. Steichele, J. Phys. C **15**, 4835 (1982).
3. I. Sosnowska and A. K. Zvezdin, J. Magn. Magn. Mater. **140–144**, 167 (1995).
4. M.-M. Tehranchi, N. F. Kubrakov, and A. K. Zvezdin, Ferroelectrics **204**, 181 (1997).
5. Yu. F. Popov, A. K. Zvezdin, G. P. Vorob'ev, *et al.*, Pis'ma Zh. Éksp. Teor. Fiz. **57** (1), 65 (1993) [JETP Lett. **57**, 69 (1993)].
6. Yu. F. Popov, A. M. Kadomtseva, G. P. Vorob'ev, and A. K. Zvezdin, Ferroelectrics **162**, 135 (1994).
7. A. M. Kadomtseva, Yu. F. Popov, G. P. Vorob'ev, and A. K. Zvezdin, Physica B (Amsterdam) **211**, 327 (1995).
8. A. V. Zalessky, A. A. Frolov, T. A. Khimich, *et al.*, Europhys. Lett. **50** (4), 547 (2000).
9. A. V. Zalesskiĭ, A. K. Zvezdin, A. A. Frolov, and A. A. Bush, Pis'ma Zh. Éksp. Teor. Fiz. **71** (11), 682 (2000) [JETP Lett. **71**, 465 (2000)].
10. Yu. E. Roginskaya, Yu. N. Venevtsev, S. A. Fedulov, and G. S. Zhdanov, Kristallografiya **8** (4), 610 (1963) [Sov. Phys. Crystallogr. **8**, 490 (1963)].
11. Yu. E. Roginskaya, Yu. N. Venevtsev, and G. S. Zhdanov, Zh. Éksp. Teor. Fiz. **44** (4), 1418 (1963) [Sov. Phys. JETP **17**, 955 (1963)].
12. M. Polomska, W. Kaczmarek, and Z. Pajak, Phys. Status Solidi A **23**, 567 (1974).
13. V. A. Murashov, D. N. Rakov, I. S. Dubenko, *et al.*, Kristallografiya **35** (4), 912 (1990) [Sov. Phys. Crystallogr. **35**, 538 (1990)].
14. Z. V. Gabbasova, M. D. Kuz'min, A. K. Zvezdin, *et al.*, Phys. Lett. A **158**, 491 (1991).
15. I. Sosnovska, R. Przenioslo, F. Fisher, and V. A. Murashov, J. Magn. Magn. Mater. **160**, 384 (1996).
16. M. A. Butler, Int. J. Magn. **4**, 131 (1973).

Translated by A. Zalesskiĭ

Physics of the Solid State, Vol. 45, No. 1, 2003, pp. 146–153. Translated from Fizika Tverdogo Tela, Vol. 45, No. 1, 2003, pp. 139–146.

MAGNETISM AND FERROELECTRICITY

A Study of Magnetic Ordering in $LaMnO_{3+\delta}$ Single Crystals

S. N. Barilo*, V. I. Gatal'skaya*, S. V. Shiryaev*, G. L. Bychkov*, L. A. Kurochkin*, S. N. Ustinovich*, R. Szymczak, M. Baran**, and B. Krzymańska****

** Institute of Solid-State and Semiconductor Physics, National Academy of Sciences, Minsk, 220072 Belarus*

e-mail: v_gatal@ifttp.bas-net.by

*** Institute of Physics, Polish Academy of Sciences, Warsaw, 02-668 Poland*

Received May 10, 2002

Abstract—The magnetic state of $LaMnO_{3+\delta}$ single crystals with different contents of nonstoichiometric oxygen grown by electric deposition is studied by measuring the temperature and field dependences of magnetization for different orientations of a magnetic field. The results obtained are analyzed in terms of a two-phase magnetic-state model. © *2003 MAIK "Nauka/Interperiodica".*

1. INTRODUCTION

The continuous interest in substituted lanthanum manganites $La_{1-x}A_xMnO_3$ (*A* stands for the doping divalent or monovalent ion) stems from the fact that these compounds exhibit a remarkable variety of properties important both from the standpoint of science and application. In particular, these compounds exhibit colossal magnetoresistance (CMR). The CMR is interpreted usually in terms of the double-exchange (DE) model [1, 2] or noncollinear antiferromagnetism (AF) [3]. The models involving a change from the polaron-mediated to hopping conduction near the paramagnetic (PM)-to-ferromagnetic (FM) phase transition at temperature T_c and melting of a charge-ordered state (see review [4] and references therein) likewise fail in satisfactorily explaining the nonstandard behavior of manganites. A model of a crystal state with two magnetic phases originating from strong *s–d* exchange [5] has frequently been invoked in recent years to account for the anomalous properties of the manganites.

$LaMnO_{3+\delta}$ is a model system for studying the magnetic interactions and disorder in mixed-valence manganites. Mn^{3+} can transfer to Mn^{4+}, in particular, in the presence of nonstoichiometric oxygen in undoped $LaMnO_{3+\delta}$ with a nominal Mn^{4+} content roughly equal to 2δ. Stoichiometric $LaMnO_3$ contains only ferromagnetically ordered Mn^{3+} ions in the (*ab*) Mn–O planes, which form, in turn, an AF lattice along the *c* axis, thus producing an *A*-type AF coupling with $T_N \sim 135$ K [4]. The FM ordering of Mn^{3+} ions is initiated by the Mn^{3+}–O– Mn^{3+} anisotropic superexchange interaction, which is stabilized at room temperature by Jahn–Teller (JT) distortions in the *O*' structure (*Pbmn*, $c/\sqrt{2} < a < b$). An increase in temperature or an excess of oxygen favors suppression of the JT effect, which results in a change in the structural, magnetic, and transport properties of $LaMnO_3$.

Nonstoichiometric $LaMnO_{3+\delta}$ typically contains manganese ions in the +3, +4, and +2 valence states, as well as vacancies on the cation sublattice [6, 7]. Its formula can be written more exactly as $(LaMn)_{1-\delta}O_3$, or $La_{3/(3+\delta)}Mn_{3/(3+\delta)}O_3$ for the case of La : Mn = 1 : 1. As δ is increased, the strongly distorted orthorhombic *O*' lattice transfers to orthorhombic (*Pbmn*, $a \le c/\sqrt{2} < b$), pseudocubic (*Pbmn*, $a \approx b \approx c/\sqrt{2}$), and, subsequently, to rhombohedral [7–10]. As the Mn^{4+} concentration decreases and the magnetization of $LaMnO_{3+\delta}$ decreases, AF ordering sets in; for $\delta = 0.05$–0.07, the magnetic moment was found to contain AF and FM components, which were assigned to the magnetic structure being noncollinear [11] or to electronic phase separation [12]. Note that the few available studies on the magnetic transport properties of $LaMnO_{3+\delta}$ provided controversial results. Most of the investigations were performed on ceramic $LaMnO_{3+\delta}$ samples, and information on measurements of lanthanum manganite single crystals with nonstoichiometric oxygen are practically lacking. To understand more clearly the processes occurring in the manganites and depending on the interaction between the magnetic, charge, and local structures, one has to carry out measurements on high-quality single crystals.

There are very few papers dealing with $LaMnO_{3+\delta}$ single crystals. Weak FM [13] and electron spin resonances [14, 15] have been studied in single crystals grown using the floating-zone technique with radiation heating. Among the numerous disadvantages involved in this method is that a crystal thus grown has twins of various types.

McCarroll *et al.* [16] proposed electrochemical deposition on a high-temperature melt solution serving as

Table 1. Structural data for $LaMnO_{3+\delta}$ single crystals

Crystal	1	2	3
δ	0.01	0.02	0.085
Mn^{4+}%	2	4	17
Formula unit	$La_{0.997}Mn^{3+}_{0.975}Mn^{4+}_{0.022}O_3$	$La_{0.993}Mn^{3+}_{0.954}Mn^{4+}_{0.049}O_3$	$La_{0.972}Mn^{3+}_{0.807}Mn^{4+}_{0.165}O_3$
Space group 300 K	*Pbnm*	*Pbnm*	
300 K *a*, Å	5.529	5.493	3.894α = 90°56′
b, Å	5.572	5.536	
c, Å	7.756	7.821	
V/*Z*, Å^3	59.73	59.45	59.06
Structure	*O*′	*O*	*R*
300 K *m*(Mn–O_I), Å	1.95	1.95	
s(Mn–O_{II}), Å	1.93	1.956	
l(Mn–O_{II}), Å	2.02	1.958	
$R_t = l/s$	1.047	~1	

an anode as a method for growing lanthanum manganite single crystals. Among the merits of this method is the absence of twins in the grown crystals. We report here on an investigation of $LaMnO_{3+\delta}$ single crystals with various oxygen contents prepared using a refined electrochemical deposition method described in detail in [17] to study the effect of oxygen nonstoichiometry on the magnetic properties and magnetic states of these single crystals. Particular attention was focused on the magnetic anisotropy of $LaMnO_{3+\delta}$ single crystals.

2. SAMPLES AND EXPERIMENTAL TECHNIQUE

The $LaMnO_{3+\delta}$ single crystals were grown by electrochemical deposition from a melt solution using platinum electrodes and a platinum crucible. The technique employed to obtain single crystals and the determination of the cation and anion composition are described in considerable detail in [17]. The single crystals thus grown were of a lustrous black and their shape was close to cubic. The cation composition was determined using x-ray fluorescence. The average manganese valence was derived in two steps; first, the oxidizing capacity was found using iodometric titration, after which the total content of manganese was measured using the photocolorimetry of a solution of permanganic acid upon complete oxidation of the manganese [18]. Assuming vacancies on the La and Mn sublattices to be present in equal numbers, the oxygen content was found based on the average manganese valence, with the concentration $Mn^{4+}\% = 2\delta \times 100\%$.

The phase composition, lattice parameters, and crystal orientation were determined using the x-ray technique. The x-ray structural measurements made on powder samples of crystalline material showed all samples to be single-phase orthorhombic or rhombohedral single crystals [17]. The measurements were performed on three $LaMnO_{3+\delta}$ single crystals with different oxygen contents: crystal 1 ($\delta = 0.01$), crystal 2 ($\delta = 0.02$), and crystal 3 ($\delta = 0.085$). Crystal 1 had orthorhombic *O′* structure, crystal 2 had orthorhombic *O* structure, and crystal 3 had rhombohedral structure. Table 1 lists the crystallographic characteristics of the three $LaMnO_{3+\delta}$ single crystals, including the distance *m* between the Mn ion and the apical oxygen ion (Mn–O_I), as well as the short (*s*) and the long (*l*) distances between the Mn and O_{II} ions in the MnO_4 plane. The values of *m*, *s*, and *l* were calculated using the technique proposed in [19]. We chose $R_t = 1/s$ as a parameter characterizing the JT distortions, as in [7].

As follows from Table 1, the distortions of the oxygen octahedra around the manganese ions decrease with increasing content of nonstoichiometric oxygen; the *O*′ structure (crystal 1, $\delta = 0.01$) transfers to the *O* structure (crystal 2, $\delta = 0.02$), and then, at the maximum value $\delta = 0.085$, we have rhombohedral crystal 3.

The magnetization of the single crystals was determined with a SQUID magnetometer (Quantum Design, MPMS-5) in magnetic fields of up to 5 T and at temperatures ranging from 4.2 to 300 K for various magnetic-field orientations with respect to the principal crystallographic axes.

3. EXPERIMENTAL RESULTS

3.1. Temperature Dependences of the Magnetization of Single Crystals 1, 2, and 3 for Various Magnetic Field Orientations

The temperature dependences of the magnetization *M*(*T*) of the three single crystals were measured in weak fields under field cooling (FC) and zero-field

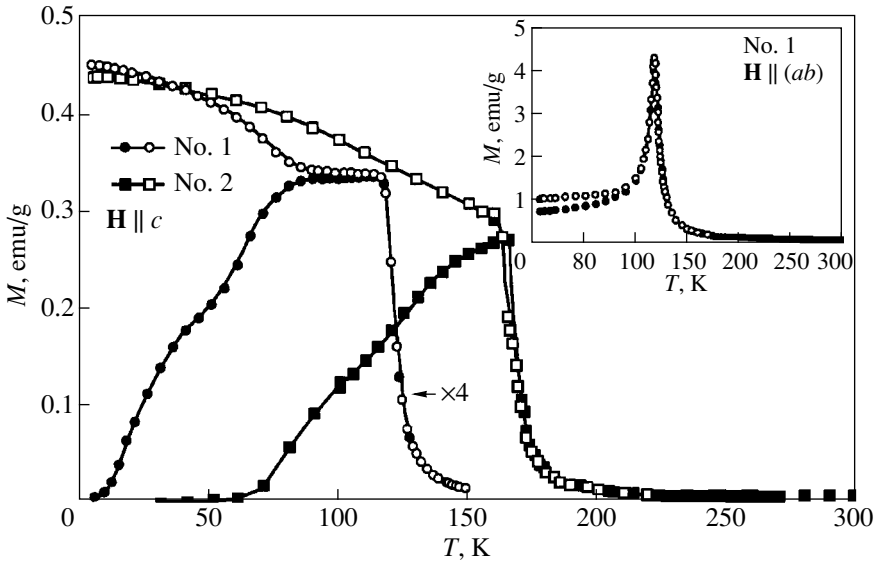

Fig. 1. Temperature dependences of the magnetizations M_{FC} (open symbols) and M_{ZFC} (filled symbols) for $LaMnO_{3+\delta}$ single crystals No. 1 at 200 Oe and No. 2 at 10 Oe (**H** || *c*); the inset shows crystal No. 1 for **H** || (*ab*).

cooling (ZFC). As seen from Fig. 1, lowering the temperature entails a fairly sharp PM-to-FM transition at T_c= 125 K (crystal 1) and 170 K (crystal 2) for **H** || *c*. For $T < T_c$, the $M_{ZFC}(T)$ and $M_{FC}(T)$ curves exhibit a clearly different behavior. In particular, M_{FC} grows with decreasing $T < T_c$ practically down to the lowest temperatures reached. At the same time, the M_{ZFC} curve reveals a broad maximum and for $T < T_f$ = 155 K (crystal 1) or 160 K (crystal 2), the $M_{ZFC}(T)$ and $M_{FC}(T)$ cease to coincide. Below T_f, M_{ZFC} decreases to reach very low values at 5 K. In the case of the magnetic field *H* lying in the (*ab*) plane in crystal 1, the behavior of the $M_{FC}(T)$ and $M_{ZFC}(T)$ relations at $T < T_f$ = 120 K is quite different (see inset to Fig. 1). First, there is practically no difference between the $M_{FC}(T)$ and $M_{ZFC}(T)$ curves. Both curves pass a sharp maximum at $T_f \approx$ 120 K. Second, both M_{ZFC} and M_{FC} decrease by more than four times with a further decrease in temperature.

Figure 2a displays the temperature dependence of the magnetization of crystal 3 measured in a weak magnetic field of 10 Oe in the temperature interval 5– 300 K for three magnetic field orientations. Single crystal 3 has rhombohedral structure (Table 1). During the measurements, the magnetic field was oriented perpendicular to the (200) growth planes. The crystal was observed to transfer to the FM state at T_c = 190 K in all three magnetic field configurations. Below ~240 K, both M_{FC} and M_{ZFC} increase strongly in magnitude for all magnetic field orientations; below ~160 K, M_{FC} has a constant value different from those of M_{ZFC}. For the first orientation of the magnetic field in Fig. 2a, the $M_{FC}(T)$ and $M_{ZFC}(T)$ curves follow a similar behavior, whereas in the other two orientations, M_{FC} and M_{ZFC} exhibit thermomagnetic irreversibility below 150 K. Note that at ~200 K, all the measured $M_{FC}(T)$ and $M_{ZFC}(T)$ curves display a certain bend (Fig. 2a). This feature, as well as the difference between M_{FC} and M_{ZFC}, becomes less pronounced in higher fields (Fig. 2b), until in such high fields as 6 and 50 kOe, all the curves practically coincide throughout the temperature interval covered, 5–300 K.

Figure 3a plots the temperature dependence of volume magnetic susceptibility $\chi_{FC}(T) = M_{FC}/H$ measured in fields of 6 and 50 kOe (*H* is directed along the *c* axis). The inset shows the temperature dependence of inverse susceptibility $1/\chi_{FC}(T)$, whose extrapolation to zero yields the PM Curie temperature Θ_p. The values of Θ_p equal to ~145 K (*H* = 6 kOe) and ~135 K (*H* = 50 kOe) are positive and higher than T_c, which implies an FM character of exchange coupling between the spins. For crystals 2 and 3, Θ_p = 177.3 and 203.4 K, respectively. Table 2 lists the Curie constant *C* and the effective number of Bohr magnetons calculated for all crystals in the PM state. It is instructive to follow the effect of the magnetic field on the magnetization of crystal 1 in the case **H** lying in the (*ab*) plane (Fig. 3b). Note that the field of 6 kOe shifts the maximum in $M_{FC}(T)$ by 10 K toward lower temperatures, while the magnetization decreases by a factor of ~1.4 as the sample is cooled to 5 K; therefore, the decrease in $M_{FC}(T)$ at 6 kOe is three times smaller than that in a field of 200 Oe (inset to Fig. 1). A further increase of the magnetic field in magnitude brings about the disappearance of the maximum in the $M_{FC}(T)$ curve for *H* = 50 kOe in the (*ab*) plane, while a weak maximum in $M_{ZFC}(T)$ at ~50 K is still seen (inset to Fig. 3b).

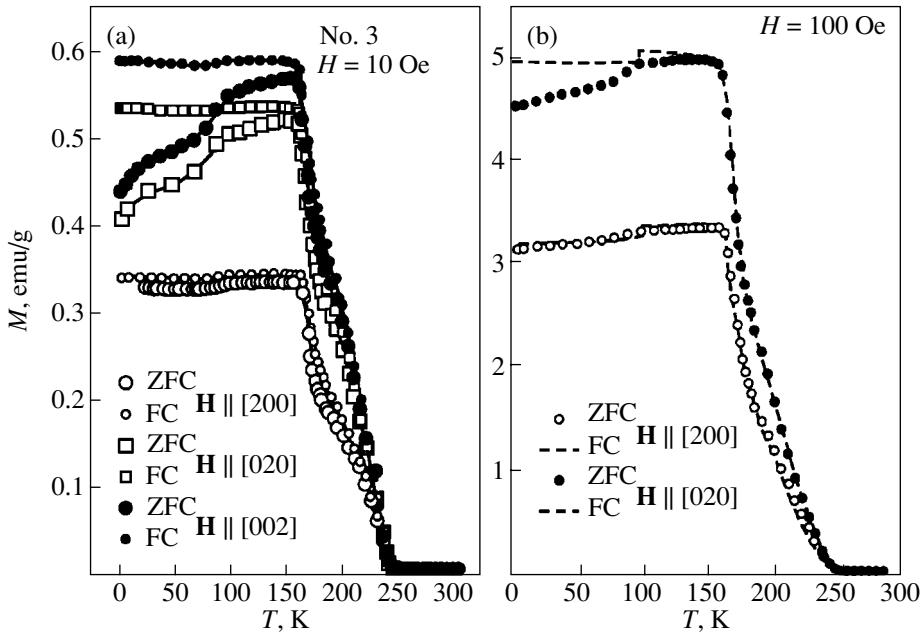

Fig. 2. Temperature dependences of M_{FC} and M_{ZFC} magnetizations obtained for $LaMnO_{3+\delta}$ single crystal No. 3 in a field of (a) 10 Oe for three different magnetic-field directions and (b) 100 Oe for two field directions.

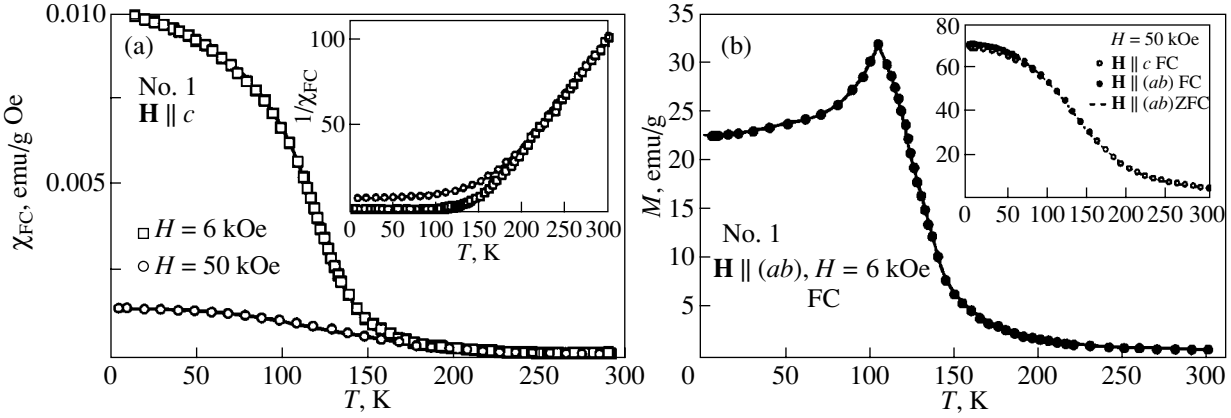

Fig. 3. Temperature dependences (a) of the susceptibility χ_{FC} and $1/\chi_{FC}$ (inset) obtained on $LaMnO_{3+\delta}$ single crystal No. 1 in fields of 6 and 50 kOe (**H** || *c*) and (b) of the magnetization obtained on $LaMnO_{3+\delta}$ single crystal No. 1 for **H** || (*ab*) at 6 kOe and (inset) 50 kOe.

3.2. Isotherms of the Field Dependences of Magnetization of Single Crystals 1, 2, and 3

The hysteresis loops measured by us (not shown in Fig. 4) are symmetric with respect to the origin; therefore, Fig. 4 shows only part of the $M(H)$ curves obtained in the measurements. For sample 1 (**H** || *c*), the coercive field H_c is ~1.5 kOe at 5 K and decreases to ~100 Oe at 50 K. Measured in the **H** || (*ab*) orientation, the value of H_c at 5 K is substantially smaller, about 200 Oe. In the other crystals, H_c is low and, at 5 K, is ~30 Oe for sample 2 and less than 10 Oe for crystal 3. Extrapolation of $M(H)$ from the saturation region to $H = 0$ yielded an estimate for the spontaneous magnetization M_s = 70 emu/g (**H** || *c*) and 67 emu/g (**H** || (*ab*)). Note that at 5 K, the magnetization saturates in fields H_s ~ 5–6 kOe (**H** || *c*) and ~10 kOe (**H** || (*ab*)). The theoretical value of saturation magnetization M_s^t at $T = 0$ as calculated for total FM spin ordering of Mn^{3+} ($S = 2$) and Mn^{4+} ($S = 3/2$) in single crystal 1 is 91.6 emu/g, which is ~25% higher than the observed M_s at 5 K. Such a low value of M_s may be due to a sizable part of the sample being in the AF state. The values of M_s(FC)

Table 2. Magnetic characteristics of $LaMnO_{3+\delta}$ single crystals

Crystal/δ	1/0.01		2/0.02	3/0.085
H orientation	‖*c*	‖(*ab*)	‖*c*	‖[200]
PM region				
C, (emu K)/mole	4.13	4.73	4.77	4.49
Θ_p, K	144.5	131.7	177.3	203.4
P_{eff}, μ_B	5.5	6.15	6.18	5.99
FM region				
T_c, K	125	~125	170	190
M_s(FC)	70	67	88	89
M_s(ZFC)	63.6	63.6	86	87
μ, μ_B	3.03	2.9	3.75	3.77
H_c (5 K), Oe	1500	200	~30	<10
H_s, kOe	5	10	7	8
χ_{HF}(5 K), cm^3/g	2×10^{-4}	9.6×10^{-4}	2.2×10^{-4}	$(6–8) \times 10^{-5}$
J_F/k_B	8.4		10.9	
J_A/k_B	–1.22		~–0.5	

and M_s(ZFC) and the corresponding effective magnetic moment are presented in Table 2. Note that the low-temperature magnetization is higher than the magnetization measured at $T \approx 100–120$ K only in fields above ~1000 Oe (Fig. 4b), whereas in lower fields, the magnetization at $T \approx 100–120$ K is noticeably higher than that at lower temperatures.

For crystal 2, M_s(5 K) is ~88 emu/g or 3.75 μ_B/Mn. The values of the saturation magnetization at 5 K derived from the field dependences $M(H)$ for all three magnetic-field orientations in crystal 3 (Fig. 4c) vary within the interval 87–89 emu/g, which corresponds to a magnetic moment of 3.68–3.77μ_B at 5 K.

3.3. Temperature Dependence of the High-Field Susceptibility of Single Crystals 1, 2, and 3

It is well known that the differential magnetization $\chi = [M(H_1) - M(H_2)]/(H_1 - H_2)$ for a fixed value of $\Delta H = H_1 - H_2$ is a characteristic of the magnetic state of a sample. In weak fields ($H \ll H_s$), the susceptibility χ of a crystal with $M_s > 0$ contains contributions due to domain wall displacement and domain magnetization vector rotation toward the magnetic-field direction. In high fields, $\chi = \chi_{HF}$ characterizes the sample susceptibility in the single-domain magnetic state. Figure 5 displays temperature dependences of the high-field susceptibility $\chi_{HF}(T)$ of crystal 1 measured for two magnetic-field orientations. The fields H_1 and H_2 are chosen to be 6 and 50 kOe, respectively. For $T \ll T_c$, χ_{HF} for $\mathbf{H} \parallel c$ is nearly constant; close to T_c, the susceptibility grows to a maximum value at $T_{max} = 140$ K (this is in agreement with the behavior of an FM material [20]) and then falls off rapidly. For $\mathbf{H} \parallel (ab)$, the $\chi_{HF}(T)$ relation follows a more complicated course for $T < T_c$, with an additional maximum appearing at ~50 K. In crystal 2, the $\chi_{HF}(T)$ curve measured for $\mathbf{H} \parallel c$ passes through a maximum at $T_{max} = 200$ K (above T_c) and remains practically constant below 100 K. The high-field susceptibility of crystal 3 in the single-domain state behaves in a similar way (Fig. 5).

4. DISCUSSION OF RESULTS

The observed behavior of magnetization in $LaMnO_{3+\delta}$ single crystals can be understood by invoking the model of the two-phase magnetic state, which assumes separation of a system, at low enough temperatures, into an AF matrix and FM clusters embedded in it. The excess oxygen in $LaMnO_{3+\delta}$ gives rise to vacancy formation on the cation (La and Mn) sublattices [6]. Each vacancy has a charge of $-3e$ and acts as an acceptor for the holes doped into the system, with the result that hole-enriched FM clusters form near the vacancies. The AF matrix is free of holes and is coupled to the FM clusters by superexchange interaction at the interface separating the two phases [10]. These assumptions, which permit one to explain the magnetic properties of $LaMnO_{3+\delta}$, draw from measurements, for instance, of inelastic neutron scattering in $La_{0.95}Ca_{0.05}MnO_3$ [21], which revealed the existence of an anisotropic AF phase and an isotropic FM phase with an FM correlation length of 8–10 Å in all directions. Neutron diffraction measurements performed on polycrystalline $LaMnO_{3+\delta}$ samples [8] likewise support the existence of phase separation, with the latter depending strongly on the actual conditions of crystal

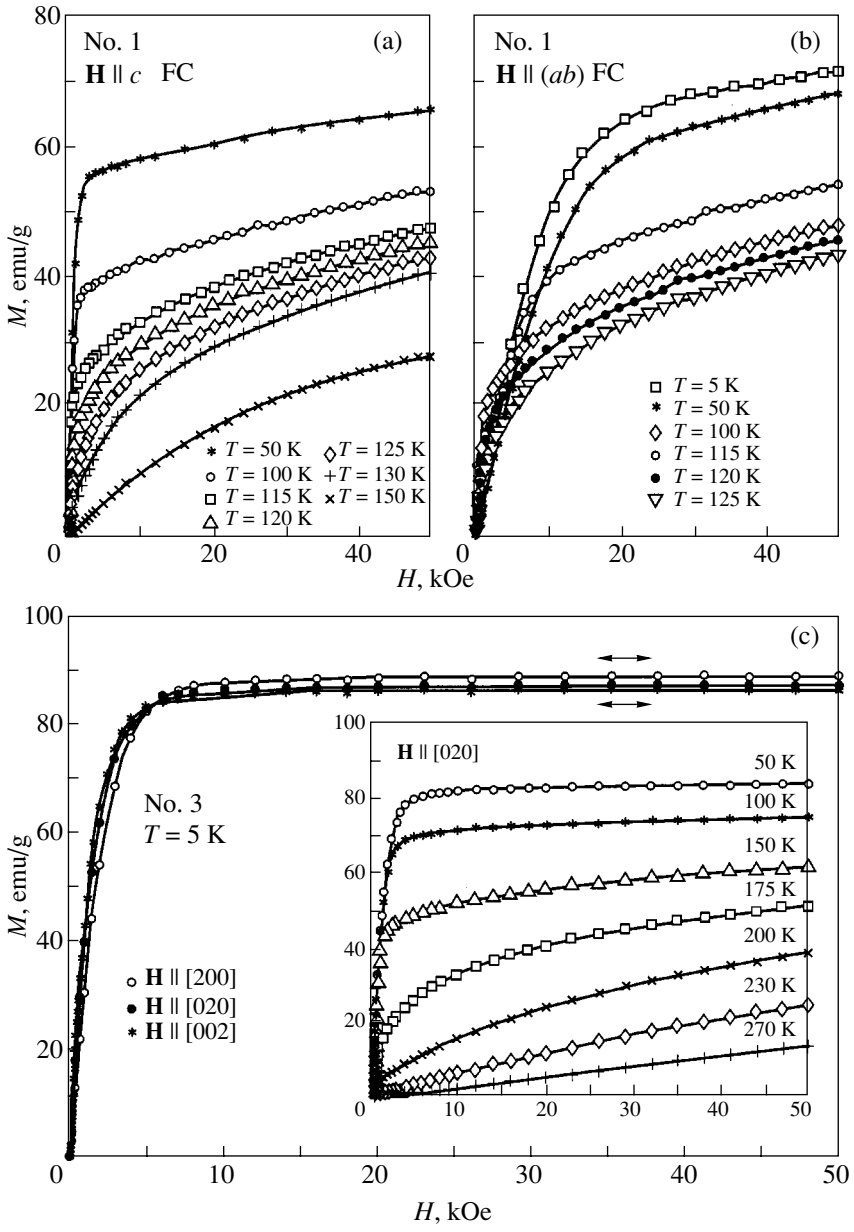

Fig. 4. Field dependences of the magnetization of $LaMnO_{3+\delta}$ single crystals (a, b) No. 1 for (a) **H** || *c* and (b) **H** || (*ab*) and (c) No. 3 for three magnetic-field orientations (T = 5 K); inset: $M(H)$ plotted for the region 50–270 K.

growth and heat treatment. This accounts for the scatter of literature data on the crystal and magnetic properties of $LaMnO_{3+\delta}$. It should be stressed that the crystal phases revealed in [8] coincide in structure with the ones identified in the present study (except the $P112_{1/a}$ phase). In what follows, we use the model proposed in [10] to explain our data.

For small values of δ and low enough temperatures, the FM clusters are separated from one another; as δ (and, hence, the cation vacancy concentration) increases, however, the distance between the FM clusters decreases, making it possible for some of them to merge into larger clusters until, eventually, an infinite cluster (for instance, for a rhombohedral structure) appears. However, in the latter case, AF regions still persist, as found in neutron diffraction studies made on $La_{1-x}Sr_xMnO_3$ for $x > 0.175$ [22] despite the fact that the sample with rhombohedral structure was in the metallic phase.

The distribution of holes and the spin configuration of the AF–FM system depend on temperature; for $T \gg T_c$, the spins are in the random state and the holes are distributed uniformly. When the sample is cooled ($T \longrightarrow T_c$), the holes are concentrated near the cation vacancies to form clusters with FM-ordered spins (through strong DE interaction). The magnetic moments

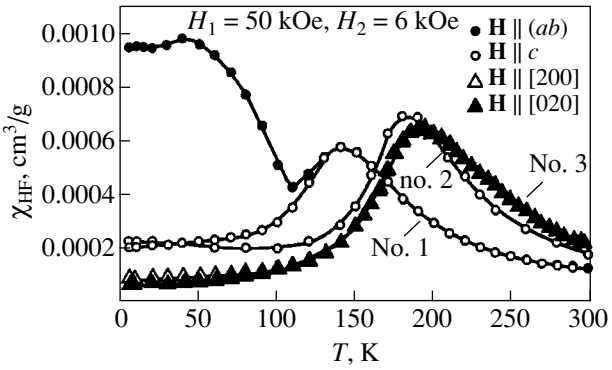

Fig. 5. Temperature dependences of the high-field susceptibility $\chi_{HF}(T)$ measured on $LaMnO_{3+\delta}$ single crystals Nos. 1, 2, and 3.

of the host ions are ordered antiferromagnetically. The exchange interactions in an AF–FM system may be considered the sum of a strong positive J_{FC} interaction inside the FM clusters and a negative interaction J_A and a positive interaction J_F between spins along and perpendicular to the *c* axis, respectively, in the AF matrix [23], as well as of the exchange interaction $J_B > 0$ at the boundary separating the two phases [10]. We estimated the exchange constants J_F and J_A using the values of T_c and Θ_p measured for $\delta = 0.01$ and 0.02 and came to the following relations [13]:

$$T_c = 2/3S(S+1)(4|J_F| + 2|J_A|)/k_B,$$

$$\Theta_p = 2/3S(S+1)(4J_F + 2J_A)/k_B.$$

The values thus obtained (Table 2) correlate well with the results for $LaMnO_{3+\delta}$ [7] found for the corresponding values of $R_t = l/s$ (Table 1). The spins of the AF matrix near the FM clusters are canted relative to the spins in the FM clusters because of the exchange interaction J_B, and the canting angle grows with increasing FM cluster density and applied magnetic field [10].

The actual character of the temperature dependences of M_{FC} and M_{ZFC} should depend on the relative magnitude of the contributions of the AF matrix and the FM clusters for a given magnetic-field orientation. In the FC case, the cluster spins align with the field with decreasing temperature $T < T_c$, so that the contribution to M_{FC} will be the largest for **H** ∥ *c*. In the ZFC case, where the sample is cooled in a zero field, there is no preferential orientation for spins in the FM clusters and the contribution that the FM phase provides to M_{ZFC} should be the lowest for **H** ∥ *c* (down to the lowest possible temperatures). If a weak field is applied to the sample, the magnetization will depend strongly on the system anisotropy. In the case of strong anisotropy, a weak magnetic field will not be able to rotate the spins and M_{ZFC} will be small. Because the magnitude of the coercive field H_c is due to the magnetic anisotropy of the AF phase, for $H < H_c$, the thermomagnetic irreversibility between M_{FC} and M_{ZFC} will be large (Fig. 1, **H** ∥ *c*; Table 2). The difference between M_{FC} and M_{ZFC} decreases with increasing magnetic field (Fig. 2; inset to Fig. 3b), a feature characteristic of the presence of FM clusters in the matrix [24].

Note that for **H** ∥ (*ab*) (crystal 1), FM ordering at $T_c \approx 125$ K is accompanied by the appearance of an additional maximum at $T = 120$ K in the $M_{FC}(T)$ relation measured at 200 Oe (inset to Fig. 1). The magnitude of T_{max} depends on the magnetic field and shifts from 120 to 110 K in a field of 6 kOe (Fig. 3b). In addition, $M_{FC}(T)$ and $M_{ZFC}(T)$ are not thermomagnetically irreversible in this field configuration (inset to Fig. 3b). Thus, the FM cluster contribution is the lowest. Such an anomaly in the behavior of $M_{FC}(T)$ has been observed in single-crystal $La_{0.9}Sr_{0.1}MnO_3$ for **H** ∥ (*ab*) [25], where FM ordering at $T_c = 150$ K was accompanied by the appearance of a maximum in the $M_{FC}(T)$ curve at 110 K and the field dependences $M(H)$ in the interval 105–118 K had a stepwise character. Metamagnetic transitions in high fields and the additional maximum in the temperature dependence of $\chi_{HF}(T)$ for $T < T_c$ were assigned [26] to a structural transition in single-crystal $La_{0.9}Sr_{0.1}MnO_3$ from the pseudocubic *O*" to orthorhombic *O*' structure occurring in the interval 100–110 K. The field dependences of $M(H)$ of single crystal 1 exhibit neither a stepwise pattern nor metamagnetic transitions in high fields. Nevertheless, an anomaly in the behavior of $M_{FC}(T)$ does exist for $T < T_c$ (**H** ∥ (*ab*)) and the value of T_{max} depends on H (Fig. 3b); also, the $\chi_{HF}(T)$ relation follows a complicated pattern in the low-temperature region (Fig. 5).

As δ (i.e., the cation vacancy concentration) increases, (i) the FM cluster density increases and, accordingly, the number of AF-matrix spins per FM cluster decreases; (ii) the spin canting angle in the AF matrix increases; and (iii) the crystal orthorhombicity decreases and, as a consequence, the crystallographic magnetic anisotropy decreases. All these processes bring about a decrease in H_c with increasing δ (Table 2). The growth of the saturation magnetization M_s with increasing δ (Table 2) is associated not only with a growth in the number of completely field-aligned spins in the FM clusters but also with an increase in the canting angle in the AF matrix. The feature observed for $T > T_c$ in the single crystal with $\delta = 0.085$ (Fig. 2) can also be assigned to the presence of clusters. As the temperature increases, the long-range order in the matrix breaks down faster than the short-range order in the clusters; therefore, the $M(T)$ curve exhibits two magnetic-ordering temperatures. In polycrystalline $LaMnO_{3+\delta}$ [12], such an anomaly was observed in $\chi_{ac}(T)$ curves. The size of the clusters can be estimated using the technique [27] relating the cluster magnetic moment to the concentration of cation vacancies. For $\delta = 0.085$, this concentration is ~0.025 and, hence, the clusters are about 15–20 Å in size. The nonlinearity of

the $M(H)$ curves for $T \gg T_c$ is likewise associated with the presence of FM clusters (Fig. 4).

5. CONCLUSION

Thus, we have reported on a study of magnetic ordering in $LaMnO_{3+\delta}$ single crystals grown by electrochemical deposition. Single crystals with the structures O' ($\delta = 0.01$), O ($\delta = 0.02$), and R ($\delta = 0.085$) exhibit FM ordering at T_c = 125, 170, and 190 K, respectively. A strong thermomagnetic irreversibility is observed between $M_{FC}(T)$ and $M_{ZFC}(T)$ for $\delta = 0.01$ and 0.02 for $\mathbf{H} \parallel c$. For $\delta = 0.01$ and $\mathbf{H} \parallel (ab)$, $M_{FC}(T)$ was observed to behave anomalously for $T < T_c$. The temperature and field dependences of magnetization obtained for $LaMnO_{3+\delta}$ single crystals are accounted for within the model of a two-phase magnetic system containing an insulating AF matrix with embedded hole-enriched FM clusters.

ACKNOWLEDGMENTS

This study was partially supported by the Scientific Research Committee, project no. 5P03B01620.

REFERENCES

1. C. Zener, Phys. Rev. **82** (3), 403 (1951).
2. P. W. Anderson and H. Hasegawa, Phys. Rev. **100** (1), 675 (1955).
3. P. G. De Gennes, Phys. Rev. **118** (1), 141 (1960).
4. J. M. D. Coey, M. Viret, and S. von Molnár, Adv. Phys. **48** (2), 167 (1999).
5. E. L. Nagaev, Usp. Fiz. Nauk **166** (8), 833 (1996) [Phys. Usp. **39**, 781 (1996)].
6. J. A. M. van Roosmalen and E. H. P. Cordfunke, J. Solid State Chem. **110** (1), 109 (1994).
7. C. Ritter, M. R. Ibarra, J. M. De Teresa, *et al.*, Phys. Rev. B **56** (12), 8902 (1997).
8. Q. Huang, A. Santoro, J. W. Lynn, *et al.*, Phys. Rev. B **55** (22), 14987 (1997).
9. F. Prado, R. D. Sánchez, A. Caneira, *et al.*, J. Solid State Chem. **146** (2), 418 (1999).
10. M. Muroi and R. Street, Aust. J. Phys. **52** (2), 208 (1999).
11. J. P. Mitchel, D. N. Argyriou, C. D. Potter, *et al.*, Phys. Rev. B **54** (9), 6172 (1996).
12. A. N. Pirogov, A. E. Teplykh, V. I. Voronin, *et al.*, Fiz. Tverd. Tela (St. Petersburg) **41** (1), 103 (1999) [Phys. Solid State **41**, 91 (1999)].
13. V. Skumryev, F. Ott, J. M. D. Coey, *et al.*, Eur. Phys. J. B **11** (3), 401 (1999).
14. S. Mitsudo, K. Hirano, H. Nojiri, *et al.*, J. Magn. Magn. Mater. **177–181** (1), 877 (1998).
15. A. M. Balbashov, M. K. Gubkin, V. V. Kireev, *et al.*, Zh. Éksp. Teor. Fiz. **117** (3), 542 (2000) [JETP **90**, 474 (2000)].
16. W. H. McCarroll, K. V. Ramanujachary, I. D. Fawcett, and M. Greenblatt, J. Solid State Chem. **145** (1), 88 (1999).
17. D. D. Khalyavin, S. V. Shiryaev, G. L. Bychkov, *et al.*, in *Proceedings of Fourth International Conference "Single Crystal Growth and Heat & Mass Transfer," Obninsk, 2001*, Vol. 2, p. 372.
18. A. G. Soldatov, S. N. Barilo, and S. V. Shiryaev, Zh. Anal. Khim. **56** (12), 1245 (2001).
19. A. K. Bogush, V. I. Pavlov, and L. V. Balyko, Cryst. Res. Technol. **18** (3), 589 (1983).
20. K. P. Belov, *Magnetic Transitions* (Fizmatgiz, Moscow, 1959; Consultants Bureau, New York, 1961).
21. M. Hennion, F. Moussa, J. Rodriguez-Carvajal, *et al.*, Phys. Rev. B **56** (1), R497 (1997).
22. D. Louca, T. Egami, E. L. Brosha, *et al.*, Phys. Rev. B **56** (14), R8475 (1977).
23. F. Moussa, M. Hennion, J. Rodriguez-Carvajal, *et al.*, Phys. Rev. B **54** (22), 15149 (1996).
24. L. Ghivelder, L. A. Castillo, M. A. Gusmâo, *et al.*, Phys. Rev. B **60** (17), 12184 (1999).
25. K. Ghosh, R. L. Greene, S. E. Lofland, *et al.*, Phys. Rev. B **58** (13), 8206 (1998).
26. A. V. Korolyov, V. Ye. Arkhipov, V. S. Gaviko, *et al.*, J. Magn. Magn. Mater. **213** (1), 63 (2000).
27. J. Z. Sun, L. Krusin-Elbaum, A. Gupta, *et al.*, Appl. Phys. Lett. **69** (7), 1002 (1996).

Translated by G. Skrebtsov

Physics of the Solid State, Vol. 45, No. 1, 2003, pp. 154–157. Translated from Fizika Tverdogo Tela, Vol. 45, No. 1, 2003, pp. 147–150.

MAGNETISM AND FERROELECTRICITY

Mechanism of the Polarization Response in the Relaxor State of Lead Scandotantalate Single Crystals with Different Levels of Ion Ordering

L. S. Kamzina and N. N. Kraĭnik

Ioffe Physicotechnical Institute, Russian Academy of Sciences, Politekhnicheskaya ul. 26, St. Petersburg, 194021 Russia

Received November 13, 2001; in final form, March 20, 2002

Abstract—The dielectric properties and optical transmission of stoichiometric lead scandotantalate (PST) single crystals in strong electric fields was studied above the temperature of the spontaneous ferroelectric phase transition (T_{sp}). It is shown that the mechanism of polarization response directly above T_{sp} is related to induced polarization effects and macrohysteretic behavior only in ac fields above 5 kV/cm. An analysis of reciprocal dielectric permittivity carried out over a broad temperature range far above the temperature at which the dielectric permittivity passes through a maximum revealed that specific features of the relaxor behavior manifest themselves up to 400°C even in highly ordered PST crystals. *© 2003 MAIK "Nauka/Interperiodica".*

1. INTRODUCTION

The nature of the dielectric response in disordered media, to which ferroelectric relaxors belong, has remained a topical problem in the physics of ferroelectricity for many years. However, obtaining an unambiguous answer to the question of which "relaxing" elements are responsible for the dielectric response within a broad temperature range is a very difficult problem. This is accounted for by the fact that interactions among the relaxing elements play a major role at low temperatures and as the temperature varies, the nature itself of these elements may change from single dipoles at high temperatures to domains and domain walls at low temperatures. At the same time, in the region of comparatively weak interactions in the ergodic phase of the relaxors (at high temperatures), one can obtain an explicit answer to this question; this could prove an important step in understanding the nature of relaxors.

Such studies have been carried out on lead magnoniobate (PMN), which is a classical relaxor [1, 2]. It has been shown experimentally that the nonlinear dielectric properties in the ergodic phase revealed in ac electric fields $0 < E < 2$ kV/cm are due only to the motion of phase boundaries of polar regions rather than to thermally activated orientation of the local spontaneous polarization vector in polar regions.

Among the specific features of relaxors (PMN and similar compounds) is that the temperature dependence of reciprocal dielectric permittivity ε in the ergodic phase immediately above the maximum in ε ($T_{max\,\varepsilon}$) is quadratic [3, 4] and that only at high temperatures in the paraelectric phase does this dependence obey the Curie–Weiss law, as is the case with conventional ferroelectrics.

The mechanism of polarization response in ac fields and the temperature dependence of ε in the relaxor state in compounds of the type $PbB'_{1/2}B''_{1/2}O_3$, which occupy an intermediate position between normal ferroelectrics and typical relaxors, are not fully understood. Among these substances is lead scandotantalate, $PbSc_{1/2}Ta_{1/2}O_3$ (PST). There is only one communication that reports on the effect of the ac field amplitude $0 < E < 4$ kV/cm on the dielectric response of PST crystals near the spontaneous phase transition temperature (T_{sp}) [5]. In that study, it was shown that in fields of up to 4 kV/cm and at temperatures slightly above T_{sp}, the observed nonlinearity is most likely associated with the dynamics of domain walls and phase boundaries. In addition to the typical relaxor behavior, these substances also exhibit a spontaneous phase transition from the relaxor state to the ferroelectric phase at a temperature below the maximum in ε. By properly changing the degree of ordering s of the Sc^{3+} and Ta^{5+} ions, one can vary not only the phase transition temperature but also the character of the transition. As s decreases, the specific features of the relaxor behavior characteristic of the diffuse ferroelectric transition are seen more clearly. An increase in s ($s \longrightarrow 1$) weakens the relaxor properties. In partially ordered PST compounds, the relaxor state extends over a fairly broad temperature interval above T_{sp} [6, 7].

This study deals with the mechanism of the polarization response of PST crystals as a function of ac field amplitude and with the effect of the degree of ion ordering s on the behavior of dielectric permittivity at temperatures above T_{sp}.

We employed not only the classical dielectric methods but also an optical technique, namely, measurement of the optical transmission (OT); the latter method is more sensitive to changes in the size of the inhomoge-

neities. If the size of the scatterers changes at the phase transition, this will entail changes not only in light scattering but also in the optical transmission. Scattering depends on the ratio of the dimensions of the scattering particle to the wavelength of light. If this ratio is small, the scattered intensity will be weak and the sample will be virtually transparent. In the absence of an electric field, such a state is characteristic of the relaxor phase. As the particle size increases, the scattering intensity grows strongly, particularly in directions making small angles with the propagation vector of the incident light. This results in a decrease in the OT. We showed in previous communications [8, 9] that the spontaneous phase transition in stoichiometric PST crystals is of percolation type. In phase transitions of the percolation type, the average size of new-phase clusters at percolation threshold approaches the size of the sample and a large-scale nonuniform structure ("infinite cluster") forms. In this case, the phase transition should be accompanied by the appearance of anomalously narrow peaks in small-angle light scattering intensity and, hence, by a minimum in the OT.

2. EXPERIMENTAL TECHNIQUE AND THE SAMPLES USED

We used stoichiometric PST crystals with different degrees of ion ordering ($0.3 < s < 0.98$). Dielectric and optical measurements were conducted on PST single crystals $1 \times 2 \times 2$ mm in size which were not subjected to any mechanical processing. The electric field was applied along the ⟨100⟩ crystallographic directions, and the light was propagated along ⟨001⟩. The dielectric permittivity was measured at frequencies of 1 kHz and 1.3 MHz on a sample heated at a rate of 2–4°C/min in the temperature range from 0 to 700°C.

The optical studies were conducted with a He–Ne laser. A low-power laser beam was passed through a sample mounted in a temperature-controlled cryostat with an aperture of ~1.5°. This aperture permitted us to effectively exclude the contribution from Rayleigh scattering on small particles to optical transmission. On passing through the crystal, the light was detected by a photodiode, whose output was fed to a lock-in detector with a time constant of 1 s. The laser beam modulation frequency was 1 kHz. A 50-Hz electric field with an amplitude of up to 8 kV/cm was applied to the sample. The time-averaged signal was measured. All the optical measurements were performed in integrated mode. After each application of the electric field, the samples were depolarized by heating to 100°C prior to subsequent measurement.

3. EXPERIMENTAL RESULTS AND DISCUSSION

Figure 1 presents OT temperature dependences obtained at different ac electric field amplitudes. The minima in the OT curves lie at the temperature of the spontaneous phase transition T_{sp}. The width of the minimum is ~1–2°C. In this region, a large-scale structure forms, small-angle scattering increases sharply, and the crystal becomes practically opaque. Immediately above T_{sp} (percolation threshold), the scatterer size decreases and the OT increases. An increase in the field amplitude to 4 kV/cm (curves *1*, *1*') virtually does not affect the magnitude of OT at temperatures above T_{sp}. The change in the OT curve shape observed to occur below T_{sp} in a field of 4 kV/cm is associated with an increase in domain size. The behavior of the OT at temperatures slightly below T_{sp} was discussed by us in more detail elsewhere [5]. In fields above 5 kV/cm, the OT falls off considerably (curves *2*, *3*) directly above T_{sp}. The increase in domain and polar region size, which entails the formation of a macrodomain cluster, may account for the above-mentioned decrease in OT. This conjecture is also corroborated by the double dielectric hysteresis loops observed immediately above T_{sp} in polycrystalline PST samples [10]. It follows from the data presented in [10] that strong nonlinearity and hysteresis effects are induced only in fields above 5 kV/cm. Double hysteresis loops appear, the inhomogeneities grow in size, and a large-scale macrodomain structure forms. The increase in inhomogeneity size brings about an increase in small-angle scattering and a decrease in the OT; this exactly is observed experimentally. This type of nonlinearity is associated with induced polarization switching and domain growth.

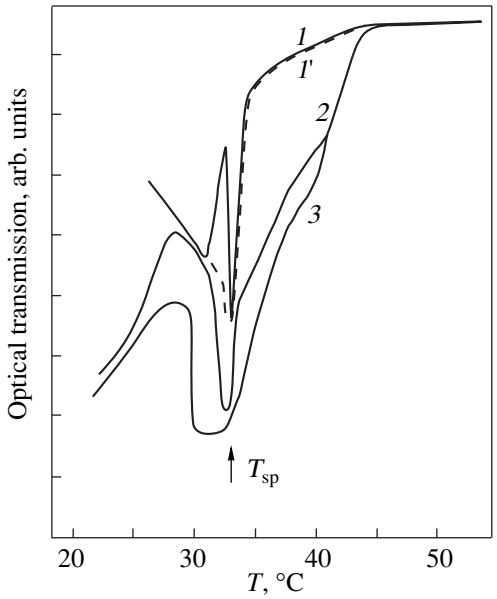

Fig. 1. Temperature dependences of optical transmission in PST crystals ($s = 0.9$) measured at different ac electric field amplitudes E: (*1*) 0, (*1*') 4, (*2*) 6, and (*3*) 8 kV/cm.

As follows from the hysteresis loops, in weak fields (below 4 kV/cm), the P vs. E relation is linear and the size of the inhomogeneities does not change; therefore at temperatures above T_{sp}, no change in the OT is

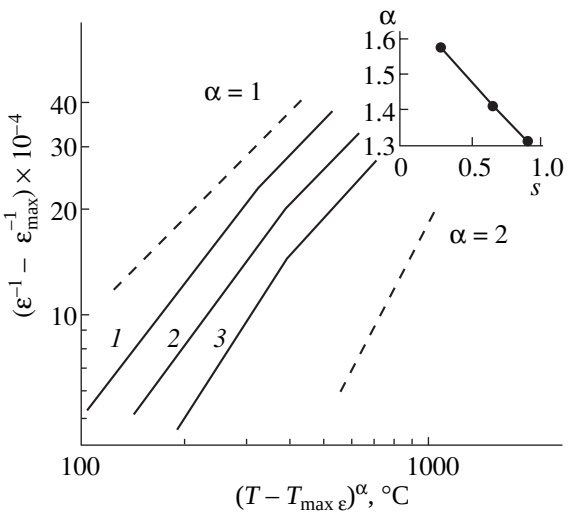

Fig. 2. Reciprocal dielectric permittivity ($\varepsilon^{-1} - \varepsilon_{max}^{-1}$) plotted vs. $(T - T_{max\,\varepsilon})^{\alpha}$ on a log–log scale for PST single crystals with the degree of ordering *s*: (*1*) 0.9, (*2*) 0.7, and (*3*) 0.3. Dashed lines are calculated for $\alpha = 1$ and 2. Inset: plot of the parameter α vs. *s*.

observed within the experimental accuracy (curve *1*' in Fig. 1). At the same time, in [5], slight variations were noticed in the dielectric permittivity of this crystal in fields below 600 V/cm; these variations are most likely associated with a change in the dynamics of domain or interphase states. The polarization induced at low temperatures in the ferroelectric state deviates from its preferred direction already in fields as weak as ~4 kV/cm for $T > T_{sp}$ and undergoes reorientation.

The upper temperature boundary of existence of an intermediate relaxor state in PST, above which the crystal transfers to a paraelectric state, is a debatable topic. In [6], indications of a relaxor behavior could be traced up to 170°C, whereas in [7], the paraelectric phase formed only above 400°C. An answer to this problem can be found by studying the behavior of dielectric permittivity over a broad temperature range, including the relaxor and paraelectric states, and by investigating the effect of ion ordering *s* on the character of this behavior. It is known that in compounds with a diffuse phase transition the temperature dependence of the reciprocal dielectric permittivity above $T_{max\,\varepsilon}$ is described by the expression [11] $(\varepsilon^{-1} - \varepsilon_{max}^{-1}) = A(T - T_{max\,\varepsilon})^{\alpha}$, where ε_{max} is the value of ε at the maximum, $T_{max\,\varepsilon}$ is the temperature of the maximum in ε, α is a critical parameter varying in the interval of 1 to 2, and *A* is a constant. In typical relaxors, such as PMN, the dielectric permittivity follows a quadratic relation with $\alpha = 2$ at temperatures approximately 200°C above $T_{max\,\varepsilon}$. Only at higher temperatures (360–400°C above $T_{max\,\varepsilon}$) is the Curie–Weiss law met and does the parameter α approach unity. In compounds of the type of PST in which not only the relaxor state exists but also a spontaneous phase transition occurs, no quadratic dependence of ε^{-1} on temperature has been observed [12]. Figure 2 shows the reciprocal dielectric permittivity plotted vs. temperature on the log–log scale for PST crystals with different values of *s*. It is seen that the slope of the straight lines (equal to α) varies depending on *s*; more specifically, the larger the degree of ordering *s* at temperatures above $T_{max\,\varepsilon}$, the closer the parameter α to unity ($\alpha = 1.3$ for $s = 0.9$, curve *1*). As *s* decreases, the parameter α approaches 2 ($\alpha = 1.58$ for $s = 0.3$, curve *3*). This is seen more clearly in the inset to Fig. 2. The reciprocal dielectric permittivity in crystals with different *s* is observed to depend on temperature with $\alpha = 1$ only at temperatures above 400°C, which implies a transition to a uniform paraelectric phase. Thus, the PST crystals studied in this work retain specific features of the relaxor behavior up to 400°C even in highly ordered compounds.

We used dielectric permittivity measurements performed with different ac electric fields to calculate the coefficient α for temperatures above T_{sp}. It was found that changing the field strength from 1 to 600 V/cm virtually does not affect the magnitude of α. This may mean that ac fields of up to 600 V/cm do not induce the formation of new polar clusters and only slightly increase the size of those that already exist. This is also confirmed by our optical measurements carried out in fields of up to 4 kV/cm (curve *1*' in Fig. 1). Otherwise, α would have grown with increasing ac field to approach 2, as was observed in [13] to occur in a PZT-based ferroelectric ceramic.

4. CONCLUSION

Thus, our dielectric and optical studies of stoichiometric disordered PST single crystals with different values of *s* clearly indicate that the mechanism of polarization response in the relaxor state immediately above T_{sp} is related to induced polarization effects and macrohysteretic behavior only in ac fields above 5 kV/cm. Growth of domains and polar regions in size, which gives rise to the formation of macrodomain clusters above T_{sp}, may account for the observed decrease in OT.

Analysis of the behavior of the dielectric permittivity over a broad temperature interval considerably above $T_{max\,\varepsilon}$ showed the relaxor-behavior features in PST crystals to persist up to 400°C even in highly ordered compounds. This behavior of ε at high temperatures in crystals with $s \longrightarrow 1$ appears to be of interest and requires further study to gain insight into the nature of relaxor phenomena in inhomogeneous ferroelectric media.

ACKNOWLEDGMENTS

This study was supported by the Russian Foundation for Basic Research, project no. 01-02-17801.

REFERENCES

1. A. K. Tagantsev and A. E. Glazounov, Phys. Rev. B **57** (1), 18 (1998).
2. A. E. Glazounov, A. K. Tagantsev, and A. J. Bell, Phys. Rev. B **53** (17), 11281 (1996).
3. G. A. Smolensky, J. Phys. Soc. Jpn., Suppl. **28**, 26 (1970).
4. V. V. Kirillov and V. A. Isupov, Ferroelectrics **5**, 3 (1973).
5. L. S. Kamzina and N. N. Kraĭnik, Fiz. Tverd. Tela (St. Petersburg) **43** (10), 1880 (2001) [Phys. Solid State **43**, 1958 (2001)].
6. F. Chu, C. R. Fox, and N. Setter, J. Am. Ceram. Soc. **81** (6), 1577 (1998).
7. L. S. Kamzina, N. N. Kraĭnik, L. M. Sapozhnikova, *et al.*, Pis'ma Zh. Tekh. Fiz. **14** (19), 1760 (1988) [Sov. Tech. Phys. Lett. **14**, 764 (1988)].
8. L. S. Kamzina and A. L. Korzhenevskiĭ, Pis'ma Zh. Éksp. Teor. Fiz. **50** (3), 146 (1989) [JETP Lett. **50**, 163 (1989)].
9. L. S. Kamzina and N. N. Kraĭnik, Fiz. Tverd. Tela (St. Petersburg) **42** (1), 136 (2000) [Phys. Solid State **42**, 142 (2000)].
10. F. Chu, N. Setter, and A. K. Tagantsev, J. Appl. Phys. **74** (8), 5129 (1993).
11. R. L. Moreira and R. P. S. M. Lobo, J. Phys. Soc. Jpn. **61** (6), 1992 (1992).
12. A. Sternberg, L. Shebanovs, E. Birks, *et al.*, Ferroelectrics **217**, 307 (1998).
13. A. V. Shilnikov, I. V. Otsarev, A. I. Burkhanov, *et al.*, Ferroelectrics **235**, 125 (1999).

Translated by G. Skrebtsov

Physics of the Solid State, Vol. 45, No. 1, 2003, pp. 158–162. Translated from Fizika Tverdogo Tela, Vol. 45, No. 1, 2003, pp. 151–155.

MAGNETISM AND FERROELECTRICITY

Acoustic Emission and Thermal Expansion of $Pb(Mg_{1/3}Nb_{2/3})O_3$ and $Pb(Mg_{1/3}Nb_{2/3})O_3$–$PbTiO_3$ Crystals

E. Dul'kin*, I. P. Raevskiĭ, and S. M. Emel'yanov****

** Advanced School of Applied Science, The Hebrew University, Jerusalem, 91904 Israel*

e-mail: dulkin@pob.huji.ac.il

*** Research Institute of Physics, Rostov State University, pr. Stachki 194, Rostov-on-Don, 344090 Russia*

e-mail: rip@ip.rsu.ru

Received April 3, 2002

Abstract—The temperature dependence of the elongation per unit length for $Pb(Mg_{1/3}Nb_{2/3})O_3$ crystals unannealed after growth and mechanical treatment is investigated in the course of thermocycling. It is revealed that this dependence deviates from linear behavior at temperatures below 350°C. The observed deviation is characteristic of relaxors, is very small in the first cycle, increases with increasing number n of thermocycles, and reaches saturation at $n \geq 3$. In the first cycle, a narrow maximum of the acoustic emission activity is observed in the vicinity of 350°C. In the course of thermocycling, the intensity of this maximum decreases and becomes zero at $n > 3$. For $(1 - x)Pb(Mg_{1/3}Nb_{2/3})O_3$–$xPbTiO_3$ crystals, the dependence of the temperature of this acoustic emission maximum on x exhibits a minimum. It is assumed that the phenomena observed are associated with the phase strain hardening due to local phase transitions occurring in compositionally ordered and polar nanoregions. © *2003 MAIK "Nauka/Interperiodica".*

1. INTRODUCTION

Lead magnoniobate $Pb(Mg_{1/3}Nb_{2/3})O_3$ (PMN) is a typical representative of relaxor ferroelectrics. These materials have been extensively investigated in recent years [1–3]. The permittivity ε of relaxor ferroelectrics shows a smeared maximum whose temperature T_m and height ε_m depend on the frequency of the measuring field. Unlike ferroelectrics, which exhibit an abrupt phase transition, relaxors do not undergo macroscopic structural transformations at temperatures close to T_m. The specific features in the properties of relaxors are associated with their inhomogeneity on the mesoscopic level, particularly with the presence of polar and compositionally ordered nanometer-sized regions in the paraelectric matrix [2–11]. The polar regions are formed in the course of cooling at a temperature $T_d \approx$ 350°C, which is considerably higher than the temperature T_m ($T_m \approx -10$°C for PMN). The number and the mean size of these regions gradually increase with decreasing temperature [2–4, 8, 9]. By contrast, the mean size (2–5 nm) and volume content (20–30% according to different estimates [5, 8]) of compositionally ordered regions remain nearly constant with a change in the temperature from 200 to 800 K [8]. For these materials, the ordered regions were long thought to be nonstoichiometric in composition with the ratio Mg : Nb = 1 : 1 and the net uncompensated charge was considered to be one of the main factors limiting their size [2, 3, 5]. In recent years, there has appeared evidence that, although PMN ferroelectrics have a composition with the ratio Mg : Nb = 2 : 1, compositional ordering in nanoregions is characterized by a ratio of 1 : 1 and occurs in accordance with the random-site model [3, 10, 11]. Within this model, the crystal lattice of PMN in an ordered state consists of two sublattices, namely, the sublattice B' containing Nb^{5+} cations alone and the sublattice B'' whose sites are randomly occupied by Nb^{5+} and Mg^{2+} cations in the ratio 1 : 2; as a result, the composition of lead magnoniobate is described by the formula $Pb(Nb)_{1/2}(Nb_{1/3}Mg_{2/3})_{1/2}O_3$.

At temperatures below T_d, the temperature dependences of the birefringence and the elongation per unit length $\Delta L/L$ for PMN deviate from linear behavior (characteristic of higher temperatures), which is associated with the formation of polar nanoregions and an increase in their total volume with a decrease in the temperature [2–4, 12–18]. The maximum deviation of the dependence $\Delta L/L(T)$ from linearity at temperatures below T_d agrees with the electrostrictive constants of PMN in order of magnitude [2, 4, 18]. It should be noted that, at temperatures above T_d, the linear thermal expansion coefficients α determined both with the dilatometric technique [2, 12, 14, 17] and from the temperature dependences of the lattice parameter [15, 16, 18] are in close agreement. At the same time, the dilatometric data obtained in different works [2, 12, 14, 17] for temperatures below T_d differ significantly.

Earlier, it was repeatedly noted that the properties of relaxors substantially depend on the prehistory of the studied samples, specifically on the conditions of preliminary annealing and mechanical treatment [2]. Although the available data on this dependence corre-

spond to temperatures below T_m, we can assume that a similar effect also manifests itself at higher temperatures. Note that, in specific cases, considerable differences between the dependences $\Delta L/L(T)$ measured for different crystals (or even for the same crystal in different cooling–heating cycles) are observed in ferroelectric materials characterized by an abrupt phase transition. One of the reasons for these differences is the phase strain hardening, which consists in generating misfit dislocations due to disturbance of coherence at the interfaces of ferroelectric nuclei or between an antiferroelectric phase and a paraelectric matrix upon a first-order phase transition [19–21]. As a rule, crystals contain grown-in dislocations. In the course of thermocycling, these dislocations interact (in particular, annihilate) with misfit dislocations, which is attended by acoustic emission [19–22]. Acoustic emission maxima are frequently observed even in the case when anomalies in the elongation per unit length $\Delta L/L$ are either absent or weakly pronounced [22]. The acoustic emission activity $\dot{N}$ (the number of pulses per unit time) is proportional to the number of annihilating dislocations. Consequently, the maximum of the acoustic emission activity, as a rule, is well pronounced only in the first heating–cooling cycles and decreases in the course of phase strain hardening. The acoustic emission technique, as applied to relaxor ferroelectrics, makes it possible to determine the phase transition temperature and to investigate manifestations of phase strain hardening.

The aim of this work was to investigate the thermal expansion and acoustic emission of $Pb(Mg_{1/3}Nb_{2/3})O_3$ and $(1 - x)Pb(Mg_{1/3}Nb_{2/3})O_3$–$xPbTiO_3$ (PMN–PT) crystals in the course of thermocycling in the vicinity of the temperature T_d under nonequilibrium conditions of relaxation of growth defects and defects produced by mechanical treatment.

2. SAMPLE PREPARATION AND EXPERIMENTAL TECHNIQUE

Transparent yellow crystals of $Pb(Mg_{1/3}Nb_{2/3})O_3$ and $(1 - x)Pb(Mg_{1/3}Nb_{2/3})O_3$–$xPbTiO_3$ (x = 0.25 and 0.40) in the form of cubes with edges up to 6 mm in length and faceting along the (001) planes of the perovskite basis were grown through spontaneous crystallization from a solution in melt with the use of a PbO–B_2O_3 mixture as a solvent [23]. The composition of PMN–PT crystals was determined using a "Camebax-Micro" scanning microscope–microanalyzer. Samples in the form of plates $4 \times 4 \times 1$ mm in size were cut parallel to the (001) natural faces of the crystal and were then ground. It should be noted that, following the purpose in hand, the studied crystals after growth and mechanical treatment were not annealed prior to measurements, unlike in the universally accepted procedure.

The measurements were performed according to a combined technique described earlier in [24]. A crystal was mounted on the polished surface of a cylindrical quartz acoustic waveguide, which was vertically inserted into the bottom of the furnace. An acoustic emission detector made from a TsTS-19 piezoelectric ceramic material was cemented to the lower cold surface of the waveguide. Two rods of a differential dilatometer with a sensitivity higher than 10^{-7} were inserted into the top of the furnace. The temperature was measured using a chromel–alumel thermocouple whose junction was in close contact with the crystal. The thermal elongation per unit length $\Delta L/L$ and the acoustic emission activity were measured simultaneously during cooling of the crystals in the course of thermocycling in the temperature range 200–500°C at a rate of 1–2 K/min.

3. RESULTS

The results of dilatometric measurements of PMN crystals in the first three thermocycles are presented in Fig. 1. In the first thermocycle, the temperature dependence $\Delta L/L(T)$ only slightly deviates from linear behavior. In the second and third thermocycles, the dependence $\Delta L/L(T)$ appreciably deviates from linearity; in this case, the deviation increases with an increase in the number of thermocycles. After the third thermocycle, the dependence $\Delta L/L(T)$ ceases to change. The deviation of the temperature dependence $\Delta L/L(T)$ for PMN crystals from linear behavior after the third thermocycle is in reasonable agreement in sign and order of magnitude with the results obtained in [2, 12–14]. The deviation of the dilatometric curves from linearity is observed beginning at 350°C and is attended by a drastic increase in the acoustic emission activity. The acoustic emission activity decreases with an increase in the number of thermocycles. After the third thermocycle, the acoustic emission is virtually absent.

Figure 2 shows the dependences $\Delta L/L(T)$ and $\dot{N}(T)$ for $(1 - x)Pb(Mg_{1/3}Nb_{2/3})O_3$–$xPbTiO_3$ (x = 0.25 and 0.40) crystals in the course of cooling in the first thermocycle. As in the case of the PMN crystal, the dependence $\Delta L/L(T)$ measured for a crystal with x = 0.25 (corresponding to relaxor compositions [3]) in the first thermocycle exhibits a nearly linear behavior. A radically different curve $\Delta L/L(T)$ is obtained for a crystal with x = 0.40, which is similar in structure and properties to conventional ferroelectrics [3, 7]. A jump corresponding to the ferroelectric phase transition in the vicinity of 220°C is observed for the elongation per unit length $\Delta L/L$ even upon the first cooling. Moreover, the dependence $\Delta L/L(T)$ deviates from linearity in the vicinity of 330°C, i.e., at a lower temperature than in the case of the PMN crystal. Unlike the PMN crystal, the crystals with x = 0.25 and 0.40 are characterized by two maxima of the acoustic emission activity. For the crystal with x = 0.40, the first maximum in the depen-

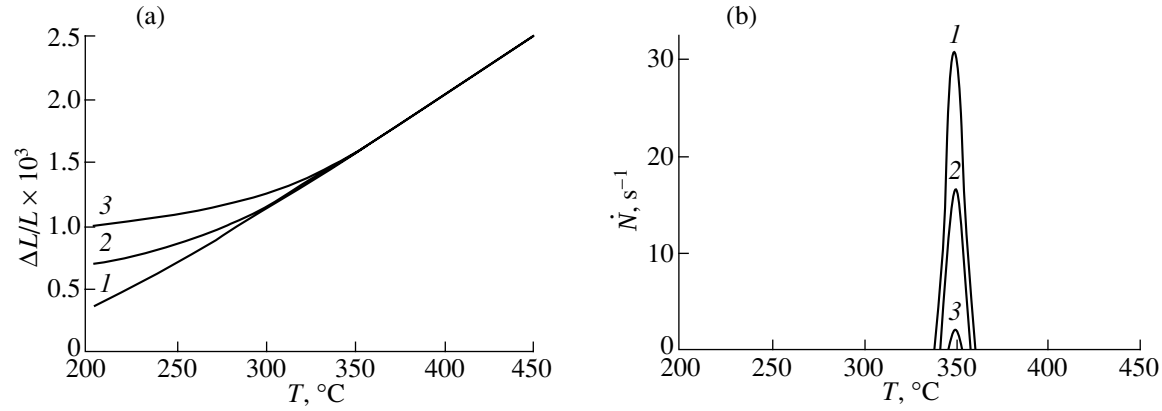

Fig. 1. Temperature dependences of (a) the elongation per unit length and (b) the acoustic emission activity $\dot{N}$ for the $Pb(Mg_{1/3}Nb_{2/3})O_3$ crystal during cooling in different heating–cooling cycles. Numerals near the curves indicate the cycle number.

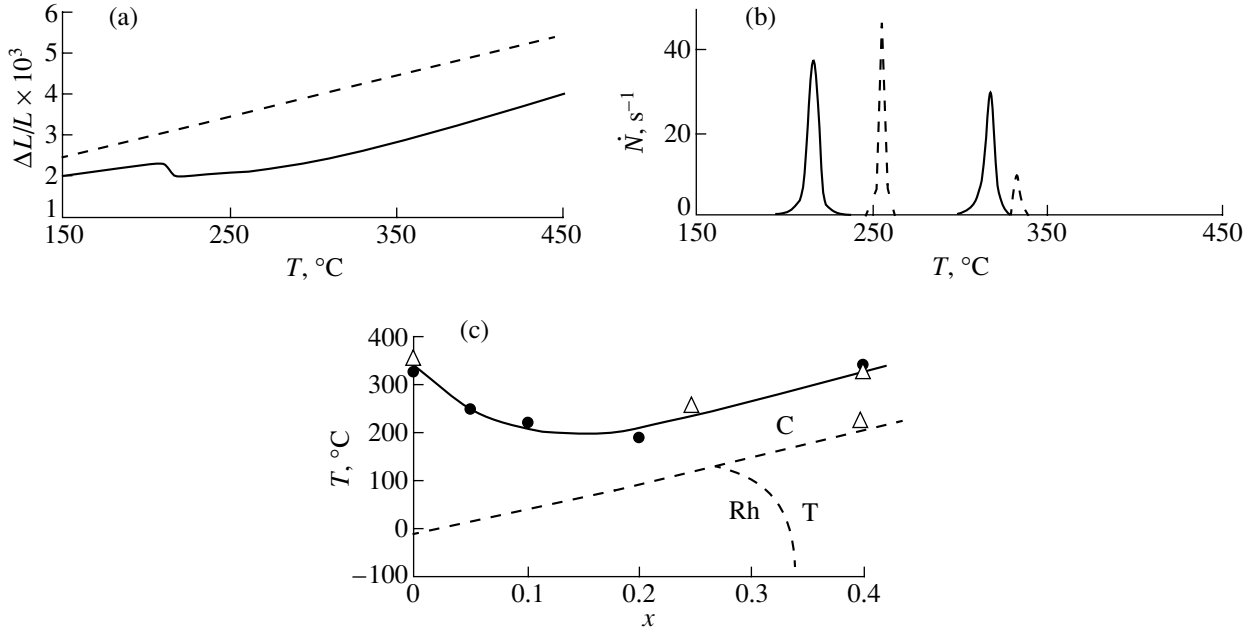

Fig. 2. Temperature dependences of (a) the elongation per unit length and (b) the acoustic emission activity $\dot{N}$ for $(1 - x)Pb(Mg_{1/3}Nb_{2/3})O_3$–$xPbTiO_3$ crystals with $x = 0.25$ (dashed lines) and $x = 0.40$ (solid lines) during cooling in the first heating–cooling cycle. (c) Temperatures of deviation of the dependences $a^*(T)$ from linear behavior according to the data taken from [16] (closed circles) and the temperature of the acoustic emission activity maximum (open triangles) as a function of the $PbTiO_3$ content in $(1 - x)Pb(Mg_{1/3}Nb_{2/3})O_3$–$xPbTiO_3$ crystals. The dashed line shows the x–T phase diagram of the $(1 - x)Pb(Mg_{1/3}Nb_{2/3})O_3$–$xPbTiO_3$ system according to the data taken from [16, 25, 26]. Designations: C is the cubic phase, Rh is the rhombohedral phase, and T is the tetragonal phase.

dence $\dot{N}(T)$ corresponds to a ferroelectric phase transition at 220°C and the second maximum is observed at 330°C, i.e., at a temperature lower than that for the PMN crystal. The main maximum in the dependence $\dot{N}(T)$ for the crystal with $x = 0.25$ occurs at 250°C, which is considerably lower than that for PMN. A weak maximum of the acoustic emission activity at a temperature of approximately 330°C, most likely, can be caused by concentration inhomogeneities in the crystal. Thus, the dependence of the temperature of the maximum in $\dot{N}(T)$ on the titanium content in PMN–PT crystals exhibits a minimum (Fig. 2c).

4. DISCUSSION

A comparison of the temperatures of the maxima revealed in the dependence $\dot{N}(T)$ and the x–T phase diagram of solid solutions in the $(1 - x)$PMN–xPT sys-

tem [16, 25, 26] demonstrates that only the low-temperature acoustic emission maximum and its attendant jump in the dependence $\Delta L/L(T)$ for crystals with $x = 0.40$ correspond in temperature to the known phase transition from the tetragonal phase to the cubic phase. All the other anomalies in the acoustic emission are observed at temperatures close to T_d. At these temperatures, as follows from the high-temperature x-ray diffraction data obtained in [16], the dependence of the mean unit-cell parameter $a^* = V^{1/3}$ (where V is the unit cell volume) for the studied crystals deviates from linear behavior (Fig. 2c).

A decrease in the acoustic emission activity due to phase strain hardening was previously observed upon thermocycling in ferroelectric crystals [19] and ferroelectric ceramic materials [20] undergoing abrupt phase transitions. In particular, for (Na,Li)NbO_3 ceramic samples, a maximum in the acoustic emission activity was revealed in the first thermocycle, whereas a minimum manifested itself after the third thermocycle, as is the case with our crystals. If the change observed in the dependences $\Delta L/L(T)$ for PMN crystals is caused by phase strain hardening, we should assume that a phase transition occurs near T_d. This assumption is consistent with data available in the literature on the anomalies observed in the temperature dependences of the permittivity $\varepsilon(T)$ [12], the mean unit-cell parameter $a^*(T)$ [16], and the heat capacity [15] for PMN crystals at temperatures close to T_d. However, the absence of macroscopic structural transformations in PMN crystals at these temperatures suggests a local character of the phase transition. As was noted above, the PMN crystals involve nanoregions of two types, namely, polar and compositionally ordered nanoregions. Since the volume content of polar nanoregions in the vicinity of T_d is close to zero [2–4, 9], it seems likely that the narrow maximum at 350°C in the dependence $\dot{N}(T)$ corresponds to a phase transition in compositionally ordered nanoregions whose volume content is relatively large and does not depend on the temperature. Apparently, this phase transition is antiferroelectric in nature, because, otherwise, the temperature dependence of the birefringence proportional to the mean square of the polarization should exhibit a jump at a temperature close to T_d; however, no jumpwise increase in the birefringence occurs [2, 4]. Furthermore, a number of authors [3, 6–8, 11] have observed ion displacements of the antiferroelectric type in compositionally ordered nanoregions of the PMN crystals. Precision x-ray diffraction investigations [16] also demonstrated that the deviation of the temperature dependence $a^*(T)$ from linearity upon cooling of PMN crystals is preceded by a jumpwise decrease in the parameter a^*, which is characteristic of antiferroelectric phase transitions [1].

The assumption regarding the antiferroelectric nature of the phase transition in compositionally ordered nanoregions at $T \approx T_d$ also offers a satisfactory explanation of the nonmonotonic dependence $T_d(x)$ for the PMN–PT system. It is known that the concentration dependence of the phase transition temperature for solid solutions of an antiferroelectric and a ferroelectric passes through a minimum (the most known examples are provided by the $NaNbO_3$–$KNbO_3$ and $PbZrO_3$–$PbTiO_3$ systems [1, 27]). Upon addition of $PbTiO_3$ to compositionally ordered antiferroelectrics, such as $PbMg_{1/2}W_{1/2}O_3$ and $PbYb_{1/2}Nb_{1/2}O_3$, this minimum in the concentration dependences becomes more pronounced [3, 27].

It should be noted that the formation of polar regions in the paraelectric matrix can also be considered a local ferroelectric phase transition; moreover, compared to the antiferroelectric phase transitions, the local ferroelectric phase transitions should make a substantially larger contribution to the acoustic emission and phase strain hardening [19–21]. This can be judged, in particular, from the more pronounced strain hardening observed in the 0.6PMN–0.4PT crystal. For this crystal, the dependence $\Delta L/L(T)$ strongly deviates from linear behavior even in the first cooling cycle. This can be explained by the occurrence of the normal ferroelectric transition, which is accompanied by a strong spontaneous strain and, consequently, by a more appreciable change in the dependence $\Delta L/L(T)$. On the other hand, since the temperatures of the local ferroelectric transitions lie in a very wide range [2], their related acoustic emission manifests itself only as a background weakly dependent on the temperature. A narrow maximum in the acoustic emission activity and anomalies in the dependence $a^*(T)$ in the temperature range of phase transitions occurring in compositionally ordered regions can be observed because the total volume of these regions is sufficiently large (up to 30% of the crystal volume [5]) and the temperatures of the phase transitions in all the regions are close to each other.

5. CONCLUSIONS

Thus, we investigated the thermal expansion and acoustic emission of PMN and PMN–PT crystals under nonequilibrium conditions of relaxation of growth defects and defects produced by mechanical treatment. It was found that the shape of the curve $\Delta L/L(T)$ depends on the number of thermocycles and that the acoustic emission activity exhibits a maximum at $T \approx T_d$. For $(1-x)$PMN–xPT crystals, the dependence of the temperature of this maximum in the acoustic emission activity on x shows a minimum. Analysis of the results obtained and the data available in the literature on the structural, dielectric, and thermal properties of PMN materials [12, 13, 16] permit the assumption that the acoustic emission maxima observed in the vicinity of T_d are associated with the local antiferroelectric phase transitions occurring in compositionally ordered nanoregions. The change in the dependence $\Delta L/L(T)$ upon thermocycling is caused by the phase strain hardening

induced by local phase transitions in both the compositionally ordered and polar nanoregions of the crystal. The considerable scatter in the data on the thermal expansion of PMN crystals at temperatures below T_d is explained by the fact that the deviation of the curve $\Delta L/L(T)$ from linear behavior at temperatures below T_d strongly depends on the degree of relaxation of the defect structure (in our case, on the conditions of annealing of the crystals after the growth, mechanical treatment, and other actions).

ACKNOWLEDGMENTS

This work was supported in part by the Russian Foundation for Basic Research (project no. 01-03-33119) and the Ministry of Education of the Russian Federation (project no. E00-3.4-287)

REFERENCES

1. G. A. Smolenskiĭ, V. A. Belov, V. A. Isupov, N. N. Kraĭnik, R. E. Pasynkov, A. I. Sokolov, and N. K. Yushin, *Physics of Ferroelectric Phenomena* (Nauka, Leningrad, 1985).
2. L. E. Cross, Ferroelectrics **76**, 241 (1987).
3. I. W. Chen, J. Phys. Chem. Solids **61**, 197 (2000).
4. G. Burns and F. H. Dacol, Solid State Commun. **48**, 853 (1983).
5. E. Prouzet, E. Husson, N. de Mathan, and A. Morell, J. Phys.: Condens. Matter **5**, 4889 (1993).
6. E. Husson, M. Chubb, and A. Morell, Mater. Res. Bull. **23**, 357 (1988).
7. S. B. Vakhrushev, Author's Abstract of Doctoral Dissertation (St. Petersburg, 1998).
8. A. Tkachuk, H. Chen, P. Zschack, and E. Colla, in *Fundamental Physics of Ferroelectrics 2000: Aspen Center for Physics Winter Workshop*, Ed. by R. E. Cohen (American Inst. of Physics, Melville, 2000); AIP Conf. Proc. **535**, 136 (2000).
9. G. K. Smolenskiĭ, N. K. Yushin, S. I. Smirnov, and S. N. Dorogovtsev, Dokl. Akad. Nauk SSSR **294**, 1366 (1987) [Sov. Phys. Dokl. **32**, 501 (1987)].
10. Y. Yan, S. J. Pennycook, Z. Xu, and D. Viehland, Appl. Phys. Lett. **72**, 3145 (1998).
11. S. Miao, J. Zhu, X. Zhang, and Z.-Y. Cheng, Phys. Rev. B **65**, 052101 (2001).
12. N. N. Krainik, L. A. Markova, V. V. Zhdanova, *et al.*, Ferroelectrics **90**, 119 (1989).
13. A. Fouskova, V. Kohl, N. N. Krainik, and I. E. Mylnikova, Ferroelectrics **34**, 119 (1981).
14. H. Arndt and F. Schmidt, Ferroelectrics **79**, 149 (1988).
15. P. Bonnneau, P. Garnier, C. Calvarin, *et al.*, J. Solid State Chem. **91**, 350 (1991).
16. O. Bunina, I. Zakharchenko, S. Yemelyanov, *et al.*, Ferroelectrics **157**, 299 (1994).
17. M. Damdekalne, K. Bormanis, L. Chakare, and A. Sternberg, Ferroelectrics **186**, 293 (1996).
18. A. E. Glazounov, J. Zhao, and Q. M. Zhang, in *Proceedings of 5th Williamsburg Workshop on First-Principles Calculations for Ferroelectrics*, Ed. by R. E. Cohen (American Inst. of Physics, Woodbury, 1998); AIP Conf. Proc. **436**, 118 (1998).
19. V. G. Gavrilyachenko, E. A. Dul'kin, and A. F. Semenchev, Fiz. Tverd. Tela (St. Petersburg) **37**, 1229 (1995) [Phys. Solid State **37**, 668 (1995)].
20. E. A. Dul'kin, L. V. Grebenkina, I. V. Pozdnyakova, *et al.*, Pis'ma Zh. Tekh. Fiz. **25** (2), 68 (1999) [Tech. Phys. Lett. **25**, 70 (1999)].
21. E. A. Dul'kin, V. G. Gavrilyachenko, and O. E. Fesenko, Fiz. Tverd. Tela (St. Petersburg) **39**, 740 (1997) [Phys. Solid State **39**, 654 (1997)].
22. E. A. Dul'kin, I. P. Raevskiĭ, and S. M. Emel'yanov, Fiz. Tverd. Tela (St. Petersburg) **39**, 363 (1997) [Phys. Solid State **39**, 316 (1997)].
23. S. M. Emel'yanov, N. P. Protsenko, V. A. Zagoruĭko, *et al.*, Izv. Akad. Nauk SSSR, Neorg. Mater. **27**, 431 (1991).
24. E. A. Dul'kin, Mater. Res. Innovations **2**, 338 (1999).
25. S. W. Choi, T. R. Shrout, S. J. Jang, and A. S. Bhalla, Ferroelectrics **100**, 29 (1989).
26. E. V. Colla, N. K. Yushin, and D. Viehland, J. Appl. Phys. **83**, 3298 (1998).
27. V. A. Isupov, Phys. Status Solidi A **181**, 211 (2000).

Translated by O. Borovik-Romanova

Physics of the Solid State, Vol. 45, No. 1, 2003, pp. 16–20. Translated from Fizika Tverdogo Tela, Vol. 45, No. 1, 2003, pp. 17–21.

METALS AND SUPERCONDUCTORS

Metastable Phases in YBCO Films Created by Short-Term Annealings

M. I. Samoĭlov*, V. A. Sukhov, and A. L. Rakhmanov***

* *Institute of Theoretical and Applied Electrodynamics, Russian Academy of Sciences, Moscow, 127412 Russia*

** *Moscow Power Engineering Institute, Moscow, 111250 Russia*

Received December 28, 2001; in final form, May 21, 2002

Abstract—The effect of short-term low-temperature annealing in air and in vacuum on the properties of HTSC films of YBCO is studied. It is shown that, under certain conditions of preparation of initial samples, a transition from the HTSC phase with the superconducting transition temperature T_c = 90 K to a phase with T_c = 60 K occurs without a noticeable change in the oxygen content. It is found that, as a result of short-term annealings, a transition from the HTSC phase with T_c = 60 K to the phase with T_c = 90 K can occur only through the vacuum annealing stage, which converts the sample into the superconducting state. Short-term annealings lead to multiple reversible "switching" of the films from one phase to another. The obtained results are of practical interest, since the proposed method can be used to quickly obtain superconducting YBCO films in various phase states. It is shown, in addition, that the annealing procedure makes it possible not only to increase the oxygen concentration but also to produce a structural rearrangement of a YBCO film. © *2003 MAIK "Nauka/Interperiodica".*

1. INTRODUCTION

It has been generally accepted that the superconducting transition temperature T_c of bulk oxide-based high-temperature superconductors (HTSCs) is practically in one-to-one correspondence with the oxygen concentration x (or the crystal lattice parameter c) [1]. In bulk $YBa_2Cu_3O_x$ (YBCO) single crystals, for example, the superconducting phase with $T_c \approx 90$ K exists for $6.8 < x < 7.0$ (1.168 nm < c < 1.170 nm) and the superconducting phase with $T_c \approx 60$ K corresponds to $6.6 < x < 6.8$ (1.172 nm < c < 1.176 nm), while for concentrations x below 6.4–6.5 (c > 1.178 nm), a semiconducting (nonsuperconducting) phase is formed. However, this regularity is not universal and the one-to-one correspondence between the superconducting transition temperature and the lattice parameter c (and, apparently, the oxygen concentration x) is violated under certain conditions. For example, this is the case with bulk samples from which oxygen is removed according to the so-called soft method, i.e., when a sample is subjected to short-term low-temperature annealing under special conditions or when oxygen is removed by substitution of hydrogen or azobenzene [1–5].

Another object in which the $T_c(c)$ dependence differs from that for single crystals is a superconducting film. The superconducting phase with T_c = 80–90 K exists in films up to values of c = 1.180–1.182 nm [6]. Unfortunately, it is quite difficult to determine the oxygen concentration in films using direct methods in view of their small mass. For this reason, the relation between the lattice parameter c and the oxygen content x in films has not been established reliably.

We studied a large number of superconducting films of the YBCO system which were subjected to short-term (5–15 min), low-temperature (400–700°C) annealing in air and in vacuum. The superconducting transition temperature T_c was determined using the standard four-probe method. The lattice parameter c was determined using x-ray diffractometry. It was shown that the $T_c(c)$ dependence for high-quality, single-phase films displays a hysteresis; i.e., superconducting phases with $T_c \approx 90$ and ≈60 K may exist at the same value of c. Moreover, we established a certain exclusion principle. For example, short-term annealings make it possible to obtain the 60-K phase and a semiconducting nonsuperconducting phase from the 90-K phase; the 60-K phase can be transformed only to a semiconducting phase, and the semiconducting phase can be used to obtain the 90- and 60-K HTSC phases. Thus, a direct transition from the 60-K phase to the 90-K phase with the help of shot-term annealings is forbidden, while the transition from the semiconducting phase to the 90-K HTSC phase is allowed.

The technological process worked out by us makes it possible to obtain films with high values of the superconducting transition temperature T_c and a large lattice parameter c directly in the course of sputtering (without subsequent processing) [7–10]. The possibility of multiple irreversible switching of the samples from the 90-K HTSC phase to the 60-K and semiconducting phases and back indicates that no damage or contamination of the films occurs as a result of the annealing regimes used by us. The obtained results combined with the available data from the literature (see above)

1063-7834/03/4501-0016$24.00 © 2003 MAIK "Nauka/Interperiodica"

Table 1. Comparison of properties of films obtained with and without post-annealing

Sample	T_c, K	c, nm	x*	Regime
YBCO (*A*)	90	1.174	6.6	Post-annealing in regime II
YBCO (*B*)	75	1.171	6.8	Without post-annealing; 40 vol % oxygen in the working mixture

* Oxygen content is recalculated from the $x(c)$ relation for bulk samples [1].

suggest that metastable superconducting phases may exist in the YBCO system.

2. SAMPLE PREPARATION AND METHODS OF MEASUREMENT

Films were obtained using dc magnetron sputtering on lithium niobate substrates (monocrystalline $LiNbO_6$ coated with a ZrO_2 layer oriented in the (100) direction) and on monocrystalline MgO (100) substrates. The sputtering system consisted of a vacuum chamber 300 mm in diameter with a bracket for clamping a cylindrical magnetron to the chamber and a heater mounted above it, whose temperature was registered with a thermocouple. The system also included blocks of evacuation, gas supply, and pressure control. A thermal molecular pump with an evacuation rate of 20 s^{-1} and a rotary pump with an evacuation rate of 100 s^{-1} ensured a residual pressure down to 2×10^{-5} Pa in the working chamber. A target with a stoichiometric composition was soldered to a water-cooled magnetron with the help of indium solder. Substrates were fixed directly to a quartz thermal ballast supplied with a heater with a nichrome strip as the resistive element. The temperature of the substrate was controlled with a chromel–alumel thermocouple. The target diameter was 100 mm, the thickness was 7 mm, and the substrate size was 20×10 mm. The substrate was mounted above the center of the target. Two gas flow rate regulators monitored the gas mixture composition in the chamber.

The films were grown *in situ* using the following procedure [7–10]. A substrate was fixed to the heater, after which the working chamber was evacuated to a pressure of 2×10^{-5} Pa. Then, the substrate was heated to the sputtering temperature 700°C and a working mixture containing 70 vol % Ar and 30 vol % O was introduced into the chamber. The working mixture pressure was 20 Pa. The magnetron discharge current was 0.8 A, and the voltage was 80 V. Prior to the next series of sputtering, the target was presputtered in pure argon for 5 h. The film deposition time was 3–5 h, and the thickness of the prepared films was 100 nm. After deposition, the films were cooled for 10 min under the pressure at which the sputtering was carried out; then, the temperature of the films remained unchanged for 15 min. For the sake of brevity, we will call this process post-annealing. We used two regimes for such processes. In the first case (regime I), the working-mixture pressure remained unchanged but a collector discharge (100 mA) was triggered. In the second case (regime II), the working-mixture pressure was raised to 1000 Pa due to oxygen puffing. After post-annealing, the films were cooled to room temperature over 30 min. Repeated annealings were carried out in the working chamber (vacuum annealing) or in a special furnace (annealing in air).

Resistance measurements were made using the standard four-probe technique. X-ray measurements were made on a Dron-4 diffractometer (CuK_α radiation) and were used to monitor the single-phase form of a sample and the orientation of the crystallographic axis *c* and to determine the crystal lattice parameter *c*. The standard methods were also used for x-ray measurements.

3. RESULTS OF MEASUREMENTS

We systematically studied the effect of technological parameters of the process on the value of T_c and on the results of x-ray structural analysis. In our experiments, we varied the separation between the target and the substrate and their relative position, the current and voltage of the magnetron discharge, the composition of the working mixture, the evacuation rate, and the temperature of the substrate and determined the optimal values of these parameters (for the given setup). The experiments proved that the properties of the films depend on the above parameters insignificantly. This fact considerably facilitates the obtaining of samples with a good reproducibility of their characteristics. It should be noted, however, that overly strong deviations of parameters from their optimal values considerably affect the properties of the samples. For example, following [6], we varied the oxygen content in the films by changing its concentration in the gas mixture, which proved to be ineffective, since the change in the working-mixture composition affected the parameters of the magnetron discharge and sharply deteriorated the reproducibility of the results. On the contrary, the post-annealing parameters significantly affect only the characteristics of the films. By varying the conditions of post-annealing, we can purposefully modify the properties of the samples over wide limits. It should be noted that optimal post-annealing is a more effective method for increasing the superconducting transition temperature than variation of the oxygen pressure in the working mixture. Table 1 gives an example of such a comparison for films obtained with post-annealing in regime II and for similar films obtained at an elevated

Table 2. Effect of annealing on the properties of a sample (successive annealings in air, each annealing lasting 15 min; the sample was obtained in regime I)

T_c, K	c, nm	Annealing temperature, °C
89.6	1.172	<400
88.5	1.174	450
71.3	1.175	530
62.4	1.175	580

Table 3. Effect of annealing on the properties of a sample (single annealing in air for 15 min; the sample was obtained in regime I)

T_c, K	c, nm	Annealing temperature, °C
90.0	1.172	Without annealing
60.8	1.175	580

Table 4. Effect of annealing on the properties of a sample (single annealing in air for 15 min; the sample was obtained in regime II)

T_c, K	c, nm	Annealing temperature, °C
89.0	1.174	Without annealing
≈60	1.174	500

oxygen concentration in the gas mixture (40 vol % instead of 30 vol %) but without post-annealing. Technological investigations are described in greater detail in [7–10].

Thus, using the two regimes with short-term (not exceeding 15 min) post-annealings at a relatively low oxygen pressure, we prepared series of homogeneous YBCO films with a stable, high superconducting transition temperature T_c (88–90 K). It should be noted that no systematic difference in the current–voltage characteristics and in the values of T_c was observed for films obtained in regimes I and II. X-ray measurements proved, however, that all the films obtained in regime II have larger values of the crystal lattice parameter c than the samples prepared in regime I: $c = 1.172$ nm (regime I) and $c = 1.174$ nm (regime II). It should be noted that our films are distinguished by a relatively large value of parameter c [which would correspond to an oxygen content $x \approx 6.8$ (regime I) or $x \approx 6.6$ (regime II) for bulk samples]. Henceforth, repeated heating of a film cooled to room temperature after its preparation will be referred to as annealing.

Then, we studied the effect of short-term (5–15 min) annealing (quenching) at temperatures of 400–700°C in air and in vacuum on the properties of the films obtained with post-annealing in regimes I and II. It can be stated that such annealings did not change the cation composition and caused no contamination or mechanical failure of the samples, since by using this method, a sample can be transformed repeatedly from the superconducting state with $T_c \approx 90$ K to the superconducting state with $T_c \approx 60$ K and to a semiconducting (nonsuperconducting) state and back. The absence of phases other than the stoichiometric phase 123 was confirmed by the x-ray structural data.

It was found that annealing of a sample in air at 400–580°C for less than 15 min makes it possible to change the value of T_c considerably. Table 2 gives an example of such a study for a sample obtained with post-annealing in regime I. It can be seen that, when the annealing temperature exceeds 400°C, the superconducting transition temperature decreases monotonically. This effect was observed for a series of samples both with repeated and single annealings (Table 3). The regular dependence of T_c on the annealing temperature indicates the formation of a stable superconducting phase under the action of only short-term heating in air under normal pressure. The decrease in T_c was accompanied by an insignificant decrease in the resistivity ratio $\gamma = \rho_{300\,K}/\rho_{100\,K}$ from $\gamma \approx 2$ at $T_c \approx 90$ K to $\gamma \approx 1.6$ for $T_c \approx 60$ K. It is worth noting that a conventional correlation between the superconducting transition temperature and the lattice parameter c is observed for the samples obtained with post-annealing in regime I: the value of T_c decreases upon an increase in c ($c = 1.72$ nm for the 90-K phase and $c = 1.75$ nm for the 60-K phase; see Tables 2, 3).

For the films obtained with post-annealing in regime II, the superconducting transition temperature also decreases monotonically with increasing annealing temperature (Table 4). An important distinguishing feature of the films prepared in regime II is that the value of T_c for such films decreases at a constant value of the crystal lattice parameter c. Thus, the crystal structure and its evolution in the course of short-term annealings differ noticeably for samples obtained in regimes I and II, while the electrical parameters are similar.

Using short-term annealings in air and in vacuum, superconducting films can be reversibly switched from one state to another. Table 5 and the figure show an example of this type of complicated sequence of switchings for one of the samples. We denote the state of the initial sample by *A*. The initial film was prepared in regime I; the parameters of the film are given in Table 5, and the temperature dependence of resistance $R(T)$ is shown in the figure (curve *A*). Then, the film was annealed at 580°C in air and was transformed into the 60-K phase (state *B* in Table 5 and curve *B* in the figure). Annealing at 400°C in air led to an increase in T_c but did not return the sample to the initial 90-K phase (state *C*). It was found that, in order to return the film to the initial state, it must first be transformed into the

Table 5. Transitions of a film from one state to another as a result of short-term annealings

State of sample	T_c, K	c, nm	x	Annealing regime
A	89	1.172	≈6.8	Without annealing
B	60	1.175	≈6.6	15-min annealing in air at 580°C
C	77	1.175	≈6.6	15-min annealing in air at 400°C
D	–	1.189	≈6.0	5-min annealing in vacuum at 630°C
E	89	1.172	≈6.8	15-min annealing in air at 400°C

semiconducting phase with the help of short-term annealing in vacuum at a sufficiently high temperature (state *D*) and then annealed in air to transform the film into the 90-K phase (state *E*).

The following interesting fact is worth noting. Short-term annealing does not return a 60-K film to the 90-K phase, but exactly the same annealing converts a semiconducting film into the superconducting phase with T_c = 89 K. This sort of exclusion principle is observed for all samples (prepared in regimes I and II) for different sequences of switchings. Moreover, even 1-h annealing in oxygen of a sample transformed to state *B* (60-K phase) did not return it to the initial 90-K superconducting state. The superconducting transition temperature remained at a level of 70–77 K.

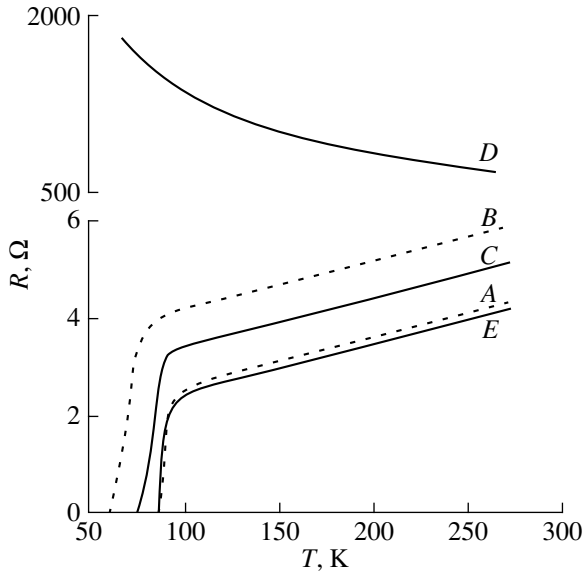

Temperature dependence of the film resistance for different annealing conditions of the initial sample. The notation on the curves corresponds to the states of the sample and the annealing regimes listed in Table 5.

It should be noted that a superconducting sample with $T_c \approx 90$ K can be transformed to a semiconducting tetragonal phase through short-term annealing in vacuum and returned to the initial 90-K superconducting phase through short-term annealing in air.

The switchings of a film from one state to another described above were carried out by us two, three, and even four times on the same sample. It is noteworthy that the reversibility of transformations is quite high (see Table 5 and figure). For the same sample in the 90-K phase, the values of parameter c and the $R(T)$ dependences for the initial and annealed states coincide within the accuracy of our measurements.

4. CONCLUSIONS

Thus, the results of our experiments indicate the richness of the phase diagram of superconducting $YBa_2Cu_3O_x$ films for a constant or slightly varying oxygen content x. The observed effects are probably associated with the phase separation characteristic of strongly correlated electron systems, e.g., with the ordering of copper ions with different valences in our deficiently doped samples or with the formation of the so-called stripe structures [1]. It is also probable that a transition from the 60- to the 90-K phase without a change in the oxygen content can be explained in the framework of the model proposed in [1, 11–13] for describing neutron and Raman scattering spectra. In this model, it is assumed that the so-called apical oxygen [O (4) ion in the Ba–O plane] may be in two states separated by a potential barrier of the order of 0.1 eV. More definite conclusions as to the reasons for the observed effects require further investigations.

The obtained results are also of purely practical importance, since, first, the technique proposed by us makes it possible to obtain superconducting YBCO films with satisfactory characteristics quite rapidly and, second, these results can be used for optimization of the film preparation process. Indeed, the short-term annealing procedure used in this work enabled us to clearly trace the second stage of the two-stage (sputtering–annealing) process of preparing HTSC films with a high T_c. It is shown that annealing increases the oxygen content x and is also required for a certain structural rearrangement of the YBCO crystal lattice.

ACKNOWLEDGMENTS

The authors are grateful to D.A. Kozlov (Moscow Institute of Steel and Alloys) for performing the x-ray structural measurements.

REFERENCES

1. N. M. Plakida, *High-Temperature Superconductivity* (Mezhdunarodnaya Programma Obrazovaniya, Moscow, 1996; Springer, Berlin, 1995).

2. Yu. M. Baĭkov, S. K. Filatov, V. V. Semin, *et al*., Pis'ma Zh. Tekh. Fiz. **16** (14), 56 (1990) [Sov. Tech. Phys. Lett. **16**, 544 (1990)].
3. A. A. Konovalov, A. A. Sidel'nikov, and R. T. Pavlyukhin, Sverkhprovodimost: Fiz., Khim., Tekh. **7**, 517 (1994).
4. V. N. Kuznetsov, Pis'ma Zh. Tekh. Fiz. **27** (10), 1 (2001) [Tech. Phys. Lett. **27**, 394 (2001)].
5. Yu. N. Drozdov, S. A. Pavlov, and A. E. Parafin, Pis'ma Zh. Tekh. Fiz. **24** (1), 55 (1998) [Tech. Phys. Lett. **24**, 24 (1998)].
6. D. K. Aswal, S. K. Gupta, S. N. Naranga, *et al.*, Thin Solid Films **292**, 277 (1997).
7. M. I. Samoilov, V. A. Sukhov, and V. A. Ryzhkov, Superlattices Microstruct., Suppl. A **21**, 307 (1997).
8. M. I. Samoilov and V. A. Sukhov, in *Proceedings of 3rd International Summer School on High-Temperature Superconductivity, Eger, 1997*, p. 51.
9. M. I. Samoilov, in *Abstracts of 5th International Workshop on High-Temperature Superconductors and Novel Inorganic Materials, Moscow, 1998*, W. 51.
10. M. I. Samoĭlov, S. P. Kobeleva, M. P. Beketov, *et al.*, in *Proceedings of International Conference "Physicotechnical Problems of Electromechanical Materials and Components," Moscow, 1999*, p. 180.
11. Yu. M. Baĭkov, Sverkhprovodimost: Fiz., Khim., Tekh. **7**, 1208 (1994).
12. A. P. Saĭko and V. E. Gusakov, Fiz. Nizk. Temp. **22**, 748 (1996) [Low Temp. Phys. **22**, 575 (1996)].
13. M. A. Obolenskiĭ, D. D. Balla, A. V. Bondarenko, *et al.*, Fiz. Nizk. Temp. **25**, 1259 (1999) [Low Temp. Phys. **25**, 943 (1999)].

Translated by N. Wadhwa

Physics of the Solid State, Vol. 45, No. 1, 2003, pp. 163–166. Translated from Fizika Tverdogo Tela, Vol. 45, No. 1, 2003, pp. 156–159.

LATTICE DYNAMICS AND PHASE TRANSITIONS

Nonequilibrium Phonon Propagation in High-Purity CdTe

A. I. Sharkov, T. I. Galkina, A. Yu. Klokov, and Yu. V. Klevkov

Lebedev Physical Institute, Russian Academy of Sciences, Leninskiĭ pr. 53, Moscow, 119991 Russia

e-mail: shark@sci.lebedev.ru

Received January 25, 2002

Abstract—Propagation of nonequilibrium acoustic phonons in samples of high-purity CdTe (impurity content ~10^{16} cm^{-3}) was studied using the heat pulse technique under pulsed photoexcitation. An analysis of nonequilibrium phonon propagation made by comparing the experimental response with Monte Carlo calculations assuming samples to be without twins provided an estimate for the spontaneous anharmonic phonon decay constant $A_L = 2 \times 10^{-52}$ s^{-1} Hz^{-5}. The probability of free phonon transit through a twin boundary in a sample with twin structure was estimated as $A_C = 0.96$. © *2003 MAIK "Nauka/Interperiodica".*

1. INTRODUCTION

Wide-band-gap II–VI compounds have been witnessing renewed interest in recent years. This stems from the need to develop both high-efficiency injection lasers (based on ZnSe, ZnSeS) that operate in the blue and violet spectral regions and (CdTe-, CdZnTe-based) detectors of x-ray and nuclear radiation. Application of the II–VI compounds meets with difficulties, because samples obtained by using traditional high-temperature methods are heavily defected and possess, as a rule, a very high electrical resistivity. The latter is due to self-compensation, an effect common to all wide-band-gap compounds.

The purest II–VI polycrystalline compounds are presently produced using low-temperature methods, for instance, repeated resublimation [1]. In order to improve the growth technology of the II–VI compounds, the complex processes of interaction responsible for the significant part of the electronic spectrum of these materials, e.g., interactions between various impurities with one another and with defects, have to be understood. Investigation of pulsed heat transport, i.e., of nonequilibrium phonon propagation modes, by using the heat pulse technique may provide additional information on the content and nature of defects in the II–VI compounds.

Moreover, devices based on these materials are, as a rule, heterostructures, which makes characterization of the interfaces an extremely important problem. Investigation of phonon propagation through interfaces provides additional information on the interface characteristics. At the same time, studies of phonon transit across interfaces of different nature, such as grain boundaries, twinning planes, and interfaces in heterostructures and superlattices, are hindered by the fact that each sample is characterized by a unique combination of the defect content, interface imperfections, etc. Therefore, understanding the phonon behavior near interfaces even on a qualitative level may yield information required to improve the technology of development of such structures.

The present study is aimed at investigating the specific features in the propagation of nonequilibrium phonons in CdTe crystals, both having a twin structure and without it, which is needed for further research in the field of nanostructures, for instance, of ZnTe/CdTe [2].

2. EXPERIMENT

Propagation of nonequilibrium phonons in CdTe was studied using the heat pulse technique. This technique and the main processes involving nonequilibrium phonons are illustrated schematically in Fig. 1. Nonequilibrium phonons are generated in sample *S* by pulsed excitation *P*. In the series of experiments reported here, phonons were excited by light with photon energy in excess of the band gap of the material

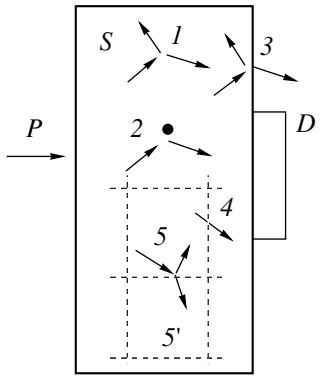

Fig. 1. Main processes taken into account in the modeling: (*1*) spontaneous decay, (*2*) elastic scattering, (*3*) effects at sample boundaries, (*4*) free transit through block boundaries, and (*5*, *5*') backward and forward scattering from block boundaries, respectively.

1063-7834/03/4501-0163$24.00

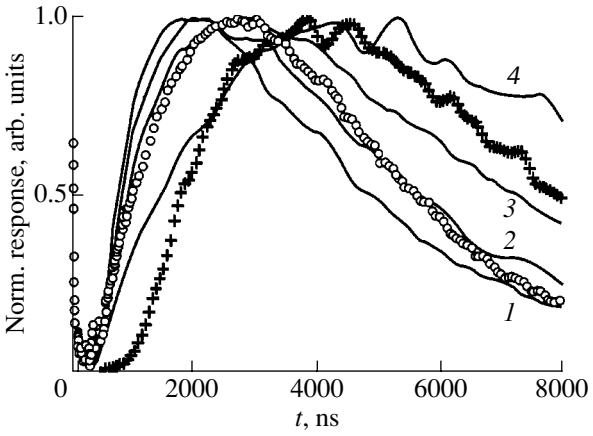

Fig. 2. Comparison of the experimental response for a twin-free sample (circles) with Monte Carlo calculations made with $A_L = 3 \times 10^{-53}$, 2×10^{-53}, 1×10^{-53}, and 3×10^{-54} s^{-1} Hz^{-5} for curves *1–4*, respectively. Crosses plot the experimental response [10] for a twinned sample.

studied; in these conditions, phonons are generated directly in the sample in the process of cooling of hot carriers or nonradiative recombination. The phonons thus produced propagate through the sample and undergo (*1*) spontaneous anharmonic decay, (*2*) elastic scattering, etc. (Fig. 1). By absorbing in detector *D*, they induce a signal. The shape of the time-resolved signal carries information on the specific features of the processes occurring with nonequilibrium phonons and on their propagation mode.

The signals can be analyzed by comparing the experimental detector response with Monte Carlo calculations [3]. This method permits one to estimate the scattering intensity of nonequilibrium acoustic phonons from point defects in the sample under study [4, 5], to determine the characteristic dimensions of the grains making up the sample [6], etc.

The polycrystalline CdTe samples of stoichiometric composition used in our experiment were prepared through repeated low-temperature sublimation–crystallization processes [7]. The total content of 65 residual impurities was 10^{-3}–10^{-4} wt %. The polycrystalline ingots prepared at $T \sim 600$°C had a textured structure with the single-crystal grains growing in the [111] direction.

The polycrystalline ingots were sliced perpendicular to the single-crystal growth direction into wafers 1 mm thick, of which samples for measurements with dimensions 8×8 mm were cut. Following grinding and polishing, the samples were etched in a Br–methanol solution to remove the damaged surface layer. X-ray analysis showed the single-crystal grains to be ~1.5–2.0 mm in diameter. Some grains were twinned.

Twinning is a characteristic feature of the II–VI compounds, including CdTe. The formation of twins is usually attributed to nonequilibrium processes associated with crystal growth at the interfaces separating two coexisting phases. The formation of twins in single-crystal grains of high-purity CdTe polycrystals with textured structure in the [111] growth direction was frequently observed by us to occur (see [10]) and, as we believe, was related to nonequilibrium conditions of vapor transport to the site of crystallization [the vapor flux density was $\sim 10^{17}$ atoms/s cm^2 at a recrystallization temperature of $(0.5–0.6)T_{melt}$]. The twin axis usually coincided with [111], and the twinning plane was parallel to the (111) plane. The twin boundaries on the twinning plane were visualized by etching the samples in $K_2Cr_2O_7 : H_2O : H_2SO_4 + AgNO_3$ (*E*Ag-1).

We chose for the study samples both with and without a twin structure.

The arrival of nonequilibrium acoustic phonons was detected with a meander-shaped, thin-film, superconducting bolometer, 0.35×0.50 mm in size, made of ~300 Å-thick granular aluminum, which was thermally evaporated on one of the sample faces. The sample surface was excited by an LGI-21 nitrogen laser (λ = 337 nm, $\tau_P \sim 7.5$ ns). The response was measured with a V9-5 computer-controlled stroboscopic voltage converter. The measurements were carried out at 1.7 K.

3. EXPERIMENTAL RESULTS AND DISCUSSION

The experimental bolometer response to pulsed excitation of a twin-free sample is shown in Fig. 2 (circles). We readily see that while the signal is fairly long, the pulse of the arriving LA phonons (shown with an arrow) is resolved. The beginning of the pulses corresponds to the phonon ballistic transit time (310 ns for LA and 550 ns for TA phonons).

The response signals were analyzed in terms of a model [3] taking into account spontaneous anharmonic decay and elastic scattering of phonons from point defects. The mean free times with respect to spontaneous decay (τ_L) and to elastic scattering from point defects (τ_S) are known to depend strongly on phonon frequency ($\tau_L^{-1} = A_L \nu^5$, $\tau_S^{-1} = A_S \nu^4$).

In our earlier modeling of the propagation of nonequilibrium acoustic phonons in silicon and diamond [4, 5], we used the known values of the constants A_L and varied A_S, which permitted us to determine the constant A_S for specific samples with an unknown impurity content. For CdTe, we did not succeed in finding calculated values of A_L in the literature. We also did not locate the values of the third-order elastic constants necessary for calculating A_L, as was done, for instance, in [8]. At the same time, as already mentioned, the studied samples of stoichiometric CdTe had an extremely low concentration of impurities ($\sim 10^{16}$ cm^{-3}). It should be pointed out that while in diamond, for instance, there are only three isotopes, with the content of the dominant isotope

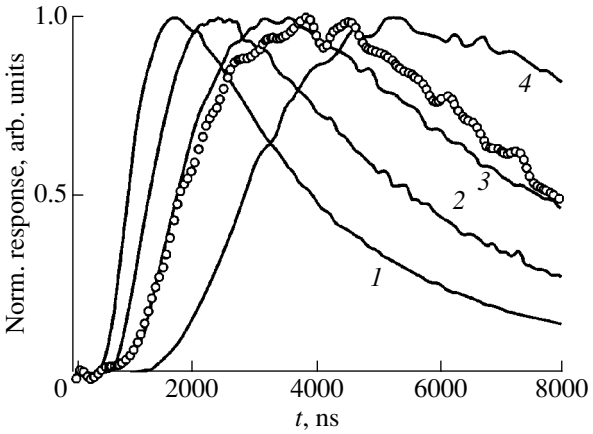

Fig. 3. Comparison of the experimental response for a sample with twin structure (circles) with Monte Carlo calculations made for different values of the phonon mean free path λ: 100, 70, 50, and 30 μm for curves *1–4*, respectively (see [10, Fig. 5]).

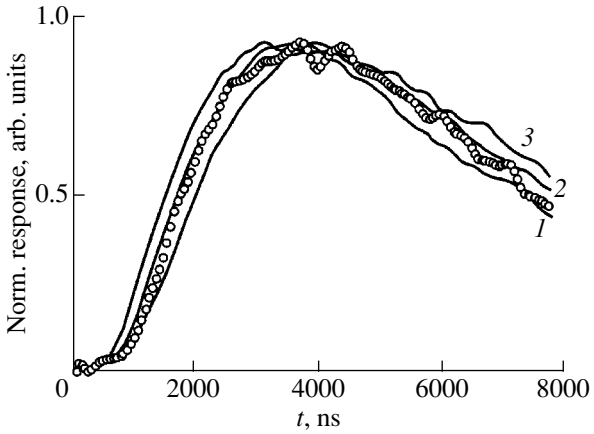

Fig. 4. Comparison of the experimental response [10] for a sample with twin structure (circles) with Monte Carlo calculations made for different probabilities of free phonon transit through the twin boundary A_C: 0.97, 0.96, and 0.95 for curves *1–3*, respectively.

$^6C_{12}$ being about 99% (whereas the content of nitrogen is not less than 10^{17} cm^{-3}), both cadmium and tellurium in CdTe have eight stable isotopes each, with the content of the most abundant ones being about 30%. All this gives one grounds, in calculations of the constant A_S, to take into account phonon scattering from the isotopes only and neglect the impurity scattering. Calculations made in accordance with [9] yield for the constant of elastic phonon scattering from the isotopes, $A_S = 2.5 \times 10^{-40}$ s^{-1} Hz^{-4}.

We used the calculated value of A_S and varied A_L in the modeling; this was carried out for the actual experimental geometry. It was assumed (due to a lack of literature data for CdTe) that the relative probabilities of phonon decay are the same as in silicon. Figure 2 compares the calculated response (solid lines) with the experimental data (circles). The best fit is seen to be achieved for $A_L = 2 \times 10^{-53}$ s^{-1} Hz^{-5}, so that, for instance, for LA phonons of frequency 1 THz, the mean free path limited by phonon decay is ~160 μm.

Also shown in Fig. 2 is the experimental response (crosses) obtained on a sample with a twin structure. One readily sees the following significant differences.

(1) Although the thickness of the sample with twin structure (800 μm) is less than that of the twin-free one (1000 μm), the response is markedly longer (7500 ns vs. 4500 ns).

(2) The beginning of the response is delayed substantially (by more than 500 ns).

(3) The pulse corresponding to the arrival of LA phonons is not resolved.

The smooth rise delayed by a time longer than the ballistic transit time implies the existence of one more scattering mechanism limiting the mean free path of phonons, including low-frequency phonons, which form the leading edge of the response for times close to that of the phonon ballistic transit through the sample. Attempts [10] to fit the calculated response to the experimental data by inclusion of spontaneous decay and elastic scattering alone on point defects (processes characterized by a strong dependence on phonon frequency) did not meet with success. Therefore, nonequilibrium phonon propagation was simulated in [10] in terms of another model assuming phonon propagation to be diffusive, the only variable parameter being the phonon mean free path λ independent of phonon frequency.

Figure 3 (cf. [10, Fig. 5]) compares the experimental response (circles) with calculations made for several

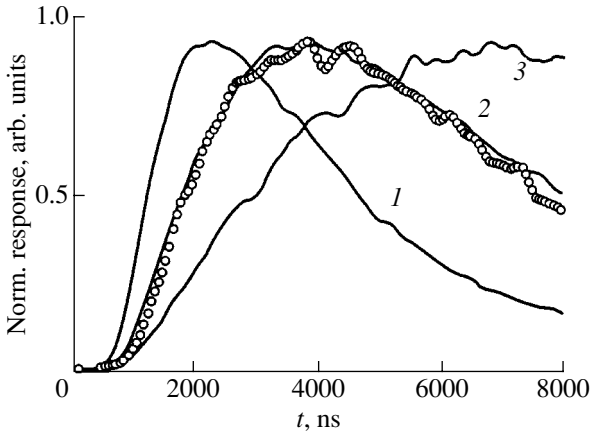

Fig. 5. Comparison of the experimental response [10] for a sample with twin structure (circles) with Monte Carlo calculations made for the same probability of free phonon transit through the twin boundary $A_C = 0.96$ but different values of A_L: 2×10^{-52}, 2×10^{-53}, and 2×10^{-54} s^{-1} Hz^{-5} for curves *1–3*, respectively.

values of the mean free path λ. It is seen that the response obtained with such modeling reproduces quite well both the shift of the leading edge and the general pattern of the experimental response, the best fit value being λ = 50 μm.

The process which only weakly depends on phonon frequency may be associated with scattering from plane interfaces. These cannot, however, be grain boundaries, because, as already mentioned, their dimensions exceed the obtained value of λ by more than an order of magnitude. At the same time, this scattering can take place on twinning planes present in the sample. Because the distance between the twinning planes is 2–8 μm, which is markedly smaller than the value of λ obtained, it can be assumed that the probability of phonon scattering from twinning planes is much less than unity.

The above estimate of the spontaneous phonon decay constant A_L in CdTe permits one to simulate the propagation of nonequilibrium phonons in this compound with allowance for the spontaneous anharmonic decay, elastic scattering, and the existence of plane interfaces in the sample (such a model has been proposed for analysis of nonequilibrium phonon propagation in CVD diamond and is described in considerable detail in [6]).

This model assumes that the sample is made up of blocks, shown schematically by dotted lines in Fig. 1, and that phonons can pass freely from one block to another (example *4*) and scatter elastically at the block boundaries (*5*, *5*'). We note that there is no consistent microscopic description of high-frequency phonon scattering from grain boundaries.

The modeling was performed under the assumption that the sample is a plate, the twinning planes are parallel to the sample surface with a separation of 5 μm, and that the grain dimensions in other directions are 500 μm. The probability A_C of free phonon transit through the plane interfaces was a variable parameter. The value of A_L used in the modeling was taken to be that obtained on the sample free of twins, $A_L = 2 \times 10^{-52}$ s^{-1} Hz^{-5}.

Figure 4 compares the responses calculated in this model for $A_C = 0.97$, 0.96, and 0.95 with the experimental data. We readily see that the calculations reproduce both the shift of the beginning of the response and the response duration. The best-fit value is $A_C = 0.96$.

It is essential that in such a modeling the value of A_L should be estimated preliminarily, because the shape of the response depends strongly on the magnitude of A_L. This conclusion follows from Fig. 5, which displays response curves calculated with the same $A_C = 0.96$ but for different values of A_L. Considered from the physical standpoint, this means that phonon propagation in CdTe is essentially affected by scattering not only from twin boundaries but also from point defects (isotopes) in the bulk of the sample.

4. CONCLUSION

Thus, we have found the anharmonic decay constants of acoustic phonons $A_L = 2 \times 10^{-52}$ s^{-1} Hz^{-5} for pure cadmium telluride ($N \sim 10^{16}$ cm^{-3}). Comparison of the experimental data obtained on CdTe samples, both with twins and twin-free, permits the conclusion that twinning planes provide a contribution to phonon scattering in addition to the dominant scattering from isotopes.

ACKNOWLEDGMENTS

The authors are indebted to N.N. Sentyurina for chemical processing of the samples and to V.P. Martovitskiĭ for x-ray diffraction measurements.

This study was supported by the Russian Foundation for Basic Research, project nos. 99-02-17183 and 01-02-16500.

REFERENCES

1. S. A. Medvedev, Yu. V. Klevkov, V. S. Bagaev, and A. F. Plotnikov, Nauka Proizvod. **6**, 16 (2000).
2. V. S. Bagaev, V. V. Zaitsev, E. E. Onishchenko, and Yu. G. Sadofyev, J. Cryst. Growth **214/215**, 250 (2000).
3. M. M. Bonch-Osmolovskiĭ, T. I. Galkina, A. Yu. Klokov, *et al.*, Fiz. Tverd. Tela (St. Petersburg) **38** (4), 1051 (1996) [Phys. Solid State **38**, 582 (1996)].
4. M. M. Bonch-Osmolovskii, T. I. Galkina, A. Yu. Klokov, *et al.*, Cryogenics **34**, 855 (1994).
5. T. I. Galkina, A. Yu. Klokov, R. A. Khmelnitskii, *et al.*, Proc. SPIE **3484**, 222 (1998).
6. A. I. Sharkov, T. I. Galkina, A. Yu. Klokov, *et al.*, Diamond Relat. Mater. **9** (3–6), 1100 (2000).
7. A. V. Kvit, Yu. V. Klevkov, S. A. Medvedev, *et al.*, Fiz. Tekh. Poluprovodn. (St. Petersburg) **34** (1), 19 (2000) [Semiconductors **34**, 17 (2000)].
8. S. Tamura, Phys. Rev. B **31** (4), 2574 (1985).
9. S. Tamura, Phys. Rev. B **30** (2), 849 (1984).
10. A. I. Sharkov, A. Yu. Klokov, T. I. Galkina, and Yu. V. Klevkov, J. Russ. Laser Res. **21**, 478 (2000).

Translated by G. Skrebtsov

Physics of the Solid State, Vol. 45, No. 1, 2003, pp. 167–170. Translated from Fizika Tverdogo Tela, Vol. 45, No. 1, 2003, pp. 160–162.

LATTICE DYNAMICS AND PHASE TRANSITIONS

Low-Temperature Specific Heat of the Rb_2KScF_6 Elpasolite

I. N. Flerov*, R. Burriel, M. V. Gorev*, P. Isla**, and V. N. Voronov***

** Kirenskiĭ Institute of Physics, Siberian Division, Russian Academy of Sciences, Akademgorodok, Krasnoyarsk, 660036 Russia*

e-mail: flerov@ksc.krasn.ru

*** Instituto de Sciencia de Materiales de Aragon, CSIC-Universidad de Zaragoza, Zaragoza, 50009 Spain*

Received February 27, 2002

Abstract—The specific heat of single-crystal Rb_2KScF_6 is measured using ac calorimetry in the range 4–280 K. The results are discussed in the context of a group-theoretical analysis of possible distortions of the elpasolite structure and of experimental data obtained earlier with an adiabatic calorimeter in a narrower temperature region. © *2003 MAIK "Nauka/Interperiodica".*

Space group $Fm\bar{3}m$ (O_h^5) is characteristic of several families of perovskite-like crystals, for instance, of those with the structure of elpasolite, cryolite, ordered ReO_3, and antifluorite. The rich variety of possible distortions in these structures is one of the factors accounting for the existence of sequences of phase transitions which may result from changes in temperature, pressure, and/or atomic substitutions [1]. As the temperature is lowered, the original G_0 structure undergoes consecutive distortions, which are usually accompanied by a gradual lowering of the symmetry.

A comprehensive group-theoretical and symmetry analysis of vibration representations in crystals with space group $Fm\bar{3}m$ (O_h^5) was reported in [2–4]. The G_0 structure, which is characteristic, in particular, of the elpasolites with a general formula $A_2BB'X_6$, was treated as being made up of rigid octahedral ionic groups $B'X_6$ and A^+ and B^+ ions. The $B'X_6$ octahedra are more rigid structural elements than BX_6 because of the large difference in charge between the B and B' ions. It was established that the structures of distorted elpasolite phases may be considered as resulting from either simple rotations of the octahedra by a small angle about one of the fourfold axes of the unit cell or from a superposition of these rotations about several axes. One may conceive of situations for which rotations of the octahedra are accompanied by displacements of the A^+ ion.

Possible combinations of two basic octahedron rotations, φ and ψ, were considered in [2–4]. In the first case, the octahedra in adjacent layers are rotated in opposite directions, and in the second case, in the same sense. Translational symmetry is changed only in the case of rotations of the ψ type. Complex combinations of simultaneous rotations of the same octahedra, $\Delta = \varphi \pm \psi$, were also found to be possible. Nineteen combinations of rotations corresponding to thirteen types of space groups were analyzed altogether. The lowest symmetry of a distorted elpasolite structure was found to be triclinic ($P\bar{1}$). However, the limiting case of superposition of rotations corresponds to trigonal symmetry (space group $R\bar{3}$) when rotations of the type ($\Delta\Delta\Delta$) are involved.

Structural studies of a large number of halogen-containing elpasolites with atomic cations, in which sequential or single displacive-type phase transitions can occur, showed their lowest symmetry to be monoclinic ($P2_1/n$, $\varphi\varphi\psi$ rotations) [1]. However, since most crystals have not been studied below 70–100 K, one cannot exclude the possibility that their structure undergoes a more complex distortion as the temperature is lowered further.

One such crystal is the Rb_2KScF_6 elpasolite. Optical, thermophysical, and structural studies carried out in the temperature region $100 < T < 310$ K revealed that this crystal undergoes two sequential phase transitions: $Fm\bar{3}m$ (G_0) $\longrightarrow$ $I4/m$ (G_1) $\longrightarrow$ $P2_1/n$ (G_2) [5]. In accordance with the entropy changes occurring at the temperatures $T_1 = 252.4$ K and $T_2 = 222.8$ K, both structural transformations were assigned to displacive phase transitions. We note that Raman investigations showed the octahedra to remain regular (rigid) structural elements in both the cubic and distorted phases of Rb_2KScF_6 [1, 6]. This experimental conclusion permits one to consider that structural distortions in the tetragonal and monoclinic phases are connected only with octahedron rotations of the type (000) $\longrightarrow$ (00φ) $\longrightarrow$ ($\varphi\varphi\psi$).

In accordance with [2–4], the phase alteration sequence observed in the Rb_2KScF_6 crystal [5] could be continued below 100 K along two paths (Fig. 1); in other words, one could conceive, besides the known phase transitions, of two or three additional phase trans-

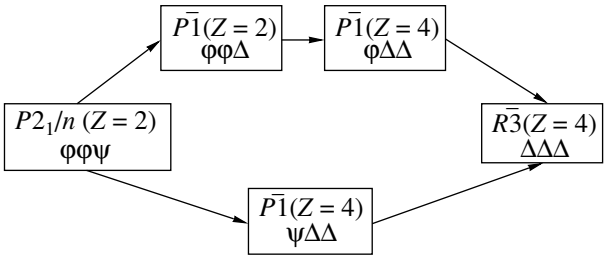

Fig. 1. Possible paths of further distortion of the monoclinic phase of crystals with elpasolite structure [2–4].

formations. The low-temperature phase was found to be triclinic in related ammonium-based $(NH_4)_2NH_4M^{3+}F_6$ crystals (M^{3+} = Ga, Sc) [7, 8] as a result of phase-transition-induced ordering of the octahedral and tetrahedral ionic groups. Note that all the phase transformations depicted schematically in Fig. 1 are clearly pronounced first-order transitions, because the number of components of the distortion that was already present in the G_{i-1} phase changes in the G_i phase.

Calorimetry is the most convenient method of searching for new phase transitions, because it reliably detects heat capacity anomalies caused by transformations of any nature. This stimulated our present measurements of the specific heat of Rb_2KScF_6 in the temperature interval 4–280 K by using a calorimetric technique based on alternating heat current (ac calorimeter). The goals of the study were as follows: (i) to search for heat capacity anomalies at temperatures below 100 K, which could be associated with a possible further symmetry lowering, and (ii) to analyze the results, taking account of the earlier data obtained by using adiabatic calorimetry, in order to find whether inclusion of the low-temperature specific heat affects the earlier determined entropy associated with phase transitions.

The sample was prepared in two stages. First, Rb_2KScF_6 was synthesized from a melt of corresponding amounts of the anhydrous starting components RbF, KF, and ScF_3 in a graphite crucible in an argon environment. Next, a transparent, colorless Rb_2KScF_6 single crystal was grown using the Bridgman method in an evacuated and sealed platinum ampule. X-ray studies carried out at room temperature (in the cubic phase) showed the single crystal thus prepared to contain no foreign phases.

Dynamic measurements of the Rb_2KScF_6 specific heat were performed in the range 4–280 K on a modified Sinku Riko ACC-1VL calorimeter. The sample for study, cut from a bulk single crystal, was a plane-parallel platelet measuring $2 \times 2 \times 0.2$ mm. The light beam emitted by a stabilized halogen lamp was chopped and, on passing through an optical waveguide, produced a periodic variation of the sample temperature within a few millikelvins. The temperature oscillations were detected with a differential chromel–alumel thermocouple made of wires 0.025 mm in diameter, whose junctions were fixed to the sample and the surrounding copper block with GE7031 varnish. Gaseous helium filling the measurement cell at a low pressure (10 mbar) provided heat removal from the sample to the copper block. The absolute value of the temperature of the block was determined with a platinum and a germanium resistance thermometer. The temperature of the sample was slightly higher than that of the copper block and was found as $T_B + \Delta T_{DC}$, where T_B is the temperature of the copper block measured with the resistance thermometer and ΔT_{DC} is the constant component of the temperature difference measured by the thermocouple.

There is a frequency range with characteristic time short as compared with the relaxation time of the sample temperature to the copper block temperature, but long as compared with the internal relaxation time. With appropriate excitation frequencies, the specific heat is inversely proportional to the amplitude of temperature oscillations ΔT_{AC} measured with the differential thermocouple. Measurements at different temperatures were made at frequencies from 2 to 20 Hz, with the larger frequency values lying in the low-temperature region. The temperature variation rates chosen in the heating and cooling runs were 10 to 30 K/h. The sample temperature was corrected taking the corresponding value of ΔT_{DC} into account.

These measurements yielded relative values of the specific heat, which were reduced to absolute values by comparing the specific heat obtained at 200 K with that measured by us earlier using adiabatic calorimetry [5]. Above and below this temperature, the specific heat measured with the latter method was found to be slightly larger. This difference reaches its largest value, 1%, at 110 and 275 K.

The temperature dependence of the specific heat of elpasolite Rb_2KScF_6 measured using the dynamic method is presented graphically in Fig. 2. In the region 4–100 K, which has not been covered previously in adiabatic-calorimetry measurements, no specific-heat anomalies were detected beyond the experimental scatter. This implies that no structural transformations with an enthalpy greater than 0.5 J/mol occur in this temperature region. Thus, the monoclinic phase of the Rb_2KScF_6 elpasolite remains stable down to very low temperatures, at least to 4 K.

It appears of interest to compare our observations with the recent nonempirical calculations of the static and dynamic properties of Rb_2KScF_6 in the three phases [9]. The results of the first-principles calculations made within a microscopic ionic-crystal model which takes into account the deformability and polarizability of ions are in qualitative agreement with experimental data related to the determination of the unit-cell parameters, angles of rotation of the octahedra, and

phase transition temperatures. Calculations of the total lattice vibration spectrum revealed the existence of unstable vibrational modes in the cubic and tetragonal phases of Rb_2KScF_6; these modes condense at the center and edge of the Brillouin zone, respectively. As for the monoclinic phase, no unstable modes were found in its vibration spectrum, because, in accordance with the above calculations, transitions to lower symmetry phases in Rb_2KScF_6 are impossible because the $P2_1/n$ phase is stable down to 0 K.

As expected from the study of Rb_2KScF_6 using adiabatic calorimetry [5], our calorimetric measurements made above 100 K revealed two anomalies in the specific heat, which are in agreement with the known phase transitions between the cubic, tetragonal, and monoclinic phases. The temperatures of the maxima in the specific heat, $T_1 = 253.4 \pm 0.2$ K and $T_2 = 224.9 \pm 0.2$ K, differ from the values $T_1 = 252.4 \pm 0.1$ K and $T_2 = 222.8 \pm 0.1$ K found using adiabatic calorimetry [5]. Note that the samples used in the present measurements and in [5] were cut from different single crystals. It is known [1] that the phase transition temperatures determined in different samples of fluorine-containing perovskite-like crystals, including the elpasolites, can differ by up to 5–7 K.

The change in enthalpy at a first-order phase transition (latent heat) cannot be measured using the above method of ac calorimetry; as a result, the shape of the specific-heat peak derived in this experiment may differ from that found from adiabatic measurements. Indeed, as seen from Fig. 2, the maximum value of the specific heat at T_2 (which corresponds to a first-order phase transition to the monoclinic phase [5]) is 260 J/mol K; this value is substantially below the value (≥310 J/mol K) found using adiabatic calorimetry [5]. This difference becomes particularly noticeable when comparing the excess specific heats, whose determination requires evaluation of the lattice contribution.

The lattice specific heat was determined by fitting the Debye and Einstein functions, $C_L(T) = A_1D(\Theta_D/T) + A_2E(\Theta_E/T)$, to the experimental values of the specific heat measured at a sufficient distance from T_1 and T_2. The $C_L(T)$ expression chosen describes the temperature dependence of the experimental specific heat satisfactorily. Within the temperature region 4–110 K, the average deviation does not exceed 1%. Varying the temperature interval that corresponds to the phase transition region and is excluded from the fitting procedure from 110–270 to 140–270 K did not bring about marked changes in the parameters Θ_D and Θ_E; these parameters were found to be 148.5 and 335.5 K, respectively. Because the excess specific heats associated with the high- and low-temperature phase transitions overlap in the region between T_1 and T_2 (Fig. 2), we determined the excess thermodynamic functions corresponding to the phase transition sequence $G_0 \longrightarrow G_1 \longrightarrow G_2$. Inte-

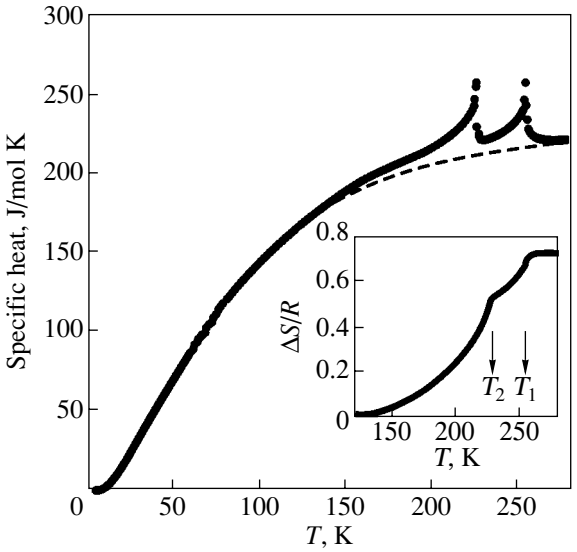

Fig. 2. Temperature dependence of the specific heat of a Rb_2KScF_6 crystal. Dashed line is the lattice specific heat. Inset: temperature dependence of the excess entropy.

gration of the $\Delta C_p(T)$ and $(\Delta C_p/T)(T)$ functions yielded values of the enthalpy $\Sigma\Delta H_i = \Delta H_1 + \Delta H_2 = 1250 \pm 70$ J mol^{-1} and of the entropy $\Sigma\Delta S_i = \Delta S_1 + \Delta S_2 = 6.0 \pm 0.3$ J (mol K)$^{-1}$. The temperature dependence of the dimensionless excess entropy $\Delta S/R$ is shown graphically in the inset to Fig. 2; its value at saturation (0.73) is in good agreement with that derived in the adiabatic calorimeter experiments (0.71) [5].

Thus, our present studies and the analysis of the low-temperature specific heat of the Rb_2KScF_6 elpasolite, considered together with the data from [5, 9], show that the monoclinic phase of this crystal remains stable down to 0 K and that allowance for the data on the $C_p(T)$ relation below 100 K does not influence the accuracy with which the thermodynamic functions of the sequential phase transitions in this crystal are determined.

ACKNOWLEDGMENTS

This study was supported by the Russian Foundation for Basic Research (project no. 00-15-96790), INTAS (grant no. 97-10177), and the Ministry of Science and Technologies of Spain (grant no. MAT2001-3607-C02-02).

REFERENCES

1. I. N. Flerov, M. V. Gorev, K. S. Aleksandrov, *et al.*, Mater. Sci. Eng. R **24** (3), 81 (1998).

2. S. V. Misyul', Kristallografiya **29**, 941 (1984) [Sov. Phys. Crystallogr. **29**, 554 (1984)].
3. K. S. Aleksandrov and S. V. Misyul', Kristallografiya **26**, 1074 (1981) [Sov. Phys. Crystallogr. **26**, 612 (1981)].
4. M. Couzi, S. Khaïroun, and T. Tressaud, Phys. Status Solidi A **98** (2), 423 (1986).
5. I. N. Flerov, M. V. Gorev, S. V. Mel' nikova, *et al.*, Fiz. Tverd. Tela (St. Petersburg) **34** (7), 2185 (1992) [Sov. Phys. Solid State **34**, 1168 (1992)].
6. A. N. Vtyurin, A. Bulou, A. S. Krylov, and V. N. Voronov, Fiz. Tverd. Tela (St. Petersburg) **43** (11), 2066 (2001) [Phys. Solid State **43**, 2154 (2001)].
7. S. V. Mel'nikova, S. V. Misyul', A. F. Bovina, and M. L. Afanas'eva, Fiz. Tverd. Tela (St. Petersburg) **42** (2), 336 (2000) [Phys. Solid State **42**, 345 (2000)].
8. M. V. Gorev, I. N. Flerov, S. V. Mel'nikova, *et al.*, Izv. Ross. Akad. Nauk, Ser. Fiz. **64** (6), 1104 (2000).
9. V. I. Zinenko and N. G. Zamkova, Fiz. Tverd. Tela (St. Petersburg) **41** (7), 1297 (1999) [Phys. Solid State **41**, 1185 (1999)].

Translated by G. Skrebtsov

Physics of the Solid State, Vol. 45, No. 1, 2003, pp. 171–175. Translated from Fizika Tverdogo Tela, Vol. 45, No. 1, 2003, pp. 163–167.

LATTICE DYNAMICS AND PHASE TRANSITIONS

Electron Correlations and Instability of a Two-Center Bipolaron

N. I. Kashirina*, V. D. Lakhno, and V. V. Sychev****

** Institute of Semiconductor Physics, National Academy of Sciences of Ukraine, Kiev, 03028 Ukraine*
e-mail: kashirin@class.semicond.kiev.ua
*** Institute of Mathematical Problems in Biology, Russian Academy of Sciences, Pushchino, Moscow oblast, 142290 Russia*

Received March 14, 2002

Abstract—The energy of a large bipolaron is calculated for various spacings between the centers of the polarization potential wells of the two polarons with allowance made for electron correlations (i.e., the explicit dependence of the wave function of the system on the distance between the electrons) and for permutation symmetry of the two-electron wave function. The lowest singlet and triplet 2^3S states of the bipolaron are considered. The singlet polaron is shown to be stable over the range of ionic-bond parameter values $\eta \le \eta_m \approx 0.143$ ($\eta = \varepsilon_\infty/\varepsilon_0$, where ε_∞ and ε_0 are the high-frequency and static dielectric constants, respectively). There is a single energy minimum, corresponding to the single-center bipolaron configuration (similar to a helium atom). The binding energy of the bipolaron for $\eta \longrightarrow 0$ is $J_{bp} = -0.136512e^4m^*/\hbar^2\varepsilon_\infty^2$ (e and m^* are the charge and effective mass of a band electron), or 25.8% of the double polaron energy. The triplet bipolaron state (similar to an orthohelium atom) is energetically unfavorable in the system at hand. The single-center configuration of the triplet bipolaron corresponds to a sharp maximum in the distance dependence of the total energy $J_{bp}(R)$; therefore, a transition of the bipolaron to the orthostate (e.g., due to exchange scattering) will lead to decay of the bound two-particle state. The exchange interaction between polarons is antiferromagnetic (AFM) in character. If the conditions for the Wigner crystallization of a polaron gas are met, the AFM exchange interaction between polarons can lead to AFM ordering in the system of polarons. © *2003 MAIK "Nauka/Interperiodica".*

1. INTRODUCTION

Interest in polarons was rekindled after the discovery of high-temperature superconductivity (HTSC). Some vexatious computational errors made in early papers on the subject of bipolarons (see review [1]) were corrected in [2]. The minimum found in [2] for the energy of the single-center bipolaron (or the Pekar bipolaron [3]) is significantly lower than the energy minimum of the two-center bipolaron first considered in [4]. Later, the results of [2] were reproduced in [5] using both Pekar and Gaussian functions. In spatial configuration, the single-center bipolaron is similar to a helium atom and the two-center bipolaron, to a hydrogen molecule.

Since the energy of the ground state of the single-center bipolaron was found to be significantly lower than that of the two-center bipolaron, investigation of the molecular configuration of the bipolaron has virtually ceased. We may only cite the papers by Mukhomorov (see, e.g., [6, 7] and references therein), in which the study into the two-center configuration was continued despite the fact that the energy minimum found in [2] was considerably lower than that obtained in [6, 7]. However, the energy of the two-electron system as a function of the distance between the centers of the polarization potential wells of two polarons has not yet been investigated with allowance for electron correlations (here and henceforth, electron correlations are taken to mean an explicit dependence of the wave function (WF) of the two-electron system on the distance between the electrons).

When the dependence of the energy of a system of two polarons on the distance between the centers of the two polarization wells is calculated using the variational method, preference should be given to the deepest minimum. In solving this problem, success will be achieved if, by taking into account electron correlations, we reproduce (or improve) the results of variational calculations performed to date for any distance between the centers of the polarization wells. Only in that case can one answer the question of whether the atomic or molecular bipolaron configuration is favorable.

Recently, interest in the subject of polarons and bipolarons has also been inspired by studies on the properties of these particles in anisotropic crystals, low-dimensional structures, and systems with quantum wells [8–13]. The proper choice of the bipolaron configuration and the electron correlation effect are also of importance in such systems.

1063-7834/03/4501-0171$24.00 © 2003 MAIK "Nauka/Interperiodica"

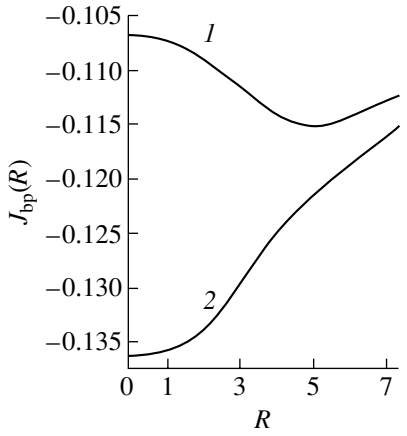

Fig. 1. Dependence of the bipolaron energy on the distance between the centers of the polarization wells (*1*) without and (*2*) with regard for electron correlations calculated for $n = 5$ in Eq. (4).

2. BASIC EQUATIONS

The Hamiltonian of the system consisting of two electrons and a phonon field is taken in the form

$$H = \hbar\omega\sum_{\mathbf{k}} a_{\mathbf{k}}^{+}a_{\mathbf{k}} + \sum_{\mathbf{k}} V_{\mathbf{k}}(a_{\mathbf{k}} - a_{-\mathbf{k}}^{+})[\exp(i\mathbf{k}\mathbf{r}_1) + \exp(i\mathbf{k}\mathbf{r}_2)] - \frac{\hbar^2}{2m^*}\Delta_1 - \frac{\hbar^2}{2m^*}\Delta_2 + \frac{e^2}{\varepsilon_\infty|\mathbf{r}_1 - \mathbf{r}_2|}, \quad (1)$$

$$V_{\mathbf{k}} = -i\frac{e}{k}\sqrt{\frac{2\pi\hbar\omega}{V\tilde{\varepsilon}}}, \quad \frac{1}{\tilde{\varepsilon}} = \frac{1}{\varepsilon_\infty} - \frac{1}{\varepsilon_0}.$$

Here, V is the volume of the crystal; ω is the frequency of an optical phonon; $\mathbf{k}$ is the wave vector of a phonon; $a_{\mathbf{k}}^{+}$ and $a_{\mathbf{k}}$ are the creation and annihilation operators, respectively, for a phonon with wave vector $\mathbf{k}$; ε_∞ and ε_0 are the high-frequency and static dielectric constants, respectively; $\mathbf{r}_1$ and $\mathbf{r}_2$ are the position vectors of the electrons; and m^* is the effective mass of an electron.

In Eq. (1), the first term is the Hamiltonian of optical phonons, the second term is the Frölich electron–phonon interaction Hamiltonian for the two-electron system, the third and fourth terms are the kinetic energy of the electrons, and the last term describes the Coulomb repulsion between the electrons.

We perform a canonical transformation of the Hamiltonian (1) $\exp(S_a)H\exp(-S_a)$ with $S_a = \sum_{\mathbf{k}} C_{\mathbf{k}}(a_{\mathbf{k}}^{+} - a_{\mathbf{k}})$, vary the Hamiltonian with respect to the parameters $C_{\mathbf{k}}$ (characterizing the shift transformation), and take the average over the phonon variables. As a result, we obtain the following functional for the ground state of the bipolaron:

$$J_{bp} = \bar{T} + \bar{V}_{ee} + \bar{V}_{ef},$$

$$\bar{T} = -\frac{\hbar^2}{2m^*}\langle\Psi(\mathbf{r}_1, \mathbf{r}_2)|\Delta_1 + \Delta_2|\Psi(\mathbf{r}_1, \mathbf{r}_2)\rangle,$$
$$\bar{V}_{ee} = \left\langle\Psi(\mathbf{r}_1, \mathbf{r}_2)\left|\frac{e^2}{\varepsilon_\infty r_{12}}\right|\Psi(\mathbf{r}_1, \mathbf{r}_2)\right\rangle, \quad (2)$$
$$\bar{V}_{ef} = -\frac{2e^2}{\tilde{\varepsilon}}\int\frac{|\Psi(\mathbf{r}_1, \mathbf{r}_2)|^2|\Psi(\mathbf{r}_3, \mathbf{r}_4)|^2}{r_{13}}d\boldsymbol{\tau}_{12}d\boldsymbol{\tau}_{34}.$$

In what follows, atomic units with an energy unit $e^4m^*/\hbar^2\varepsilon_\infty^2$ and an effective Bohr radius $a_0^* = \hbar^2\varepsilon_\infty/m^*e^2$ as a unit of length are used.

As a trial WF, we take the following linear combination of Gaussian functions:

$$\Psi_S(\mathbf{r}_1, \mathbf{r}_2) = \Phi(\mathbf{r}_1, \mathbf{r}_2) + (-1)^S\Phi(\mathbf{r}_2, \mathbf{r}_1), \quad (3)$$

$$\Phi(\mathbf{r}_1, \mathbf{r}_2) = \sum_{i=1}^{n} C_i\exp(-a_{1i}r_{a1}^2 - 2a_{2i}(\mathbf{r}_1\mathbf{r}_2) - a_{3i}r_{b2}^2), \quad (4)$$

where $S = 0$ for the singlet state (symmetric with respect to the permutation of the coordinates of the electrons), $S = 1$ for the triplet (antisymmetric) state of the bipolaron, and $\mathbf{r}_1(\mathbf{r}_2)$ is the position vector of the first (second) electron, with the origin taken at a point midway between the points a and b (the centers of the polarization wells). The z axis passes from the point a to the point b. The distance between these points is R. The quantities C_i, a_{1i}, a_{2i}, and a_{3i} are variational parameters. Electron correlations are taken into account by the term $\exp[-2a_{2i}(\mathbf{r}_1\mathbf{r}_2)]$ in Eq. (4). The polaron WF is taken in the form

$$\Psi_p(\mathbf{r}) = \sum_{i=1}^{n} c_i\exp(-\alpha_i r^2), \quad (5)$$

where c_i and α_i are variational parameters.

3. RESULTS OF COMPUTATIONS

3.1. Singlet Bipolaron

Figure 1 shows the dependence of the energy of the ground (singlet) state of the bipolaron on the distance between the centers of the polarization wells calculated for $\eta = \varepsilon_\infty/\varepsilon_0 = 0$ using wave function (3) with $n = 5$ in Eq. (4) without regard for electron correlations ($a_{1i} = a_{3i}$, $a_{2i} = 0$, $i = 1, \ldots, n$) and with allowance for them. It can be seen from Fig. 1 that as the distance between the polarons increases, the effect of electron correlations decreases; the energy functional of the bipolaron approaches the product of the two functionals corresponding to two noninteracting polarons and the bipolaron energy tends to twice the polaron energy calculated within this approximation ($J_p = -0.0542564$). We note that this value of the polaron energy is calculated

by us using a polaron wave function approximation (5) with five exponentials and exactly reproduces the result obtained in [14].

Thus, the minimum corresponding to the two-center bipolaron state in the distance dependence of the energy calculated without regard for electron correlations (curve *1* in Fig. 1) is due to a poor choice of the trial electron wave function. Such minima were considered in [4, 6, 7]. We note that, to our knowledge, Vinetskiĭ and Gitterman [4] were the first to demonstrate (on the basis of microscopic calculations) the possible existence of a bipolaron, which sets off their paper from the later publications devoted to bipolarons, in spite of the fact that the choice of the trial WF in [4] was not the best.

When comparing the results of variational calculations based on different trial WFs, one should compare the absolute values of the minima of the energy functional under study. However, the binding energy is presented, as a rule, in units of the polaron energy calculated within the same approximation. The results obtained in [2] using the Pekar trial WF $\Psi(\mathbf{r}_1, \mathbf{r}_2) = N(1 + \gamma r_{12})(1 + \alpha r_1)(1 + \alpha r_2)\exp[-\alpha(r_1 + r_2)]$ were reproduced in [5]. With this trial function, it was found that $\Delta E/2J_p \approx 0.22$ for $\eta = 0$. The binding energy of the bipolaron is defined as $\Delta E = J_{bp} - 2J_p$, where $J_p = -0.0542564$ is the exact value of the polaron energy calculated in [14] using a numerical method within the strong-coupling approximation. The region of existence of the bipolaron with the Pekar trial WF is $\eta \leq \eta_m = 0.125$. In [2], the absolute values of the ground-state energy of the bipolaron were not presented and the binding energy and the range of existence of the bipolaron ($\Delta E/2J_p \approx 0.25$, $\eta_m \approx 0.14$) were somewhat overestimated, because the binding energy of the bipolaron was calculated using a somewhat overestimated value of the polaron energy, which was found for the trial WF in the form $(1 + \alpha r)\exp(-\alpha r)$. The bipolaron binding energy for $\eta \longrightarrow 0$ presented in [15] is also overestimated ($\Delta E/2J_{pol} \approx 0.22$, $J_{pol} = 1/6\pi$), because the calculations were performed with the polaron WF taken in the form of a single Gaussian. If we replace J_{pol} by the exact strong-coupling approximation value of J_p for the two-electron WF $\varphi(r_1, r_2) = N(1 + \gamma r_{12}^2)\exp(-\mu^2(r_1^2 + r_2^2))$ used in [15], we will obtain $\Delta E/2J_p \approx 0.193$.

The absolute value of the ground-state energy found by us using WF (3) with $n = 11$ in Eq. (4) is $J_{bp} = -0.136512$ or, in dimensionless units, $\Delta E/2J_p \approx 0.258$, and $\eta_m \approx 0.143$.

Figure 2 shows the dependence of the bipolaron binding energy on the distance between the centers of the polarization wells for various values of η and $n = 5$ in Eq. (4).

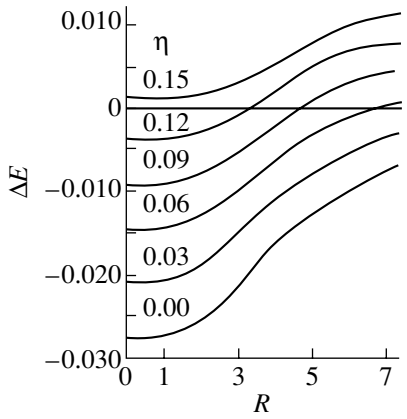

Fig. 2. Dependence of the bipolaron binding energy on the distance between the centers of the polarization wells calculated for various values of the ionic-bond parameter η and $n = 5$ in Eq. (4).

3.2. Triplet Bipolaron

When studying photoconductivity in YBCO, Deving and Salje [16] observed a wide absorption band in the infrared region with a peak near 5.5×10^3 cm^{-1} and assigned this peak to transitions of bosons from the ground (singlet) state to the excited metastable triplet state. It was also assumed in [16] that, in addition to singlet bipolarons, there exist triplet bipolarons in a certain temperature range and that it is the triplet bipolarons that are responsible for the broadening of the NMR lines of Cu and O in YBCO. The population of the triplet levels was assumed to increase with temperature, so that at $T \approx 200$ K, the conductivity was due predominantly to the triplet bipolarons. Later, the change in the shape of the conductivity versus temperature curve predicted in [16] was indeed observed in the vicinity of the temperature indicated above (see review [17] and references therein).

We calculated the energy of the triplet bipolaron (similarly to an orthohelium atom). The lowest numerical value of the energy obtained using WF (3) for $\eta = 0$ for the single-center ($R = 0$) configuration of the triplet bipolaron was $J_{or} = -0.076082$.

As the distance between the centers of the polarization wells increases, the energy corresponding to the triplet bipolaron term decreases monotonically (in perfect analogy with the $^3\Sigma_u$ term of the hydrogen molecule). At $R = 0$, a fairly sharp peak is observed on the energy versus distance curve. This peak is indicative of the instability of the triplet 2^3S state, which can occur, for example, under nonequilibrium conditions where exchange scattering of band electrons by bipolarons takes place. In this case, bipolarons break down into single polarons.

3.3. Interaction between Polarons at Large Distances

Now, we will show that there is antiferromagnetic (AFM) exchange interaction between polarons. Indeed, at sufficiently large distances between polarons, the correlation effects become insignificant and the bipolaron WF can be written as a symmetrized or antisymmetrized product of the polaron WFs for the singlet and triplet states, respectively. In this case, to within the terms quadratic in the overlap integral K, the interaction energy of the two polarons has the form

$$E_{\text{int}} = E_1 - J_{\text{ex}} S_1 S_2, \tag{6}$$

where S_1 and S_2 are the spins of the first and second electrons,

$$E_1 = \frac{1}{\varepsilon_0}\int \frac{a(1)^2 b(2)^2}{r_{12}} d\boldsymbol{\tau}_{12}, \tag{7}$$

$$J_{\text{ex}} = \frac{1}{\varepsilon_\infty} K_1 - \frac{4}{\tilde{\varepsilon}} K_2 K,$$

$$K_1 = \int \frac{a(1)b(1)a(2)b(2)}{r_{12}} d\boldsymbol{\tau}_{12}, \tag{8}$$

$$K_2 = \int \frac{a(1)b(1)b(2)^2}{r_{12}} d\boldsymbol{\tau}_{12}, \quad K = \int a(1)b(1) d\boldsymbol{\tau}_1.$$

Here, we introduced the notation common for two-center systems: $a(1)$ and $b(1)$ are the polaron WFs centered at the points a and b, respectively; i.e., $a(1) \equiv \Psi_{\text{p}}(\mathbf{r}_{a1})$ and $b(1) \equiv \Psi_{\text{p}}(\mathbf{r}_{b1})$.

In Eq. (8), the first term corresponds to ferromagnetic Coulomb exchange and the second term describes AFM interaction between the polarons via phonons.

Thus, at large distances, the polarons repel each other and the spin-dependent part of the interaction (total exchange) is antiferromagnetic in nature (at $\eta \longrightarrow 0$, we have $E_1 \approx 1/\varepsilon_0 R$, $J_{\text{ex}} \approx -3K^2/R$). We also note that there is a potential barrier to the formation of the bipolaron state.

4. DISCUSSION

Thus, polarons repel one another at large distances and, therefore, a system of polarons may behave as an electron gas with Coulomb repulsion between particles. If the concentration of polarons is sufficiently low, a transition may occur (as in an electron gas [18]) to the Wigner crystal state, provided that $k_{\text{B}}T < e^2/\varepsilon_0 a$ (a is the distance between particles). There are a number of papers devoted to the Wigner crystallization of a polaron gas. For example, it was shown in [19, 20] that a system of polarons (considered within a continuum approximation) can crystallize into a hexagonal lattice with a period which depends on the polaron concentration, as in the Wigner theory. In [21], the stability of the polaronic Wigner crystal was investigated and the possibility of the insulator–superconductor transition in the process of destruction of a polaron lattice was substantiated theoretically. Without going into details, we will simply note that when the conditions for the Wigner crystallization are met, the AFM exchange interaction between polarons can cause AFM ordering to occur in a system of polarons. Antiferromagnetism in the electronic Wigner crystal was discussed in [22, 23].

The AFM interaction between polarons can also lead to a decrease in the paramagnetic component of the magnetic susceptibility of a polaron gas with increasing polaron concentration, even if bound bipolaron states do not arise.

The instability of the 2^3S term of the bipolaron with respect to its decay into single polarons, shown by us in terms of the Fröhlich Hamiltonian describing the interaction of electrons with optical phonons, does not rule out the possible formation of bound triplet states of the two-electron system [13] or the existence of triplet bipolarons resulting from the interaction of electrons with elementary excitations of other types, e.g., with spin waves. The formation of self-localized electronic states in antiferromagnets with a low Néel temperature (a spin polaron in an AFM crystal) was considered in [24, 25]. In [17], it was supposed that high-temperature superconductivity is due to a triplet bound state of spin polarons, which forms in much the same way as the bipolaron.

Based on the Fröhlich Hamiltonian, we can consider only large polarons and bipolarons. The continuum approximation is applicable if the effective polarization potential in which self-trapped electrons move varies smoothly over distances of the order of the lattice constant b [3]. In [3], the effective polarization radius r_{p} of an electron was defined as the length over which the self-consistent polarization potential decreases by a factor of 2. For the simplest, hydrogenic, polaron WF, we have $r_{\text{p}} \approx 10\hbar^2\tilde{\varepsilon}/m^*e^2$.

The continuum approximation can be applied if $r_{\text{p}} > b$. In the opposite case of $r_b \le b$, the spatial dispersion of the dielectric constants ε_0 and ε_∞ becomes significant; the difference in value between ε_0 and ε_∞ decreases with decreasing size of the region of polaron localization, and we have $\varepsilon_0 \approx \varepsilon_\infty \approx 1$. In most ionic crystals, $SrTiO_3$, and layered cuprates (along an "easy-plane" direction), the value of r_{p} is approximately 3–5 lattice constants.

The spatial dispersion of the dielectric constants can be included in a qualitative way by using the phenomenological interpolation model by Inkson [26]. In this case, an increase in the electron–phonon coupling is compensated by the dielectric-constant dispersion; as a result, if we take into account only the interaction of electrons with optical phonons, the case of $r_{\text{p}} \le b$ is not realized in nearly all ionic crystals. It should also be noted that spatial dispersion of the dielectric constants (in the case of polarons and bipolarons of an intermedi-

ate radius) causes the bipolaron binding energy to decrease in absolute value, whereas any anisotropy of the crystal increases the ratio $\Delta E/2J_p$ [8, 9].

Interaction of carriers with acoustic phonons [27] or with short-wavelength optical phonons may lead to the formation of self-trapped states of a small radius. In this case, the continuum model is inadequate. Small-radius bipolarons treated within the strong-coupling approximation and superconductivity caused by their Bose condensation in narrow-band metals were considered in [28]. When considering such states, the binding energy of the bipolaron is generally taken to be a phenomenological parameter. Various aspects of the large-bipolaron theory as applied to the HTSC problem are discussed in [1, 8, 9, 29]. Review [17] is concerned with small-bipolaron states. In [19, 20], a system of large bipolarons in a layered high-temperature superconductor is treated as a Wigner crystal, in which plasma oscillations occur and favor carrier pairing in the conducting layers.

ACKNOWLEDGMENTS

This study was supported by the Russian Foundation for Basic Research, project no. 01-07-90317.

REFERENCES

1. V. L. Vinetskiĭ, N. I. Kashirina, and É. A. Pashitskiĭ, Ukr. Fiz. Zh. **37** (1), 77 (1992).
2. S. G. Suprun and B. Ya. Moĭzhes, Fiz. Tverd. Tela (Leningrad) **24** (5), 1571 (1982) [Sov. Phys. Solid State **24**, 903 (1982)].
3. S. I. Pekar, *Investigations on Electron Theory of Crystals* (Gostekhizdat, Moscow, 1951).
4. V. L. Vinetskiĭ and M. Sh. Gitterman, Zh. Éksp. Teor. Fiz. **33** (3), 730 (1957) [Sov. Phys. JETP **6**, 560 (1958)].
5. V. L. Vinetskiĭ, O. Meredov, and V. A. Yanchuk, Teor. Éksp. Khim. **25** (6), 641 (1989).
6. V. K. Mukhomorov, Opt. Spektrosk. **86** (1), 50 (1999) [Opt. Spectrosc. **86**, 41 (1999)].
7. V. K. Mukhomorov, Zh. Tekh. Fiz. **67** (8), 1 (1997) [Tech. Phys. **42**, 855 (1997)].
8. N. I. Kashirina, E. M. Mozdor, É. A. Pashitskiĭ, and V. A. Sheka, Izv. Ross. Akad. Nauk, Ser. Fiz. **59** (8), 127 (1995).
9. N. I. Kashirina, E. V. Mozdor, E. A. Pashitskij, and V. I. Sheka, Quantum Electron. Optoelectron. **2** (2), 7 (1999).
10. V. D. Lakhno, Izv. Ross. Akad. Nauk, Ser. Fiz. **60** (9), 69 (1996).
11. E. P. Pokatilov, V. M. Fomin, J. T. Devreese, *et al.*, Phys. Rev. B **61** (4), 2721 (2000).
12. J. T. Devreese, V. M. Fomin, E. P. Pokatilov, *et al.*, Phys. Rev. B **63** (18), 184304 (2001).
13. J. Adamovski, M. Sobkowicz, and B. Szafran, Phys. Rev. B **62** (7), 4234 (2000).
14. S. J. Miyake, J. Phys. Soc. Jpn. **41** (3), 747 (1976).
15. P. Zh. Baĭmatov, D. Ch. Khuzhakulov, and Kh. T. Sharipov, Fiz. Tverd. Tela (St. Petersburg) **39** (2), 284 (1997) [Phys. Solid State **39**, 248 (1997)].
16. H. L. Deving and E. Salje, Supercond. Sci. Technol. **5** (1), 50 (1992).
17. N. F. Mott, J. Phys.: Condens. Matter **5** (22), 3487 (1993).
18. É. G. Batyev, Pis'ma Zh. Éksp. Teor. Fiz. **73** (10), 635 (2001) [JETP Lett. **73**, 566 (2001)].
19. A. A. Remova and B. Ya. Shapiro, Physica C (Amsterdam) **160** (2), 202 (1989).
20. A. A. Remova and B. Ya. Shapiro, Physica C (Amsterdam) **172** (1&2), 105 (1990).
21. P. Quemerais and S. Fratini, Physica C (Amsterdam) **341** (1), 229 (2000).
22. R. Rajeswarapalanichamy and K. Iyakutti, Int. J. Mod. Phys. B **15** (15), 2147 (2001).
23. D. S. Hirashima, J. Phys. Soc. Jpn. **70** (4), 931 (2001).
24. V. D. Lakhno and É. L. Nagaev, Fiz. Tverd. Tela (Leningrad) **20** (1), 82 (1978) [Sov. Phys. Solid State **20**, 44 (1978)].
25. V. D. Lakhno, Fiz. Tverd. Tela (Leningrad) **27** (3), 669 (1985) [Sov. Phys. Solid State **27**, 414 (1985)].
26. J. C. Inkson, J. Phys. C **6** (2), 181 (1973).
27. M. F. Deĭgen and S. I. Pekar, Zh. Éksp. Teor. Fiz. **21** (7), 803 (1951).
28. A. Alexandrov and J. Ranninger, Phys. Rev. B **24** (3), 1164 (1981).
29. G. Verbist, F. M. Peeters, and J. T. Devreese, Phys. Rev. B **43** (4), 2712 (1991).

Translated by Yu. Epifanov

Physics of the Solid State, Vol. 45, No. 1, 2003, pp. 176–182. Translated from Fizika Tverdogo Tela, Vol. 45, No. 1, 2003, pp. 168–173.

LOW-DIMENSIONAL SYSTEMS AND SURFACE PHYSICS

Resonance Reflection of Light from Two-Dimensional Superlattice Structures

M. M. Voronov and E. L. Ivchenko

Ioffe Physicotechnical Institute, Russian Academy of Sciences, Politekhnicheskaya ul. 26, St. Petersburg, 194021 Russia

Received February 21, 2002

Abstract—The exciton Bloch states in a quantum well with a two-dimensional periodic potential are studied theoretically. Expressions are derived for the light reflection coefficient and the exciton oscillator strength for a structure with this type of lateral superlattice. The redistribution of the oscillator strength between exciton states with varying period and depth of the potential is analyzed. The limiting cases where the nearly free exciton and tight-binding approximations are applicable are considered. *© 2003 MAIK "Nauka/Interperiodica".*

1. INTRODUCTION

The first theoretical analysis of resonant optical reflection from a structure with a planar quantum dot array was reported in [1]. The reflection coefficient was calculated for two limiting cases, more specifically, for short-period structures and in the dc field approximation. Recently, analytical results have been obtained for an arbitrary relation between the lateral period and the wavelength of light, in addition to between the radiative and nonradiative exciton damping [2]. The theory developed in [1, 2], as well as the optical spectroscopy studies of three-dimensional quantum dot arrays performed in [3–5], neglected the overlap of exciton wave functions bound to different quantum dots. In the present study, the theory of optical reflection and transmission is generalized to take into account coherent exciton tunneling from one potential minimum to another.

We consider a semiconductor quantum well with a periodic two-dimensional (2D) potential,

$$V(x, y) = V(x + a, y) = V(x, y + a), \qquad (1)$$

which acts on the exciton as a whole while not affecting the exciton internal state. For the sake of simplicity, the potential is assumed to be characterized by the point symmetry of a square:

$$V(x, y) = V(\pm x, \pm y) = V(y, x).$$

This potential transforms the exciton energy spectrum from a parabolic dispersion $E_{\rm exc}(k_x, k_y) = \hbar^2(k_x^2 + k_y^2)/2M$ in an ideal quantum well with $V \equiv 0$ (M is the translational effective mass of the 2D exciton) to a series of two-dimensional minibands defined in the Brillouin zone $-\pi/a < (k_x, k_y) \le \pi/a$.

The two-particle envelopes of electron–hole wave functions are written in the form

$$\Psi_{\rm exc}(\mathbf{r}_e, \mathbf{r}_h) = \psi(\boldsymbol{\rho})F(|\boldsymbol{\rho}_e - \boldsymbol{\rho}_h|)\phi_e(z_e)\phi_h(z_h). \qquad (2)$$

Here, the functions ϕ_e and ϕ_h describe single-particle quantum confinement of the electron (*e*) and the hole (*h*) along the growth axis z, $\boldsymbol{\rho}_{e,h}$ is the electron or hole position vector in the interface plane, F is a function of relative exciton motion in an ideal quantum well with no additional lateral potential present (the 1*s* exciton is considered subsequently), and the envelope ψ depends on the position vector of the exciton center of mass $\boldsymbol{\rho} = (x, y)$. Note that the effect of the lateral potential $V(\boldsymbol{\rho})$ on internal exciton motion can be neglected if the effective two-dimensional Bohr radius of the exciton is smaller than the characteristic scale of variation of this potential.

Normally incident light excites only exciton states with $k_x = k_y = 0$ (Γ point of the 2D Brillouin zone). In this case, the envelopes $\psi^\nu(\boldsymbol{\rho})$ labeled by a discrete index ν are periodic with the lattice period and can be expanded in a Fourier series,

$$\psi^\nu(\boldsymbol{\rho}) = \frac{1}{a}\sum_{\mathbf{b}} c_{\mathbf{b}}^{(\nu)} \exp(i\mathbf{b}\boldsymbol{\rho}),$$

$$c_{\mathbf{b}}^{(\nu)} = \frac{1}{a}\int_{\Omega_0} \psi^\nu(\boldsymbol{\rho}) \exp(-i\mathbf{b}\boldsymbol{\rho}) d\boldsymbol{\rho}, \qquad (3)$$

over the vectors of the reciprocal two-dimensional lattice $\mathbf{b} = (2\pi/a)(l, m)$, where l and m are the integers 0, ±1, …. The functions ψ^ν are normalized by the condition

$$\int_{\Omega_0} |\psi|^2 d\boldsymbol{\rho} = 1,$$

where Ω_0 is the unit cell, which can be chosen, for instance, in the form of a square $-a/2 < (x, y) < a/2$. Hence, the expansion coefficients $c_{\mathbf{b}}$ satisfy the identity

$$\sum_{\mathbf{b}} \left|c_{\mathbf{b}}^{(\nu)}\right|^2 = 1.$$

In view of the fact that the states with $\nu \neq \nu'$ are mutually orthogonal, we obtain

$$\sum_{\mathbf{b}} c_{\mathbf{b}}^{(\nu)*} c_{\mathbf{b}}^{(\nu')} = \delta_{\nu\nu'},$$

whence it also follows that

$$\sum_{\nu} c_{\mathbf{b}}^{(\nu)*} c_{\mathbf{b}'}^{(\nu)} = \delta_{\mathbf{b}\mathbf{b}'}. \quad (4)$$

Note that Bloch functions at the Γ point can be made real by properly choosing the phase factors. In this case, because of the high symmetry of the $V(\boldsymbol{\rho})$ potential, the coefficients $c_{\mathbf{b}}^{(\nu)}$ are real and the complex-conjugation sign in Eq. (4) can be dropped.

For the sake of convenience, we introduce a star β of the two-dimensional vector $\mathbf{b} = (2\pi/a)(l, m)$ which contains vectors $(2\pi/a)(\pm l, \pm m)$ and $(2\pi/a)(\pm m, \pm l)$. For $l \neq m \neq 0$, the star consists of eight different vectors; in other cases, the star includes four vectors if $l = m \neq 0$, $l = 0$ and $m \neq 0$, or $l \neq 0$ and $m = 0$ and one vector in the particular case of $l = m = 0$. In what follows, symbol β denotes both the star of the reciprocal-lattice vectors and the magnitude of these vectors $(2\pi/a)\sqrt{l^2 + m^2}$.

It is known that in bulk materials with a conduction and a valence band connected by optical transitions which are allowed at the Γ point, only the *s* excitons (1*s*, 2*s*, etc.) are optically active. For the same reason, only states (2) with a totally symmetric $\psi^{\nu}(\boldsymbol{\rho})$ function (Γ_1 representation) are optically active in the case of normal light incidence on the lateral superlattice. For such states, the coefficients $c_{\mathbf{b}}$ in Eq. (3) for vectors belonging to the same star β coincide and index $\mathbf{b}$ on these coefficients may be replaced by index β, $c_{\mathbf{b}} \equiv c_{\beta}$.

2. REFLECTION COEFFICIENT OF LIGHT AND OSCILLATOR STRENGTH FOR TWO-DIMENSIONAL EXCITONS

The system to be considered is a quantum well with a lateral potential $V(\boldsymbol{\rho})$, which is placed between semi-infinite barriers. The difference between the dielectric constant ε_b of the barrier material of the well and the background dielectric constant ε_a is neglected. In this case, the constitute equation coupling the electric induction $\mathbf{D}$ with electric field $\mathbf{E}$ can be written as $\mathbf{D} = \varepsilon_b\mathbf{E} + 4\pi\mathbf{P}_{\text{exc}}$, where $\mathbf{P}_{\text{exc}}$ is the excitonic contribution to the dielectric polarization, which, in turn, is related to the field $\mathbf{E}$ and functions ψ^{ν} through [1, 2, 6]

$$4\pi\mathbf{P}_{\text{exc}}(\mathbf{r}) = \varepsilon_b\omega_{LT}\pi a_B^3 \sum_{\nu} \frac{\Psi_{\text{exc}}^{\nu}(\mathbf{r}, \mathbf{r})}{\omega_{0\nu} - \omega - i\Gamma_{\nu}}\Lambda_{\nu}, \quad (5)$$

where

$$\Lambda_{\nu} = \int dz \int_{\Omega_0} d\boldsymbol{\rho}\Psi_{\text{exc}}^{\nu *}(\mathbf{r}, \mathbf{r})\mathbf{E}(\mathbf{r}),$$

$\omega_{0\nu}$ is the resonant frequency of the exciton in state ν, and integration in the (x, y) plane is performed over the unit cell Ω_0; for the sake of convenience, the cubed Bohr radius a_B^3 and the longitudinal–transverse splitting ω_{LT} of the three-dimensional exciton are isolated in an explicit form as dimension factors.

By solving the wave equation with exciton polarization (5), one can calculate the coefficients of reflection, transmission, and diffraction of light similarly to as was done in [2] for a two-dimensional quantum-dot superlattice. We present here only the expression for the amplitude reflection coefficient:

$$r(\omega) = i\Gamma_0^{QW} \sum_{\nu} \frac{c_0^{(\nu)}\eta_0}{\omega_{0\nu} - \omega - i\Gamma_{\nu}} \frac{\Lambda_{\nu}}{E_0}, \quad (6)$$

where $c_0^{(\nu)}$ are the expansion coefficients in Eq. (3) for $\mathbf{b} = 0$, E_0 is the scalar amplitude of the light-wave electric field, and the quantities Λ_{ν} satisfy the coupled equations

$$\Lambda_{\nu} = \Lambda_{\nu}^0 + i\sum_{\nu'} \Lambda_{\nu'} \frac{\Gamma_0^{QW}}{\omega_{0\nu} - \omega - i\Gamma_{\nu}} \times [A_{\nu\nu'} + i(B_{\nu\nu'} + C_{\nu\nu'})]. \quad (7)$$

Here,

$$\Lambda_{\nu}^0 = E_0 c_0^{(\nu)}\eta_0, \quad \eta_0 = \int \phi_e(z)\phi_h(z)\cos kz dz, \quad (8)$$

$k = (\omega/c)\sqrt{\varepsilon_b}$,

$$\Gamma_0^{QW} = \frac{1}{2}k\omega_{LT}\pi a_B^3 F^2(0)\eta_0^2 \quad (9)$$

is radiative exciton damping in the ideal quantum well:

$$A_{\nu\nu'} + iB_{\nu\nu'} = \sum_{\beta \in B_1} n_{\beta}\frac{k}{k_{\beta}}\left(1 - \frac{\beta^2}{2k^2}\right) \times c_{\beta}^{(\nu)} c_{\beta}^{(\nu')}\left[\left(\frac{\eta_{\beta}}{\eta_0}\right)^2 + iI_{\nu\beta}\right], \quad (10)$$

$$C_{\nu\nu'} = -\sum_{\beta \in B_2} n_{\beta}\frac{k}{\kappa_{\beta}}\left(1 - \frac{\beta^2}{2k^2}\right) c_{\beta}^{(\nu)} c_{\beta}^{(\nu')} J_{\nu\beta}, \quad (11)$$

$$\eta_{\beta} = \int \phi_e(z)\phi_h(z)\cos k_{\beta} z dz,$$

B_1 and B_2 are subsets of the reciprocal-lattice vectors which satisfy the conditions $|\mathbf{b}| < k$ and $|\mathbf{b}| > k$, respectively, n_β is the number of vectors in the star β, $k_\beta = \sqrt{k^2 - \beta^2}$, $\kappa_\beta = \sqrt{\beta^2 - k^2}$,

$$I_{\nu\beta} = \eta_0^{-2}\iint dz dz' S_{eh}(z, z')\sin k_\beta |z - z'|,$$

$$J_{\nu\beta} = \eta_0^{-2}\iint dz dz' S_{eh}(z, z') e^{-\kappa_\beta |z - z'|},$$

$$S_{eh}(z, z') = \phi_e(z)\phi_h(z)\phi_e(z')\phi_h(z').$$

Equations (10) and (11) were derived taking into account that the quantities b_x^2, b_y^2, and $b_x b_y$ averaged over vectors $\mathbf{b} = (b_x, b_y)$ of the star β are equal to $\beta^2/2$, $\beta^2/2$, and 0, respectively.

Because for the function $\psi(\boldsymbol{\rho})$ with symmetry other than Γ_1 we have

$$\sum_{\mathbf{b} \in \beta} c_\beta^{(\nu)} = 0$$

and, in particular, $c_0^{(\nu)} = 0$, it is only the totally symmetric Bloch states Γ_1 that contribute to reflection.

If the separation between the resonance frequency of exciton ν and the adjacent frequency of another optically active exciton is larger than the exciton damping, only one term can be retained in sum (6) within the frequency interval near the given resonance; this term has the form

$$r_\nu(\omega) = \frac{i\Gamma_0^{QW} c_0^{(\nu)2}}{\tilde{\omega}_{0\nu} - \omega - i(\Gamma_\nu + \Gamma_{0\nu})}, \tag{12}$$

where

$$\Gamma_{0\nu} = \Gamma_0^{QW} \sum_{\beta \in B_1} c_\beta^{(\nu)2} n_\beta \frac{k}{k_\beta}\left(\frac{\eta_\beta}{\eta_0}\right)^2\left(1 - \frac{\beta^2}{2k^2}\right), \tag{13}$$

$$\tilde{\omega}_{0\nu} - \omega_{0\nu} = \Gamma_0^{QW}(B_{\nu\nu} + C_{\nu\nu}). \tag{14}$$

In this case, the quantity $\Gamma_{0\nu}$ is the total radiative damping of the given exciton and $\tilde{\omega}_{0\nu}$ is the resonance frequency renormalized with due account of the light–exciton coupling. Note that for $2\pi/a > k$, the subset B_1 consists of only one element, $\mathbf{b} = 0$, while subset B_2 contains all reciprocal-lattice vectors except the zero vector. In this case, $\Gamma_{0\nu}$ coincides with the quantity $\Gamma_0^{QW} c_0^{(\nu)2}$ entering the numerator in the right-hand member of Eq. (12). One may conveniently introduce a dimensionless oscillator strength of the νth exciton in the form

$$f_\nu = c_0^{(\nu)2}. \tag{15}$$

The sum of the oscillator strengths is preserved, because, by virtue of Eq. (4) for $\mathbf{b} = \mathbf{b}' = 0$, we have

$$\sum_\nu c_0^{(\nu)2} = 1. \tag{16}$$

3. TWO-DIMENSIONAL Γ_1 EXCITONS IN A LATERAL SUPERLATTICE

Using the plane-wave formalism based on expansion (3), the Schrödinger equation can be reduced to a system of coupled linear equations:

$$\left(\frac{\hbar^2}{2M}\beta^2 - E\right)c_\beta + \sum_{\beta'} c_{\beta'} \sum_{(l', m') \in \beta'} V_{lm, l'm'} = 0,$$

$$V_{lm, l'm'} = \frac{1}{a^2}\iint_{\Omega_0} V(x, y) \times \cos\left\{\frac{2\pi}{a}[(l' - l)x + (m' - m)y]\right\} dxdy, \tag{17}$$

where $\beta^2 = (2\pi/a)^2(l^2 + m^2)$ and E is the energy reckoned from the excitation energy of the exciton at rest in the ideal quantum well. In what follows, we assume the lateral potential to be a periodic set of discs, so that

$$V(x, y) = \sum_{lm} v(x - la, y - ma),$$

$$v(x, y) \equiv v(\rho) = \begin{cases} -v_0, & \rho \le R \\ 0, & \rho > R, \end{cases} \tag{18}$$

where $\rho = \sqrt{x^2 + y^2}$. In this case, the matrix elements of the periodic potential can be written as

$$V_{lm, l'm'} = -v_0 \frac{R}{a}\frac{J_1(2\pi\sqrt{(l' - l)^2 + (m' - m)^2}R/a)}{\sqrt{(l' - l)^2 + (m' - m)^2}}, \tag{19}$$

where $J_1(t)$ is the Bessel function.

One may conveniently transfer to dimensionless quantities,

$$\varepsilon = \frac{E}{E_0}, \quad u_0 = \frac{v_0}{E_0}, \quad \mu = \frac{R}{a},$$

where

$$E_0 = \frac{\hbar^2}{2M}\left(\frac{2\pi}{R}\right)^2,$$

$$\tilde{\beta} = \frac{a}{2\pi}\beta = \sqrt{l^2 + m^2}, \tag{20}$$

and to coefficients,

$$C_\beta = \sqrt{n_\beta} c_\beta. \tag{21}$$

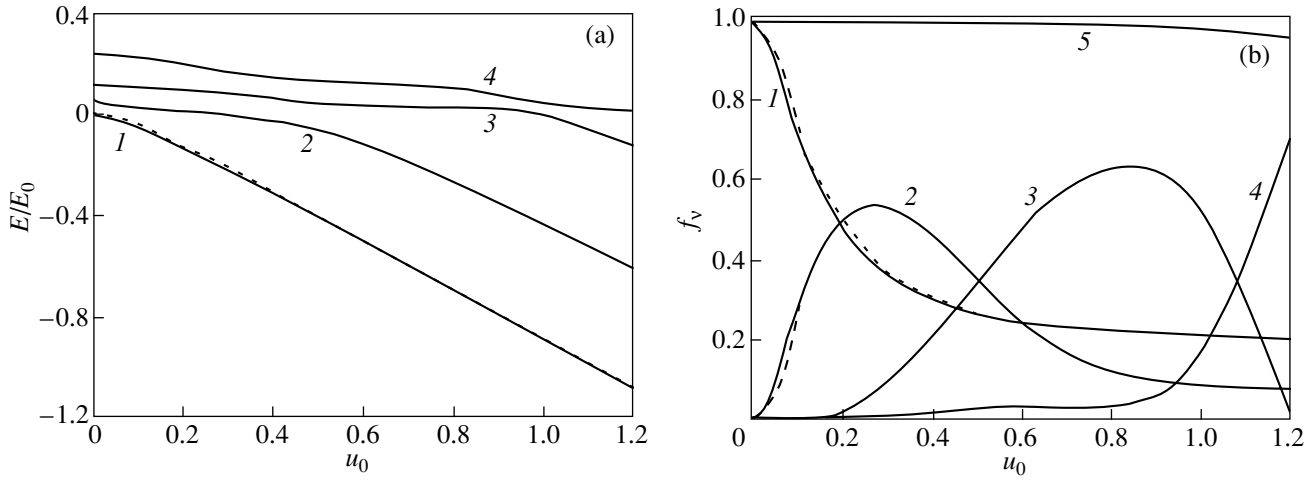

Fig. 1. (a) Dimensionless energy and (b) oscillator strength plotted vs. dimensionless depth of a potential disc for the lowest four exciton states $\nu = 1$–4. The calculation was carried out for a lateral array of quantum discs of radius $R = a/4$. Solid curves are exact plane-wave calculations, dashed lines *1* and *2* in Fig. 1b are calculated in terms of the model of nearly free excitons, and dotted lines relate to a calculation of (a) ε_1 and (b) f_1 made in the tight-binding approximation. Curve *5* plots the sum of the oscillator strengths for the above four states.

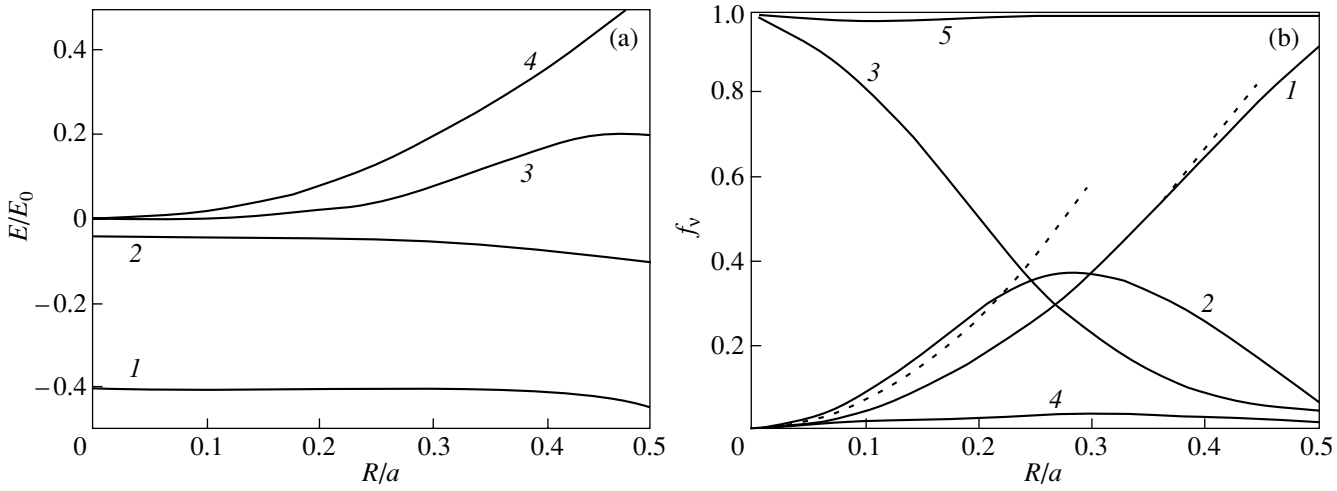

Fig. 2. Dependence of (a) energy and (b) oscillator strength on the ratio R/a for excitons with $\nu = 1$–4 in a superlattice with a periodic array of quantum discs. The dimensionless depth of a potential disc is $u_0 = V_0/E_0 = 0.5$. Dotted lines *1* and *2* in Fig. 2b plot the calculation made in the tight-binding approximation. Curve *5* plots the sum of the oscillator strengths for the above four states.

This permits one to recast Eqs. (17) in the form

$$(\mu^2\tilde{\beta}^2 - \varepsilon)C_\beta - u_0\sum_{\beta'} U_{\beta\beta'}C_{\beta'} = 0,$$

$$U_{\beta\beta'} = -\frac{1}{V_0\sqrt{n_\beta n_{\beta'}}}\sum_{\substack{(l,m)\in\beta\\(l',m')\in\beta'}} V_{lm,l'm'}. \qquad (22)$$

Thus, formulation of the problem in dimensionless units leaves only two independent parameters, u_0 and μ. The next section presents the results of an exact calculation of dimensionless energy $\varepsilon_\nu(u_0, \mu)$ and oscillator strength $f_\nu(u_0, \mu)$ by using the plane wave method, and Sections 5 and 6 analyze interesting, nearly free-exciton and tight-binding approximations.

4. CALCULATION FOR A QUANTUM DISC ARRAY

Figures 1–3 display energy and oscillator strength as functions of the potential-disc depth and of the R/a ratio for the four lowest Γ_1 exciton states in the two-dimensional superlattice. The dimensionless energy of

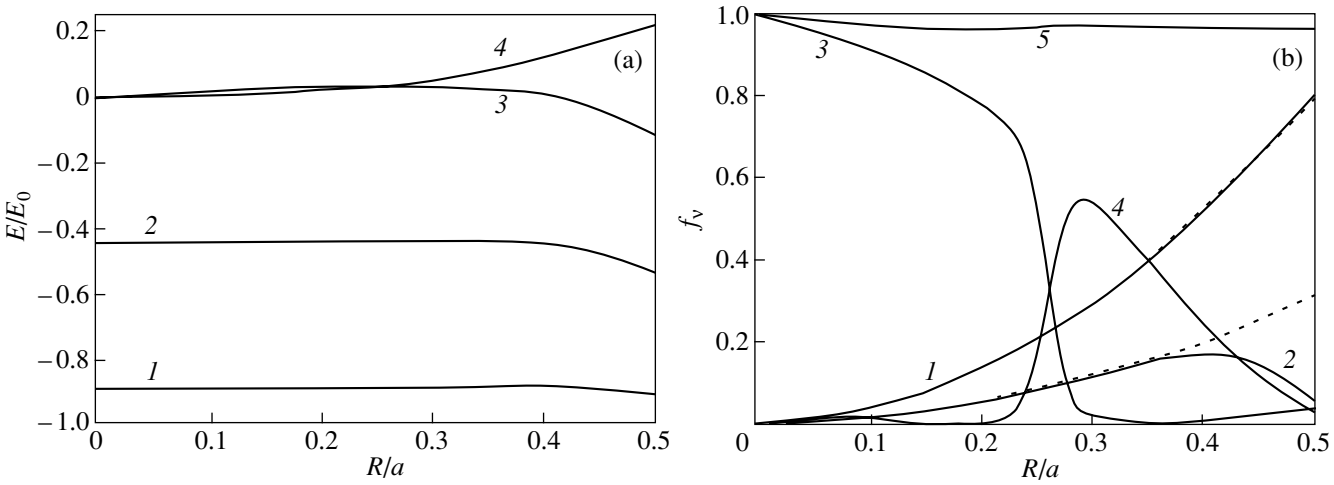

Fig. 3. Same as in Fig. 2, but for $u_0 = 1$.

the ν exciton in the ideal quantum well, i.e., for $u_0 = 0$, is $\mu^2\tilde{\beta}^2$ and successively takes on the values 0, μ^2, $2\mu^2$, $4\mu^2$, …, with only exciton ν = 1 being optically active, which is in accord with the behavior of the curves in Figs. 1a and 1b as u_0 tends to zero. For $u_0 \neq 0$, spatial harmonics with wave vectors belonging to different β stars mix, so that the upper exciton states also become optically active. In the interval from $u_0 = 0$ to $u_0 = 0.2$, the oscillator strength transfers from exciton *1* predominantly to exciton *2* alone; the oscillator strength of exciton *3* becomes noticeable for $u_0 > 0.3$. The oscillator strength also undergoes a similar redistribution when the ratio of the disc radius to the superlattice period is varied (see Figs. 2, 3). As the period increases (with $R/a \longrightarrow 0$), the negative energies ε_1 and ε_2 approach the energy of an exciton bound to a single potential disc; because only two such bound states exist for $u_0 = 0.5$ or 1, the energies ε_ν with $\nu > 2$ converge to zero. Curves *5* in these figures plot the sum of the oscillator strengths for the four lowest exciton states. Because this sum is close to unity, excitons with $\nu > 4$ are practically not excited by light in the range of parameters studied.

The behavior of the $\varepsilon_\nu(u_0, \mu)$ and $f_\nu(u_0, \mu)$ curves characteristic of level anticrossing is of particular interest. For instance, for $u_0 = 1$–1.2 in Fig. 1 and near $R/a = 0.25$ in Fig. 3, the difference $\varepsilon_4 - \varepsilon_3$ reaches a minimum, while the oscillator strengths f_3 and f_4 depend linearly on u_0 and R/a (the sum $f_3 + f_4$ being nearly constant) and become equal at a certain point. A similar pattern of mutual repulsion of states *1* and *2* is observed within the interval $0 < u_0 < 0.3$. Consider this phenomenon in a simplified but revealing model where only stars (0, 0) and (1, 0) are included in expansion (3), so that coupled equations (22) reduce to two equations:

$$(\varepsilon_0^1 - \varepsilon)C_{0,0} + VC_{1,0} = 0,$$

$$VC_{0,0} + (\varepsilon_2^0 - \varepsilon)C_{1,0} = 0,$$

where

$$\varepsilon_1^0 = -\pi\mu^2 u_0,$$

$$\varepsilon_2^0 = \frac{1}{2}\mu^2 - \frac{1}{2}\pi\mu^2 u_0 - \frac{1}{4}\mu u_0 J_1(4\pi\mu) - \frac{1}{\sqrt{2}}\mu u_0 J_1(2\sqrt{2}\pi\mu),$$

$$V = -2u_0\mu J_1(2\pi\mu).$$

Considered in terms of this approximate description, the diagonal energies ε_1^0 and ε_2^0 become equal at

$$u_0 = \frac{\mu}{0.5J_1(4\pi\mu) + \sqrt{2}J_1(2\sqrt{2}\pi\mu)}.$$

At this value of u_0, the separation between ε_2 and ε_1 is $2|V|$ and the oscillator strengths coincide. For $\mu = 0.25$, this value for u_0 is 0.27, whereas an exact calculation suggests that the oscillator strengths f_1 and f_2 become equal at a somewhat smaller value $u_0 \approx 0.2$.

5. NEARLY FREE TWO-DIMENSIONAL EXCITON APPROXIMATION

In the free-exciton approximation, Bloch functions of symmetry Γ_1 are obtained through symmetrization of

plane waves with wave vectors belonging to a definite star β:

$$\psi^{\beta}(x, y) = \frac{1}{a}\sum_{(l, m) \in \beta}\frac{1}{\sqrt{n_\beta}}\exp\left[i\frac{2\pi}{a}(lx + my)\right]. \quad (23)$$

In this case, the state index ν can be conveniently replaced by β. Thus, in the zeroth approximation, we have $c^{\beta}_{\beta'} = n_\beta^{-1/2}\delta_{\beta, \beta'}$ and $C^{\beta}_{\beta} = 1$.

In first order in parameter $(u_0/\mu^2\tilde{\beta}^2) \ll 1$, admixture of the (0, 0) wave to the symmetrized combination (23) with $\beta \neq 0$ is described by the coefficient

$$c^{\beta}_0 = -\frac{u_0}{\varepsilon^0_\beta}U_{0, \beta}, \quad \varepsilon^0_\beta = \mu^2\tilde{\beta}^2.$$

Therefore, in second order in the above parameter, one obtains for the dimensionless oscillator strength

$$f_{\beta \neq 0} \approx \left(\frac{u_0}{\varepsilon^0_\beta}\frac{V_{0, 0; l, m}}{v_0}\right)^2 = n_\beta\left[\frac{u_0}{\mu\tilde{\beta}^3}J_1(2\pi\tilde{\beta}\mu)\right]^2,$$

$$f_0 \approx 1 - \sum_{\beta \neq 0} f_\beta. \quad (24)$$

In Fig. 1b, the dashed curves show the dependences of the oscillator strength on u_0 calculated for the two lowest exciton Γ_1 states in the nearly free exciton approximation, i.e., from Eq. (24).

6. TIGHT-BINDING APPROXIMATION

The Bloch states ν with negative energy E can be analyzed in terms of the tight-binding approximation. Considered in this approximation, the functions $\psi^{\nu}(x, y)$ at the Γ point can be written as

$$\psi^{\nu}(x, y) = \sum_{lm}\varphi_\nu(x - la, y - ma), \quad (25)$$

where $\varphi_\nu(x, y)$ are the normalized wave functions of the exciton bound to a single potential disc centered at the point $x = y = 0$. Bloch states of symmetry Γ_1 in a square lattice made up of circular potential discs can be derived only from the states $\varphi_\nu(x, y)$ in which the projection l_z of the orbital angular momentum on the z axis is either zero or a multiple of four. We denote the energy of such states, reckoned from the potential disc bottom and expressed in units of E_0, by $e_\nu(u_0)$, so that

$$\varepsilon_\nu(u_0) = e_\nu(u_0) - u_0. \quad (26)$$

The ground level e_1 is characterized by a zero angular momentum projection. For states with $l_z = 0$, the solutions inside and outside a disc are proportional to the Bessel functions $J_0(2\pi\sqrt{e_\nu}\,\rho/R)$ and $K_0(2\pi\sqrt{u_0 - e_\nu}\,\rho/R)$ and the values of e_ν satisfy the transcendental equation

$$\sqrt{u_0 - e_\nu}J_0(2\pi\sqrt{e_\nu})K_1(2\pi\sqrt{u_0 - e_\nu}) = \sqrt{e_\nu}J_1(2\pi\sqrt{e_\nu})K_0(2\pi\sqrt{u_0 - e_\nu}).$$

Representation (25) is valid for small overlaps of the functions φ_ν centered at two neighboring sites of a lateral superlattice. This condition is upheld for a large enough superlattice period a or a large enough potential depth v_0. According to Eqs. (3) and (15), the oscillator strength of exciton ν in the tight-binding approximation is given by

$$f_\nu = \frac{1}{a^2}\left(\iint\varphi_\nu(x, y)dxdy\right)^2. \quad (27)$$

The dashed lines in Figs. 1a and 1b plot the $\varepsilon_1(u_0)$ and $f_1(u_0)$ dependences calculated from Eqs. (26) and (27), respectively. As u_0 increases, the energy e_ν tends to its limiting value $e_\nu(\infty) = (t_\nu/2\pi)^2$, where t_ν are roots of the equation $J_0(t) = 0$. The first few limiting values of $e_\nu(\infty)$ for levels with $l_z = 0$ are 0.1465, 0.7718, 1.8969, …. The region of validity of the tight-binding approximation can also be estimated by comparing solid lines *1* and *2* with the dotted curves calculated using Eq. (27).

7. CONCLUSION

Thus, we have developed a theory of resonance reflection of light from a structure with a two-dimensional lateral superlattice whose period is large compared to the Bohr radius of the quasi-two-dimensional exciton. The Bloch states of the exciton of symmetry Γ_1 excited by light propagating along the principal axis of the structure were calculated. The dependence of exciton energy in these states on the potential-relief amplitude and on the superlattice period, as well as the corresponding redistribution of oscillator strength between various states, was analyzed. While the calculation was performed for a periodic array of quantum discs, the theory is capable of treating potentials of a more complicated shape. The theory may also be of advantage in a qualitative analysis of the relation between the oscillator strengths of the free exciton X and of the train X^- in doped quantum-well structures and is capable of accounting for the oscillator strength redistribution in favor of the trion resonance with increasing concentration of free carriers which was observed experimentally in [7].

ACKNOWLEDGMENTS

This study was supported by the Ministry of Science of the Russian Federation, program “Nanostructures.”

REFERENCES

1. E. L. Ivchenko and A. V. Kavokin, Fiz. Tverd. Tela (St. Petersburg) **34**, 1815 (1992) [Sov. Phys. Solid State **34**, 968 (1992)].
2. E. L. Ivchenko, Y. Fu, and M. Willander, Fiz. Tverd. Tela (St. Petersburg) **42**, 1707 (2000) [Phys. Solid State **42**, 1756 (2000)].
3. E. L. Ivchenko, Y. Fu, and M. Willander, in *Proceedings of 6th International Symposium "Nanostructures: Physics and Technology," St. Petersburg, Russia, 1998*, p. 374; M. Willander, E. L. Ivchenko, and Y. Fu, in *Proceedings of 2nd International Workshop on Physics and Modeling of Devices Based on Low-Dimensional Structures, Aizu-Wakamatsu, Japan, 1998*, p. 10.
4. G. Ya. Slepyan, S. A. Maksimenko, V. P. Kalosha, *et al.*, Phys. Rev. B **59**, 12275 (1999).
5. S. A. Maksimenko, G. Ya. Slepyan, N. N. Ledentsov, *et al.*, Semicond. Sci. Technol. **15**, 491 (2000).
6. Y. Fu, M. Willander, E. L. Ivchenko, and A. A. Kiselev, Phys. Rev. B **55**, 9872 (1997).
7. K. Kheng, R. T. Cox, Y. Merle d'Aubigné, *et al.*, Phys. Rev. Lett. **71**, 1752 (1993).

Translated by G. Skrebtsov

Physics of the Solid State, Vol. 45, No. 1, 2003, pp. 183–188. Translated from Fizika Tverdogo Tela, Vol. 45, No. 1, 2003, pp. 174–179.

POLYMERS AND LIQUID CRYSTALS

Dynamic and Dielectric Properties of Liquid Crystals

A. V. Zakharov and L. V. Mirantsev

Institute for Problems of Mechanical Engineering, Russian Academy of Sciences, Bol'shoĭ pr. 61, Vasil'evskiĭ ostrov, St. Petersburg, 199178 Russia

e-mail: miran@microm.ipme.ru

Received April 9, 2002

Abstract—The structural properties, static ε_j and relaxation $\varepsilon_j(\omega)$ permittivities ($j = \parallel, \perp$), time correlation functions $\Phi^1_{i0}(t)$ ($i = 0, 1$) and $\Phi^2_{00}(t)$, and orientational relaxation times $\tau^1_{i0}(t)$ ($i = 0, 1$) of 4-*n*-pentyl-4'-cyanobiphenyl (5CB) molecules in the nematic phase are investigated in the framework of the statistical–mechanical theory and the molecular dynamics method. The permittivities ε_j are calculated within a statistical–mechanical approach with the inclusion of translational, orientational, and mixed correlations in the description of the anisotropic systems. The time correlation functions $\Phi^1_{i0}(t)$ and $\Phi^2_{00}(t)$ and the orientational relaxation times $\tau^1_{i0}(t)$ of 5CB molecules are calculated using the molecular dynamics method for liquid-crystal systems simulated by realistic intramolecular and intermolecular atom–atom interactions. The results of calculations and the experimental data for 5CB are in good agreement. © *2003 MAIK "Nauka/Interperiodica".*

1. INTRODUCTION

The characteristic feature of anisotropic systems such as liquid crystals is that they exhibit a long-range orientational order due to an anisotropic nature of intermolecular interaction. There exist a number of theoretical approaches to analyzing the relation between the measured macroscopic parameters and the microscopic structure of liquid-crystal systems [1]. Among these methods, the statistical–mechanical approach and molecular dynamics calculations seem to hold the greatest promise. This can be explained by the fact that these techniques make it possible, on the one hand, to calculate directly the macroscopic characteristics of liquid crystals in the framework of reasonable approximations using model intermolecular interaction potentials and, on the other hand, to determine the averaged parameters on the basis of realistic interaction potentials both between atoms inside molecules forming an anisotropic system and between atoms of different molecules [1, 2].

In the present work, the above theoretical approaches were used to investigate the dynamic and dielectric properties of the nematic phase of 4-*n*-pentyl-4'-cyanobiphenyl (5CB). For this purpose, the time correlation functions, orientational relaxation times, and orientation distribution functions were derived by the molecular dynamics method [3, 4]. The choice of the nematic phase of 5CB was made primarily for the following reasons: (i) this compound has a simple phase diagram, and (ii) the nematic phase is observed in the temperature range 295–307 K [5], which is convenient for experimental investigations. Investigations into the dielectric characteristics of nematic liquid crystals have long attracted the particular attention of researchers engaged in the field of liquid-crystal materials [6–11]. However, direct experimental measurements of the permittivities and self-diffusion coefficients are rather complicated. In this respect, theoretical studies have assumed a new significance, because they can provide answers to a number of fundamental questions. For example, how much do the microscopic parameters responsible for the character of intermolecular interactions in a liquid-crystal system affect measured macroscopic characteristics (such as the self-diffusion coefficient or orientational relaxation times) of real liquid crystals? In the present study, we used the statistical–mechanical theory based on the method of conditional distribution functions [12]. This method makes it possible to take into account not only translational and orientational correlations but also mixed correlations of the molecules involved. As a model intermolecular interaction potential, we chose the dipolar Gay–Berne (GB) potential [13]. The dipoles were assumed to be aligned parallel to the long axes of the molecules forming a liquid crystal. Earlier [5], it was experimentally revealed that mesogenic molecules of cyanobiphenyl compounds consist of flexible hydrocarbon chains attached to a rigid core. The flexibility of the hydrocarbon chains determines the physical properties of liquid crystals in many respects. Moreover, these molecules possess a sufficiently large dipole moment (~4.5–5.0 D [14]), which is directed from the polar core to the molecular tail. The pair correlation functions of the distribution and the orientation distribution function of 5CB molecules in the temperature range corresponding to the nematic phase were calculated in the framework of the statistical–mechanical theory. Moreover, the time correlation functions were obtained from molecular

1063-7834/03/4501-0183$24.00

dynamics calculations, which made it possible to calculate the orientational relaxation times with the use of realistic interatomic interaction potentials [3, 4].

This paper is organized as follows. Section 2 covers the basic principles of the statistical–mechanical description of a system of interacting dipoles. Within this approach, we calculated the orientation distribution functions, the pair correlation functions, and the order parameters. Sections 3 and 4 present the results of calculations of the relaxation times and the static and relaxation permittivities of a nematic liquid crystal formed by 5CB molecules.

2. THE PAIR CORRELATION FUNCTION

The pair correlation functions for the nematic phase of 5CB are calculated in the framework of the equilibrium statistical mechanics [15] based on the method of conditional distributions [12]. We consider a single-component system composed of ellipsoidal molecules of length $\sigma_\parallel$ and width $\sigma_\perp$ in a volume V at a temperature T. The volume of the system is divided into N cells, each occupying a volume $v = V/N$. As a first approximation, we take into account only the states of the system for which each cell contains one molecule [16]. The potential energy of this system can be represented in the form $U = \sum_{i<j}\Phi(i, j)$, where $\Phi(i, j)$ is the pair intermolecular interaction potential, $i \equiv (\mathbf{r}_i, \mathbf{e}_i)$, and $\mathbf{r}_i$ and $\mathbf{e}_i$ are the vectors specifying the position and the orientation of the ith molecule, respectively. Now, we perform the integration of the quantity $\exp[-U/k_BT]$ (where k_B is the Boltzmann constant), which is the probability density of finding the system at points 1, 2, 3, …, N at a temperature T [12, 15]. As a result, we determine partial distribution functions, namely, the one-particle distribution function $F(i)$ (the probability density of finding a particle inside the ith cell), the pair distribution function $F(i, j)$ (the probability density of finding two particles in the ith and jth cells), etc. [12, 16]. In the present work, we will restrict our consideration to the case of two-particle correlations.

The functions $F(i)$ and $F(i, j)$ can be expressed in terms of the mean-force potentials [12, 16]

$$F(i) = \frac{\Psi(i)}{\int_i \Psi_i(i)d(i)}, \tag{1}$$

$$F(i, j) = F(i)F(j)V(i, j)\Psi^{-1}_{i, j}(i)\Psi^{-1}_{j, i}(j), \tag{2}$$

where $\Psi_j(j) = \prod_{i\neq j}\Psi_{j, i}(j)$, $\int_j d(j) \equiv \int_v d\mathbf{r}_j\int_\alpha d\mathbf{e}_j$, $V(i, j) = \exp[-\Phi(i, j)/k_BT]$, and α is the volume associated with the orientation of the ith molecule. The functions $F(i)$ satisfy the normalizing condition $\int_i F(i)d(i) = 1$, and the constraint $F(i) = \int_j F(i, j)d(j)$, which relates the one-particle and two-particle distribution functions, allows us to derive a closed integral equation with respect to the mean-force potential $\Psi_{i, j}(i)$ [12, 16]:

$$\Psi_{i, j}(i) = \int_j V(i, j)\Psi^{-1}_{j, i}(j)F(j)d(j). \tag{3}$$

Equation (3) can be solved only by the numerical method described in detail in [16, 17]. With the use of the solution $\Psi_{i, j}(i)$ and Eq. (2), we can calculate the pair correlation function $F(i, j)$, the orientation distribution function $f_0(\cos\beta_i) = \int_i F(i)d\mathbf{r}_i d\varphi_i$ (where φ_i is the azimuthal angle of the unit vector $\mathbf{e}_i$), the order parameters of the liquid-crystal system

$$\bar{P}_{2L} = \int_i F(i)P_{2L}(\cos\beta_i)d(i), \tag{4}$$

the correlators

$$\langle \mathbf{e}_i \cdot \mathbf{e}_j\rangle = \int_i d(i)\int_j d(j)F(i, j)(\mathbf{e}_i \cdot \mathbf{e}_j), \tag{5}$$

$$\bar{\chi} = \int_i d(i)F(i)\cos(2\pi z_i/d)P_2(\cos\beta_i), \tag{6}$$

and the Helmholtz free energy

$$f = \frac{F}{N} = -k_BT\ln\int_i d(i)\Psi_i(i). \tag{7}$$

Here, P_{2L} (L = 1, 2, and 3) are the Legendre polynomials, β is the polar angle formed by the long molecular axis and the director $\mathbf{n}$ aligned along the z axis, and d is the distance between two layers of the smectic-A phase. The parameter $\bar{\chi}$ is the measure of the density wave amplitude of the layered structure of the phase. The nematic phase is characterized by $\bar{\chi} = 0$ and $P_{2L} \neq 0$. The kernel $V(i, j)$ of the integral equation (3) is determined by the pair intermolecular interaction potential chosen as the sum of the Gay–Berne potential and the dipole–dipole interaction potential: $\Phi(i, j) = \Phi_{GB}(i, j) + \Phi_{DD}(i, j)$. The former potential can be written in the form $\Phi_{GB}(i, j) = 4\varepsilon_0\varepsilon(R^{-12} - R^{-6})$, where $R = (r - \sigma + \sigma_\perp)/\sigma_\perp$ and $r = [\mathbf{r}_i - \mathbf{r}_j]$. The parameters σ and ε are the width and the depth of the potential well, respectively. These parameters depend on the orientation of the unit vectors $\mathbf{e}_i$ and $\mathbf{e}_j$ (where $\mathbf{e} = \mathbf{r}/|\mathbf{r}|$), the geometric parameter of the molecule $\gamma = \sigma_\parallel/\sigma_\perp$, and the two exponents ν and μ in the relationship $\varepsilon = \varepsilon_1^\nu(\mathbf{e}_i, \mathbf{e}_j)\varepsilon_2^\mu(\mathbf{e}_i, \mathbf{e}_j, \mathbf{e})$. The formulas for ε_1 and ε_2 are given in [13]. The dipole–dipole interaction potential has the form $\Phi_{DD}(i, j) = \frac{\Delta^2}{r^3}[(\mathbf{e}_i \cdot \mathbf{e}_j) - 3(\mathbf{e}_i \cdot \mathbf{e})(\mathbf{e}_j \cdot \mathbf{e})]$, where Δ is the dipole moment of the 5CB molecule ($\Delta \sim 5$ D [14]). The intermolecular interaction parameters used in our calcula-

tions are as follows: $\gamma = \sigma_\parallel/\sigma_\perp = 3$ ($\sigma_\parallel \approx 1.8$ nm and $\sigma_\perp \approx 0.6$ nm), $\nu = 2.0$, $\mu = 0.98$, and $\varepsilon_0 = 2.07 \times 10^{-21}$ J. In addition, we used the following dimensionless parameters: the density $\rho = N\sigma_\perp^3/V \approx 0.512$ (corresponding to a density of 10^3 kg/m^3 for 5CB), the temperature $\Theta = k_B T/\varepsilon_0$, and the dimensionless dipole moment $\mu^* = \dfrac{\Delta}{(\varepsilon_0\sigma_\perp^3)^{1/2}} \approx 2.5$. It should be noted that the calculations were performed only for a cubic structure with six nearest neighbors and twelve next-to-nearest neighbors. In this case, we solved 18 nonlinear integral equations (3) in five-dimensional space. The molecular dynamics calculations included 120 5CB molecules enclosed in a cubic cell with an edge of 3.65 nm, which corresponds to a density of 10^3 kg/m^3. The temperature was maintained at 300 K ($\Theta = 2.0$). The equations of motion of 5CB molecules were solved using the Verlet algorithm [18] with a step of 2 fs [3, 4]. The starting configuration corresponded to the smectic phase of 5CB [4]. The director orientation **n** was determined with the use of the matrix $Q_{zz}^{\nu\nu'}$ written in the form [19]

$$Q_{zz}^{\nu\nu'} = \frac{1}{N}\sum_{j=1}^{N}\frac{1}{2}(3\cos\beta_{z\nu}^j\cos\beta_{z\nu'}^j - \delta_{\nu\nu'}), \qquad (8)$$

where N is the number of 5CB molecules and $\beta_{z\nu}^j$ is the angle between the long axis of the jth molecule and the ν axis related to the cubic cell. The molecular coordinates of the system were constructed using the eigenvectors of the tensor of the moment of inertia [3, 4]. By diagonalizing the matrix $Q_{zz}^{\nu\nu'}$, we obtained all the eigenvectors, of which the largest vector corresponds to the director orientation **n**. Figure 1 depicts the orientation distribution function $f_0(\cos\beta_i)$ calculated by the molecular dynamics method with due regard for the potential energy involving the intramolecular and intermolecular atom–atom contributions in the system at $T = 300$ K [3, 4]. The orientation distribution functions derived with the use of the integral equation for polar ($\mu^* \approx 2.5$) and nonpolar ($\mu^* = 0$) systems at $T = 300$ K are also displayed in Fig. 1. Making allowance for the fact that the calculations were performed using different potentials of the intermolecular interaction, the results obtained with different methods are in good agreement. Moreover, the order parameters $\bar{P}_2$ and $\bar{P}_4$ were calculated in the framework of the statistical–mechanical theory ($\bar{P}_2 = 0.78$ and $\bar{P}_4 = 0.35$) and the molecular dynamics method ($\bar{P}_2 = 0.504$ and $\bar{P}_4 = 0.188$). The theoretical results were compared with the experimental data obtained using NMR spectroscopy ($\bar{P}_2 = 0.61$ and $\bar{P}_4 = 0.15$) [20]. It should be noted that the order parameters calculated by the molecular dynamics method with different parametrizations of the potential energy of the system [3, 4, 20] and molecular coordinate systems [21] considerably differ from each other [22]: $0.5 \le \bar{P}_2 \le 0.72$ and $0.18 \le \bar{P}_4 \le 0.31$. The interpretation of the experimental data also depends on the choice of the coordinate system [23]. Compound 5CB over the entire range of the existence of the nematic phase is characterized by the parameter $\bar{\chi} = 9.5 \times 10^{-2}$, which confirms that there is a nematic ordering in the phase. It was also found that the dimensionless Helmholtz free energy f/ε_0 of the system is equal to –15.55 with due regard only for the nearest neighbors and –15.67 with allowance made for the nearest and next-to-nearest neighbors. Such an insignificant change in this integral characteristic indicates that, in the framework of the statistical theory allowing for the translational, orientational, and mixed correlations, it is quite reasonable to take into account the nearest and next-to-nearest neighbors.

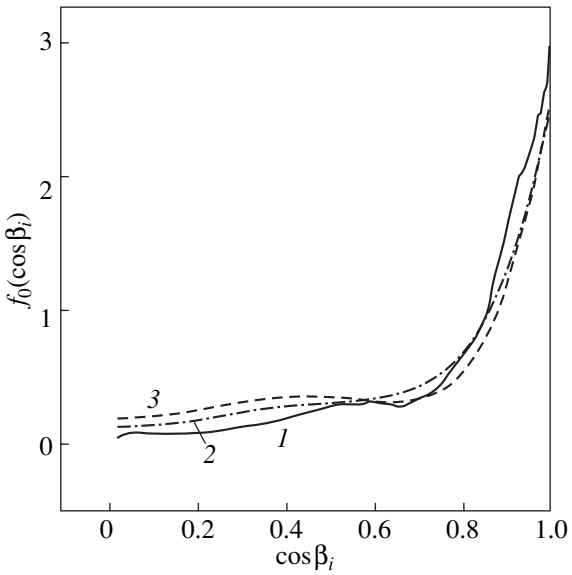

Fig. 1. Orientation distribution function for 5CB molecules at $T = 300$ K according to calculations in the framework of (*1*) the molecular dynamics method, (*2*) the statistical–mechanical theory with inclusion of the dipole–dipole interaction, and (*3*) the statistical–mechanical theory without regard for the dipole–dipole interaction.

3. STATIC PERMITTIVITY OF A NEMATIC LIQUID CRYSTAL

The static permittivity of an isotropic liquid is determined by the scalar quantity ε_i [24]. The dielectric properties of uniaxial liquid-crystal systems are characterized by two permittivity tensor components ε_{ij}, which are parallel ($\varepsilon_\parallel = \varepsilon_{zz}$) and perpendicular ($\varepsilon_\perp = \varepsilon_{xx} = \varepsilon_{yy}$) to the director orientation **n** [5]. The difference between $\varepsilon_\parallel$ and $\varepsilon_\perp$ is insignificant for nonpolar liquid crystals but is substantial for polar liquid crystals such

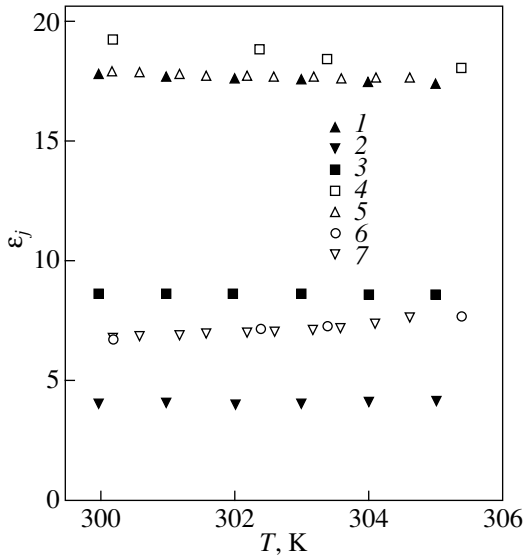

Fig. 2. (*1–3*) Calculated and (*4–7*) experimental temperature dependences of the static permittivity ε_j ($j = \parallel, \perp$) for 5CB: (*1*, *4*, *5*) $\varepsilon_\parallel$, (*2*, *6*, *7*) $\varepsilon_\perp$, and (*3*) $\bar{\varepsilon}$. Calculations are performed using relationships (9) and (10). Experimental data are taken from [6, 11].

as 5CB. For these two components, the mean permittivity $\bar{\varepsilon}$ can be defined by the expression

$$\bar{\varepsilon} = \frac{2\varepsilon_\perp + \varepsilon_\parallel}{3}. \quad (9)$$

For 5CB, the value of $\delta\varepsilon_{NI} = \bar{\varepsilon} - \varepsilon_i$ at the temperature T_{NI} of the nematic–isotropic liquid phase transition is negative and the permittivity $\bar{\varepsilon}$ slowly decreases with a decrease in the temperature [5]. According to the molecular theory proposed by Edwards and Madden [25], the permittivity tensor components can be calculated from the quadratic equation

$$\varepsilon_j^2 - B_j\varepsilon_j - D_j = 0, \quad (10)$$

where $B_j = \dfrac{A_j + 1 - y_j}{1 + y_j}$ and $D_j = \dfrac{y_j}{1 + y_j}$ ($j = \parallel, \perp$). The unknown coefficients A_j and y_j are functions of t_j and ε_j, respectively. The quantity t_j is given by the formula

$$t_j = \left\langle \mathbf{e}_j \cdot \sum_{m \in R_0} \mathbf{e}_m \right\rangle, \quad (11)$$

where $m \neq j$ and $\langle \ldots \rangle$ is defined by relationship (5). Summation in formula (11) is carried out over all the dipoles located inside the sphere of radius R_0 with the center at the jth molecule. All correlators of the type $\langle \mathbf{e}_j \cdot \mathbf{e}_m \rangle$ can be calculated in terms of the statistical–mechanical theory described in Section 2. The relationships for A_j and y_j have the form [25]

$$A_j = \frac{4\pi\rho\mu^{*2}}{\Theta} t_j, \quad y_\parallel = \frac{\xi}{\Omega}\left(1 - \frac{1}{\Omega^{1/2}}\tan^{-1}\Omega^{1/2}\right),$$
$$y_\perp = \frac{1}{\Omega}\left(-1 + \frac{\xi}{\Omega^{1/2}}\tan^{-1}\Omega^{1/2}\right), \quad (12)$$

where $\Omega = \xi - 1$ and $\xi = \varepsilon_\parallel/\varepsilon_\perp$. Equation (10) can be solved using the iterative procedure

$$\varepsilon_j^{[k+1]} = \frac{B_j(\varepsilon_j^{[k]})}{2} + \left[\frac{B_j^2(\varepsilon_j^{[k]})}{4} + D_j(\varepsilon_j^{[k]})\right]^{1/2}, \quad (13)$$

where k is the iteration number. Figure 2 shows the temperature dependences of the permittivities ε_j ($j = \parallel, \perp$) calculated according to Eq. (10) with the use of the correlators t_j obtained in the framework of the statistical–mechanical theory. The experimental data on the static permittivity for the nematic phase of 5CB [6, 11] are also presented in Fig. 2. It should be noted that the calculated and experimental data are in good agreement.

4. DIELECTRIC RELAXATION AND THE RELAXATION TIMES OF 5CB

For 5CB, the permittivity relaxation tensor $\varepsilon_{ik}(\omega) = \mathrm{Re}\varepsilon_{ik}(\omega) - i\,\mathrm{Im}\varepsilon_{ik}(\omega)$, which was measured over a wide frequency range ($1\ \mathrm{kHz} \le \omega/2\pi \le 13\ \mathrm{MHz}$ [9]), is characterized by a Debye relaxation. In the laboratory coordinate system with the z axis coinciding with the director orientation $\mathbf{n}$, the tensor components $\varepsilon_{ik}(\omega)$ for uniaxial nematics can be written in the following form [26]:

$$\frac{\varepsilon_i(\omega) - 1}{\varepsilon_j - 1} = 1 - i\omega\int_0^\infty C_j(t)\exp(-i\omega t)\,dt, \quad (14)$$

where $C_j(t)$ are the tensor components of the dipole autocorrelation function. These components can be represented by the relationships

$$C_\parallel = \langle e_z(0)e_z(t)\rangle = \Phi_{00}^1(t), \quad (15)$$

$$C_\perp = \langle e_x(0)e_x(t)\rangle = \langle e_y(0)e_y(t)\rangle = \Phi_{10}^1(t). \quad (16)$$

Here, $\Phi_{i0}^1(t)$ ($i = 0, 1$) are the first-rank time correlation functions and e_α ($e_\alpha \equiv e_{i\alpha}$) are the projections of the unit vector $\mathbf{e}$ onto the α axes ($\alpha = x, y, z$). The functions $\Phi_{i0}^1(t)$ can be written in the exponential form [2]

$$\Phi_{00}^1(t) = \Phi_{00}^1(0)\exp(-t/\tau_{00}^1) = \frac{1 + 2\bar{P}_2}{3}\exp(-t/\tau_{00}^1), \quad (17)$$

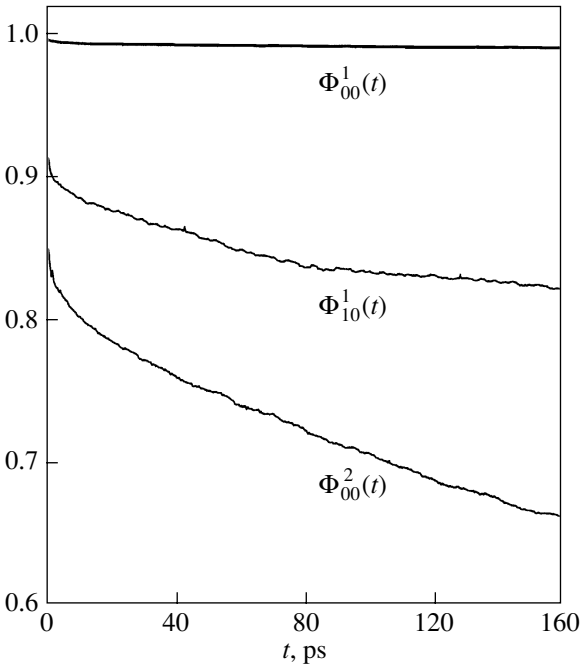

Fig. 3. Time correlation functions for 5CB molecules in the nematic phase according to molecular dynamics calculations.

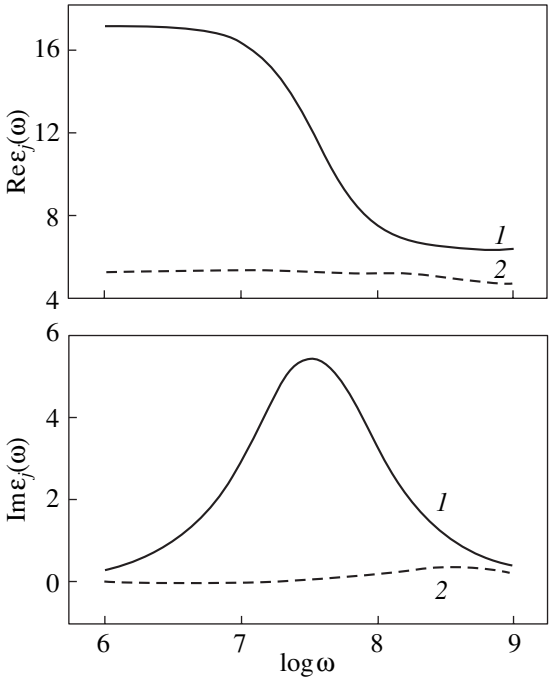

Fig. 4. Real and imaginary parts of the permittivity tensor $\varepsilon_j(\omega)$ ($j = \parallel, \perp$) calculated according to relationships (19) and (20) for (*1*) longitudinal and (*2*) transverse components $\varepsilon_j(\omega)$ ($\omega/2\pi$ in Hz) at a temperature of 300 K.

$$\Phi^1_{00}(t) = \Phi^1_{10}(0)\exp(-t/\tau^1_{10}) = \frac{1-\bar{P}_2}{3}\exp(-t/\tau^1_{10}). \quad (18)$$

Next, Eq. (14) can be rewritten as follows:

$$\frac{\varepsilon_\parallel(\omega)-1}{\varepsilon_\parallel-1} = 1-\Phi^1_{00}(0)\frac{i\omega\tau^1_{00}}{1+i\omega\tau^1_{00}}, \quad (19)$$

$$\frac{\varepsilon_\perp(\omega)-1}{\varepsilon_\perp-1} = 1-\Phi^1_{10}(0)\frac{i\omega\tau^1_{10}}{1+i\omega\tau^1_{10}}. \quad (20)$$

It should be noted that different spectroscopic techniques make it possible to determine the relaxation times τ^L_{mn} and the time correlation functions Φ^L_{mn} at specific values of L. In particular, the first-rank time correlation functions ($L = 1$) can be obtained using IR and dielectric spectroscopy [27], whereas the second-rank time correlation functions ($L = 2$) can be determined by NMR spectroscopy [28]. Three time correlation functions, $\Phi^1_{i0}(t)$ ($j = 0, 1$) and $\Phi^2_{00}(t)$, calculated in terms of the molecular dynamics method described in Section 2 are shown in Fig. 3. A technique for calculating these functions and the orientational relaxation times τ^1_{i0} ($i = 0, 1$) was described in detail in [3, 4]. The relaxation times τ^1_{i0} calculated within the molecular dynamics formalism and determined using NMR spectroscopy [29] for the nematic phase of 5CB at 300 K are presented in the table.

From relationships (19) and (20) and the relaxation times τ^1_{i0} ($i = 0, 1$), we can calculate the coefficients of the complex permittivity tensor $\varepsilon_j(\omega)$ ($j = \parallel, \perp$). Figure 4 presents the real parts $\mathrm{Re}\varepsilon_j(\omega)$ and the imaginary parts $\mathrm{Im}\varepsilon_j(\omega)$ of the permittivity tensor components $\varepsilon_j(\omega)$ calculated for the nematic phase of 5CB at a temperature of 300 K. The frequency $\nu = \dfrac{\omega}{2\pi}$ at which both longitudinal $\mathrm{Im}\varepsilon_\parallel(\omega)$ and transverse $\mathrm{Im}\varepsilon_\perp(\omega)$ components of the permittivity tensor $\varepsilon_j(\omega)$ exhibit a maximum of the dielectric loss is in close agreement with the frequency $\nu_{exp} \approx 6$ MHz determined experimentally for the nematic phase of 5CB at atmospheric pressure [9].

Orientational relaxation times τ^1_{i0} ($i = 0, 1$) calculated by the molecular dynamics method and determined using NMR spectroscopy for 5CB molecules in the nematic phase at a temperature of 300 K

Molecular dynamics method		NMR spectroscopy	
τ^1_{00}, ns	τ^1_{10}, ns	τ^1_{00}, ns	τ^1_{10}, ns
38.6	3.66	28.9	2.83

5. CONCLUSIONS

Thus, in the present work, the dynamic and dielectric properties of the nematic liquid crystal formed by 5CB molecules were investigated in the framework of the statistical–mechanical theory (based on the method of conditional distributions) and the molecular dynamics method (with the use of realistic interatomic interaction potentials). Within these approaches, we calculated the orientation distribution functions $f_0(\cos\beta_i)$ of 5CB molecules, the order parameters $\bar{P}_{2L}$ ($L = 1$ and 2), the orientational correlators $\langle \mathbf{e}_i \cdot \mathbf{e}_j \rangle$, the static ($\varepsilon_j$) and relaxation [$\varepsilon_j(\omega)$] permittivities ($j = \parallel, \perp$), the orientational relaxation times τ^1_{i0} ($i = 0$, 1), and the time correlation functions $\Phi^1_{i0}(t)$ ($i = 0$, 1) and $\Phi^2_{00}(t)$. The results obtained were compared with the available experimental data and with the results derived within other independent theoretical approaches. In particular, the relaxation times τ^1_{i0} ($i = 0$, 1) and the order parameter $\bar{P}_2 = 0.504$ ($T = 300$ K) determined in our work permitted us to calculate the rotational self-diffusion coefficient $D_\perp$ for 5CB molecules according to the equation $\tau^1_{10} = [D_\perp(2 + \bar{P}_2)/(1 - \bar{P}_2)]^{-1}$ [27]. The result obtained ($D_\perp = 1.4 \times 10^8$ s^{-1}) was compared with the self-diffusion coefficient ($D_\perp = 5.32 \times 10^8$ s^{-1}) determined from the experimental NMR data [29]. The above results give grounds to make the inference that the molecular dynamics method used in combination with the statistical–mechanical theory is a valuable tool for studying the macroscopic and microscopic properties of real liquid-crystal materials.

ACKNOWLEDGMENTS

This work was supported by the Russian Foundation for Basic Research, project no. 01-03-32084.

REFERENCES

1. P. G. de Gennes and J. Prost, *The Physics of Liquid Crystals* (Oxford Univ. Press, Oxford, 1995, 2nd ed.), p. 360.
2. G. R. Luckhurst and C. A. Veracini, *Molecular Dynamics of Liquid Crystals* (Kluwer, Dordrecht, 1994), p. 280.
3. A. V. Zakharov, A. V. Komolkin, and A. Maliniak, Phys. Rev. E **59**, 6802 (1999).
4. A. V. Zakharov and A. Maliniak, Eur. Phys. J. E **4**, 435 (2001).
5. W. H. de Jeu, *Physical Properties of Liquid Crystal Materials* (Gordon and Breach, New York, 1986), p. 240.
6. D. A. Dunmur, M. R. Manterfield, W. H. Miller, and J. K. Dunleavy, Mol. Cryst. Liq. Cryst. **45**, 127 (1978).
7. D. A. Dunmur and K. Toriyama, Liq. Cryst. **1**, 169 (1986).
8. J. Jadzyn, S. Czerbas, G. Czechowski, *et al.*, Liq. Cryst. **26**, 432 (1999).
9. S. Urban, A. Wurflinger, and B. Gestblom, Phys. Chem. Chem. Phys. **11**, 2787 (1999).
10. D. Demus and T. Inukai, Liq. Cryst. **26**, 1257 (1999).
11. S. R. Sarma, Mol. Phys. **78**, 733 (1993).
12. L. A. Rott, *The Statistical Theory of Molecular Systems* (Nauka, Moscow, 1978).
13. J. G. Gay and B. J. Berne, J. Chem. Phys. **74**, 3316 (1981).
14. K. P. Gueu, E. Magnassau, and A. Proutiere, Mol. Cryst. Liq. Cryst. **132**, 303 (1986).
15. R. Balescu, *Equilibrium and Nonequilibrium Statistical Mechanics* (Wiley, New York, 1978), p. 440.
16. A. V. Zakharov, Physica A (Amsterdam) **166**, 540 (1990); **175**, 327 (1991); Phys. Rev. E **51**, 5880 (1995).
17. A. V. Zakharov and S. Romano, Phys. Rev. E **58**, 7428 (1998).
18. M. P. Allen and D. J. Tildesley, *Computer Simulation of Liquids* (Clarendon, Oxford, 1989), p. 350.
19. R. Eppenga and D. Frenkel, Mol. Phys. **52**, 1303 (1984).
20. R. Y. Dong, Phys. Rev. E **57**, 4316 (1998).
21. A. V. Komolkin, A. Laaksonen, and A. Maliniak, J. Chem. Phys. **101**, 4103 (1994).
22. C. W. Cross and B. M. Fung, J. Chem. Phys. **101**, 6839 (1994).
23. T. Koboyashi, H. Yoshida, A. D. L. Chandani, *et al.*, Mol. Cryst. Liq. Cryst. **136**, 267 (1986).
24. G. S. Rushbrooke, *Introduction to Statistical Mechanics* (Clarendon, Oxford, 1949), p. 310.
25. D. M. F. Edwards and P. A. Madden, Mol. Phys. **48**, 471 (1983).
26. G. R. Luckhurst and C. Zannoni, Proc. R. Soc. London, Ser. A **343**, 389 (1975).
27. I. Dozov, N. Kirov, and M. P. Fontana, J. Chem. Phys. **81**, 2585 (1984).
28. R. Y. Dong, *Nuclear Magnetic Resonance in Liquid Crystals* (Springer-Verlag, New York, 1997, 2nd ed.), p. 225.
29. A. V. Zakharov and R. Y. Dong, Phys. Rev. E **64**, 031701 (2001).

Translated by O. Borovik-Romanova

Physics of the Solid State, Vol. 45, No. 1, 2003, pp. 189–196. Translated from Fizika Tverdogo Tela, Vol. 45, No. 1, 2003, pp. 180–186.

FULLERENES AND ATOMIC CLUSTERS

Equilibrium State of C_{60}, C_{70}, and C_{72} Nanoclusters and Local Defects of the Molecular Skeleton

O. E. Glukhova and A. I. Zhbanov

Saratov State University, ul. Astrakhanskaya 83, Saratov, 410012 Russia
e-mail: GlukhovaOE@info.sgu.ru; ZhbanovAI@info.sgu.ru

Received February 19, 2002

Abstract—The stability of C_{60} and C_{70} fullerenes and C_{60} and C_{72} nanotubes devoid of 2–12 atoms of the cluster skeleton was theoretically studied. It was established that C_n molecules with an even number of atoms remain stable, which was confirmed by experimental studies of monomolecular decay of clusters with the number of atoms $n \geq 30$. The change in the internuclear distances and in the ionization potential of nanoclusters was determined depending on the number of eliminated atoms. Such defects were shown to decrease the ionization potential of nanoclusters by 0.5–0.8 eV. The electron spectrum was calculated within the Harrison semiempirical tight-binding model in the Goodwin modification. A new parametrization of interatomic matrix elements of the Hamiltonian and atomic terms for carbon nanoclusters was suggested. © *2003 MAIK "Nauka/Interperiodica".*

1. INTRODUCTION

Since the discovery of carbon nanoclusters, interest in their properties has significantly increased from year to year. The reason for this is the technological advancement made in the field of cluster synthesis in a macroscopic volume with significant potential for practical applications.

Currently, many efficient methods of nanocluster production are being developed, among them the burning of hydrocarbons using the contact arc, resistive and high-frequency heating in inert gas atmospheres, and evaporation of graphite microparticles in thermal plasmas at normal pressure (see [1]). The simplest, most efficient, and most widely used method is arc discharge in inert-gas atmospheres with the use of graphite electrodes [2, 3]. However, many problems of nanocluster formation from hot chaotic carbon plasmas [4] remain to be solved. A number of studies [1, 4, 5] have been dedicated to the discussion of these problems.

The development of efficient technologies of nanocluster synthesis has led to the advent of novel lines of inquiry. The discovery of superconducting properties of doped fullerites [6] stimulated interest in the fullerene crystalline phase [7] and gave rise to a new field of physics of molecular crystals, namely, i.e., the physics of fullerites. The possibility of producing metal-containing organic compounds with the participation of fullerenes exhibiting ferromagnetism [8] created significant prospects in the development of the metalloorganic chemistry of fullerenes [9]. Another priority direction in cluster application is synthesis based on fullerene–polymers [10] whose molecules are bound chemically, rather than by van der Waals forces as in crystalline fullerite. Films with nanotube clusters (nanotubes) represent a promising material for designing subminiature electrovacuum devices [11].

Due to the wide application of nanoclusters in various branches of chemistry and physics and continuous advancement in the synthesis technologies of nanoclusters and nanocluster-based complex compounds, interest expressed in the properties of these many-particle molecules remains pertinent. As is known, C_{60} fullerenes are characterized by high chemical and mechanical stability. Their stability to external deformations is studied. A formal estimation [12] of the modulus of dilatation shows C_{60} fullerene to be characterized by a smaller compressibility than diamond crystal.

Alongside the above-mentioned, the application of nanoclusters calls for studies of their electronic structure, affinity to electrons, and molecule ionization potential, all of which control the chemical properties of clusters (in particular, in the synthesis of organic semiconductors with the participation of fullerenes), and of the emission properties when using films with nanotube clusters as field emitting arrays.

As has been shown in many studies dedicated to the physical properties and synthesis of carbon nanoclusters, clusters with a skeleton devoid of some atoms are formed alongside typical perfect clusters with a regular molecular structure [11].

The problem of cluster stability in the case of elimination of several pairs of atoms and even fragments has been theoretically studied by many scientists in the lines of (i) predictions of the molecular stability to the detachment of atoms, as well as to changes in bond lengths and in the skeleton configuration as a whole; (ii) estimations of enthalpy changes due to decomposition;

1063-7834/03/4501-0189$24.00

(iii) study of the electron shell of a molecule with broken bonds; and (iv) study of endohedral-compound formation by incorporating a foreign atom into the opening fullerene.

The studies into the cluster stability were carried out within two fragmentation models. In [13, 14], the Rice method was considered to be the mechanism of fullerene fragmentation. In this method, the preliminary Stone–Wales isomerization [15] is performed before the elimination of atom pairs, which transfers the initial fullerene into an isomer with a lower symmetry (C_{2v}) as a result of 90° rotation of the C–C bond between neighboring hexagons. According to the Rice method, elimination of one or more atom pairs leaves the electron shell closed but changes the symmetry group. The authors of [13] theoretically confirmed the stability of the C_{60} fullerene against elimination of C_2, C_4, and C_6 and the stability of C_{62} against C_2 elimination; estimated the enthalpy of Stone–Wales isomerization and decomposition of C_{60}; and substantiated the existence of at least one stable C_{30} fullerene isomer. The authors of [14] studied fragmentation of carbon cluster cations C_n^+ ($3 \le n \le 60$) within the Rice method and showed the high thermodynamic stability of the clusters.

An alternative method of fullerene fragmentation was employed in [16] with the intent of studying the formation of endohedral compounds. The latter method is based on the tight-binding approximation of molecular dynamics. The authors of [16] confirmed the high thermal stability of the C_{60} fullerene, which retains its skeleton with a bond length fluctuation of ±0.4 Å ("floppy phase" [17]) up to 3000 K, and studied the model of fullerene decomposition with the opening of a "window" formed initially by 9 and then by 13 and 16 atoms as C_2, C_4, and C_5 fragments were eliminated on reaching a temperature of ~5000 K. The energy barrier for a helium atom passing inside the fullerene through a 9-atomic window was shown to decrease from 8.7 to 3.5 eV in comparison with one passing through a hexagon ring.

Apart from fullerenes, the physical properties of single-walled nanotube carbon structures were theoretically studied *ab initio* in the case where the structures have no dome, as well as in the case of detachment of more extended fragments with the formation of an opened nanotube with flat and oblique edges [18]. It was shown in [18] that broken bonds become closed onto one of the bonds of the sp^2 hybridization as unpaired electrons appear, thus closing the electron shell of the molecule. In this case, a tight double bond is formed, shortening the distance between the nuclei from 1.41 Å (for the initial molecule) to 1.27 Å.

We studied the models of clusters devoid of several atoms under the assumption of the shell being closed, as in [18].

2. NEW PARAMETRIZATION OF THE HARRISON TIGHT-BINDING MODEL IN THE GOODWIN MODIFICATION FOR CALCULATING THE ELECTRONIC STRUCTURE OF CARBON NANOCLUSTERS

We calculated the metric characteristics of the skeleton and the electron spectrum of carbon nanoclusters using the Harrison modified semiempirical model of tight binding [19]. We chose this model for several reasons. An *ab initio* theoretical calculation of the electron spectrum of polyatomic molecules requires significant computer resources [6], while semiempirical methods can be efficiently applied to calculate micro- and macroscopic carbon systems [20]. An advantage of the Harrison scheme is that it operates with the Hamiltonian constructed in real space, in the basis of *s* and *p* orbitals of outer electron layers of carbon atoms. This allows one to calculate the skeleton metric characteristics and the electron energy levels at various local changes in the molecule structure. The wave functions of valence electrons of neighboring atoms are considered to be nonoverlapping. There exist a few modifications of the Harrison scheme, for example, the Goodwin modification for calculating the band structure of diamond and graphite [21].

To calculate the metric characteristics of the skeleton and the electron spectrum of the cluster, the total energy E of the cluster is minimized with respect to bond lengths:

$$E = E_{\text{bond}} + E_{\text{rep}}, \tag{1}$$

where E_{bond} is the band structure energy and E_{rep} is the phenomenological energy taking into account the electron–electron and internuclear interactions.

The phenomenological energy is written as the sum of pair repulsing potentials:

$$E_{\text{rep}} = \sum_{i<j} V_{\text{rep}}(|r_i - r_j|), \tag{2}$$

where i and j are indices of interacting atoms and r_i and r_j are the Cartesian coordinates. The function V_{rep} is given by (see [21])

$$V_{\text{rep}}(r) = V_{\text{rep}}^0\left(\frac{1.54}{r}\right)^{4.455} \times \exp\left\{4.455\left[-\left(\frac{r}{2.32}\right)^{22} + \left(\frac{1.54}{2.32}\right)^{22}\right]\right\}, \tag{3}$$

where $V_{\text{rep}}^0 = 10.92$ eV. The band structure energy is given by

$$E_{\text{bond}} = 2\sum_n \varepsilon_n, \tag{4}$$

Table 1. Carbon atom terms and equilibrium overlap integrals (eV)

Parametrization	ε_s	ε_p	$V^0_{ss\sigma}$	$V^0_{sp\sigma}$	$V^0_{pp\sigma}$	$V^0_{pp\pi}$
Goodwin [21]	–5.163331	2.28887	–4.43338	3.78614	5.65984	–1.82861
His study	–10.932	–5.991	–4.344	3.969	5.457	–1.938

where ε_n is the energy of the occupied state with index n, i.e., the Hamiltonian eigenvalue (the factor of two takes into account the electron spin).

Interatomic matrix elements of the Hamiltonian were determined from the formula [21]

$$V_{ij\alpha}(r) = V^0_{ij\alpha}\left(\frac{1.54}{r}\right)^{2.796} \times \exp\left\{2.796\left[-\left(\frac{r}{2.32}\right)^{22} + \left(\frac{1.54}{2.32}\right)^{22}\right]\right\}, \quad (5)$$

where r is the interatomic spacing, i and j are the orbital quantum numbers of the wave functions, and α is the subscript indicating the bond type (σ or π). The values of the atomic terms ε_s and ε_p and the equilibrium overlap integrals $V^0_{ss\sigma}$, $V^0_{sp\sigma}$, $V^0_{pp\sigma}$, and $V^0_{pp\pi}$ suggested by Goodwin are listed in Table 1. This modification was used in [22] to calculate the electronic and vibrational spectra of the C_{60} fullerene (see Fig. 1). The bond lengths (r_1 = 1.463 Å and r_2 = 1.418 Å for single and double bonds, respectively) obtained in [22] for the fullerene, as well as the energy gap between the last highest occupied and the lowest empty level in the electronic spectrum (E_g = 1.7 eV), were in quite good agreement with the experimental data from [23]: r_1 = 1.45 ± 0.01 Å, r_2 = 1.4 ± 0.01 Å, and E_g = 1.7–1.9 eV. However, the immediate application of the Goodwin parametrization to matrix elements of the Hamiltonian does not allow one to determine the ionization potential from the electronic spectrum, which somewhat narrows the applicability range of this parametrization.

We suggest a new parametrization of interatomic and diagonal matrix elements of carbon nanoclusters having none of the above limitations.

The first attempt that we undertook to improve the parametrization consisted in the following. We left the equilibrium overlap integrals $V^0_{ss\sigma}$, $V^0_{sp\sigma}$, $V^0_{pp\sigma}$, and $V^0_{pp\pi}$ unchanged, i.e., the same as in the Goodwin modification. As a first approximation to the carbon atomic terms ε_s and ε_p, we took the values suggested by Harrison [19] (ε_s = –17.52, ε_p = –5.97 eV) and then varied them. We increased ε_s and ε_p by the same amount and shifted the electronic spectrum such that the energy position of the highest electron energy level corresponded to the experimental value of the ionization potential I = 7.61 eV [6] of the C_{60} fullerene (the best studied carbon cluster). The carbon atomic terms were found to be higher by 3 eV in comparison with the Harrison values (see the Harrison–Goodwin parametrization in Table 1). However, the fullerene bond lengths (r_1 = 1.470 Å, r_2 = 1.425 Å) and the energy gap (E_g = 1.64 eV) calculated for these values of ε_s and ε_p were significantly more different (a change for the worse) from the experimental values in comparison with the same quantities obtained theoretically with the Goodwin parametrization [23].

Therefore, we attempted to improve the parametrization in another way and varied both the carbon atomic terms and the interatomic matrix elements. We modified the carbon atomic terms and the equilibrium overlap integrals such that the bond lengths r_1 and r_2, the energy gap E_g, and the ionization potential I corresponded to the experimental values for the C_{60} fullerene. To do this, the sum of squared deviations of the calculated bond lengths r_1 and r_2, energy gap E_g, and ionization potential I from their true (experimental) values (see above) was minimized. At each change of one of the optimized parameters (carbon atomic terms and equilibrium overlap integrals), we calculated the values r_1, r_2, E_g, and I by minimizing the total energy of the molecule with respect to bond lengths, which takes approximately 80 iterations; i.e., a 240 × 240 matrix was diagonalized 80 times. As a result, the carbon

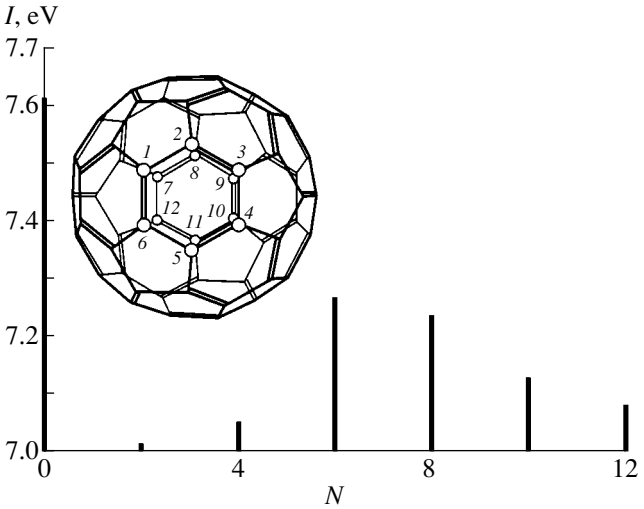

Fig. 1. Change in the ionization potential of fullerene C_{60} after elimination of twelve atoms; N is the number of sequentially eliminated atoms.

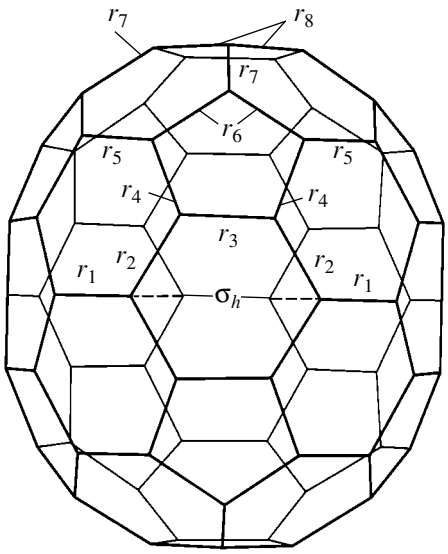

Fig. 2. C_{70} fullerene.

atomic terms and the interatomic matrix elements were determined by performing 1000 iterations to an accuracy of 10^{-4}. To calculate the Hamiltonian eigenvalues, we invoked the Householder method [24], as in [22]. Minimization was carried out with the Hooke–Jeeves method. The calculated Hamiltonian matrix elements are listed in Table 1. For the fullerene, we obtained r_1 = 1.4495 Å, r_2 = 1.4005 Å, E_g = 1.96 eV, and I = 7.6099 eV. For all three Harrison scheme modifications under consideration, according to the dimensions of the irreducible *a*, *t*, *g*, and *h* representations of the point symmetry group Y_h to which the C_{60} fullerene is related, the electron spectrum is characterized by singly, triply, quadruply, and fivefold degenerate states, respectively.

To check the new parametrization of matrix elements in the Harrison modified scheme, the calculated metric characteristics of the C_{70} fullerene skeleton were compared to the known values numerically calculated from the electron energy loss spectrum for elastic scattering in C_{70} in the gaseous state [20].

3. STABLE STATE OF C_{60} AND C_{70} FULLERENES AND C_{60} AND C_{72} NANOTUBES

Experimental studies of C_{60} fullerenes demonstrate the extraordinarily high stability of these clusters [20]. High survival of molecules with even numbers of atoms was observed in the course of monomolecular decomposition of carbon clusters with $n \geq 30$ or photodissociation. This stability is explained by the structural fragment C_2 detachment [20].

We theoretically studied the geometrical parameters of the molecular skeleton and the electronic spectrum of carbon clusters in the case of elimination of fragments with even numbers of atoms.

The metric characteristics of the skeleton and the electronic spectrum of the cluster are calculated as follows.

The total energy of the molecule is calculated. The internuclear distances are specified in the initial approximation. Then, these distances are determined more accurately by minimizing the molecule energy with respect to the sought-for internuclear distances. The number of internuclear distances to be calculated is limited by the calculating time. For example, determination of the values of eight bond lengths and four skeleton diameters of the C_{70} fullerene takes computer time that is several tens of times longer than that taken for determination of two bond lengths of the C_{60} fullerene. In the case of optimization of additional internuclear distances or coordinates of separate atoms with the intent of correcting the skeleton configuration, the computing time significantly increases. In this way, we calculated the molecule skeleton configuration and the electronic spectrum.

As is known, the ionization potential of a molecule can be estimated from the electronic spectrum. According to the Koopmans theorem, this potential represents the total energy of an ion produced by the elimination of one electron and can be determined from the energy spectrum of the molecule as the absolute value of the energy of the highest occupied level. In this case, the configuration change accompanying ionization, as well as the fact that the electron shell of the new system becomes open, can be neglected for large molecules [25].

It appears of interest to study the multiplicity of the stable state of carbon clusters. This study requires a group-theoretical analysis of each cluster; however, the method we applied to calculate the electronic spectrum does not make it possible to account for the multiplicity. Within the method under consideration, the ground (many-electron) state of molecule C_n is controlled by population of the lowest $2n$ single-electron states by $4n$ valence electrons (single-electron approximation). Nevertheless, a survey of some papers on fullerene stability [13–15], nanotube electronic structure [20], physical properties of fullerenes [26], hyperfullerenes [27], and nanotubes [28, 29] shows that the cluster state multiplicity can be neglected in this case.

4. C_{70} FULLERENE

The C_{70} fullerene belongs to the point symmetry group D_{5h} and is a closed spheroid molecule consisting of 25 hexagons and 12 pentagons. Two pentagons form opposite faces, distance with the between them being maximum for this molecule (Fig. 2). The skeleton configuration is characterized by four diameters, height, and eight different internuclear distances [30]. One of the diameters, d_1 (Table 2), characterizes a circle lying in the symmetry plane σ_h perpendicular to the principal rotation axis C_5 passing through the centers of the pen-

tagons. The three other diameters define the circles lying in the planes parallel to σ_h. The diameter d_2 (Table 2) of the circle spaced from σ_h by one layer is smaller than d_1; therefore, there is a waist in the plane σ_h [30]. The fullerene height h (Table 2) is understood as the distance between opposite pentagons. The internuclear distances are determined by the following C–C bonds (Table 2): the bond r_1 between the hexagons, which lies in the plane σ_h; the bond r_2 between the pentagon and the hexagon whose one side lies in the σ_h plane; the bond r_3 lying in a pentagon and also belonging to the hexagon crossed by σ_h; the bond r_4, common for a pentagon and the hexagon which is based on σ_h; the bond r_5 between the irregular pentagons; the bond r_6 which lies in the pentagon and also belongs to the hexagon contiguous to the pentagon; the bond r_7 between a pentagon and an irregular pentagon; and the bond r_8 lying in a pentagon.

Using the technique described above, we calculated the geometrical parameters of the C_{70} fullerene with various parametrizations of matrix elements, namely, the Goodwin and Harrison–Goodwin parametrizations and ours (Table 1). The results are listed in Table 2. From the calculations, it follows that our parametrization is adequate. The metric parameters of the fullerene structure conform well to the values given in [30]. The electronic spectrum is controlled by singly and doubly degenerate orbital multiplets of different energy according to the dimensions of the irreducible *a* and *e* representations of the D_{5h} group. As follows from a comparison of the circle diameter (Table 2) in σ_h with other diameters, no waists in the fullerene symmetry plane σ_h exist. This result is qualitatively confirmed by calculations with various parametrizations of the matrix elements (Table 2).

We studied the C_{70} fullerene behavior in the course of sequential elimination in two or more atoms from hexagons. The coordinates of atoms with broken bonds were optimized, and the electronic spectra of C_{68}, C_{66}, C_{64}, C_{62}, C_{60}, and C_{58} were calculated. The sequence of eliminations is shown in Fig. 3. The first to be eliminated from the cluster were two atoms with indices 1 and 2, then four atoms with indices 1–4; two fragments containing atoms 1–12 were removed in the last reaction. As indicated above, the electron shell of the cluster remains closed after elimination of several atoms or a whole fragment. Elimination of atoms from the cluster was accompanied by an increase in the total energy, a displacement of the highest populated electron term to the region of positive values, and an increase in the decomposition heat. The ionization potential variation is shown in Fig. 3. The reaction heat increase due to the cluster losing more and more atoms is shown in Table 3. However, the enthalpy calculations show that the reaction heat can be lowered by eliminating a single C_6 ring instead of several C_2 pairs (for C_{64}) or by eliminating one or two C_6 rings alongside several C_2 pairs (for C_{62}, C_{60}, C_{58}). This conforms to the results of similar studies of the C_{60} fullerene [13].

Table 2. Some metric characteristics (Å) of the C_{70} fullerene skeleton

	Experiment [30]	Parametrization	
		Goodwin	this study
Bond lengths			
r_1	$1.41^{+0.03}_{-0.01}$	1.466	1.454
r_2	1.39 ± 0.01	1.438	1.421
r_3	$1.47^{+0.01}_{-0.03}$	1.448	1.433
r_4	1.46 ± 0.01	1.462	1.448
r_5	1.37 ± 0.01	1.414	1.396
r_6	1.47 ± 0.01	1.459	1.446
r_7	1.37 ± 0.01	1.419	1.401
r_8	1.464 ± 0.009	1.462	1.449
Diameters and height			
d_1	6.94 ± 0.05	7.18	7.12
d_2	6.99 ± 0.05	7.01	6.93
h	7.8 ± 0.01	8.00	7.92

5. C_{60} FULLERENE

Now, we consider the case when atoms that are arranged in two opposite hexagons are sequentially broken away in pairs from the molecule. The coordinates of atoms with broken bonds were optimized, and

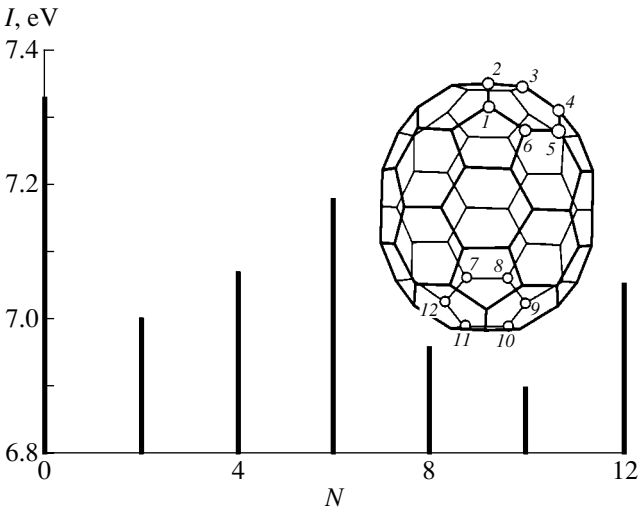

Fig. 3. Variation in the C_{70} fullerene ionization potential in the case of elimination of twelve atoms.

Table 3. Enthalpy of C_{60}, C_{70}, and C_{72} carbon cluster decomposition

C_{60} fullerene (Y_h)		C_{60} nanotube (D_{6h})	
reaction: $C_{60} \longrightarrow$	heat ΔH, kcal/mol	reaction: $C_{60} \longrightarrow$	heat ΔH, kcal/mol
$C_{58} + C_2$	392.58 (17.07 eV)	$C_{58} + C_2$	5947.52 (258.59 eV)
$C_{56} + 2C_2$	610.42	$C_{56} + 2C_2$	6116.83
$C_{54} + 3C_2$	816.75	$C_{54} + 3C_2$	6285.93
$C_{54} + C_6$	631.48	$C_{54} + C_6$	6100.66
$C_{52} + 4C_2$	1235.24	$C_{52} + 4C_2$	6634.69
$C_{52} + C_2 + C_6$	1049.97	$C_{52} + C_2 + C_6$	6449.40
$C_{50} + 5C_2$	1440.12	$C_{50} + 5C_2$	6826.15
$C_{50} + 2C_2 + C_6$	1049.97	$C_{50} + 2C_2 + C_6$	6640.87
$C_{48} + 6C_2$	1640.04	$C_{48} + 6C_2$	7003.26
$C_{48} + 2C_6$	1269.49	$C_{48} + 2C_6$	6632.71
C_{70} fullerene (D_{5h})		C_{72} nanotube (D_{6d})	
reaction $C_{70} \longrightarrow$	heat ΔH, kcal/mol	reaction $C_{72} \longrightarrow$	heat ΔH, kcal/mol
$C_{68} + C_2$	393.23 (17.10 eV)	$C_{70} + C_2$	7080.84 (307.86 eV)
$C_{66} + 2C_2$	599.22	$C_{68} + 2C_2$	7253.89
$C_{64} + 3C_2$	797.86	$C_{66} + 3C_2$	7476.48
$C_{64} + C_6$	612.60	$C_{66} + C_6$	7256.21
$C_{62} + 4C_2$	1191.43	$C_{64} + 4C_2$	7894.69
$C_{62} + C_2 + C_6$	1006.17	$C_{64} + C_2 + C_6$	7676.21
$C_{60} + 5C_2$	1407.85	$C_{62} + 5C_2$	8112.14
$C_{60} + 2C_2 + C_6$	1222.59	$C_{62} + 2C_2 + C_6$	7901.87
$C_{58} + 6C_2$	1596.83	$C_{60} + 6C_2$	8334.86
$C_{58} + 2C_6$	1226.30	$C_{60} + 2C_6$	7908.31

the electronic spectra of C_{58}, C_{56}, C_{54}, C_{52}, C_{50}, and C_{48} molecules were calculated (Fig. 1). The atom elimination sequence remained as before (for the C_{70} fullerene). The bond lengths of the symmetric C_{48} molecule were different: $r_1 = 1.466$ Å and $r_2 = 1.378$ Å. As in the case of C_{70} fullerene, the total energy increases, the ionization potential is lowered (Fig. 1), and the decomposition enthalpy increases (Table 3) as atoms are eliminated from the cluster. The values of the reaction heat for the C_{58}, C_{56}, and C_{54} production are in general agreement with the corresponding values from [13, 14] but do not completely coincide, since the authors of [13, 14] used an alternative fullerene C_{60} decomposing procedure (the Rice method) and the MNDO calculation method. Moreover, the authors of [14] studied the C_{60}^+ cation rather than the neutral fullerene. As in the case of the C_{70} fullerene, the reaction heat tended to decrease after elimination of one or two C_6 rings.

It can be concluded that the C_{60} and C_{70} fullerenes remain stable, notwithstanding some imperfections in the configuration of their skeleton.

6. C_{60} AND C_{72} NANOTUBES

We also studied the C_{60} and C_{72} nanotube clusters (Figs. 4, 5), which have identical dome shapes and differ only in the number of hexagons in their skeletons. The C_{60} and C_{72} nanotubes are poorly studied in comparison with the C_{60} and C_{70} fullerenes; therefore, we first determined their bond lengths. Unlike the authors of [20], we detected five C–C bond lengths rather than four: the bond in the hexagon at the "cover" (r_1 = 1.452 Å), the bond common to two pentagons (r_2 = 1.475 Å), and the bond also belonging to the hexagon lying outside the cluster cover (r_3 = 1.460 Å); this last hexagon is also characterized by two more bond types (r_4 = 1.448 Å, r_5 = 1.467 Å). The electronic spectrum of the nanotubes is formed by singly and doubly degenerate multiplets according to the dimensions of the irreducible *a*, *b*, and *e* representations of the D_{6h} group (for the C_{60} nanotube) and D_{6d} group (for the C_{72} nanotube) whose reducible-representation basis is formed by *p* orbitals.

A study of nanotubes with deformed domes (C_{58}, C_{56}, C_{54}, C_{52}, C_{50}, C_{48}; C_{70}, C_{68}, C_{66}, C_{64}, C_{62}, C_{60}) and

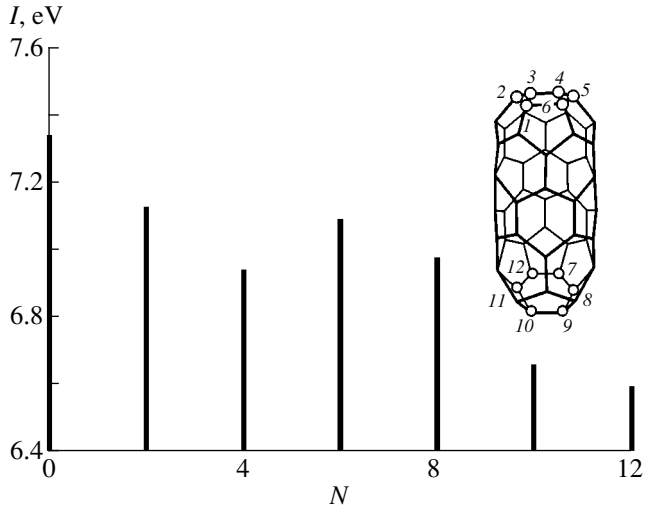

Fig. 4. Variation in the ionization potential of the C_{60} nanotube in the case of elimination of twelve atoms.

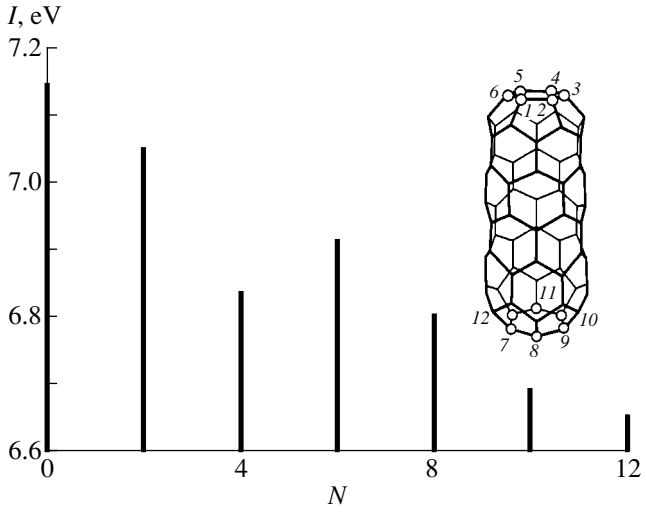

Fig. 5. Variation in the ionization potential of the C_{72} nanotube in the case of elimination of twelve atoms.

without domes (C_{54}, C_{48}; C_{66}, C_{60}; Figs. 3, 4) showed cluster stability to such defects of the molecular skeleton, a rather small change in the coordinates of atoms with broken bonds, and an increase in the molecule energy and in the energy of the highest occupied energy level. The ionization potential variation due to a decrease in the number of carbon atoms in the dome is shown in Figs. 4 and 5 (the sequence of atom eliminations is the same as for fullerenes). The skeleton of nanotubes whose symmetry remains unchanged was corrected by optimizing the bond lengths. For the C_{54} and C_{66} nanotubes, we have $r_1 = 1.421$, $r_2 = 1.476$, r_3, $r_4 = 1.428$, and $r_5 = 1.441$ Å. For the C_{48} and C_{60} nanotubes, we have $r_3 = 1.410$, $r_4 = 1.441$, and $r_5 = 1.432$ Å. The reaction enthalpy variation is shown in Table 3. As in the case of fullerenes, the enthalpy is lowered as one or two C_6 rings are eliminated alongside C atom pairs.

7. DISCUSSION

The theoretical study of the stability of the C_{60} and C_{70} fullerenes and the C_{60} and C_{72} nanotubes with defects in their molecular structure showed the following.

In the case of elimination of an even number of atoms, the nanoclusters do not decompose. At the points of local defects, a correction to the cluster skeleton is observed which corresponds to the recovery of equilibrium.

The ionization potential of clusters devoid of several atom pairs was found to decrease. This is probably explained by a correction to the skeleton and by a large ratio of the number of removed atoms to the total number of atoms in the molecule. It has also been established that the decrease in the ionization potential becomes less appreciable and then the potential increases slowly with the number of eliminated atoms.

It has been shown that the enthalpy of fullerene fragmentation can decrease if elimination of whole fragments (one or more C_6 rings), rather than of carbon atom pairs, is performed. A similar enthalpy tendency is observed during decomposition of carbon tubes. In this case, much larger fragmentation heats of carbon tubes are observed in comparison with those for fullerenes. The reason for this effect is unclear, and, as far as we know, there are no publications on this problem.

The results of this study allow one to predict some properties of molecules with a deformed skeleton devoid of certain atoms. Such molecules are formed in the course of carbon nanocluster synthesis in macroscopic volumes. In particular, the emissivity can be qualitatively estimated from changes in the electronic spectrum and the ionization potential. This study allows us to conclude that a purposeful generation of certain defects in the course of carbon nanocluster synthesis can allow one to achieve required properties.

ACKNOWLEDGMENTS

This study was supported in part by the Russian Foundation for Basic Research (project no. 98-02-17970) and the International Science and Technology Center (project no. 1024f-99).

REFERENCES

1. D. Afanas'ev, I. Blinov, A. Bogdanov, *et al.*, Zh. Tekh. Fiz. **64** (10), 77 (1994) [Tech. Phys. **39**, 1017 (1994)].
2. J. P. Hare, H. W. Kroto, and R. Taylor, Chem. Phys. Lett. **177**, 394 (1991).

3. W. A. Scrivens and J. M. Tour, J. Org. Chem. **57**, 6932 (1992).
4. H. Kroto, Pure Appl. Chem. **62**, 407 (1990).
5. R. F. Curl, Nature **363**, 14 (1993).
6. V. M. Loktev, Fiz. Nizk. Temp. **18** (3), 217 (1992) [Sov. J. Low Temp. Phys. **18**, 149 (1992)].
7. S. V. Kozyrev and V. V. Rotkin, Fiz. Tekh. Poluprovodn. (St. Petersburg) **27** (9), 1409 (1993) [Semiconductors **27**, 777 (1993)].
8. B. Morosin, C. Henderson, and J. E. Schrieber, Appl. Phys. A **59**, 179 (1994).
9. P. J. Fagan, J. C. Calabrese, and B. Malone, Acc. Chem. Res. **25**, 134 (1992).
10. F. Wudl, Acc. Chem. Res. **25**, 157 (1992).
11. N. I. Sinitsyn, Yu. V. Gulyaev, G. V. Torgashov, *et al.*, Appl. Surf. Sci. **111**, 145 (1997).
12. R. S. Ruoff and A. L. Rouff, Appl. Phys. Lett. **59**, 1553 (1991).
13. R. E. Stanton, J. Phys. Chem. **96**, 111 (1992).
14. J. J. Novoa and M.-H. Whangbo, New J. Chem. **18**, 457 (1994).
15. R. E. Stanton and D. J. Wales, Chem. Phys. Lett. **128**, 501 (1986).
16. E. Kim, D.-H. Oh, C. W. Oh, and Y. H. Lee, Synth. Met. **70**, 1495 (1995).
17. S. G. Kim and D. Tomanek, Phys. Rev. Lett. **72**, 2418 (1994).
18. S. Han and J. Ihm, Phys. Rev. B **61** (15), 9986 (2000).
19. W. A. Harrison, *Electronic Structure and the Properties of Solids: The Physics of the Chemical Bond* (Freeman, San Francisco, 1980; Mir, Moscow, 1983), Vol. 1.
20. E. G. Gal'pern, I. V. Stankevich, L. A. Chernozatonskiĭ, and A. L. Chistyakov, Pis'ma Zh. Éksp. Teor. Fiz. **55** (8), 469 (1992) [JETP Lett. **55**, 483 (1992)].
21. L. Goodwin, J. Phys.: Condens. Matter **3**, 3869 (1991).
22. N. V. Khokhryakov and S. S. Savinskiĭ, Fiz. Tverd. Tela (St. Petersburg) **36** (12), 3524 (1994) [Phys. Solid State **36**, 1872 (1994)].
23. J. R. D. Copley, D. A. Neumann, R. L. Cappelletti, and W. A. Kamitakahara, Phys. Chem. Solids **53** (1), 1353 (1992).
24. J. H. Wilkinson and C. Reinsch, *Linear Algebra* (Springer, Berlin, 1971; Mashinostroenie, Moscow, 1976).
25. R. Zahradnik and R. Polak, *Zaklady kvantove chemie* (SNTL, Prague, 1976; Mir, Moscow, 1979).
26. T. L. Makarova, Fiz. Tekh. Poluprovodn. (St. Petersburg) **35** (3), 257 (2001) [Semiconductors **35**, 243 (2001)].
27. M. I. Heggie, M. Terrones, B. R. Eggen, *et al.*, Phys. Rev. B **57** (21), 13339 (1998).
28. L. Lou, P. Nordlander, and R. E. Smalley, Phys. Rev. B **52** (3), 1429 (1995).
29. L. Lou and P. Nordlander, Phys. Rev. B **54** (23), 16659 (1996).
30. A. V. Eletskiĭ and B. M. Smirnov, Usp. Fiz. Nauk **163** (2), 33 (1993) [Phys. Usp. **36**, 202 (1993)].

Translated by A. Kazantsev

Physics of the Solid State, Vol. 45, No. 1, 2003, pp. 197–200. Translated from Fizika Tverdogo Tela, Vol. 45, No. 1, 2003, pp. 187–190.

FULLERENES AND ATOMIC CLUSTERS

The Influence of Ultraweak Ionizing Irradiation on the Magnetoplastic Effect in Single Crystals of a C_{60} Fullerite

Yu. I. Golovin*, A. A. Dmitrievskiĭ*, R. K. Nikolaev, and I. A. Pushnin***

** Tambov State University, Internatsional'naya ul. 33, Tambov, 392622 Russia*

*** Institute of Solid-State Physics, Russian Academy of Sciences, Chernogolovka, Moscow oblast, 142432 Russia*

e-mail: golovin@tsu.tmb.ru, golovinyi@mail.ru

Received March 12, 2002

Abstract—The suppression of plasticity sensitivity of a C_{60} fullerite to the action of a magnetic field is revealed. It is found that the C_{60} fullerite undergoes temporary softening due to irradiation with ultralow (<0.1 cGy) doses of β and γ radiation. © *2003 MAIK "Nauka/Interperiodica".*

Numerous magnetoplastic effects have been revealed in magnetically disordered solids since the first publication in this field [1]. Until presently, the nontrivial nature of these effects had remained unclear in many respects and continues to be of interest in physical chemistry. There are some difficulties in interpreting magnetoplastic effects. One of these difficulties is associated with the fact that the magnetic energy $E_m \approx \mu_B B$ in a laboratory magnetic field $B \sim 1$ T (μ_B is the Bohr magneton) is incommensurate to any characteristic energy of a nonmagnetic solid at room temperature T_r (it is at this temperature that the majority of experiments were carried out). Specifically, $E_m/kT_r \approx 10^{-2}$, $E_m/E_a \approx 10^{-3}$–10^{-4}, and $E_m/E_b \approx 10^{-4}$–10^{-5}. Here, k is the Boltzmann constant, $E_a \approx 0.1$–1 eV is the activation energy of overcoming the stoppers by dislocations, and $E_b \approx 1$–10 eV is the binding energy in the solid. Another difficulty encountered in interpreting the magnetoplastic effects is as follows. The observed macroscopic effect of softening (an increase in the mobility of individual dislocations [2–5], an increase in the damping decrement of internal friction [6, 7], a decrease in the yield point [8] and the strain-hardening coefficient [9], etc.) is a consequence of the multistage process of structural relaxation. The result of this process manifests itself well apart from the elementary acts in the electron-spin subsystem, which, strictly speaking, can be affected by the magnetic field [10–13]. In most cases, the limiting stage is likely to be the spin-dependent stage of switching of bonds in complexes of point defects and bonds between a dislocation core and a stopper [11, 14, 15]. It is known that even a weak magnetic field can affect the multiplicity of short-lived excited spin pairs, cause spin conversion in these pairs, and open (or close) some of the existing channels in reactions between radicals with several possible results [16–18].

Investigation into optical and radiation effects under simultaneous (or alternating) exposure to a magnetic field can provide additional information on the nature of the aforementioned processes. In particular, it was found that weak x-ray irradiation [19] and light in the optical range [20] affect the magnetoplastic effects in ionic crystals. The problem of low radiation doses is of current concern in itself, because, as in the case of a weak magnetic field, there often arise effects that have defied explanation. These are softening (instead of conventional radiation hardening at moderate absorbed doses) [21, 22], fast relaxation of internal stresses [23], an increase in the internal friction [24], etc. [25]. The effect of irradiation with α and β particles on the properties of fullerenes was considered in [26–28], and the influence of the magnetic field on these materials was analyzed in [29, 30]. However, systematic information on the influence of low radiation doses and magnetic fields on fullerites is unavailable.

In this connection, the purpose of this work was to investigate the alternating effects of a pulsed magnetic field with an induction B up to 24 T and small (<1 cGy) doses of β and γ radiation on the mechanical properties of single-crystal fullerite C_{60} (>99.95%) grown from the vapor phase. Magnetic-field pulses with the amplitude B_m = 24 T were generated using a capacitor bank discharged through a solenoid with a small number of turns. The pulses had a shape close to that of a half-sinusoid and a duration of ~150 μs.

The radioactive source used in the experiments was based on a $^{137}_{55}Cs$ radionuclide with the activity A = 4.2 MBq. The source emitted γ quanta with a maximum energy of 0.66 MeV and a quantum yield of 0.85 per decay. In addition, this source emitted β^- particles into two bands of the energy spectrum with maximum energies E'_m = 0.564 MeV (the quantum yield is 0.947 per

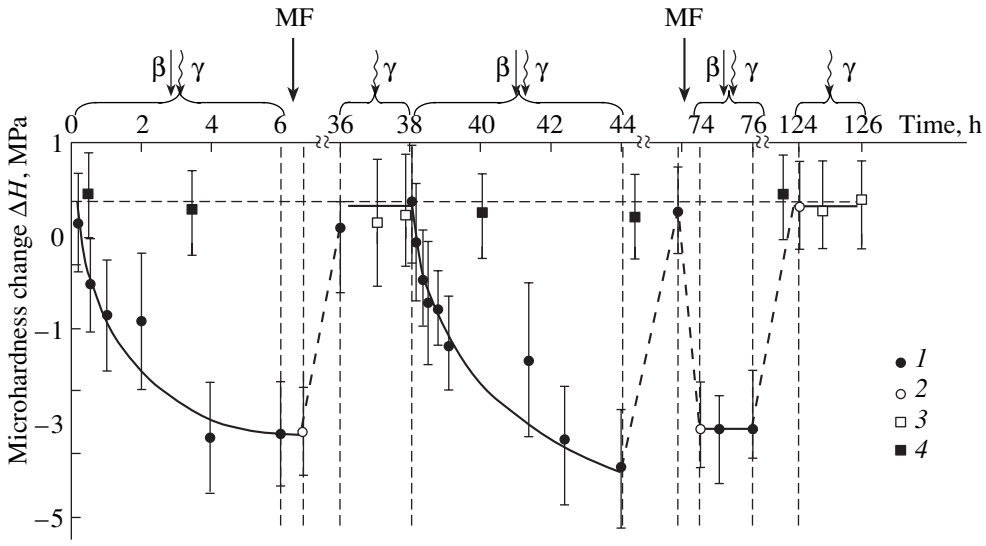

Fig. 1. Change in the microhardness H of the C_{60} fullerite with time due to alternating actions of irradiation and pulses of the magnetic field with the induction B = 25 T: (*1*) β + γ irradiation, (*2*) treatment with a pulsed magnetic field, (*3*) γ irradiation, and (*4*) grinding.

decay) and E''_m = 1.176 MeV (the quantum yield is 0.053) [31].

Since the depth of penetration of β^- particles with energies <1 MeV into the crystal under investigation was relatively small (tens of micrometers), their possible influence on the mechanical properties of thin surface layers was investigated using dynamic nanoindentation [32]. In all the experiments, the maximum load was 200 mN and the indentation depth was approximately 7 μm. In order to prevent rapid oxidation of the surface, all manipulations (irradiation, microhardness measurements, and rest after irradiation) were carried out either in the dark or in the presence of weak red light.

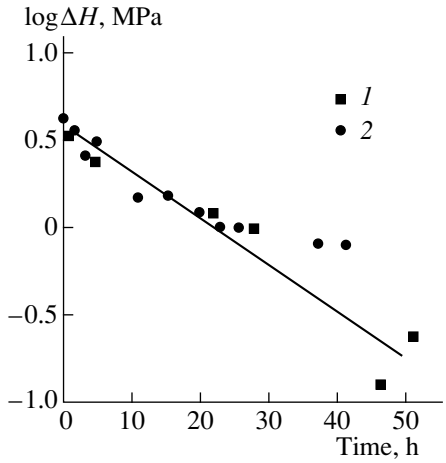

Fig. 2. Kinetics of recovery of the initial microhardness H after the action of (*1*) the pulse of the magnetic field B = 25 T and (*2*) β + γ irradiation.

As can be seen form Fig. 1 (in which each point is obtained by averaging 15–20 individual measurements), the β + γ irradiation leads to a decrease in the microhardness H with an increase in the radiation dose D to saturation after a time $t_{sat} \sim 6$ h. In the saturation state, no additional decrease in the microhardness H is observed in the sample exposed to a magnetic field. After the rest for ~30 h at room temperature in the absence of irradiation and a magnetic field, the microhardness completely regains its initial value. Repeated irradiation after the rest brings about a decrease in the same quantity as after the first irradiation. A decrease in the radiation intensity leads to a decrease not only in the softening rate but also in the softening magnitude at saturation. It is worth noting that the sample subjected to a magnetic-field pulse after relaxation undergoes approximately the same softening as in the case of β and γ irradiation. However, in this case, irradiation does not result in an additional decrease in the microhardness H. It should be noted that exposure to β + γ irradiation and a pulsed magnetic field leads not only to close magnitudes of reversible softening but also to the same type of kinetics (the first-order reaction) and close rates of relaxation to the initial state after these treatments (Fig. 2).

In our experiments, we examined about 20 samples. Each sample was used repeatedly. In order to remove the oxidized layer, a 50- to 100-μm-thick surface layer was periodically ground away from the sample. The test experiments demonstrated that, after grinding, the possible change in the microhardness H due to slow oxidation of the surface under the aforementioned

experimental conditions remains negligible for at least a few days after the preparation of the surface.

The sample was screened using a 2-mm-thick aluminum plate, which completely absorbed the β radiation and had no effect on the intensity of the γ radiation. This screening led to suppression of the softening effect. Therefore, the γ irradiation with the doses used had no noticeable effect on the microhardness H. The elucidation of the role played by the γ irradiation under the joint action of the β and γ radiation calls for special consideration. Let us now assume that the particle fluxes and the energies transferred by the β and γ radiation are approximately equal to each other. It is clear that, under these conditions, the contribution of the β radiation to the changes observed in the surface properties should be substantially larger than that of the γ radiation. Actually, in the case when the weighted-mean energy of β particles in a flux emitted by the $^{137}_{55}$Cs radionuclide is taken as $\langle E_\beta \rangle = 179.8$ keV [12], the absorbing layer thickness for these particles is approximately 10^3 times smaller than that for γ quanta with an energy $E_\gamma = 0.66$ MeV and the bulk density of induced excited states in the surface layers is higher by approximately the same factor.

Now, we estimate the number n of atomic defects produced by a flux of β^- particles with a maximum fluence $F = I_\beta t_{sat} \approx 2 \times 10^8$ cm^{-2}. As a rule, the energy required to produce atomic radiation damage is taken to be $E_0 = 20$–30 eV. In this case, the number of radiation defects formed in a surface layer of thickness $h_{1/2} \approx 13$ μm that absorbs one-half the electron flux with energy $\langle E_\beta \rangle = 0.18$ MeV is determined to be $n = F\langle E_\beta \rangle/(h_{1/2}E_0) \approx 10^{15}$ cm^{-3}. For such a low concentration of structural defects, the mechanisms of their influence on the plastic characteristics call for special analysis. We can suggest at least three possible reasons for an effective action of β^- radiation with low doses on fullerites.

(1) Plasticity of the fcc crystals is limited by the occurrence of local stoppers for glide dislocations. In the C_{60} single crystals under investigation, these stoppers can be carbon molecules with a different molecular weight (mainly, C_{70}), dimers (C_{60}–C_{60}), oxidized molecules, impurities of other elements, etc. Their total concentration in the surface layers amounts to ~10^{-3}–10^{-4}. By modifying even a small number of the most efficient stoppers under irradiation, it is possible to increase the dislocation mobility and to decrease the microhardness H.

(2) Excitations induced by a flux of β^- particles produce quasi-one-dimensional tracks with a macroscopic length $h_{1/2} \sim 10$ μm rather than point defects stochastically distributed over the bulk as in the case of γ irradiation. These tracks can exert a stronger softening effect.

(3) Saturation and closure of intramolecular covalent bonds in C_{60} lead to the fact that the plastic strain of the fullerite occurs predominantly through breaking of weaker intermolecular bonds. A knocking-out of one or two carbon atoms from a symmetric molecule of C_{60} can result both in loss of molecular stability under load and in macroscopic strain not only due to slip of some spherical molecules relative to others but also due to decay of molecules themselves. This process of multiplying the action of a vacancy in the structure of the C_{60} molecule can substantially increase the efficiency of radiation influence.

The reversible effect of a magnetic field and irradiation on the microhardness, the dependence of the saturation level on the irradiation intensity, repeated recovery of softening after relaxation of treatment-induced states, and a number of other factors indicate that these two types of weak fields affect objects close to thermodynamic equilibrium. The pulsed magnetic field and radiation affect the same objects in the crystal, or, at least, their actions occur through similar mechanisms. This can be judged from the following factors: (i) the depths of softening effects caused by the magnetic field and irradiation are equal to each other; (ii) the time constants of exponential relaxation of the microhardness H to the initial value are also equal to each other; and (iii) the sensitivity to one of these factors is suppressed immediately after the action of the other factor.

The mechanisms of the influence of weak magnetic and radiation fields on fullerites call for further investigation. However, the mere fact that fullerite softening occurs under such weak actions has stimulated a search for similar effects in other cyclic carbon-containing substances (for example, single crystals of an aromatic series, polymers, etc.); moreover, caution should be exercised when dealing with possible consequences of exposure even in very weak fields.

ACKNOWLEDGMENTS

This work was supported by the Program "Fullerenes and Atomic Clusters" (project no. 2008), the Russian Foundation for Basic Research (project no. 00-02-16094), and the Ministry of Education (project no. E00-3.4-552).

REFERENCES

1. V. I. Al'shits, E. V. Darinskaya, T. M. Perekalina, and A. A. Urusovskaya, Fiz. Tverd. Tela (Leningrad) **29** (2), 467 (1987) [Sov. Phys. Solid State **29**, 265 (1987)].
2. Yu. I. Golovin and R. B. Morgunov, Pis'ma Zh. Éksp. Teor. Fiz. **58** (3), 189 (1993) [JETP Lett. **58**, 191 (1993)].
3. Yu. I. Golovin and R. B. Morgunov, Zh. Éksp. Teor. Fiz. **115** (2), 605 (1999) [JETP **88**, 332 (1999)].
4. A. A. Skvortsov, A. M. Orlov, L. I. Gonchar, *et al.*, Fiz. Tverd. Tela (St. Petersburg) **42** (10), 1814 (2000) [Phys. Solid State **42**, 1861 (2000)].
5. V. A. Makara, L. P. Steblenko, N. Ya. Gorid'ko, *et al.*, Fiz. Tverd. Tela (St. Petersburg) **43** (3), 462 (2001) [Phys. Solid State **43**, 480 (2001)].

6. M. I. Molotskii, R. E. Kris, and V. Fleurov, Phys. Rev. B **51** (20), 12531 (1995).
7. N. A. Tyapunina, V. L. Krasnov, and E. P. Belozerova, Fiz. Tverd. Tela (St. Petersburg) **41** (6), 1035 (1999) [Phys. Solid State **41**, 942 (1999)].
8. A. A. Urusovskaya, V. I. Al'shits, A. E. Smirnov, and N. N. Bekkauer, Pis'ma Zh. Éksp. Teor. Fiz. **65** (6), 470 (1997) [JETP Lett. **65**, 497 (1997)].
9. Yu. I. Golovin and R. B. Morgunov, Pis'ma Zh. Éksp. Teor. Fiz. **61** (7), 583 (1995) [JETP Lett. **61**, 596 (1995)].
10. M. I. Molotskiĭ, Fiz. Tverd. Tela (Leningrad) **33** (10), 3112 (1991) [Sov. Phys. Solid State **33**, 1760 (1991)].
11. V. I. Al'shits and E. V. Darinskaya, Pis'ma Zh. Éksp. Teor. Fiz. **70** (11), 749 (1999) [JETP Lett. **70**, 761 (1999)].
12. M. I. Molotskii and V. Fleurov, Phys. Rev. B **56** (18), 10809 (1997).
13. Yu. I. Golovin and R. B. Morgunov, Materialovedenie, Nos. 3–6, 2 (2000).
14. Yu. I. Golovin, R. B. Morgunov, A. A. Dmitrievskiĭ, *et al.*, Pis'ma Zh. Éksp. Teor. Fiz. **68** (5), 400 (1998) [JETP Lett. **68**, 426 (1998)].
15. Yu. I. Golovin, R. B. Morgunov, A. A. Dmitrievskiĭ, and V. E. Ivanov, Zh. Éksp. Teor. Fiz. **117** (6), 1080 (2000) [JETP **90**, 939 (2000)].
16. B. Brocklehurst, Nature **221**, 921 (1969).
17. B. Ya. Zel'dovich, A. L. Buchachenko, and E. L. Frankevich, Usp. Fiz. Nauk **155** (1), 3 (1988) [Sov. Phys. Usp. **31**, 385 (1988)].
18. K. M. Salikhov, Yu. N. Molin, R. Z. Sagdeev, and A. L. Buchachenko, *Spin Polarization and Magnetic Effects in Radical Reactions* (Nauka, Novosibirsk, 1978; Elsevier, Amsterdam, 1984).
19. V. I. Al'shits, E. V. Darinskaya, and O. L. Kazakova, Pis'ma Zh. Éksp. Teor. Fiz. **62** (4), 352 (1995) [JETP Lett. **62**, 375 (1995)].
20. Yu. I. Golovin, R. B. Morgunov, and S. Z. Shmurak, Dokl. Akad. Nauk **360** (6), 753 (1998) [Phys. Dokl. **43**, 340 (1998)].
21. V. A. Makara and N. N. Novikov, Fiz. Khim. Obrab. Mater., No. 6, 137 (1973).
22. S. Fujita, K. Maeda, and S. Hyodo, Phys. Status Solidi A **109** (2), 383 (1988).
23. A. G. Lipson, D. M. Sakov, V. I. Savenko, and E. I. Saunin, Pis'ma Zh. Éksp. Teor. Fiz. **70** (2), 118 (1999) [JETP Lett. **70**, 123 (1999)].
24. V. A. Lomovskoĭ, A. G. Lipson, N. Yu. Lomovskaya, and I. A. Gagina, Vysokomol. Soedin., Ser. A **42** (6), 980 (2000).
25. V. L. Indenbom, V. V. Kirsanov, and A. N. Orlov, Vopr. At. Nauki Tekh., Ser. Fiz. Radiats. Povrezhdeniĭ Radiats. Materialov. **10** (2), 3 (1982).
26. C. E. Foerster, C. M. Lepienski, F. C. Serbena, and F. C. Zawislak, Thin Solid Films **340** (2), 201 (1999).
27. V. M. Mikushkin and V. V. Shnitov, Fiz. Tverd. Tela (St. Petersburg) **39** (1), 187 (1997) [Phys. Solid State **39**, 164 (1997)].
28. Yu. S. Gordeev, V. M. Mikushkin, and V. V. Shnitov, Fiz. Tverd. Tela (St. Petersburg) **42** (2), 371 (2000) [Phys. Solid State **42**, 381 (2000)].
29. Yu. A. Osip'yan, Yu. I. Golovin, D. V. Lopatin, *et al.*, Pis'ma Zh. Éksp. Teor. Fiz. **69** (2), 110 (1999) [JETP Lett. **69**, 123 (1999)].
30. Yu. A. Osip'yan, Yu. I. Golovin, R. B. Morgunov, *et al.*, Fiz. Tverd. Tela (St. Petersburg) **43** (7), 1333 (2001) [Phys. Solid State **43**, 1389 (2001)].
31. V. F. Kozlov, *Handbook on Radiation Safety* (Énergoatomizdat, Moscow, 1991).
32. Yu. I. Golovin, V. I. Ivolgin, V. V. Korenkov, and B. Ya. Farber, Fiz. Tverd. Tela (St. Petersburg) **43** (11), 2021 (2001) [Phys. Solid State **43**, 2105 (2001)].

Translated by N. Korovin

Physics of the Solid State, Vol. 45, No. 1, 2003, pp. 21–27. Translated from Fizika Tverdogo Tela, Vol. 45, No. 1, 2003, pp. 22–28.

SEMICONDUCTORS AND DIELECTRICS

Interference Effect in Combined Elastic and Inelastic Scattering of an Energetic Electron Reflected from a Disordered Medium with Generation of a Surface Plasmon

B. N. Libenson

St. Petersburg Scientists' Union, St. Petersburg, 199034 Russia

e-mail: Surfplasmon@mail.ru

Received January 15, 2002; in final form, February 26, 2002

Abstract—Quantum interference in combined elastic and inelastic scattering of an energetic electron with excitation of a surface plasmon leads to a change in the shape of the corresponding peak in the electron-energy-loss spectrum. The plasmon generation is suppressed near the frequency $\omega_p/\sqrt{2}$. The suppression increases with increasing surface-plasmon wave length, because the interference of the energetic-electron scattering processes differing in the sequential order of elastic and inelastic scattering becomes progressively more destructive. The decrease in the height of the surface-plasmon peak in the electron-energy-loss spectrum leads to a nondissipative broadening in this peak. Quantum interference also causes a specific feature to occur in the azimuth-angle dependence of the spectral intensity as the electron energy loss increases in the immediate vicinity of the surface-plasmon peak. © *2003 MAIK "Nauka/Interperiodica".*

1. INTRODUCTION

As shown in [1–4], the features of quantum transport of energetic electrons in the inelastic-scattering channel differ significantly from the features of conventional weak localization in the elastic scattering of energetic electrons. The main coherent effect which arises in the inelastic scattering of an electron in the bulk of a disordered medium is associated with interference in the process of single inelastic scattering combined with single elastic large-angle scattering. A distinctive feature of this coherent effect is that the cross section of inelastic electron scattering is anisotropic in this case; in particular, the cross section decreases as the scattering angle χ approaches π. This decrease in the inelastic electron scattering cross section occurs over a χ-value range much wider than the angular width of the backward peak in the case of conventional weak localization in the elastic-scattering channel. As shown in [3], the angular range in which the feature of the inelastic cross section mentioned above arises can be determined in a qualitative way if all acts of electron scattering are assumed to occur in the bulk of the disordered medium far from its boundary.

In this paper, we study the influence of the surface of a disordered medium on the interference correction to the inelastic scattering cross section in the case where the inelastic electron scattering is accompanied by a single excitation of a surface plasmon at the boundary between the disordered medium and vacuum. We restrict our consideration to the case where the absorption of the electron wave field by the disordered medium is so strong that $l \ll v/\omega$, where l is the coherence length, v is the velocity of an energetic electron, and ω is the frequency corresponding to the electron energy loss. In such a medium, elastic large-angle scattering of electrons with a high energy E (of several hundreds of electronvolts) occurs in a few near-surface atomic layers [5]. It is well known that bulk plasmons, which are oscillations of a longitudinal electric field, can be generated only when electrons move in the medium. Surface plasmons are not quanta of a longitudinal electric field and can be excited by electrons moving both in the medium and vacuum.

Therefore, the coherent effect is predominantly a result of the interference of two processes. In one of them, an energetic electron first experiences a single elastic noncoherent large-angle scattering from the centers located near the surface of the strongly absorbing disordered medium and then passes from the medium to vacuum and excites a plasmon. In the other process, the sequential order of the electron scattering and plasmon excitation is reversed. The quantum interference of these processes affects the shape of the surface-plasmon peak in the characteristic energy loss spectrum: this peak becomes lower in the vicinity of the energy $\hbar\omega_p/\sqrt{2}$, because the long-wavelength part of the surface-plasmon generation spectrum is suppressed.

In an infinite medium, the interference effect in question leads to a dependence of the inelastic scattering cross section on the scattering angle χ. For a finite medium, this dependence on χ transforms into a dependence on the angle of incidence α_i and the exit angle α_f of electrons, as well as on the azimuth angle ϕ_p between the projections of the velocities $\mathbf{v}$ and $\mathbf{v}'$ of the incident

and escaping electrons, respectively, onto the plane surface of the medium. The dependence of the inelastic scattering cross section on the angles α_i and α_f is basically not associated with the interference in question, whereas the dependence on the azimuth angle ϕ_p is due to the quantum interference in the process of electron transport alone. Therefore, the azimuthal dependence of the electron-energy-loss spectrum can be taken as evidence of the occurrence of the coherent effect.

2. INCOHERENT ELASTIC SCATTERING OF AN ENERGETIC ELECTRON IN A DISORDERED MEDIUM

We will describe disordered elastic-scattering centers located in the bulk of the medium with the expression

$$U_{bs}(\mathbf{r}) = \sum_{j=1}^{N} V_{bs}(\mathbf{r}-\mathbf{r}_j) = \frac{1}{(2\pi)^3}\int d\mathbf{k}_a u_{bs}(\mathbf{k}_a)\sum_{j=1}^{N}\exp[i\mathbf{k}_a(\mathbf{r}-\mathbf{r}_j)], \quad (1)$$

where $U_{bs}(\mathbf{r})$ is the three-dimensional potential responsible for elastic large-angle (backward) scattering of an energetic electron, N is the number of randomly distributed elastic-scattering centers, and $u_{bs}(\mathbf{k}_a)$ is the electron scattering amplitude for such a center. Upon averaging over the randomly distributed scatterers, the product $U_{bs}(\mathbf{r})U^*_{bs}(\mathbf{r}')$ takes the form

$$\langle U_{bs}(\mathbf{r})U^*_{bs}(\mathbf{r}')\rangle\big|_{rd} = \frac{n}{(2\pi)^3}\int d\mathbf{k}_a|u_{bs}(\mathbf{k}_a)|^2 \times\exp[i\mathbf{k}_a(\mathbf{r}-\mathbf{r}')], \quad (2)$$

where n is the concentration of the elastic-scattering centers. Elastic large-angle scattering of an energetic electron is characterized by a length $(k_p)^{-1}$, which is much smaller than atomic-scale lengths. Nevertheless, the elastic large-angle scattering potential for electrons can be replaced by the Fermi potential. Of course, the anisotropy of elastic scattering is neglected in this approximation. However, in the case of a strongly absorbing medium, an electron can undergo only a single elastic large-angle scattering and our simplification is justified. Within this approximation, as shown in [1, 2, 6], the square of the elastic-scattering amplitude modulus of an electron depends, to first order in $\hbar\omega/E \ll 1$, only on the total momentum transfer and the dependence on the momentum transfer in inelastic scattering can be ignored. Therefore, the cross section of the entire process contains the elastic cross section as a factor; the inelastic cross section we are interested in is the ratio of the total cross section to the elastic cross section and does not depend on the structure of the latter cross section.

Using the Fermi potential, the inelastic part of the electron scattering cross section can be simply calculated.

For the Fermi potential, we have $|u_{bs}(\mathbf{k}_a)|^2 = |u_{bs}|^2 =$ const (independent of $\mathbf{k}_a$) and, hence,

$$\langle U_{bs}(\mathbf{r})U^*_{bs}(\mathbf{r}')\rangle\big|_{rd} = n|u_{bs}|^2\delta(\mathbf{r}-\mathbf{r}').$$

The differential cross section of the elastic electron scattering by the potential $U_{bs}(\mathbf{r})$ is written as

$$\frac{d\sigma_{\rm el}}{d\Omega} = \frac{S}{4\pi}\frac{\sigma_{bs}}{\sigma_t[\cos(\alpha_i)^{-1}+\cos(\alpha_f)^{-1}]}. \quad (3)$$

Here, S is the surface area of the medium,

$$\sigma_{bs} = \frac{m^2|u_{bs}|^2}{\pi\hbar^4};$$

$\sigma_t = \frac{4\pi}{k_p}\mathrm{Im}\,f(\theta = 0)$ is the total cross section of energetic-electron scattering, with $f(\theta = 0)$ being the forward scattering amplitude.

3. SCATTERING CROSS SECTION FOR A STRONGLY ABSORBING MEDIUM

The wave function of an electron interacting with a semi-infinite medium with randomly distributed elastic-scattering centers and exciting a surface plasmon at the boundary between the medium and vacuum can be found using the conventional perturbation methods. The coherent wave field and the Green's function of the energetic electron are calculated in the same way as in [7]. The differential scattering cross section is determined by the second-order correction to the wave function. We have

$$\frac{d\sigma}{d\Omega d\omega} = \frac{d\sigma_{\rm el}}{d\Omega}\frac{e^2}{\pi^2\hbar}\int_0^\infty dq\,\mathrm{Im}\frac{1}{\Xi_s(q,\omega)} \times F(q, v, \alpha_i, \alpha_f, \phi_p, \kappa_i+\kappa_f, E_q). \quad (4)$$

Here, q and $\hbar\omega$ are the wave vector and the energy, respectively, transferred by the electron to an excited surface plasmon. The condition $\Xi_s(q,\omega) = 0$ determines the pole corresponding to an excited surface plasmon. The localization function $F(q, v, \alpha_i, \alpha_f, \phi_p, \kappa_i+\kappa_f, E_q)$ is given by a cumbersome expression and is presented in the Appendix. The velocity $\mathbf{v}$ of the energetic electron in the initial state has components v_z and $\mathbf{v}_\rho$; the components of the velocity $\mathbf{v}'$ of the electron in the final state are v_{fz} and $\mathbf{v}'_\rho$ ($v_{fz} > 0$). The parameters involved in the localization function are defined as

$$E_q = \frac{\hbar^2q^2}{2m},$$

$$\kappa_i = \mathrm{Im}\sqrt{k_z^2 + ikn\sigma_t}, \quad \kappa_f = \mathrm{Im}\sqrt{k_{fz}^2 + ikn\sigma_t}.$$

The dependence of the quantity F on the angle ϕ_p between $\mathbf{v}_\rho$ and $\mathbf{v}'_\rho$ is determined only by the quantum interference.

Equation (4) is valid for an arbitrary absorbing medium. The inelastic-scattering intensity (which also characterizes the surface-plasmon generation) is defined as

$$S1_{\mathrm{inel}} = \frac{d\sigma/d\Omega d\omega}{d\sigma_{\mathrm{el}}/d\Omega}. \tag{5}$$

For a medium strongly absorbing an electron wave field, Eq. (5) is significantly simplified:

$$S1_{\mathrm{inel}}(\phi_p, \omega) = \frac{e^2}{\pi\hbar}\int\frac{d\mathbf{q}}{q}\mathrm{Im}\frac{1}{\Xi_s(q,\omega)} \times\left|\frac{1}{\omega + \mathbf{q}\mathbf{v}_\rho + \hbar^{-1}E_q - iqv_z} + \frac{1}{-\omega - \mathbf{q}\mathbf{v}'_\rho + \hbar^{-1}E_q - iqv_{fz}}\right|^2. \tag{6}$$

In the limit of a strongly absorbing medium,

$$q \ll \kappa_i + \kappa_f,$$

$$\omega \ll 2(\kappa_i + \kappa_f)v_z, \quad \omega \ll 2(\kappa_i + \kappa_f)v_{fz},$$

the terms retained in Eq. (4) are represented in Eq. (6) as the square of the modulus of the sum of the Green's functions describing the system consisting of the energetic electron, the boundary of the disordered medium, and the excited surface plasmon. Each of these two vacuum components of the Green's function corresponds to the amplitude of one of the two possible realizations of the combined elastic and inelastic scattering. The zeros of the real parts of the denominators in the Green's functions correspond to the conservation of the normal component of the wave vector in the processes with different sequential order of elastic and inelastic scattering, while the imaginary parts of the denominators determine the spatial-decay frequencies of the electric field of a plasmon along the direction of motion of the electron. Equation (6) describes the quantum interference of processes differing in the sequential order of two spatially separated acts of elastic and inelastic electron scattering. The main consequence of this interference is suppression of surface excitations with very long wavelengths.[1]

Indeed, the square of the modulus of the sum in Eq. (6) tends to zero as $q \longrightarrow 0$. For this reason, the dependence of the localization function on the wave vector q

$$F(q) = \int_0^{2\pi} d\phi\left|\frac{1}{\omega + \mathbf{q}\mathbf{v}_\rho + \hbar^{-1}E_q - iqv_z} + \frac{1}{-\omega - \mathbf{q}\mathbf{v}'_\rho + \hbar^{-1}E_q - iqv_{fz}}\right|^2 \tag{7}$$

has a sharp maximum, whose width and height depend on the energy E and the angles α_i, α_f, and ϕ_p. An analytical expression for the localization function $F(q)$ can be found in the form

$$F(q) = \frac{2\pi}{qv_z}\mathrm{Im}\frac{1}{\sqrt{(\omega + \hbar^{-1}E_q - iqv_z)^2 - (qv_\rho)^2}} + \frac{2\pi}{qv_{fz}}\mathrm{Im}\frac{1}{\sqrt{(\omega - \hbar^{-1}E_q - iqv_{fz})^2 - (qv'_\rho)^2}} - 4\pi\mathrm{Re}\left\{\frac{1}{[\mathbf{v}_\rho(\omega + \hbar^{-1}E_q - iqv_z) - \mathbf{v}'_\rho(\omega - \hbar^{-1}E_q - iqv_{fz})]^2 - [q\mathbf{v}_\rho \times \mathbf{v}'_\rho]^2}\right. \times\left.\left[\frac{v_\rho^2(\omega + \hbar^{-1}E_q - iqv_z) - \mathbf{v}_\rho \cdot \mathbf{v}'_\rho(\omega + \hbar^{-1}E_q - iqv_z)}{\sqrt{(\omega + \hbar^{-1}E_q - iqv_z)^2 - (qv_\rho)^2}} + \frac{v'^2_\rho(\omega - \hbar^{-1}E_q - iqv_z) - \mathbf{v}_\rho \cdot \mathbf{v}'_\rho(\omega - \hbar^{-1}E_q - iqv_{fz})}{\sqrt{(\omega - \hbar^{-1}E_q - iqv_{fz})^2 - (qv'_\rho)^2}}\right]\right\}. \tag{8}$$

Equation (8) contains terms that are different in nature. The terms with the sign Im are not associated with interference; these terms describe the probabilities of two possible processes that differ in the sequential order of elastic scattering of the energetic electron and of the generation of a surface plasmon. The term containing the sign Re describes the interference of these two processes. A direct analysis of this term involves intricate calculations, because the expression is fairly cumbersome. However, such an analysis becomes much simpler in the case of $\alpha_i = \alpha_f = \alpha$ and $E_q \ll \hbar\omega$, which is of considerable practical importance.

[1] As shown in [1, 6], the suppression of bulk plasmons with very long wavelengths caused by destructive interference does not lead to a decrease in the intensity of the peak in the vicinity of the plasma frequency in the electron-energy-loss spectrum, because in an infinite medium (in contrast to vacuum), the imaginary parts of the denominators in the Green's functions have constant components (independent of the wave vector **q**) that are proportional to the imaginary part of the forward scattering amplitude of an energetic electron.

Let us introduce the notation $z = qv/\omega$. It can be shown that the interference term in Eq. (8) changes its sign when

$$z^2[\cos^2(\alpha) + \sin^2(\alpha)\cos^2(\phi_p/2)] + 2z\cos(\alpha)\frac{g(z,\alpha) - z\cos(\alpha)}{1 + z\cos(\alpha)g(z,\alpha)} - 1 = 0. \quad (9)$$

Here,

$$g(z,\alpha) = \frac{\mathrm{Im}\sqrt{[1 - iz\cos(\alpha)]^2 - z^2\sin^2(\alpha)}}{\mathrm{Re}\sqrt{[1 - iz\cos(\alpha)]^2 - z^2\sin^2(\alpha)}}.$$

Equation (9) has a root $z_c(\alpha, \phi_p)$ whose position determines the character of the interference. In the wave-vector range $qv < z_c(\alpha, \phi_p = 0°)\omega$, the interference term in Eq. (8) is negative for any value of ϕ_p. Therefore, in this range, the interference of the two scattering processes of interest is destructive. In contrast, when $qv > z_c(\alpha, \phi_p = 180°)\omega$, the interference of these processes is constructive for any value of ϕ_p. In the wave-vector range

$$\frac{\omega}{v}z_c(\alpha, \phi_p = 0°) < q < \frac{\omega}{v}z_c(\alpha, \phi_p = 180°),$$

the interference is not as unambiguous in character.

At a fixed value of $z = qv/\omega$, the dependence of the interference term in Eq. (8) on the azimuth angle ϕ_p has the form of a function of $\cos^2(\phi_p/2)$. Such a dependence has extrema at $\phi_p = 0°$ and 180°. In addition, this dependence may have an extremum at

$$\phi_p = 2\arccos\sqrt{\frac{1 - y(z) - z^2\cos^2(\alpha)}{z\cos(\alpha)}}, \quad (10)$$

the extremum being a maximum if

$$y(z) = -2z\cos(\alpha) \times \frac{z\cos(\alpha) - g(z,\alpha) + \sqrt{(1 + z^2\cos^2(\alpha))(1 + g^2(z,\alpha))}}{1 + z\cos(\alpha)g(z,\alpha)} \quad (11)$$

and a minimum if

$$y(z) = -2z\cos(\alpha) \times \frac{z\cos(\alpha) - g(z,\alpha) - \sqrt{(1 + z^2\cos^2(\alpha))(1 + g^2(z,\alpha))}}{1 + z\cos(\alpha)g(z,\alpha)}. \quad (12)$$

The extrema at $\phi_p = 0°$ and 180°, on the contrary, will be minima in the former case and maxima in the latter.

A detailed investigation of the dynamics of the interfering processes can be performed only on the basis of Eq. (6), which involves not only the localization function $F(q, \alpha, \phi_p)$ considered above but also the surface-plasmon excitation function $\mathrm{Im}[\Xi_s(q, \omega)]^{-1}$.

4. THE DEPENDENCE OF THE ANGULAR STRUCTURE OF THE INTERFERENCE EFFECT ON THE ELECTRON ENERGY LOSS $\hbar\omega$

It was shown in Section 3 that the interference being constructive or destructive depends on the surface-plasmon wavelength. In order to include the spatial dispersion described by the surface-plasmon excitation function, we should investigate the reflection of the intrinsic electrons of the medium from the boundary. We will use the results obtained in [8], where the bulk dielectric properties of a medium were described within a hydrodynamic model. The properties of the surface of a medium will be described in terms of phenomenological parameters R and P, which are the fractions of intrinsic electrons experiencing elastic and specular reflections, respectively, from the boundary of the medium. We will restrict our consideration to the case where the medium strongly absorbs an electron wave field and, therefore, $R \ll 1$ and $P \ll 1$.

In this case, the expansion of the function $\Xi_s(q, \omega)$ in powers of the small parameter qv_F/ω has the form

$$\Xi_s(q,\omega) = 1 + \varepsilon(\omega) - i\sqrt{\beta}\frac{qv_F}{\omega} \times \left[\frac{1 - PR}{2} + \frac{(1 + R)[1 - R - i(1 + R)]}{(1 + R^2)}\right] - \beta\frac{(qv_F)^2}{\omega^2}\left[\frac{1 + R + 4R^2 + PR(2 - R - R^2)}{2(1 + R^2)} - \frac{(1 + R^2)(1 - 4R + R^2)}{(1 + R^2)^2}\right] - i\beta\frac{(qv_F)^2}{\omega^2} \times \left[\frac{1 + 5R + 3R^2 - 2PR - PR^2 + PR^3}{2(1 + R^2)} + \frac{(1 - R)(1 + 4R + 2R^2)}{(1 + R^2)^2}\right] + \ldots. \quad (13)$$

Here, v_F is the Fermi velocity, $\beta = 4/9$, and $\varepsilon(\omega) = 1 - \omega_p^2/\omega(\omega - i\nu)$, with ν being the collision frequency of intrinsic electrons of the medium.

Substituting Eq. (13) into Eq. (6), we can find the function $S1_{\mathrm{inel}}(\phi_p, \omega)$. In the figures presented below, this function is designated as $S1$. The figures also show the quantity $S2$, which is the contribution to the surface-plasmon generation intensity from the sum of the squared moduli of the amplitudes of two scattering processes differing in the sequential order of collisions of an energetic electron. This quantity has nothing to do with the interference and is independent of the angle ϕ_p.

The angular dependence of $S1(\phi_p)$ presented in Fig. 1 corresponds to the localization function $F(\phi_p,$

$qv/\omega \approx 1$). Using Eq. (10), we find the values of the roots determining the q-value ranges of the constructive and destructive interference: $z_c(\alpha = 70°, \phi_p = 0°) = 0.89$ and z_c ($\alpha = 70°$, $\phi_p = 180°$) = 1.34. According to Eq. (13), the intensity of generation of surface plasmons with $\omega = 0.707\omega_p$ is maximum for $qv/\omega \approx 0.1$ and plasmons are generated predominantly over the range

$$q \ll \frac{\omega}{v} z_c(\alpha, \phi_p = 0°).$$

The suppression of generation of such long-wavelength plasmons is so strong that the dominant contribution to the quantity $S1$ comes from plasmons with $qv/\omega \approx 1$. The intensity $S2$, which does not contain interference terms, is nearly twice as large as the intensity $S1$ for any value of the angle ϕ_p.

Figure 2 shows the $S1(\phi_p)$ and $S2$ curves for the case of $\omega = 0.74\omega_p$. It is seen that these curves intersect. The range of azimuth angles where $S1(\phi_p) > S2$ corresponds to the constructive interference of the scattering amplitudes. This range includes the angle $\phi_p = 0°$ and makes up the greater part of the entire azimuth-angle range. Weak destructive interference of the amplitudes takes place in the vicinity of the angle $\phi_p = 180°$, where $S1(\phi_p) < S2$. The intensity of generation of plasmons with $\omega = 0.74\omega_p$ is maximum at $qv/\omega \approx 1.2$. The angular dependence of $S1(\phi_p)$ is close to that of the function

$$F\left(\phi_p, \frac{qv}{\omega} \approx 1.2\right).$$

A similar azimuth-angle dependence of the localization function was also found in [1] for the interference correction to the electron scattering cross section involving the generation of bulk plasmons.

Figure 3 presents the $S1(\phi_p)$ and $S2$ angular dependences for $\omega = 0.79\omega_p$. It is seen that the interference correction is positive over the entire azimuth-angle range, which is due to the fact that the dominant contribution to the integral with respect to q in Eq. (6) comes from plasmons with $qv > \omega z_c(\alpha, \phi_p = 180°)$. The intensity of generation of plasmons with $\omega = 0.79\omega_p$ is maximum for $qv/\omega \approx 2.5$. The angular dependence of $S1(\phi_p)$ exhibits a maximum at $\phi_p = 110°$ and is similar to that of the localization function $F(\phi_p, qv/\omega = 1.95)$, for which the maximum is also located at 110°, as follows from Eq. (10). The localization function $F(qv/\omega = 2, \chi)$ corresponding to a new type of weak localization in the bulk-plasmon generation channel [1] also exhibits a maximum at the scattering angle $\chi \approx 110°$.

A comparison of Figs. 1–3 shows that the $S1(\phi_p)$ angular dependence undergoes a significant change as the electron energy loss increases within the range of 10% near $\hbar\omega_p/\sqrt{2}$. This specific feature of the angular dependence of the interference correction can be used to detect the coherent effect in the electron-energy-loss spectrum associated with surface-plasmon excitation.

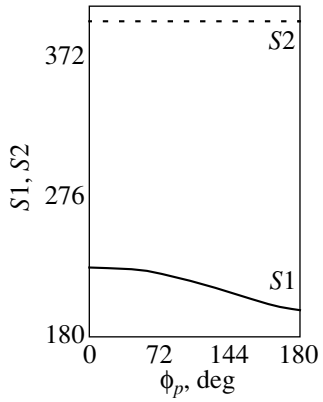

Fig. 1. Dependence of the intensity of electron energy loss equal to $\hbar\omega = 0.707\hbar\omega_p$ on the azimuth angle ϕ_p for E = 1000 eV, E_F = 11.6 eV, $\alpha_i = \alpha_f = 70°$, and $R = P = 0$.

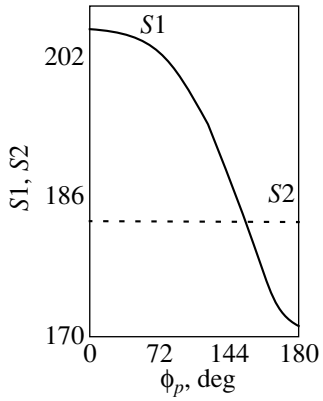

Fig. 2. Same as in Fig. 1 but for $\hbar\omega = 0.74\hbar\omega_p$.

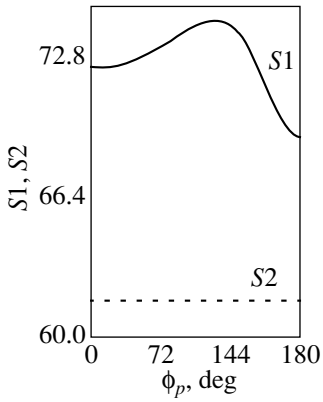

Fig. 3. Same as in Fig. 1 but for $\hbar\omega = 0.79\hbar\omega_p$.

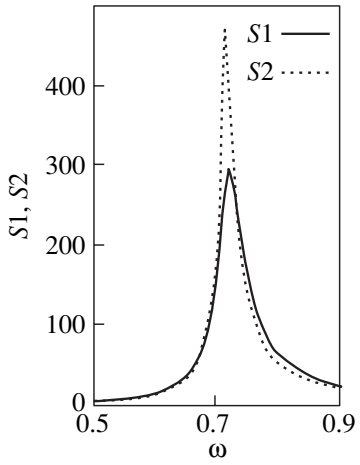

Fig. 4. Effect of the interference in combined elastic and inelastic scattering on the intensity of the electron-energy-loss spectral peak for $\alpha = 70°$ and $\phi_p = 0°$.

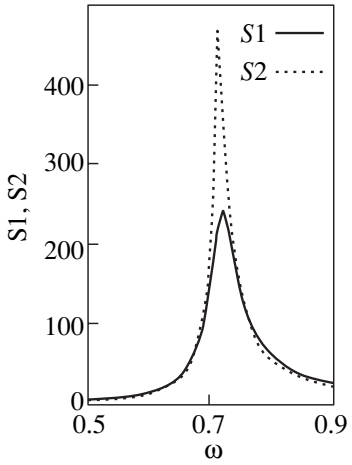

Fig. 5. Same as in Fig. 4 but for $\alpha = 70°$ and $\phi_p = 180°$.

5. INTERFERENTIAL BROADENING OF THE ELECTRON ENERGY LOSS SPECTRUM

The spectral distribution of the inelastic-scattering intensity without regard for the interference correction can be found from Eq. (6) to be

$$S2_{\text{inel}}(\omega) = \frac{e^2}{\pi\hbar}\int\frac{d\mathbf{q}}{q}\text{Im}\frac{1}{\Xi_s(q,\omega)}$$

$$\times\left\{\frac{1}{[\omega + \mathbf{q}\mathbf{v}_\rho + \hbar^{-1}E_q]^2 + (qv_z)^2}\right. \qquad (14)$$

$$\left. + \frac{1}{[\omega + \mathbf{q}\mathbf{v}'_\rho - \hbar^{-1}E_q]^2 + (qv_{fz})^2}\right\}.$$

The spectra described by Eqs. (6) and (14) are compared in Figs. 4 and 5. It is seen that the quantum interference in combined elastic and inelastic scattering leads to suppression of the excitation of a plasmon with energy close to $\hbar\omega_p/\sqrt{2}$. The effect is equivalent to broadening of the surface-plasmon peak; however, this broadening is not associated with decay of the excitation and, hence, is nondissipative. The effective broadening of the surface-plasmon peak in the energy-loss spectrum can be as large as 100% of the width of the "initial" peak described by Eq. (14). The destructive interference in the vicinity of the energy loss $\hbar\omega_p/\sqrt{2}$ is dependent on the azimuth angle ϕ_p. The suppression of excitation of a surface plasmon at $\phi_p = 180°$ is somewhat stronger than that at $\phi_p = 0°$ (as can be seen from the spectra presented in Figs. 4, 5), and the same is true for the broadening of the corresponding peak in the energy-loss spectrum.

The characteristic energy loss spectra presented in Figs. 4 and 5 are calculated for a polycrystalline aluminum target. The realistic peak width is obtained without involving an additional nondispersive mechanism of plasmon decay. The collision frequency of intrinsic electrons of the disordered medium is assumed to be $\nu \ll v_F\omega_p/v$.

6. CONCLUSIONS

The following practical importance can be inferred.

(1) The quantum interference in the process of combined elastic and inelastic scattering of an energetic electron causes significant additional broadening of the surface-plasmon peak in the energy loss spectrum. Therefore, there is no need to search for an additional plasmon decay mechanism to explain the experimental values of the spectral-peak width.

(2) The specific features of the azimuthal dependence of the electron-energy-loss spectrum predicted in this paper can be presently observed experimentally. For this purpose, one needs to measure the ratio of the energetic-electron flux reflected from a disordered medium with a fixed deviation of the energy loss from that corresponding to the central peak to the elastically reflected electron flux for different values of the azimuth angle.

(3) The main features of the interference corrections to the bulk- and surface-plasmon peaks in the energy loss spectrum of energetic electrons are identical, in spite of the fact that the theoretical description of this phenomenon occurring in the bulk of a disordered medium and near its surface is different.

The results obtained in this paper can be used to experimentally detect the azimuthal dependence inherent in the interference in combined elastic and inelastic scattering of energetic electrons reflected from a disor-

dered medium. The angular and energy resolutions attainable in the currently available characteristic-energy-loss spectroscopic methods allow one to perform such experiments.

APPENDIX

The localization function for an arbitrary medium absorbing an electron wave field has the form

$$
\begin{aligned}
F(q, v, \alpha_i, \alpha_f, \phi_p, \kappa_i + \kappa_f, E_q) = \frac{e^2}{\pi^2\hbar}\int_0^{2\pi} d\phi_{\mathbf{q}}\Bigg\{ & \frac{q + 2(\kappa_i + \kappa_f)}{2(\kappa_i + \kappa_f)}\Bigg[\frac{1}{(\omega + \mathbf{q}\mathbf{v}_\rho + \hbar^{-1}E_q)^2 + (qv_z)^2} \\
& + \frac{1}{(\omega + \mathbf{q}\mathbf{v}'_\rho - \hbar^{-1}E_q)^2 + (qv_{fz})^2}\Bigg] + \frac{[q + 2(\kappa_i + \kappa_f)](\kappa_i + \kappa_f - q)}{2(\kappa_i + \kappa_f)(q + \kappa_i + \kappa_f)} \\
& \times\Bigg[\frac{1}{(\omega + \mathbf{q}\mathbf{v}_\rho + \hbar^{-1}E_q)^2 + [q + 2(\kappa_i + \kappa_f)]^2 v_z^2} + \frac{1}{(\omega + \mathbf{q}\mathbf{v}'_\rho - \hbar^{-1}E_q)^2 + [q + 2(\kappa_i + \kappa_f)]^2 v_{fz}^2}\Bigg] \\
& + 2(\kappa_i + \kappa_f)\mathrm{Re}\Bigg\langle \frac{v_z v_{fz}}{2(\kappa_i + \kappa_f)v_z v_{fz} + i[v_{fz}(\omega + \mathbf{q}\mathbf{v}_\rho + \hbar^{-1}E_q) + v_z(\omega + \mathbf{q}\mathbf{v}'_\rho - \hbar^{-1}E_q)]} \\
& \times\Bigg\{\frac{1}{(q + \kappa_i + \kappa_f)}\Bigg[\frac{1}{v_z(v_{fz}[q + 2(\kappa_i + \kappa_f)] + i[\omega + \mathbf{q}\mathbf{v}'_\rho - \hbar^{-1}E_q])} + \frac{1}{v_{fz}(v_z[q + 2(\kappa_i + \kappa_f)] + i[\omega + \mathbf{q}\mathbf{v}_\rho + \hbar^{-1}E_q])}\Bigg] \\
& + \frac{2}{[qv_z + i(\omega + \mathbf{q}\mathbf{v}_\rho + \hbar^{-1}E_q)]([q + 2(\kappa_i + \kappa_f)]v_z + i(\omega + \mathbf{q}\mathbf{v}_\rho + \hbar^{-1}E_q))} \\
& + \frac{2}{[qv_{fz} + i(\omega + \mathbf{q}\mathbf{v}'_\rho - \hbar^{-1}E_q)]([q + 2(\kappa_i + \kappa_f)]v_{fz} + i(\omega + \mathbf{q}\mathbf{v}'_\rho - \hbar^{-1}E_q))} \\
& + \frac{2}{[qv_z + i(\omega + \mathbf{q}\mathbf{v}_\rho + \hbar^{-1}E_q)][qv_{fz} + i(\omega + \mathbf{q}\mathbf{v}'_\rho - \hbar^{-1}E_q)]}\Bigg\}\Bigg\rangle\Bigg\}.
\end{aligned}
$$

REFERENCES

1. B. N. Libenson, K. Yu. Platonov, and V. V. Rumyantsev, Zh. Éksp. Teor. Fiz. **101** (2), 614 (1992) [Sov. Phys. JETP **74**, 326 (1992)].
2. V. V. Rumyantsev and V. V. Doubov, Phys. Rev. B **49** (13), 8643 (1994).
3. V. V. Rumyantsev, E. V. Orlenko, and B. N. Libenson, Z. Phys. B **103**, 53 (1997).
4. B. N. Libenson and V. V. Rumyantsev, Fiz. Tverd. Tela (St. Petersburg) **40** (8), 1413 (1998) [Phys. Solid State **40**, 1283 (1998)].
5. I. M. Bronshteĭn and I. P. Pronin, Fiz. Tverd. Tela (Leningrad) **17**, 2431 (1975) [Sov. Phys. Solid State **17**, 1610 (1975)]; Fiz. Tverd. Tela (Leningrad) **17**, 2502 (1975) [Sov. Phys. Solid State **17**, 1672 (1975)].
6. V. V. Rumyantsev and B. N. Libenson, Ann. Phys. **111**, 152 (1978).
7. E. E. Gorodnichev, S. L. Dudarev, D. B. Rogozkin, and M. I. Ryazanov, Preprint No. 025-87, MIFI (Moscow Engineering Physics Institute, Moscow, 1987).
8. B. N. Libenson, Fiz. Tverd. Tela (St. Petersburg) **36** (8), 2283 (1994) [Phys. Solid State **36**, 1243 (1994)].

Translated by Yu. Epifanov

Physics of the Solid State, Vol. 45, No. 1, 2003, pp. 28–31. Translated from Fizika Tverdogo Tela, Vol. 45, No. 1, 2003, pp. 29–32.

SEMICONDUCTORS AND DIELECTRICS

Effect of Correlation between the Shallow and Deep Metastable Level Subsystems on the Excitonic Photoluminescence Spectra in *n*-GaAs

V. V. Krivolapchuk, M. M. Mezdrogina, and N. K. Poletaev

Ioffe Physicotechnical Institute, Russian Academy of Sciences, Politekhnicheskaya ul. 26, St. Petersburg, 194021 Russia

e-mail: vlad.krivol@pop.ioffe.rssi.ru

Received February 28, 2002; in final form, April 19, 2002

Abstract—The excitonic photoluminescence spectra of GaAs epitaxial layers are studied. Changes in the relative arrangement of shallow and deep centers in the tetrahedral lattice are shown to bring about changes in the decay kinetics and the shape of the (D^0, x) emission line (corresponding to an exciton bound to a shallow neutral donor). This change in the excitonic photoluminescence spectra is caused by dispersion in the exciton binding energy of shallow donors E_D, the dispersion being a result of the influence of the subsystem of deep metastable defects in *n*-GaAs crystals. © *2003 MAIK "Nauka/Interperiodica"*.

1. INTRODUCTION

The ordering and correlation between shallow and deep defect subsystems has recently become a subject of considerable interest. The ordering processes manifest themselves both in a variation of the concentration of the impurity doped into a semiconductor and in fluctuations in the composition [1, 2].

It is known that at low temperatures, exciton states are the final stage in the electronic excitation relaxation in energy, which is affected in a large measure by exciton interaction with defects and impurities. The characteristics of exciton luminescence (the presence of specific lines, their shape, intensity, halfwidth, decay time) provide a sufficiently correct idea of the dynamics of nonequilibrium carriers in GaAs crystals and, therefore, permit one to gain an understanding of the extent to which they are affected by processes involving various defects in the material.

The objective of the present work is to investigate the connection between shallow and deep impurity subsystems and the influence of this mutually related defect configuration on the specific features of the excitonic spectra in gallium arsenide epitaxial layers.

2. SAMPLES AND EXPERIMENTAL ARRANGEMENT

We studied epitaxial layers of *n*-GaAs grown by gas-phase epitaxy in a chloride system on gallium arsenide substrates. The shallow impurity concentration N_{eff} ($N_D - N_A$) in the samples measured using the *C–V* technique was 10^{13}–10^{14} cm^{-3}. The concentration of deep levels, as determined using DLTS, did not exceed that of the shallow levels. The photoluminescence spectra (studied in the reflection geometry, with the epitaxial layer plane normal to the spectrometer optical axis) were obtained on samples immersed in liquid helium in vacuum (T = 1.8 K). The photoluminescence (PL) was excited by the radiation of a cw He–Ne laser (λ = 6328 Å) focused to a spot about 150 μm in diameter. The PL decay kinetics was studied under pumping with a pulsed semiconductor laser (λ = 7980 Å). The PL spectra and kinetics were investigated in the lock-in photon-counting mode using a DFS-52 double-grating diffraction spectrometer. To adequately compare the emission spectra of various samples, the controllable experimental conditions (temperature, excitation density, spectral resolution, laser beam incidence angle) were maintained unchanged.

3. RESULTS OF THE MEASUREMENTS

As studied at pumping levels providing the created electron–hole pairs in numbers comparable to N_{eff}, the emission spectra of *n*-GaAs epitaxial layers contain the following spectral components: a polariton emission of free excitons, a line due to excitons bound to shallow neutral donors (D^0, x), a line originating from the recombination of a neutral-donor electron with a valence-band hole (D^0, h), and, if the compensation by shallow acceptors is high enough, a line of excitons bound to neutral acceptors (A^0, x) (Fig. 1). The (D^0, x) line is the strongest in all samples. The spectra of the samples investigated differ noticeably from one another in intensity (by an order of magnitude) and in the halfwidth (FWHM = 0.15–0.30 meV) and position of the (D^0, x) line (Fig. 2).

1063-7834/03/4501-0028$24.00

4. DISCUSSION

To understand the relation between the shallow- and deep-level subsystems, let us consider how the emission spectrum of bound and free excitons (polaritons) in a crystal depends on the presence of defects.

In general, the radiation intensity I_r at a pumping level $g = f(I_{ex})$ depends on the total lifetime of nonequilibrium carriers (excitons) τ, which, in turn, is determined by the radiative (τ_r) and nonradiative (τ_{nr}) lifetimes of excitons (carriers) as $1/\tau = 1/\tau_r + 1/\tau_{nr}$. Therefore, the radiation intensity can be written as $I_r = g/(1 + \tau_r/\tau_{nr})$.

Because for the given material (GaAs) and the experimental conditions chosen we have τ_r = const, the intensity depends on τ_{nr} alone. The nonradiative lifetime τ_{nr} is determined by exciton trapping (the trapping cross section σ_i) into deep states (with concentration N_i) associated with various defects: $1/\tau_{nr} = \sum_i v\sigma_i N_i^{NR}$ (here, v is the thermal velocity and i labels the defect type). It thus follows that samples with different PL intensities measured under the same experimental conditions differ primarily in the concentration of nonradiative recombination centers, which are associated with deep levels. The lower the concentration of the centers (deep levels) responsible for nonradiative exciton annihilation, the higher the integrated PL intensity, and vice versa.

In what follows, we focus our attention primarily on the emission spectrum of excitons bound to shallow donors (D^0, x). The above reasoning suggests that the intensity of the radiation involving shallow centers should depend on the concentrations of shallow and deep centers, their mutual arrangement in the lattice, and on free exciton transport to the trapping centers (both shallow and deep). One should, therefore, consider the factors governing the relative contribution of free and bound excitons to the observed emission spectrum.

The radiation intensity of free excitons (polaritons) can be represented in a simplified way as [3]

$$I(E) \approx \sum_r T_r(E)F(x, E)_{x=0},$$

where $T_r(E)$ is the coefficient of polariton conversion to external radiation at the crystal boundary (transmission coefficient) and $F(x, E)$ is the polariton distribution function in space and energy in the crystal. It thus follows that the polariton luminescence in a given material is determined primarily by the distribution function in space and energy $F(x, E)$. In a first approximation, this function can be written in a factorized form, $F(x, E) = f(E)*C(x)$. To be able to describe the PL spectrum, one has to determine $F(x, E)$ in an explicit form in each specific case, which is a very difficult problem. For our further analysis of the GaAs emission spectra, however, it may be sufficient to note that both $f(E)$ and $C(x)$ are determined by the total exciton lifetime τ. As the lifetime τ increases, both the energy and the spatial distribution functions change. The maximum of the polariton energy distribution function $f(E)$ shifts into the res-

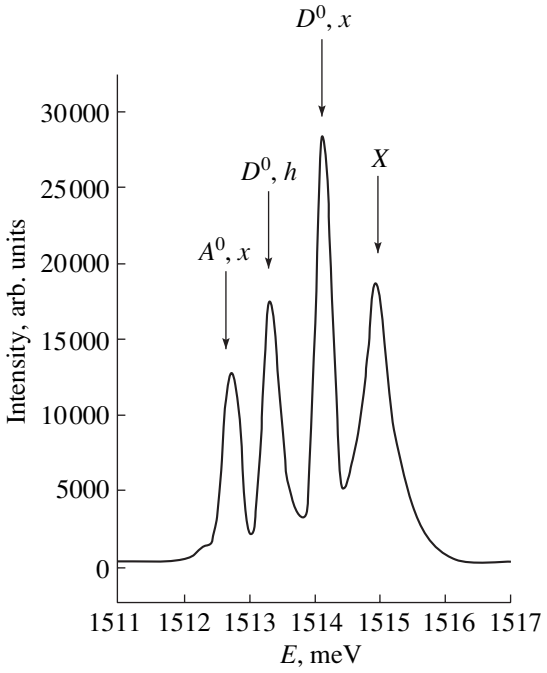

Fig. 1. Typical *n*-GaAs photoluminescence spectrum in the exciton region measured at T = 1.8 K.

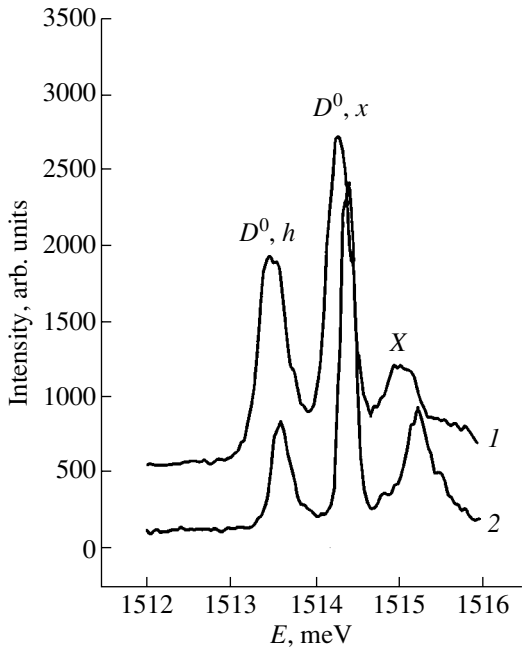

Fig. 2. Photoluminescence spectra (translated as a whole) of two different *n*-GaAs samples measured under identical pumping and measurement conditions.

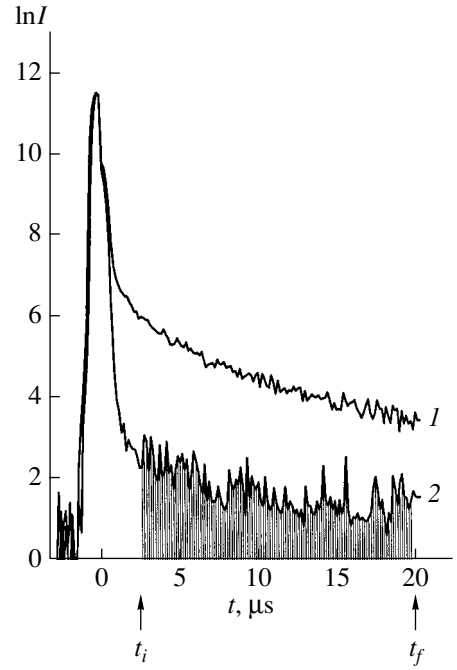

Fig. 3. Decay kinetics of the (D^0, x) emission line in two GaAs samples with FWHM equal to (*1*) 0.31 and (*2*) 0.14 meV. The integration region bounded by t_i and t_f is hatched. The figures label the spectra displayed in Fig. 2.

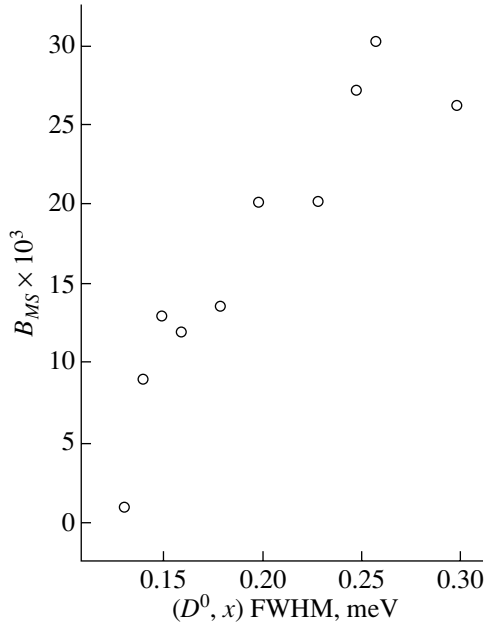

Fig. 4. Area B_{MS} bounded by the (D^0, x) decay curve as a function of the halfwidth (FWHM) of this line in different *n*-GaAs samples.

onance region E_{LT} and the maximum of the spatial distribution function $C(x)$ shifts into the bulk of the crystal because of the increasing diffusion length both of free excitons, $L = (1/3\langle v\rangle^2\tau_k\tau)^{1/3}$, and of carriers [4]. As a result, with increasing τ (and, hence, L), the sample volume occupied by free excitons and the number of neutral donors D^0 in this volume increase. Trapping of free excitons by shallow neutral donors D^0 produces an emission line (D^0, x) whose intensity is determined by the neutral-donor concentration. The relative intensity of the spectral lines produced by free and bound excitons is determined by the radiation imprisonment effect, which plays a major role in samples with long lifetimes [5]. Whence it follows that samples with different total lifetimes τ differ substantially in PL intensity from one another; therefore, the intensity of the (D^0, x) line (for samples with shallow donor concentrations 10^{13}–10^{14} cm^{-3}) can be considered a parameter that qualitatively characterizes the concentration of nonradiative exciton annihilation centers N_i^{NR} in a sample.

The energy position and FWHM of the (D^0, x) emission line are important spectral characteristics. In the samples studied, the halfwidth of the (D^0, x) line varied from 0.12 to 0.31 meV.

The (D^0, x) emission line is known to be inhomogeneously broadened. Its inhomogeneous broadening is due to the fact that the excitons bound to different donors D^0 emit radiation of slightly different wavelengths. This difference originates from the dispersion of thermal activation energy of shallow donors E_{DT} (and, hence, of the excitons bound to them). The reason for the E_{DT} dispersion, in turn, lies in the different values of the local potential V_{loc} at donor impurity sites. This means that the various defects located close to shallow donors D^0 change the crystal field. The assumption that both deep nonradiative annihilation centers and shallow acceptors can act as such defects was not confirmed. Indeed, an analysis of the spectra of samples differing in the (D^0, x) emission line intensity by more than an order of magnitude and, hence, in the concentration of deep nonradiative annihilation centers N_i^{NR} showed the (D^0, x) halfwidth to be independent of the concentration N_i^{NR}. The halfwidth also does not depend on the shallow acceptor concentration. [We note that the high concentration of shallow acceptors is indicated by the presence of a strong (A^0, x) line.] It thus follows that the E_{DT} dispersion is dominated not by the nonradiative annihilation centers and shallow acceptors but rather by a subsystem of defects of another nature that are responsible for the deep levels.

The key to understanding the origin of the E_{DT} dispersion [i.e., of the (D^0, x) line broadening] lies in the difference in the spectral position of this line and in the decay kinetics of the (D^0, x) emission line between different samples. It was shown in [6] that the slow decay ($\tau \approx 10^{-6}$ s) of the (D^0, x) line is due to the existence of local metastable centers donating holes to the valence

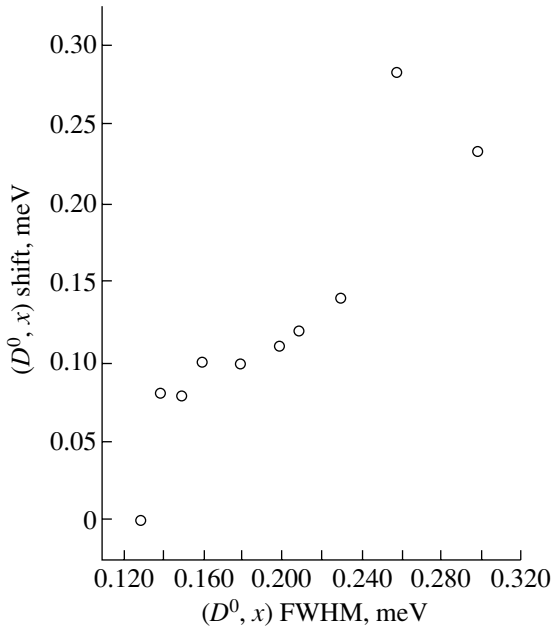

Fig. 5. Spectral position of the (D^0, x) emission line plotted as a function of its FWHM.

band. The number of these centers is related to the area B_{MS} bounded by the PL decay curve of the (D^0, x) line [7, 8] (Fig. 3). It was found that there is no slow decay in uncompensated samples exhibiting a (D^0, x) line halfwidth less than 0.12 meV. Figure 4 presents the values of B_{MS} and FWHM for a number of samples with a high emission intensity (large τ). We readily see a noticeable correlation between these quantities. Because the inhomogeneous halfwidth is due to the shallow-donor E_{DT} dispersion and the area B_{MS} reflects the number of deep metastable states, this correlation implies the existence of a connection between the shallow- and deep-level subsystems. The scatter (1.5143–1.5158 eV) in the energy position of the maximum of the (D^0, x) line, which varies from sample to sample, originates from the samples being differently strained [9], as a result of which the PL spectra are shifted as a whole with respect to one another (Fig. 2). Figure 5 plots the deviation of the (D^0, x) spectral position from a reference value in different samples as a function of the FWHM of this line for each sample. [This relation was obtained in the following way: the (D^0, x) line position in the sample with the minimum FWHM (0.12 meV) which exhibits the smallest E_{DT} dispersion was taken as the reference.] Thus, the spectral position and the halfwidth of the (D^0, x) emission line and the value of the area B_{MS} were found to be interrelated, which may be due to reconstruction of the tetrahedral lattice [10] and the formation of deep centers as a result of impurity ions transferring from the lattice sites to tetrahedral interstitial sites [11–14]. Such a reconstruction is possible in samples with strains manifested as a spread in the (D^0, x) line position.

Thus, the analysis of the variation of the exciton photoluminescence spectra combined with the investigation of their decay kinetics permits us to suggest a consistent interpretation of coupling between the subsystems of deep and shallow defects in *n*-type gallium arsenide.

ACKNOWLEDGMENTS

The authors are indebted to V.M. Botnaryuk and L.M. Fedorov for providing the samples.

REFERENCES

1. M. M. Mezdrogina, T. I. Mosina, E. I. Terukov, and I. N. Trapeznikova, Fiz. Tekh. Poluprovodn. (St. Petersburg) **35**, 714 (2001) [Semiconductors **35**, 684 (2001)].
2. V. A. Shchukin and A. N. Starodubtsev, in *Proceedings of 8th International Symposium "Nanostructures: Physics and Technology," Ioffe Institute, St. Petersburg, 2000*, p. 137.
3. Y. Toyozava, Prog. Theor. Phys. **20**, 53 (1958).
4. V. V. Krivolapchuk, S. A. Permogorov, and V. V. Travnikov, Fiz. Tverd. Tela (Leningrad) **23**, 606 (1981) [Sov. Phys. Solid State **23**, 343 (1981)]; V. V. Travnikov and V. V. Krivolapchuk, Fiz. Tverd. Tela (Leningrad) **24**, 961 (1982) [Sov. Phys. Solid State **24**, 547 (1982)].
5. V. V. Travnikov and V. V. Krivolapchuk, Pis'ma Zh. Éksp. Teor. Fiz. **37**, 419 (1983) [JETP Lett. **37**, 496 (1983)].
6. A. V. Akimov, A. A. Kaplyanskiĭ, V. V. Krivolapchuk, and E. S. Moskalenko, Pis'ma Zh. Éksp. Teor. Fiz. **46**, 35 (1987) [JETP Lett. **46**, 42 (1987)].
7. A. V. Akimov, V. V. Krivolapchuk, N. K. Poletaev, and V. G. Shofman, Fiz. Tekh. Poluprovodn. (St. Petersburg) **27**, 310 (1993) [Semiconductors **27**, 171 (1993)].
8. V. V. Krivolapchuk, N. K. Poletaev, and L. M. Fedorov, Fiz. Tekh. Poluprovodn. (St. Petersburg) **28**, 310 (1994) [Semiconductors **28**, 188 (1994)].
9. G. L. Bir and G. E. Pikus, *Symmetry and Stain-Induced Effects in Semiconductors* (Nauka, Moscow, 1972; Wiley, New York, 1975), Chap. 7.
10. D. E. Onopko, N. T. Bagraev, and A. I. Ryskin, Fiz. Tekh. Poluprovodn. (St. Petersburg) **30**, 142 (1996) [Semiconductors **30**, 82 (1996)].
11. P. M. Moony, J. Appl. Phys. **67**, R1 (1990).
12. D. J. Chadi and K. J. Chang, Phys. Rev. B **39**, 10063 (1989).
13. T. N. Morgan, Mater. Sci. Forum **38–41**, 1079 (1989).
14. D. J. Chadi and K. J. Chang, Phys. Rev. Lett. **61**, 873 (1988).

Translated by G. Skrebtsov

Physics of the Solid State, Vol. 45, No. 1, 2003, pp. 32–35. Translated from Fizika Tverdogo Tela, Vol. 45, No. 1, 2003, pp. 33–36.

SEMICONDUCTORS AND DIELECTRICS

On the Determination of the Debye Temperature from Experimental Data

M. N. Magomedov

Institute of Geothermy, Dagestan Scientific Center, Russian Academy of Sciences, pr. Kalinina 3, Makhachkala, 367003 Russia

e-mail: danterm@dinet.ru

Received April 9, 2002

Abstract—It is shown that the Debye temperature as a function of temperature must satisfy certain equations in order for the thermodynamic functions calculated in terms of the Debye temperature to satisfy both the third law of thermodynamics and the law of equipartition of energy. A general expression for the $\Theta(T)$ function satisfying these thermodynamic laws is found. © *2003 MAIK "Nauka/Interperiodica".*

In the traditional Debye theory [1–6], integration with respect to frequency is performed over the range from zero to a certain value ω_D called the Debye frequency. If ω_D is assumed to be independent of temperature T, then the free energy F_D, entropy S_D, and the specific heat at constant volume C_D of a three-dimensional crystal are found to be [1–6]

$$\begin{aligned} F_D/3N_An_ik_B &= 3\Theta/8 + T\ln[1-\exp(-\Theta/T)] \\ &\quad -(T/3)D_3(\Theta/T), \\ S_D/3N_An_ik_B &= -\ln[1-\exp(-\Theta/T)] \\ &\quad +(4/3)D_3(\Theta/T), \\ C_D/3N_An_ik_B &= 4D_3(\Theta/T) \\ &\quad -3(\Theta/T)/[\exp(\Theta/T)-1]. \end{aligned} \tag{1}$$

Here, N_A is the Avogadro constant, n_i is the number of atoms in a molecule, $\Theta = \hbar\omega_D/k_B$ is the Debye temperature, $\hbar$ is the Planck constant, k_B is the Boltzmann constant, and $D_n(x)$ is the Debye function for an n-dimensional crystal, which has the form

$$D_n(x) = (n/x^n)\int_0^x \{t^n[\exp(t)-1]\}dt. \tag{2}$$

For some substances, however, the parameter Θ depends on temperature. In this case, the expressions for the entropy and specific heat at constant volume involve derivatives of the function $\Theta(T)$ and have the form

$$\begin{aligned} S/3N_An_ik_B &= S_D/3N_An_ik_B \\ &\quad -[3/8+(T/\Theta)D_3(\Theta/T)](d\Theta/dT)_v, \end{aligned} \tag{3}$$

$$\begin{aligned} C/3N_An_ik_B &= (C_D/3N_An_ik_B) \\ &\quad \times[1-(T/\Theta)(d\Theta/dT)_v]^2 \\ &\quad -[3/8+(T/\Theta)D_3(\Theta/T)]T(d^2\Theta/dT^2)_v. \end{aligned} \tag{4}$$

At low temperatures $T \ll \Theta(T)$, functions (3) and (4) must satisfy the third law of thermodynamics, which, following Planck [2, 6], can be written in the form

$$\lim_{T/\Theta\to 0} S/3N_An_ik_B = 0, \quad \lim_{T/\Theta\to 0} C/3N_An_ik_B = 0. \tag{5}$$

At high temperatures $T \gg \Theta(T)$, function (4) must satisfy the classical law of equipartition of energy [2, 6], a consequence of which is the Dulong–Petit law [1–6]:

$$\lim_{T/\Theta\to\infty} C/3N_An_ik_B = 1. \tag{6}$$

The boundary conditions defined by Eqs. (5) and (6) impose certain restrictions on the function $\Theta(T)$ in Eqs. (3) and (4). At low temperatures $T \ll \Theta(T)$, the Debye function can be written as [1–6] $D_3(\Theta/T) \cong (\pi^4/5)[T/\Theta(T)]^3$ and Eqs. (3) and (4) take the form

$$\begin{aligned} (S/3N_An_ik_B)_{\text{low}} &\simeq (S_D/3N_An_ik_B)_{\text{low}} \\ &\quad -(3/8)(d\Theta/dT)_v, \end{aligned} \tag{7}$$

$$\begin{aligned} (C/3N_An_ik_B)_{\text{low}} &\simeq (C_D/3N_An_ik_B)_{\text{low}} \\ &\quad \times[1-(T/\Theta)(d\Theta/dT)_v]^2 - (3/8)T(d^2\Theta/dT^2)_v. \end{aligned} \tag{8}$$

Here, we introduced the following designation of the functions, which is commonly used when $\Theta(T)$ is defined at low temperatures [1–6]:

$$\begin{aligned} (S_D/3N_An_ik_B)_{\text{low}} &\simeq (4\pi^4/15)[T/\Theta(T)]^3, \\ (C_D/3N_An_ik_B)_{\text{low}} &\simeq (4\pi^4/5)[T/\Theta(T)]^3. \end{aligned} \tag{9}$$

It is easy to see that the third law of thermodynamics in the form of Eqs. (5) will be obeyed if the function

$\Theta(T)$ does not contain terms linear in T as $T \longrightarrow 0$ K. This fact was pointed out by Born and von Karman [1] and was used in [3, 5, 7].

We assume that, at $T \ll \Theta_0$, the $\Theta(T)$ dependence has the form

$$\Theta(T)_{\text{low}} \cong \Theta_0[1 - \chi(T/\Theta_0)^k], \tag{10}$$

where $\Theta_0 = \lim \Theta(T)$ as $T \longrightarrow 0$ K. This dependence is a generalization of the expressions for $\Theta(T)_{\text{low}}$ used in [1, 3, 5, 7] and reduces to them when $k = 2$. The factor χ is found by calculating the function $\Theta(T)_{\text{low}}$.

Since Eq. (10) is commonly obtained at $T \ll \Theta_0$ as a result of expansion in powers of the small quantity $\chi(T/\Theta_0)^k \ll 1$, the function $\Theta(T)_{\text{low}}$ can also be represented as

$$\Theta(T)_{\text{low}} \cong \Theta_0 \exp[-\chi(T/\Theta_0)^k]. \tag{11}$$

Substituting Eq. (11) or (10) into Eqs. (7) and (8) for $T \ll \Theta_0$, we find

$$\begin{aligned}(S/3N_An_ik_B)_{\text{low}} &\cong (4\pi^4/15)(T/\Theta_0)^3 \\ &+ (3/8)k\chi(T/\Theta_0)^{k-1}, \\ (C/3N_An_ik_B)_{\text{low}} &\cong (4\pi^4/5)(T/\Theta_0)^3 \\ &+ (3/8)k(k-1)\chi(T/\Theta_0)^{k-1}.\end{aligned} \tag{12}$$

It is seen from Eq. (12) that if $k = 1$ (as was assumed in [8, 9]), the third law of thermodynamics (5) is not obeyed.

If $k = 2$ (as was the case in [1, 3, 5, 7]), then from Eq. (12) it follows that the crystal lattice entropy and heat capacity at low temperatures follow a linear law (S, $C \sim T$). This contradicts the experimental data and is incompatible with the experimental determination of the electronic specific heat, which is assumed to be dominant (due to its linear dependence on T) over the lattice specific heat at $T \longrightarrow 0$ K (see, e.g., [1–6, 8, 9]). At $k = 3$, we have S, $C \sim T^2$. This behavior also contradicts the experimental evidence for the cubic temperature dependence of the lattice specific heat of three-dimensional crystals at $T \longrightarrow 0$ K.

In the case of $k = 4$, the temperature dependence given by Eq. (12) agrees with the experimental data; however, the value of Θ_0 should be defined in this case not from Eq. (9) but rather from Eq. (12):

$$(C/3N_An_ik_B)_{\text{low}} \cong [(4\pi^4/5) + (9/2)\chi](T/\Theta_0)^3.$$

This definition leads to a correction to the Debye temperature calculated from Eq. (9):

$$\Theta_0 = \Theta_0^s[1 + (45\chi/8\pi^4)]^{1/3}, \tag{13}$$

where Θ_0^s is the value determined from the experimental data on the specific heat without regard for the temperature dependence of $\Theta(T)_{\text{low}}$; that is, Θ_0^s is calculated directly from Eq. (9).

We note that some authors have calculated the function $\Theta(T)_{\text{low}}$ using methods which give $\chi < 0$ for $k = 2$ (see, e.g., [3, Chapter 4], where this was the case for lead). Such methods are not quite adequate. Indeed, if $\chi < 0$ for $k = 2$, then it follows from Eq. (12) that the functions $S(T)_{\text{low}}$ and $C(T)_{\text{low}}$ have minima and their minimum values are negative for $1 < k < 3$. For this reason, we assume that $\chi \geq 0$ and $k \geq 4$ in Eqs. (10) and (11).

At high temperatures $T \gg \Theta(T)$, the Debye function can be written as [1–6]

$$D_3(\Theta/T) \cong 1 - (3/8)(\Theta/T) + (1/20)(\Theta/T)^2$$

and Eq. (4) reduces to

$$\begin{aligned}(C/3N_An_ik_B)_{\text{high}} &\cong [1 - (1/20)(\Theta/T)^2] \\ &\times [1 - (T/\Theta)(d\Theta/dT)_v]^2 - (T^2/\Theta)(d^2\Theta/dT^2)_v.\end{aligned} \tag{14}$$

The function $\Theta(T)$ at high temperatures is commonly found by equating the experimental values of $[C(T)/3N_An_ik_B]_{\text{high}}$ to the expression $\{1 - (1/20)[\Theta(T)/T]^2\}$ (see [1–6]). Therefore, the contributions from both the first and second derivatives of the function $\Theta(T)$ to the lattice specific heat of a crystal at $T \gg \Theta(T)$ are ignored.

From Eqs. (6) and (14), we obtain a differential equation for the function $\Theta(T)$ at $[T/\Theta(T)] \longrightarrow \infty$:

$$\begin{aligned}T(d^2\Theta/dT^2)_v - (T/\Theta)[(d\Theta/dT)_v]^2 \\ + 2(d\Theta/dT)_v = 0.\end{aligned} \tag{15}$$

A trivial solution to this equation is the constant Θ_∞ independent of T. A more general solution to Eq. (15) has the form

$$\Theta(T)_{\text{high}} = \Theta_\infty \exp(-\alpha\Theta_\infty/T),$$

where $\Theta_\infty = \lim\Theta(T)$ as $T/\Theta_\infty \longrightarrow \infty$; the fitting parameter α controls the rate of increase in the function T/Θ_{high} as $T/\Theta_\infty \longrightarrow \infty$.

The interpolation of the low-temperature expression (11) and the high-temperature function $\Theta(T)$ over the entire temperature range can be written as

$$\begin{aligned}\Theta(T) &= \Theta_0 \exp[-\chi(T/\Theta_0)^k] \\ &+ \Theta_\infty \exp(-\alpha\Theta_\infty/T).\end{aligned} \tag{16}$$

Thus, the function $\Theta(T)$ decreases smoothly from Θ_0 (at $T = 0$ K) to a minimum value and then increases, approaching the asymptotic value Θ_∞ as $T \longrightarrow \infty$. The function $\Theta(T)$ given by Eq. (16) is characterized by five fitting parameters Θ_0, χ, k, Θ_∞, and α and does not contradict the laws of thermodynamics.

For n-dimensional crystals of elementary substances (consisting of monatomic molecules, $n_i = 1$), the function $\Theta(T)$ can be found using a procedure proposed in [7] if one knows the parameters of the interatomic interaction described by the Mie–Lennard–Jones potential:

$$\varphi(r) = [\varepsilon/(b-a)]\{a[r_0/(c+r)]^b - b[r_0/(c+r)]^a\}. \quad (17)$$

Here, ε and r_0 are the depth and coordinate of the minimum of the potential well, respectively; b and a are parameters characterizing the stiffness and range of the potential, respectively; and c is the distance between the centers of nearest neighbor atoms in the n-dimensional crystal.

Let us consider a model proposed by Frenkel' [10] for crystals consisting of triatomic molecules. The central atom in a molecule is assumed to oscillate within the potential well formed by the "core branches" of the pairwise interaction potential produced by the other two atoms (which are assumed to be fixed, with the separation between them being $2c$) [7]:

$$\nu(r) = [\varepsilon^* a/2(b-a)] \times \{[r_0/(c-r)]^b - 4(r_0/c)^b + [r_0/(c+r)]^b\}. \quad (18)$$

Here, ε^* is the effective depth of potential well (18):

$$\varepsilon^* = \varepsilon - E_n/(k_n/2), \quad (19)$$

where E_n and k_n are the oscillation energy and the first-neighbor coordination number of an atom in the n-dimensional crystal, respectively; i.e., $(k_n/2)$ is the number of pairs of oppositely positioned nearest neighbors of a given atom.

Using the Debye model with the function $\Theta(T)$, the energy E_n can be found to be

$$E_n = nk_B\Theta\{[n/2(n+1)] + (T/\Theta)D_n(\Theta/T)\} \times [1 - (T/\Theta)(d\Theta/dT)_v]. \quad (20)$$

Here, the first term is the zero-point energy and the second term is the thermal excitation energy of a system of harmonic oscillators characterized by a Debye frequency spectrum.

It should be noted that in [7], when considering the oscillation of an atom between its two nearest neighbors in an n-dimensional crystal, we assumed this oscillation to be one-dimensional and, instead of Eq. (19), used the relation $\varepsilon^* = \varepsilon - E_{n=1}$, where the second term was expressed in terms of the one-dimensional Debye function. This was the reason why, in [7], expression (10) was obtained with $k = 2$ and $\chi = (4/3)\pi^2$ for an n-dimensional crystal. As will be shown below, Eq. (19) leads to thermodynamically more self-consistent forms of Eqs. (10) and (11) with $k = n + 1$.

Using Eqs. (19) and (20) and performing the same mathematical manipulation as in [7], the function $\Theta(T)$ can be found to be

$$\Theta(T) = A\xi_0\{-1 + [1 + (8\varepsilon/k_BA\xi_0^2) \times (1 - (k_BT/4\varepsilon)S_n)]^{1/2}\}, \quad (21)$$

where m is the mass of an atom,

$$A = K_R[5k_nab(b+1)/144(b-a)](r_0/c)^{b+2},$$
$$K_R = \hbar^2/k_Br_0^2m,$$
$$\xi_0 = 4n^2/k_n(n+1), \quad (22)$$
$$S_n = -\xi_0(d\Theta/dT)_v + (8n/k_n)[1 - (T/\Theta)(d\Theta/dT)_v]D_n(\Theta/T).$$

It is easy to show that the function $\Theta(T)$ given by Eq. (21) reaches a maximum at $T = 0$ K, which agrees with the experimental data. This maximum value can be found from Eq. (21) to be

$$\Theta_0 = A\xi_0\{-1 + [1 + (8\varepsilon/k_BA\xi_0^2)]^{1/2}\}. \quad (23)$$

Equation (23) is a generalization of the corresponding expression obtained for Θ_0 in [7] and reduces to it when $\xi_0 = 1$. For three-dimensional cubic crystals, the value of ξ_0 is

$$\xi_0(n=3) = (9/k_{n=3}) = \begin{cases} 0.750 & \text{for } k_{n=3} = 12 \\ 1.125 & \text{for } k_{n=3} = 8 \\ 1.500 & \text{for } k_{n=3} = 6 \\ 2.250 & \text{for } k_{n=3} = 4. \end{cases} \quad (24)$$

Thus, for closely packed structures, the value of ξ_0 is close to unity.

At temperatures close to 0 K, i.e., for $(\Theta/T) \gg 1$, the Debye function can be written as $D_n(\Theta/T) \cong nn!\zeta(n+1)(T/\Theta)^n$ [11]. Here, $\zeta(n+1)$ is the Riemann zeta function and is equal to $\zeta(2) = \pi^2/6$, $\zeta(3) = 1.202$, and $\zeta(4) = \pi^4/90$ for one-, two-, and three-dimensional systems, respectively. In this case, the function $\Theta(T)_{\text{low}}$ has the form of Eq. (10) with $k = n + 1$. Therefore, for three-dimensional crystals, we have $k = 4$ in Eq. (16).

For an n-dimensional crystal of a monatomic substance, in the case where the zero-point energy is small in comparison with the depth of the potential well described by Eq. (17), i.e., where

$$8\varepsilon/k_BA \gg \xi_0^2[\xi_0^2(n+1)^2 - 1], \quad (25)$$

the function χ has the form

$$\chi = (n^2/k_n)n!\zeta(n+1)(k_B\Theta_0/\varepsilon). \quad (26)$$

We note that inequality (25) is satisfied for three-dimensional crystals of all elementary substances except helium.

Thus, for three-dimensional crystals of elementary substances, we have

$$\chi = (3\pi^4/5k_{n=3})(k_B\Theta_0/\varepsilon). \quad (27)$$

In this case, Eq. (13) reduces to the following expression, which enables one to calculate Θ_0 from the known values of Θ_0^s [found using Eq. (9)], of the coordination number, and of the depth of potential (17):

$$\Theta_0 = \Theta_0^s[1 + (27/8k_{n=3})(k_B\Theta_0^s/\varepsilon)]^{1/3}. \quad (28)$$

Numerical calculations based on the values of Θ_0^s and ε/k_B taken from [7] showed that Θ_0 is greater than Θ_0^s by 25–30% for He, ortho-H_2, and para-D_2; by 12–16% for Ne; by 5–7% for Ar; and by 2–4% for Kr and Xe. Therefore, in calculating Θ_0 for cryocrystals, one should take into account the correction to Θ_0^s found from Eq. (9) without regard for the temperature dependence of $\Theta(T)$. As for other crystals, the correction to Θ_0^s for them is very small, since $k_B\Theta_0^s/\varepsilon \ll 1$. Even for Li, we have $\Theta_0 - \Theta_0^s/\Theta_0^s \le 0.01$.

Thus, for three-dimensional fcc and bcc crystals, inequality (25) holds within a large margin, the value of χ is small, and ξ_0 is close to unity. This is the reason why both the Debye temperature and the Grüneisen parameter calculated in [7] were in good agreement with the experimental data. The calculational technique was then extended in [12, 13] to the case of binary ionic cubic crystals of the *AB* type and the agreement with the experimental data was found to be good. For the same reason, the parameters of potential (17) determined in [14–16] must differ only slightly from the values of these parameters calculated on the basis of the expression for the Debye temperature derived in this paper.

The quantity Θ_∞ can be calculated using the methods described in the literature. It should be noted that the high-temperature value of the Debye temperature Θ_∞ is determined experimentally much more accurately than is Θ_0 because of the weak temperature dependence of the specific heat at constant volume for $T/\Theta_\infty \longrightarrow \infty$ and can be found in many handbooks. Therefore, only the parameter α should be fitted in calculating $\Theta(T)$.

ACKNOWLEDGMENTS

The author is grateful to K.M. Magomedov, as well as K.N. Magomedov and Z.M. Surkhaeva, for their assistance throughout this work.

This study was supported by the Russian Foundation for Basic Research, project no. 02-03-33301.

REFERENCES

1. *Physical Acoustics: Principles and Methods*, Vol. 3, Part B: *Lattice Dynamics*, Ed. by W. P. Mason (Academic, New York, 1965; Mir, Moscow, 1968).
2. J. E. Mayer and M. Goeppert-Mayer, *Statistical Mechanics* (Wiley, New York, 1977).
3. A. A. Maradudin, E. W. Montroll, and G. H. Weiss, *Theory of Lattice Dynamics in the Harmonic Approximation* (Academic, London, 1963).
4. Ch. Kittel, *Introduction to Solid State Physics* (Wiley, New York, 1976, 5th ed.).
5. G. Grimvall, *Thermophysical Properties of Materials* (North-Holland, Amsterdam, 1986).
6. H. Schilling, *Statische Physik in Beispielen* (VEB Fachbuchverlag, Leipzig, 1972).
7. M. N. Magomedov, Zh. Fiz. Khim. **61** (4), 1003 (1987).
8. V. Yu. Bodryakov and V. M. Zamyatin, Fiz. Met. Metalloved. **85** (4), 18 (1998).
9. V. Yu. Bodryakov and V. M. Zamyatin, Teplofiz. Vys. Temp. **38** (5), 724 (2000).
10. Ya. I. Frenkel', *Introduction to the Theory of Metals* (GIFML, Moscow, 1958).
11. *Handbook of Mathematical Functions*, Ed. by M. Abramowitz and I. A. Stegun (National Bureau of Standards, Washington, 1964).
12. M. N. Magomedov, Teplofiz. Vys. Temp. **30** (6), 1110 (1992).
13. M. N. Magomedov, Zh. Fiz. Khim. **67** (11), 2280 (1993).
14. M. N. Magomedov, Zh. Fiz. Khim. **62** (8), 2103 (1988).
15. M. N. Magomedov, Zh. Fiz. Khim. **63** (11), 2943 (1989).
16. M. N. Magomedov, Teplofiz. Vys. Temp. **32** (5), 686 (1994).

Translated by Yu. Epifanov

Physics of the Solid State, Vol. 45, No. 1, 2003, pp. 36–40. Translated from Fizika Tverdogo Tela, Vol. 45, No. 1, 2003, pp. 37–41.

SEMICONDUCTORS AND DIELECTRICS

The Distribution of the Valence Electron Density in Predominantly Ionic Crystals with Different Bravais Sublattices

Yu. N. Zhuravlev and A. S. Poplavnoĭ

Kemerovo State University, ul. Krasnaya 6, Kemerovo, 650043 Russia

e-mail: zhur@phys.kemsu.ru

Received February 20, 2002

Abstract—Based on the theory of the local-density functional, self-consistent valence electron densities are calculated for CaO with a rock-salt lattice, CaF_2 with a fluorite lattice, K_2O with an antifluorite lattice, and for their constituent sublattices. It is shown that in the crystals with different Bravais sublattices, the anionic sublattice is a framework with covalent bonds containing a metal sublattice inside of them. The coupling between the sublattices is characterized by the density difference, which is defined as the difference between the total electron density and the densities of the individual sublattices. The density difference is found to be an order of magnitude smaller than the crystal and sublattice densities, which is evidence of weak hybridization of the sublattices and of the predominately ionic character of the bonding between them. © *2003 MAIK "Nauka/Interperiodica".*

1. INTRODUCTION

The sublattice technique for studying the electronic structure of crystals was developed by us in [1–3]. It has been shown that some peculiarities in the electron density are due to long-range interaction between identical atoms of the sublattices. From this point of view, crystals with different Bravais sublattices are of particular interest. The difference between the basis vectors of the sublattices in these crystals results in peculiarities in the electron density which cannot be interpreted in terms of translation symmetry of the entire crystal. Fluorides of alkali-earth metals with a fluorite lattice (for example, CaF_2) and oxides and sulfides of alkali metals with an antifluorite lattice (for example, K_2O) are the most suitable objects for use in investigating cases where the anionic and cationic Bravais sublattices are different. For reference, a crystal with identical anionic and cationic sublattices should be considered; in our case, this crystal is CaO.

The fluorite structure consists of two cubic cationic and anionic sublattices. The cations form an fcc sublattice into which a simple cubic anionic sublattice is incorporated. The sublattices are arranged in such a way that the cations are placed at the centers of every second anionic unit cube along any coordinate axis. This leads to such an alternation of the occupied and empty positions that the empty positions form an fcc lattice. In terms of the interchange between anions and cations, the antifluorite structure is reciprocal to the fluorite structure. In the CaF_2 crystal, the ions of the bivalent alkali-earth metal occupy fcc-sublattice sites and the septivalent anions, the sites of the simple cubic sublattice. In the K_2O crystal, the fcc-sublattice sites are occupied by ions of the univalent alkali metal and the sites of the simple cubic sublattice, by sexivalent anions. In the CaO crystal, both cations and anions are located at fcc-sublattice sites, which makes the crystal suitable for comparison with fluorite and antifluorite.

In this paper, we carried out calculations in the framework of the local-density-functional theory by using the pseudopotential method and the basis of numerical atomic $s^1p^3d^5$ pseudoorbitals expanded in terms of plane waves [4].

2. ROCK-SALT STRUCTURE

Let us consider CaO as an example of a crystal with identical fcc Bravais sublattices. The valence electron densities of the crystal and sublattices calculated for the [110] plane are shown in Fig. 1. The numerical values of the densities are given in units of $e \cdot Å^{-3}$ (e is the electron charge). The valence density of the crystal $\rho(CaO)$ is an electron density typical of ionic compounds. The electron density is concentrated predominantly in the vicinity of the anion and cation positions, where its distribution is almost spherically symmetric. The small density maximum between the metal ions corresponds to the saddle point of the $\rho(CaO)$ level surface, because there is a minimum in the anion plane at this point.

Now, let us consider the formation of the crystal density $\rho(CaO)$ from the densities of the anionic and cationic sublattices. In the oxygen sublattice, the electron density $\rho(O)$ is concentrated mainly around the anions and is partially transferred to the empty positions of the metal ions; therefore, the oxygen sublattice

1063-7834/03/4501-0036$24.00

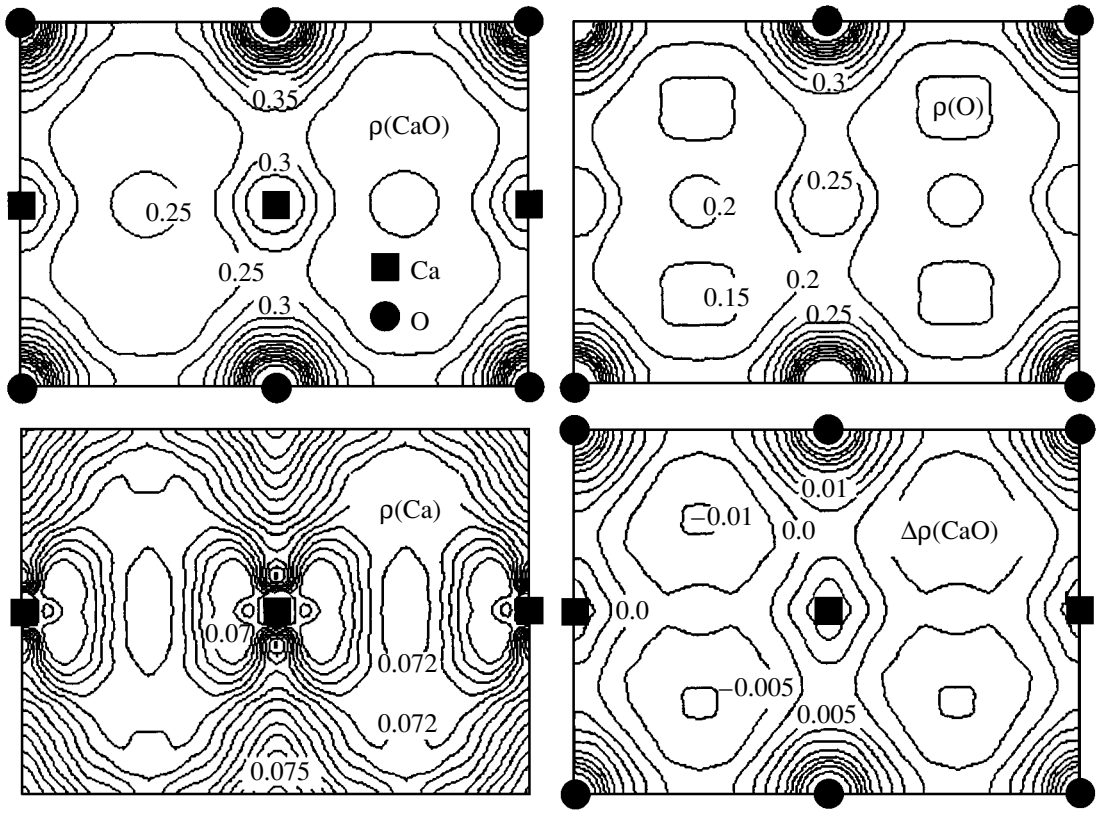

Fig. 1. Distribution of the valence crystal density ρ(CaO), the calcium and oxygen sublattice densities [ρ(Ca) and ρ(O), respectively], and the density difference Δρ(CaO) in the [110] plane of the calcium oxide.

is an anionic framework with covalent bonds. In the metal sublattice, the electron density is smeared quite uniformly over the unit cell with an average density of 0.073; however, a small charge is also transferred from the positions of the metal ions to the empty oxygen positions. The density difference Δρ(CaO) is an order of magnitude smaller than the total density ρ(CaO) in this case, which indicates that the hybridization between the sublattices is weak. As seen from the distribution of the negative (in units of *e*) and positive values of Δρ(CaO), this effect is reduced to charge transfer from the interstitials to the positions of the anions and cations.

Thus, in the case of a crystal with identical Bravais sublattices, the main peculiarity of the sublattice electron densities is the charge transfer from the occupied sites of one sublattice to the empty sites of the other. For this reason, the summation of the sublattice densities results in a simple pattern characterizing the ionic crystal. In terms of the sublattices, the hybridization of the wave functions of different atoms is explained by the tendency of the identical atoms of a sublattice to form a chemical bond of covalent type by means of charge transfer to interstitial sites that exactly coincide with the empty sites of the second sublattice.

Within the local model, the electron exchange between atoms of different sublattices is explained in terms of the overlapping of corresponding wave functions of neighboring sites. From the above, it is clear that if the Bravais sublattices are different, the pattern of the formation of the total electron density will be completely different.

3. FLUORITE STRUCTURE

In [5], full-electron calculations of the band structure, the charge-density distribution, and the optical functions of CaF_2 were carried out using the *ab initio* method of the local-density functional. The calculated total electron density is almost spherically symmetric and is concentrated in the vicinity of the metal and anion atoms. Based on the estimated values of the ion charges, it was concluded in [5] that the ionicity of the bond in CaF_2 is high.

It is well known that maps of the total electron density are less informative than those of the valence density. For this reason, we carried out self-consistent calculations of both the crystal and sublattice valence densities of CaF_2 corresponding to the [110] plane (Fig. 2). The map of crystal valence density $\rho(CaF_2)$ shows that, in the vicinity of the F atoms, the valence-density distribution is nearly spherically symmetric. The nearest neighbor F atoms are surrounded by the common con-

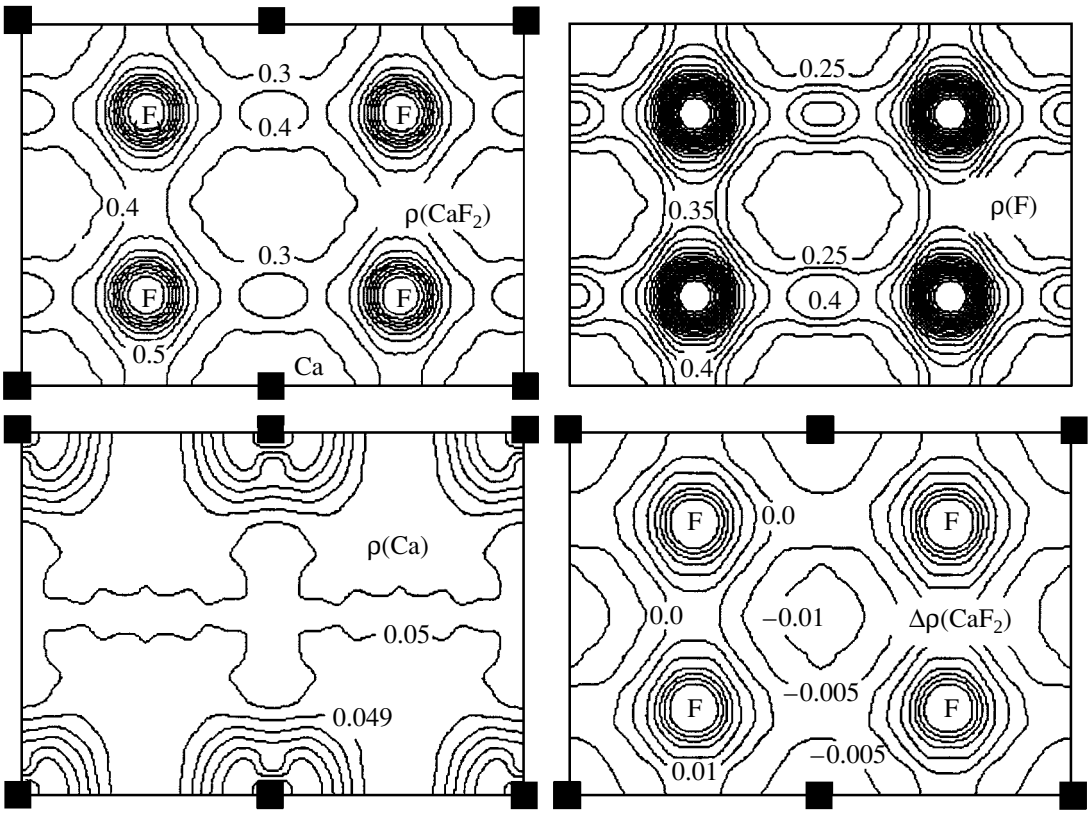

Fig. 2. Distribution of the valence crystal density $\rho(CaF_2)$, calcium and fluorine sublattice densities [ρ(Ca) and ρ(F), respectively], and density difference $\Delta\rho(CaF_2)$ in the [110] plane of the calcium fluoride.

tour of the valence-density distribution, which is in agreement with the data on the total electron density presented in [5]. At the same time, there are significant peculiarities in the $\rho(CaF_2)$ map (Fig. 2) which are not revealed in the map of the total electron density: valence-density peaks of height 0.4 appear between the next-to-nearest neighbor anions and occupy the face-central positions.

Now, let us analyze the role of the sublattices in the formation of the crystal valence density. First, we consider the electron density of the fluorine sublattice ρ(F). In comparing it with $\rho(CaF_2)$, one can see that the distribution of electron density over the fluorine sublattice closely repeats the main peculiarities of the valence density of the crystal. This conclusion relates to the formation of the common contours "embracing" the nearest neighbor fluorine atoms, as well as to the presence of the maxima of the density between the next-to-nearest neighbors. Thus, the origin of these peculiarities becomes clear: it can be stated that the anionic sublattice is the framework with covalent bonds into which the cationic sublattice is inserted.

Now, we consider the metal sublattice. Figure 2 shows that the valence density ρ(Ca) is smeared quite uniformly over the entire space with an average value of ~0.048. The density minima are located at the positions of the metal ions and are equal to 0.046. The maximum density is concentrated in the sufficiently narrow strip between the metal planes with convexities towards the atomic sites. It should be noted that the maxima of the crystal density are also located in the region of these convexities; therefore, the valence density of the metal also favors the enhancement of the covalent coupling between the next-to-nearest neighbor anions.

The density difference $\Delta\rho$, which is defined as the difference between the electron density of the crystal and the densities of the separate sublattices, is positive (in units of e) inside the anion region and negative in the rest of the crystal, including the cation positions. The density difference is an order of magnitude smaller than the crystal and sublattice densities, which indicates that the hybridization of the sublattices is weak and that the coupling between them is mainly ionic.

Now, we compare these results with those for CaO. First, we note that the CaO and CaF_2 sublattices are significantly different. The fluorine sublattice in CaF_2 is a simple cubic lattice, whereas the oxygen sublattice in CaO is an fcc lattice with doubled (with respect to the simple cubic lattice) period. Since the Bravais sublattices in CaO are identical, the framework of the oxygen sublattice with covalent bonds no longer arise as the total density ρ(CaO) is formed, because the metal sites

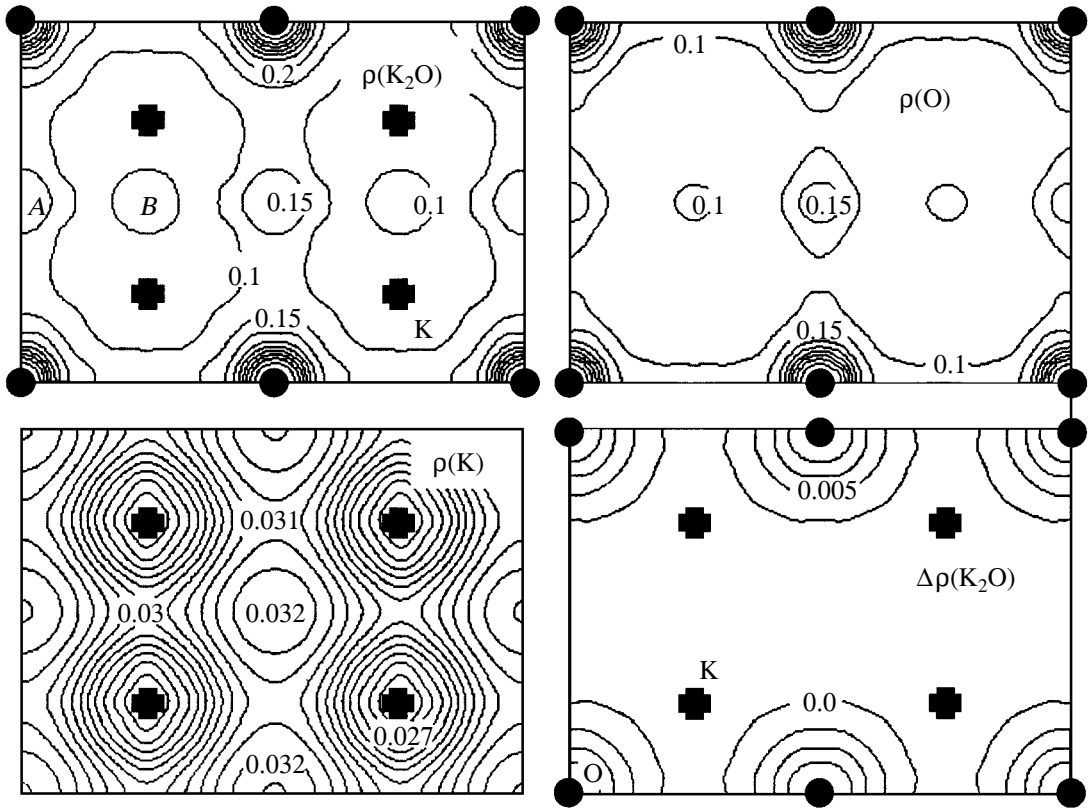

Fig. 3. Distribution of the valence crystal density $\rho(K_2O)$, potassium and oxygen sublattice densities [$\rho(K)$ and $\rho(O)$, respectively], and density difference $\Delta\rho(K_2O)$ in the [110] plane of the potassium oxide.

are located at the positions of the bond charges of this framework. On the contrary, the anionic framework with covalent bonds survives upon the formation of the total density $\rho(CaF_2)$ due to the difference between the Bravais sublattices of CaF_2. Herein lies the principal difference in the formation of the electron density between compounds with identical and different Bravais sublattices.

It should be noted that the metal sublattices in CaO and CaF_2 are similar and differ only in the value of the lattice constant; this explains the differences between the $\rho(Ca)$ maps shown in Figs. 1 and 2.

4. ANTIFLUORITE STRUCTURE

We illustrate the results of our calculations using the example of K_2O (Fig. 3). First, let us take a look at the map of the crystal density $\rho(K_2O)$. The electron-density minima correspond to the cation positions, while the density maxima are at the anion positions and in the interstices. The main maximum in the interstices is at the position *A* midway between the next-to-nearest neighbor anions, and another maximum is seen at the points with coordinates (1/4, 1/4, 1/2) (position *B* in Fig. 3). It should be noted that an electron density minimum localized between two oxygen atoms is located at position *B* in the anion plane. Hence, position *B* corresponds to a saddle point of the electron-density level surface.

Now, let us compare the electron density of the oxygen sublattice $\rho(O)$ with $\rho(K_2O)$. One can see that the distribution of $\rho(O)$ closely repeats the main peculiarities of the valence density of the crystal. The most significant fact is that electrons are transferred from the anion ions to positions *A* (which are midway between the next-to-nearest neighbor anions), which leads to the formation of a covalently bonded framework due to the anion–anion bonds. Moreover, saddle point *B* is also formed basically by the anion electrons.

A comparison of the $\rho(O)$ maps for CaO (Fig. 1) and K_2O (Fig. 3) shows that these maps are qualitatively similar and that the quantitative differences between them are due to the different lattice constants of these compounds. As in the case of fluorite, the anionic framework with covalent bonds (but with an fcc Bravais lattice) survives in the total density $\rho(K_2O)$.

In the metal sublattice, the valence density is smeared quite uniformly with an average density of ~0.019. Weakly pronounced maxima (equal to ~0.02) are situated at the empty positions of oxygen atoms and in the interstices midway between the empty positions of the next-to-nearest neighbor anions. At the metal

positions themselves, there are density minima equal to 0.018. Thus, the valence density of the metal also favors the enhancement of the covalent bonds of the anionic sublattice.

The density difference is positive inside the anion region and negative in the rest of the space, including the cation positions. The absolute values of $\Delta\rho$ are an order of magnitude smaller than the crystal and sublattice densities; this indicates that the hybridization between the sublattices is weak and the coupling between them is mainly ionic.

5. RESULTS AND DISCUSSION

Based on the calculated crystal and sublattice valence electron densities of the compounds with rock-salt, fluorite, and antifluorite lattices (possessing both identical and different Bravais sublattices), one may draw the following conclusions. Identical sublattice atoms form a covalent type of chemical bond by transferring a certain charge to the interstices, where maxima in the electron density are formed. From symmetry considerations, it is obvious that these maxima possess the translation symmetry of the corresponding sublattice. If, upon summation of the sublattice densities with the formation of the crystal density, the peaks of the electron density at interstitial sites coincide with the sublattice sites (as is the case in the rock-salt structure), then a purely ionic chemical bond is realized. However, this is the case only if the Bravais sublattices are identical. When different Bravais sublattices are superposed, the electron-density maxima are necessarily left at the interstitial sites, forming the covalent component of the chemical bond. It is obvious that the electron density maxima at interstitial sites are the higher, the larger the number of electrons in the sublattice where these maxima arise. That is the reason why the framework with covalent bonds originates due to the anions in the crystals under investigation. Covalent bonding of the cations can occur in metals with localized *d* and *f* states in the valence region.

The ionic conductivity of a number of crystals with a fluorite or an antifluorite lattice is sufficiently high; that is why these crystals are classified as solid electrolytes [6]. As underlined in [6], the ionic conductivity is favored by the presence of tunnels or layers in the crystal structure. Our calculations of the electron density in K_2O crystals indicate that there are wells with minimum electron density in the anionic framework with covalent bonds, which can be channels for the motion of the alkali-metal ions. An analysis of the experimental data [6] shows that the ionic conductivity in crystals with an antifluorite lattice is due to the transfer of the metal ions.

In the fluorite lattice, the situation is different; since the volume of the unit cell of the simple cubic sublattice is smaller than that of the fcc lattice, there are no tunnels or wells in the anionic framework with covalent bonds in this lattice. However, as was previously mentioned, there are metal vacancies in the centers of the next-to-nearest cubes in this framework. This favors the generation of anionic Frenkel defects, which can provide ionic conductivity. As noticed in [6], the ionic conductivity in fluorite crystals increases when the order in the anionic sublattice is destroyed. The electronic structure of a number of alkali-earth fluorides with Frenkel defects theoretically calculated on the basis of the linear muffin-tin orbital method supports this model [7]. The energies of the formation and migration of the defects estimated for two possible mechanisms of the ionic conductivity (the motion of vacancies associated with anionic Frenkel defects and the motion of interstitial ions) indicate that the smaller migration energies correspond to the motion of anionic vacancies.

REFERENCES

1. Yu. N. Zhuravlev, Yu. M. Basalaev, and A. S. Poplavnoĭ, Zh. Strukt. Khim. **42** (2), 210 (2001).
2. Yu. N. Zhuravlev and A. S. Poplavnoĭ, Zh. Strukt. Khim. **42** (5), 860 (2001).
3. Yu. N. Zhuravlev and A. S. Poplavnoĭ, Fiz. Tverd. Tela (St. Petersburg) **43** (11), 1984 (2001) [Phys. Solid State **43**, 2067 (2001)].
4. Yu. N. Zhuravlev, Yu. M. Basalaev, and A. S. Poplavnoĭ, Izv. Vyssh. Uchebn. Zaved., Fiz., No. 3, 96 (2000).
5. F. Gan, Y.-N. Xu, M.-Z. Huang, *et al.*, Phys. Rev. B **45** (15), 8248 (1992).
6. A. West, *Solid State Chemistry and Its Applications* (Wiley, Chichester, 1984; Mir, Moscow, 1988), Part 2.
7. V. P. Zhukov and V. M. Zaĭnullina, Fiz. Tverd. Tela (St. Petersburg) **40** (11), 2019 (1998) [Phys. Solid State **40**, 1827 (1998)].

Translated by A. Poushnov

Physics of the Solid State, Vol. 45, No. 1, 2003, pp. 41–45. Translated from Fizika Tverdogo Tela, Vol. 45, No. 1, 2003, pp. 42–45.

SEMICONDUCTORS AND DIELECTRICS

Electromechanical Properties and Anisotropy of Acoustic Wave Propagation in CuB_2O_4 Copper Metaborate

K. S. Aleksandrov*, B. P. Sorokin, D. A. Glushkov**, L. N. Bezmaternykh*, S. I. Burkov**, and S. V. Belushchenko***

** Kirensky Institute of Physics, Siberian Division, Russian Academy of Sciences, Akademgorodok, Krasnoyarsk, 660036 Russia*

*** Krasnoyarsk State University, Krasnoyarsk, 660041 Russia*

e-mail: bsorokin@lan.krasu.ru

Received March 12, 2002

Abstract—The propagation of bulk acoustic waves in single-crystal CuB_2O_4 copper metaborate is studied. The elastic, piezoelectric, and dielectric constants are calculated. The anisotropy in the parameters of bulk acoustic wave propagation in this crystal are determined. © *2003 MAIK "Nauka/Interperiodica".*

1. The interest in undertaking a coordinated investigation of the properties of single-crystal copper oxyborates has been spurred by recent studies on their low-temperature magnetism [1–6]. The most comprehensive data, including determination of the magnetic structure using neutron diffraction [4], were obtained for the CuB_2O_4 copper metaborate. This tetragonal noncentrosymmetric crystal [7], belonging to space group $D_{2d}^{12} = 1\bar{4}2d$, with the lattice parameters a = 11.528 Å and c = 5. 607 Å, remains paramagnetic down to 21 K. At lower temperatures, the crystal transfers to the antiferromagnetic state and its weak ferromagnetic moment of approximately 0.56 emu/g is accounted for by the two coupled sublattices being slightly misoriented [1]. Below 10 K, the compound undergoes a second phase transition to an incommensurate spiral structure, which is due primarily to the Dzyaloshinsky–Moriya antisymmetric exchange interaction [5]. Optical absorption spectra of CuB_2O_4 are discussed in [8].

At the same time, we are not aware of any publications dealing with such properties as the elasticity and piezoelectric effect of this crystal. The present paper reports on a measurement of the bulk acoustic wave (BAW) velocities and determination of the elastic, dielectric, and piezoelectric constants of this crystal, as well as on a calculation of the anisotropy in the BAW parameters.

Single crystals of copper metaborate, up to 10–15 cm^3 in volume, were grown, as in [9], from lithium borate melt solutions diluted by MoO_3. In such melt solutions, the growing face also maintains stability with a seed growing from the melt-solution surface, which made possible a stable Kyropoulos process with a lowered temperature in the interval 920–850°C.

2. BAW propagation in a crystal is described by the Green–Christoffel equation [10], whose solution yields the velocities and polarization vectors of BAWs propagating in a given crystal direction. Expressions for BAW velocities, which, in general, are combinations of elastic, piezoelectric, and dielectric constants, are presented in Table 1 for some directions in crystals of point symmetry group $\bar{4}2m$, to which the copper metaborate CuB_2O_4 belongs.

The BAW velocities in CuB_2O_4 were measured using the pulsed ultrasonic technique (30 MHz) [10] based on measuring the time of ultrasonic pulse propagation in a sample. This method ensures an accuracy of not worse than 10^{-4} in absolute measurements and a sensitivity of 10^{-6} in relative measurements. The CuB_2O_4 samples, shaped as polished-face rectangular parallelepipeds with linear dimensions ≈1 cm, were cut from the same boule. The crystallographic orientation of the samples was checked with an x-ray diffractometer to within ±3′. The sample orientations are shown in Fig. 1. The results of the BAW velocity measurements are listed in Table 2.

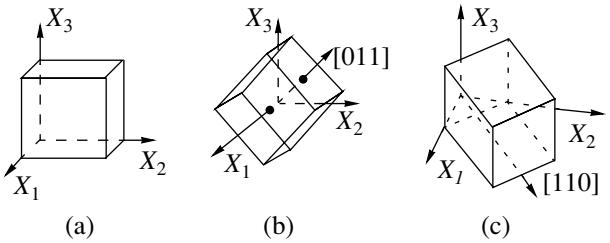

Fig. 1. Sample orientation. (a) Sample *1*, (b) sample *2*, and (c) sample *3*.

1063-7834/03/4501-0041$24.00 © 2003 MAIK "Nauka/Interperiodica"

Table 1. BAW velocities and electromechanical constants in crystals of $\bar{4}2m$ symmetry

Direction of propagation	Type of wave	Direction of polarization vector	ρV^2
[100]	L	[100]	C_{11}^E
	S	[010]	C_{66}^E
	S	[001]	C_{44}^E
[001]	L	[001]	C_{33}^E
	S		C_{44}^E
[110]	L	[110]	$1/2(C_{11}^E + C_{12}^E) + C_{66}^E$
	S	[001]	$C_{44}^E + \dfrac{e_{14}^2}{\varepsilon_{11}^\eta}$
	S	$[\bar{1}10]$	$1/2(C_{11}^E - C_{12}^E)$
[011]	S	[100]	$0.19C_{66}^E + 0.81C_{44}^E + \dfrac{0.16(e_{14}+e_{36})^2}{0.19\varepsilon_{11}^\eta + 0.81\varepsilon_{33}^\eta}$
	QS		$1/2(0.19C_{11}^E + 0.81C_{33}^E + C_{44}^E)$ $- 1/2\sqrt{[0.19(C_{11}^E - C_{44}^E) + 0.81(C_{44}^E - C_{33}^E)]^2 + 0.62(C_{44}^E + C_{13}^E)^2}$

Note: L is longitudinal, S shear, and QS quasi-shear mode.

The dielectric permittivities of mechanically free samples ε_{11}^σ and ε_{33}^σ were derived from the capacity of planar capacitors prepared from *X*- and *Z*-cut plates; the capacity was measured with an E8–4 high-precision semiautomatic bridge (1 kHz). These data were used to determine the elastic and piezoelectric constants of CuB_2O_4 from the BAW velocities.

Table 2. BAW velocities in single-crystal CuB_2O_4 (20°C)

Direction of propagation	Type of wave	Direction of polarization vector	Velocity, m/s
[100]	L	[100]	9917.6 ± 0.1
	S	[010]	4867.7 ± 0.1
	S	[001]	5307.0 ± 0.5
[001]	L	[001]	8882.5 ± 1.2
	S		5307.0 ± 0.5
[110]	L	[110]	9227.3 ± 1.4
	S	[001]	5317.3 ± 0.3
	S	$[\bar{1}10]$	6073.4 ± 0.2
[011]	S	[100]	5234.9 ± 1.1
	QS		5471.9 ± 1.3

3. As seen from Table 1, the signs of the piezoelectric constants e_{14} and e_{36} cannot be determined from the BAW velocities alone. The relative sign of these constants has to be found independently. It should be pointed out that crystals belonging to point symmetry group $\bar{4}2m$ permit the existence of two inequivalent sets of crystallographic coordinate systems (CCSs). In choosing the CCS, we were guided by the rules proposed in [11], according to which the proper CCS is that in which the condition for the piezoelectric modulus $d_{36} > 0$ is met. Therefore, we chose the proper CCS and analyzed the signs of the piezoelectric constants by using the static direct piezoelectric effect.

Consider the behavior of a sample oriented as shown in Fig. 1c under the application of uniaxial mechanical compression along the [011] direction. The equation of state for this case can be written as

$$D_i' = d_{ikl}'\sigma_{kl}', \quad (1)$$

where all quantities are defined relative to the "rotated" coordinate system (Fig. 2a). In this coordinate system, the mechanical stress tensor corresponding to uniaxial compression has the form

$$\sigma'_{kl} = \begin{pmatrix} -p & 0 & 0 \\ 0 & 0 & 0 \\ 0 & 0 & 0 \end{pmatrix} \quad (2)$$

in the case of compression along the X'_1 axis and

$$\sigma'_{kl} = \begin{pmatrix} 0 & 0 & 0 \\ 0 & -p & 0 \\ 0 & 0 & 0 \end{pmatrix} \quad (3)$$

for compression along the X'_2 axis. The pressure is assumed to be negative. Then, the electric induction vector should have only one nonzero component, either

$$D'_3 = -d'_{31} p_{X'_1} = -\frac{1}{2} d_{36} p_{X'_1} \quad (4)$$

or

$$D'_3 = -d'_{32} p_{X'_2} = \frac{1}{2} d_{36} p_{X'_2}. \quad (5)$$

Thus, by measuring the sign of the charges produced by the direct piezoelectric effect at the sample faces perpendicular to the X'_3 axis under uniaxial mechanical stress along X'_1 or X'_2 and assuming $d_{36} > 0$, one can choose the direction of axes of the original coordinate system in a given sample. After this, because all the samples were prepared from the same boule and their mutual orientation is known, we fix the axes of the original CCS in sample *2* (Fig. 1b). Following the same reasoning, we find that the nonzero component of the electric induction vector in the case of uniaxial mechanical compression applied to sample *2* along X'_2 (Fig. 2b) is

$$D'_1 = -k d_{14} p_{X'_2}, \quad (6)$$

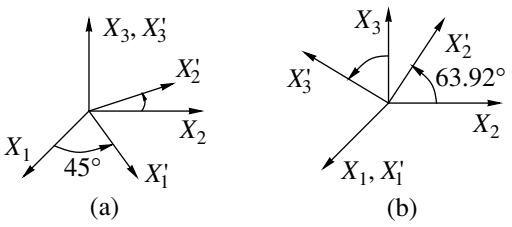

Fig. 2. Rotated coordinate systems (a) for sample *3* and (b) for sample *2*.

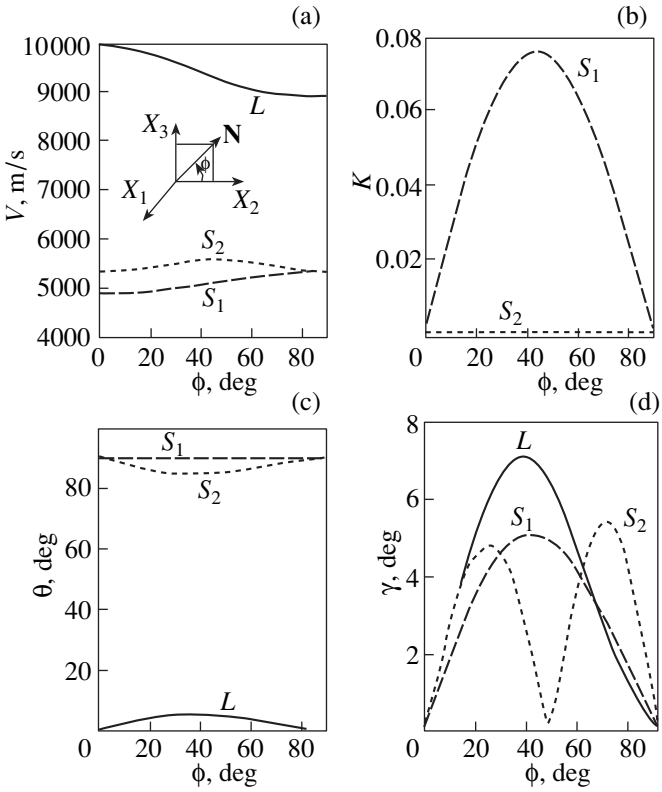

Fig. 3. Anisotropy in the BAW propagation parameters for CuB_2O_4 in the (100) plane. (a) BAW phase velocities, (b) electromechanical coupling coefficients, (c) angles between the polarization vector and direction of BAW propagation, and (d) angles of BAW energy flow deviation. **N** is the wave normal vector.

where k is a positive coefficient depending on the rotation angle of the coordinate system. Measurements performed in accordance with Eqs. (4)–(6) showed that in CuB_2O_4 for $d_{36} > 0$ the inequality $d_{14} > 0$ is met.

Table 3. Material constants of single-crystal CuB_2O_4 (20°C)

$C^E_{\lambda\mu}$, 10^{10} Pa	C^E_{11}	C^E_{12}	C^E_{13}	C^E_{33}	C^E_{44}	C^E_{66}
	39.54 ± 0.01	9.86 ± 0.02	10.56 ± 0.02	31.72 ± 0.01	11.32 ± 0.01	9.53 ± 0.01
ρ, kg/m^3 [7]	$e_{i\lambda}$, C/m^2	e_{14}	e_{36}	ε^σ_{ij}	ε^σ_{11}	ε^σ_{33}
4020		0.14 ± 0.01	0.22 ± 0.01		6.09 ± 0.05	6.14 ± 0.05

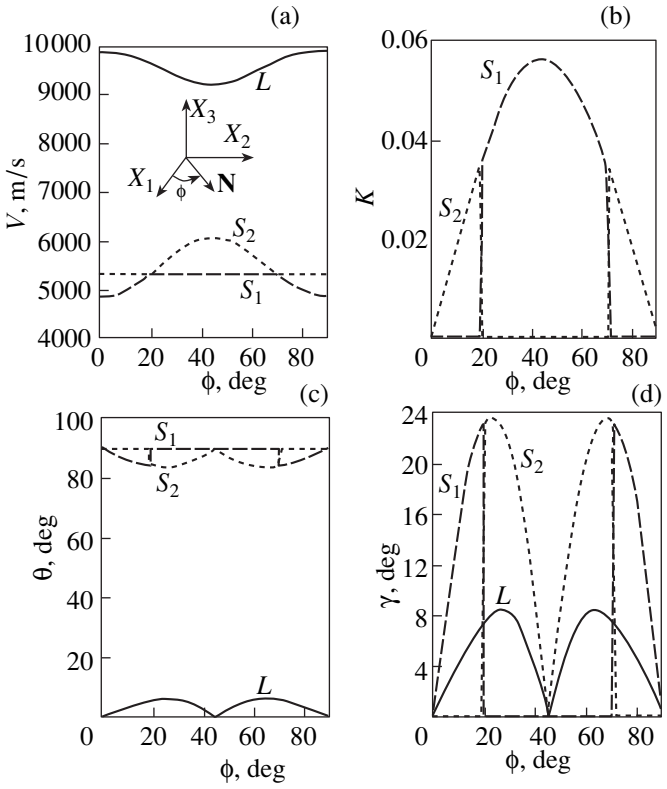

Fig. 4. Anisotropy in the BAW propagation parameters for CuB_2O_4 in the (001) plane. (a) BAW phase velocities, (b) electromechanical coupling coefficients, (c) angles between the polarization vector and direction of BAW propagation, and (d) angles of BAW energy flow deviation. **N** is the wave normal vector.

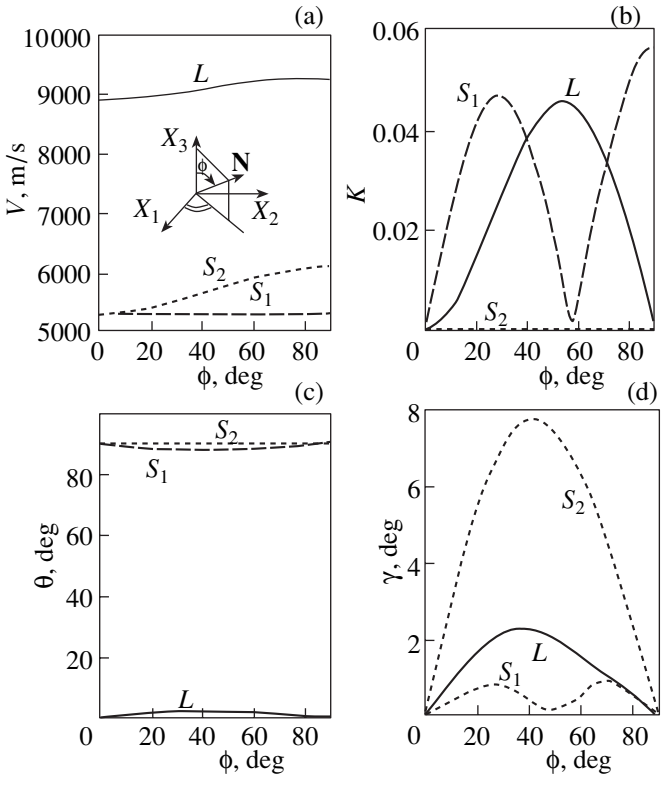

Fig. 5. Anisotropy in the BAW propagation parameters for CuB_2O_4 in the $(1\bar{1}0)$ plane. (a) BAW phase velocities, (b) electromechanical coupling coefficients, (c) angles between the polarization vector and direction of BAW propagation, and (d) angles of BAW energy flow deviation. **N** is the wave normal vector.

The relation connecting the piezoelectric constants with piezoelectric moduli presented in [11] reduces in our case to

$$e_{14} = d_{14}C_{44}^E, \quad (7)$$

$$e_{36} = d_{36}C_{66}^E. \quad (8)$$

Because the elastic constants are $C_{44} > 0$ and $C_{66} > 0$ (see Tables 1, 2), the piezoelectric constants are $e_{14} > 0$ and $e_{36} > 0$.

The Mohs hardness of the copper metaborate is more than seven units (a single crystal scratches quartz). The deep blue color, chemical stability, homogeneity, and fairly large dimensions of this crystal make it attractive as material for use in jewelry; its refractive indices $N_o = 1.69$ and $N_e = 1.582$ were determined in [12].

4. The material constants thus obtained (Table 3) were used to calculate the anisotropy in the BAW parameters for some planes of the CuB_2O_4 crystal. The results are presented in Figs. 3–5. Figure 3a shows the anisotropy of the BAW velocities for propagation in directions lying in the (100) plane. The velocities of longitudinal waves in this plane reach a maximal value, which is relatively high (about 10000 m/s), in the X_1 (X_2) directions. The X_3 direction (fourfold inversion axis) is the acoustic axis. Figure 3b displays the anisotropy of the electromechanical coupling coefficient (ECC). Only the slow shear wave polarized along [100] is accompanied by the longitudinal piezoelectric activity. For propagation at an angle $\phi \approx 44°$, the ECC for this mode reaches a maximum value $k \approx 7.6\%$. This value characterizes the copper metaborate as a weak piezoelectric crystal. Figure 3c shows the BAW polarization angles, which can be used to determine the directions of the "pure" modes. In this plane, pure modes propagate along crystallographic axes. Figure 3d illustrates the angles of the BAW energy flow deviation. Shown graphically in Fig. 4 are the results of similar calculations made for the (001) plane. Note the presence of acoustic axes which do not coincide with the crystallographic directions and lie at angles $\phi \approx 20°$ and 70°. As one crosses the acoustic axis, the polarization vector solutions, as it were, become replaced; more specifically, the shear-wave polarization vectors rotate by 90°. The shear wave polarized along [001] is an elastically isotropic wave. As follows from Fig. 5 [the $(1\bar{1}0)$

plane], the longitudinal mode, as well as the slow shear wave, is accompanied by the longitudinal piezoelectric activity.

ACKNOWLEDGMENTS

This study was supported by the Russian Foundation for Basic Research (project no. 00-15-96790) and the Federal Program "Integration" (project no. 69).

REFERENCES

1. G. Petrakovskii, D. Velikanov, A. Vorotinov, *et al.*, J. Magn. Magn. Mater. **205**, 105 (1999).
2. G. A. Petrakovskiĭ, A. D. Balaev, and A. M. Vorotynov, Fiz. Tverd. Tela (St. Petersburg) **42** (2), 313 (2000) [Phys. Solid State **42**, 321 (2000)].
3. G. A. Petrakovskiĭ, K. A. Sablina, D. A. Velikanov, *et al.*, Kristallografiya **45** (5), 926 (2000) [Crystallogr. Rep. **45**, 853 (2000)].
4. B. Roessli, J. Schefer, G. Petrakovskii, *et al.*, Phys. Rev. Lett. **86** (9), 1885 (2001).
5. G. A. Petrakovskiĭ, M. A. Popov, B. Roessli, and B. Ouladdiaf, Zh. Éksp. Teor. Fiz. **120** (4), 926 (2001) [JETP **93**, 809 (2001)].
6. H. Kageyama, K. Onizuka, T. Yamauchi, and Y. Ueda, J. Cryst. Growth **206**, 65 (1999).
7. M. Martinez-Ripoll, S. Martinez-Carrera, and S. Garcia-Blanco, Acta Crystallogr. B **27**, 677 (1971).
8. L. N. Bezmaternykh, A. M. Potseluĭko, E. A. Erlykova, and I. S. Édel'man, Fiz. Tverd. Tela (St. Petersburg) **43** (2), 297 (2001) [Phys. Solid State **43**, 309 (2001)].
9. L. N. Bezmaternykh, A. D. Vasil'ev, I. A. Gudim, *et al.*, in *Proceedings of the IX National Conference on Crystal Growth, Moscow, 2000*, p. 457.
10. M. P. Zaĭtseva, Yu. I. Kokorin, Yu. M. Sandler, V. M. Zrazhevskiĭ, B. P. Sorokin, and A. M. Sysoev, *Nonlinear Electromechanical Properties of Noncentrosymmetric Crystals* (Nauka, Novosibirsk, 1986).
11. Yu. I. Sirotin and M. P. Shaskolskaya, *Fundamentals of Crystal Physics* (Nauka, Moscow, 1979; Mir, Moscow, 1982).
12. G. K. Avdulaev, P. F. Rza-Zade, and S. Kh. Mamedov, Zh. Neorg. Khim. **27** (7), 1837 (1982).

Translated by G. Skrebtsov

Physics of the Solid State, Vol. 45, No. 1, 2003, pp. 46–50. Translated from Fizika Tverdogo Tela, Vol. 45, No. 1, 2003, pp. 46–50.

SEMICONDUCTORS AND DIELECTRICS

The Features of the EPR Spectrum in the Vicinity of Accidental Coincidence of Interacting Transitions

V. A. Vazhenin, V. B. Guseva, and M. Yu. Artemov

Institute of Physics and Applied Mathematics, Ural State University, Yekaterinburg, 620083 Russia

e-mail: vladimir.vazhenin@usu.ru

Received April 2, 2002

Abstract—The mechanisms of the inhomogeneous broadening of the EPR spectra of exchange-coupled copper dimers, high-spin iron centers in lithium germanate, and off-center Tl^{2+} ions in potassium sulfate are analyzed. It is shown that the additional EPR signals observed for these materials when two EPR lines are nearly coincident can be due to averaging of a portion of the spin packets associated with these lines. © *2003 MAIK "Nauka/Interperiodica".*

1. It is well known that investigation of the electron paramagnetic resonance (EPR) spectrum near an accidental crossing of electronic levels of a high-spin center allows one to detect fairly subtle effects associated with noticeable splitting of degenerate levels due to very weak interactions. These effects, for instance, carry information on defect-induced low-symmetry distortions of the crystal which affect the centers under study. In a number of experimental papers [1–6], specific features (an additional signal and a dip) were also reported to be observed when two EPR lines were nearly coincident; these features could not be explained in terms of the spin Hamiltonian involving only averaged values of the parameters.

In [1], for example, the dip in the absorption line of two coincident EPR transitions in Ni^{2+} ions in MgO was explained as resulting form static fluctuations of the initial splitting of the form $\varepsilon(S_z^2 - 2/3)$, which can be associated with random strains. It was shown that fast cross relaxation between closely spaced spin packets of the two EPR transitions at the center of the absorption line can give rise to homogeneous broadening of these spin packets and, as a consequence, to a dip in the absorption line. A similar effect has recently been observed in the EPR spectrum of axial centers Ni^{2+} in a single crystal of $Zn(BF_4)_2 \cdot 6H_2O$ in the case where the initial splitting became zero under hydrostatic pressure [6].

In [2], an additional signal was observed between the two EPR lines of the 3–4 and 5–6 transitions of trigonal centers Gd^{3+} in ferroelectric lead germanate ($Pb_5Ge_3O_{11}$, T_c = 450 K) in the vicinity of the coincidence of these two lines. The amplitude of the additional signal increased as the distance between the initial lines decreased or as T_c was approached. The reason for the appearance of this signal was found to be the averaging (caused by relaxation transitions between the 3–4 and 5–6 doublets) of the internal part of the quasi-symmetrical spin packets corresponding to the two initial EPR lines [7, 8]. The quasi-symmetrical structure of these spin packets is due to the spread in the spin-Hamiltonian parameters b_{21} and b_{43}, which increases as the ferroelectric phase transition point is approached [9].

By using computer simulation of the shape of the experimentally observed EPR spectrum over a wide temperature range around the structural phase transition point, the temperature dependences of the inhomogeneous-broadening parameters and of the relaxation both within each doublet and between the doublets have been found. It should be noted that the feature of the EPR spectrum observed in lead germanate is similar in nature to the cross-singular effects observed in NMR of polycrystals [10], as well as to the effects that occur when relaxation without spin flipping is taken into account between Kramers doublets originating from a vibronic doublet split by a random strain field [11]. An additional signal similar in shape was observed by the authors of [3] in the vicinity of one of the crossings of the angular dependences of the EPR-line positions corresponding to transitions in the triplet of dimeric exchange clusters $[Cu(PU)_5(ClO_4)_2]_2$ and by the authors of [4] near three points of coincidence of EPR transitions involving fine-structure spectral lines of Fe^{3+} ions in the "weak"-ferroelectric lithium germanate ($Li_2Ge_7O_{15}$, T_c = 283.5 K). Coexistence of the high- and low-temperature EPR spectra of off-center Tl^{2+} ions in K_2SO_4 near the crossover between the fast- and slow-motion regimes, which can be thought of as the appearance of an additional signal in the low-temperature EPR spectrum, was observed in [5].

The objective of this paper is to interpret the effects observed in [3–5] in the vicinity of coincidence of EPR transitions in terms of the model of relaxation averag-

1063-7834/03/4501-0046$24.00

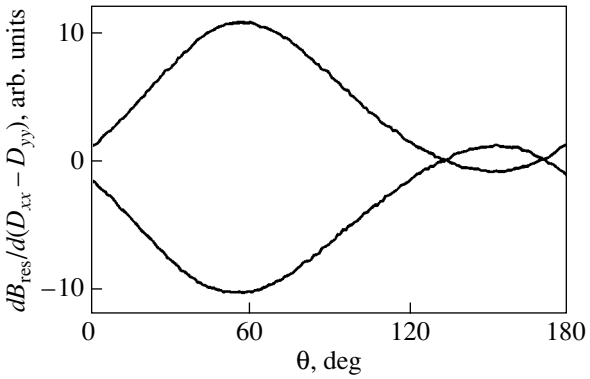

Fig. 1. Angular dependence (in the *zx* plane) of the shift in the position of the EPR signal from the dimeric cluster caused by a change in $(D_{xx} - D_{yy})$.

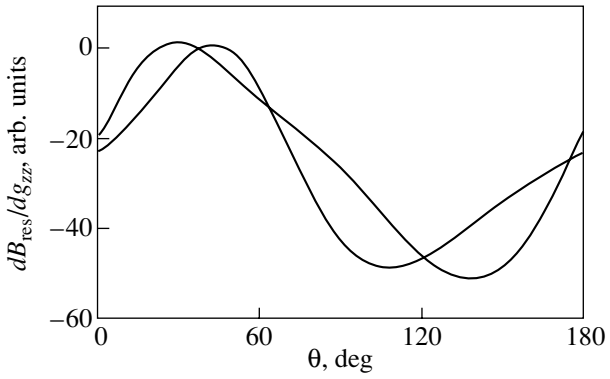

Fig. 2. Angular dependence (in the *zx* plane) of the shift in the position of the EPR signal from the dimeric cluster caused by a change in g_{zz}.

ing of part of the inhomogeneously broadened initial lines [7, 8].

2. The angular dependences (in the *zx* plane) of the EPR-line positions associated with the two transitions in the triplet of the centrosymmetric dimeric cluster $[Cu(PU)_5(ClO_4)_2]_2$ cross each other twice (at polar angles $\theta \approx 36°$ and 107°) and are adequately described by the spin Hamiltonian (with $S = 1$)

$$\mathbf{H} = \beta \mathbf{B} \cdot \mathbf{g} \cdot \mathbf{S} + (1/2)\mathbf{S} \cdot \mathbf{D} \cdot \mathbf{S}, \qquad (1)$$

where β is the Bohr magneton, **B** is the magnetic induction, **g** is the **g** tensor, and **D** is the fine-structure tensor, whose parameters are defined in [3]. The additional (anomalous) signal is observed in the vicinity of $\theta_0 \approx 36°$ and only for $\theta > \theta_0$.

In a model where the triplet states are single-ion states, the observed signals can be interpreted as transitions of an ion subjected to the local field produced by the spin of another ion. When the state of the other ion is changed, crossover occurs between the observed resonance transitions. If the frequency of relaxation transitions is comparable to the spacing between the EPR lines, the components of the EPR spectrum are shifted and broadened. As the relaxation rate increases further and becomes noticeably higher than the line splitting, the EPR spectrum is fully averaged. This motion-induced destruction of the fine structure of the EPR spectrum was considered in detail in [12].

Inhomogeneous electric fields and elastic strains, which always exist in actual crystals, give rise to a spread in the spin-Hamiltonian parameters. Calculations showed that a change in the components of the tensor **D** always causes symmetric shifts in the position of a pair of fine-structure lines, these shifts being strongly dependent on the angle θ (Fig. 1). In contrast, the shifts in the pair of lines produced by variations in the diagonal components of the **g** tensor are of the same sign (Fig. 2). A spread in the off-diagonal components of the **g** tensor causes shifts in the EPR-line positions which may be arbitrary in character for different values of the polar angle.

It was shown in [7, 8] that if the positions of spin packets are approximately symmetric and a mechanism causing a crossover between EPR transitions operates, then an additional signal appears between the initial EPR lines in the vicinity of coincidence of these lines. To calculate the EPR spectrum, we use the following formula from [8], which is a generalization of the corresponding expression from [12] to the case where the positions and widths of the EPR lines are affected by relaxation transitions between these lines:

$$I(B) = \sum_m \exp(-mc/\sigma_2)^2$$

$$\times \left[\sum_n \mathrm{Re}(\mathbf{W} \cdot \mathbf{A}(B)^{-1} \cdot \mathbf{1}) \cdot \exp(-nd/\sigma_1^2) \right],$$

$$\mathbf{A}(B) = \Omega(B) + \breve{\mathbf{I}}, \quad \breve{\mathbf{I}} = \begin{vmatrix} -V & V \\ V & -V \end{vmatrix}, \qquad (2)$$

$$\Omega(B)$$

$$= \begin{vmatrix} i\alpha(a + nd + mc - B) - V_0 & 0 \\ 0 & i\alpha(b - nd + mc - B) - V_0 \end{vmatrix},$$

where **W** is a vector whose components are the probabilities of the initial transitions induced by a microwave field; **1** is the unit vector; $\breve{\mathbf{I}}$ is the matrix of the probabilities of relaxation transitions between the EPR lines; $\Omega(B)$ is a matrix of the parameters of the initial spin packets (V_0 is the probability of relaxation transitions); a and b are the positions of the initial EPR lines; $\alpha = g_{\mathrm{eff}}\beta$, $2n + 1$, and $2m + 1$ are the numbers of spin packets characterized by the symmetric and antisymmetric distribution, respectively; d and c are the distances between neighboring spin packets; and V is the proba-

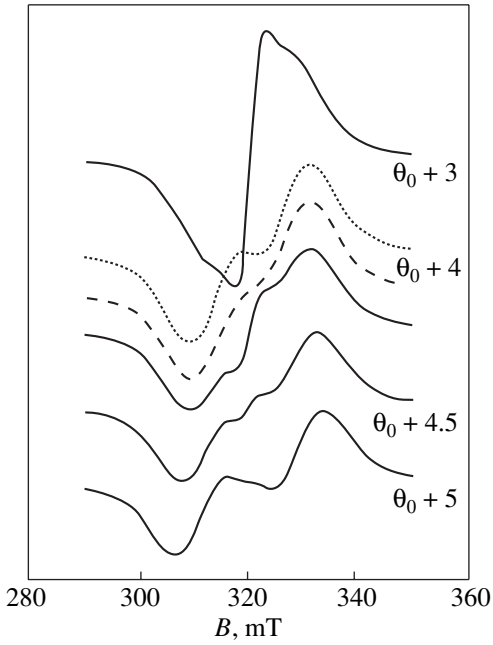

Fig. 3. Dependence of the first derivative of the EPR spectrum of the dimeric cluster on the polar angle in the *zx* plane. The parameters characterizing the shape of the initial signals are presented in the text.

bility of the relaxation transition between the EPR lines, which is equal to V_0 in the case under study.

The calculated first derivative of $I(B)$ is shown in Fig. 3 for several values of the polar angle and demonstrates the ability of the model under consideration to qualitatively describe the experimental data [3]. In order to calculate the EPR spectrum more accurately, we need the experimental values of the spin-packet widths, as well as information on the character and magnitude of the inhomogeneous broadening. In Eq. (2), the distribution of spin-packet intensity is assumed to be normal, with $\sigma_1 = 4.3$ mT for symmetric spin packets and $\sigma_2 = 0$ for antisymmetric ones; we also assumed that the relaxation transition probability is $V = 9 \times 10^7$ Hz and that $B_i(\theta)$ are linear functions in the range of interest. The parameters are adjusted so as to fit the experimental data on the widths and splittings of the EPR signals.

The absence of an additional signal for $\theta < \theta_0 = 36°$ and near the crossing of the angular dependences of the EPR-line positions at $\theta_0 = 107°$ is most likely due to the large (relative) contribution from antisymmetric spin packets to the inhomogeneous broadening of the EPR lines, because the anisotropy of the line broadening is very high (Figs. 1, 2). As an illustration, Fig. 3 shows the spectrum at $\theta = \theta_0 + 4°$ calculated for $\sigma_1 = \sigma_2 = 3$ mT (dashed curve) and for $\sigma_1 = 0$, $\sigma_2 = 4.3$ mT (dotted curve).

3. The situation in the EPR spectrum of $Li_2Ge_7O_{15}$: Fe^{3+} [4] is very similar to that for lead germanate doped with Gd^{3+} [2]. At room temperature, i.e., near the ferroelectric phase transition point, additional signals appear in the spectra of two of the four inequivalent high-spin Fe^{3+} centers in the vicinity of three coincidences of EPR transitions ($M \longleftrightarrow M + 1$, $M + 2 \longleftrightarrow M + 3$); the intensity of these signals increases rapidly as a point of coincidence is approached. We note that, as in the case of lead germanate, anomalous signals were observed in the vicinity of coincidence of EPR transitions within doublets separated by an energy interval.

It is obvious that the doublets within which EPR transitions are observed are always coupled by relaxation transitions controlled by spin–lattice or spin–spin interactions. Our calculations showed that a change in any fine-structure parameter (second-rank tensor) causes symmetric shifts in the position of the EPR lines in the vicinity of their coincidence. Therefore, there exist conditions for the formation of an additional signal in the vicinity of coincidence of EPR transitions within different doublets. The intensity of the EPR line that forms when two initial lines exactly coincide is higher than the sum of the intensities of these two lines [4], because the width of the resulting line is noticeably smaller. This last fact was indicated in [8] and is due to the averaging and to the close approach of symmetric spin packets when the initial lines coincide.

4. According to [5, 11], a thallium ion introduced into K_2SO_4 (D_{2h}) occupies the potassium ion position of local symmetry C_s. The inversion and U_2 operators take one pair of the four translationally inequivalent potassium ion positions in the unit cell into the other pair; therefore, the magnetic multiplicity of the Tl^{2+} centers (effective symmetry C_s) is $K_M = 2$. For these two types of centers, the hyperfine interaction tensor **A** and the **g** tensor (which are of importance in the spin Hamiltonian for Tl^{2+}) in the system of the principal axes differ only in the sign of their *xy* components, which will lead to different spectra in the *xy* plane for these two types of centers; the other off-diagonal components are zero.

Since the Tl^{2+} ion is displaced from the symmetry plane (off-center localization [5]), there are two types of Tl^{2+} centers of symmetry C_1 (related by mirror symmetry) and their spin Hamiltonians differ in the sign of the *xz*, *zx*, *yz*, and *zy* components of the **A** and **g** tensors.

The splitting of an EPR line (corresponding to one of the Tl^{2+} ion transitions within the triplet resulting from hyperfine interaction with a large value of $A \approx 115$ GHz) observed in [5, 11] at temperatures below 40 K is due to the contributions to the line position that are linear in the off-diagonal **g**- and **A**-tensor components indicated above. For the orientation $\mathbf{B} \parallel z \parallel \mathbf{c}$, there are no such contributions and only one EPR line is observed. At $\theta \neq 0$ and $\varphi = 0$ (φ is the azimuth angle of the magnetic field), in the coordinate system following

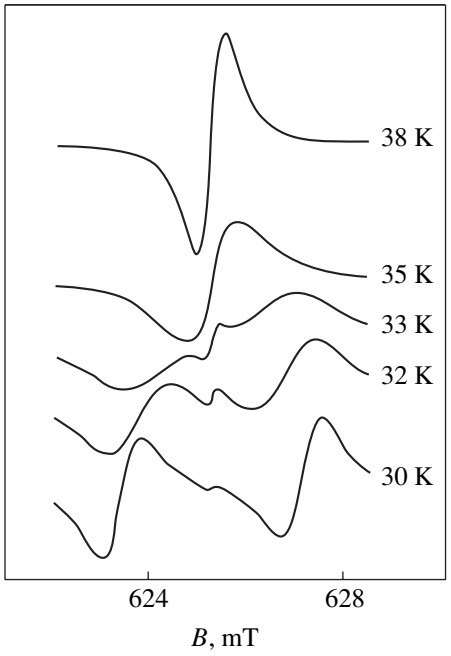

Fig. 4. Temperature dependence of the EPR spectrum of the off-center Tl^{2+} ion in K_2SO_4 for a small misorientation with respect to **B** ∥ *z* ∥ **c**.

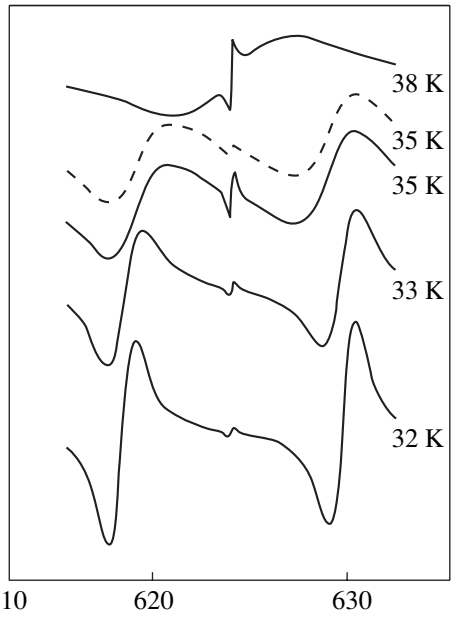

Fig. 5. EPR spectrum of the off-center Tl^{2+} ion in K_2SO_4 for a large misorientation with respect to **B** ∥ *z* ∥ **c**.

the field, the shifts in the position of the EPR line are found to be

$$\Delta B \sim \pm|g_{xz} + g_{zx}|B\sin 2\theta/g_{\text{eff}}, \quad (3)$$

$$\Delta B \sim \pm|A_{zx} + A_{xz}|\sin 2\theta/g_{\text{eff}}\beta; \quad (4)$$

these shifts for the inequivalent off-center positions of the Tl^{2+} ion differ in sign and lead to a splitting of the EPR line [5, 11]. When the direction of the magnetic field lies in the *zy* plane, the components g_{zy}, g_{yz}, A_{yz}, and A_{zy} are of importance in the formation of the EPR doublet.

The coexistence of the high- and low-temperature EPR spectra of Tl^{2+} centers in K_2SO_4, mentioned in Section 1, is observed only in the case of small misorientations ($\theta < 5°$) [5]. At a large deviation of the magnetic field direction from the *z* axis, only the typical crossover between the regimes of fast and slow motion of the off-center ion [13] is observed in the temperature dependence of the EPR spectrum.

Let us consider the effect of a spread in the value of different components of the **g** and **A** tensors on the arrangement of spin packets in the EPR spectrum of Tl^{2+} ions in off-center positions of both types. It is obvious that a deviation of an off-diagonal component from its average value, in accordance with Eqs. (3) and (4), leads to EPR-line shifts that are different in sign for the two different types of off-center Tl^{2+} positions and, as a result, a "quasi-symmetric" structure of spin packets forms in the EPR doublet [7, 8]. The line shifts due to the terms quadratic in variations of the off-diagonal components of the **g** and **A** tensors are small and of the same sign for off-center Tl^{2+} positions of both types.

Let us suppose that, at a small misorientation relative to the orientation **B** ∥ *z* ∥ **c**, a quasi-symmetric structure of spin packets with a Lorentzian intensity distribution is realized in the doublet under discussion (such a shape is characteristic of line broadening due to random strains or chaotically distributed electric dipoles [14]), with the distribution width being $2\lambda = 0.1$ mT and the spin-packet width being 0.1 mT. The relaxation time of the off-center impurity in the double-well potential is assumed to be $\tau = 1/V = 5 \times 10^{-13}\exp(357/T)$ [15].

In this case, using a modified formula based on Eq. (2),

$$I(B) = \left[\sum_n \text{Re}(\mathbf{W}\cdot\mathbf{A}(B)^{-1}\cdot\mathbf{1})\frac{1}{1+(nd/\lambda)^2}\right], \quad (5)$$

we obtain the EPR spectrum shown in Fig. 4 as a function of temperature. This spectrum qualitatively explains the experimental data presented in [5, 13, 15]. As the angle θ is increased, which corresponds to increasing the spacing between the initial EPR lines, the peak intensity of the additional signal decreases (Fig. 5). The values of the splitting in Figs. 4 and 5 are taken to be roughly equal to the experimental values [5, 13, 15].

For a large misorientation (when the lines virtually do not overlap) and a moderate hopping frequency of the off-center ion, only the spin packets of low intensity

are averaged and the additional peak is small. As the hopping frequency of the ion in the double-well potential increases with temperature, the initial lines approach each other and become broader, with the result that progressively more intense spin packets are averaged.

Obviously, in the case where only initial lines with symmetric spin-packet structure are inhomogeneously broadened, the width of the additional signal will be of the order of the spin-packet width [16]. However, as indicated in Section 2, the width of the additional peak essentially depends on the degree of inhomogeneous broadening characterized by antisymmetric packet structure. It is easily understood that static fluctuations in the diagonal components of the tensors lead to EPR-line shifts of the same sign for the different types of off-center ion positions (the shifts being proportional to $\Delta g_{zz}\beta B\cos^2\theta$, $\Delta g_{xx}\beta B\sin^2\theta$, $\Delta g_{yy}\beta B\sin^2\theta$, $\Delta A_{zz}\cos^2\theta$, $\Delta A_{xx}\sin^2\theta$, and $\Delta A_{yy}\sin^2\theta$) and, therefore, give rise to line broadening characterized by antisymmetric arrangement of the spin packets in the EPR doublet. Since the polar-angle dependence of some antisymmetric contributions ($\sim\sin^2\theta$) is stronger than that of the symmetric contributions ($\sim\sin\theta\cos\theta$), the former dependence can lead to a noticeable spread in the additional peak (see, e.g., the dashed curve in Fig. 5, which is calculated with allowance for both the symmetric and antisymmetric broadening described by a Lorentzian 0.1 mT wide). This spread is likely the reason why no additional signal is observed for large misorientations relative to $\mathbf{B} \parallel z$ [5, 13, 15].

5. Thus, the appearance of an additional signal in the vicinity of accidental coincidence of the two EPR transitions considered in Sections 2–4 can be explained qualitatively in terms of selective averaging of the interacting spin packets associated with these transitions. Computer simulation of experimental EPR spectra will allow one to determine the parameters characterizing the broadening and interaction of the EPR lines.

In closing, it is worth remarking on the anomalous shape of an EPR signal resulting from a superposition of allowed and forbidden transitions of Ni^{2+} centers in $Zn(BF_4)_2 \cdot 6H_2O$ [6]. Since these transitions involve accidentally degenerate states $\langle +1|$ and $\langle 0|$, even very weak low-symmetric distortions can affect the shape of the observed EPR line, which will make exact coincidence of the transitions impossible. For example, if the spin Hamiltonian contains the term $(1/3)b_{21}O_{21}$ with $b_{21} = 0.1$ GHz, the resonance positions of the two transitions at the "level crossing" will differ by approximately 0.5 mT. In our opinion, low-symmetric distortions of the environment of a paramagnetic center can become fairly large under a quasi-hydrostatic pressure.

ACKNOWLEDGMENTS

The authors are grateful to V.K. Voronkova, V.N. Efimov, and A.A. Galeev for helpful discussions.

This study was supported by the US Civilian Research and Development Foundation for the CIS Countries, grant no. REC-005.

REFERENCES

1. S. R. P. Smith, F. Dravnieks, and J. E. Wertz, Phys. Rev. **178** (2), 471 (1969).
2. V. A. Vazhenin and K. M. Starichenko, Pis'ma Zh. Éksp. Teor. Fiz. **51** (8), 406 (1990) [JETP Lett. **51**, 461 (1990)].
3. V. K. Voronkova, L. V. Mosina, Yu. V. Yablokov, *et al.*, Mol. Phys. **75** (6), 1275 (1992).
4. A. A. Galeev, N. M. Khasanova, A. V. Bykov, *et al.*, Appl. Magn. Reson. **11**, 61 (1996).
5. G. V. Mamin and V. N. Efimov, Mod. Phys. Lett. B **12** (22), 929 (1998).
6. I. M. Krygin, A. A. Prokhorov, G. N. Neĭlo, and A. D. Prokhorov, Fiz. Tverd. Tela (St. Petersburg) **43** (12), 2147 (2001) [Phys. Solid State **43**, 2242 (2001)].
7. V. A. Vazhenin, K. M. Starichenko, and A. D. Gorlov, Fiz. Tverd. Tela (St. Petersburg) **35** (9), 2449 (1993) [Phys. Solid State **35**, 1214 (1993)].
8. V. A. Vazhenin, V. B. Guseva, and M. Yu. Artemov, Fiz. Tverd. Tela (St. Petersburg) **44** (6), 1096 (2002) [Phys. Solid State **44**, 1145 (2002)].
9. V. A. Vazhenin, E. L. Rumyantsev, M. Yu. Artemov, and K. M. Starichenko, Fiz. Tverd. Tela (St. Petersburg) **40** (2), 321 (1998) [Phys. Solid State **40**, 293 (1998)].
10. É. P. Zeer, V. E. Zobov, and O. V. Falaleev, *Novel Effects in NMR of Polycrystals* (Nauka, Novosibirsk, 1991).
11. J. R. Herrington, T. L. Estle, and L. A. Boatner, Phys. Rev. B **13** (9), 2933 (1971).
12. A. Abragam, *The Principles of Nuclear Magnetism* (Clarendon, Oxford, 1961; Inostrannaya Literatura, Moscow, 1963).
13. V. N. Efimov and G. V. Mamin, Mod. Phys. Lett. B **11** (13), 579 (1997).
14. A. B. Roĭtsin, in *Radiospectroscopy of Solid: Collection of Scientific Works of Academy of Sciences of Ukraine* (Naukova Dumka, Kiev, 1987), p. 89.
15. G. V. Mamin, Author's Abstract of Candidate's Dissertation (Kazanskiĭ Gos. Univ., Kazan, 1999).
16. J. E. Wertz and J. R. Bolton, *Electronic Spin Resonance: Elementary Theory and Practical Applications* (McGraw-Hill, New York, 1972; Mir, Moscow, 1975).

Translated by Yu. Epifanov

Physics of the Solid State, Vol. 45, No. 1, 2003, pp. 51–56. Translated from Fizika Tverdogo Tela, Vol. 45, No. 1, 2003, pp. 51–55.

SEMICONDUCTORS AND DIELECTRICS

Electron Paramagnetic Resonance of Cr^{3+}–Li^{+} Centers in (Cr,Li) : Mg_2SiO_4 Synthetic Forsterite

I. D. Ryabov*, A. V. Gaĭster, and E. V. Zharikov****

** Institute of the Lithosphere of Marginal Seas, Russian Academy of Sciences, Staromonetnyĭ per. 22, Moscow, 119180 Russia*

*** Research Center of Laser Materials and Technologies, Institute of General Physics, Russian Academy of Sciences, ul. Vavilova 38, Moscow, 119991 Russia*

Received January 14, 2002; in final form, April 9, 2002

Abstract—Synthetic single crystals of chromium- and lithium-doped forsterite, namely, (Cr,Li) : Mg_2SiO_4, are studied using electron paramagnetic resonance spectroscopy. It is revealed that, apart from the known centers $Cr^{3+}(M1)$ and $Cr^{3+}(M2)$ (with local symmetries C_i and C_s, respectively), these crystals involve two new types of centers with C_1 symmetry, namely, $Cr^{3+}(M1)'$ and $Cr^{3+}(M2)'$ centers. The standard parameters D and E in a zero magnetic field [zero-field splitting (ZFS) parameters expressed in GHz] and principal components of the **g** tensor are determined as follows: $D = 31.35$, $E = 8.28$, and **g** = (1.9797, 1.9801, 1.9759) for $Cr^{3+}(M1)'$ centers and $D = 15.171$, $E = 2.283$, and **g** = (1.9747, 1.9769, 1.9710) for $Cr^{3+}(M2)'$ centers. It is found that the low-symmetric effect of misalignment of the principal axes of the ZFS and g tensors most clearly manifests itself (i.e., its magnitude reaches 19°) in the case of $Cr^{3+}(M2)'$ centers. The structural models $Cr^{3+}(M1)$–$Li^{+}(M2)$ and $Cr^{3+}(M2)$–$Li^{+}(M1)$ are proposed for the $Cr^{3+}(M1)'$ and $Cr^{3+}(M2)'$ centers, respectively. The concentrations of both centers are determined. It is demonstrated that, upon the formation of Cr^{3+}–Li^{+} ion pairs, the $M1$ position for chromium appears to be two times more preferable than the $M2$ position. Reasoning from the results obtained, the R_1 line (the $^2E \longrightarrow {}^4A_2$ transition) observed in the luminescence spectra of (Cr,Li) : Mg_2SiO_4 crystals in the vicinity of 699.6 nm is assigned to the $Cr^{3+}(M1)'$ center. © *2003 MAIK "Nauka/Interperiodica".*

1. INTRODUCTION

Chromium-doped forsterite (Cr : Mg_2SiO_4 or chromium forsterite) has found wide use as an active medium in tunable near-infrared lasers [1–3]. Tetravalent chromium ions play the role of active laser centers. The Cr^{4+} ions located at tetrahedrally coordinated silicon positions with C_s local symmetry have been recently identified using electron paramagnetic resonance (EPR) spectroscopy [4–9]. According to the EPR data [10, 11], chromium-doped forsterite also contains Cr^{3+} and Cr^{2+} ions in two structurally nonequivalent, octahedrally coordinated positions of Mg^{2+} ions, namely, the $M1$ and $M2$ positions with local symmetries C_i and C_s, respectively. Bershov *et al.* [12–14] studied crystals of chromium- and aluminum-doped forsterite (Cr,Al) : Mg_2SiO_4 and revealed that, in addition to individual ions $Cr^{3+}(M1)$ and $Cr^{3+}(M2)$, these crystals contain $Cr^{3+}(M1)$–Al^{3+} and $Cr^{3+}(M2)$–Al^{3+} ion pairs (in this case, Al^{3+} ions substitute for Si^{4+} ions and play the role of charge compensators). More recently, Mass *et al.* [15] showed that the formation of these pairs in (Cr,Al) : Mg_2SiO_4 crystals encourages quenching of Cr^{3+} luminescence and an increase in the relative intensity of Cr^{4+} luminescence in the near-IR range, which, in turn, results in an improvement of the laser properties of chromium forsterite.

Earlier [16–19], it was found that the introduction of lithium dopants also brings about a considerable change in the luminescence properties of chromium forsterite. However, the origin of chromium active centers in (Cr,Li) : Mg_2SiO_4 crystals cannot be elucidated using optical spectroscopy alone. In the present work, a detailed EPR investigation of two new Cr^{3+} centers formed in (Cr,Li) : Mg_2SiO_4 crystals was performed for the first time. Preliminary results were reported in our recent work [20].

2. SAMPLE PREPARATION AND EXPERIMENTAL TECHNIQUE

The experiments were performed with single crystals of (Cr,Li) : Mg_2SiO_4 and Cr : Mg_2SiO_4 (for comparison) grown by the Czochralski method using a Kristall-2 apparatus. The batch contained MgO (OSCh 11-2) and finely dispersed SiO_2 (99.99+%, Wacker). Doping impurities in the form of Cr_2O_3 and Li_2CO_3 were introduced into an iridium crucible ($\varnothing 30 \times 30$ mm) immediately prior to the crystal growth. The pulling speed of crystals was 3 mm/h, and the rotational speed was 12 rpm. The crystals were grown in a 100% Ar atmosphere.

Samples were prepared from grown crystals in the form of cubes ($5 \times 5 \times 5$ or $3 \times 3 \times 3$ mm in size). The

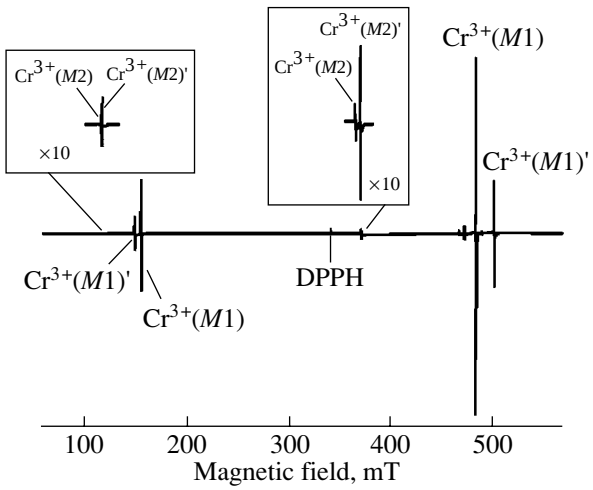

Fig. 1. EPR spectrum of Cr^{3+} centers in a (Cr,Li) : Mg_2SiO_4 crystal in the magnetic field $\mathbf{B}_0 \parallel \mathbf{a}$ ($\mathbf{B}_1 \parallel \mathbf{b}$) at the frequency $\nu_0 = 9.52$ GHz. The most intense narrow lines corresponding to the resonance transitions *1* ⟶ *2* and *3* ⟶ *4* (indicated by arrows in Fig. 3) are shown.

edges of cubic samples were oriented parallel to the **a**, **b**, and **c** crystallographic axes with an accuracy of better than 1.5°. Initially, the orientation of the crystals under investigation was determined from their growth facet and natural pleochroism (the crystals were green, blue, and red in appearance in the **a**, **b**, and **c** directions, respectively). Then, the crystal orientation was refined on a DRON-2 diffractometer. (In what follows, all crystallographic data will be given in the *Pbnm* setting.)

The EPR spectra were recorded on a Varian E-115 spectrometer operating in the *X* band (at a frequency of approximately 9.5 GHz) at room temperature with the use of an E-231/E-232 duplex rectangular cavity (TE_{104} mode) at a modulation frequency of 100 kHz. The static magnetic field was determined using an IMI Sh1-1 magnetic induction meter and a Ch3-38 frequency meter. The calibration was performed against a D-688 DPPH reference sample (Research Institute of Physicotechnical and Radio Engineering Measurements, Russia) containing 4.04×10^{16} paramagnetic centers ($g = 2.0036$). The crystal was rotated in the cavity about two mutually perpendicular axes with the use of a goniometer consisting of two circles, namely, a large horizontal circle with a vernier dial (0.1°) and a small vertical circle with a dial. In order to obtain the angular dependences of the location of the EPR lines (in five degree intervals) in the **ab**, **bc**, and **ca** crystallographic planes, the crystal under investigation was rotated about the **a**, **b**, and **c** axes, respectively. The orientation of the crystal was controlled using the EPR spectrum so that, if required, the sample could be slightly reoriented (to within 1.5°) with the use of the vertical circle of the goniometer through confluence of four (for the orientation of the static magnetic field $\mathbf{B}_0 \parallel \mathbf{a}$, **b**, or **c**) or two (for other directions of the magnetic field $\mathbf{B}_0$ in the crystallographic planes **ab**, **bc**, and **ca**) EPR lines taken from magnetically nonequivalent positions of paramagnetic centers with the magnetic multiplicity $K_m = 4$.

The concentration of paramagnetic centers in the studied samples was determined by comparing the integrated intensities of the EPR lines attributed to these centers and the DPPH reference sample. The double integration of the measured EPR lines was performed according to a standard procedure described in [21].

3. RESULTS

We performed a comparative analysis of the EPR spectra recorded at different orientations of the magnetic field $\mathbf{B}_0$ in the **ab**, **bc**, and **ca** crystallographic planes for both Cr : Mg_2SiO_4 and (Cr,Li) : Mg_2SiO_4 crystals with approximately the same content of chromium and different contents of lithium. It was revealed that the (Cr,Li) : Mg_2SiO_4 crystals contain four types of Cr^{3+} paramagnetic centers (Fig. 1), namely, the two known centers $Cr^{3+}(M1)$ and $Cr^{3+}(M2)$ and two new centers that were preliminarily designated as $Cr^{3+}(M1)'$ and $Cr^{3+}(M2)'$. The number of magnetically nonequivalent positions K_m for both new centers was found to be equal to 4. Recall that, for the known centers $Cr^{3+}(M1)$ and $Cr^{3+}(M2)$, these numbers are equal to 4 and 2, respectively [10].

The angular dependences of the location of the EPR lines for $^{52}Cr^{3+}(M1)'$ and $^{52}Cr^{3+}(M2)'$ centers (Fig. 2) can be adequately described by the spin Hamiltonian

$$H = H_{\mathrm{ZFS}} + H_{\mathrm{Ze}}. \tag{1}$$

Here, the first term characterizes the splitting of the ground level ($^4A_2$) in a zero magnetic field [i.e., zero-field splitting (ZFS)],

$$H_{\mathrm{ZFS}} = \mathbf{S} \cdot \mathbf{D} \cdot \mathbf{S} = D_X S_X^2 + D_Y S_Y^2 + D_Z S_Z^2, \tag{2}$$

and the second term describes the electron Zeeman interaction,

$$\begin{aligned} H_{\mathrm{Ze}} &= \beta \mathbf{B}_0 \cdot \mathbf{g} \cdot \mathbf{S} \\ &= \beta(g_{X'} B_{X'} S_{X'} + g_{Y'} B_{Y'} S_{Y'} + g_{Z'} B_{Z'} S_{Z'}). \end{aligned} \tag{3}$$

Table 1 presents the principal components and directions of the principal axes of the **D** and **g** tensors calculated in terms of the Levenberg–Marquardt nonlinear least-squares method [22] using 204 and 186 experimental points for $Cr^{3+}(M1)'$ and $Cr^{3+}(M2)'$ centers, respectively. This table also lists the standard ZFS parameters $D = 3D_Z/2$ and $E = (D_X - D_Y)/2$ and the splittings δ of the $^4A_2$ orbital singlet into two Kramers doublets $\varepsilon_{\pm 1/2}$ and $\varepsilon_{\pm 3/2}$:

$$\delta = |\varepsilon_{\pm 3/2} - \varepsilon_{\pm 1/2}| = 2\sqrt{D^2 + 3E^2}. \tag{4}$$

It is known [23, 24] that, for a constant frequency ν_0 of the microwave field $B_1\cos 2\pi\nu_0 t$ and scanning of the magnetic field B_0, the integrated intensity I_{int} of the EPR lines is proportional to the concentration of paramagnetic centers in the sample; that is,

$$I_{\text{int}} \propto \frac{N|U_{ji}|^2}{(2S+1)|U_{jj}-U_{ii}|}. \quad (5)$$

Here, N is the concentration of paramagnetic centers in the studied sample and subscripts i and j refer to the levels (with energies E_i and E_j, respectively) characterized by the resonance transition:

$$U_{ji} = \langle j|\mathbf{B}_1 \cdot \mathbf{g} \cdot \mathbf{S}|i\rangle/B_1, \quad (6)$$

$$U_{jj} - U_{ii} = \frac{\partial(E_j - E_i)}{\partial(\beta B_0)} = (\langle j|\mathbf{B}_0 \cdot \mathbf{g} \cdot \mathbf{S}|j\rangle - \langle i|\mathbf{B}_0 \cdot \mathbf{g} \cdot \mathbf{S}|i\rangle)/B_0. \quad (7)$$

The quantities $|U_{ji}|^2$ and $U_{jj} - U_{ii}$ (for the orientations of the magnetic field vectors $\mathbf{B}_0 \parallel \mathbf{a}$ and $\mathbf{B}_1 \parallel \mathbf{b}$ calculated for $Cr^{3+}(M1)'$ and $Cr^{3+}(M2)'$ centers with $S = 3/2$ are given in Table 2. For the DPPH reference, we obtained $S = 1/2$, $|U_{21}|^2 = (g_{\text{DPPH}}/2)^2$, and $U_{22} - U_{11} = g_{\text{DPPH}} = 2.0036$. The concentrations of $Cr^{3+}(M1)'$ and $Cr^{3+}(M2)'$ centers in (Cr,Li) : Mg_2SiO_4 crystals grown from melts with different contents of lithium and approximately the same content of chromium were determined from the intensities of the EPR lines of the transitions *1* ⟶ *2* and *3* ⟶ *4* (indicated by arrows in Fig. 3) with due regard for the parameters given in Table 2. The results obtained are presented in Fig. 4. The mean values (closed and open circles or closed and open squares depicted in Fig. 4) are taken into account in the approximation (nonlinear regression) with the use of the relationship (represented by lines in Fig. 4)

$$N_C = A[1 - \exp(-BN_{\text{Li}})], \quad (8)$$

where N_C is the concentration of paramagnetic centers of the same type (expressed in terms of $N_0 = 4.04 \times 10^{16}$ ions/mg) and N_{Li} is the lithium content in the melt (wt %). As a result, we obtained the following parameters: $A = (0.093 \pm 0.003) \times N_0$ and $B = 15 \pm 2$ wt $\%^{-1}$ for $Cr^{3+}(M1)'$ centers and $A = (0.043 \pm 0.002) \times N_0$ and $B = 16 \pm 3$ wt $\%^{-1}$ for $Cr^{3+}(M2)'$ centers.

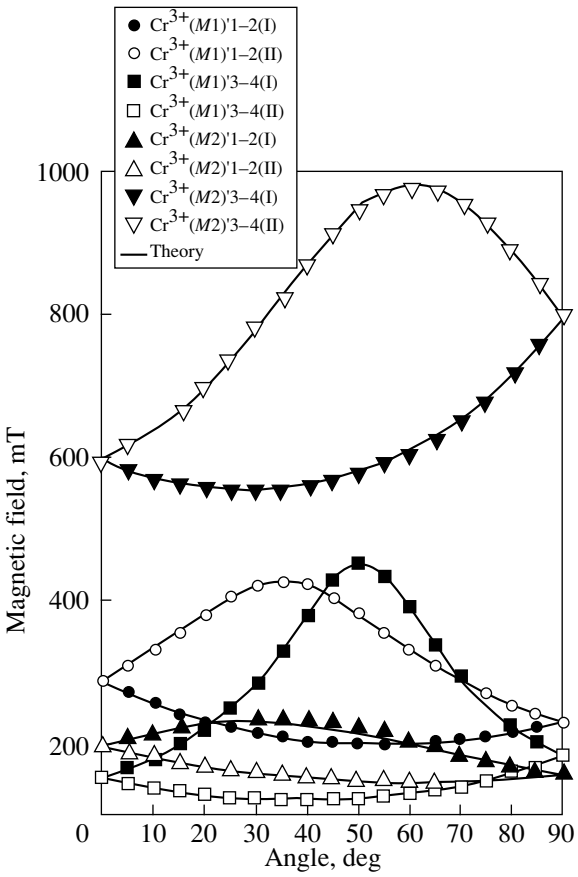

Fig. 2. Angular dependences of the location of the EPR lines (resonance transitions *1* ⟶ *2* and *3* ⟶ *4*) for two pairs (I and II) of magnetically nonequivalent positions of $Cr^{3+}(M1)'$ and $Cr^{3+}(M2)'$ centers in the crystallographic plane **bc**. Points are the experimental data, and solid lines correspond to the results of theoretical calculations (ν_0 = 9.5 GHz).

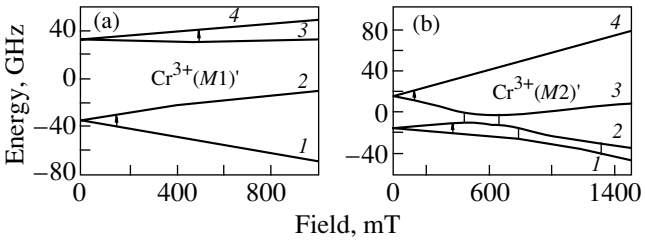

Fig. 3. Energy levels and resonance transitions at different magnetic field strengths (mT): (a) 148.9 and 500.6 for $Cr^{3+}(M1)'$ and (b) 118.4, 369.5, 447.7, 666.7, 792.8, and 1318.6 for $Cr^{3+}(M2)'$. ν_0 = 9.52 GHz. $\mathbf{B}_0 \parallel \mathbf{a}$.

4. DISCUSSION

Paramagnetic centers belonging to one of the two new types were initially designated as $Cr^{3+}(M1)'$, because they are characterized by spin Hamiltonian parameters, directions of the principal axes of the ZFS tensor (Table 1), and angular dependences of the location of the EPR lines (Fig. 2) that are close to the corresponding characteristics of $Cr^{3+}(M1)$ centers [10, 12–14]. For comparison, the parameters taken from [12, 14] for $Cr^{3+}(M1)$ centers are given below: $D = 30.6 \pm 0.2$ GHz, $E = 8.48 \pm 0.05$ GHz, $g_X = g_Y = 1.980 \pm 0.002$, and $g_Z = 1.974 \pm 0.002$. Since the new centers $Cr^{3+}(M1)'$ are observed only in chromium forsterite samples containing lithium, it is reasonable to assume that

Table 1. EPR parameters of Cr^{3+}–Li^+ centers in (Cr,Li) : Mg_2SiO_4 forsterite

Parameters	$Cr^{3+}(M1)'$	$Cr^{3+}(M2)'$
D_X, GHz	–2.17(4)	–2.774(1)
	(58.1, 55.1, 51.1)	(89.2, 30.2, 59.9)
D_Y, GHz	–18.73(5)	–7.340(1)
	(147.8, 73.2, 63.4)	(96.3, 119.9, 30.7)
D_Z, GHz	20.90(5)	10.114(2)
	(85.8, 140.2, 50.5)	(6.4, 93.8, 84.9)
D, GHz	31.35(8)	15.171(3)
E, GHz	8.28(3)	2.283(1)
δ, cm^{-1}	2.300(5)	1.0459(2)
$g_{X'}$	1.9797(3)	1.9747(3)
	(54.6, 59.7, 50.3)	(81.6, 15.1, 77.6)
$g_{Y'}$	1.9801(4)	1.9769(3)
	(144.6, 68.3, 63.5)	(96.5, 101.5, 13.3)
$g_{Z'}$	1.9759(3)	1.9710(2)
	(90.6, 141.2, 51.2)	(10.7, 99.6, 85.4)

Note: The sign of ZFS parameters is not determined. The directions (deg) of the principal axes of the **D** and **g** tensors (for one of four magnetically nonequivalent positions of each center) are specified with respect to the crystallographic axes **a**, **b**, and **c**. The root-mean-square errors in the last significant digit are given in parentheses.

Table 2. Parameters characterizing the integrated intensities [see formula (5)] of EPR lines of the resonance transitions *1* ⟶ *2* and *3* ⟶ *4* (indicated by arrows in Fig. 3) in the magnetic field $\mathbf{B}_0 \parallel \mathbf{a}$ ($\mathbf{B}_1 \parallel \mathbf{b}$) at the frequency $\nu_0 = 9.52$ GHz

Center	Magnetic field B_0, mT	Transition $i \longrightarrow j$	$\lvert U_{ji}\rvert^2$	$U_{jj} - U_{ii}$
$Cr^{3+}(M1)'$	148.9	*1* ⟶ *2*	1.11	4.55
$Cr^{3+}(M1)'$	500.6	*3* ⟶ *4*	4.54	1.25
$Cr^{3+}(M2)'$	369.5	*1* ⟶ *2*	2.51	1.64
$Cr^{3+}(M2)'$	118.4	*3* ⟶ *4*	0.22	5.74

$Cr^{3+}(M1)$–Li^+ ion pairs are formed in these crystals. In particular, earlier EPR investigations revealed Cr^{3+}–Li^+ ion pairs in crystals of (Cr,Li) : Cs_2CdCl_4 [25] and (Cr,Li) : A_2MF_4 (A = K, Rb, or Cs and M = Zn or Cd) [26, 27] (see also theoretical studies [28, 29]). In these crystals, two impurity ions, namely, trivalent chromium Cr^{3+} and monovalent lithium Li^+, substitute for two nearest neighbor bivalent ions M^{2+}, thus retaining the electric charge balance. A similar situation, i.e., when two ions of different valences (Cr^{3+} and Li^+) substitute for two bivalent ions Mg^{2+} simultaneously, occurs in chromium- and lithium-doped forsterite.

When identifying $Cr^{3+}(M2)$–Li^+ centers of the other new type, which were initially designated as $Cr^{3+}(M2)'$, we were guided by similar considerations. These centers are analogs of the known $Cr^{3+}(M2)$ centers with the following spin Hamiltonian parameters [12, 14]: $D = 21.1 \pm 0.4$ GHz, $E = 2.60 \pm 0.05$ GHz, $g_X = g_Z = 1.970 \pm 0.002$, and $g_Y = 1.979 \pm 0.002$. It should be noted that, compared to the $Cr^{3+}(M1)$–Li^+ centers, the $Cr^{3+}(M2)$–Li^+ centers are more strongly affected by the nearest neighbor ions Li^+. This manifests itself in an appreciable decrease in the magnitude of the ZFS parameters (Table 1), an increase in the magnetic multiplicity to $K_m = 4$, and a rotation of the **X** and **Y** axes of the ZFS tensor through an angle of ~30° with respect to the corresponding axes for $Cr^{3+}(M2)$ centers [13, 14].

It is known [30] that crystals with space group $Pbnm(D_{2h}^{16})$ contain no active centers other than those with local symmetries C_i, C_s, and C_1. For symmetry C_i [as in the case of $Cr^{3+}(M1)$ centers] or C_1, the number of magnetically nonequivalent positions of a particular center is determined to be $K_m = 4$ and the preferred direction is absent [30]. For symmetry C_s [as in the case of $Cr^{3+}(M2)$ and $Cr^{3+}(M2)$–Al^{3+} centers], the number of magnetically nonequivalent positions of a particular center in the forsterite is $K_m = 2$ and there exists only one preferred direction (the principal axis **Y** [13, 14]) along the **c** axis. It is evident that, when the Cr^{3+} ion occupies the $M2$ position within the mirror-reflection plane in the neighborhood of an Li^+ ion lying off this plane, the newly formed center $Cr^{3+}(M2)$–Li^+ has a lower C_1 symmetry instead of C_s symmetry. Similarly, the stabilization of the $Cr^{3+}(M1)$–Li^+ ion pair is accompanied by a lowering of the symmetry from C_i to C_1 (in our opinion, the formation of an Li^+–$Cr^{3+}(M1)$–Li^+ ion triad with C_i symmetry is unlikely).

Our calculations (with structural data taken from [31]) of different interatomic distances and the corresponding directions in the forsterite unit cell demonstrated that the vector **M2**–**M1** with direction cosines (0.0126, 0.8842, 0.4669) and a magnitude of 0.3202 nm is very similar in orientation to the principal axis **X** of the **D** tensor for $Cr^{3+}(M2)'$ centers (Table 1); in this case, the angle between the two directions is equal to 3.1°. This gives grounds to assume that the Cr^{3+} and Li^+ ions are located at the adjacent positions $M2$ and $M1$ (Fig. 5). Hence, the hypothetical model of a $Cr^{3+}(M2)'$ center can be represented as $Cr^{3+}(M2)$–$Li^+(M1)$. Let us now consider a $Cr^{3+}(M1)'$ center. In this case also, among all the vectors **M1**–**Mj** (j = 1, 2) in the forsterite unit cell, the vector **M1**–**M2**, having the same magnitude but opposite direction, is close in orientation to the principal axis **Z** of the ZFS tensor (the corresponding angle is equal to 12.3°) for one of the four magnetically nonequivalent positions of this center, except for the $M1$ and $M2$ positions separated by a distance of 0.8632 nm (the angle is 9.2°). Therefore, we can make the assumption that, upon the formation of a $Cr^{3+}(M1)'$

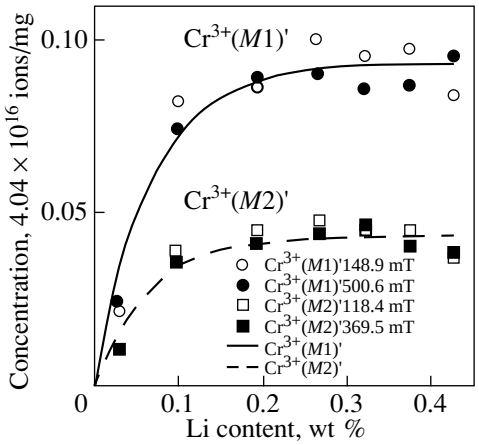

Fig. 4. Concentration of $Cr^{3+}(M1)'$ and $Cr^{3+}(M2)'$ centers in (Cr,Li) : Mg_2SiO_4 crystals (expressed in units of 4.04×10^{16} ions/mg) as a function of the lithium content in the melt. The chromium content in the melt is approximately equal to 0.05–0.06 wt %.

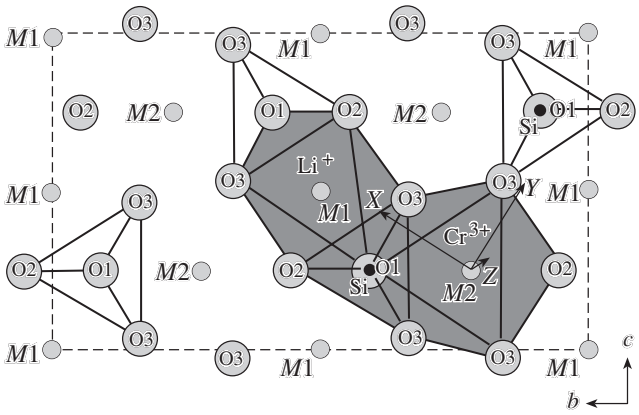

Fig. 5. Structural model of a $Cr^{3+}(M2)$–$Li^{+}(M1)$ center.

center, as for the $Cr^{3+}(M2)'$ center, the same adjacent Mg^{2+} positions ($M1$ and $M2$) are occupied by Cr^{3+} and Li^{+} ions but in the reverse order; i.e., the structural model of a $Cr^{3+}(M1)'$ center can be represented as $Cr^{3+}(M1)$–$Li^{+}(M2)$.

Analysis of the concentrations of $Cr^{3+}(M1)'$ and $Cr^{3+}(M2)'$ centers in chromium- and lithium-doped forsterite crystals [see Fig. 4 and compare the constants A for $Cr^{3+}(M1)'$ and $Cr^{3+}(M2)'$ in the text below formula (8)] revealed that, upon formation of Cr^{3+}–Li^{+} ion pairs in (Cr,Li) : Mg_2SiO_4 crystals, the $M1$ position for chromium is two times more preferable than the $M2$ position. According to different authors, this ratio for individual ions $Cr^{3+}(M1)$ and $Cr^{3+}(M2)$ varies from 3 : 2 [10] to 4 : 1 [32].

In our consideration of the experimental results, we did not proceed *a priori* from the assumption that the principal axes of the **D** tensor are aligned with those of the **g** tensor, unlike the authors of all the works mentioned in the introduction and concerned with EPR investigations of chromium ions in chromium-doped forsterite. Generally speaking, this assumption is incorrect because low-symmetric effects can manifest themselves in the case of centers with local symmetries C_i, C_s, and C_1 [30]. It is found that the low-symmetric effect of misalignment of the aforementioned axes is most clearly pronounced for $Cr^{3+}(M2)$–$Li^{+}(M1)$ centers (Table 1): the misalignment of the principal axes **X** and **X'** (**Y** and **Y'**) amounts to approximately 19°.

In the luminescence spectra of Cr : Mg_2SiO_4 crystals at a relatively low temperature, the R_1 line observed in the vicinity of 692.7 nm is attributed to $Cr^{3+}(M1)$ centers [33, 34]. It turned out that the ZFS parameters for centers $Cr^{3+}(M1)$ [12, 14] and $Cr^{3+}(M1)'$ (Table 1) are close in magnitude. This suggests that the introduction of Li^{+} ion impurities into the forsterite crystal brings about a weak disturbance of the crystal field experienced by the nearest neighbor ions $Cr^{3+}(M1)$. As a consequence, the coexistence of $Cr^{3+}(M1)$ and $Cr^{3+}(M1)'$ centers in (Cr,Li) : Mg_2SiO_4 crystals should manifest itself in the luminescence spectra of these crystals in the form of two R_1 lines (the $^2E \longrightarrow {}^4A_2$ transition) that are almost equally split ($\delta \approx 2.3$ cm^{-1}) at sufficiently low temperatures. In actual fact, the luminescence spectra of (Cr,Li) : Mg_2SiO_4 crystals at $T = 77$ K exhibit two narrow R_1 lines in the vicinity of 692.7 and 699.6 nm [19]. Reasoning from the results obtained in the present work, the R_1 line observed at 699.6 nm in the luminescence spectra of (Cr,Li) : Mg_2SiO_4 crystals was assigned to the $Cr^{3+}(M1)'$ center for the first time.

ACKNOWLEDGMENTS

We would like to thank L.D. Iskhakova and A.G. Makarevich (Research Center of Fiber Optics, Institute of General Physics, Russian Academy of Sciences) for their assistance in preparing the oriented samples used in our investigation.

This work was supported by the Russian Foundation for Basic Research, project nos. 00-15-96715, 00-02-16103, and 01-05-65348.

REFERENCES

1. V. Petricevic, S. K. Gayen, and R. R. Alfano, Appl. Phys. Lett. **53** (26), 2590 (1988).
2. H. R. Verdun, L. M. Thomas, D. M. Andrauskas, *et al.*, Appl. Phys. Lett. **53** (26), 2593 (1988).
3. V. G. Baryshevskiĭ, M. V. Korzhik, A. E. Kimaev, *et al.*, Zh. Prikl. Spektrosk. **53** (1), 7 (1990).

4. V. G. Baryshevski, M. V. Korzhik, M. G. Livshitz, *et al.*, OSA Proc. Adv. Solid-State Lasers **10**, 26 (1991).
5. M. H. Garrett, V. H. Chan, H. P. Jenssen, *et al.*, OSA Proc. Adv. Solid-State Lasers **10**, 76 (1991).
6. K. R. Hoffman, J. Casas-Gonzalez, S. M. Jacobsen, and W. M. Yen, Phys. Rev. B **44** (22), 12589 (1991).
7. M. L. Meilman and M. G. Livshitz, OSA Proc. Adv. Solid-State Lasers **13**, 39 (1992).
8. M. H. Whitmore, A. Sacra, and D. J. Singel, J. Chem. Phys. **98** (5), 3656 (1993).
9. D. E. Budil, D. G. Park, J. M. Burlitch, *et al.*, J. Chem. Phys. **101** (5), 3538 (1994).
10. H. Rager, Phys. Chem. Miner. **1** (4), 371 (1977).
11. V. F. Tarasov, G. S. Shakurov, and A. N. Gavrilenko, Fiz. Tverd. Tela (St. Petersburg) **37** (2), 499 (1995) [Phys. Solid State **37**, 270 (1995)].
12. L. V. Bershov, R. M. Mineeva, A. V. Speranskiĭ, and S. Hafner, Dokl. Akad. Nauk SSSR **260** (1), 191 (1981).
13. L. V. Bershov, R. M. Mineeva, A. V. Speranskiĭ, and S. Hafner, Mineral. Zh., No. 3, 62 (1981).
14. L. V. Bershov, J.-M. Gaite, S. S. Hafner, and H. Rager, Phys. Chem. Miner. **9** (3–4), 95 (1983).
15. J. L. Mass, J. M. Burlitch, D. E. Budil, *et al.*, Chem. Mater. **7** (5), 1008 (1995).
16. N. Nishide, Y. Segawa, P. H. Kim, *et al.*, Resa Kagaku Kenkyu, No. 7, 89 (1985).
17. N. Nishide, Y. Segawa, P. H. Kim, and S. Namba, Resa Kagaku Kenkyu, No. 8, 97 (1986).
18. A. Sugimoto, Y. Nobe, T. Yamazaki, *et al.*, Phys. Chem. Miner. **24** (5), 333 (1997).
19. A. V. Gaister, V. A. Smirnov, and E. V. Zharikov, in *Proceedings of the Fourth International Conference "Single Crystal Growth and Heat & Mass Transfer," Obninsk, 2001*, Vol. 2, p. 272.
20. I. D. Ryabov, A. V. Gaister, and E. V. Zharikov, Bull. Soc. Fr. Mineral. Cristallogr. **13** (3), 106 (2001).
21. T.-T. Chang, Magn. Reson. Rev. **9** (1–3), 65 (1984).
22. W. H. Press, B. P. Flannery, S. A. Teukolsky, and W. T. Vetterling, *Numerical Recipes: The Art of Scientific Computing* (Cambridge Univ. Press, Cambridge, 1986), p. 523.
23. T.-T. Chang, D. Foster, and A. H. Kahn, J. Res. Natl. Bur. Stand. **83** (2), 133 (1978).
24. C. E. Forbes, J. Chem. Phys. **79** (6), 2590 (1983).
25. D. Kay and G. L. McPherson, J. Phys. C **14** (22), 3247 (1981).
26. H. Takeuchi and M. Arakawa, J. Phys. Soc. Jpn. **52** (1), 279 (1983).
27. M. Arakawa, H. Ebisu, and H. Takeuchi, J. Phys. Soc. Jpn. **55** (8), 2853 (1986).
28. M.-L. Du and M.-G. Zhao, Solid State Commun. **76** (4), 565 (1990).
29. S.-Y. Wu and W.-C. Zheng, Physica B (Amsterdam) **262** (1–2), 84 (1999).
30. M. L. Meĭl'man and M. I. Samoĭlovich, *Introduction to the Spectroscopy of Electron Paramagnetic Resonance of Activated Single Crystals* (Atomizdat, Moscow, 1977).
31. J. R. Smyth and R. M. Hazen, Am. Mineral. **58** (7–8), 588 (1973).
32. J. L. Mass, J. M. Burlitch, D. E. Budil, *et al.*, Chem. Mater. **7** (5), 1008 (1995).
33. W. Jia, H. Liu, S. Jaffe, *et al.*, Phys. Rev. B **43** (7), 5234 (1991).
34. T. J. Glynn, G. F. Imbusch, and G. Walker, J. Lumin. **48–49** (2), 541 (1991).

Translated by O. Borovik-Romanova

Physics of the Solid State, Vol. 45, No. 1, 2003, pp. 57–60. Translated from Fizika Tverdogo Tela, Vol. 45, No. 1, 2003, pp. 56–59.

SEMICONDUCTORS AND DIELECTRICS

Thermal Conductivity of Crystalline Chrysotile Asbestos

Yu. A. Kumzerov*, L. S. Parfen'eva*, I. A. Smirnov*, H. Misiorek, J. Mucha**, and A. Jezowski****

** Ioffe Physicotechnical Institute, Russian Academy of Sciences, Politekhnicheskaya ul. 26, St. Petersburg, 194021 Russia*
e-mail: Igor.Smirnov@pop.ioffe.rssi.ru

*** Institute of Low-Temperature and Structural Research, Polish Academy of Sciences, Wroclaw, 50-950 Poland*

Received April 9, 2002

Abstract—The thermal conductivity of crystalline chrysotile asbestos made up of hollow tubular $Mg_3Si_2O_5(OH)_4$ filaments is measured in the range 5–300 K. The paper discusses the possibility of using this material in studies of the thermal conductivity of thin filaments of metals and semiconductors incorporated into the channels of crystalline chrysotile asbestos tubes. © *2003 MAIK "Nauka/Interperiodica".*

Considerable effort has been recently focused in leading research laboratories of Europe, the USA, and Japan, on studies of the physical properties of small metal and semiconductor particles in the form of clusters, cluster crystals, ultrathin filaments, and nanocomposites; these studies were undertaken with the intention to develop new materials for use in present-day technology and nanoelectronics and to investigate their fundamental physical characteristics [1, 2].

Studying the physical properties of these objects in the free state is usually impossible. Therefore, they are loaded in nanopores or narrow channels of various dielectric porous host matrices, more specifically, porous glasses, zeolites, opals, and asbestos.

Here, we deal with the dielectric host matrix of crystalline chrysotile asbestos.

Chrysotile asbestos, the hydrated magnesium silicate $Mg_3Si_2O_5(OH)_4$, is a filamentary material of the serpentine group with the following chemical composition (which can vary from one deposit to another): ~37–44% SiO_2, ~39–44% MgO, and ~12–15% H_2O (bound water). It may have Fe, Al, Ca, Ni, Mn, and Na impurities.

Chrysotile asbestos has a remarkable, highly unusual structure. It consists essentially of structural layers confined on the inside by a framework of silica and on the outside by a framework of magnesium hydroxide [2–5] (Fig. 1a). Because of the inner framework being smaller in size than the outer one, the chrysotile asbestos layers tend to roll into cylinders (tubes), with the silica layer on the inner side. Such tubes have an outer diameter d_1 ~ 300–500 Å and an inner diameter d_2 ~ 20–150 Å [2, 4] (Figs. 1b, 1c). The space between the tubes (denoted by *1* in Fig. 1b) is usually filled by an amorphous mass of the tube material. On the whole, the crystal lattice of the asbestos layers belongs to the monoclinic system [4, 6–14] with the following parameters: a = 5.30 Å, b = 9.10 Å, c = 7.32 Å, and $\beta = 93°$ [14]. The a axis is directed along the tube channels (Fig. 1d). The tube packing structure is close to hexagonal [2].

The porosity of chrysotile asbestos (the ratio of the channel to the total sample volume) is ~5–6% [2]. The porous structure of chrysotile asbestos was directly studied using electron microscopy in [14].

The channels of the chrysotile asbestos tubes can be filled under pressure by molten Hg, Sn, Bi, In, Pb, Se, and Te [2, 15] to form regular systems of ultrathin parallel filaments, which do not interact with one another due to their large separation. These filaments are similar, in many respects, to quantum wires.

The physical properties of such thin metal and semiconductor filaments that fill the channels of chrysotile asbestos tubes have been extensively studied in recent years. The effect of channel size on the superconducting transition temperature, the melting and solidification points, current–voltage characteristics, electrical resistivity, heat capacity, and other properties of materials loaded in chrysotile asbestos have been investigated (see, e.g., [16–24]).

The physics of quasi-one-dimensional metal and semiconductor systems has aroused considerable research interest, because such objects possess properties that are radically different from those of bulk materials [1, 2].

The behavior of thermal conductivity κ of ultrathin filaments (quantum wires) has also attracted recent attention (primarily that of theoreticians). However, experimental data on the magnitude of κ of metals and semiconductors incorporated in asbestos channels are presently lacking. There is likewise no information available on the thermal conductivity of crystalline chrysotile asbestos over a broad temperature range. This prompted us to attempt to determine the magnitude of thermal conductivity of crystalline chrysotile asbestos at temperatures from 5 to 300 K and to esti-

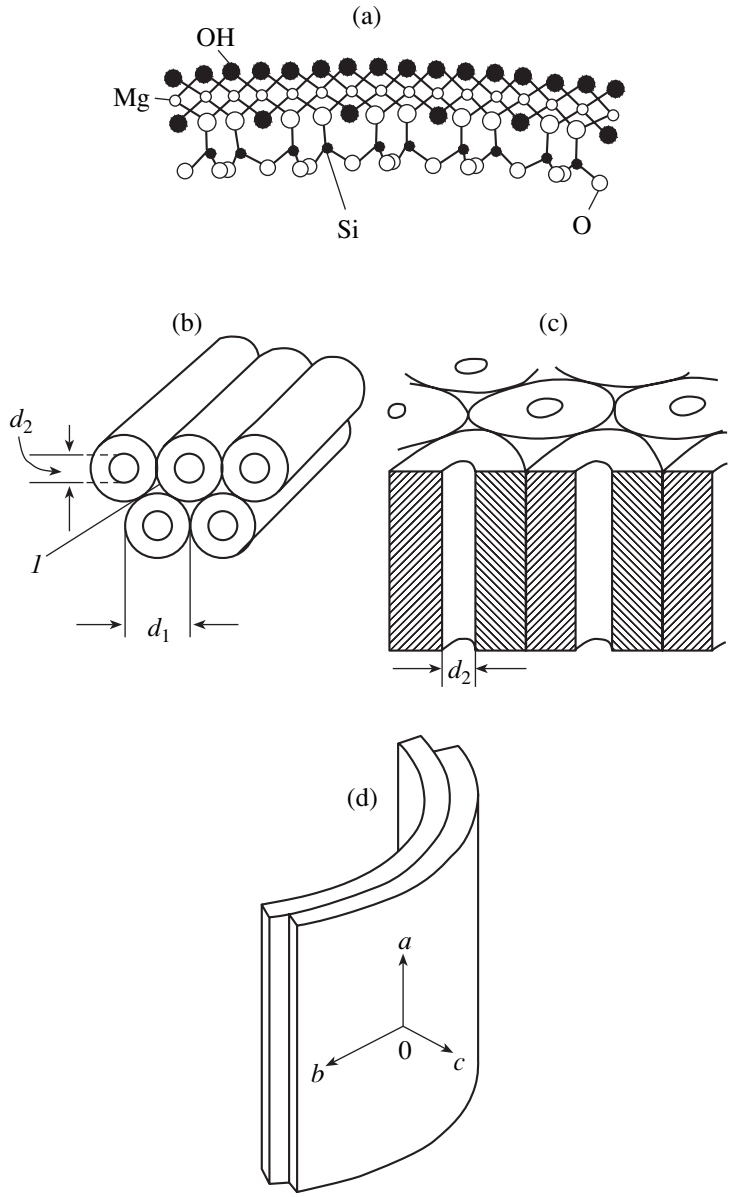

Fig. 1. (a) Crystal layers forming the filamentary structure of chrysotile asbestos [5]; (b) system of closely packed tubular filaments of chrysotile asbestos [2]: (*1*) space between asbestos tubes; (c) schematic representation of a cut through the tubular filaments of chrysotile asbestos [2]; and (d) diagram illustrating the orientation of the unit-cell axes of chrysotile asbestos with respect to the curved layers of the structure [4].

mate the possibility of its use as a dielectric host matrix in studies of κ of thin metal and semiconductor filaments incorporated in the nanochannels of asbestos tubes.

We measured the thermal conductivity of a sample of natural "brittle" chrysotile asbestos from an Uzbekistan deposit. The sample size was $5.5 \times 6.5 \times 12$ mm. Its inner and outer tube diameters were $d_2 \sim 50$ Å and $d_1 = 300$ Å, respectively.

Before the κ measurements, the sample was annealed in air at ~150°C to remove the water possibly present in the tubes. The bound water was not lost from the sample at this temperature [25]. After the annealing, a thin layer of varnish was deposited on the sample end faces to prevent penetration of atmospheric water into the asbestos tubes when mounting the sample in the experimental setup. The thermal conductivity of asbestos was measured within the temperature range 5–300 K on a setup similar to that employed in [26].

The experimental data obtained on the κ of crystalline chrysotile asbestos are displayed in Fig. 2. Since chrysotile asbestos is an insulator, the experimentally measured κ is actually the lattice heat conductivity κ_{ph} ($\kappa = \kappa_{ph}$).

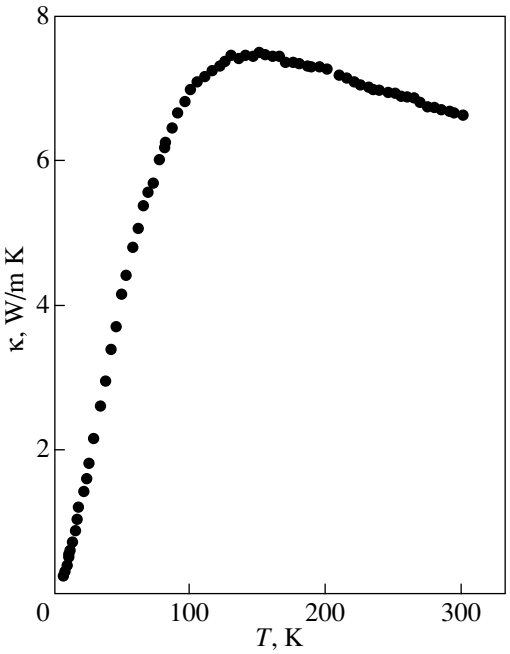

Fig. 2. Thermal conductivity of crystalline chrysotile asbestos plotted as a function of temperature. The heat flux was directed along the asbestos tubes (along the *a* direction).

We note two features observed in the $\kappa(T)$ dependence of chrysotile asbestos: (i) the presence of a maximum in the thermal conductivity at a fairly high temperature, ~150 K, and (ii) the relatively small magnitude of κ at low temperatures ($T \lesssim 20$–30 K).

Figure 3 compares our data on κ of crystalline chrysotile asbestos (curve *1*) with the literature data on κ_{ph} of single crystals of MgO [27] (*2*) and SiO_2 [28] (*3*) (the main components of the chrysotile asbestos $Mg_3Si_2O_5(OH)_4$), as well as information on the thermal conductivity of asbestos wool (*4*) [29]. Curve 5 was derived from data on crystalline chrysotile asbestos calculated using a relation from [30] with account taken of the porosity of our sample (~5%).

The appearance of a maximum in $\kappa(T)$ of crystalline chrysotile asbestos at fairly high temperatures, as compared, for instance, to those for MgO and SiO_2 single crystals (Fig. 3), can be qualitatively accounted for by the size effect, whereby the phonon mean free path becomes comparable to the thickness of the asbestos tube wall. In the sample studied by us, this thickness was ~100–125 Å. Unfortunately, we did not succeed in finding any literature data on the sound velocity v and

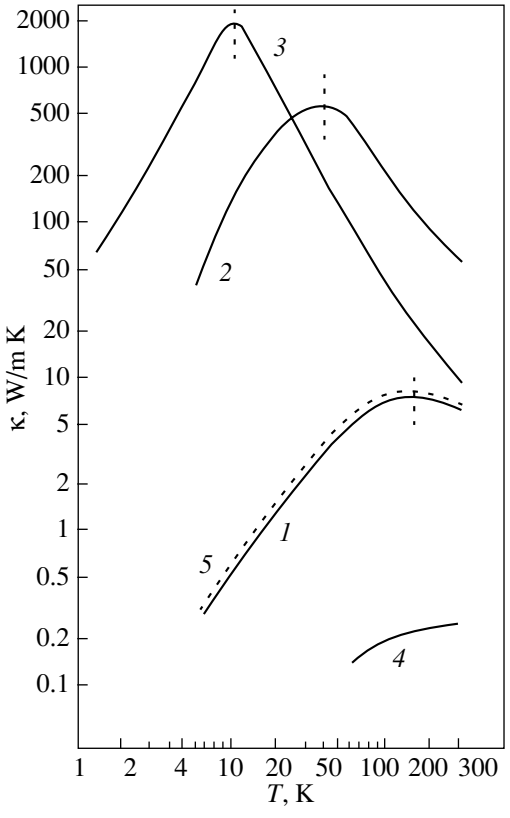

Fig. 3. Temperature dependence of the thermal conductivity of (*1*) crystalline chrysotile asbestos, (*2*) single-crystal MgO [27], (*3*) SiO_2 along the *c* axis [28], and (*4*) asbestos wool [29]; (*5*) thermal conductivity of crystalline chrysotile asbestos calculated with inclusion of sample porosity. Vertical dashed lines on the curves specify the temperature of the maximum for the corresponding material.

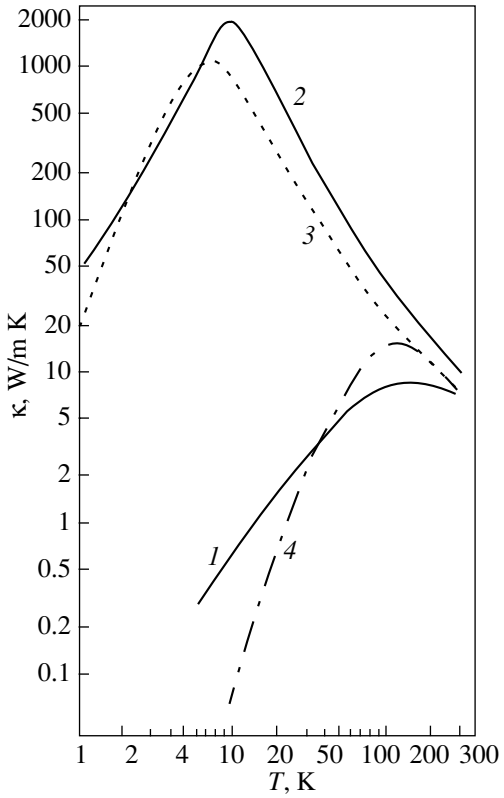

Fig. 4. Temperature dependence of the thermal conductivity of (*1*) crystalline chrysotile asbestos, (*2*) single crystals of SiO_2 [28] and (*3*) of NaCl [28], and (*4*) crystalline NaCl for l = const = 100 Å [31].

specific heat $C_v(T)$ for crystalline chrysotile asbestos, and, therefore, we could not calculate the mean free path l in this material from the well-known expression

$$l = \frac{3\kappa_{ph}}{C_v \bar{v}}.$$

Figure 4 qualitatively compares the behavior of κ_{ph} for chrysotile asbestos (*1*) and for an NaCl single crystal experiencing the size effect, with l = const = 100 Å [31] (curves *3*, *4*). Also shown are the data on κ_{ph} for a SiO_2 single crystal [28] (*2*). The conclusion as to the $\kappa(T)$ of crystalline chrysotile asbestos being dominated by the size effect can be drawn, however, only after experimental data are obtained on $C_v(T)$ and $\bar{v}$.

A comparison of our data on $\kappa(T)$ of crystalline chrysotile asbestos with the available information on the thermal conductivity of pure metals and some semiconductors [28] allows us to conclude that this material can be used as a dielectric host matrix over a fairly broad temperature range (where κ of asbestos is lower by several orders of magnitude than that of the filler materials) in studies of the thermal conductivity of thin filaments of metals and semiconductors incorporated into asbestos tubes. We hope to obtain evidence supporting this conclusion in the experiments recently begun at our laboratories.

ACKNOWLEDGMENTS

This work was conducted within bilateral agreements between the Russian and Polish Academies of Sciences and was supported by the Russian Foundation for Basic Research, project no. 02-02-17657.

REFERENCES

1. V. N. Bogomolov and Yu. A. Kumzerov, Preprint No. 971, FTI im. A. F. Ioffe AN SSSR (Ioffe Physicotechnical Institute, Academy of Sciences of USSR, Leningrad, 1985).
2. Yu. A. Kumzerov, in *Nanostructured Films and Coatings*, Ed. by Gan-Moog Chow, I. A. Ovid'ko, and T. Tsakalakos (Kluwer, Dordrecht, 2000), NATO ASI Series, Partnership Sub-series 3: High Technology, Vol. 78, p. 63.
3. V. V. Bekhterev and V. I. Solomonov, Neorg. Mater. **31** (4), 567 (1995).
4. W. L. Bragg and G. F. Claringbull, *Crystal Structure of Minerals* (Bell, London, 1965; Mir, Moscow, 1967).
5. V. N. Bogomolov, Usp. Fiz. Nauk **124** (1), 171 (1978) [Sov. Phys. Usp. **21**, 77 (1978)].
6. B. E. Warren and W. L. Bragg, Z. Kristallogr. **76**, 201 (1930).
7. B. E. Warren and K. W. Herring, Phys. Rev. **59**, 925 (1941).
8. E. Aruya, Miner. Mag. **27**, 188 (1945).
9. N. N. Padurow, Acta Crystallogr. **3**, 200 (1950).
10. E. J. W. Whittaker, Acta Crystallogr. **9**, 855 (1956).
11. G. W. Brindley, *X-ray Identification of Crystal Structures of Clay Minerals* (Mineralogical Society, London, 1952), Chap. 2.
12. H. Jagodzinski and G. Kunze, Neues Jahrb. Mineral., Monatsh., No. 7, 134 (1954).
13. J. E. W. Whittaker and J. Zussmann, Miner. Mag. **31**, 107 (1956).
14. K. Yada, Acta Crystallogr. **23**, 704 (1967).
15. V. N. Bogomolov, Fiz. Tverd. Tela (Leningrad) **13** (3), 815 (1971) [Sov. Phys. Solid State **13**, 672 (1971)].
16. V. N. Bogomolov, V. K. Krivosheev, and Yu. A. Kumzerov, Fiz. Tverd. Tela (Leningrad) **13** (5), 3720 (1971) [Sov. Phys. Solid State **13**, 3148 (1971)].
17. V. N. Bogomolov and V. K. Krivosheev, Fiz. Tverd. Tela (Leningrad) **14** (4), 1238 (1972) [Sov. Phys. Solid State **14**, 1059 (1972)].
18. V. N. Bogomolov and Yu. A. Kumzerov, Pis'ma Zh. Éksp. Teor. Fiz. **21** (7), 434 (1975) [JETP Lett. **21**, 198 (1975)].
19. V. N. Bogomolov, E. V. Kolla, Yu. A. Kumzerov, *et al.*, Solid State Commun. **35** (4), 363 (1980).
20. V. N. Bogomolov, B. E. Kvyatkovskiĭ, E. V. Kolla, *et al.*, Fiz. Tverd. Tela (Leningrad) **23** (7), 2173 (1981) [Sov. Phys. Solid State **23**, 1271 (1981)].
21. V. N. Bogomolov, Yu. A. Kumzerov, and V. A. Pimenov, Fiz. Tverd. Tela (Leningrad) **23** (8), 2506 (1981) [Sov. Phys. Solid State **23**, 1471 (1981)].
22. V. N. Bogomolov, E. V. Kolla, and Yu. A. Kumzerov, Solid State Commun. **46** (2), 159 (1983).
23. V. N. Bogomolov, E. V. Kolla, and Yu. A. Kumzerov, Solid State Commun. **46** (5), 383 (1983).
24. V. N. Bogomolov, K. V. Kolla, and Yu. A. Kumzerov, Pis'ma Zh. Éksp. Teor. Fiz. **41** (1), 28 (1985) [JETP Lett. **41**, 34 (1985)].
25. L. A. Drobyshev and Ya. Ya. Govorova, Kristallografiya **16** (3), 544 (1971) [Sov. Phys. Crystallogr. **16**, 460 (1971)].
26. A. Jezowski, J. Mucha, and G. Pompe, J. Phys. D **7**, 1247 (1974).
27. I. P. Morton and M. F. Lewis, Phys. Rev. B **3** (2), 552 (1971).
28. *Heat Conductivity of Solids: A Handbook*, Ed. by F. S. Okhotin (Énergoatomizdat, Moscow, 1984).
29. *Thermophysical Properties of Materials under Low Temperatures: A Handbook* (Mashinostroenie, Moscow, 1982).
30. E. Ya. Litovskiĭ, Izv. Akad. Nauk SSSR, Neorg. Mater. **16** (3), 559 (1980).
31. V. N. Bogomolov, N. F. Kartenko, D. A. Kurdyukov, *et al.*, Fiz. Tverd. Tela (St. Petersburg) **41** (2), 348 (1999) [Phys. Solid State **41**, 313 (1999)].

Translated by G. Skrebtsov

Physics of the Solid State, Vol. 45, No. 1, 2003, pp. 6–10. Translated from Fizika Tverdogo Tela, Vol. 45, No. 1, 2003, pp. 8–11.

METALS AND SUPERCONDUCTORS

Low-Temperature Anomalies in MgB_2 Thermal Expansion

N. V. Anshukova*, B. M. Bulychev, A. I. Golovashkin*, L. I. Ivanova***, I. B. Krynetskiĭ**, and A. P. Rusakov*****

** Lebedev Physical Institute, Russian Academy of Sciences, Leninskiĭ pr. 53, Moscow, 119991 Russia*

e-mail: golov@sci.lebedev.ru

*** Moscow State University, Vorob'evy gory, Moscow, 119899 Russia*

**** Moscow State Institute of Steel and Alloys, Leninskiĭ pr. 4, Moscow, 117936 Russia*

Received January 31, 2002

Abstract—The thermal expansion coefficient $\alpha(T)$ of MgB_2 was measured at low temperatures both in a zero magnetic field and at $H = 36$ kOe. As in the oxide HTSCs, a region of anomalous (negative) thermal expansion and a strong effect of magnetic field on $\alpha(T)$ were revealed. The results obtained indicate the anomalous properties of MgB_2 and the oxide HTSCs to follow a common pattern. *© 2003 MAIK "Nauka/Interperiodica".*

The discovery of superconductivity with a critical temperature $T_c = 40$ K in MgB_2 was recently announced [1]. The new superconductor is highly promising for potential application. The currently available information on the properties of MgB_2 allow only controversial conclusions to be drawn as to the nature of superconductivity in this compound [2–5]; in other words, there are still no grounds to unambiguously decide whether MgB_2 belongs to conventional or oxide high-temperature superconductors (HTSCs).

The oxide HTSCs are known to exhibit a number of characteristic anomalies in their properties. In particular, thermal expansion of high-quality oxide HTSCs reveals a low-temperature anomaly, namely, a negative thermal expansion coefficient α [6]. Furthermore, magnetic field was found to exert a strong effect on the anomalous temperature dependence $\alpha(T)$ [7]. These anomalies are not observed in conventional superconductors. Thus, measurement of these characteristics in MgB_2 will make it possible to establish to which group of superconductors this compound belongs, which is an important aspect in revealing the mechanism of its superconductivity.

We report here on measurements of the temperature dependence of thermal expansion of MgB_2 both in a zero magnetic field and in a field $H = 36$ kOe. In addition, we measured the dependence of thermal expansion on a magnetic field up to $H \approx 42$ kOe at a fixed temperature. At low temperatures for $H = 0$, a region of negative thermal expansion characteristic of the oxide HTSCs was found. It was also found that the magnetic field weakens this anomaly.

MgB_2 samples were prepared by hot pressing. The starting magnesium diboride was synthesized by reacting metallic magnesium with elemental boron using the standard technique at a temperature of 950–1000°C for 5 h under atmospheric pressure. The single-phase material thus obtained contained more than 98% of the main compound. MgB_2 pellets were sintered under a pressure of 50 kbar at a temperature of 950–1000°C. The density of the sintered samples was 97% of the figure obtained by x-ray diffraction. The x-ray diffractogram of a single-phase sample recorded on a DRON-4 diffractometer is in full agreement with the figures listed in the ASTM standard catalog. It is on such samples that we measured the specific heat and other characteristics and revealed a jump in the specific heat at the superconducting transition at $T \approx 39$ K.

The sample chosen for dilatometric measurements was a 4-mm-high cylinder 3 mm in diameter. The change in sample length $\Delta L/L$ was measured with a strain pickup with a sensitivity of $\sim 10^{-7}$ [7]. The magnetic field was oriented parallel to the direction of strain measurement. The setup was calibrated through repeated measurement of the temperature dependence of thermal expansion $\alpha(T)$ of rare-earth oxide samples. These measurements showed $\alpha(T)$ of the above samples to follow a normal course throughout the low-temperature region covered; i.e., the thermal expansion coefficient of these compounds is positive ($\alpha > 0$) and does not reverse sign.

Figure 1a displays the temperature dependence of the quantity $\Delta L/L$ (L is the sample length) obtained in this study on MgB_2 for $H = 0$. Also presented for comparison in Fig. 1b are data for $YBa_2Cu_3O_{7-x}$ [8], $Bi_2Sr_2CaCu_2O_8$ [9], $La_{2-x}Sr_xCuO_4$ ($x = 0.1$) [7], and $Ba_{1-x}K_xBiO_3$ ($x = 0.13$) [7] obtained earlier. For MgB_2, $\Delta L/L < 0$ in the interval $7 \le T \le 16.5$ K. The thermal expansion coefficient $\alpha = (1/L)dL/dT$ is negative in the temperature interval of approximately 7–11 K. As seen from Fig. 1b, oxide HTSCs also exhibit negative thermal expansion $\alpha(T)$ at low temperatures; i.e., MgB_2

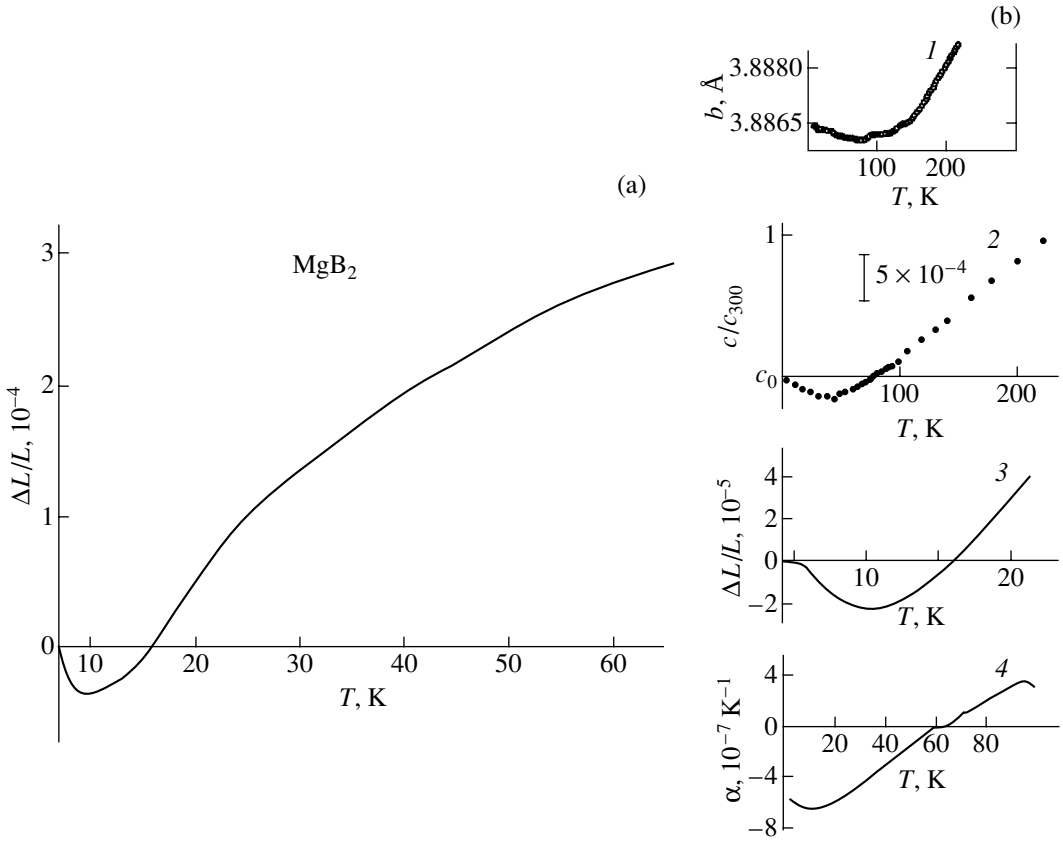

Fig. 1. (a) Temperature dependence of thermal expansion $\Delta L/L$ for MgB_2 and (b) its comparison with the data obtained for other HTSCs. (*1*) $YBa_2Cu_3O_{7-x}$ (*b* is the lattice constant along the *b* axis) [8]; (*2*) $Bi_2Sr_2CaCu_2O_8$ (*c* is the lattice constant along the *c* axis, c_{300} is the lattice constant at $T = 300$ K) [9]; (*3*) $La_{2-x}Sr_xCuO_4$ ($x = 0.1$, *ab* plane) [7]; and (*4*) $Ba_{1-x}K_xBiO_3$ ($x = 0.13$, α is the thermal expansion coefficient) [7].

possesses the same anomalous property ($\alpha < 0$) as the oxide HTSCs whose characteristics are plotted in Fig. 1b.

Figure 2a illustrates the effect of the magnetic field $H = 36$ kOe on the temperature dependence of $\Delta L/L$ for MgB_2. For comparison, Fig. 2b shows the magnetic-field dependence of $\Delta L/L$ obtained earlier for $Ba_{0.6}K_{0.4}BiO_3$ and $La_{1.9}Sr_{0.1}CuO_4$ samples [7]. It is seen that the magnetic field $H \approx 40$ kOe exerts an anomalously strong effect on $\alpha(T)$ of this class of compounds at low temperatures.

Figure 3 plots $\Delta L/L$ vs. magnetic field H dependences obtained at different temperatures for MgB_2. We readily see that the dependence of $\Delta L/L$ on H measured at $T = 12.1$ K, i.e., in the region of negative values of $\Delta L/L$ ($T \le 16.5$ K), differs qualitatively from those obtained for $T > 16.5$ K (this case is illustrated using only the three curves measured at $T = 18.8$, 28.2, and 37.5 K). The behavior of the curves measured at $T > 16.5$ K can be accounted for by the effect of magnetostriction, whereas at $T = 12.1$ K, the variation of $\Delta L/L$ with magnetic field has opposite sign. Therefore, this behavior cannot be explained in terms of magnetostriction. Magnetostriction has been recently studied in considerable detail for $T < T_c$ on the HTSC compound $Ba_{0.6}K_{0.4}BiO_3$ [10]. It was shown in [10] that samples contract as the magnetic field is increased to 5 T at a fixed temperature, which means that $\Delta L/L$ is negative and grows in absolute magnitude. The magnetic-field dependences of $\Delta L/L$ obtained by us are in full agreement with this behavior for temperatures $16.5 \text{ K} < T < T_c$. Thus, the $\Delta L/L$ vs. H dependence plotted in Fig. 3 for $T = 18.8$, 28.2, and 37.5 K can be accounted for by magnetostriction. At low temperatures, however (see, for instance, the curve for $T = 12.1$ K in Fig. 3), the sign of the $\Delta L/L$ vs. H dependence is opposite to that of magnetostriction; i.e., $\Delta L/L > 0$ and grows with H. Thus, in addition to the magnetostriction, MgB_2 exhibits an effect of opposite sign, which becomes stronger for $T < 16.5$ K. Both these effects have also been observed in a number of other HTSCs [7].

For $T > T_c$, where MgB_2 is in a normal state, the $\alpha(T)$ and $\alpha(H)$ relations resemble those of conventional metals. Samples of the $Ba_{1-x}K_xBiO_3$ system with metallic

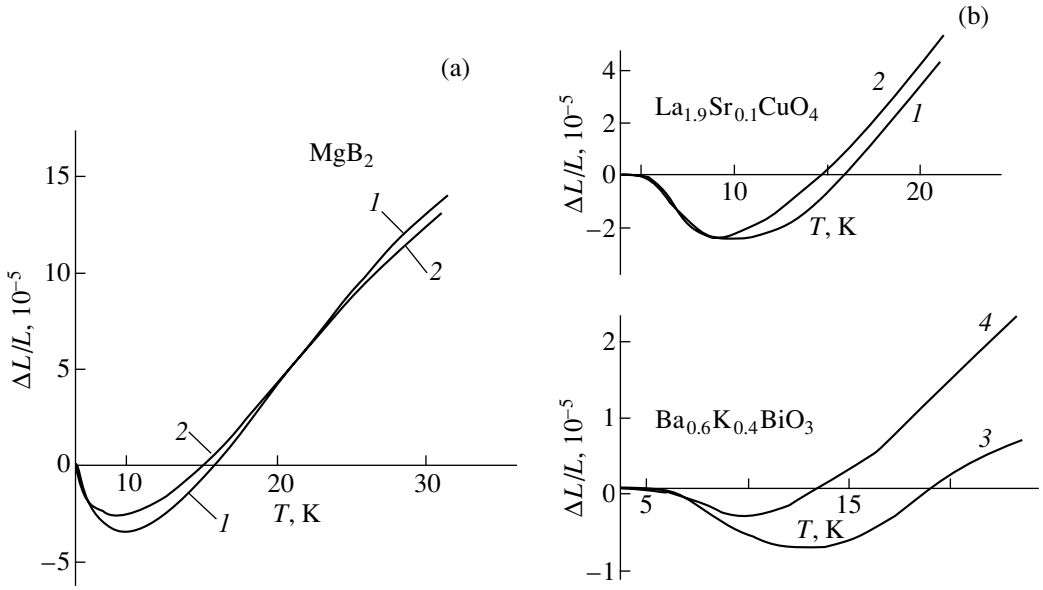

Fig. 2. Effect of magnetic field on the temperature dependence of thermal expansion. (a) MgB_2 [(*1*) $H = 0$, (*2*) $H = 36$ kOe]; (b) $La_{1.9}Sr_{0.1}CuO_4$ [(*1*) $H = 0$, (*2*) $H \approx 4$ T], and $Ba_{0.6}K_{0.4}BiO_3$ [(*3*) $H = 0$, (*4*) $H = 4$ T] [7].

conduction for $x > 0.4$ are characterized by the same properties [11].

Both in MgB_2 and in the oxide HTSC systems, the anomalous (negative) thermal expansion can be explained by the effect of charge density waves (CDW) on crystal lattice stability [12]. However, no comprehensive microscopic-scale analysis of the effect of negative $\alpha(T)$ has been carried out for the HTSCs, or even for simpler substances of the type of tetrahedral semiconductors (Si, Ge, etc.), where one also observes $\alpha < 0$ in the low-temperature domain. Current phenomenological calculations, which take into account only anharmonicity with a large number of fitting parameters, fail to explain why in such materials as Si, the Debye temperature $\theta \approx 600$ K α is negative at liquid-helium temperatures, i.e., in the region where the harmonic approximation is undoubtedly valid [13]. It turns out that if the additional Coulomb interaction of bond-localized charges (an analog of CDW) in tetrahedral semiconductors or the CDW in HTSCs with an ionic lattice are neglected, the crystal structure of these systems becomes unstable; i.e., the transverse acoustic phonon frequency ω_{TA} at the Brillouin zone boundary vanishes. As a result of the interaction of bond-localized charges in tetrahedral semiconductors or of CDW in ionic HTSCs, the Brillouin zone edge frequency ω_{TA} becomes positive ($\omega_{TA} > 0$), which is a necessary condition for crystal lattice stability [12, 13]. Thus, in compounds with $\alpha < 0$ at low temperatures ($T \ll \theta$), such as HTSCs, tetrahedral semiconductors, and MgB_2, the crystal lattice stability is provided by a nonuniform electron density distribution in the crystal.

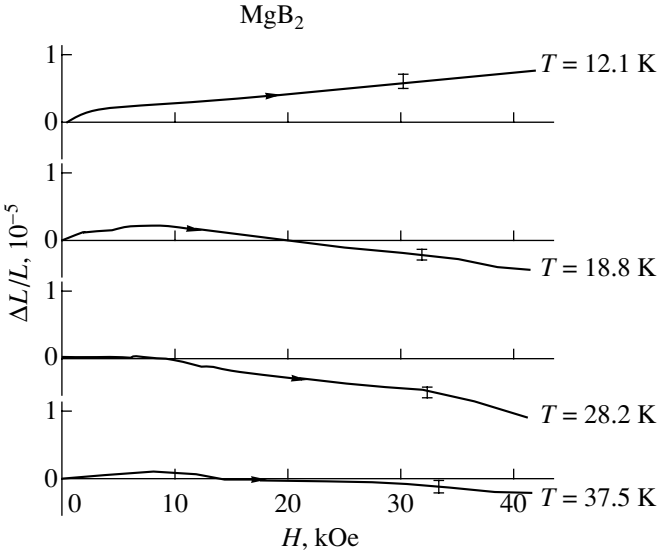

Fig. 3. Thermal expansion $\Delta L/L$ of MgB_2 plotted vs. magnetic field for fixed temperatures. The measurement temperatures are specified in the graphs. The measurement errors are shown with bars. The arrows identify the direction of magnetic-field variation.

To arrive at a qualitative explanation of the anomalous temperature dependence $\alpha(T)$ for the above materials, including MgB_2, we consider a model phonon spectrum of a diatomic metal, which is presented in a simplified form in Fig. 4. We do not have at our disposal an experimental dependence of the frequency ω on wave vector $\mathbf{Q}$ for MgB_2. For illustration, we took typ-

ical dispersion relations $\omega(\mathbf{Q})$ in a high symmetry direction (Fig. 4a). This scheme is appropriate for the MgB_2 spectrum only at low frequencies (acoustic branches).

The first to be excited under heating from $T = 0$ are the low-frequency branches of the phonon spectrum, $\omega \approx kT/\hbar$. The lowest frequency phonon branch ω_{TA} near the Brillouin zone edge (frequency ω^*_{TA}) is characterized by a high density of phonon states (the low-frequency peak in $F(\omega)$ in Fig. 4b). The major contribution to the frequency ω^*_{TA} near the Brillouin zone boundary is due to the CDW interaction with the ionic lattice [12, 13]. A charge density wave, for instance, on the oxygen sublattice of an HTSC system, appears when the effect of the Brillouin zone boundaries on electron scattering is included. Electron–phonon coupling considered with inclusion of this effect results in a divergence of the dielectric susceptibility, and the dielectric permittivity $\varepsilon(\omega, \mathbf{Q})$ becomes negative for wave vectors $\mathbf{Q}$ connecting such boundaries [12]. Therefore, when phonons with such $\mathbf{Q}$ and ω are excited, the crystal must contract, because $\varepsilon(\omega^*, \mathbf{Q}) < 0$. To this region of frequencies ω^* corresponds the temperature $T^* = \hbar\omega^*/k$, and it is near this temperature that negative α values should be observed (Fig. 4c). When heating is continued further, phonons of other branches with higher frequencies are excited. For these phonons, we have $\varepsilon(\omega, \mathbf{Q}) > 0$, which accounts for the normal behavior of $\alpha(T)$ (i.e., $\alpha > 0$).

The effect of a magnetic field on the thermal-expansion anomaly in MgB_2 and other HTSCs [14] is easier to consider using a model dielectric state. A strong magnetic field will tend to destroy singlet-paired electrons and holes forming a CDW and, hence, reduce the CDW amplitude. This will bring about a decrease in the phonon frequencies ω^*_{TA} near the Brillouin zone boundary, as shown by the dashed line in Fig. 4a. The peak in the phonon density of states will decrease in magnitude and shift toward lower frequencies (dashed line in Fig. 4b). As a result, the temperature T^* [temperature of the minimum in $\alpha(T)$] will decrease, the temperature region over which $\alpha < 0$ will narrow, and the negative α will reduce in absolute value (dashed line in Fig. 4c).

This decrease in T^* with increasing H agrees qualitatively with the measurements shown in Fig. 2a for MgB_2 and in Fig. 2b for other HTSC compounds. To analyze this effect on a microscopic scale quantitatively, one would have to have experimental phonon dispersion curves $\omega(\mathbf{Q})$, which are presently not available for MgB_2 [15].

Thus, it has been found that at low temperatures, MgB_2 has a negative thermal expansion coefficient, $\alpha < 0$, as do oxide HTSCs. As in the case of HTSC systems, a magnetic field was shown to strongly affect the low-temperature anomaly in thermal expansion $\alpha(T)$; this effect cannot be explained as being due solely to magnetostriction. All these findings imply that the anomalies in the properties of MgB_2 are similar in nature to those of the oxide HTSCs.

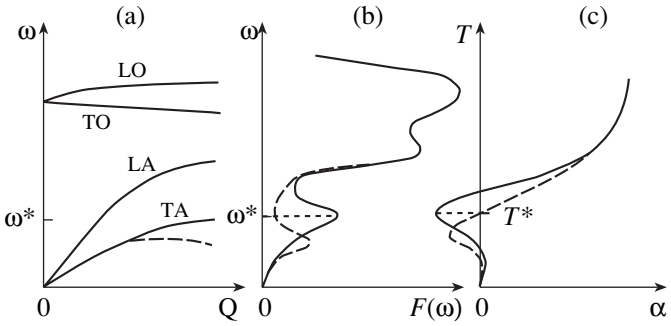

Fig. 4. Schematic of the relation between (a) phonon dispersion $\omega(\mathbf{Q})$, (b) phonon spectrum $F(\omega)$, and (c) anomalous temperature dependence of the thermal expansion coefficient $\alpha(T)$ and of the magnetic field effect on these characteristics (solid lines for $H = 0$, dashed lines for $H \neq 0$). For the sake of simplicity, only four phonon branches are shown for the diatomic-metal model in a high-symmetry direction: LO denotes longitudinal optical; TO, transverse optical; LA, longitudinal acoustic; and TA, transverse acoustic phonons. ω^* is the transverse acoustic phonon frequency at the Brillouin zone boundary, and T^* is the temperature corresponding to the maximum absolute value of negative $\alpha(T)$.

ACKNOWLEDGMENTS

The authors are indebted to Ya.G. Ponomarev for assistance in the present study.

This study was supported by the Russian Foundation for Basic Research (project no. 01-02-16395) and the Scientific Council program "Topical Problems in the Physics of Condensed Matter" (subprogram "Superconductivity").

REFERENCES

1. J. Nagamatsu, N. Nakagawa, T. Nuranaka, *et al.*, Nature **410**, 63 (2001).
2. S. L. Li, H. H. Wen, Z. W. Zhao, *et al.*, Phys. Rev. B **64** (9), 094522 (2001).
3. S. L. Bud'ko, C. Petrovic, G. Lapertot, *et al.*, cond-mat/0102413 (2001).
4. N. V. Anshukova, A. I. Golovashkin, L. I. Ivanova, and A. P. Rusakov, Usp. Fiz. Nauk **167** (8), 887 (1997) [Phys. Usp. **40**, 843 (1997)].
5. J. Kortus, I. I. Mazin, K. D. Belashchenko, *et al.*, cond-mat/0101446 (2001).
6. N. V. Anshukova, A. I. Golovashkin, L. I. Ivanova, *et al.*, Int. J. Mod. Phys. B **12** (29–31), 3251 (1998).

7. N. V. Anshukova, A. I. Golovashkin, L. I. Ivanova, and A. P. Rusakov, Pis'ma Zh. Éksp. Teor. Fiz. **71** (9), 550 (2000) [JETP Lett. **71**, 377 (2000)].
8. H. You, U. Welp, and Y. Fang, Phys. Rev. B **43** (4), 3660 (1991).
9. Z. J. Yang, M. Yewondwossen, D. W. Lawther, and S. P. Ritcey, J. Supercond. **8**, 223 (1995).
10. V. V. Eremenko, V. A. Sirenko, G. Shimchak, *et al.*, Fiz. Tverd. Tela (St. Petersburg) **40** (7), 1199 (1998) [Phys. Solid State **40**, 1091 (1998)].
11. N. V. Anshukova, A. I. Golovashkin, Yu. V. Bugoslavskii, *et al.*, J. Supercond. **7** (2), 427 (1994).
12. L. N. Bulaevskiĭ, V. L. Ginzburg, G. F. Zharkov, D. A. Kirzhnits, Yu. V. Kopaev, E. G. Maksimov, and D. I. Khomskiĭ, *Problems in High-Temperature Superconductivity*, Ed. by V. L. Ginzburg and D. A. Kirzhnits (Nauka, Moscow, 1977).
13. H. Wendel and R. M. Martin, Phys. Rev. B **19** (10), 5251 (1979).
14. A. I. Golovashkin and A. P. Rusakov, Usp. Fiz. Nauk **170** (2), 192 (2000) [Phys. Usp. **43**, 184 (2000)].
15. C. Buzea and T. Yamashita, cond-mat/0108265 (2001).

Translated by G. Skrebtsov

Physics of the Solid State, Vol. 45, No. 1, 2003, pp. 61–68. Translated from Fizika Tverdogo Tela, Vol. 45, No. 1, 2003, pp. 60–67.

SEMICONDUCTORS AND DIELECTRICS

Thermal Conductivity of Opal Filled with a $LiIO_3$ Ionic Conductor

A. É. Aliev*, N. Kh. Akhmedzhanova, V. F. Krivorotov**, I. N. Kholmanov**, and A. A. Fridman****

** Institute of Technologies LG-Elite, LG-Electronics Corporation, Seoul, 137724 Korea*

*** Department of Thermal Physics, Academy of Sciences of Uzbekistan, ul. Katartal 28, kvartal Ts, Chilanzar, Tashkent, 700135 Uzbekistan*

e-mail: AliAliev@hotmail.com

Received April 28, 2002

Abstract—The temperature dependences of the thermal conductivity of a synthetic opal and opal-based nanocomposites prepared by introducing a $LiIO_3$ superionic conductor into pores of the opal matrix from an aqueous solution or melt are measured by the hot-wire technique in the temperature range 290–420 K. It is demonstrated that the thermal conductivity of pure opal increases with an increase in the diameter of the SiO_2 spheres forming a face-centered cubic lattice of an opal and is determined by the total thermal resistance of interfaces between the spheres. Filling of opal pores with the ionic conductor leads to an increase in the thermal conductivity. The behavior of the thermal conductivity and its magnitude in opal-based nanocomposites depend to a large extent on the method of filling the matrix pores. *© 2003 MAIK "Nauka/Interperiodica".*

1. INTRODUCTION

Research into composites with a characteristic particle size of the order of several tens of nanometers, including filled porous materials, has attracted the attention of many scientists owing to the prospects of designing new materials with unusual properties. Recent investigations of nanostructures have aroused particular scientific interest due to the fresh opportunities they offer for detailed study of the size effects, surface phenomena, and the influence of pore geometry on the physicochemical properties of materials incorporated into porous matrices.

Among the most extensively studied nanostructures, porous matrices with a regular system of interconnecting pores (such as zeolites, fullerenes, opals, and porous glasses) have drawn special attention, because they are convenient model objects [1]. A great diversity of processes—melting, crystallization, phase transitions to superfluid and superconducting states, phase separation in binary liquids, ferroelectric phase transitions, structural transformations in solids, transitions to the vitreous state, and others—have been investigated in filled porous glasses. In particular, Molz *et al.* [2] studied porous glasses filled with different inert gases and found that their temperatures of melting and solidification are considerably lower than those for bulk materials. In porous glasses filled with gallium, size effects were observed by Bogomolov *et al.* [3] and a change in the symmetry of the gallium lattice was found by Sorina *et al.* [4]. Hysteresis phenomena indicating heterogeneous crystallization of gallium in pores of glasses [5] and opal [6] were revealed using acoustical spectroscopy.

Owing to their strictly periodic three-dimensional lattice, which are composed of SiO_2 spheres interacting mechanically, opals are also of particular interest for use as structural materials of photonic crystals [7–9] and thermoelectric devices [1]. Taking into account that the electrical and thermal conductivities of a nanocomposite based on opal filled with bismuth decrease out of proportion to each other (as compared to those of bulk bismuth), Baughman *et al.* [10] succeeded in increasing the thermoelectric conversion efficiency $ZT = \alpha^2\sigma T/(\chi_l + \chi_c)$ (the Ioffe criterion) by a factor of two. Here, α is the Seebeck coefficient; σ is the electrical conductivity; χ_l and χ_c are the phonon and electron thermal conductivity components, respectively; and T is the temperature.

Recent interest expressed in the behavior of thermal conductivity in similar structures and a more fundamental problem concerning the behavior of phonon spectra in a system of mechanically coupling nanoparticles and composites developed on their basis have lent impetus to a series of investigations into the thermal conduction of nanocomposites based on opal and porous glasses [11–14]. It has been found that impregnation of opal with a saturated aqueous solution of NaCl does not affect the thermal properties of the nanocomposite. Arutyunyan *et al.* [11] explained this finding by the fact that the matrix pores are occupied by NaCl in the form of needles that are not in contact; consequently, heat transfer through NaCl is absent. Bogomolov *et al.* [13] obtained better filling upon immersing

the opal matrix in an NaCl melt at $T = 900°C$. These authors were the first to reveal an unusual low-temperature peak in the thermal conductivity (at 35 K) due to the size effect limiting the mean free path of phonons. The results obtained were explained under the assumption that, apart from the standard mechanism observed in a conventional composite involving a matrix and a filler, heat transfer in an opal–NaCl nanocomposite proceeds through an additional mechanism typical of bulk crystals. The filler introduced into a cubic lattice of opal pores forms a matrix quasi-lattice consisting of microcrystallites. This leads to a manifestation of the coherent effects and properties characteristic of bulk crystals.

A nearly perfect crystal system of pores in opal is of scientific interest from the standpoint of the behavior of a quasi-liquid ionic subsystem involved in nanocomposites based on opal and superionic conductors (solid electrolytes). First, the large contact area between the surface of the introduced solid electrolyte and the inner surface of the pores can substantially increase the ionic conductivity at the expense of a decrease in the activation energy of ion migration along the interface between two media [15]. Second, the size effects in a bounded pore space can bring about a decrease in the internal energy of the introduced material and, hence, a decrease in the activation energy of ions. In particular, Molz *et al.* [2] demonstrated with the use of a geometric model that an increase in the surface-to-volume ratio $S/V = (4\pi r^2)/\left(\frac{4}{3}\pi r^3\right)$ with a decrease in the pore size to several tens of nanometers can lead to a considerable change in the melting temperature of the material introduced, that is,

$$\Delta T = 3k\vartheta_{\text{mol}}T_m/Lr, \quad (1)$$

where k is the surface tension coefficient, ϑ_{mol} is the molar volume of the introduced material, T_m is the melting temperature of the initial bulk material introduced into the pores, L is the heat of melting or solidification, and r is the mean pore radius.

We investigated the electrical and thermal properties of a nanocomposite based on synthetic opal and a lithium-conducting ionic conductor $LiIO_3$. This paper reports only part of the results obtained in our investigation, namely, the description of the behavior of the thermal conductivity coefficient in pure opals with different diameters of SiO_2 spheres and in opals filled with lithium iodate from a saturated aqueous solution and a melt. The electrical properties of the opal–$LiIO_3$ nanocomposite will be published in separate papers.

2. MATERIALS AND EXPERIMENTAL TECHNIQUE

Lithium iodate of the α modification, namely, α-$LiIO_3$ ($P6_3$), already at room temperature is a good conductor with a quasi-one-dimensional ionic conductivity along the optic axis C [$\sigma_{33(300\text{ K})} = 5.6 \times 10^{-4}$ $(\Omega\text{ m})^{-1}$] [16–19]. As a rule, α-$LiIO_3$ hexagonal prisms with high optical quality can be grown from an aqueous solution and are characterized by a high hygroscopicity. At a temperature of ~247°C, α-$LiIO_3$ lithium iodate transforms into a low-conductivity orthorhombic γ phase with a hysteresis of 46°C; as the temperature increases, this compounds undergoes a destructive phase transition at a temperature of 256°C and subsequent melting at 420°C [20]. Consequently, α-$LiIO_3$ is a convenient model object and can be introduced into opal pores from a saturated aqueous solution and a melt at relatively low temperatures. The choice of the filler material with a low melting temperature was made for two reasons; namely, it was necessary, first, to prevent interaction between the filler and the matrix material and, second, to avoid further sintering of close-packed spheres consisting of amorphous SiO_2 in the course of filling from the melt.

The synthetic opal was grown through deposition of an aqueous colloidal suspension (Nissan Chemical Inc.). This compound has a close-packed face-centered cubic lattice formed by SiO_2 spheres of identical diameter with a lattice spacing of 250–400 nm. Suspensions containing spheres of different diameters (180 ± 4, 220 ± 5, and 300 ± 6 nm) were treated in separating columns and poured into Petri dishes. The time it takes for high-quality opals to be grown through slow crystallization of a monodisperse aqueous colloidal solution is approximately equal to ten months. Although the deposition and crystallization of opals can occur through a variety of processes described in the literature [21], these methods are not essentially different from each other. After drying in air, the resultant precipitate was similar in hardness to chalk (talc). In order to obtain mechanically high-strength opal, the precipitate was annealed initially at 120°C for 10 h and then at 750°C for 4 h.

The thermal conductivity coefficients were measured using the hot-wire technique in the temperature range 290–420°C in an inert gas (N_2) atmosphere or under vacuum. At room temperature, the measurements were performed for the most part under vacuum in order to provide better desorption of water vapors from the opal matrix. At temperatures above 150°C, the thermal conductivities measured in the nitrogen atmosphere and under vacuum did not differ from each other. The hot-wire technique used in the thermal experiments was described in detail in [22, 23]. A thin tungsten wire 12 μm in diameter was clamped between two plane-parallel opal plates $10 \times 10 \times 2$ mm in size. A rectangular pulse (width, 0.5 s; amplitude, 0.4 V) was applied to the probe completely embedded between the plates. Depending on the rate of heat transfer from the probe to the sample, the probe temperature and, hence, the probe resistance increased as $\sqrt{t}$. The slope of the curve characterizing an increase in the temperature

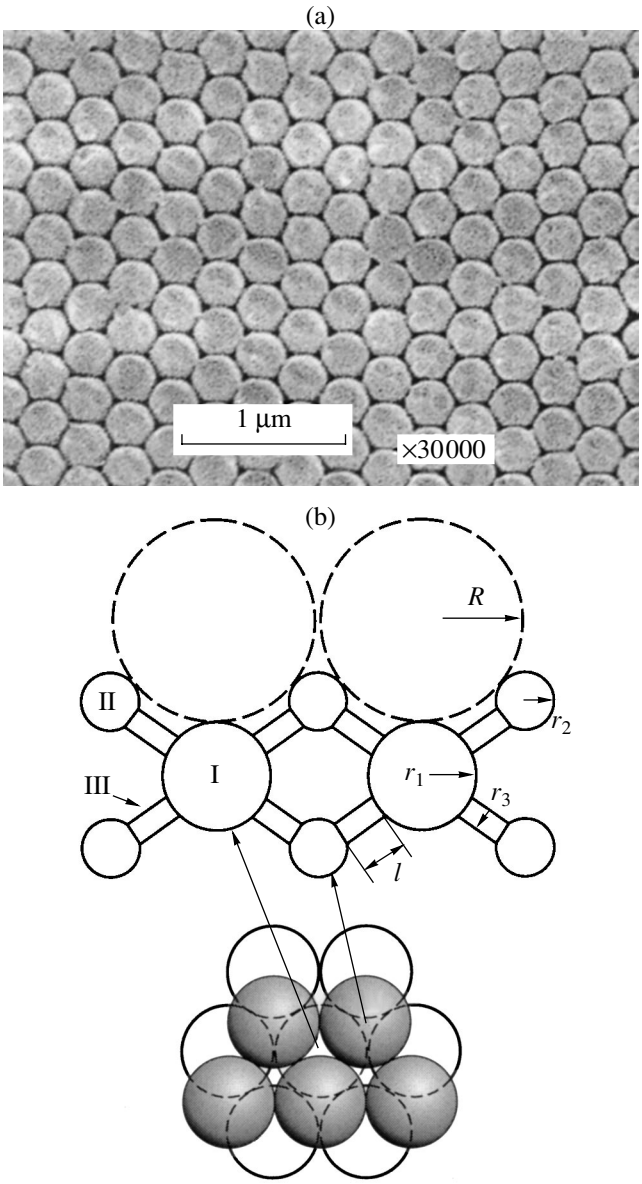

Fig. 1. (a) Electron micrograph of the fractured surface of a synthetic opal with SiO_2 spheres 300 nm in diameter and (b) schematic diagram of the opal structure and the cavity lattice represented as a network of connected spherical elements [1]. D = 160–300 nm, $r_1 = R(\sqrt{2} - 1)$, $r_2 = R(\sqrt{3/2} - 1)$, $r_3 = R(2\sqrt{3} - 1)$, and $l = R(2 - \sqrt{2})$.

(resistance) is inversely proportional to the thermal conductivity in the direction perpendicular to the probe location. With the aim of improving the thermal contact between the probe and the sample plates, the plates were pressed to each other under a pressure of ~2 kg/cm^2. The mean temperature of the sample was measured using a chromel–alumel thermocouple. The instrumental error in measuring the thermal conductivity coefficient $\chi(T)$ was determined with the use of Al_2O_3, KCl, and SiO_2 reference samples [for the fused silica reference sample, χ(300 K) = 1.358 W/(m K)] and did not exceed 3% in the temperature range $100 < T < 300$ K and 5% in the range $300 < T < 450$ K.

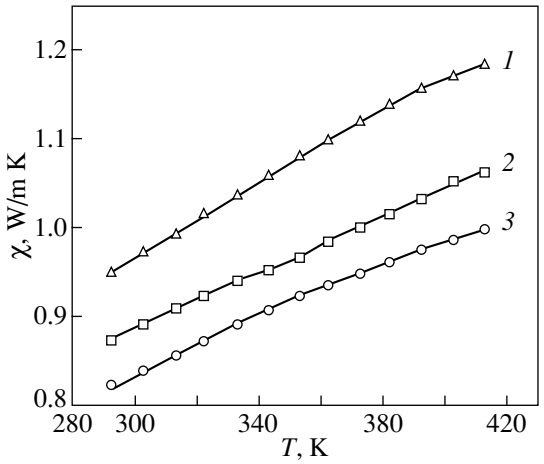

Fig. 2. Temperature dependences of the thermal conductivity coefficient χ for synthetic opals containing SiO_2 spheres with diameters of (*1*) 300, (*2*) 220, and (*3*) 180 nm.

The surface structure and the specific features in the filling of internal regions of opal were examined using a JSM-6300 (JEOL, Japan) scanning electron microscope. X-ray diffraction analysis was performed on a DRON-2 diffractometer (CuK_α radiation).

3. RESULTS AND DISCUSSION

The electron micrograph of the fractured surface of a synthetic opal is displayed in Fig. 1a. The observed perfect structure of hexagonal packing of SiO_2 spheres corresponds to the (111) plane of a face-centered cubic lattice. Traces of the sintering of the cleaved layer are clearly seen on the surface of the spheres. The close-packed lattice of SiO_2 spheres involves octahedral (I) and tetrahedral (II) holes, which, according to [1], can be represented as spheres connected through cylindrical channels (III) 30–40 nm in diameter (Fig. 1b). The area of the inner surface of pores in opal can be as large as ~10 m^2/g.

The temperature dependences of the thermal conductivity coefficient χ_{12} measured along the [111] direction [perpendicular to the (111) plane shown in Fig. 1a] for synthetic opals containing SiO_2 spheres with diameters of 180, 220, and 300 nm are plotted in Fig. 2. An increase in the thermal conductivity with an increase in the temperature is characteristic of the amorphous state. As follows from the kinetic equation for thermal conductivity, according to which phonons are treated as an ideal quasiparticle gas, the thermal conductivity coefficient χ is proportional to the heat capacity C_v at constant volume, the velocity V of sound

(averaged over all the directions and modes), and the mean free path l of phonons; that is,

$$\chi = \frac{1}{3} C_v \bar{V} \bar{l}. \quad (2)$$

The relative increments of the thermal conductivity with an increase in the temperature virtually coincide for all three opal samples,

$$\Delta\chi = \frac{\chi_{413\ \mathrm{K}} - \chi_{293\ \mathrm{K}}}{\chi_{293\ \mathrm{K}}} = 0.22\text{–}0.23. \quad (3)$$

This suggests the same nature of heat transfer in three similar structures.

However, the magnitudes of the thermal conductivity differ considerably. An increase in the diameter of SiO_2 spheres is accompanied by a proportional increase in the thermal conductivity. An insignificant increase in the opal density ($\rho_{300}/\rho_{160} = 1.05$ [10]) with an increase in the sphere diameter cannot be responsible for the observed increase in the thermal conductivity ($\chi_{300}/\chi_{180} = 1.16$).

When analyzing the heat transfer over SiO_2 spheres, we can assume that opals of the three types under investigation differ in the mean free path of phonons. The averaged velocities of sound and the heat capacities in relationship (2) should be identical for SiO_2 spheres of different diameters. The sphere size can limit the mean free path of phonons and, correspondingly, the thermal conductivity of the sample at low temperatures. The calculated mean free paths of phonons in red opal with spheres of diameter $D = 300$ nm (light reflected from the surface has a red hue) indicate that, even at room temperature, the condition $l \le 3$ nm is satisfied; i.e., the mean free path l is two orders of magnitude smaller than the sphere size.

Under the given conditions of sintering, the ratio of the sphere diameter D to the minimum distance d between the sphere centers lies in the range from 1.05 to 1.055 [24]. In this case, the diameter of the contact neck between spheres in red opal is determined as $a = (D^2 - d^2)^{1/2} = 90\text{–}95$ nm. Therefore, the contact neck between spheres also cannot limit the mean free path of phonons.

On the other hand, the diameter of the contact neck between spheres increases with an increase in the sphere diameter and, seemingly, might affect the through heat transfer. However, an increase in the sphere diameter is accompanied by a proportional increase in the cross-sectional area of the pores; as a result, the specific surface of heat transfer remains unchanged. At the same time, the number of contact necks per unit length in the direction of propagation of a heat wave depends on the sphere size. With the Wiener model of successive layers [25], it can be easily shown that the thermal conductivity of a composite consisting of ordered layers formed by identical particles is determined primarily by the total thermal resistance of contact regions per unit thickness of the sample. Let us consider the propagation of a heat wave along the [111] direction in opals containing SiO_2 spheres of different diameters: 180, 220, 250, and 300 nm.[1] The total thermal resistance of the sample is equal to the sum of thermal resistances of all n_1 layers of the spheres and thermal resistances of n_2 layers of the interfaces between the spheres; that is,

$$\frac{1}{\chi} = \frac{n_1}{\chi_1} + \frac{n_2}{\chi_2}, \quad (4)$$

where $1/\chi_1$ is the thermal resistance of one layer of the SiO_2 spheres and $1/\chi_2$ is the thermal resistance of one layer of the interfaces. It is evident that the number n_1 of layers of the spheres and the number n_2 of layers of the interfaces in the direction of the heat flux φ_{12} across the sample thickness can be considered nearly identical ($n_2 = n_1 - 1$) and determined to be $n_{1,2} = h/(d(2/3)^{1/2})$, where h is the sample thickness and d is the distance between the centers of the spheres.

The first sample ($D = 180$ nm), which is 2 mm thick with a surface area of 100 mm^2, has a thermal resistance of 24.39 K W^{-1}. For the distance between the sphere centers $d = D/1.055 = 170$ nm, this sample contains 14410 layers of SiO_2 spheres in the direction of the heat flux φ_{12}. The second sample, which is of the same size, has a thermal resistance of 22.81 K W^{-1} and involves 11664 layers of SiO_2 spheres with a sphere diameter of 220 nm ($d = 210$ nm). For a sample with a smaller sphere diameter, 2746 additional layers of the interfaces bring about an increase in the thermal resistance by 1.58 K W^{-1}. Therefore, irrespective of the seal diameter and the number of contacts per sphere, the thermal resistance of one contact layer is equal to 0.575×10^{-3} K W^{-1}. A comparative analysis of other opals leads to a similar result. The table presents the calculated thermal resistances of interfaces (χ_2^{-1}) and SiO_2 spheres (χ_1^{-1}) for all the opal samples studied. The specific thermal conductivity χ_0 of an individual SiO_2 sphere was estimated (for four samples) at ~1.24 W/m K. This value is close to the thermal conductivity of fused silica (1.36 W/m K at $T = 293$ K) but exceeds the thermal conductivity of SiO_2 ceramic materials (0.76 W/m K at $T = 293$ K) [26]. Most likely, the SiO_2 spheres were partly fused together upon heat treatment. This is indicated by the low porosity ($P = 0.27\text{–}0.30$) measured for these samples by Baughman *et al.* [10]. In general, the temperature dependence of the thermal conductivity of the aforementioned opals is similar to that of fused silica and ceramic materials.

Figure 3 shows the dependence of the thermal conductivity on the sphere size. This dependence is nearly

[1] The thermal conductivity of the opal sample with $D = 250$ nm was measured only at $T = 20$°C.

Thermal resistances of interfaces χ_2^{-1} and SiO_2 spheres χ_1^{-1} for four types of opals with different distances between the centers of SiO_2 spheres according to calculations from the experimental thermal conductivities χ measured at 20°C

d, nm	χ, W/m K (20°C)	χ^{-1}, K W^{-1} ($10 \times 10 \times 2$ mm)	n	χ_2^{-1}, K W^{-1}	χ_1^{-1}, K W^{-1}	χ_0, W/m K (20°C)
170	0.82	24.39	14410	8.29	16.10	1.24
210	0.87	22.81	11664	6.7	16.11	1.24
240	0.91	21.98	10206	5.87	16.11	1.24
280	0.95	21.14	8748	5.02	16.12	1.24

linear, in accordance with the predictions of the above model. Fayette *et al.* [27] observed a similar behavior of the thermal conductivity in SnO_2 ceramic materials over a narrow range of particle sizes. It is evident that, as the sphere size substantially increases or decreases, the thermal conductivity exhibits nonlinear behavior. It seems likely that there exist other mechanisms limiting an increase in the thermal conductivity. In particular, Kitayama *et al.* [28] studied β-Si_3N_4 ceramics and experimentally derived the relationship $\chi = C_1 \ln A + C_2$, where C_1 and C_2 are constants and A is the mean particle size.

As was shown in [27], additional annealing of ceramic samples results in a decrease in the thickness of the contact region between crystal grains and an appreciable increase in the thermal conductivity. For spherical structural units of opal, additional annealing can lead not only to a decrease in the thickness of the contact neck but also to an increase in the contact area. This is not necessarily desirable because superfluous annealing brings about a decrease in the opal porosity. Figure 4 depicts the temperature dependences of the thermal conductivity of red opal (D = 300 nm) after a series of additional annealings for 1 h at 750°C. Initial sample *1* was first annealed for 4 h at 750°C and was then kept in a desiccator for a month. The first additional annealing results in a change in the slope of the thermal conductivity curve. This can be associated with hydrothermal treatment of the inner cavities in the porous matrix. Even at T > 360 K, the thermal conductivity is 1.5% higher than its initial value. The next additional annealing brings about an increase in the thermal conductivity of opal by 4.2%. However, a further increase in the magnitude of the thermal conductivity is less pronounced. The temperature behavior of the thermal conductivity remains virtually unchanged after each annealing. The thermal conductivity as a function of the number of sequential annealings at T = 413 K is shown in the inset to Fig. 4. The total change in the thermal conductivity (after the fourth annealing as compared to the thermal conductivity of the initial sample) is more than 10%. If this change can result only from the increase in the diameter of the contact neck between the spheres (by ignoring the decrease in the thickness of the contact layer), the resulting shrinkage of channels connecting octahedral and tetrahedral holes will appear to be critical.

The channel radius can be estimated from the relationship $r_{min} = (3)^{-1/2}d - (D/2)$. As was noted above,

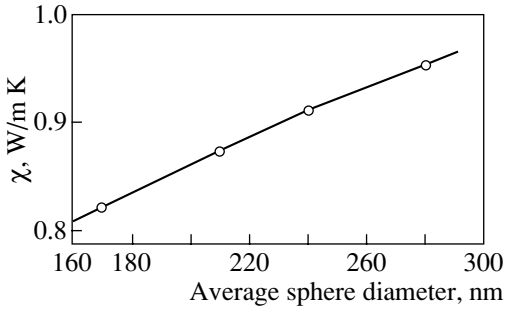

Fig. 3. Dependence of the thermal conductivity coefficient on the size of SiO_2 spheres forming the face-centered cubic structure of a synthetic opal. T = 20°C.

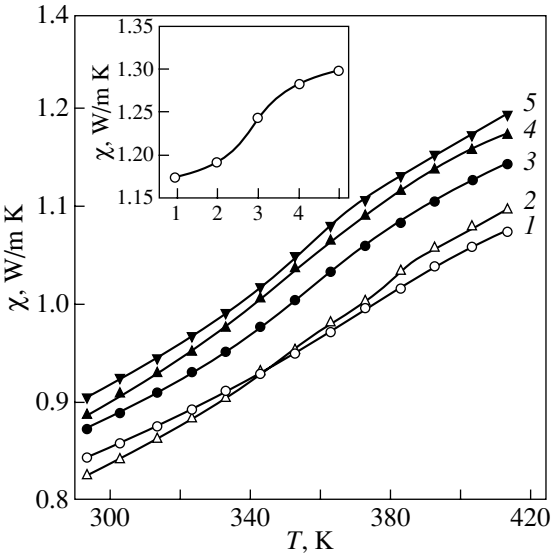

Fig. 4. Temperature dependences of the thermal conductivity of red opal (D = 300 nm) after a series of additional annealings for 1 h at 750°C. (*1*) Thermal conductivity curve for the initial sample. The inset shows the dependence of the thermal conductivity on the number of additional annealing cycles at 413 K.

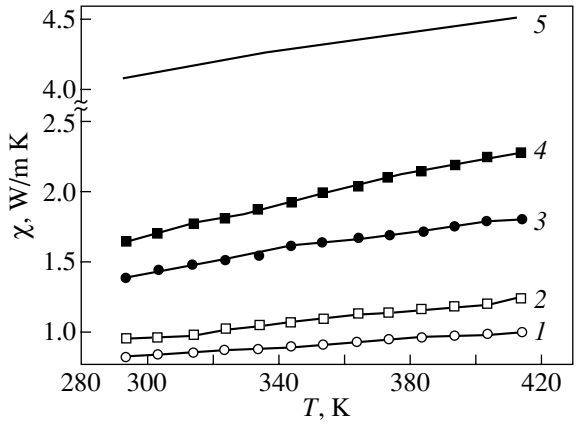

Fig. 5. Temperature dependences of the thermal conductivity of (*1*, *3*) blue (D = 180 nm) and (*2*, *4*) red (D = 300 nm) opals: (*1*, *2*) the initial unfilled samples and (*3*, *4*) opals filled with $LiIO_3$ from an aqueous solution (60°C). (*5*) Dependence of the thermal conductivity of α-$LiIO_3$ measured along the [001] direction.

under the initial conditions of sintering (at 750°C for 4 h), the ratio D/d of the sphere diameter to the minimum distance between the sphere centers falls in the range 1.05–1.055. The channels collapse at $D/d = 1.155$ [10]. Therefore, additional thermal annealing that becomes possible in the course of filling of opal pores with a high-temperature liquid melt is undesirable.

Figure 5 displays the temperature dependences of the thermal conductivity for blue and red opals prior to and after filling with an $LiIO_3$ ionic conductor. For comparison, curve *5* shows the dependence of the thermal conductivity χ_{33} for an α-$LiIO_3$ bulk single crystal along the [001] direction, which was measured by Abdulchalikova *et al.* [29]. Opals were filled by repeated immersion in a saturated aqueous solution of lithium iodate at a temperature of 60°C. After each immersion, the sample was dried first in air for 1 h and then in a vacuum furnace for 1 h at 120°C, weighed, and immersed again in the solution for 10 min. The percolation of the solution through the opal pores was controlled visually: as the liquid penetrates into the pores, opal changes its transparency. After the fifth immersion, the channels connecting the opal pores were filled, thus preventing further incorporation of $LiIO_3$. This can be judged from the electron micrograph in Fig. 6b, which displays the image of the central region in the cleavage of a sample ($10 \times 10 \times 2$ mm in size) filled at room temperature. Lithium iodate is concentrated in narrow necks of the channels and prevents further filling of the pores. The degree of filling of the sample surface (Fig. 6a) is considerably higher than that of the inner regions. Analysis of the experimental data on the density of the prepared composites demonstrated that the highest degree of pore filling, which can be achieved by immersing opals in aqueous solutions at room temperature, does not exceed 15% of the pore volume.

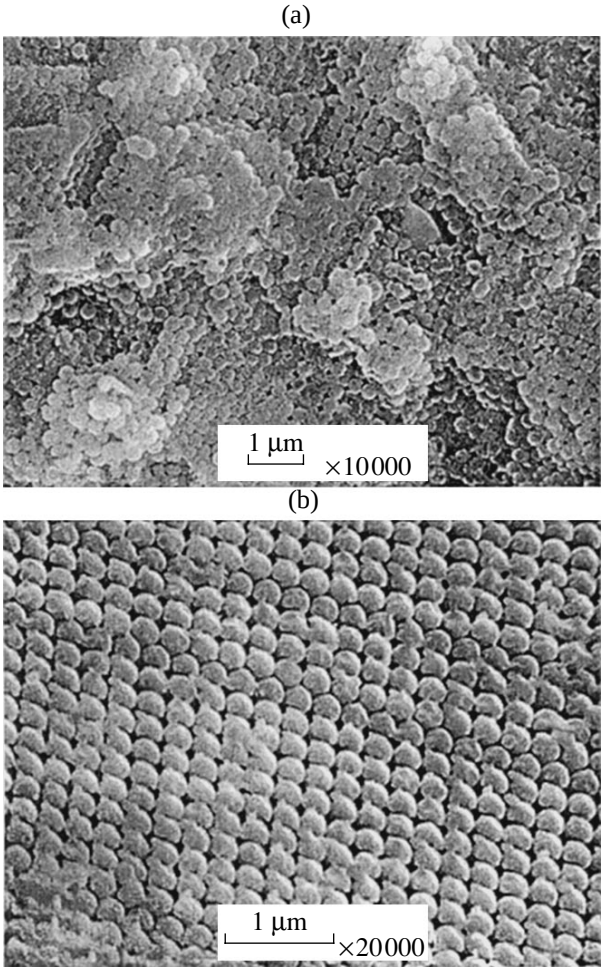

Fig. 6. Electron micrographs of (a) the surface and (b) the cleavage of the inner region of green opal (D = 220 nm) filled with $LiIO_3$ from a saturated aqueous solution at room temperature.

An increase in the solution temperature makes it possible to increase the solution saturation and the mean degree of pore filling. At a solution temperature of 60°C, the mean degree of filling reaches 25% of the pore volume. However, even under these conditions, the inner regions of the sample remain not easily accessible. Analysis of the data on the thermal conductivity of the nanocomposites filled at room temperature and 60°C revealed that, even at such a low density of the incorporated material, the thermal conductivity increases in proportion when changing over from the initial opal to the completely impregnated nanocomposite. In the narrow range of sphere sizes studied in this work, the empirical dependence of the effective thermal conductivity on the sphere diameter D (nm) and the degree of pore filling P can be approximately written in the following form:

$$\chi_{\text{eff}} = DC_1 + C_2 + PC_3/D, \qquad (5)$$

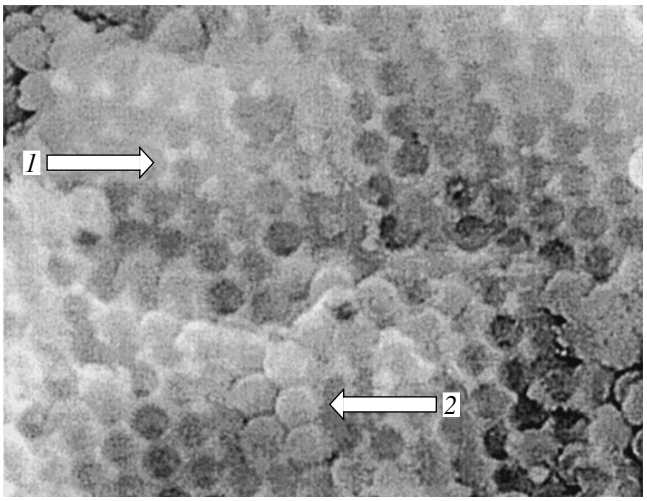

Fig. 7. Electron micrograph of the cleavage of green opal (D = 220 nm) filled with $LiIO_3$ from the melt under a pressure of 5 kbar. Arrows *1* and *2* indicate the filler SiO_2 spheres, respectively.

where $C_1 = 1.2 \times 10^{-3}$ W/m K, $C_2 = 0.6$ W/m K, and $C_3 = 750$ W/m K.

A further increase in the degree of pore filling can be achieved by immersion in a melt. An examination of the electron micrograph of the cleavage of green opal (D = 220 nm) filled from a lithium iodate melt at 450°C revealed that lithium iodate occupies, on average, up to 60% of the pore volume across the whole thickness of the sample. Note that, in this case, the surface and central regions of the sample are filled to the same extent.

Finally, the pores can be almost completely filled upon filling from a melt under pressure. At a pressure of 5 kbar and a melt temperature of 450°C, we succeeded in filling 90% of the pore volume. The electron micrograph of the central region in the cleavage of green opal (D = 220 nm) filled from the melt under pressure is displayed in Fig. 7. This cleavage represents a replica of the opal characterized by a nearly complete filling of the pores. However, the thermal conductivity of this composite does not fit into the aforementioned empirical dependence on the degree of filling.

X-ray diffraction analysis performed on a DRON-2 diffractometer (CuK_α radiation) demonstrated that the crystallization of lithium iodate in opal pores depends on the filling method. The hexagonal α phase with a high ionic conductivity dominates upon filling from a saturated aqueous solution. However, this method has failed to attain a high degree of pore filling. Upon filling from a melt at 450°C, the tetrahedral β and orthorhombic γ low-conductivity phases, which are characterized by a lower thermal conductivity of the initial bulk material, predominantly crystallize in the opal pores. In this case, the relative integrated intensity of the peaks attributed to the β and γ phases of lithium iodate (Fig. 8) is no less than 75%.

The preparation of nanocomposites with a high ionic conductivity calls for further investigation into the

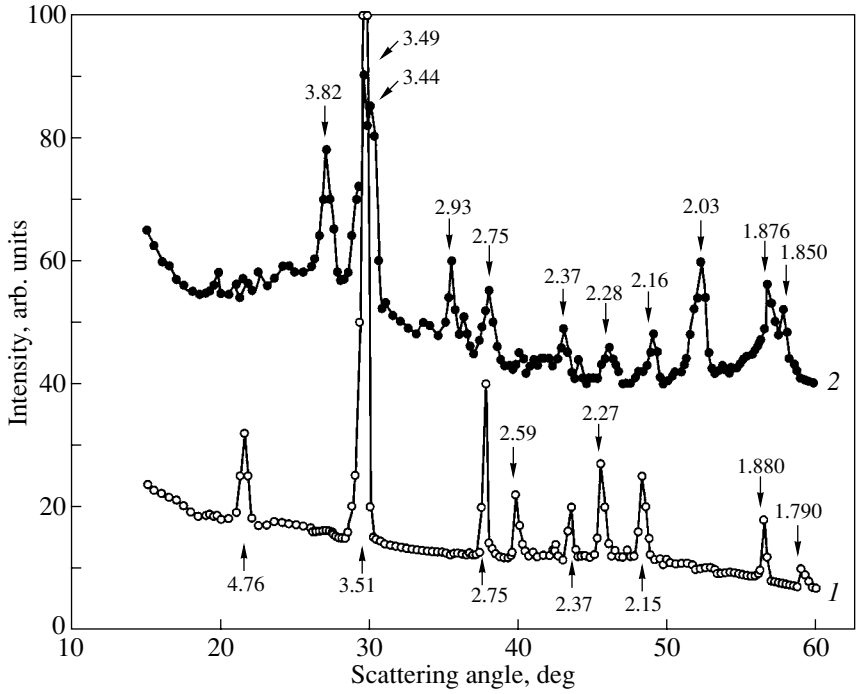

Fig. 8. Diffraction patterns of (*1*) an α-$LiIO_3$ single crystal and (*2*) a nanocomposite comprised of opal filled with $LiIO_3$ from the melt. Intense peaks at 1.85, 2.03, 2.93, and 3.82 Å correspond to the β phase of lithium iodate.

stabilization of the hexagonal α phase of lithium iodate in pores of opal filled from the melt.

ACKNOWLEDGMENTS

This work was supported by the Scientific Technological Center (Ukraine), project no. Uzb-05.

REFERENCES

1. V. N. Bogomolov and T. M. Pavlova, Fiz. Tekh. Poluprovodn. (St. Petersburg) **29** (5), 826 (1995) [Semiconductors **29**, 428 (1995)].
2. E. Molz, A. P. Wong, M. H. W. Chan, and J. R. Beamish, Phys. Rev. B **48**, 5741 (1993).
3. V. N. Bogomolov, R. Sh. Malkovich, I. A. Smirnov, *et al.*, Fiz. Tverd. Tela (Leningrad) **12**, 1204 (1970) [Sov. Phys. Solid State **12**, 938 (1970)].
4. I. G. Sorina, C. Tien, E. V. Charnaya, *et al.*, Fiz. Tverd. Tela (St. Petersburg) **40** (8), 1552 (1998) [Phys. Solid State **40**, 1407 (1998)].
5. B. F. Borisov, E. V. Charnaya, Yu. A. Kumzerov, *et al.*, Solid State Commun. **92** (6), 531 (1994).
6. J. M. Dereppe, B. F. Borisov, E. V. Charnaya, *et al.*, Fiz. Tverd. Tela (St. Petersburg) **42**, 184 (2000) [Phys. Solid State **42**, 193 (2000)].
7. E. Yablonovitch, Phys. Rev. Lett. **58**, 2059 (1987).
8. S. John, Phys. Rev. Lett. **58**, 2486 (1987).
9. S. John and T. Quang, Phys. Rev. Lett. **74**, 3419 (1995).
10. R. H. Baughman, A. A. Zakhidov, I. I. Khayrullin, *et al.*, in *Proceedings of the XVII International Conference on Thermoelectrics (ICT'98), Nagoya, Japan, 1998.*
11. L. I. Arutyunyan, V. N. Bogomolov, N. F. Kartenko, *et al.*, Fiz. Tverd. Tela (St. Petersburg) **40** (2), 379 (1998) [Phys. Solid State **40**, 348 (1998)].
12. V. N. Bogomolov, N. F. Kartenko, L. S. Parfen'eva, *et al.*, Fiz. Tverd. Tela (St. Petersburg) **40** (3), 573 (1998) [Phys. Solid State **40**, 528 (1998)].
13. V. N. Bogomolov, N. F. Kartenko, L. S. Parfen'eva, *et al.*, Fiz. Tverd. Tela (St. Petersburg) **41** (2), 348 (1999) [Phys. Solid State **41**, 313 (1999)].
14. A. E. Aliev and N. Kh. Akhmedjanova, Uzb. Fiz. Zh., No. 1, 373 (1999).
15. J. Maier, J. Phys. Chem. Solids **46**, 309 (1985).
16. A. É. Aliev and A. Sh. Akramov, Izv. Akad. Nauk Uz. SSR, No. 1, 76 (1987).
17. A. A. Abramovich, A. Sh. Akramov, A. É. Aliev, and L. N. Fershtat, Fiz. Tverd. Tela (Leningrad) **29** (8), 2479 (1987) [Sov. Phys. Solid State **29**, 1426 (1987)].
18. A. E. Aliev, A. Sh. Akramov, L. N. Fershtat, and P. K. Khabibullaev, Phys. Status Solidi A **108**, 189 (1988).
19. A. É. Aliev, A. Sh. Akramov, and R. R. Valetov, Fiz. Tverd. Tela (Leningrad) **31** (12), 178 (1989) [Sov. Phys. Solid State **31**, 2127 (1989)].
20. K. I. Avdienko, S. V. Bogdanov, S. M. Arkhirov, B. I. Kidyarov, V. V. Lebedev, Yu. E. Nevskiĭ, V. I. Trunov, D. V. Sheloput, and R. M. Shklovskaya, *Lithium Iodate: Growth of Crystals, Their Properties and Applications* (Nauka, Novosibirsk, 1980).
21. A. P. Philipse, J. Mater. Sci. Lett. **8**, 1371 (1989).
22. N. R. Abdulkhalikova and A. E. Aliev, Uzb. Fiz. Zh., No. 4, 50 (1991).
23. N. R. Abdulchalikova and A. E. Aliev, Synth. Met. **71**, 1929 (1995).
24. A. A. Zakhidov, R. H. Baughman, Z. Igbal, *et al.*, Science **282** (5390), 897 (1998).
25. O. Wiener, Phys. Z. **5**, 332 (1904).
26. *Acoustical Crystals*, Ed. by M. P. Shaskol'skaya (Nauka, Moscow, 1982).
27. S. Fayette, D. S. Smith, A. Smith, and C. Martin, J. Eur. Ceram. Soc. **20**, 297 (2000).
28. M. Kitayama, K. Hirao, M. Toriyama, and Sh. Kanzaki, J. Am. Ceram. Soc. **82** (11), 3105 (1999).
29. N. R. Abdulchalikova, A. E. Aliev, V. F. Krivorotov, and P. K. Khabibullaev, Solid State Ionics **107**, 59 (1998).

Translated by O. Borovik-Romanova

Physics of the Solid State, Vol. 45, No. 1, 2003, pp. 69–72. Translated from Fizika Tverdogo Tela, Vol. 45, No. 1, 2003, pp. 68–70.

SEMICONDUCTORS AND DIELECTRICS

Effect of Gamma Radiation on the Permittivity and Electrical Conductivity of $TlGaS_2$ Crystals

A. U. Sheleg, K. V. Iodkovskaya, and N. F. Kurilovich

Institute of Solid-State and Semiconductor Physics, Belarussian National Academy of Sciences, ul. Brovki 17, Minsk, 220072 Belarus

e-mail: sheleg@ifttp.bas-net.by

Received February 20, 2002; in final form, May 13, 2002

Abstract—The effect of gamma radiation on the permittivity ε and the electrical conductivity σ of $TlGaS_2$ crystals is investigated at frequencies of 0.1, 1, and 10 kHz and 1 MHz in the temperature range 200–370 K. It is shown that an increase in the temperature leads to an increase in the permittivity ε and the electrical conductivity σ. The electrical conductivity σ of $TlGaS_2$ samples irradiated with a dose of 10 MR and then measured at all frequencies and the permittivity ε of samples irradiated with a dose of 1 MR and then measured at frequencies of 10 kHz and 1 MHz increase, whereas further accumulation of the dose results in a decrease in the values of ε and σ. The parameters studied are characterized by a considerable dispersion: as the frequency increases, the permittivity ε decreases and the electrical conductivity σ increases. © *2003 MAIK "Nauka/Interperiodica".*

1. INTRODUCTION

Crystals of $TlGaS_2$ belong to semiconductors–ferroelectrics of the $TlA^{III}B_2^{VI}$ type (*A* is In or Ga and *B* is S or Se) with a layered structure and a number of interesting physical properties. The layered structure of these crystals is responsible for the strong anisotropy of their dynamic characteristics. Moreover, it has been demonstrated that representatives of this family, such as $TlGaSe_2$ and $TlInS_2$ crystals, have incommensurate phases and, correspondingly, undergo sequences of phase transitions from a highly symmetric phase to an incommensurate phase and, then, to a ferroelectric commensurate phase [1–3]. Although $TlGaSe_2$ and $TlInS_2$ compounds have been thoroughly studied, there exists some discrepancy between the phase transition temperatures determined by different authors. Earlier, Abdullaev *et al.* [4] assumed that these crystals are susceptible to polytypism due to their layered structure. More recently [5], different polytypic modifications of $TlGaSe_2$ and $TlInS_2$ crystals were revealed with x-ray diffraction. The above difference in the phase transition temperatures determined by different authors can be explained by the fact that the samples used in these studies belong to different polytypic modifications.

As regards $TlGaS_2$ crystals, they have been studied to a lesser degree as compared to $TlGaSe_2$ and $TlInS_2$ crystals. The data available in the literature on $TlGaS_2$ crystals are few in number and contradictory. In particular, Abdullaeva *et al.* [6] measured the heat capacity of $TlGaS_2$ in the temperature range 3–300 K and did not revealed anomalies in the heat capacity in the temperature range covered. Krupnikov and Abutalybov [7] observed anomalies in the curve $C_p = f(T)$ at temperatures $T_1 = 73.5$, $T_2 = 91$, $T_3 = 101$, $T_4 = 114$, $T_5 = 133.5$, and $T_6 = 187$ K. According to the authors' opinion [7], this indicates a sequence of phase transitions in the $TlGaS_2$ crystal. Mal'sagov *et al.* [8] analyzed the temperature dependences of the unit cell parameters of a $TlGaS_2$ crystal and revealed jumps in the parameters at $T = 121$ K, which suggests the occurrence of a phase transition at this temperature. Aliev *et al.* [9] reported the results of the dielectric measurements of a $TlGaS_2$ crystal at a frequency of 100 kHz in the temperature range 80–300 K. These authors found no anomalies in the temperature dependence of the permittivity $\varepsilon = f(T)$. It is quite possible that the contradictory results relating to $TlGaS_2$, $TlGaSe_2$, and $TlInS_2$ crystals are due to the existence of $TlGaS_2$ polytypes. Therefore, the use of different samples leads to different results.

This paper reports on the results of investigating the effect of gamma radiation on the permittivity ε and the electrical conductivity σ of $TlGaS_2$ crystals. The measurements were carried out at different frequencies in the temperature range 200–370 K.

2. SAMPLES AND EXPERIMENTAL TECHNIQUE

The permittivity and electrical conductivity of $TlGaS_2$ crystals were measured on an E7-12 digital meter at a frequency of 1 MHz and an E7-14 meter at frequencies of 0.1, 1, and 10 kHz. The measurements were performed using continuous heating at a rate of 0.5 K/min.

1063-7834/03/4501-0069$24.00

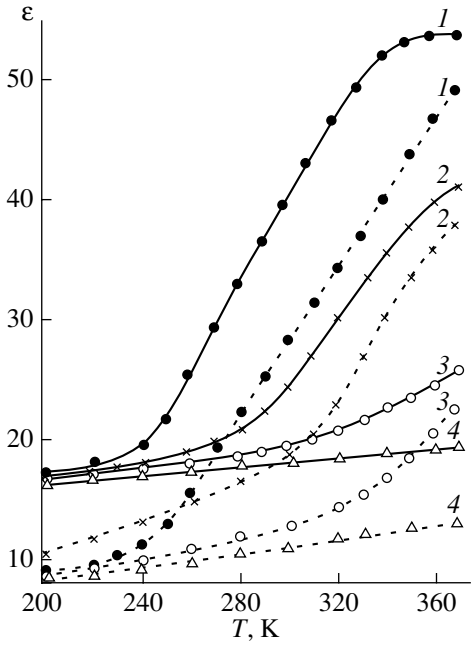

Fig. 1. Temperature dependences of the permittivity ε of the $TlGaS_2$ samples measured at frequencies of (*1*) 0.1, (*2*) 1, and (*3*) 10 kHz and (*4*) 1 MHz before (solid lines) and after (dashed lines) irradiation with a dose of 100 MR.

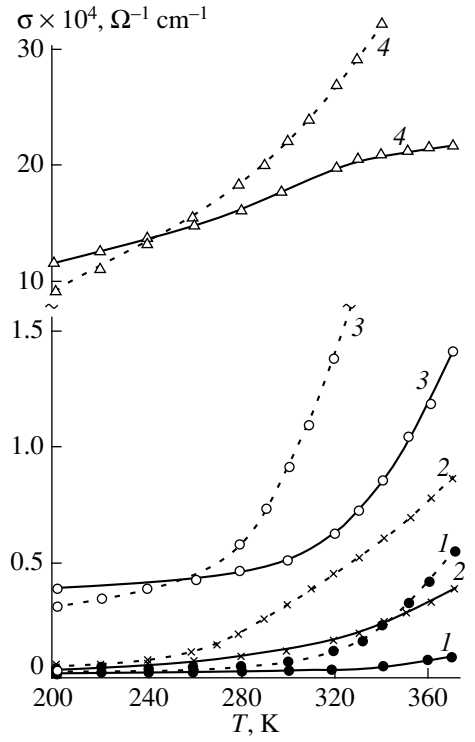

Fig. 2. Temperature dependences of the electrical conductivity σ of the $TlGaS_2$ samples measured at frequencies of (*1*) 0.1, (*2*) 1, and (*3*) 10 kHz and (*4*) 1 MHz before (solid lines) and after (dashed lines) irradiation with a dose of 100 MR.

Samples were prepared in the form of 0.5- to 0.7-mm-thick single-crystal plates. The surfaces of these plates were (001) cleavages. The electrodes used were made of a silver paste. The studied sample was placed in a special holder and immersed in nitrogen vapor. The temperature of the sample was measured by a chromel–copel thermocouple whose junction was located at the sample surface. The temperature was controlled using a heater mounted in the holder of the sample. The samples were irradiated on a gamma setup with a ^{60}Co source at room temperature. The power of the ^{60}Co source in the irradiation zone was ~180 R/s. The irradiation dose was accumulated in the same sample through consecutive exposures and amounted to 1, 10, 50, and 100 MR. The permittivity ε and the electrical conductivity σ were measured after each irradiation.

3. RESULTS AND DISCUSSION

Figures 1 and 2 show the temperature dependences of the permittivity and the electrical conductivity of a $TlGaS_2$ crystal measured at frequencies of 0.1, 1, and 10 kHz and 1 MHz (solid lines) and the permittivity $\varepsilon = f(T)$ and the electrical conductivity $\sigma = f(T)$ obtained using the same sample irradiated with a dose of 100 MR (dashed lines). It can be seen that, as the temperature increases, the permittivity ε and the electrical conductivity σ also increase for all the frequencies used in the measurements. This is due to an increase in the concentration of free charge carriers (manifestation of the semiconductor properties) and an increase in the mobility of the domain boundaries (manifestation of the ferroelectric properties) with an increase in the temperature.

It can be seen from Fig. 1 that gamma radiation with a dose of 100 MR results in a decrease in the permittivity ε over the entire temperature range studied and for all the frequencies used. This behavior of the permittivity of $TlGaS_2$ can be associated with the radiation-stimulated ageing of the samples due to gamma-activated migration of natural defects, which leads to stabilization of the domain structure and a decrease in the permittivity ε [10]. It should be noted that, at high frequencies, the electrical conductivity σ of $TlGaS_2$ irradiated samples is substantially higher than that of unirradiated samples (Fig. 2). As is known, the main gamma-radiation effect is induced by secondary Compton electrons and secondary photoelectrons [10]. The generation of secondary electrons and ionization of the medium bring about an increase in the electrical conductivity of the irradiated samples. Analysis of the experimental results demonstrates that the permittivities ε of $TlGaS_2$ samples irradiated with doses of 10 and 50 MR are intermediate between the permittivities of the samples measured before and after irradiation with a dose of 100 MR.

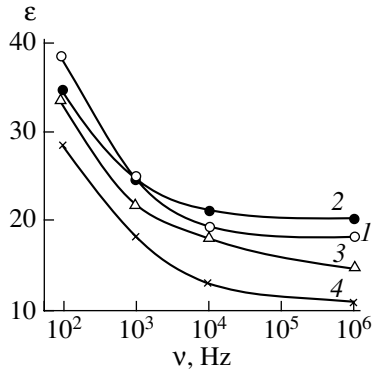

Fig. 3. Dispersion curves $\varepsilon = f(\nu)$ of $TlGaS_2$ samples (*1*) before and after irradiation with doses of (*2*) 1, (*3*) 10, and (*4*) 100 MR. $T = 300$ K.

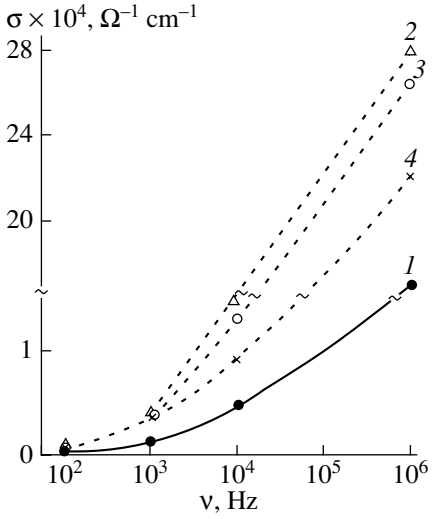

Fig. 4. Dispersion curves $\sigma = f(\nu)$ of $TlGaS_2$ samples (*1*) before and after irradiation with doses of (*2*) 10, (*3*) 50, and (*4*) 100 MR. $T = 300$ K.

The dispersion curves $\varepsilon = f(\nu)$ and $\sigma = f(\nu)$ at $T = 300$ K for $TlGaS_2$ crystals prior to and after irradiation with different doses are depicted in Figs. 3 and 4, respectively. It is evident that the permittivity ε for all the studied samples decreases with an increase in the frequency. The permittivities ε of the samples irradiated with a dose of 1 MR and measured at frequencies of 10 kHz and 1 MHz are somewhat larger than those of the unirradiated samples (Fig. 3). Further irradiation leads to a decrease in the permittivity ε as the irradiation dose accumulates. It can be seen from Fig. 4 that the electrical conductivity σ increases with increasing frequency. Mustafaev *et al.* [11] obtained similar experimental results for the isostructural composition $TlInS_2$. From analyzing the frequency dependence of the electrical conductivity, these authors made the inference that, in $TlInS_2$ semiconductors, the charge transfer occurs through the hopping mechanism and electrical conduction is due to optical transitions [11]. This can also explain the frequency dependence of the electrical conductivity $\sigma = f(\nu)$ in $TlGaS_2$. The electrical conductivity $\sigma(\nu)$ first increases as a result of irradiation with a dose of 10 MR and then decreases with a further increase in the irradiation dose, as is the case with the permittivity. This is associated with the fact that, when the irradiation doses are relatively small, defects in the irradiated crystal undergo annealing (the so-called effect of small doses). As was already mentioned, an increase in the irradiation dose brings about radiation-stimulated ageing of the sample and an increase in the concentration of defects in the crystal. Most probably, the scattering of charge carriers by defects leads to a decrease in the electrical conductivity $\sigma(\nu)$. Note that, at high frequencies, the permittivity $\varepsilon(\nu)$ of the irradiated samples, except for the case of the 1-MR dose, turned out to be smaller than that of the unirradiated samples (Fig. 3).

Analysis of the results obtained demonstrates that the permittivity ε and electrical conductivity σ of the $TlGaS_2$ crystal under study exhibit a pronounced dispersion. As the temperature increases, the permittivity ε drastically increases at low frequencies and weakly varies at high frequencies (Fig. 1). In actual fact, at a frequency of 1 MHz, the permittivity ε only slightly increases with increasing temperature. It seems likely that the decrease in the sensitivity of the permittivity ε with an increase in the frequency is due to relaxation processes occurring in the high-frequency range.

It should be noted that no anomalies are found in the curves $\varepsilon(T)$ and $\sigma(T)$. This indicates that the $TlGaS_2$ crystal does not undergo a sequence of phase transitions from a high symmetric phase to an incommensurate phase and then to a ferroelectric commensurate phase, which are typical of $TlGaSe_2$ and $TlInS_2$ crystals belonging to the same family as $TlGaS_2$.

ACKNOWLEDGMENTS

This work was supported by the Belarussian Foundation for Basic Research, project no. F99-043.

REFERENCES

1. S. B. Vakhrushev, V. V. Zhdanova, B. E. Kvyatkovskiĭ, *et al.*, Pis'ma Zh. Éksp. Teor. Fiz. **39** (6), 245 (1984) [JETP Lett. **39**, 291 (1984)].
2. D. F. McMorrow, R. A. Cowley, P. D. Hatton, and I. Banys, J. Phys.: Condens. Matter **2** (16), 3699 (1990).
3. A. U. Sheleg, O. B. Plyushch, and V. A. Aliev, Fiz. Tverd. Tela (St. Petersburg) **36** (1), 226 (1994) [Phys. Solid State **36**, 124 (1994)].
4. G. B. Abdullaev, G. I. Abutalybov, A. A. Aliev, *et al.*, Pis'ma Zh. Éksp. Teor. Fiz. **38** (11), 525 (1983) [JETP Lett. **38**, 632 (1983)].

5. O. B. Plyushch and A. U. Sheleg, Kristallografiya **44** (5), 873 (1999) [Crystallogr. Rep. **44**, 813 (1999)].
6. S. G. Abdullaeva, A. M. Abdullaev, K. K. Mamedov, and N. G. Mamedov, Fiz. Tverd. Tela (Leningrad) **26** (2), 618 (1984) [Sov. Phys. Solid State **26**, 375 (1984)].
7. E. S. Krupnikov and G. I. Abutalybov, Fiz. Tverd. Tela (St. Petersburg) **34** (9), 2964 (1992) [Sov. Phys. Solid State **34**, 1591 (1992)].
8. A. U. Mal'sagov, B. S. Kul'buzhev, and B. M. Khamkhoev, Izv. Akad. Nauk SSSR, Neorg. Mater. **25** (2), 216 (1989).
9. R. A. Aliev, K. R. Allakhverdiev, A. I. Baranov, *et al.*, Fiz. Tverd. Tela (Leningrad) **26** (5), 1271 (1984) [Sov. Phys. Solid State **26**, 775 (1984)].
10. E. V. Peshikov, *Radiation Effects in Ferroelectrics* (Tashkent, 1986).
11. S. N. Mustafaev, M. M. Asadov, and V. A. Ramazanzade, Fiz. Tverd. Tela (St. Petersburg) **38** (1), 14 (1996) [Phys. Solid State **38**, 7 (1996)].

Translated by O. Moskalev

Physics of the Solid State, Vol. 45, No. 1, 2003, pp. 73–77. Translated from Fizika Tverdogo Tela, Vol. 45, No. 1, 2003, pp. 71–75.

SEMICONDUCTORS AND DIELECTRICS

Trimers of Bivalent Copper Impurity Ions in CaF_2 Crystals: The Structure and Mechanism of Formation

V. A. Ulanov, M. M. Zaripov, E. P. Zheglov, and R. M. Eremina

Kazan Physicotechnical Institute, Russian Academy of Sciences, Sibirskiĭ trakt 10/7, Kazan 29, 420029 Tatarstan, Russia
e-mail: ulanov@dionis.kfti.kcn.ru

Received February 18, 2002; in final form, May 14, 2002

Abstract—Crystals of CaF_2 : Cu (with a copper impurity content higher than 0.1 at. %) grown by the Czochralski method from a melt in a mixed helium–fluorine atmosphere are investigated using electron paramagnetic resonance (EPR) spectroscopy. It is found that the crystals contain paramagnetic centers whose magnetic properties at low temperatures are identical to those of $[CuF_4F_4]^{6-}$ ($S = 1/2$) single centers. The magnetic properties of the centers exhibit a qualitative change in the temperature range 77–300 K. These changes are described within a model according to which the center is treated as a cluster composed of three $[CuF_4F_4]^{6-}$ impurity complexes involved in exchange interactions and interactions occurring in the field of Jahn–Teller lattice distortions. © *2003 MAIK "Nauka/Interperiodica".*

1. INTRODUCTION

It is known that crystals belonging to the fluorite structural family (CdF_2, CaF_2, SrF_2, and BaF_2) have a loose-packed lattice with predominantly ionic bonds between atoms. Consequently, at high temperatures, intensive correlated diffusion of both host-lattice and impurity ions occurs in response to an external electric field or in the presence of an impurity concentration gradient in the lattice [1]. This diffusion of copper impurity ions in a BaF_2 crystal brings about the formation of copper stable dimers [2]. Under certain conditions, the concentration of copper stable dimers in the crystal can turn out to be higher than that of copper single centers. Apparently, two impurity paramagnetic centers of bivalent copper are bound into a thermally stable dimer due to an interaction between impurity single centers, which, in turn, leads to a decrease in the lattice energy. For copper dimers in a BaF_2 crystal, the nature of this interaction can be better understood when it is considered that, upon replacement of a Ba^{2+} cation by a bivalent copper impurity ion, this ion is located at the center of a regular cube and its orbital ground state is represented by the $^2T_{2g}$ triplet. In this situation, lattice vibrations should significantly affect the bivalent copper states and, particularly, result in substantial displacements of ions surrounding the copper impurity to new equilibrium positions (the Jahn–Teller effect). In the case of a BaF_2 : Cu crystal, the copper impurity ion is also appreciably displaced (by ~1 Å). This brings about a considerable polarization of the lattice in the vicinity of the copper impurity ion and gives rise to large electric dipole moments. The energy of interaction between copper off-center complexes ~5 Å apart with parallel electric dipole moments is roughly estimated at ~0.1–0.2 eV. This energy accounts for the dimerization of impurity ions in the host lattice of the crystal under conditions of intensive diffusion.

The purpose of this work was to analyze the possibility of forming copper impurity clusters in a CaF_2 crystal and to investigate their magnetic properties. We believed that clusters of a new type could be formed in a matrix with a unit cell of considerably smaller size.

2. SAMPLE PREPARATION, EXPERIMENTAL TECHNIQUE, AND RESULTS

The crystals to be studied were grown by the Czochralski method. The crucibles used for the crystal growth were produced from chemically pure graphite. Impurities in the form of carefully dried CuF_2 were introduced into a melt of chemically pure calcium fluoride. With the aim of maintaining equilibrium between the processes of thermal decomposition and formation of copper fluoride, gaseous fluorine was added in small amounts to the helium atmosphere used in the crystal growth.

The grown crystals were examined using electron paramagnetic resonance (EPR) spectroscopy on an E-12 Varian spectrometer operating in the *X* and *Q* bands (9.3 and 37 GHz, respectively) at liquid-helium temperature and in the temperature range 77–300 K. It was found that, in the case when the impurity concentration was less than or equal to 0.5 at. % and the temperature gradient in the vicinity of the crystallization front was greater than or equal to 20 K/mm, the grown crystals predominantly contained $[CuF_4F_4]^{6-}$ orthorhombic centers, whose structure and magnetic parameters were described in our earlier work [3]. For the crystals grown at higher impurity concentrations and smaller temperature gradients (≤5 K/mm), the EPR

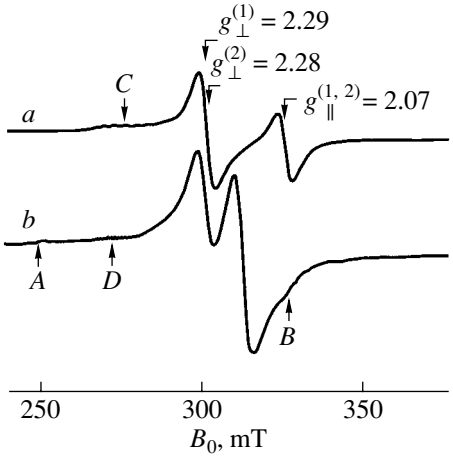

Fig. 1. EPR spectra of the CaF_2 : Cu (0.2 at. %) sample measured in the *X* band at a temperature of 77 K for two principal orientations of the crystal: (*a*) $\mathbf{B}_0 \parallel \langle 001 \rangle$ and (*b*) $\mathbf{B}_0 \parallel \langle 110 \rangle$.

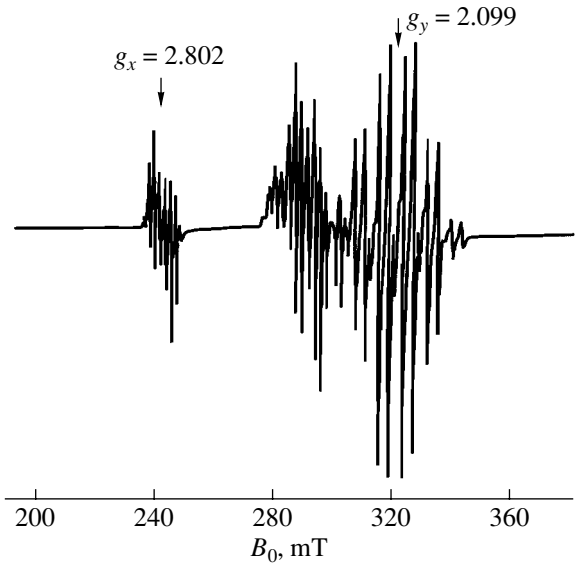

Fig. 2. EPR spectrum of the CaF_2 : Cu (0.2 at. %) sample measured in the *X* band at a temperature of 4.2 K for the orientation $\mathbf{B}_0 \parallel \langle 110 \rangle$.

spectra measured at temperatures in the range 77–300 K exhibited intense lines attributed to paramagnetic centers with axial symmetry of the magnetic properties. In this case, the crystals had a red color.

The EPR spectrum of a crystal arbitrarily oriented with respect to the external dc magnetic field vector contains six structureless lines, each approximately 5 mT wide. Moreover, these lines overlap with each other in pairs. Figure 1 shows the EPR spectra measured in the *X* band at a temperature of 77 K for the two most important orientations of the crystal with respect to the external magnetic field, namely, $\mathbf{B}_0 \parallel \langle 001 \rangle$ (spectrum *a*) and $\mathbf{B}_0 \parallel \langle 110 \rangle$ (spectrum *b*). The angular dependences of the line position turned out to be characteristic of transitions between states of two spin doublets with the effective spin moments $S^{(1)} = S^{(2)} = 1/2$.

These dependences can be adequately described by two orthorhombic tensors of the electron Zeeman interaction with the following principal components: $g_x^{(1)} = g_y^{(1)} = g_\perp^{(1)} = 2.28 \pm 0.01$, $g_z^{(1)} = 2.075 \pm 0.005$, $g_x^{(2)} = g_y^{(2)} = g_\perp^{(2)} = 2.29 \pm 0.01$, and $g_z^{(2)} = 2.075 \pm 0.005$. In the temperature range 77–300 K, these components do not depend on the temperature within the limits of experimental error. Investigations performed at frequencies of 9.3 and 37.3 GHz revealed that the electron Zeeman interaction almost linearly depends on the magnetic field (i.e., the components of the tensors $g^{(1)}$ and $g^{(2)}$ are independent of the magnetic field strength).

In addition to the intense structureless lines, the EPR spectra measured for the principal orientations of the crystal contain several groups of weak lines (Fig. 1). Since these lines were masked by noise arising upon rotations of the crystal through small angles, we failed to obtain the angular dependences of their positions.

Figure 2 displays the EPR spectrum of the studied crystal at a low temperature (4.2 K) for the orientation $\mathbf{B}_0 \parallel \langle 110 \rangle$. This spectrum coincides in every detail with the spectrum of $[CuF_4F_4]^{6-}$ impurity single centers, which was thoroughly examined in [3]. The sole difference resides in the fact that the line width for lightly doped samples is two or three times smaller. No signals other than those observed in the aforementioned spectra are revealed at this temperature (with the aim of searching for broad lines, the electromagnetic field power in the cavity was reduced to a level of 0.01 mW, at which the possibility of saturating a resonance transition was ruled out).

An important experimental characteristic is the temperature dependence of the intensity ratio of spectral lines of the second and first groups, which, in turn, can be characterized by the tensors $g^{(2)}$ and $g^{(1)}$, respectively. It was found that this ratio increases with increasing temperature.

We examined the crystals grown at different concentrations of copper impurities in the CaF_2 melts. It was revealed that a decrease in the content of copper introduced into the melt leads to a drastic decrease in the concentration of the centers under investigation. However, in this case, the components of the electron Zeeman interaction tensor and the EPR line shape remain unchanged. Moreover, these parameters prove to be independent of the shape of the studied samples.

3. DISCUSSION

In order to answer the question as to the nature of the magnetic centers revealed in the crystals under investigation, we analyzed different variants of defect structures in the samples. For this purpose, we considered the characteristic temperature dependence of the intensity ratio of two groups of structureless resonance lines, their widths, the electron Zeeman interaction tensor components characterizing the angular dependences of these lines, the dynamic properties of copper single complexes, and the character of local lattice distortions produced by these complexes. In addition, we took into account that no impurities other than copper ions were introduced into the crystal. The hypothetical model of the centers under consideration should also explain their relatively high concentration.

The experimental fact that the measurements performed at a temperature of 4.2 K under conditions far from saturation revealed no broad structureless lines is of crucial importance. It turned out that the spectra observed are characteristic of $[CuF_4F_4]^{6-}$ orthorhombic complexes. It is also important that the intensity ratio of the two groups of structureless resonance lines observed at temperatures ranging from 77 to 300 K depends on the temperature. These findings allow us to draw the inference that one of the groups of structureless resonance lines whose relative intensity increases with increasing temperature corresponds to EPR transitions within a certain excited spin doublet of a paramagnetic center created in the crystal. As follows from analyzing the obtained temperature dependence of the relative intensity of the structureless lines, the energy separation between the ground spin state of the center and this doublet is of the order of 30–50 cm^{-1}. It is clear that, if the above assumption holds true, this group of lines should not be observed at 4.2 K. It is also evident that the ground state of this center should be represented by a spin multiplet with a half-integer effective spin moment. Consequently, the other group of more intense structureless lines is associated with the transitions within this ground spin multiplet (according to our experimental data, this is a doublet).

Therefore, the hypothetical model of the clusters under investigation must satisfy the following three main requirements.

(1) At low temperatures, the EPR spectra of the ground spin doublet of the studied cluster should be similar to the spectra of a copper impurity single complex with orthorhombic symmetry [3].

(2) In the temperature range 77–300 K, these spectra should transform into structureless lines whose angular dependences can be described by the axial tensor $g^{(1)}$.

(3) The angular dependences of the EPR spectra of the excited doublet in the temperature range 77–300 K should correspond to experimental angular dependences of the structureless resonance lines characterized by the tensor $g^{(2)}$.

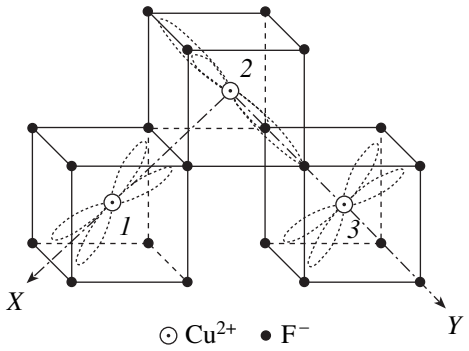

Fig. 3. A model of the copper trimer in a CaF_2 : Cu crystal. The t_2 orbitals occupied by an electron hole of Cu^{2+} ions are shown. The coordination cubes of Cu^{2+} ions are contracted along the C_2 axis lying in the plane of the t_2 orbital.

On this basis, we proposed a model according to which the cluster is treated as a copper trimer formed by three bivalent copper single complexes with orthorhombic symmetry (Fig. 3). The electron Zeeman interaction in orthorhombic fragments of the trimer ($S = 1/2$) is characterized by a g tensor with the following components: $g_x = 2.099$, $g_y = 2.147$, and $g_z = 2.802$. Figure 3 corresponds to one of the molecular configurations of the trimer at low temperatures of the crystal. In this configuration, each orthorhombic fragment of the trimer is localized in one out of six equivalent wells of the adiabatic potential. It can be seen that, within the proposed model, orthorhombic Jahn–Teller distortions (corresponding to a contraction of the coordination cube along one of the twofold axes [3]) correlate with each other. Note that the total energy of elastic strains produced by Jahn–Teller distortions in the host lattice of the crystal in the vicinity of the trimer appears to be less than the total energy of strains arising around widely spaced Jahn–Teller single centers. Since the copper nuclei in the trimer are located in the plane aligned parallel to one of the (001) planes in the crystal, it is obvious that the number of different cluster orientations in the CaF_2 crystal is equal to the product $3 \times 4 \times 2 = 24$. The number 2 in this product corresponds to the number of ground nuclear configurations of each particular cluster, i.e., to the number of wells of the adiabatic potential for this cluster. One of these configurations is depicted in Fig. 3. The other configuration can be obtained by transferring a hole in the Cu 3d filled shell from one orbital t_2 to another orbital t_2 in each of the three complexes forming the trimer. In this case, care should be taken to see that the Jahn–Teller distortions remain correlated. Taking into account that the frequency of transitions between wells of the adiabatic potential for a copper single complex drastically increases at temperatures of 25–30 K [4], we believe that similar transitions in the trimer should be intensive at slightly higher temperatures (40–60 K). At temperatures above 60 K, the EPR spectra of the trimer should

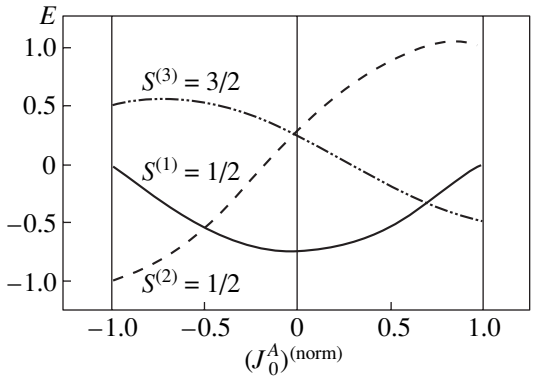

Fig. 4. Changes in the energy diagram for spin levels of the orbital ground state of a trimer localized in one of the two wells of the adiabatic potential as a function of the quantity $(J_0^A)^{(\mathrm{norm})}$.

transform in such a manner that they can be adequately described by the averaged perpendicular components of the low-temperature *g* tensors; that is,

$$g_\perp^{(i)} = \frac{g_x^{(i)} + g_y^{(i)}}{2},$$

where $g_x^{(i)}$ and $g_y^{(i)}$ are the *x* and *y* components of the *g* tensors for the ground and excited spin doublets (i = 1 and 2, respectively) of the trimer.

The positions of groups *A* and *B* of weak lines in Fig. 1 coincide with those of the lines in the low-temperature spectrum. This experimental finding indicates that certain trimers at T = 77 K remain localized in their wells of the adiabatic potential. It seems likely that local strains in the crystal appear to be the strongest in the vicinity of these trimers. As regards groups *C* and *D* of resonance lines in Fig. 1, they can be associated with the resonance transitions between excited spin states of these trimers. However, these lines can also be attributed to the transitions between excited spin states of copper clusters of another type (for example, copper dimers, which can be formed in the crystal with a sufficiently high probability).

The parameters of the model proposed were calculated within the approximation of pair exchange coupling between trimer fragments. The numbering of single complexes (trimer fragments) is shown in Fig. 3. Within a rough approximation in which the anisotropic parts of the exchange interaction tensors can be ignored, the spin Hamiltonian of the orbital ground state of the trimer can be represented as follows:

$$\mathbf{H}_S = -\mathbf{S}_1 \cdot J_0^A \cdot \mathbf{S}_2 - \mathbf{S}_2 \cdot J_0^A \cdot \mathbf{S}_3 - \mathbf{S}_1 \cdot J_0^B \cdot \mathbf{S}_3, \quad (1)$$

where S_j are the electron spin operators for the copper single complexes forming the trimer and J_0^A and J_0^B are the isotropic exchange constants. The eigenvalues of the spin Hamiltonian are the energies of three spin multiplets, namely, a quartet (S = 3/2) and two doublets (S = 1/2). The relative positions of these multiplets on the energy axis can differ depending on the magnitudes and signs of the isotropic exchange constants (J_0^A and J_0^B). Figure 4 depicts the dependences of the energy of the spin multiplets on the quantity $(J_0^A)^{(\mathrm{norm})} = J_0^A/((J_0^A)^2 + (J_0^B)^2)^{1/2}$ {the energy E is expressed in terms of $[(J_0^A)^2 + (J_0^B)^2]^{1/2}$}.

When analyzing the electron Zeeman interaction of the trimer with an external dc magnetic field, we restrict our consideration to the approximation in which the operator of this interaction can be written in the form

$$\mathbf{H}_Z = \beta_e(\mathbf{S}_1 \cdot \mathbf{g}_1 + \mathbf{S}_2 \cdot \mathbf{g}_2 + \mathbf{S}_3 \cdot \mathbf{g}_3) \cdot \mathbf{B}_0, \quad (2)$$

where g_1, g_2, and g_3 are the Zeeman interaction tensors for three orthorhombic copper complexes (trimer fragments) and $\mathbf{B}_0$ is the external dc magnetic field vector. In the framework of our approximation, the components of these tensors are taken to be equal to the corresponding components for the copper single complexes. In actual fact, these components for trimer fragments can be different, because the trimer fragments interact with each other; i.e., they can be involved in the Coulomb interaction and the interaction occurring in the field of Jahn–Teller distortions. To a first approximation, the components of the *g* tensor for the excited spin doublet (with an intermediate spin moment S_{13} = 1) of the trimer can be represented by the relationships

$$g_x^{(2)} = -\frac{2g_{1x} - g_{2x} + 2g_{3x}}{3},$$

$$g_y^{(2)} = -\frac{2g_{1y} - g_{2y} + 2g_{3y}}{3}, \quad (3)$$

$$g_z^{(2)} = -\frac{2g_{1z} - g_{2z} + 2g_{3z}}{3}.$$

For the ground spin doublet (S_{13} = 0), we have

$$g_x^{(1)} = g_{2x}, \quad g_y^{(1)} = g_{2y}, \quad g_z^{(1)} = g_{2z}. \quad (4)$$

Here, g_{jx}, g_{jy}, and g_{jz} are the components of the electron Zeeman interaction tensors for copper single centers forming the trimer under investigation (the tensors are represented in the general coordinate system *XYZ*) and j = 1–3 are the numbers of these fragments of the trimer according to the numbering shown in Fig. 3. Within this approximation, the magnitudes of the components of the *g* tensor for the excited spin doublet of the trimer are as follows:

$$g_x^{(2)} = 3.03, \quad g_y^{(2)} = 1.87, \quad g_z^{(2)} = 2.14.$$

The components of the electron Zeeman interaction tensor for the ground spin doublet coincide with the corresponding components of the *g* tensor for an impu-

rity single center oriented in the crystal in the same manner as fragment *2* in the trimer; that is,

$$g_x^{(1)} = 2.802, \quad g_y^{(1)} = 2.099, \quad g_z^{(1)} = 2.147.$$

For a temperature of 77 K and higher (at which the frequency of internuclear transitions in the trimer becomes considerably higher than the EPR frequency), the mean value of the perpendicular component of the *g* tensor for the excited spin doublet was calculated in the above approximation and amounted to 2.45. For the ground doublet, we obtained approximately the same value (~2.45). The parallel component of the *g* tensor for both doublets was not averaged and remained equal to 2.147. These components (calculated to the second order in the perturbation theory) of the electron Zeeman interaction tensors are appreciably larger than the experimental components:

$$g_\perp^{(1)} = 2.28, \quad g_z^{(1)} = 2.075,$$

$$g_\perp^{(2)} = 2.29, \quad g_z^{(2)} = 2.075.$$

This discrepancy can be explained by the fact that the dynamic properties of the trimer were ignored in these calculations. Let us assume that, during internuclear transitions in the trimer, molecular motions in its fragments occur not synchronously but with a certain lag. Under this assumption, negative corrections to the components of the aforementioned tensors *g* arise already within the second order in the perturbation theory and lead to an improvement in the results of calculations.

For the ground spin doublet, we performed a more detailed calculation of the hyperfine and superhyperfine structures of the EPR spectra of the trimer. The spin Hamiltonian of electron–nucleus interactions was represented as the sum $\mathbf{H}_{en} = \mathbf{H}_{hfi} + \mathbf{H}_{shfi}$. Here,

$$\mathbf{H}_{hfi} = \sum_i (\mathbf{S}_i \cdot \mathbf{a}_i \cdot \mathbf{I}_i^{Cu} + \mathbf{I}_i^{Cu} \cdot \mathbf{Q}_i \cdot \mathbf{I}_i^{Cu} - \beta_n g_n^{Cu} I_i^{Cu} \cdot \mathbf{B}_0), \quad (5a)$$

$$\mathbf{H}_{shfi} = \sum_i \sum_j (\mathbf{S}_i \cdot \mathbf{A}_{ij} \cdot \mathbf{I}_{ij}^F - \beta_n g_n^F \mathbf{I}_{ij}^F \cdot \mathbf{B}_0). \quad (5b)$$

In Hamiltonians (5a) and (5b), subscript *i* refers to the copper ions in the trimer; subscript *j* indicates fluorine nuclei that are ligands of the *i*th impurity ion; $\mathbf{S}_i$ is the operator of the electron spin of the *i*th copper ion; $\mathbf{a}_i$ and $\mathbf{Q}_i$ are the hyperfine and quadrupole interaction tensors for the *i*th copper ion, respectively; $\mathbf{A}_{ij}$ is the tensor of the superhyperfine interaction between the electron spin moment of the *i*th copper ion and the nucleus of the *j*th ligand; and $\mathbf{I}_{ij}^F$ is the operator of the nuclear spin of the *j*th ligand of the *i*th copper impurity ion. According to the results of our calculations, the EPR spectrum of the ground spin doublet of the trimer coincides (to the second order in the perturbation theory) with the spectrum of a copper single complex with orthorhombic symmetry.

4. CONCLUSIONS

Thus, the results obtained in the present work and in our earlier experimental studies [2, 4] demonstrated that a large number of complex paramagnetic clusters that are formed by impurity ions of the iron group and have a regular molecular structure can be created in the bulk of crystals belonging to the fluorite structural family. The copper impurity clusters (copper trimers) formed in CaF_2 crystals are adequately described in the framework of the model presented in Fig. 3. These clusters are characterized by a multiple-well adiabatic potential and a complex system of low-lying spin energy levels. As a consequence, their physical properties are extremely sensitive to distortions of the host lattice of the crystal and a change in the temperature. One of the main reasons for the formation of the trimer under investigation is the interaction between the trimer fragments in the field of Jahn–Teller distortions.

ACKNOWLEDGMENTS

This work was supported by the Russian Foundation for Basic Research, project no. 01-02-17718.

REFERENCES

1. G. C. Benson and E. Dempsey, Proc. R. Soc. London, Ser. A **226**, 344 (1962).
2. M. M. Zaripov and V. A. Ulanov, Fiz. Tverd. Tela (Leningrad) **31** (10), 254 (1989) [Sov. Phys. Solid State **31**, 1798 (1989)].
3. M. M. Zaripov and V. A. Ulanov, Fiz. Tverd. Tela (Leningrad) **30**, 1547 (1988) [Sov. Phys. Solid State **30**, 896 (1988)].
4. V. A. Ulanov, M. M. Zaripov, and E. P. Zheglov, in *Abstracts of XI Feofilov Symposium on Spectroscopy of Crystals Activated by Rare-Earth and Transition-Metal Ions, Kazan, 2001*, p. 52.

Translated by O. Borovik-Romanova

Physics of the Solid State, Vol. 45, No. 1, 2003, pp. 78–81. Translated from Fizika Tverdogo Tela, Vol. 45, No. 1, 2003, pp. 76–79.

SEMICONDUCTORS AND DIELECTRICS

Ligand Hyperfine Interaction in Gd^{3+} Tetragonal Centers in CaF_2 and SrF_2 and the Structure of the Impurity Nearest Surroundings

A. D. Gorlov

Institute of Physics and Applied Mathematics, Ural State University, pr. Lenina 51, Yekaterinburg, 620083 Russia
e-mail: Anatoliy.Gorlov@usu.ru

Received February 12, 2002; in final form, May 18, 2002.

Abstract—ENDOR experimental spectra of Gd^{3+} tetragonal impurity centers in CaF_2 and SrF_2 crystals were used to determine the superhyperfine interaction (SHFI) constants of the impurity with ^{19}F nuclear spins of its first coordination sphere and the compensator ion. The distances in the $Cd^{3+}F_9^-$ complex were estimated within the model of isotropic SHFI constants suggested in [1]. An analysis of the data on the SHFI and spin-Hamiltonian constants [2] in terms of the superposition model indicates significant changes in the contributions (due to the Gd^{3+} mixed states) to these parameters for the tetragonal centers in comparison with the corresponding contributions for the cubic and trigonal centers in the same crystals. © *2003 MAIK "Nauka/Interperiodica".*

1. INTRODUCTION

A specific feature of tetragonal Gd^{3+} impurity centers (ICs) in CaF_2 and SrF_2 crystals is that the fluorine ion (F^-) in the nearest neighbor interstice along the axis C_4 is a compensator (F^k) of the surplus positive charge of the impurity. The Coulomb interaction between the IC and F^k causes opposite displacements of Gd^{3+} (from the $8F^-$ cube center) and F^k [3]. A comparison of the coordinates of ^{19}F nuclei located in the 2nd–4th shells of the neighbor (hereinafter, the anion environment is meant) with the positions of ligands in the undistorted lattice and the Gd^{3+} cubic centers in the same crystals [4] shows that the most significant displacements take place in the region close to the compensator. In this paper, we consider the displacements of atoms of the nearest ligands and the compensator using the results of ENDOR studies of the superhyperfine interaction (SHFI) between Gd^{3+} (electron spin $S = 7/2$) and ^{19}F nuclei (nuclear spin $I = 1/2$), as well as of studies of the parameters of initial splitting and the quadrupole and intrinsic hyperfine (HFI) interactions [2] for ^{157}Gd in CaF_2 and SrF_2.

2. ENDOR DATA AND DISCUSSION

CaF_2 and SrF_2 crystals grown by the Stockbarger method with a GdF_3 impurity (0.015 wt % in blend) exhibited tetragonal and cubic Gd^{3+} ESR spectra, and SrF_2 also exhibited an additional trigonal spectrum, with intensity ratios of 3 : 1 and 5 : 1 : 4, respectively. The ESP of the tetragonal centers in the range of 3 cm at temperature $T = 4.2$ K was described by the conventional spin Hamiltonian (SH) with the parameters given in [2] in the laboratory system of coordinates, where the principal symmetry axis C_4 of the center is parallel to the Z and [001] axes and the X and Y axes are parallel to [100] and [010], respectively.

The ENDOR spectra in an external magnetic field **H** directed along the crystal symmetry axes (C_4, C_3, C_2) and the angular dependences in the plane {001} were studied. The IC displacement along the C_4 axis caused by F^k results in the eight fluorine nuclei (with local symmetry C_s) nearest to Gd^{3+} being divided into two groups. For the orientations $\mathbf{H} \parallel (C_2, C_4)$ and $\mathbf{H} \perp C_4$, the ENDOR signals for both groups of ^{19}F ions [forming regular quadrangles lying above (111-type nuclei close to the compensator) and under the {001} plane ($\bar{1}\bar{1}\bar{1}$-type nuclei)] had a fine structure caused by the indirect nucleus–nucleus interaction through the impurity ion [5, 6], with the center of this structure coinciding with the signal positions in the absence of this interaction.

The procedure of SHFI constant determination used was the same as that in [1]. The Hamiltonian H_n adequately describing the electron–nucleus interaction between Gd^{3+} and ^{19}F is given by

$$H_n = (A_s + 2A_p)O_1^0(S)O_1^0(I) + (A_s - A_p - A_E) \times O_1^1(S)O_1^1(I) + (A_s - A_p + A_E)\Omega_1^1(S)\Omega_1^1(I) + (A_1 + 4A_2)O_3^0(S)O_1^0(I) + (A_1 - 3A_2) \quad (1)$$

Experimental SHFI constants and the angular coordinates of the nearest ligands at the Gd^{3+} tetragonal centers in CaF_2 and SrF_2, as well as the model isotropic constants, distances, and induced dipole moments

Crystal	CaF_2			SrF_2		
Nucleus type	111	$\bar{1}\bar{1}\bar{1}$	F^k	111	$\bar{1}\bar{1}\bar{1}$	F^k
Ligand local symmetry	C_s	C_s	C_{4v}	C_s	C_s	C_{4v}
A_s, MHz	–1.994(3)	–1.315(3)	–0.842(3)	–2.236(4)	–1.179(4)	–0.522(3)
A_p, MHz	4.984(3)	4.576(3)	4.391(3)	4.841(2)	4.279(3)	3.919(3)
A_E, kHz	–42(4)	–50(3)	–	–55(6)	–31(4)	–
$A_1 \times 10$, kHz	–4(3)	0.9(19)	–9(2)	–4(3)	–0.7(32)	–4(2)
$A_2 \times 10$, kHz	–0.8(4)	0.2(35)	0(1)	–1.6(6)	–0.8(6)	0(1)
$A_3 \times 10$, kHz	1.8(4)	0(7)	–	1(4)	0.6(6)	–
$A_4 \times 10$, kHz	5(2)	0(7)	–	0(2)	6(3)	–
θ, deg	63.7(1)	129.1(1)	0	63.8(1)	129.4(1)	0
A_s, MHz, calculation	–1.99	–1.27	–0.80	–2.22	–1.22	–0.47
R, Å, calculation	2.30	2.40	2.32	2.33	2.42	2.35
D_i, e Å, calculation	0.14	0.08	0.2	0.125	0.085	0.21
$D\cos\theta$, e Å, calculation	0.035	–0.05	0.08	0.033	–0.048	0.075

Note: The F^- ion polarizability α is taken from [7]; α = 1 for the IC.

$$\times (O_3^1(S)O_1^1(I) + \Omega_3^1(S)\Omega_1^1(I)) + (A_3 + A_4)$$
$$\times (O_3^1(S)O_1^1(I) - \Omega_3^1(S)\Omega_1^1(I)) - g_n\beta_n(HI).$$

The notation in Eq. (1) is conventional [5, 6]. We emphasize that H_n contains only the terms whose contributions to the ENDOR frequencies exceed the experimental errors. Therefore, Eq. (1) in fact corresponds to the higher local symmetry C_{2v} of nuclei. Equation (1) yields the SH for F^k with local symmetry C_{4v} at A_E and $A_2 = A_4 = 0$. The SHFI constants are defined in the local frame of reference of a separated nucleus (the z axis is parallel to the Gd^{3+}–^{19}F bond axis, and the x axis lies in the plane containing the bond axis and C_3). The ligand angular coordinates θ (between the Gd^{3+}–^{19}F bond axis and axis Z) and φ (between the projection of the bond axis onto plane XY and axis X) were determined as in [1]. Axis C_4 is retained at the tetragonal centers; therefore, φ = 45° for the nearest ligands.

The table lists the experimentally determined SHFI constants and the angular coordinates of the nearest neighbor anions and F^k (the IC is at the origin of coordinates). One can see that nuclei of type 111 ($\bar{1}\bar{1}\bar{1}$) are characterized by angles θ > 54.74° (125.24°), which are appreciably larger than those for the cubic centers. This is obviously caused both by F^k forcing the 111-type nuclei apart and by the IC displacement to the compensator. The results of [4] show that the positions of ^{19}F nuclei far from the compensator (2nd–4th shells of the IC environment) virtually coincide (to within the experimental error) with the coordinates of the same anions for cubic ICs in these crystals when the Gd^{3+} displacement is taken into account. Assuming that the displacements of the nearest $\bar{1}\bar{1}\bar{1}$-type ligands are also small in comparison with those for cubic ICs and that the increase in θ is caused only by Gd^{3+} displacement along the C_4 axis, we approximate the distances $R(\bar{1}\bar{1}\bar{1})$ as 2.40 and 2.42 Å for CaF_2 and SrF_2, respectively. The same result was previously obtained in [3] in theoretical calculations of the local structure of the tetragonal rare-earth impurity centers in MeF_2.

The distance R for ^{19}F in the 2nd–4th shells close to the compensator is shorter than that for cubic ICs in these crystals. This can take place only under the condition that F^k is significantly displaced to Gd^{3+} from the center of the nearest neighbor interstice. Otherwise, Coulomb repulsion of like charges would result not only in a change in the angle θ but also in an increase in R for these ^{19}F nuclei in comparison with the case of cubic ICs even for a Gd^{3+} displacement along the C_4 axis. As was indicated in [3], $R(111)$ is roughly equal to the IC–F^k distance $R(k)$.

3. ANALYSIS OF THE ISOTROPIC SHFI AND SH CONSTANTS

The distances $R(111)$ and $R(k)$ were estimated within the model proposed in [1], but the equation for the constant A_s defined in [1, Eq. (3)] was modified as

$$A_s = [A_s(R_0) + K_s'D\cos\theta_i](1 + K_sD_i)(R_0/R_i)^3. \quad (2)$$

The parameters $A_s(R_0)$, K_s, and K_s' have the same meaning as in [1]. The dipole moments of F^- (D_i) and Gd^{3+}

(D) were also determined in a similar way. For rough estimations, we neglect the radial dependence of the parameter K_s' because of its small contribution (K_s' = –50(4) MHz/e Å for the trigonal center in this approximation). This equation is more adequate, since it takes the dependence of A_s on the overlapping of outer electrons of the polarized IC with electrons of the polarized ligand into account more correctly [8].

The values of A_s were calculated as in [1], i.e., by varying $R(111)$, $R(k)$, D_i, and D. The coordinates of the ^{19}F atoms in the second and more distant shells of neighbors were taken from [4]. The positions of cations in CaF_2were taken from [3], taking into account that the minimum Ca^{2+}–^{19}F distance is no shorter than the sum of their ionic radii (the distances in SrF_2 were increased proportionally to the lattice parameter).

Calculations of A_s with the model parameters from [1] showed that the values of R for the ligands nearest to the IC cannot be adjusted such that the calculated constants A_s for the two groups of fluorine nuclei nearest to Gd^{3+} and for the compensator are close to their experimental values. On the other hand, if the structure of the surroundings of the nearest IC is taken to be close to that calculated in [3] and the contributions due to the F^- polarization (with the model parameter K_s from [1]) are subtracted from the experimental values of A_s, then the values obtained will be regularly arranged (according to the sign of the projections $D_z = D\cos\theta_i$ onto the Gd^{3+}–^{19}F bond axis directions) with respect to $A_s(R)$ for Gd^{3+} cubic centers in fluorite-structured crystals. This means that the model suggested for the trigonal centers is also applicable to the tetragonal centers, but the contributions to the isotropic SHFI related to the polarization and mixing of the Gd^{3+} electron shells differ from those suggested in [1].

To determine the parameter K_s', we used three equations (2) for A_s, taken in pairs under the condition that $R(111) = R(k) = 2.305$ Å for CaF_2, since it is hardly probable that $R(111)$ is shorter than its corresponding value for the cubic IC. The values obtained were different and were smaller in magnitude than those in [1]. This was also the case with the results for SrF_2 determined under the same conditions. By only having put $R(111) < R(k)$ and varying them, a complete set of experimental constants A_s was obtained (see table) with the same parameter K_s' = –32(3) MHz/e Å for both crystals. However, this value of K_s' is smaller than that for the trigonal center by a factor of 1.56 [1].

In our opinion, this difference is qualitatively explained by more efficient mixing of the $4f^7$ ground state of Gd^{3+} not only with unfilled 5d but also with the filled 5p state, since the matrix elements A_n^m of even and odd components of the crystalline field (CF) relating such electron states [5, 6, 9–11] are larger in this case (A_n^m(tetr) > A_n^m(trig) [3, 6]). This appreciably changes the overlap parameters of the outer electron shells of the RE^{3+} ion with the electron shells of the F^- ion in comparison with trigonal ICs. Optical spectra of $MeF_2 : RE^{3+}$ of various local symmetries also indicate an increase in the CF strength when passing from trigonal to tetragonal centers in these crystals [3].

Small changes in the radial distribution of the electron density of outer 5p electrons (even A_n^m couple the 4f and 5p states [5, 9, 10]) cause a reduction of the unpaired spin density both in the ligand region and at the RE^{3+} nucleus site, which can cause changes in both SHFI and HFI [5–8, 10–13]. Indeed, studies of the HFI in tetragonal $^{157}Gd^{3+}$ in CaF_2 and SrF_2 [1, 2] showed the hyperfine isotropic constants $A(s) = (A + 2B)/3$ to be appreciably larger than those for trigonal and cubic ICs. The increase in A_s is undeniably caused by a change in the unpaired spin density of outer-shell electrons at the Gd^{3+} nucleus site as they are most sensitive to the CF [5, 6, 9–12]. It is also worth noting that the increase in $A(s)$ cannot be caused by a change in the spin density of 6s electrons (if this density is present), since their contribution would decrease this constant [5, 11, 12]. The electron density of populated 5p states is only decreased due to mixing; this explains the increase in $A(s)$ due to a decrease of the negative-contribution fraction in $A(s)$ caused by the interaction of 5(s, p) electron shells, which also takes place in the free Gd^{3+} ion [11, 12]. The reduction of the unpaired spin density of 5p electrons at ligands results in a positive contribution to A_s [11, 13], i.e., to a decrease in $|K_s'|$ in the model we suggested, since this parameter now describes two contributions: the negative one is due to the mixing of states by the odd CF (or Gd^{3+} polarization), and the positive one is related to the action of the even CF on already mixed states.

As was shown in [9, 10] in microscopic calculations of A_2^0, the contribution from the mixing of the 4f and 5p electron states is opposite in sign to the contribution from the 4f–5d mixing. A similar conclusion as to the contributions to A_s follows from the data presented in [14], where the SHFI of the tetragonal Ce^{3+} in CaF_2 was considered. In our opinion, all these facts explain the decrease in $|K_s'|$ for tetragonal ICs.

Presuming the values R to be correct, we calculated the values Z_2^0 ($Z_2^0 = A_2^0$, b_2^0, P_2^0, with P_2^0 being the quadrupole interaction constant) for the tetragonal ^{157}Gd in CaF_2 and SrF_2 within the superposition model [9, 15] with intrinsic parameters Z_p and Z_s taken from [2, 9]. The signs of A_2^0 and P_2^0 were found to be identical to the experimental ones [2, 16]; however, the values are three to four times larger. In the case of b_2^0, the signs also coincide, but the calculated values are three

times smaller than the experimental ones. The A_2^0 and b_2^0 fit to the experiment can be improved by varying Z_s; however, this is impossible for P_2^0. This does not contradict the superposition model but calls for inclusion of the additional contributions to Z_2^0 from the mixing of the half-filled $4f$ shell with other shells induced by the CF, which was ignored in [9]. This approach can lead to changed intrinsic parameters and radial dependences.

On the other hand, it was found that the experimental values of Z_2^0 correlate. This is apparent if they are determined as

$$Z_2^0 = Z_p k(p) + Z_s k(s), \quad (3)$$

where $k(p)$ and $k(s)$ are the effective parameters of the model [16], including the radial and angular dependences of the point Coulomb and short-range-interaction contributions in the $Gd^{3+}F_9^-$ complex. Having solved the set of two equations with respect to $k(p, s)$ with Z_p and Z_s taken from [2, 9], we find the third Z_2^0 to be close to the experimental value. For example, the values A_2^0 calculated for CaF_2 and SrF_2 are 390 and 190 cm^{-1}, while the experimental values are 339 and 204 cm^{-1}, respectively [16].

4. CONCLUSIONS

Thus, the basic results of this study can be summarized as follows.

(i) The SHFI constants for tetragonal Gd^{3+} centers in CaF_2 and SrF_2 were determined from the experimental ENDOR spectra. These spectra are well described by the SH corresponding to a higher local symmetry of fluorine nuclei than the actual symmetry in the $Gd^{3+}F_9^-$ complex.

(ii) The empirical model describing the SHFI isotropic constants in the trigonal Gd^{3+} center in BaF2 is also applicable to the tetragonal ICs considered in this paper if one changes the contribution to the isotropic SHFI from the mixing of the outer IC electron states caused by both even (A_n^m) and odd ($A_1^0 \sim D$) components of the ligand crystalline field.

(iii) The distances to the nearest neighbor ^{19}F nuclei and the compensating fluorine atom were determined within this model. The $Gd^{3+}F_9^-$ complex structure obtained is similar to that calculated within the exchange-charge model.

(iv) An analysis of the constants A_2^0, b_2^0, and P_2^0 within the superposition model requires the intrinsic parameters be changed, which is also due to the influence of even and odd CF components on the Gd^{3+} outer electron shells, manifesting itself in tetragonal ICs.

ACKNOWLEDGMENTS

A.D. Gorlov thanks A.I. Rokeakh and A.S. Moskvin for the experimental data and valuable discussions.

This study was supported in part by the Civilian Research and Development Foundation for the New Independent States of the Former Soviet Union (grant no. REC-005).

REFERENCES

1. A. D. Gorlov, V. B. Guseva, A. P. Potapov, and I. A. Rokeakh, Fiz. Tverd. Tela (St. Petersburg) **43** (3), 456 (2001) [Phys. Solid State **43**, 473 (2001)].
2. A. D. Gorlov, A. P. Potapov, V. I. Levin, and V. A. Ulanov, Fiz. Tverd. Tela (Leningrad) **33** (5), 1422 (1991) [Sov. Phys. Solid State **33**, 801 (1991)]; A. D. Gorlov and A. P. Potapov, Fiz. Tverd. Tela (St. Petersburg) **42** (1), 49 (2000) [Phys. Solid State **42**, 51 (2000)].
3. M. P. Davydova, B. Z. Malkin, and A. L. Stolov, in *Spectroscopy of Crystals* (Nauka, Leningrad, 1978), p. 27; S. M. Arkhipov and B. Z. Malkin, Fiz. Tverd. Tela (Leningrad) **22** (5), 1471 (1980) [Sov. Phys. Solid State **22**, 857 (1980)].
4. A. I. Rokeakh, A. A. Mekhonoshin, N. V. Legkikh, and A. M. Batin, Fiz. Tverd. Tela (St. Petersburg) **37** (10), 3135 (1995) [Phys. Solid State **37**, 1728 (1995)].
5. A. Abragam and B. Bleaney, *Electron Paramagnetic Resonance of Transition Ions* (Clarendon, Oxford, 1970; Mir, Moscow, 1972), Vol. 1.
6. S. A. Al'tshuler and B. M. Kozyrev, *Electron Paramagnetic Resonance* (Nauka, Moscow, 1972).
7. C. Fainstein, M. Tovar, and C. Ramos, Phys. Rev. B **25** (5), 3039 (1982).
8. J. M. Baker, J. Phys. C **12** (19), 4093 (1979).
9. L. I. Levin, Phys. Status Solidi B **134** (2), 275 (1986).
10. M. V. Eremin, in *Spectroscopy of Crystals* (Nauka, Leningrad, 1989), p. 30.
11. R. Watson and A. J. Freeman, in *Hyperfine Interactions*, Ed. by A. J. Freeman and R. B. Frankel (Academic, New York, 1967; Mir, Moscow, 1970).
12. J. Andriessen, D. van Ormondt, S. N. Ray, and T. P. Das, J. Phys. B **11** (15), 2601 (1978).
13. J. Casas, P. Stydzinski, J. Andriessen, *et al.*, J. Phys. C **19** (34), 6767 (1986).
14. O. A. Anikienok, M. V. Eremin, and O. G. Khutsishvili, Fiz. Tverd. Tela (Leningrad) **28** (6), 1690 (1986) [Sov. Phys. Solid State **28**, 935 (1986)].
15. D. J. Newman and W. Uraban, Adv. Phys. **24** (2), 793 (1973).
16. L. I. Levin and A. D. Gorlov, J. Phys.: Condens. Matter **4** (2), 1981 (1992).

Translated by A. Kazantsev

Physics of the Solid State, Vol. 45, No. 1, 2003, pp. 82–86. Translated from Fizika Tverdogo Tela, Vol. 45, No. 1, 2003, pp. 80–83.

DEFECTS, DISLOCATIONS, AND PHYSICS OF STRENGTH

Internal Friction of $Li_2B_4O_7$ Single Crystals

V. S. Bilanych, N. D. Baĭsa, V. M. Rizak, I. M. Rizak, and V. M. Holovey

Uzhgorod National University, ul. Podgornaya 46, Uzhgorod, 88000 Ukraine

e-mail: rizak@univ.uzhgorod.ua

Received March 26, 2002

Abstract—This paper reports on the results of measurements of the internal friction Q^{-1} and the shear modulus G of $Li_2B_4O_7$ single crystals along the crystallographic directions [100] and [001] in the temperature range 300–550 K for strain amplitudes of $(2–10) \times 10^{-5}$ at infralow frequencies. The anomalies observed in Q^{-1} and G in the temperature range 390–410 K are due to thermal activation of the mobility of lithium cations and their migration from one energetically equivalent position to another. A jump in the internal friction background is revealed in the vicinity of the Q^{-1} and G anomalies for the $Li_2B_4O_7$ crystal. The magnitude of this jump depends on the crystallographic direction. © *2003 MAIK "Nauka/Interperiodica".*

1. INTRODUCTION

Single crystals of $Li_2B_4O_7$ lithium tetraborate are promising materials for use in piezotechnology, because they not only have a high ionic conduction [1, 2] and exhibit anomalous behavior in a number of physical parameters but also possess unique elastic properties.

Earlier [3, 4], the elastic properties of $Li_2B_4O_7$ single crystals and their temperature behavior were studied mainly in the frequency range 0.1–800 MHz. Additional information on the specific features of the behavior of elastic moduli and the mechanisms of interaction of an acoustic wave with the crystal structure can be obtained from analyzing the influence of the amplitude of an external stress field on dissipative processes.

The goal of this work was to investigate the lattice dynamics of an $Li_2B_4O_7$ single crystal through an analysis of the temperature–frequency dependences of the internal friction Q^{-1} and the shear modulus G for different amplitudes of an external stress field.

2. EXPERIMENTAL TECHNIQUE

The internal friction Q^{-1} and the shear modulus G of an $Li_2B_4O_7$ single crystal at different temperatures were measured under quasi-static loading in the frequency range 10^{-3}–10^{-1} Hz according to an automated experimental procedure based on the use of an inverse-type torsion pendulum [5].

In order to determine the internal friction and the shear modulus at infralow frequencies ($f = 10^{-3}$–10^{-1} Hz) of forced torsional vibrations, we recorded the curves $\varepsilon = F(M_{cr})$, where M_{cr} is the harmonically variable torque moment under whose action the sample was deformed and ε is the strain of the sample. The values of Q^{-1} and G were calculated from the obtained loops of the mechanical hysteresis according to the formulas

$$Q^{-1} = \tan\delta = \frac{\sin\delta}{\sqrt{1-\sin^2\delta}},$$

$$\sin\delta = \frac{\Delta\varepsilon}{\varepsilon_m}, \quad G = A\frac{M_{cr\,m}}{\varepsilon_m},$$

where $\Delta\varepsilon$ is the residual strain at the instant when $M_{cr} = 0$, ε_m is the maximum strain, $M_{cr\,m}$ is the maximum torque moment, and A is the coefficient determined by the geometric parameters of the sample under study. The temperature dependences $Q^{-1}(T)$ and $G(T)$ were obtained upon heating at a constant rate $v_H = 37.5$ K/h. Samples in the form of parallelepipeds (cross section, 2×2 mm; length, 20 mm) were prepared from bulk single crystals oriented along the crystallographic directions [100] and [001].

The initial compound $Li_2B_4O_7$ was prepared by melting boron oxide (OSCh 12-3) and lithium carbonate (OSCh 20-2) in platinum crucibles in air. The temperature and time parameters of the synthesis were optimized taking into account the specific features of the thermal decomposition of lithium carbonate, the dehydration of the initial components, and the nature of their interaction [6]. In order to compensate for the loss of boron oxide due to incongruent evaporation of the melt during the growth of single crystals, an excess of B_2O_3 (up to 0.5 mol %) was added to the reaction product. The single crystals were grown by the Czochralski method along the crystallographic direction [001] or [100]. The pulling speed was 3–6 mm/day, and the rotational speed was 4–5 min^{-1}.

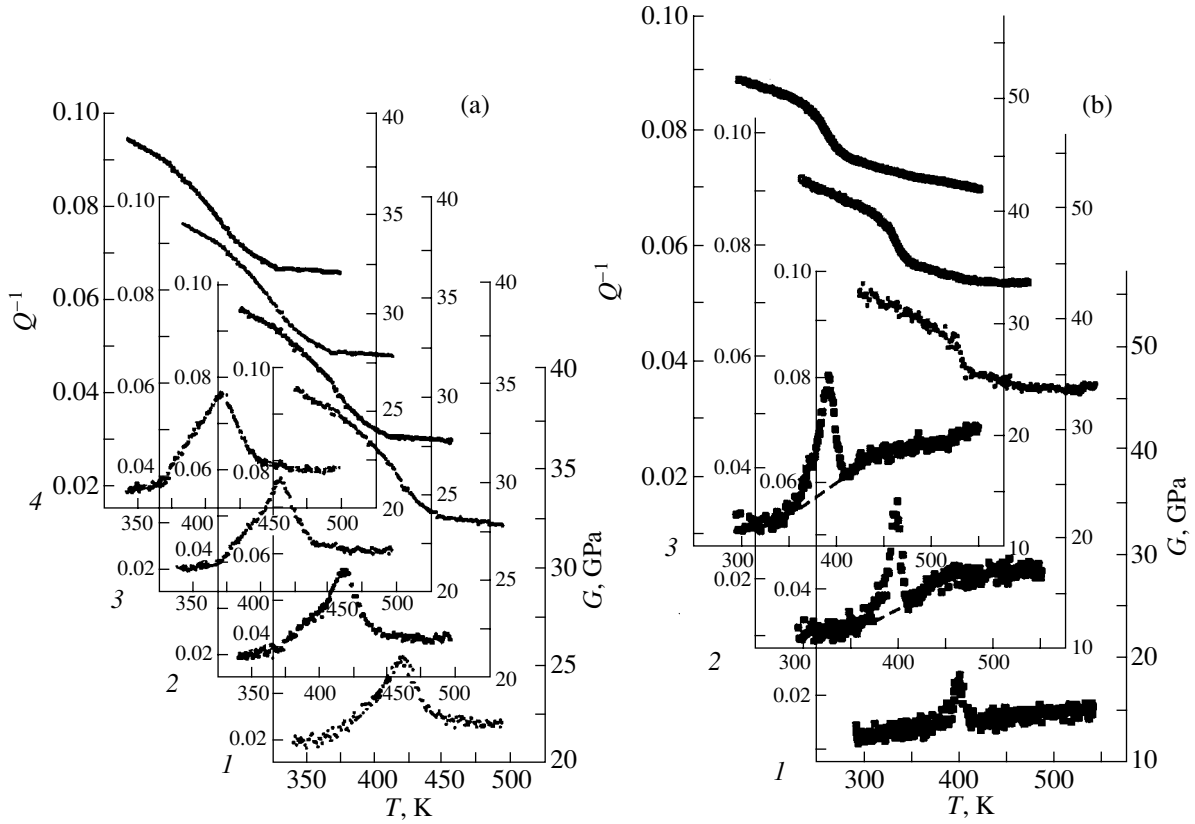

Fig. 1. Temperature dependences of the internal friction Q^{-1} and the shear modulus G of the $Li_2B_4O_7$ single crystal at a frequency of 30 mHz for the crystallographic directions (a) [100] and (b) [001] at different strain amplitudes ε. ε, 10^{-5}: (a) (*1*) 4, (*2*) 6, (*3*) 8, and (*4*) 10 and (b) (*1*) 2, (*2*) 6, and (*3*) 10.

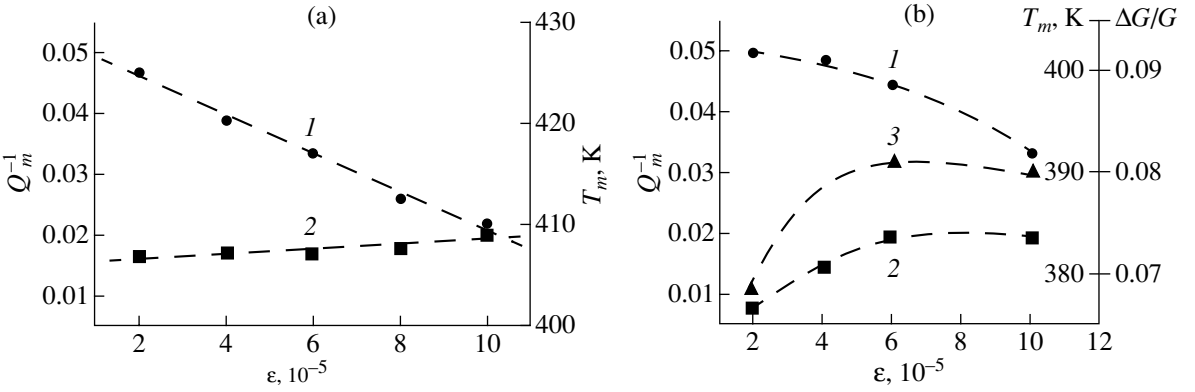

Fig. 2. Dependences of the parameters of the dissipative process (*1*) T_m, (*2*) Q_m^{-1}, and (*3*) $\Delta G/G$ on the strain ε of the $Li_2B_4O_7$ single crystal for the crystallographic directions (a) [100] and (b) [001].

3. RESULTS AND DISCUSSION

Figure 1 shows the temperature dependences of the internal friction Q^{-1} and the shear modulus G of an $Li_2B_4O_7$ single crystal for different amplitudes of shear strain $\varepsilon = (2–10) \times 10^{-5}$. The experimental dependences $Q^{-1}(T)$ exhibit a maximum in the internal friction in the temperature range 390–410 K. This maximum corresponds to a decrease in the shear modulus $G(T)$. The anomaly observed in the shear modulus $G(T)$ of the $Li_2B_4O_7$ single crystal is similar to the anomaly found in the temperature dependence of the velocity of longitudinal ultrasonic waves at a frequency of 150 kHz [3].

It is evident from Fig. 2 that the parameters of the aforementioned anomalies depend on the strain amplitude. As the strain amplitude ε increases, the temperature T_m at the maximum of the internal friction somewhat decreases, whereas its amplitude Q^{-1}, the half-width $\Delta T_{1/2}$, and the defect of the shear modulus $\Delta G/G$ increase. Here, $\Delta G = G_0 - G_\infty$, G_0 is the shear modulus before the anomaly, and $G_\infty$is the shear modulus after the anomaly. At $\varepsilon = 10 \times 10^{-5}$, these parameters are as follows: $T_m = 410$ K, $Q_m^{-1} = 20 \times 10^{-3}$, $\Delta T_{1/2} = 33$ K, and $\Delta G/G = 0.12$ for the [100] direction and $T_m = 392$ K, $Q_m^{-1} = 20 \times 10^{-3}$, $\Delta T_{1/2} = 21$ K, and $\Delta G/G = 0.08$ for the [001] direction.

Apart from the maximum observed in the dependence $Q^{-1}(T)$, there also exists a difference in the background of the internal friction Q_f^{-1} before the anomaly and after it. In the temperature range $T < T_m$, the background of the internal friction Q_f^{-1} is approximately equal to 10×10^{-3}. At temperatures $T > T_m$, the background values of Q_f^{-1} for the [001] and [100] directions increase by 12×10^{-3} and 4×10^{-3}, respectively.

The aforementioned features in the behavior of $Q^{-1}(T)$ and $G(T)$ at different values of ε indicate that, in the studied ranges of frequencies and temperatures, the internal friction in single-crystal lithium tetraborate depends on the strain amplitude.

As is known [7, 8], the amplitude-dependent effects of internal friction in crystals are frequently interpreted in the framework of a concept according to which a diffusing particle executes a thermally activated motion within a multistep potential relief that is a superposition of potential wells of equal depths. On this basis, for a crystal subjected to a harmonically variable strain, we consider an ensemble of kinetic structural units moving along a potential relief of height H whose slope varies with frequency f. The velocity of motion of a kinetic particle (kinetic unit) in a homogeneous periodic potential field can be represented by the following relationship [7]:

$$\frac{dx}{dt} = \nu_0 a\left\{\exp\left[-\left(\frac{H - v\sigma}{kT}\right)\right] - \exp\left[-\left(\frac{H + v\sigma}{kT}\right)\right]\right\}, \quad (1)$$

where ν_0 is the frequency of attempts made by the kinetic particle to pass through the potential barrier, a is the distance between the potential barriers, $v = -\dfrac{\partial H}{\partial \sigma}$ is the rate of decrease in the height H with an increase in the mechanical stress σ (v is often called the activation volume), and $v\sigma$ is the work done by the external field on a kinetic particle with an effective activation volume to move it through a potential barrier of height H. The first and second terms in Eq. (1) characterize the velocity of jumps in direct and opposite directions, respectively.

For strong mechanical stresses ($v\sigma \gg kT$), expression (1) can be rewritten in the form

$$\frac{dx}{dt} = \nu_0 a \exp\left[-\left(\frac{H - v\sigma}{kT}\right)\right]. \quad (2)$$

In this case, the mobility of a kinetic particle depends on the temperature and mechanical stress through the term $v\sigma$, which contains the activation volume. It is evident that, under the action of an external stress field, the potential barrier decreases when the particle attempts to pass through it "along the field" and increases in the opposite case. It follows from the above considerations that, under the condition $v\sigma \gg kT$, an increase in the mechanical stress at a constant frequency of deformation (f = const) should lead to a decrease in the temperature T_m at the maximum in the internal friction, which is observed in Figs. 1 and 2. According to the data presented in Figs. 1 and 2, the maximum in the internal friction Q_m^{-1} at $\varepsilon < 6 \times 10^{-5}$ sharply decreases with decreasing ε. It should be expected that, when the strains are significantly smaller (of the order of 10^{-6}–10^{-7}), this maximum can be lower than the background loss in the sample. The jump in the background loss decreases in a similar manner. The amplitude of the anomaly also noticeably decreases with a decrease in the amplitude of the exciting field.

The change in the frequency of the exciting stress field does not lead to a shift in either the temperature of the internal friction maximum or the range of variation in $\partial G/\partial T$. The dependences $Q^{-1}(T)$ and $G(T)$ at different infralow frequencies of mechanical vibrations are depicted in Fig. 3. As can be seen from Fig. 3, the curve $G(T)$ in the temperature range 380–420 K is similar to that of the elastic moduli in the relaxation processes. At the same time, the location of the maxima in the aforementioned anomalies of the strength properties and the temperature range of their manifestation weakly depend on the frequency. This suggests the absence of a pronounced dispersion and makes reliable estimation of the activation energy from the frequency shift of the maxima difficult. This frequency behavior of the strength properties is typical of the amplitude-dependent internal friction [8].

It is known [9] that the crystal structure of $Li_2B_4O_7$ is based on an anion sublattice formed by a three-dimensional network consisting of boron–oxygen triangles and tetrahedra with channels occupied by tetrahedrally coordinated lithium ions. The lithium ions are rather weakly bound to the anion sublattice and can occupy several energetically equivalent positions; hence, during thermal motion, they can pass from one equilibrium position to another. The thermal activation of the mobility of these ions in $Li_2B_4O_7$ occurs at $T >$ 350 K. This is responsible for both the dielectric loss and ionic conduction in these single crystals. Note that

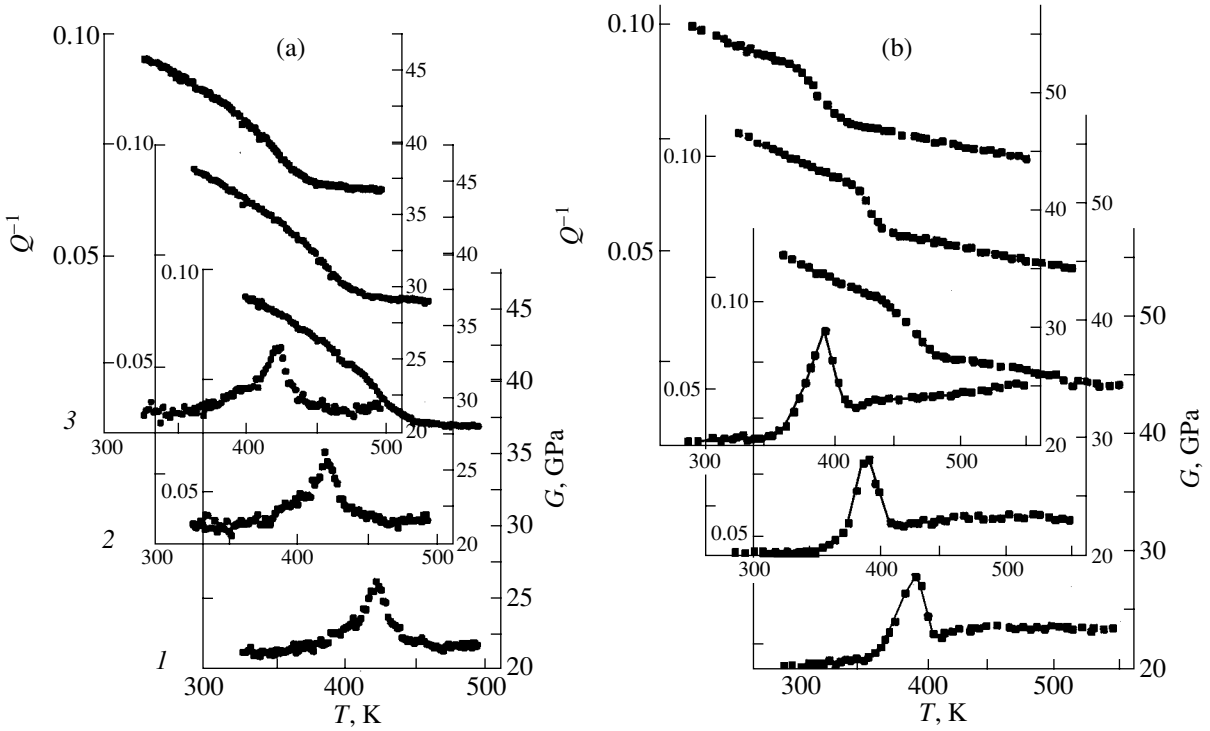

Fig. 3. Temperature dependences of the internal friction Q^{-1} and the shear modulus G of the $Li_2B_4O_7$ single crystal at different infralow frequencies for the crystallographic directions (a) [100] and (b) [001]. *f*, mHz: (a) (*1*) 30, (*2*) 50, and (*3*) 80 and (b) (*1*) 10, (*2*) 50, and (*3*) 10.

the temperature range of manifestation of the anomalies observed in the strength properties of $Li_2B_4O_7$ single crystals at infralow frequencies (Fig. 1) virtually coincides with the range of thermal activation of lithium ions. Therefore, it can be assumed that the observed maximum in the mechanical loss is attributed to the activation of the mobility of the lithium ions. In the temperature range 300–600 K, the lattice of $Li_2B_4O_7$ single crystals can be considered as two structural subsystems differing in the temperature behavior of mechanical rigidity. In this case, the totality of lithium ions can be treated as one of these subsystems. An increase in the temperature gives rise to a peak in the internal friction against the background of the mechanical loss in $Li_2B_4O_7$ in the temperature range 390–410 K. The results obtained are consistent with available data on the dielectric properties of lithium tetraborate [10–12]. According to these data, lithium tetraborate possesses ionic conduction due to the Li^+ mobility of a thermoactivation nature.

Judging from the intensity of the maximum in the internal friction of $Li_2B_4O_7$ and its temperature location and using the formula taken from [13],

$$v = \left(\frac{2kT_mQ_m^{-1}}{N_0G_0}\right)^{\frac{1}{2}}, \qquad (3)$$

we estimated the activation volume and determined the radius of the kinetic particle: $r = 0.50$ Å. This value is close to the classical radius of lithium ions [14].

It is evident from Figs. 1 and 2 that, over the entire temperature range under investigation, the magnitudes of the shear modulus for the sample oriented along the [001] direction are, on average, 25% greater than those for the sample oriented along the [100] orientation. Moreover, the jump in the background value of the internal friction (at $T > 450$ K) as a result of the activation of the dissipative process for the [001] direction is also considerably larger. This anisotropy of the strength properties suggests that the cation sublattice is characterized by different mobilities in different crystallographic directions. Since the difference between the background losses in the internal friction upon the passage through the maximum is larger for the [001] direction, it is natural to assume that the mobility of lithium cations is also larger in this direction.

4. CONCLUSIONS

Thus, the internal friction and the shear modulus of $Li_2B_4O_7$ single crystals along the crystallographic directions [100] and [001] at infralow frequencies were investigated by the method of torsional vibrations. Analysis of the results obtained revealed a dissipative process occurring in the temperature range 390–410 K

and anisotropy of the strength properties. The activation volume and the radius of kinetic particles were determined. The radius of kinetic particles proved to be close to the classical radius of lithium ions.

It was established that the maximum in the internal friction in the range 390–410 K is associated with the migration of lithium ions from one energetically equivalent position to another under the action of a periodic external stress field.

In the range $T > T_m$, there occurs a jump in the background of the internal friction due to absorption of mechanical energy by the mobile cation sublattice at temperatures higher than the temperature of the anomalies in $Q^{-1}(T)$ and $G(T)$. The difference between the jumps in the background of Q^{-1} for the crystallographic directions [100] and [001] can be explained by the anisotropy of the mobility of lithium cations.

REFERENCES

1. V. M. Rizak, I. M. Rizak, N. D. Baisa, *et al.*, in *Proceedings of the IFM-10, Madrid, Spain, 2001*, p. 219.
2. A. É. Aliev, Ya. V. Burak, and I. T. Lyseĭko, Izv. Akad. Nauk SSSR, Neorg. Mater. **26** (9), 1991 (1990).
3. A. É. Aliev and R. R. Valetov, Fiz. Tverd. Tela (St. Petersburg) **34** (10), 3061 (1992) [Sov. Phys. Solid State **34**, 1639 (1992)].
4. A. É. Aliev, Ya. V. Burak, V. V. Vorob'ev, *et al.*, Fiz. Tverd. Tela (Leningrad) **32** (9), 2826 (1990) [Sov. Phys. Solid State **32**, 1641 (1990)].
5. V. S. Bilanych, Author's Abstract of Candidate's Dissertation (Uzhgorod. Univ., Uzhgorod, 1993).
6. I. I. Turok, V. M. Holovey, and P. P. Puga, Declaration Ukraine Patent No. 32242, MPK^6 S01 V 35/12.
7. *Physical Acoustics: Principles and Methods*, Vol. 3, Part A: *The Effect of Imperfections*, Ed. by W. P. Mason (Academic, New York, 1966; Mir, Moscow, 1969).
8. V. S. Postnikov, *Internal Friction in Metals* (Metallurgiya, Moscow, 1969).
9. S. F. Radaev, L. A. Muradyan, L. F. Malakhova, *et al.*, Kristallografiya **34** (6), 1400 (1989) [Sov. Phys. Crystallogr. **34**, 842 (1989)].
10. Ya. V. Burak, I. T. Lyseĭko, and I. V. Garapin, Ukr. Fiz. Zh. **34** (2), 226 (1989).
11. A. É. Aliev and R. R. Valetov, Kristallografiya **36** (6), 1507 (1991) [Sov. Phys. Crystallogr. **36**, 855 (1991)].
12. M. M. Nassar, B. F. Borisov, E. V. Charnaya, *et al.*, Vestn. Leningr. Univ., Ser. 4: Fiz., Khim., No. 2, 82 (1991).
13. V. A. Bershteĭn, Yu. A. Emel'yanov, and V. A. Stepanov, Fiz. Tverd. Tela (St. Petersburg) **22** (2), 399 (1980) [Sov. Phys. Solid State **22**, 234 (1980)].
14. B. K. Vainshtein, V. M. Fridkin, and V. L. Indenbom, *Modern Crystallography*, Vol. 2: *Structure of Crystals* (Nauka, Moscow, 1979; Springer-Verlag, Berlin, 1982).

Translated by O. Moskalev

Physics of the Solid State, Vol. 45, No. 1, 2003, pp. 87–93. Translated from Fizika Tverdogo Tela, Vol. 45, No. 1, 2003, pp. 84–90.

DEFECTS, DISLOCATIONS, AND PHYSICS OF STRENGTH

Observation of Structural Vacancies in Titanium Monoxide Using Transmission Electron Microscopy

A. A. Valeeva*, G. Tang, A. I. Gusev*, and A. A. Rempel'***

** Institute of Solid-State Chemistry, Ural Division, Russian Academy of Sciences, ul. Pervomaĭskaya 91, Yekaterinburg, 620219 Russia*

e-mail: valeeva@ihim.uran.ru

*** Institut für Theoretische und Angewandte Physik, Universität Stuttgart, Pfaffenwaldring 57/VI, Stuttgart, 70550 Germany*

Received May 8, 2002

Abstract—Structural vacancies were directly observed in nonstoichiometric ordered titanium monoxide using high-resolution transmission electron microscopy under a magnification of 4×10^6. The observation of structural vacancies became possible due to their ordering and the formation of continuous vacancy channels in certain crystallographic directions. Microdiffraction was employed to orient the sample in the direction permitting the observation of vacancy channels. Transmission electron microscopy providing a magnification of tens of thousands of times revealed that titanium monoxide grains do not contain cracks and macropores and confirmed that the free volume detected picnometrically in the titanium monoxide is concentrated in structural vacancies on the titanium and oxygen sublattices. © *2003 MAIK "Nauka/Interperiodica".*

1. INTRODUCTION

Structural vacancies are an essential element of crystal structure, as they affect the diffusion, mechanical, electrical, and magnetic properties of solids [1]. The existence of structural vacancies has thus far been established indirectly, for instance, through the combined application of three methods, namely, chemical, picnometric, and x-ray diffraction. Structural vacancies are a fundamental element of the crystal structure of transition-metal compounds, such as the carbides, nitrides, and oxides. The concentration of structural vacancies in these substances may be as high as a few tens of percent, which accounts for these compounds being termed strongly nonstoichiometric [1, 2]. Interparticle interaction forces structural vacancies in strongly nonstoichiometric compounds to order [3], and the appearance of superstructure reflections in the x-ray and neutron diffractograms may be considered additional indirect evidence of the existence of vacancies.

In the present study, we used high-resolution transmission electron microscopy (HTEM) [4] to observe structural vacancies directly. This method makes it possible to observe atomic rows in crystals. The image thus obtained results from a superposition of tens of atomic layers. In the disordered state, structural vacancies are distributed at random and, therefore, each column of lattice sites contains both atoms and structural vacancies. Structural vacancies are, however, not seen because different columns do not differ in the relative content of atoms and structural vacancies, thus producing no contrast. For the same reason, thermal structural vacancies have thus far not been observed, despite the fact that they exist in all crystals at any finite temperature. In this study, we propose to use the ordered state of strongly nonstoichiometric compounds for the observation of vacancies. In this case, structural vacancies are arranged in an orderly way, so that directions in a crystal which pass only through vacant sites to form continuous vacancy channels can be found. When ideally ordered, the atom columns and the vacancy channels are arranged with a certain periodicity and the atomic rows in HTEM images should exhibit contrast at the points where they are broken by vacancy channels directed perpendicular to the image plane.

Nonstoichiometric cubic titanium monoxide TiO_y with $B1$-type basal structure is the most promising among the nonstoichiometric compounds for direct observation of vacancies. The nonstoichiometric cubic titanium monoxide belongs to strongly nonstoichiometric interstitial compounds [1, 2] and exhibits a very broad range of homogeneity, from $TiO_{0.7}$ to $TiO_{1.25}$. A specific feature of the titanium monoxide is that it has heavily defected sublattices not only of the oxygen but also of the metal [5, 6]. It is the high concentration of vacancies on the metal sublattice that makes their observation by HTEM possible. The fact is that most of the information seen in HTEM images is provided by metal atoms and structural vacancies of the metal sublattice because of the low scattering capacity of the atoms of oxygen compared to that of titanium. For the same reason, one cannot observe structural vacancies in strongly nonstoichiometric carbides, because the vacancies exist on the carbon sublattice only.

1063-7834/03/4501-0087$24.00

The first studies [6, 7] of titanium monoxide using the chemical, picnometric, and x-ray diffraction methods already revealed that the monoxide of equiatomic composition, $TiO_{1.00}$, has 15–16 at. % vacant sites on each sublattice. This finding was questioned in [8], where it was assumed that the free volume available in titanium monoxide derives from the presence of microvoids and pores rather than from metal sublattice vacancies. According to [8], picnometric determination of density entails a large inherent error, because in this case, the free volume is detected not only in the vacant sites but also in such defects as microcracks and pores. It is the presence of microcracks and micropores that accounts for the large difference of the picnometric from the so-called x-ray diffraction density, which is calculated using data on the composition and lattice period of the monoxide under the assumption of the absence of metal vacancies.

The viewpoint expressed in [8] did not receive subsequent support, because the results obtained in numerous structural studies could be accounted for only for the case of metal vacancies existing in TiO_y. However, no direct evidence of the existence of metal vacancies in the TiO_y monoxide had been presented until recently.

This has stimulated us to attempt a direct observation of structural vacancies in ordered Ti_5O_5 oxide using high-resolution transmission microscopy.

2. SAMPLES AND EXPERIMENTAL TECHNIQUES

A sample of the $TiO_{1.087}$ titanium monoxide was prepared by reacting titanium with titanium dioxide powder at a high temperature in vacuum. To reach a disordered distribution of structural vacancies, the sample thus prepared was quenched from 1330 to 300 K at a rate of 200 K s^{-1}. The measured picnometric density of the sample (4.968 g cm^{-3}) was found to be 20% less than the theoretical density (5.962 g cm^{-3}), which was calculated taking into account the chemical composition and experimentally determined cubic-lattice period (a_{B1} = 0.4174 nm) under the assumption of the metal sublattice having no defects. A comparison of the picnometric with theoretical density, made with due account of the relative content of titanium and oxygen, yields the formula $Ti_{0.833}O_{0.906}$. This means that 0.167 of all sites on the titanium sublattice and 0.094 of the oxygen sublattice sites are vacant.

The ordered titanium monoxide was obtained by annealing the synthesized sample at 1330 K for 4 h, with subsequent slow cooling to 300 K at a rate of 10 K h^{-1}. The technique employed and the conditions of preparation and characterization of nonstoichiometric disordered and ordered titanium monoxide samples throughout the interval in which the cubic phase exists are described in [9].

The crystal structure of the titanium monoxide was studied using x-ray diffraction on a Siemens D-500 diffractometer ($CuK\alpha_{1,2}$ radiation) in the Bragg–Brentano geometry in the 2θ angle interval from 10° to 160° in steps of $\Delta(2\theta) = 0.025°$. The samples used were finely dispersed powders of titanium monoxide.

The microscopic and crystalline structure of the titanium monoxide was also studied using electron microscopy and diffraction. Samples for these studies were prepared as follows. The sample surface was ground, and its central part was thinned with a dimple machine (Gatan, USA). After cleaning in alcohol, the sample was ion-milled to make a hole. The surface was milled by Ar ions at a voltage of 5 kV. The microstructure was studied at the edge of the foil, whose thickness did not exceed 50 nm.

Images with a high atomic resolution were obtained using a JEM-4000FX electron microscope (wavelength, λ = 0.00164 nm; voltage, 400 kV). The microdiffraction and microstructure were studied with a Philips CM-200 electron microscope (beam width, 70 nm; wavelength, λ = 0.00251 nm; voltage, 200 kV). Microdiffraction was observed at zero angle with respect to the high-resolution images. The aperture permitted the observation of $[111]]_{B1}$ ND $[220]_{B1}$ diffraction spots. The bright-field image was obtained in the central spot $[000]_{B1}$; the dark-field image, in the $[111]_{B1}$ reflection. The instrumental constant was $L\lambda = Rd_{hkl}$ = 2.33–2.51 mm nm, where L is the chamber length, R is the distance between the diffracted $[hkl]_{B1}$ and direct $[000]_{B1}$ beams, and d_{hkl} is the interplanar distance.

3. RESULTS AND DISCUSSION

Figure 1 presents x-ray diffraction patterns of the ordered and disordered titanium monoxide $TiO_{1.087}$. The x-ray diffractogram of the disordered sample obtained by quenching from 1330 K contains only the structural reflections due to the basal cubic phase. The x-ray pattern of the sample subjected to annealing and subsequent slow cooling to room temperature revealed additional weak reflections. This indicates the formation of a superstructure in the annealed titanium monoxide. A thorough analysis of the position and intensity of the additional reflections showed the ordering of atoms and structural vacancies of titanium and oxygen in TiO_y to correspond to the Ti_5O_5 monoclinic superstructure with space group $C2/m$ ($A12m/1$).

The monoclinic ordered structure Ti_5O_5 has been detected with x-ray [10–12] and electron [13] diffraction in titanium monoxide annealed at a temperature below 1263 K. The low-temperature modification of titanium monoxide was found to be stable within the composition region $0.9 < O/Ti < 1.1$. The low-temperature ordered phase has also been observed to form in the phase transition from the high-temperature cubic disordered phase in titanium monoxide single crystals by using transmission electron microscopy [14] and x-

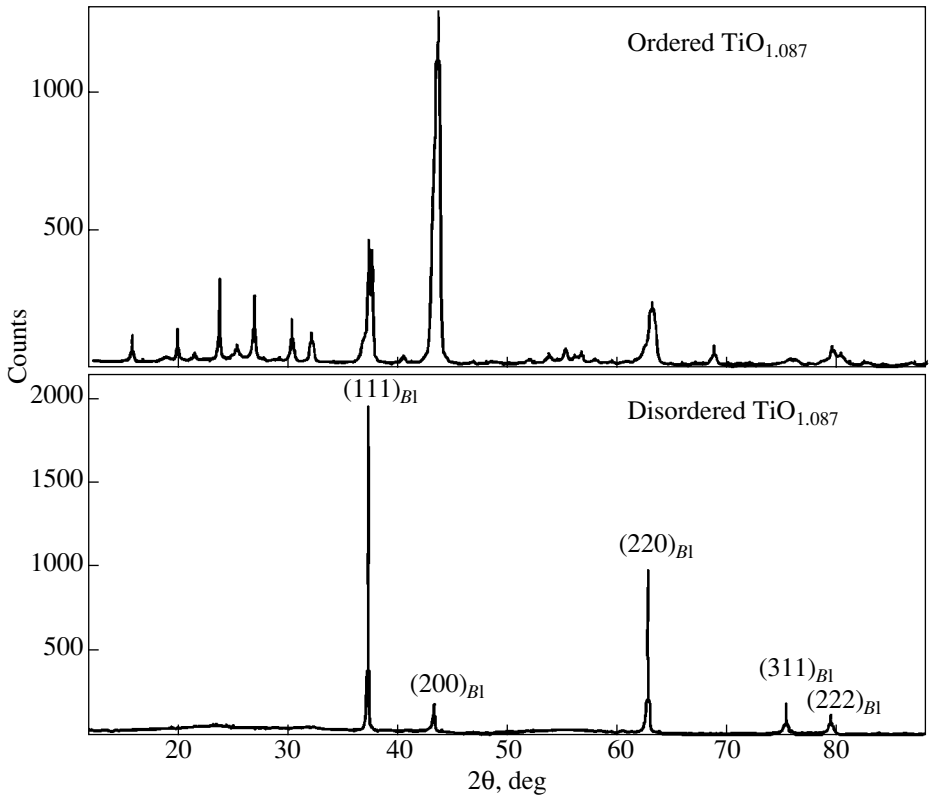

Fig. 1. X-ray diffractogram of disordered (the structural lines of the *B*1 phase are identified) and ordered titanium monoxide $TiO_{1.087}$. The x-ray diffractogram of the ordered sample clearly exhibits the structural and additional superstructure lines.

ray diffraction analysis [15]. The same phase transition was detected, using electron diffraction, in polycrystalline samples of cubic titanium monoxide $TiO_{0.7}$, $TiO_{1.03}$, $TiO_{1.13}$, and $TiO_{1.19}$ [14].

The experimental microdiffraction pattern of the ordered $TiO_{1.087}$ monoxide (Fig. 2a) contains structural reflections (high-intensity spots) and a number of additional reflections. Computer modeling of microdiffraction made for the Ti_5O_5 titanium monoxide with space group *C*2/*m* identifies those reflections that are due to a superstructure (spots with an intensity weaker by a few times than that from the basal phase in Fig. 2). The model pattern shows the indices of the structural reflections. A comparison of the experimental (Fig. 2a) with the model pattern (Fig. 2b) reveals that the additional reflections contain superstructure features and, in addition, reflections which are not connected with ordering but originate from the presence of twins, which are seen clearly in the photomicrographs (Fig. 3).

The upward-pointing normal to the plane of Fig. 2 is oriented along $[0\bar{1}\bar{1}]_{C2/m}$ or $[\bar{1}\bar{1}\bar{2}]_{B1}$. The distances from the central spot to the two nearest structural spots arranged at 90° are 9.98 and 15.90 mm. The interplanar distances d_{hkl} calculated using the instrumental constant Rd_{hkl} = 2.33–2.51 mm nm are 0.238 ± 0.012 and 0.147 ± 0.007 nm and correspond to the $[111]_{B1}$ and $[220]_{B1}$ reflections from the basal cubic phase. Calculation of the position of the superstructure reflections (Fig. 2) in the reciprocal-space cross section containing the $[111]_{B1}$ and $[220]_{B1}$ reflections from the basal phase permitted us to assign these basal-phase reflections to the $[21\bar{1}]_{C2/m}$ and $[\bar{2}2\bar{2}]_{C2/m}$ superstructure spots, respectively.

Thus, the presence of a large number of structural vacancies on the oxygen and titanium sublattices favors the formation of an ordered titanium monoxide phase. As shown by an analysis of the position and intensity of the superstructure reflections in the x-ray diffractogram and of spots in the microdiffraction pattern, the ordering of the oxygen and titanium vacancies corresponds to the ordered monoclinic Ti_5O_5 phase (space group *C*2/*m*).

The TEM microphotographs of $TiO_{1.087}$ obtained with a magnification of 38000, 50000, and 115000 show the samples studied to be polycrystals with a minimum grain size of about 100 nm (Fig. 3) and a high density of grain boundaries. Electron microscopy revealed that monoxide grains do not contain macropores or cracks and that the content of small pores is so small (Fig. 3c) as not to affect the picnometric density noticeably. Thus, the large free volume

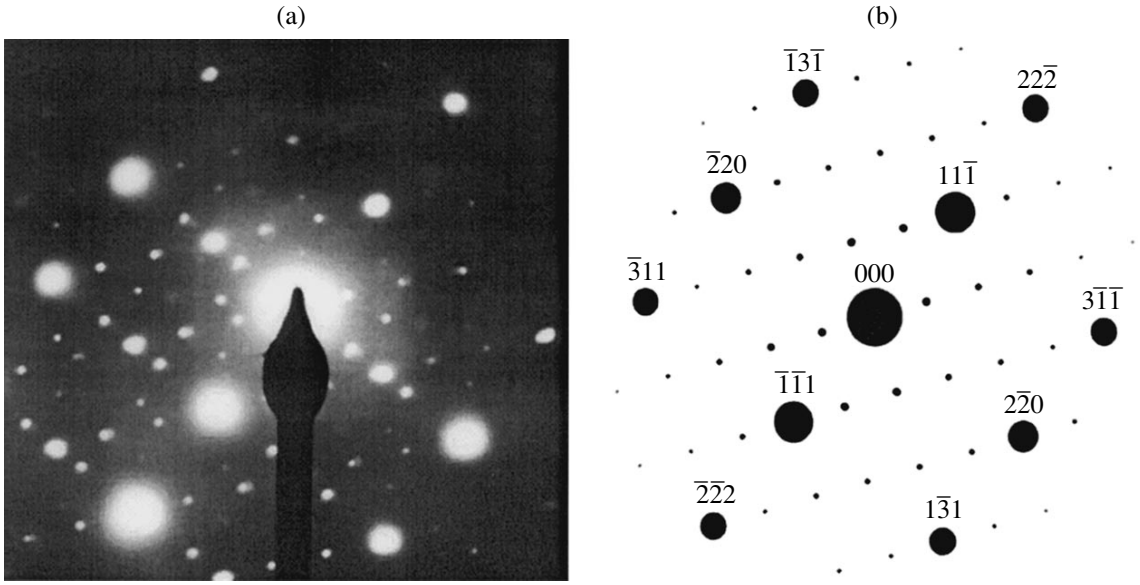

Fig. 2. (a) Experimental microdiffraction pattern of the $TiO_{1.087}$ titanium monoxide and (b) computer simulation of microdiffraction for the $TiO_{1.087}$ monoxide with the basal lattice parameter a_{B1} = 0.4174 nm (electron beam direction $[011]_{C2/m} \equiv [112]_{B1}$). The structural reflection indices are specified.

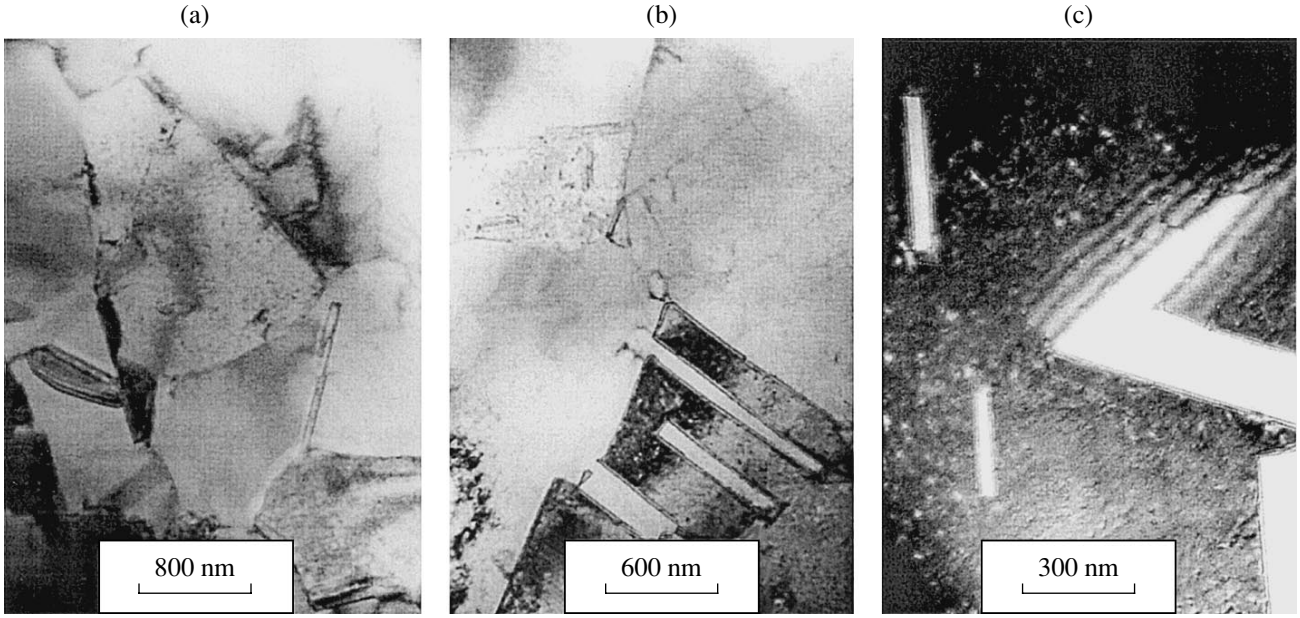

Fig. 3. Photomicrographs of a $TiO_{1.087}$ sample obtained using transmission electron microscopy [magnification (a) 38000, (b) 50000, and (c) 115000] show the sample to be polycrystalline with a minimum grain size of approximately 100 nm and a very low micropore content.

detected in titanium monoxide is due to structural vacancies rather than to pores, cracks, or other defects.

Twins are clearly seen in the photomicrographs (Figs. 3b, 3c). They are shaped as elongated rectangles and, in some cases (Fig. 3c), are interconnected. The interfaces of the twins with the host matrix exhibit striped contrast in the form of rows of parallel lines; these lines are extinction thickness contours. Judging from the extinction contours (Fig. 3c), the observed five twins can be classed into at least two families. Belong-

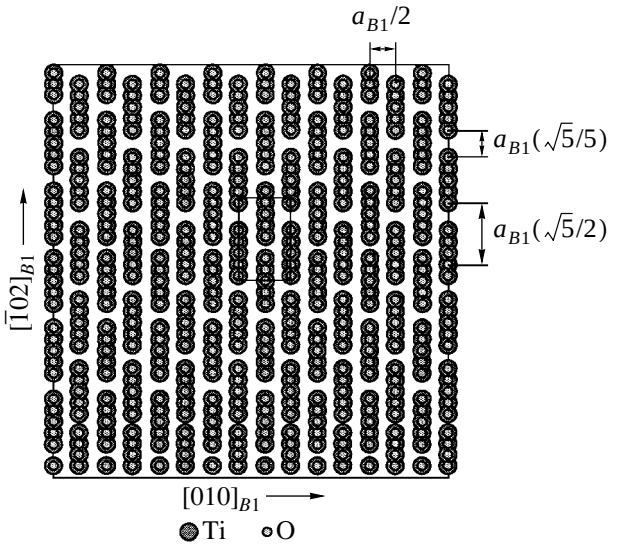

Fig. 4. Distribution of structural vacancies and titanium and oxygen atoms (observed in projection along $[101]_{C2/m} \equiv [201]_{B1}$) of ordered monoclinic titanium monoxide Ti_5O_5 (space group $C2/m$) onto the $(104)_{C2/m} \equiv (201)_{B1}$ plane. The visible distance between rows of like atoms is $d_{row} = a_{B1}/2$. The breaks between atoms in the same row specify vacancy channels oriented along $[101]_{C2/m} \equiv [201]_{B1}$. The distance between atoms separated by a vacancy is $(\sqrt{5}/5)a_{B1}$. The contour of the cross section of the Ti_5O_5 phase unit cell by the $(104)_{C2/m} \equiv (201)_{B1}$ plane is shown.

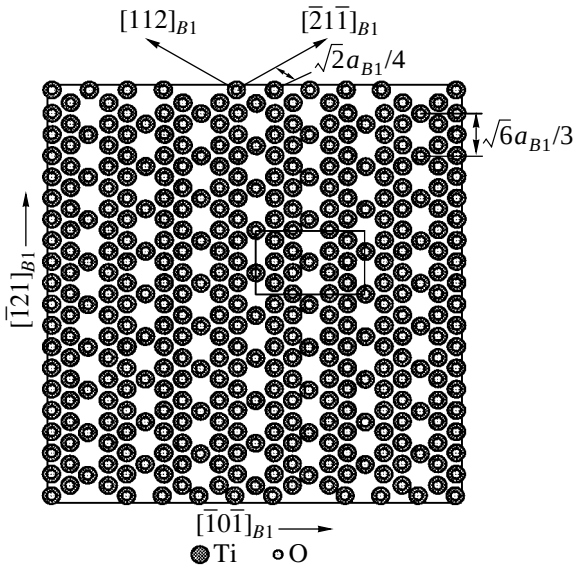

Fig. 5. Projection of the atoms and vacancies of the ordered Ti_5O_5 monoclinic phase in the $[110]_{C2/m} \equiv [11\bar{1}]_{B1}$ direction onto the $(21\bar{1})_{C2/m} \equiv (11\bar{1})_{B1}$ plane. The visible distance between rows of like atoms is $d_{row} = (\sqrt{2}/4)a_{B1}$. The vacancy channels are oriented along $[110]_{C2/m} \equiv [11\bar{1}]_{B1}$; the distance between atoms separated by a vacancy is $(\sqrt{6}/3)a_{B1}$. The contour of the cross section of the Ti_5O_5 phase unit cell by the $(21\bar{1})_{C2/m} \equiv (11\bar{1})_{B1}$ plane is shown.

ing to the first family is the twin lying slightly above the midpoint of Fig. 3c and bounded by broad contour lines. The other twins are members of the second family. The rotation angles between the twins of the second family are 67°–68°. In crystals with a structure of the $B1$ type, such a rotation angle (~65°) can occur in twinning along the $(111)_{B1}$ family planes if the matrix zone axis is directed along $[112]_{B1}$ [16]. One of the possible explanations for the appearance of striped contrast lies in the existence of a displacement field at the twin–matrix interface. One could conceive, however, of a more likely reason; namely, the presence of an extinction contour implies that the depth of the twin location is at an angle to the surface of the sample (foil) under study. This angle φ can be found as the angle between the host zone axis ($[112]_{B1}$ direction) and the normal to the twinning plane. For the twinning plane $(111)_{B1}$, we have $\varphi \approx 19.5°$; for the planes $(\bar{1}11)_{B1}$ and $(1\bar{1}1)_{B1}$, $\varphi \approx 61.9°$; and for the $(\bar{1}\bar{1}1)_{B1}$ plane, the angle is 90°. Since the extinction contours of the twins of the second family are fairly narrow, their angle φ does not reach 90°; we may thus accept that twinning occurs along the $(111)_{B1}$ or $(\bar{1}11)_{B1}$ and $(1\bar{1}1)_{B1}$ planes. The foil thickness t can be found as $t = n\xi_g$, where n is the number of extinction contours, $\xi_g = \pi V_c \cos\theta/\lambda F_g$ is the extinction length, V_c is the unit-cell volume, λ is the wavelength, F_g is the structural factor, and θ is the angle of crystal deviation from the exact reflecting position. For low-order reflections in metals, the structural factor is about 1 nm and the electron wavelength for an accelerating voltage 200 kV is 0.00251 nm; in the case where the angle between the crystal and the incident beam coincides with the Bragg angle, $\cos\theta \approx 1$ [17]. Calculation of the extinction length yields $\xi_g \approx 22 \pm 5$ nm. Taking $n = 2$ for the number of extinction contours, we obtain an approximate estimate of $t \approx 45$ nm for the foil thickness. This estimate seems realistic; indeed, the foil thickness does not exceed 50 nm, because with a larger thickness one would not have reached the atomic resolution attained in this study.

We performed computer simulation for an ordered monoclinic titanium monoxide Ti_5O_5 (space group $C2/m$) to find the directions most favorable for the observation of vacancy channels using high-resolution electron microscopy. These are the directions in which the vacancy channels lie along the direction of propagation of the electron beam. As shown by an analysis of the crystal lattice of ordered titanium monoxide, the three directions most favorable for the observation of vacancy channels are $[101]_{C2/m} \equiv [201]_{B1}$ (Fig. 4), $[110]_{C2/m} \equiv [11\bar{1}]_{B1}$ (Fig. 5), and $[011]_{C2/m} \equiv [112]_{B1}$

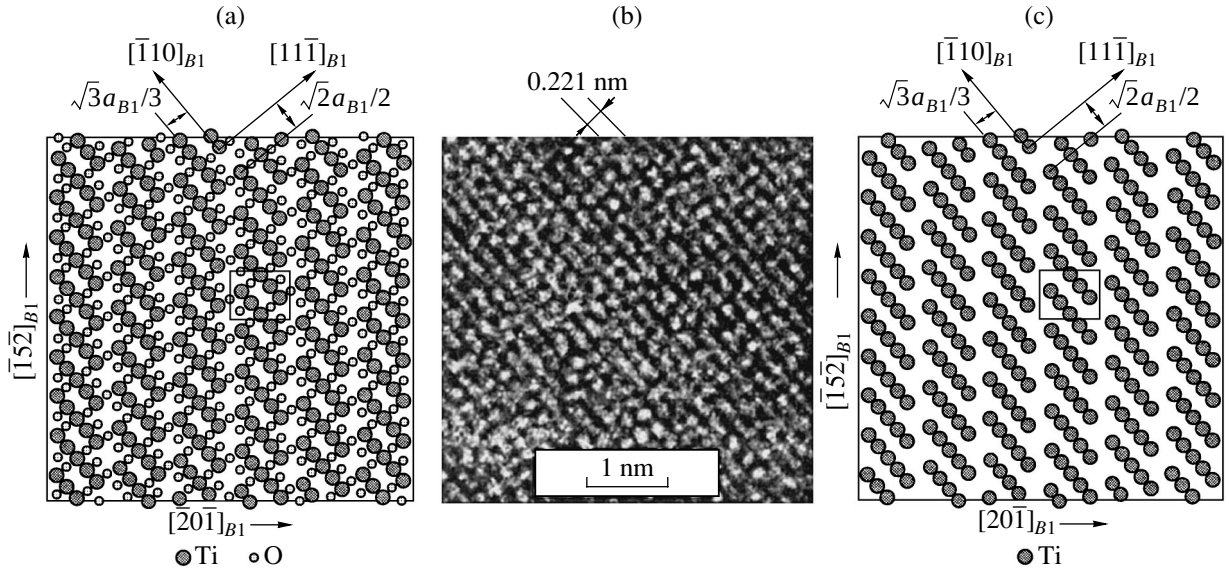

Fig. 6. Distribution of structural vacancies and Ti and O atoms seen in the $[011]_{C2/m} \equiv [112]_{B1}$ direction relative to the unit cell of ordered monoclinic Ti_5O_5 oxide (space group $C2/m$) (projection of atoms and vacancies of the Ti_5O_5 phase in the $[011]_{C2/m} \equiv [112]_{B1}$ direction onto the $(\bar{1}\,14)_{C2/m} \equiv (112)_{B1}$ plane). (a) Simulation with inclusion of Ti and O atoms, (b) experimental pattern obtained with a high atomic resolution (magnification 4×10^6), and (c) simulation made neglecting O atoms. The visible model distance between rows of like atoms is $d_{row} = \sqrt{3}/3a_{B1} = 0.241$ nm (for $a_{B1} = 0.4174$ nm), and the experimental row separation is $d_{row} = 0.221$ nm. The breaks between atoms in the same row in the model patterns correspond to vacancy channels in the $[011]_{C2/m}$ direction. The visible distance between atoms separated by a vacancy is $\sqrt{2}/2a_{B1} = 0.295$ nm. Model patterns show the contour of the cross section of the Ti_5O_5 phase unit cell by the $(\bar{1}\,14)_{C2/m}$ plane.

(Fig. 6a). Viewed in other directions, each column contains both vacancies and atoms, so that the HTEM contrast will be either low or altogether zero. To visualize the arrangement of atoms and vacancies in a cross section perpendicular to the chosen direction, we determined the projections of atoms and vacancies of the Ti_5O_5 monoclinic phase onto the planes perpendicular to each of the directions indicated above. The vacant sites in the projections identify the vacancy channels.

Vacancy channels can be visualized in the $[101]_{C2/m} \equiv [201]_{B1}$ direction, i.e., along the normal to the $(104)_{C2/m}$ plane family (Fig. 4), or along $[110]_{C2/m} \equiv [11\bar{1}]_{B1}$, i.e., along the normal to the $(21\bar{1})_{C2/m}$ planes (Fig. 5). In both directions, the channel passes through alternating nonmetal and metal vacancies. The third direction of the vacancy channel is $[011]_{C2/m} \equiv [112]_{B1}$, i.e., the normal to the $(\bar{1}\,14)_{C2/m}$ planes (Fig. 6a). In this case, the vacancy channel passes through vacant sites belonging only to the metal or only to the nonmetal sublattice. Figures 4, 5, and 6a specify the atomic-row directions, the visible distances d_{row} between rows of like atoms, and visible distances between two atoms separated by a vacancy. Also shown are the contours of the cut of the unit cell made by the above planes.

The visible distance between two atoms separated by a vacancy is a maximum (equal to $(\sqrt{6}/3)a_{B1}$ or 0.3408 nm for $a_{B1} = 0.4174$ nm) when the $(21\bar{1})_{C2/m}$ atomic planes are observed in the $[110]_{C2/m} \equiv [11\bar{1}]_{B1}$ direction (Fig. 5). In the other two directions, the visible distances between two atoms separated by a vacancy is smaller: $(\sqrt{2}/2)a_{B1} = 0.2951$ nm for the $[011]_{C2/m} \equiv [112]_{B1}$ direction (Fig. 6a) and $(\sqrt{5}/5)a_{B1} = 0.1867$ nm for $[101]_{C2/m} \equiv [201]_{B1}$ (Fig. 4). Thus, the $[110]_{C2/m} \equiv [11\bar{1}]_{B1}$ direction is preferable for direct observation of vacancies using high-resolution electron microscopy.

The visible distance between rows of like atoms $d_{row} = d_{Ti-Ti} \equiv d_{O-O}$ is maximum if atoms and vacancies of the Ti_5O_5 ordered phase are projected in the $[011]_{C2/m} \equiv [112]_{B1}$ direction onto the $(\bar{1}\,14)_{C2/m} \equiv (112)_{B1}$ plane, which is perpendicular to the direction of projection (Fig. 6a); in this case, $d_{row} = (\sqrt{3}/3)a_{B1}$ or 0.2410 nm for $a_{B1} = 0.4174$ nm. If the atoms are projected in the $[101]_{C2/m} \equiv [201]_{B1}$ direction onto a plane of the $(104)_{C2/m} \equiv (201)_{B1}$ family, the visible distance is $d_{row} = a_{B1}/2 = 0.2087$ nm; for the projection in the

$[110]_{C2/m} \equiv [11\bar{1}]_{B1}$ direction onto the $(21\bar{1})_{C2/m} \equiv (11\bar{1})_{B1}$ plane, this distance is $(\sqrt{2}/4)a_{B1} = 0.1476$ nm. Thus, atomic rows are most clearly visualized in the $[011]_{C2/m}$ direction. Figure 6b displays an experimental pattern obtained with a high atomic resolution (magnification 4×10^6 times) for the ordered monoclinic $TiO_{1.087}$ monoxide (space group $C2/m$). The image was obtained in the $(\bar{1}14)_{C2/m} \equiv (112)_{B1}$ plane (perpendicular to the $[011]_{C2/m} \equiv [112]_{B1}$ direction) and clearly reveals atomic rows.

The sample studied is about 45 nm thick; therefore, the observed pattern results from a superposition of several tens of layers, but only in one direction within the region covered are atoms arranged in distinct rows. The atomic chains in a row undergo breaks; these breaks are associated with vacancies, but their arrangement is not fully periodic. The presence of regions with a darker background in the photomicrograph (Fig. 6b) means that the sample has a larger thickness there. We do not see oxygen atoms in the experimental pattern, because their scattering factor is one third that of the titanium atoms. For comparison, Fig. 6c shows a computer simulation pattern; it exhibits only the titanium atoms and, therefore, more closely approaches the experimental image of Fig. 6b. In the model pattern, each five titanium atoms are separated by a metal structural vacancy. While in the experimental image there is no strict periodicity in the alternation of atoms and vacancies, this image is, on the whole, similar to the model one. The absence of exact periodicity in the atomic rows is accounted for by the fact that the composition of the experimentally studied titanium monoxide $TiO_{1.087}$ differs from that of monoxide $TiO_{1.00}$ ($Ti_{0.833}O_{0.833}$); the latter can form a perfect ordered phase.

4. CONCLUSION

Thus, the analysis of the microdiffraction pattern has shown the ordering of the titanium and oxygen atoms and vacancies to correspond to the ordered Ti_5O_5 phase with the monoclinic structure $C2/m$. Transmission electron microscopy performed with a magnification of tens of thousands of times revealed that titanium monoxide grains are dense and do not contain large pores. This provided evidence supporting the earlier conjectures that the free volume detected in titanium monoxide using the picnometric method is due to the presence of a large number of structural vacancies on the titanium and oxygen sublattices. High-resolution transmission electron microscopy permitted the detection and observation of structural vacancies in titanium monoxide. The observation of structural vacancies in $TiO_{1.087}$ at a magnification of 4×10^6 became possible due to vacancy ordering, which gave rise to the formation of continuous vacancy channels.

ACKNOWLEDGMENTS

The authors are indebted to Dr. Phillipp and Mrs. M. Kelsch (Max Planck Institute, Stuttgart, Germany) for assistance in the experiment and to Prof. H.-E. Schaefer (Institute of Theoretical and Applied Physics, Stuttgart University) and Dr. E.V. Shalaeva (Institute of Solid-State Physics, Ural Division, Russian Academy of Sciences) for valuable discussions.

REFERENCES

1. A. I. Gusev and A. A. Rempel', *Nonstoichiometry, Disorder, and Order in Solids* (Ural. Otd. Ross. Akad. Nauk, Yekaterinburg, 2001).
2. A. I. Gusev, A. A. Rempel, and A. A. Magerl, *Disorder and Order in Strongly Non-Stoichiometric Compounds: Transition Metal Carbides, Nitrides, and Oxides* (Springer, Berlin, 2001).
3. A. A. Rempel', *Ordering Effects in Non-Stoichiometric Interstitial Compounds* (Nauka, Yekaterinburg, 1992).
4. D. Shindo and K. Hiraga, *High-Resolution Electron Microscopy for Materials Science* (Springer, Berlin, 1998).
5. A. A. Valeeva, A. A. Rempel, M. A. Müller, *et al.*, Phys. Status Solidi B **224** (2), R1 (2001).
6. P. Ehrlich, Z. Elektrochem. **45** (5), 362 (1939).
7. S. Andersson, B. Collen, U. Kuylenstierna, and A. Magneli, Acta Chem. Scand. **11** (10), 1641 (1957).
8. B. F. Ormont, *Structures of Inorganic Substances* (Tekhteoretizdat, Moscow, 1950), p. 462.
9. A. A. Valeeva, A. A. Rempel', and A. I. Gusev, Neorg. Mater. **37** (6), 716 (2001).
10. D. Watanabe, J. R. Castles, A. Jostson, and A. S. Malin, Nature **210** (5039), 934 (1966).
11. D. Watanabe, J. R. Castles, A. Jostson, and A. S. Malin, Acta Crystallogr. **23** (2), 307 (1967).
12. E. Hilti and F. Laves, Naturwissenschaften **55** (3), 131 (1968).
13. D. Watanabe, O. Terasaki, A. Jostsons, and J. R. Castles, in *The Chemistry of Extended Defects in Non-Metallic Solids*, Ed. by L. Eyring and M. O. Keeffe (North-Holland, Amsterdam, 1970), p. 238.
14. A. W. Vere and R. E. Smallman, *Mechanism of Phase Transformation in Crystalline Solids* (Institute of Metals, London, 1969), p. 212.
15. H. Terauchi, J. B. Cohen, and T. B. Reed, Acta Crystallogr. A **34** (4), 556 (1978).
16. L. M. Utevskiĭ**,** *Electron Diffraction Microscopy in Physical Metallurgy* (Metallurgiya, Moscow, 1973).
17. *Electron Microscopy of Thin Crystals*, Ed. by P. B. Hirsch, A. Howie, R. B. Nicholson, D. W. Pashley, and M. J. Whelan (Plenum, New York, 1965; Mir, Moscow, 1968).

Translated by G. Skrebtsov

Physics of the Solid State, Vol. 45, No. 1, 2003, pp. 94–97. Translated from Fizika Tverdogo Tela, Vol. 45, No. 1, 2003, pp. 91–94.

DEFECTS, DISLOCATIONS, AND PHYSICS OF STRENGTH

A Correlation between Manifestations of the Magnetoplastic Effect and Changes in the Electron Paramagnetic Resonance Spectra after Quenching of NaCl : Eu Single Crystals

R. B. Morgunov and A. A. Baskakov

Institute of Solid-State Physics, Russian Academy of Sciences, Chernogolovka, Moscow oblast, 142432 Russia
e-mail: morgunov@issp.ac.ru

Received February 19, 2002

Abstract—The electron paramagnetic resonance (EPR) spectra of Eu^{2+} impurity ions in NaCl : Eu single crystals are investigated. It is found that the intensity of the EPR spectra undergoes prolonged (~200 h) multistage variations after quenching of NaCl : Eu single crystals. The variations observed in the EPR signal intensity are explained by the aggregation of impurity–vacancy dipoles into complexes. It is revealed that the magnetoplastic effect (a change in the microhardness in a magnetic field with an induction of 6 T) in these crystals manifests itself at an intermediate stage of impurity aggregation when all individual impurity–vacancy dipoles are temporarily stabilized in the sample. This can be associated with the thermally activated transformation of the internal atomic structure in the majority of already existing complexes. *© 2003 MAIK "Nauka/Interperiodica".*

1. INTRODUCTION

The first reliable experimental evidence supporting the existence of the magnetoplastic effect in ionic crystals was obtained by Al'shits *et al.* [1–5], who revealed and thoroughly investigated the influence of a magnetic field with an induction $B \sim 1$ T on the mobility of individual dislocations [1–3] and the yield point [4, 5]. At present, it has been reliably established that the magnetoplastic effect in ionic crystals is caused, among other factors, by magnetic-field-induced changes in both the kinetics of aggregation and the atomic configuration of intermediate nonequilibrium complexes formed by paramagnetic point defects serving as stoppers for dislocations [6–10]. In order to gain a deeper insight into the microscopic mechanism of the influence of a magnetic field on the structure of the aforementioned complexes and to elucidate their atomic structure, it is necessary to answer the following questions. What happens to the majority of impurity point defects at the instant the magnetoplastic effect manifests itself? How much do their magnetic properties change with time after quenching? What are the specific features in the behavior of spins of defects at the stage of nucleation of magnetosensitive defect configurations? In this respect, the purpose of the present work was to elucidate how the formation of magnetosensitive states of the complexes formed by point defects affects the electron paramagnetic resonance (EPR) spectra, whose variations, in turn, reflect the aggregation of Eu^{2+} paramagnetic impurity–vacancy dipoles into complexes.

2. SAMPLES AND EXPERIMENTAL TECHNIQUE

The experiments were performed with quenched crystals of NaCl : Eu (0.1 at. %). The choice of europium impurities was made for the following reason: the use of europium-doped crystals provided a means for observing the magnetoplastic effect [6, 7] and monitoring the state of paramagnetic point defects through recording and analyzing the EPR spectra [11]. The crystals were quenched by heating at a temperature of 770 K for 1 h followed by cooling in a copper vessel to a temperature of 293 K at a mean rate of ~5 K/s. In order to prevent diffusion of oxygen and hydroxyl groups into the crystals under investigation, their heating in all experiments was performed in a helium or argon atmosphere.

The presence of magnetosensitive defect complexes in the studied crystal was revealed as follows. The crystal was quenched and allowed to stand for a certain time (from 1 min to 200 h) followed by measurement of the microhardness H. Then, the crystal was exposed to a magnetic field with an induction of 6 T for 10 ms and the microhardness H was measured once again. The magnitude of the difference ΔH between these microhardnesses served as a quantitative measure of the magnetoplastic effect and indirectly characterized the concentration of magnetosensitive centers generated in the crystal. In all the experiments, the Vickers microhardness of the crystals was measured under an indenter load of 0.2 N and the loading time was 10 s. The indentation diagonals were oriented along directions of the [110] type. Each point in the graphs was obtained by averaging over 20–30 measurements. As a result, the

error in the microhardness measurement was reduced to 1–1.5%. This is a typical error in measurements of the microhardness in ionic crystals (see, for example, [12, 13]). It should be noted that, in all the experiments, the microhardness measurements and exposure of the studied crystals to a magnetic field were carried out at a temperature precisely equal to 293 K and the total duration of these procedures (taken together) was considerably shorter than that of the transient processes examined in this work.

The crystal contained europium impurities in the form of Eu^{2+}–V_k impurity–vacancy dipoles in which the cation vacancy compensated for an excess positive charge of the impurity ion. According to the estimates made by Ruiz-Mejia *et al.* [14], the free energy of defects of all other types (for example, individual ions and neutral atoms of europium) is substantially higher than that of the Eu^{2+}–V_k system; hence, the probability of their formation is negligible. The aggregation kinetics of impurity–vacancy dipoles after quenching was judged from the changes in the characteristics of the EPR spectra. The EPR spectra were recorded on a standard radiospectrometer operating in the *X* band at a modulation frequency of 100 kHz in the dc magnetic field scan range B_0 = 0.7–4 kOe. Earlier [6, 7], it was demonstrated that, when the microwave magnetic field power in the spectrometer is of the order of 100 mW, crystals undergo resonance-induced disordering. Moreover, the procedure of measuring the spectra, in principle, can affect their form. For this reason, the power used in our experiments was two orders of magnitude less (~1 mW) than that in [6, 7] (~100 mW).

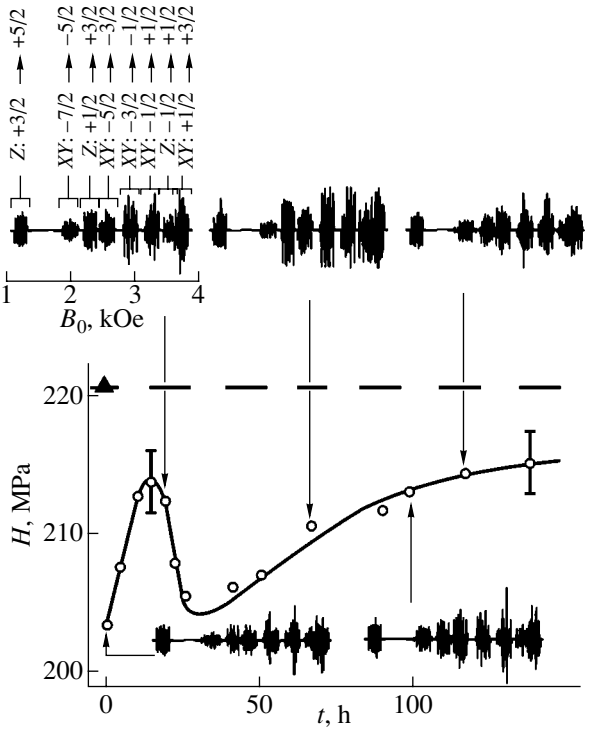

Fig. 1. Dependence of the microhardness *H* of the NaCl : Eu crystal on the time elapsed after quenching in the absence of a magnetic field. The EPR spectra shown are measured at the instants of indentation. The transitions between different Eu^{2+} electron spin states split in the crystal field are indicated at the upper left of the figure.

3. RESULTS AND DISCUSSION

The EPR spectrum of Eu^{2+}–V_k impurity–vacancy dipoles consists of 14 groups of narrow lines [11]. The Eu^{2+} ion has spin $S = 7/2$, and the Zeeman splitting for the Eu^{2+} *f* electrons partially screened by the *d* electron shell is larger than the splitting in the crystal field. Consequently, it can be expected that the EPR spectrum will contain $2S = 7$ groups of lines; each group corresponds to transitions between $2S + 1 = 8$ spin sublevels split by the crystal field in the Eu^{2+} ion. However, since the impurity–vacancy dipoles have the C_{2v} symmetry, which is lower than the symmetry of the crystal lattice, the locations of the groups of lines for the dipoles oriented parallel and perpendicular to the constant magnetic field differ from each other. Therefore, the total number of groups of lines in the EPR spectrum is equal to 14. According to Aguilar *et al.* [11], the principal magnetic axes of the impurity–vacancy dipole system are aligned parallel to the [001] direction and, in the perpendicular plane, along the [110] direction. In our experiments, the constant magnetic field was aligned parallel to the [001] direction in order to ensure the maximum distance from the groups of lines to the center of the spectrum and the possibility of processing individual lines. The limited scan range of the dc magnetic field used made it possible to observe only eight groups of lines among the above set of groups (Fig. 1). The line splitting within a particular group is associated with the hyperfine interaction of unpaired electrons with europium nuclei. In the crystal, there are isotopes of two sorts (^{151}Eu and ^{153}Eu) with an approximately identical abundance, the same nuclear spins $I = 5/2$, but different hyperfine interaction constants. Therefore, each group involves $2(2I + 1) = 12$ lines.

As can be seen from Fig. 1, the microhardness of the crystals nonmonotonically varies with time *t* after their quenching. The EPR spectra also change significantly (Fig. 1). These changes can be caused not only by variations in the hyperfine interactions occurring in the complexes and the associated change in the overlap between individual spectral lines but also by variations in the signal amplitudes corresponding to these lines. In order to separate these factors and to analyze the changes in the number of free impurity–vacancy dipoles in a pure form, we chose several nonoverlapping individual lines of two types characterizing free impurity–vacancy dipoles (not aggregated into complexes) oriented along the [001] direction and in the perpendicular plane (see, for example, the inset in Fig. 2). The intensity of the chosen lines decreases with time elapsed after the quenching of the crystal (see the inset in Fig. 2). The shape of these lines is described by

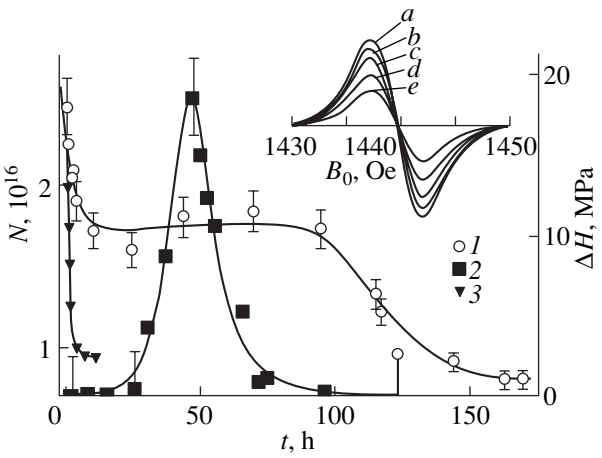

Fig. 2. Dependences of (*1*) the number *N* of spins of free impurity–vacancy dipoles (not aggregated into complexes) and (*2*) the magnitude of crystal softening (the difference between microhardnesses) ΔH upon exposure to a magnetic-field pulse (amplitude, 6 T; pulse width, 10 ms) on the time *t* elapsed after quenching of the crystal. (*3*) Dependence of the number *N* of spins of free impurity–vacancy dipoles on the time *t* elapsed after quenching of the crystal from 550 K according to the data taken from [15] (measurements were performed at a temperature of 373 K). The inset shows single EPR lines (associated with the electron spin transitions + 3/2 ⟷ +5/2 for the projection of the ^{153}Eu nuclear spin onto the direction of the dc magnetic field of the spectrometer I_z = + 5/2) within (*a*) 1, (*b*) 5, (*c*) 100, (*d*) 120, and (*e*) 170 h after the quenching of the crystal.

a Gaussian function with a high accuracy (95%). By performing double integration of the Gaussian function and normalizing the result of this integration to the area of the reference Mn^{2+} EPR spectrum of MgO, we determined the number *N* of spins of free impurity–vacancy dipoles (not aggregated into complexes) and obtained the dependence of *N* on the time *t* elapsed after the quenching of the crystal. The systematic error in the determination of *N* was approximately equal to 30%, and the scatter in the data on *N* from experiment to experiment (determined for six measurements) did not exceed 6%.

The dependence $N(t)$ is represented by a compound curve; it steeply falls off at $t < 20$ h, flattens out in the range 20 h $< t <$ 90 h, and again falls off at $t > 100$ h (curve *1* in Fig. 2). Special investigations demonstrated that this dependence is identical for all individual lines belonging to any group involved in the spectrum. Of particular interest is the fact that the magnetoplastic effect (characterized by a nonzero value of ΔH and corresponding to softening of crystals) is observed in the range 20 h $< t <$ 90 h, i.e., at the stage of relaxation of the point defect subsystem when all spins of free impurity–vacancy dipoles in the sample are temporarily stabilized (curve *2* in Fig. 2).

Before proceeding to the discussion of the results obtained, one additional essential remark needs to be made. The upper estimate of the total area of the spectrum and a standard recalculation in terms of the total concentration of free impurity–vacancy dipole spins indicate that, within a few minutes after the quenching of the crystal, this concentration is approximately equal to 1.3×10^{-2} at. %, which is substantially less than the total concentration of europium ions in the sample ($\sim 10^{-1}$ at. %). This suggests that the time of heat treatment of the crystal at a high temperature (or the heat treatment temperature itself) is less than that required to dissolve all the complexes involved in the sample. Consequently, in principle, there is a potentiality for increasing the number of magnetosensitive complexes in the crystal and enhancing the magnetoplastic effect.

A decrease in the intensity of the EPR spectra of NaCl : Eu single crystals within a few hours after quenching from a temperature of 550 K was revealed by Rubio [15], who investigated this phenomenon at $T = 373$ K (curve *3* in Fig. 2). However, long-term evolution in the intensity of the EPR spectra at $T = 293$ K (observations at this temperature are of prime interest for revealing a correlation with the kinetics of formation of magnetosensitive complexes) was not examined in [15]. The general tendency to a decrease in the EPR signal intensity with time elapsed from the quenching of samples can be explained in terms of the formation of impurity–vacancy dipole complexes that experience the internal transformations responsible for the considerable changes observed in the EPR spectra of the defect complexes as compared to the spectrum of individual impurity–vacancy dipoles. In particular, these transformations, which take part of the spins "out of the game," can be associated with the following features: (i) a substantial broadening of the spectral line due to dipole–dipole or exchange interactions between impurity–vacancy dipoles; (ii) a change in the effective *g* factor; (iii) the formation of chemical bonds between individual paramagnetic defects and, consequently, spin pairing; and (iv) an additional splitting of spin levels due to a change in the crystal field in the complexes. It should be noted that the decrease observed in the intensity of the spectral line with time elapsed after the quenching is not attended by variations in its width and shape (see the inset in Fig. 2). Therefore, only defects of the same type, namely, free impurity–vacancy dipoles, make a contribution to the EPR signal over a period of 200 h after the quenching of the crystal.

The plateau observed in the dependence $N(t)$ directly indicates the occurrence of several different processes responsible for the magnetic properties of the formed complexes and, apparently, for their atomic configuration. The change in the atomic configuration of these complexes can be judged from the nonmonotonic change in the microhardness that is sensitive to the mobility of dislocations, which, in turn, depends on the elastic stress fields induced by impurity–vacancy dipole complexes (Fig. 1). The inhibition of spin pairing can be explained under the assumption that a number of defects formed at the initial stage that do not contribute to the EPR signal appear to be thermally unstable and unfavorable for further growth through the

attachment of new impurity–vacancy dipoles. Consequently, after a time, these complexes can decay into individual impurity–vacancy dipoles due to thermal fluctuations. This process competes with the formation of favorable configurations, leads to the escape of dipoles from the complexes, and, apparently, cancels out the general tendency to a decrease in N in our experiments. The above assumption is in good agreement with the obtained dependence of the magnitude of the microhardness H on the time elapsed after the quenching of the crystal under investigation (Fig. 1). In actual fact, according to the universally accepted concepts, the larger the size of defect complexes, the stronger the dislocation motion drag [16]. On this basis, the increase observed in the microhardness H in the early stage of relaxation (at $t < 20$ h) can be explained by the increase in the size of complexes at this stage. The subsequent decrease in the microhardness H in the range $20\ \text{h} < t < 40\ \text{h}$ corresponds to a plateau in the dependence $N(t)$ and, hence, can be associated with the decay of a number of already existing complexes. Finally, the increase observed in the microhardness H at $t > 50$ h approximately corresponds to the second descending portion in the dependence $N(t)$ and can be attributed to a continuation of the aggregation from favorable configurations of the complexes.

Thus, the magnetoplastic effect manifests itself only at the stage of relaxation of the excited subsystem of point defects in the case when individual impurity–vacancy dipoles already form a number of complexes capable of dissociating (possibly, in part) or undergoing transformations in their internal atomic configurations due to thermal fluctuations. Note that the stability of complexes depends not only on the elastic potential but also on the exchange interaction and the mutual orientation of spins inside the complexes. Therefore, the concentration ratio of complexes with particular configurations can be controlled by varying the spin orientation in a specified magnetic field over a short period when terms of different multiplicities approach each other. This assumption is consistent with the concepts regarding the influence of a magnetic field on spin-dependent reactions [17]. The analogy between this phenomenon and the magnetoplastic effect was first drawn by Al'shits *et al.* [18].

4. CONCLUSIONS

The experimental data obtained allowed us to draw the following inferences. The multistage stepwise decrease in the intensity of the EPR spectra during relaxation of the subsystem of point defects excited by quenching of the crystal indicates that the processes associated with the aggregation of free impurity–vacancy dipoles into complexes compete with the processes of internal transformation and decay of the complexes into individual dipoles. The magnetosensitive states of defects arise at the stage of relaxation of the above subsystem when the aggregation is retarded as a result of the decay of already existing complexes. The role played by the magnetic field, most likely, is reduced to a change in the probability of spin-dependent transitions occurring inside the complexes and the probability of forming their intermediate configurations differing in atomic structure.

ACKNOWLEDGMENTS

This work was supported by the Russian Foundation for Basic Research, project nos. 01-03-42501 and 01-02-06307.

REFERENCES

1. V. I. Al'shits, E. V. Darinskaya, T. M. Perekalina, and A. A. Urusovskaya, Fiz. Tverd. Tela (Leningrad) **29**, 467 (1987) [Sov. Phys. Solid State **29**, 265 (1987)].
2. V. I. Al'shits, E. V. Darinskaya, and O. L. Kazakova, Pis'ma Zh. Éksp. Teor. Fiz. **62**, 352 (1995) [JETP Lett. **62**, 375 (1995)].
3. V. I. Al'shits, E. V. Darinskaya, and O. L. Kazakova, Zh. Éksp. Teor. Fiz. **111**, 615 (1997) [JETP **84**, 338 (1997)].
4. A. A. Urusovskaya, V. I. Al'shits, A. E. Smirnov, and N. N. Bekkauér, Pis'ma Zh. Éksp. Teor. Fiz. **65**, 470 (1997) [JETP Lett. **65**, 497 (1997)].
5. V. I. Al'shits, N. N. Bekkauér, A. E. Smirnov, and A. A. Urusovskaya, Zh. Éksp. Teor. Fiz. **115**, 951 (1999) [JETP **88**, 523 (1999)].
6. Yu. I. Golovin, R. B. Morgunov, V. E. Ivanov, and A. A. Dmitrievskiĭ, Zh. Éksp. Teor. Fiz. **117**, 1080 (2000) [JETP **90**, 939 (2000)].
7. Yu. I. Golovin, R. B. Morgunov, and A. A. Dmitrievskii, Mater. Sci. Eng. A **288** (2), 261 (2000).
8. Yu. I. Golovin and R. B. Morgunov, Fiz. Tverd. Tela (St. Petersburg) **37** (5), 1352 (1995) [Phys. Solid State **37**, 734 (1995)].
9. R. B. Morgunov and A. A. Baskakov, Fiz. Tverd. Tela (St. Petersburg) **43** (9), 1632 (2001) [Phys. Solid State **43**, 1700 (2001)].
10. R. B. Morgunov, A. A. Baskakov, D. V. Yakunin, and I. N. Trofimova, Fiz. Tverd. Tela (St. Petersburg) **44** (9), 2525 (2002) [Phys. Solid State **44**, (2002)].
11. G. Aguilar, E. Munoz, H. Murrieta, *et al.*, J. Chem. Phys. **60**, 4665 (1974).
12. M. Suszynska, P. Grau, M. Szmida, and D. Nowak-Wozny, Mater. Sci. Eng. A **234–236**, 747 (1997).
13. Yu. S. Boyarskaya, D. Z. Grabko, and M. S. Kats, *Physics of Microindentation* (Shtiintsa, Kishinev, 1986), pp. 10–12.
14. C. Ruiz-Mejia, U. Oseguera, H. Murrieta, and J. Rubio, J. Chem. Phys. **73**, 60 (1980).
15. J. Rubio, J. Phys. Chem. Solids **52**, 101 (1991).
16. E. Orozco and J. Soullard, Philos. Mag. A **50**, 425 (1984).
17. K. M. Salikhov, Yu. N. Molin, R. Z. Sagdeev, and A. L. Buchachenko, in *Spin Polarization and Magnetic Field Effects in Radical Reactions*, Ed. by Yu. N. Molin (Elsevier, Amsterdam, 1984).
18. V. I. Al'shits, E. V. Darinskaya, and E. A. Petrzhik, Fiz. Tverd. Tela (Leningrad) **33** (10), 3001 (1991) [Sov. Phys. Solid State **33**, 1694 (1991)].

Translated by O. Borovik-Romanova

Physics of the Solid State, Vol. 45, No. 1, 2003, pp. 98–103. Translated from Fizika Tverdogo Tela, Vol. 45, No. 1, 2003, pp. 95–100.

DEFECTS, DISLOCATIONS, AND PHYSICS OF STRENGTH

Effect of Magnetic Field on Dislocation-Induced Unelasticity and Plasticity of LiF Crystals with Various Impurities

N. A. Tyapunina*, V. L. Krasnikov, É. P. Belozerova***, and V. N. Vinogradov*****

** Moscow State University, Vorob'evy gory, Moscow, 119899 Russia*

*** Nekrasov State University, Kostroma, Russia*

**** Kostroma State Technological University, Kostroma, 156005 Russia*

e-mail: ovg@kstu.edu.ru

Received February 20, 2002; in final form, April 22, 2002

Abstract—The effect of a magnetic field of 0.04–0.8 T on the amplitude dependence of the internal friction in LiF crystals with various impurities is studied using a two-component resonant-oscillator method at a frequency of 80 kHz. The state of the samples was controlled *in situ* from the current–voltage characteristics of a compound oscillator. It is found that the state of the dislocations-pinning-centers system changes in the presence of a magnetic field; this leads to an increase in the internal friction and plasticity of the samples. The effect of the magnetic field is sensitive to the impurity composition in the crystal. © *2003 MAIK "Nauka/Interperiodica".*

1. INTRODUCTION

It is well known that inelastic properties of crystals, such as the internal friction (IF) and elastic-modulus defect (EMD), are determined by dislocation mechanisms in the kilohertz frequency range. The mechanical-energy loss at room temperature is associated with energy transfer from vibrating dislocations to the phonon subsystem of the crystal. Experiments show that the IF and EMD also respond to external agencies which directly affect the electron subsystem of the crystal. For example, inelastic properties of alkali-halide crystals (AHCs) change under the action of a magnetic field [1–3].

This work aims at studying the effect of a magnetic field on the unelasticity of LiF crystals with different impurity compositions. Among other things, we analyzed the effect of Ni impurity on the unelasticity of LiF crystals. According to Al'shits *et al.* [4], the presence of the Ni impurity considerably intensifies the magnetoplastic effect in AHCs.

2. EXPERIMENTAL TECHNIQUE AND MATERIALS

We studied the effect of a magnetic field on the IF and the Young modulus defect in AHCs in the kilohertz frequency range by using the method of a compound piezoelectric-quartz oscillator [5]. A longitudinal standing ultrasonic wave was excited at a fundamental frequency of 80 kHz over the sample length. The maximum amplitude of strain ε_0 at an antinode of the standing wave was varied from 10^{-7} to 10^{-3}.

The magnetic field, with induction vector **B** perpendicular to the direction of propagation of ultrasound, was produced by a permanent magnet (0.04–0.3 T) and an electromagnet (0.4–1 T).

The state of the sample was traced *in situ* from the current–voltage characteristics of the compound oscillator [6, 7]. The density and distribution of dislocations were controlled with the help of the selective etching method. Data concerning the initial state of the crystals are given in Table 1.

The rod-shaped samples were cleaved from crystals along the cleavage planes. The sample length corre-

Table 1. Data on the initial state of LiF crystals under investigation

Material, labeling	Main impurities	Yield stress σ_{cr}, MPa	Dislocation Density ρ, 10^9 m^{-2}	Internal friction δ_0, 10^{-4}
LiF_I	Mg	7.8	2–6	0.9
LiF_{II}	Ca, Ba	3.9	3–8	2.4
LiF_{III}	Mg, Ni	10.3	0.8–2	0.5

Note: The composition of impurities was determined spectrographically. The total molar fraction of impurities was $C \sim 10^{-5}$.

1063-7834/03/4501-0098$24.00 © 2003 MAIK "Nauka/Interperiodica"

sponded to the condition of resonance excitation of the oscillator at the fundamental frequency. After preparation, the samples were subjected to prolonged ageing (for three years) at room temperature. No fresh dislocations were introduced before measurements.

3. EXPERIMENTAL RESULTS AND DISCUSSION

Let us first consider the effect of magnetic and ultrasonic fields on LiF samples.

Test experiments based on repetitive selective etching before and after holding of the samples in a magnetic field of induction $B < 1$ T did not reveal motion or multiplication of dislocations. However, preliminary long-term holding of samples in a magnetic field produced a considerable effect on the inelastic properties (IF and Young modulus defect) of LiF crystals, as described in [8, 9].

Ultrasound can produce both reversible and irreversible changes in the dislocation structure of crystals, which are manifested in the current–voltage characteristics of the oscillator and in the results of IF measurements.

Let us analyze the dependence of IF on the strain amplitude for $B = 0$, which is typical of LiF (Fig. 1). Curves *1* and *2* in Fig. 1 correspond to two successive tests on the LiF_{III} sample. It can be seen from Fig. 1 that the height and position of the IF peak appearing at the amplitude $\varepsilon_0 \approx 2 \times 10^{-4}$ remain unchanged in repeated tests.

The ascending branches of the IF peaks are linearized in the Granato–Lucke coordinates [10]:

$$\ln[(\delta(\varepsilon_0) - \delta_{01})\varepsilon_0] = C_0 - \Gamma\varepsilon_0^{-1}, \qquad (1)$$

where δ_{01} is the amplitude-independent IF corresponding to small values of ε_0 and C_0 and Γ are constants related to the dislocation structure parameters. In both cases, the squares of the correlation coefficients were $r^2 = 0.97$.

The values of IF on the descending branches of the peaks are proportional to ε_0^{-2} with $r^2 = 0.79$ and 0.96 in the first and second tests, respectively. Consequently, the IF peaks are associated with the hysteresis mechanism of dislocation-induced internal friction and can be interpreted using the Rogers–Suprun model [11, 12].

The simultaneous effect of ultrasound and a magnetic field on the unelasticity of LiF crystals was studied on a batch of samples, as well as on the same sample. IF and EMD measurements on the same sample were made in alternating tests in the presence and in the absence of a magnetic field.

The influence of the magnetic field is illustrated in Figs. 2 and 3, showing the current–voltage characteristics $V_p(V)$ of the compound oscillator with LiF_{II} and LiF_{III} samples, respectively. As a response to the action of a magnetic field, we considered the quantity V_p proportional to the strain amplitude at the antinode ε_0 of the standing wave. As a magnetic field is applied, for a constant voltage V supplied to the quartz plates, the value of V_p (and, hence, of ε_0) decreases. This means

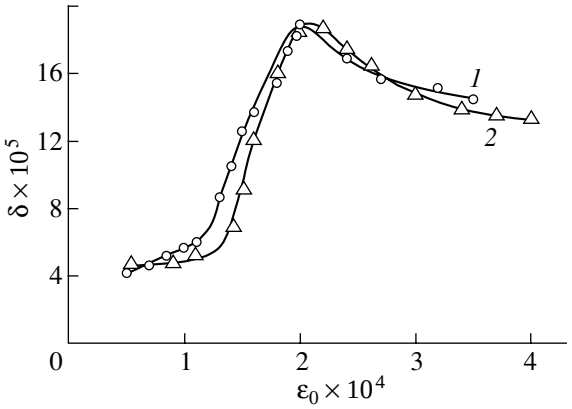

Fig. 1. Amplitude dependence of the internal friction of an LiF_{III} sample: (*1*) first test; (*2*) second test carried out 1.5 h after the first test.

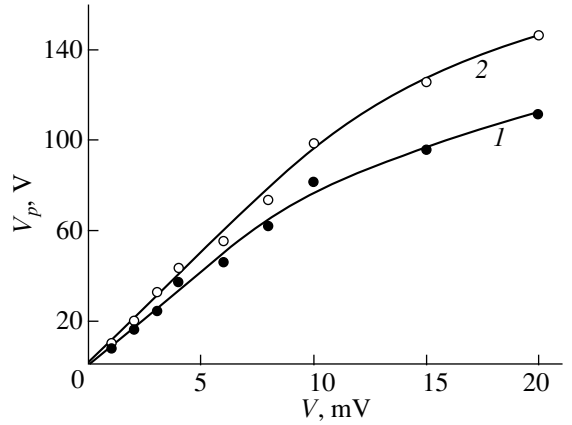

Fig. 2. Current–voltage characteristics of an LiF_{II} sample tested in a magnetic field (*1*) $B = 0.3$ T and (*2*) $B = 0$.

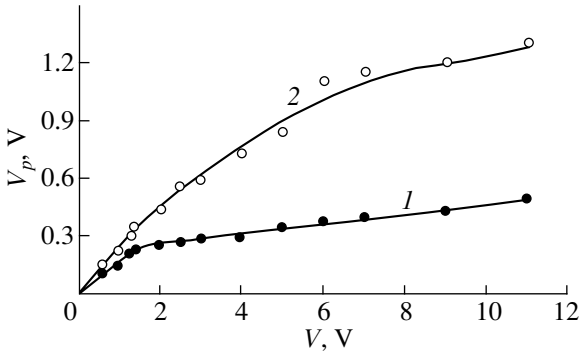

Fig. 3. Current–voltage characteristics of an LiF_{III} sample tested in a magnetic field (*1*) $B = 0.08$ T and (*2*) $B = 0$.

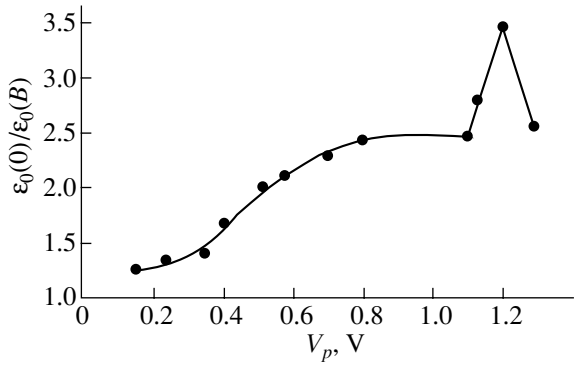

Fig. 4. Dependence of $\varepsilon_0(0)/\varepsilon_0(B)$ on V_p for an LiF_{III} sample. V_p is proportional to the amplitude $\varepsilon_0(0)$ before the application of a magnetic field.

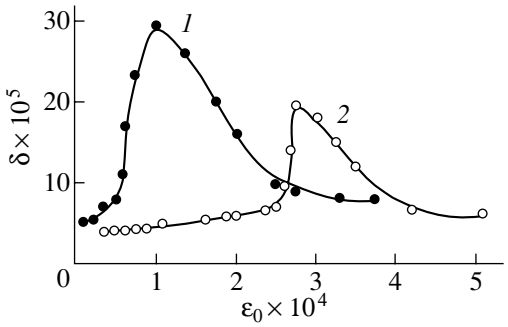

Fig. 5. Amplitude dependence of the internal friction of an LiF_{III} sample tested in a magnetic field (*1*) $B = 0.08$ T and (*2*) $B = 0$.

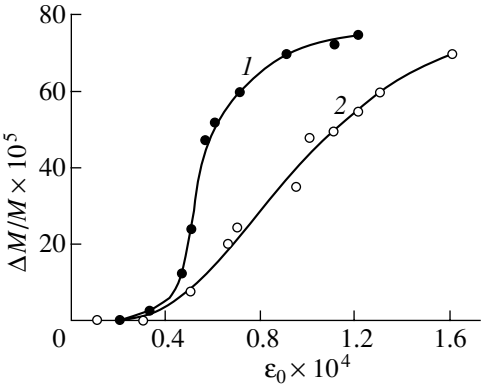

Fig. 6. Amplitude dependence of the Young modulus defect for an LiF_{III} sample tested in a magnetic field (*1*) $B = 0.08$ T and (*2*) $B = 0$.

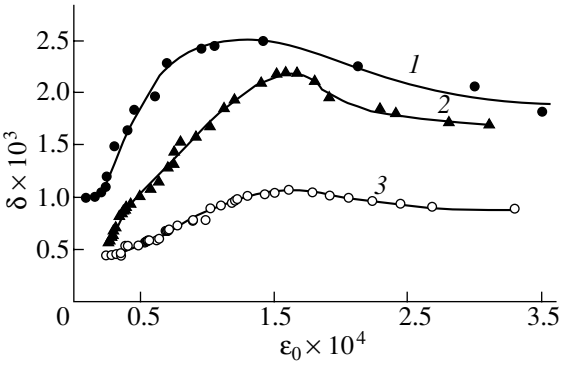

Fig. 7. Effect of magnetic field on the amplitude dependences of internal friction for LiF_{II} samples for B equal to (*1*) 0, (*2*) 0.3, and (*3*) 0.6 T.

that the value of IF increases jumpwise upon application of the magnetic field and the sample becomes more plastic. It was shown earlier that this effect is not a consequence of the emergence of a vortex electric field at the instants of application and removal of the magnetic field [1, 3].

The strain amplitude jump under the action of the magnetic field can be characterized by the ratio $\varepsilon_0(0)/\varepsilon_0(B)$, where $\varepsilon_0(0)$ is the amplitude in zero field and $\varepsilon_0(B)$ is the same in the magnetic field. This ratio for fixed V varies depending on the magnetic induction B and the ultrasound amplitude ε_0. The dependence of this ratio on ε_0 for LiF_{III} in the field $B = 0.08$ T is shown in Fig. 4. The values of $V_p \sim \varepsilon_0$ lying on the abscissa axis were obtained in a zero magnetic field. It can be seen that, for a certain amplitude ε_{0m}, the ratio $\varepsilon_0(0)/\varepsilon_0(B)$ attains its maximum value and then decreases upon an increase in ε_0. A similar dependence of the ratio $\varepsilon_0(0)/\varepsilon_0(B)$ on ε_0 has also been observed for an LiF_{II} sample [1], but the values of the ratio $\varepsilon_0(0)/\varepsilon_0(B)$ and of the quantity ε_{0m} were different; i.e., these values were determined by the impurity composition of the crystal.

The results of IF measurements on the LiF_{III} sample in the regime of alternating tests in a magnetic field and in zero field are presented in Fig. 5. The points corresponding to curve *1* in Fig. 5 were obtained in a magnetic field $B = 0.08$ T, while the points corresponding to curve *2* were obtained for $B = 0$. A comparison of curves *1* and *2* in Fig. 5 shows that the height of the IF peak in a magnetic field is larger ($\delta_{max}(B)/\delta_{max}(0) = 1.54$ in the present case) and the position of the peak is shifted towards smaller amplitudes ε_0.

Figure 6 shows the amplitude dependences of the Young modulus defect for the same LiF_{III} sample for the amplitudes corresponding to ascending segments of the IF peaks in Fig. 5. The points on curve *1* in Fig. 6 were obtained in a magnetic field $B = 0.08$ T, while the points on curve *2* were obtained for $B = 0$. It can be seen that, in the presence of a magnetic field, the amplitude dependence of the EMD is manifested for smaller values of ε_0 and the EMD values attained are higher than for $B = 0$.

The amplitude dependences $\delta(\varepsilon_0)$ for different values of the magnetic induction B are shown in Figs. 7 and 8. The curves in Fig. 7 were obtained for three LiF_{II} samples with mirror cleavage faces for $B = 0$ (curve *1*), 0.3 (curve *2*), and 0.6 T (curve *3*). Curves *1–5* in Fig. 8 correspond to the same LiF_I sample. Each series of points corresponding to the same amplitude ε_0 on this curve was obtained for the induction $B = 0$, 0.25, 0.35, 0.6, and 0.8 T, respectively. The height of the IF peak and its position on the ε_0 axis depend on the magnetic induction B. This can be seen from Fig. 9, showing the dependences of the peak heights δ_{max} (curve *1*) and of the amplitudes ε_{0m} corresponding to these peaks (curve *2*) on the magnetic induction.

Thus, our experiments revealed the following.

(1) The magnetic field affects the IF and EMD both in the amplitude-independent and in the amplitude-dependent regions. In analogy with the magnetoplastic and photoacoustic effects, we will refer to the changes in the inelastic properties of crystals under the combined action of ultrasound and a magnetic field as the magnetoacoustic effect (MAE). The strongest MAE is observed for amplitudes of ultrasound corresponding to dislocation depinning from impurity centers.

(2) There exists a threshold value B_0 of magnetic induction starting from which the effect of a magnetic field on AHC unelasticity is detectable. The values of B_0 for LiF crystals with different impurity compositions differed considerably. For example, the threshold value $B_0 = 0.14$ T for LiF_{II} crystals, while $B_0 < 0.08$ T for LiF_{III} containing Ni.

An analysis of the IF and EMD data revealed that the application of a magnetic field changes the parameters characterizing the motion of dislocations: the starting stresses τ_{st}, the dislocation segment length L_N, the number N_0 of pinning points on the segment L_N, the maximum force F_m of interaction of a dislocation with a pinning center, and the binding energy U. These data are given in Tables 2–4 for LiF_I, LiF_{II}, and LiF_{III} samples, respectively.

The data describing the variation of the dislocation structure parameters in a magnetic field for the above-mentioned LiF crystals with various impurities are compared in Fig. 5.

It can be seen from Table 5 that the dislocation density ρ remained unchanged in all crystals in the ultrasound-amplitude and magnetic-induction ranges covered. Let us first compare the data for LiF_I and LiF_{II} with those for LiF_{III}. The yield stress σ_{cr} (Table 1) of LiF_{II} crystals is half the value for LiF_I and is smaller than that for LiF_{III} by a factor of 2.5. We may conclude that the LiF_{II} is the "softest" crystal. Table 5 shows that the magnetic field changes the dislocation structure parameters for LiF_{II} to the smallest extent. The values of σ_{cr} for LiF_I and LiF_{II} samples are of the same order of magnitude. However, the MAE for LiF_{III} is manifested much more clearly than that for the remaining crystals. The height of the IF peak increases considerably in the magnetic field $B = 0.08$ T, and the displacement of the peak position towards smaller amplitudes for $B = 0.08$ T exceeds the corresponding displacement for the LiF_I sample for $B = 0.3$ T. The length L_N of a dislocation loop for LiF_{III} in a magnetic field increases more than twofold (row 4 in Table 5), while the corresponding values for LiF_I and LiF_{II} increase by a factor of 1.66 and 1.15, respectively. The binding energy of an impurity center and a dislocation, as well as the starting stresses, for LiF_{III} in a magnetic field are reduced to a greater extent than for crystals free of Ni impurity (rows 7, 8 in Table 5).

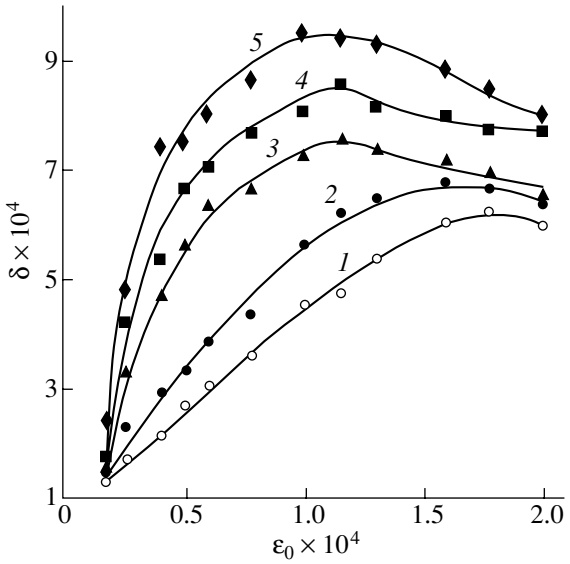

Fig. 8. Amplitude dependence of the internal friction of an LiF_I sample for various values of magnetic induction B: (*1*) 0, (*2*) 0.25, (*3*) 0.35, (*4*) 0.6, and (*5*) 0.8 T.

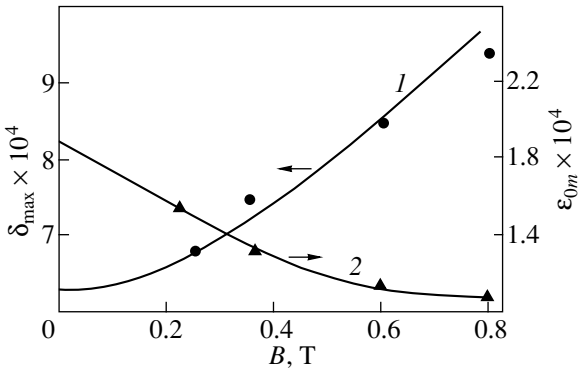

Fig. 9. (*1*) Peak heights δ_{max} and (*2*) corresponding amplitudes ε_{0m} as functions of the magnetic field for a LiF_I sample.

Table 2. Parameters of dislocation structure of LiF_I samples

Parameter	B = 0.3 T	Reference sample (B = 0)
ε_{0m}, 10^{-4}	1.0	2.1
ρ, 10^9 m^{-2}	3	3
Γ, 10^{-4}	1.61	4.92
L_N, 10^{-6} m	1.0	0.6
N_0	3	4
F_m, 10^{-10} N	5.24	6.88
U, eV	0.93	1.22
τ_{st}, MPa	0.73	1.20

Table 3. Parameters of dislocation structure of LiF_{II} samples

Parameter	B = 0.3 T	Reference sample (B = 0)
ε_{0m}, 10^{-4}	1.60	1.65
ρ, 10^9 m^{-2}	3	3
Γ, 10^{-4}	1.81	4.58
L_N, 10^{-6} m	0.45	0.39
N_0	3	7
F_m, 10^{-10} N	3.17	3.99
U, eV	0.56	0.71
τ_{st}, MPa	0.27	0.42

Table 4. Parameters of dislocation structure of LiF_{III} samples

Parameter	B = 0.08 T	Reference sample (B = 0)
ε_{0m}, 10^{-4}	1.0	2.6
ρ, 10^9 m^{-2}	1.0	1.0
Γ, 10^{-4}	2.03	3.74
L_N, 10^{-6} m	0.87	0.36
N_0	3	4
F_m, 10^{-10} N	4.39	6.62
U, eV	0.78	1.18
τ_{st}, MPa	0.63	1.10

Table 5. Variation of dislocation structure parameters of LiF crystals in a magnetic field

Parameter ratio	LiF_I(Mg), B = 0.3 T	LiF_{II}(Ca, Ba), B = 0.3 T	LiF_{III}(Mg, Ni), B = 0.08 T
$\varepsilon_{0m}(B)/\varepsilon_{0m}(0)$	0.48	0.97	0.38
$\rho(B)/\rho(0)$	1	1	1
$\Gamma(B)/\Gamma(0)$	0.33	0.40	0.54
$L_N(B)/L_N(0)$	1.66	1.15	2.40
$N_0(B)/N_0(0)$	0.75	0.43	0.75
$F_m(B)/F_m(0)$	0.76	0.79	0.66
$U(B)/U(0)$	0.76	0.79	0.66
$\tau_{st}(B)/\tau_{st}(0)$	0.61	0.64	0.57

The changes in the macroscopically measured yield stress σ_{cr} of the crystals in a magnetic field can be estimated from the data on the starting stresses τ_{st}. Indeed, σ_{cr} and τ_{st} are connected through a linear dependence [13]. Knowing the ratio $\tau_{st}(0)/\tau_{st}(B)$, we can find the variation of the yield stress under the action of a magnetic field. The results of such estimation for LiF_I and LiF_{II} crystals are given in Table 6, which also contains the results of direct measurements for LiF crystals with Mg impurity [14].

It can be seen from Table 6 that our results and the data from [14] for samples with Mg impurity are similar. The yield stresses σ_{cr} for crystals with different impurity compositions for the same values of magnetic induction vary in different manners. For example, σ_{cr} decreases in the field B = 0.48 T by a factor of 2.5 for LiF_I crystals and by a factor of 1.7 for LiF_{II} crystals.

The LiF_{III} samples containing Ni were investigated by us for B = 0, 0.04, and 0.08 T. The ratio $\sigma_{cr}(0)/\sigma_{cr}(B)$ calculated from the current–voltage characteristics was equal to unity for B = 0.04 T and to 1.88 for B = 0.08 T. A comparison of these results with the data presented in Table 6 for LiF_I shows that the critical value of B for which the yield stress starts to decrease for LiF_{III} crystals is lower than that for LiF_I crystals free of Ni. The ratio $\sigma_{cr}(0)/\sigma_{cr}(B)$ for LiF_{III} in the field B = 0.08 T is 1.3 times larger than the corresponding ratio for LiF_{II} for B = 0.3 T. The obtained results, demonstrating a

Table 6. Variation of the yield stress of LiF crystals under the action of a magnetic field

Variation of yield stress	B, T					Sample
	0.1	0.2	0.3	0.4	0.48	
$\sigma_{cr}(0)/\sigma_{cr}(B)$	1	1.3	2.07	2.6	2.7	LiF(Mg) [14]
$\tau_{st}(0)/\tau_{st}(B)$ =	–	1.44	2.2	–	2.5	LiF_I(Mg)
$\sigma_{cr}(0)/\sigma_{cr}B$	1	1.15	1.50	–	1.67	LiF_{II}(Ca, Ba)

considerable effect of Ni impurity on the yield stress of AHCs in a magnetic field, are in accord with the results of direct measurements [15].

4. CONCLUSIONS

Thus, the above results lead to the conclusion that the MAE is sensitive to the impurity composition and that the presence of Ni impurity enhances the MAE, as in the case of the magnetoplastic effect. Since the dislocation density remained unchanged upon the action of a magnetic field on a crystal, while the parameters characterizing the system of dislocations and their pinning centers varied significantly, we can conclude that the magnetic field affects the interaction of dislocations with their pinning centers, as well as the structure of the centers themselves. It was found that magnetically sensitive centers containing Ni impurity are the most sensitive to a magnetic field (have the lowest threshold value B_0) and their structure experiences the strongest changes under the action of a magnetic field. This is manifested in strong changes in the starting stresses and the binding energy of a dislocation and an impurity center in Ni-doped LiF crystals.

REFERENCES

1. N. A. Tyapunina, É. P. Belozerova, and V. L. Krasnikov, Materialovedenie, No. 12, 21 (1999).
2. N. A. Tyapunina, É. P. Belozerova, and V. L. Krasnikov, Materialovedenie, No. 2, 29 (2000).
3. N. A. Tyapunina, V. L. Krasnikov, and É. P. Belozerova, Fiz. Tverd. Tela (St. Petersburg) **41** (6), 1035 (1999) [Phys. Solid State **41**, 942 (1999)].
4. V. I. Al'shits, E. V. Darinskaya, O. L. Kazakova, *et al.*, Izv. Akad. Nauk, Ser. Fiz. **57** (11), 2 (1993).
5. S. P. Nikanorov and B. K. Kardashev, *Elasticity and Dislocation-Induced Inelasticity of Crystals* (Nauka, Moscow, 1985).
6. É. P. Belozerova, Available form VINITI, No. 5059 (1984).
7. E. K. Naimi, Available form VINITI, No. 2589 (1985).
8. N. A. Tyapunina, É. P. Belozerova, V. L. Krasnikov, and V. N. Vinogradov, Vestn. Tambov. Univ., Ser. Estestv. Tekh. Nauki **5** (3), 345 (2000).
9. N. A. Tyapunina, V. L. Krasnikov, and É. P. Belozerova, Izv. Akad. Nauk, Ser. Fiz. **64** (9), 1776 (2000).
10. A. Granato and K. Lucke, in *Ultrasonic Methods for Studying Dislocations* (Inostrannaya Literatura, Moscow, 1963), p. 27.
11. D. G. Blair, T. S. Hutchison, and D. H. Rogers, Can. J. Phys. **49** (6), 635 (1971).
12. I. T. Suprun, Phys. Status Solidi A **120**, 363 (1990).
13. N. A. Tyapunina, E. K. Naimi, and G. M. Zimenkova, *Ultrasound Action on Crystals with Defects* (Mosk. Gos. Univ., Moscow, 1999), p. 126.
14. A. A. Urusovskaya, V. I. Al'shits, A. E. Smirnov, and N. N. Bekkauer, Pis'ma Zh. Éksp. Teor. Fiz. **65** (6), 470 (1997) [JETP Lett. **65**, 497 (1997)].
15. A. A. Urusovskaya, V. I. Al'shits, A. E. Smirnov, and N. N. Bekkauer, in *Proceedings of the International Conference on Growth and Physics of Crystals, Moscow Institute of Steel and Alloys, Moscow, 1998*, p. 190.

Translated by N. Wadhwa